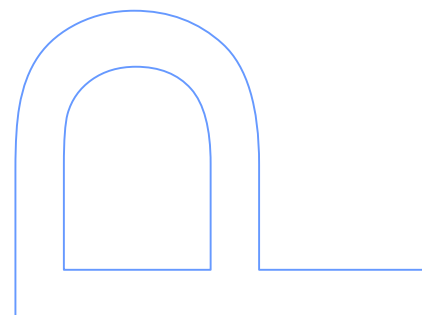
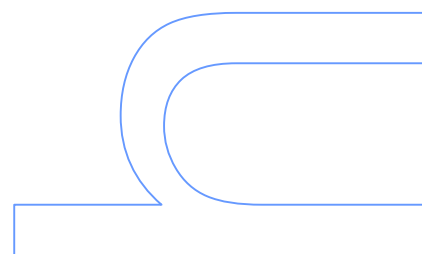
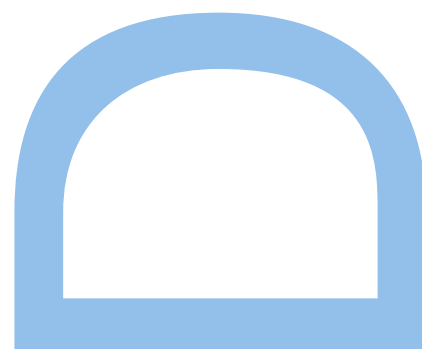


Solvation of Alcohols in Ionic Liquids

Inês Catarina Moreira Vaz
Doutoramento em Química Sustentável
Departamento de Química e Bioquímica
2020

Luís Manuel das Neves Belchior Faia dos Santos
Professor Associado com Agregação
Faculdade de Ciências da Universidade do Porto

Artur Manuel Soares da Silva
Professor Catedrático
Departamento de Química da Universidade de Aveiro



"I am among those who think that science has great beauty. A scientist in his laboratory is not only a technician: he is also a child placed before natural phenomena which impress him like a fairy tale."

Maria Skłodowska-Curie

Nobel Prize in Physics (1903) and in Chemistry (1911)

"Satisfaction of one's curiosity is one of the greatest sources of happiness in life"

Linus Pauling

Nobel Prize in Chemistry (1954) and of Peace (1962)

"I have not any special talent, I'm only passionately curious"

Einstein

Nobel Prize in Physics (1921)

To my family, for all the love and support.

Acknowledgments

Expresso aqui a minha gratidão a todos que contribuíram para a conclusão deste percurso, que não seria o mesmo sem a contribuição de todos vós.

Começo por agradecer ao Professor Luís Belchior Santos, orientador deste projeto. Muito obrigada pelo seu dinamismo, entusiasmo e pela oportunidade de ter trabalhado consigo durante os últimos anos. Agradeço todos os conhecimentos transmitidos e a transmissão da sua visão, em ciência e em tantas outras coisas. Muito obrigada por tudo professor! Foi um orgulho fazer parte do seu grupo de investigação!

Ao Professor Artur Silva, co-orientador deste projeto, agradeço a oportunidade, a confiança, a simpatia e o apoio.

À Professora Margarida Bastos agradeço a oportunidade de ter trabalhado no calorímetro de titulação, todos os conhecimentos de microcalorimetria e de solução, a disponibilidade e a simpatia durante estes anos.

Ao Senhor Carlos Torres, ao Engenheiro Francisco Carpinteiro e ao Fernando Silva agradeço a enorme ajuda, disponibilidade e prontidão. Agradeço a imensa colaboração na construção do μ FlowCal e na melhoria e criação de peças de enorme valor metodológico. Agradeço também a vossa amabilidade todos estes anos, assim como o conhecimento que me foram transmitindo. Cada ida à oficina é uma descoberta! Obrigada! Vou ter saudades.

Ao Óscar Fernandes agradeço toda a colaboração e ajuda, que foi indispensável à construção do μ FlowCal. Obrigada pela tua disponibilidade e pela enorme paciência.

À Dra. Paula, à Professora Ana Reis, ao Professor Eduardo Marques, à Professora João Sottomayor, ao Professor Jorge Gonçalves, à Professora Maria das Dores Ribeiro da Silva, ao Professor Manuel João Monte e à Professora Agostinha Matos agradeço a amabilidade, a simpatia com que me receberam no grupo de Química Física e me brindaram nos últimos anos.

À Professora Cristina Freire agradeço a exigência, a simpatia, a enorme humanidade e a oportunidade de ter feito parte do seu grupo ainda que por pouco tempo. Não tendo tido intervenção nesta tese, teve-o no meu percurso pessoal, que provavelmente teria sido muito diferente se não tivesse passado pelo seu grupo. Muito obrigada pela oportunidade e por todos os ensinamentos!

À Ana Lobo e ao Carlos Lima agradeço a pronta e indispensável ajuda ao longo destes anos. Obrigada por estarem sempre disponíveis. Agradeço-vos também a amizade e o carinho de todos os dias, as longas conversas e o vosso apoio. Obrigada!

À Ana Rodrigues, ao Nuno Branco, ao José Carlos, à Marisa Rocha, à Isabel Oliveira, à Bárbara Claro, à Bárbara Abreu, ao Carlos Silva, ao Carlos Miranda, ao Filipe Ribeiro, à Rita Almeida, à Juliana Oliveira, à Francisca, ao Ricardo Fernandes, à Sandra Silva, à Catarina, à Vera Freitas, à Ana Luísa e ao Bruno agradeço a alegria e a boa disposição. Foi um prazer partilhar o local de trabalho convosco! Em especial à Ana Rodrigues, ao Nuno Branco e ao José Carlos agradeço a amizade e o apoio. À Isabel Oliveira agradeço a companhia, a amizade, a espontaneidade e a boa disposição contagiante. À Barbara Abreu, à Barbara Claro e ao Carlos, meus colegas desde 2010, agradeço por partilharem todo este percurso comigo.

Aos meus colegas do PDQS, em especial à Carla, à Paula, ao Sarmento e ao Ricardo agradeço os bons momentos que passamos. Estes anos não teriam sido o mesmo sem vocês!

À Tânia, à Viviana, ao Vítor e à Soraia agradeço a companhia, os maravilhosos almoços e o vosso companheirismo.

Ao Departamento de Química e Bioquímica da Faculdade de Ciências da Universidade do Porto (FCUP) e ao Centro de Investigação em Química (CIQ), agradeço as condições disponibilizadas para a execução deste trabalho.

À Fundação para a Ciência e Tecnologia e ao Fundo Social Europeu, agradeço o financiamento ao Centro de Investigação em Química da Universidade do Porto (projeto estratégico PEst-C/QUI/UI0081/2013 e projeto SAM Norte-01-0145-FEDER-000028) e a concessão da bolsa de doutoramento de referência PD/BD/114575/2016.

Por fim, agradeço às pessoas mais importantes da minha vida, que estão sempre presentes e que são o motivo de conseguir alcançar os objetivos a que me proponho. Obrigada por estarem sempre presentes, pelo apoio incondicional e por acreditarem sempre em mim. As palavras não chegarão para vos agradecer por tudo.

À Sara, à Daniela e à Filipa por provarem que é verdade quando dizem que na faculdade se fazem amigos para a vida toda! Mais do que amigas, vocês são família. Obrigada!

Aos meus amigos de sempre, agradeço por terem estado sempre presentes e por serem o meu significado de amizade incondicional. Rui Moreira, Rafael Pinheiro, Tiago Sousa (Spiki), Rita Pontes e Vanessa Oliveira agradeço o vosso carinho, a amizade, as histórias partilhadas, a cumplicidade e tantas, tantas outras coisas...

À minha família: madrinha, tios, primos e avós, agradeço a permanente presença na minha vida, o apoio e incentivo constantes e o carinho sem limites. Hugo, Mãe, Pai, Marta, sem vós não teria sido possível! Nunca conseguirei agradecer o suficiente! Por isso, uma única palavra para vós: OBRIGADA!

Abstract

In this work, the solvation properties of Ionic Liquids (ILs) were explored, using alcohols as molecular probes. Different combination of alcohols and ILs were selected, exploring the ability of the hydroxyl group of the alcohol to interact with the IL by dispersive or hydrogen bond interactions, as well as, the ability of the nonpolar tail to interact with the nonpolar moieties of the IL by dispersive interactions. Due to alcohols and ILs similarities, it was considered that these studies constitute an excellent path to probe the ILs solvation characteristics.

Along this PhD project, the effects of the nature of the cation, as well as, the hydrogen bond basicity of the anion on the solvation process of alcohols in ILs were explored. In this study, it was evident the preferential location of the alcohol hydroxyl group in the polar domains of ionic liquids, interacting preferentially with basic anions. To complement this study, the effect of the alcohol acidity in the solvation of alcohols in ionic liquids was also evaluated.

To access the interactions existent in the nonpolar domains and the interplay between polar and nonpolar domains, alcohols of several alkyl chain length were solvated in ILs with different alkyl chain length. Results regarding the solvation of 1-propanol, 1-butanol and 1-pentanol were obtained before the beginning of this project. This study has evidenced the effect of nanostructuration of the ILs in the trend of the solution/solvation behaviour. During this PhD project, the solvation of bigger alcohols of this series (1-hexanol, 1-heptanol and 1-octanol) in two IL families expanded the knowledge on this topic. The results obtained in this study are in accordance with the model of the preferential location of the alcohols at both polar and nonpolar domains.

The discussion of these topics was based in results of enthalpy of solvation, derived from the enthalpy of solution. The enthalpy of solution of alcohols in ionic liquids was obtained in an Isothermal Titration Calorimeter (ITC), close to infinite dilution conditions.

The expansion of the previous solvation studies, involving the exploration of the effect of the alcohol concentration in ILs, was also part of this PhD project. In order to study the effect of the alcohol concentration, a new high precision flow microcalorimeter based in a micromixer/microreactor has been designed, constructed and tested in this PhD project, the μ FlowCal calorimeter. This microcalorimeter allowed to broad the concentration range of the previous study, as well as, the expansion of the scientific equipment of the group.

The excess molar enthalpy of an alcohol-IL binary mixture was measured in this calorimeter in a wide concentration range. Despite of the preliminary character of the obtained results, it was found a relation between the enthalpic quantities and the different structuration regimes present in the mixture.

Keywords: Ionic Liquids; molecular solutes/solvents; mixtures; solvation; molecular interactions; nanostructuration; molecular probes; microcalorimetry; ITC; methodologies.

Resumo

Neste trabalho, as propriedades de solvatação de líquidos iónicos (ILs) foram exploradas utilizando álcoois como sondas moleculares. Diferentes combinações de álcoois e ILs foram selecionadas, explorando a capacidade de interação (dispersiva ou por ponte de hidrogénio) do grupo hidroxilo do álcool com os domínios polares dos líquidos iónicos, bem como a capacidade de interação (interações dispersivas) da cadeia alquílica do álcool com os domínios não polares dos líquidos iónicos. Devido às semelhanças existentes entre os álcoois e os líquidos iónicos, considerou-se que a investigação das suas misturas constitui uma estratégia interessante para investigar as características de solvatação dos ILs.

Ao longo deste projeto de doutoramento foram explorados os efeitos da natureza do catião e da basicidade do anião no processo de solvatação de álcoois em ILs. Este estudo evidenciou a localização preferencial do grupo hidroxilo dos álcoois nos domínios polares dos líquidos iónicos, interagindo preferencialmente com aniões de características básicas. Para complementar este estudo, foi também avaliado o efeito da acidez do álcool na solvatação de líquidos iónicos.

Para explorar os domínios polares e não polares dos líquidos iónicos e a relação destes com as propriedades de solvatação dos ILs, foi explorada a solução/ solvatação de álcoois de vários comprimentos de cadeia alquílica em líquidos iónicos com diferentes comprimentos de cadeia alquílica. Os resultados referentes à solução/solvatação de 1-propanol, 1-butanol e 1-pentanol foram obtidos antes do início deste projeto. Estes resultados evidenciaram o efeito da nanoestruturação dos líquidos iónicos no comportamento da solução / solvatação dos álcoois estudados. Durante este projeto de doutoramento, este estudo foi revisitado e ampliado, tendo-se estudado a solvatação de álcoois com maior comprimento da cadeia alquílica: 1-hexanol, 1-heptanol e 1-octanol em duas famílias de líquidos iónicos. Os resultados obtidos neste estudo estão de acordo com a localização preferencial dos álcoois em ambos os domínios, polares e não polares, dos líquidos iónicos.

Estes estudos de solução / solvatação foram efetuados com base em resultados de entalpia de solvatação, derivados da entalpia de solução. A entalpia de solução foi obtida num calorímetro de titulação isotérmico (ITC), em condições experimentais próximas da diluição infinita.

O efeito da concentração do álcool nos líquidos iónicos foi também estudado no âmbito deste projeto de doutoramento. Este estudo envolveu o desenho, construção e

teste de um novo microcalorímetro de fluxo de alta precisão, o calorímetro μ FlowCal, baseado num micromisturador / microrreator. O desenvolvimento desta nova metodologia permitiu ampliar a faixa de concentração do estudo anterior, assim como, expandir os equipamentos científicos do grupo.

A entalpia molar de excesso de uma mistura binária álcool-IL foi medida no μ FlowCal numa gama ampla de concentração. Apesar do carácter preliminar dos resultados obtidos, foi encontrada uma relação entre os resultados obtidos e os diferentes regimes de estruturação presentes na mistura.

Palavras-Chave: Líquidos Iónicos; solventes/solutos moleculares; misturas; solvatação; interações moleculares; nanoestruturação; sondas moleculares; microcalorimetria; ITC; metodologias.

Table of Contents

Acknowledgments	III
Abstract	V
Resumo	VII
Table of Contents	IX
List of Tables	XVII
List of Figures	XXI
List of Symbols and Abbreviations	XXXIII
Symbols and Abbreviations associated to Physical Properties and Constants	XXXIII
Ionic Liquids Abbreviation Nomenclature	XXXVII
Alcohols Abbreviation Nomenclature	XXXVIII
Others	XXXIX
Units, Conversion Factors and Constants	XLI
Organization of the Thesis	XLIII
 Chapter 1 – Introduction	 1
1.1. State of Art	6
1.1.1. Structural Organization of Ionic Liquids	6
1.1.2. Intermolecular Interactions in Ionic Liquids	10
1.1.3. Characterization of the Polarity of Ionic Liquids	14
1.1.4. Solvation in Ionic Liquids	21
1.1.4.1. Liquid – Liquid Equilibria	22

1.1.4.2. Structuration of Mixtures	25
1.1.4.3. Dynamics and Transport Properties	30
1.1.4.4. Excess Volume	33
1.1.4.5. Enthalpic Properties of Mixing	37
1.2. Concepts on the Enthalpic Properties of Mixing	42
1.2.1. Solvation	42
Cavitation	43
Solute-solvent Interaction	45
1.2.2. Solution	45
1.2.3. Excess Enthalpy of Mixing	48
1.2.4. Partial Excess Enthalpy of Mixing	51
1.2.5. Redlich-Kister Equations	52
1.2.6. Relevance of the Enthalpic Properties of Mixing	53
1.3. Aim and Strategy	55
1.3.1. Motivation and Aim	55
1.3.2. Strategy	57
References	59
 Chapter 2 – Materials and Sample Preparation	 67
2.1. Compounds Studied	69
2.2. Purification of Alcohols and Ionic Liquids	75
2.2.1. Purification of Ionic Liquids	75
2.2.2. Purification of Molecular Solutes	77
2.3. Sample Handling	78
2.4. Additional Materials	78
References	80

Chapter 3 – Experimental Methodologies **81**

Calorimetry

3.1. Concepts in Calorimetry	83
3.1.1. Heat Transfer	84
3.1.1.1. Heat Transfer by Radiation	84
3.1.1.2. Heat Transfer by Conduction	85
3.1.1.3. Heat Transfer by Convection	86
3.1.2. Principle of Heat Measurement	86
3.1.2.1. Heat Accumulation Calorimeters	87
3.1.2.2. Heat Compensation Calorimeters	90
3.1.2.3. Heat Conduction/Flow Calorimeters	91
The Twin Design	94
3.1.3. Measurement of Heat	95
3.1.3.1. Seebeck Effect and Heat Flow Sensor	95
3.1.3.2. Fraction of Heat Measured - Sensitivity	100
3.1.3.3. Heat Flow Signal	102
3.1.4. Other concepts	104
3.1.4.1. Closed or Open Calorimetry	105
3.1.4.2. Batch or Flow Calorimetry	106
3.1.4.3. Scanning or Isothermal Calorimetry	107
3.2. Experimental Methodologies	108
3.2.1. <i>DropCalvet</i> – Drop Type Calvet Calorimetry	108
3.2.1.1. The <i>DropCalvet</i> Calorimeter	109
3.2.1.2. Calorimetric Cells	110
3.2.1.3. Heat of Vaporization Measurement	111
3.2.1.4. Summary of the Measurements	113

3.2.2. ITC – Isothermal Titration Calorimetry	114
3.2.2.1. The Calorimetric Channel	116
3.2.2.2. The Insertion Vessel	120
3.2.2.3. Multichannel Thermostat System	121
3.2.2.4. Injection System	122
3.2.2.5. Data Acquisition and System Control	122
3.2.2.6. Calorimetric Data Analysis	123
3.2.2.7. Summary of the Experimental Procedure	125
3.2.3. μ FlowCal – Isothermal Micromixer Calorimetry	128
3.2.3.1. The Working Principle	128
3.2.3.2. The Micromixer	130
3.2.3.3. Calorimeter Design	132
3.2.3.4. Calorimeter Thermostatization	136
3.2.3.5. The Flow System	139
3.2.3.6. The Fluid Thermostatization	144
3.2.3.7. Nitrogen Line	146
3.2.3.8. Heat Flow Signals	146
3.2.3.9. Customized Software	151
3.2.3.10. Summary of the Experimental Procedure	152
3.3. Calibration and Test of the Calorimetric Systems	153
3.3.1. Calibration of <i>DropCalvet</i>	154
3.3.2. Electrical Calibration of ITC and μ FlowCal	155
3.3.2.1. Calibration of ITC	158
Insertion Heaters	158
Electrical Circuit	159
Thermal Power, Time and Energy Effect	160
Comment on the Calibration Results	162

3.3.2.2. Calibration of μ FlowCal Prototype Calorimeter	163
Built-in Heaters	163
Electrical Circuit	164
Summary of the Experiments	165
Thermal Power Effect	169
Energy Effect	171
Time Effect	172
Comment on the Calibration Results	173
3.3.3. Chemical Calibration of μ FlowCal with a Mixing Process	174
3.3.4. Performance and Accuracy Test of ITC	178
3.3.5. Performance and Accuracy Test of μ FlowCal	182
3.3.5.1. Dilution of Aqueous Sucrose Solutions	182
Dependence on the Injected Volume	183
Dependence on the Magnitude of the Flow	187
Dependence on the Flow Effect & Viscosity of the Fluid	188
Comment on the Obtained Results	193
3.3.5.2. Binary Mixtures Decane-Octanol	194
3.3.5.3. Comments on the Test Results	198
References	199

Chapter 4 – Results and Discussion **201**

Solvation of Alcohols in Ionic Liquids

4.1. Study of the Anion and Cation Effect on the Solvation of Alcohols in Ionic Liquids	204
4.1.1. Strategy	204

4.1.2. Results and Discussion	207
4.1.2.1. Effect of the Cation Nature	208
4.1.2.2. Effect of the IL Anion Nature	212
4.2. Exploration of the Fluorination / Acidity Effect of the Alcohol in Ionic Liquids	221
4.2.1. Strategy	222
4.2.2. Results and Discussion	224
4.3. The Effect of the Alkyl Chain Length on the Solvation of Alcohols in Ionic Liquids	237
4.3.1. Strategy	238
4.3.2. Results and Discussion	239
4.4. Enthalpy of Mixing of a Binary Mixture of Alcohol – IL	252
4.4.1. Experimental Methodology	253
4.4.2. Results and Discussion	254
4.4.2.1. Comparison with other Binary Mixtures	257
4.4.2.2. Structuration and Energetics of the BuOH + [C ₆ C ₁ im][NTf ₂] Mixture	266
References	273
Chapter 5 – Conclusions and Achievements	279
5.1. Overview	281
5.1.1. New Experimental Methodologies	281
5.1.2. Solvation of Alcohols in Ionic Liquids	284
At Infinite Dilution	284
At the Full Concentration Range	285

5.2. Contribution and Relevance	286
Preferential Solvation in ILs	286
μ FlowCal and the Study of Mixtures	287
5.3. Still to be done	288
Solvation of Alcohols in Ionic Liquids at Infinite Dilution	288
μ FlowCal and the Study of Mixtures	289
References	290
Appendix	291
Appendix A	293
A.1. Thermostatization of μ FlowCal Calorimeter	293
A.2. Determination of the Time Constant of μ FlowCal Calorimeter	299
Appendix B	303
B.1. Data Acquisition Software of μ FlowCal Calorimeter	303
B.2. Data Treatment Software of μ FlowCal Calorimeter	306
B.3. Temperature Monitor Software of μ FlowCal Calorimeter	310
Appendix C	315
C.1. Quantum Chemical Calculation of Propanol-Anion Interaction	315
C.2. Quantum Chemical Calculation of Alcohol-[NTf ₂] Interaction	316
C.3. Quantum Chemical Calculation of Alcohol-Alcohol and Alcohol-Alkane Interaction	318
Appendix D	319
D.1. Redlich-Kister Fittings of the Mixture BuOH and [C ₆ C ₁ im][NTf ₂]	319
Appendix E	331
E.1. Cost Evaluation of μ FlowCal Calorimeter Prototype	331
References	334

List of Tables

Chapter 1 – Introduction

Table 1.1. Summary of the literature data concerning the dielectric constant, the $E_T^N(30)$ scale, the hydrogen bond acidity, the hydrogen bond basicity and the dipolarity/polarizability obtained experimentally, as well as, the hydrogen bond basicity and acidity predicted by COSMO-RS.	19
Table 1.2. Summary of the miscibility of binary mixtures constituted by $[C_nC_{1m}][\text{Anion}]$ and linear alcohols, at 298.15 K.	24

Chapter 2 – Materials and Sample Preparation

Table 2.1. Summary of the ionic liquids used in this work.	69
Table 2.2. Summary of the alcohols used in this work.	70
Table 2.3. Summary of the ionic liquids studied in this thesis.	71
Table 2.4. Summary of the alcohols studied in this thesis.	74
Table 2.5. Summary of the calibrants and test compounds used in calibration / performance tests and the techniques where they were used.	79

Chapter 3 – Experimental Methodologies... *Calorimetry*

Table 3.1. List of the alcohols studied in <i>DropCalvet</i> calorimeter.	114
Table 3.2. List of the systems ionic liquid + alcohol studied, at the infinite dilution of the alcohol, by isothermal titration calorimetry, in the context of this thesis.	126
Table 3.3. List of the systems ionic liquid + alcohol studied, at the infinite dilution of the alcohol, by isothermal titration calorimetry, before the beginning of the work that had conducted to this thesis, and of the experimentalist that have performed the measurements.	127
Table 3.4. Volume of the tubing and other parts that constitute the flow system of the $\mu\text{FlowCal}$.	142
Table 3.5. Summary of the nomenclature, the average of the results obtained for the calibration constant and the conditions associated to the electrical calibrations performed in ITC.	161
Table 3.6. Summary of the nomenclature, the average of the results obtained for the calibration constant and the conditions associated to the electrical calibrations performed in the sample side of $\mu\text{FlowCal}$.	167

Table 3.7. Summary of the nomenclature, the average of the results obtained for the calibration constant and the conditions associated to the electrical calibrations performed in the reference side of μ FlowCal.	168
Table 3.8. Summary of the experimental sensitivity and constant of calibration of μ FlowCal determined by electrical calibration and chemical calibration.	177
Table 3.9. Summary of the standard molar enthalpy of solution, at infinite dilution, of propanol in water, at 298 K, reported in the literature and obtained experimentally in ITC, in the context of this thesis.	180
Table 3.10. Summary of the details associated with the study of the flow effect on the experiments of dilution of aqueous sucrose solution, performed in μ FlowCal calorimeter.	189
Table 3.11. Summary of the details associated to the concentration and viscosity of the aqueous sucrose solutions before dilution experiments.	190

Chapter 4 – Results and Discussion... *Solvation of Alcohols in Ionic Liquids*

Table 4.1. Summary of the standard molar enthalpy of solution and solvation, at infinite dilution, of ProOH in ILs constituted by different cations and anions, at the reference temperature ($T = 298.15$ K), obtained experimentally in ITC, and comparison with correspondent data reported in the literature.	207
Table 4.2. Summary of the standard molar enthalpy of solution and solvation, at infinite dilution, of different alcohols in $[C_4C_1im][NTf_2]$ ionic liquid, at the reference temperature ($T = 298.15$ K).	224
Table 4.3. Summary of the standard molar enthalpy of vaporization, at the reference temperature ($T = 298.15$ K), obtained experimentally in <i>DropCalvet</i> , in the context of this work, and reported in literature by other authors.	225
Table 4.4. Summary of the standard molar enthalpy of solution, at infinite dilution, of alcohols of different alkyl chain length in $[C_NC_1im][NTf_2]$ IL series, at the reference temperature ($T = 298.15$ K), obtained experimentally in ITC.	239
Table 4.5. Summary of the standard molar enthalpy of solution and solvation, at infinite dilution, of alcohols of different alkyl chain length in $[C_NC_1im][PF_6]$ IL series, at the reference temperature ($T = 298.15$ K), obtained experimentally in ITC.	240
Table 4.6. Summary of the standard molar enthalpy of solvation, at infinite dilution, of alcohols of different alkyl chain length in $[C_NC_1im][NTf_2]$ IL series, at the reference temperature ($T = 298.15$ K).	240
Table 4.7. Comparison of standard molar enthalpy of solution, at infinite dilution, of alcohols in $[C_NC_1im][NTf_2]$ IL series obtained experimentally in ITC, at the reference temperature ($T = 298.15$ K), with literature data.	241
Table 4.8. Comparison of standard molar enthalpy of solution, at infinite dilution, of alcohols in $[C_NC_1im][PF_6]$ IL series obtained experimentally in ITC, at the reference temperature ($T = 298.15$ K), with literature data.	242
Table 4.9. Summary of the excess molar enthalpy of the binary mixture BuOH + $[C_6C_1im][NTf_2]$, determined experimentally in μ FlowCal, at the reference temperature ($T = 298.15$ K), and of the correspondent BuOH molar fraction.	255

Table 4.10. Summary of the increasing/decreasing rates of each regime, in the partial molar excess enthalpy of BuOH and [C ₆ C ₁ im][NTf ₂], in relation to the molar fraction and volume fraction of the alcohol.	269
---	-----

Chapter 5 – Conclusions and Achievements

Table 5.1. Summary of the specifications of μ FlowCal prototype calorimeter.	283
---	-----

Appendix

Table C.1. Results of the quantum chemical calculations regarding the structure and orientation of the propanol-anion pair, as well as, the energy of interaction established in the gas phase.	315
Table C.2. Results of the quantum chemical calculations regarding the structure and orientation of the BuOH-[NTf ₂] pair (and BuOH derivatives), as well as, the energy of interaction established in the gas phase.	316
Table C.3. Results of the quantum chemical calculations regarding the structure and orientation of the ProOH-[NTf ₂] pair (and ProOH derivatives), as well as, the energy of interaction established in the gas phase.	317
Table C.4. Results of the quantum chemical calculations regarding the structure and orientation of the propanol-propanol and propanol – propane, as well as, the energy of interaction established in the gas phase.	318
Table D.1. Summary of the parameters used in the fitting of the experimental data with the Redlich-Kister equation using two parameters.	320
Table D.2. Comparison of the excess molar enthalpy obtained with the fitting of the experimental data with the Redlich-Kister equation using two parameters.	320
Table D.3. Summary of the parameters used in the fitting of the experimental data with the Redlich-Kister equation using three parameters.	321
Table D.4. Comparison of the excess molar enthalpy obtained with the fitting of the experimental data with the Redlich-Kister equation using three parameters.	321
Table D.5. Summary of the parameters used in the fitting of the experimental data with the Redlich-Kister equation using four parameters.	322
Table D.6. Comparison of the excess molar enthalpy obtained with the fitting of the experimental data with the Redlich-Kister equation using four parameters.	322
Table D.7. Summary of the parameters used in the fitting of the experimental data with the Redlich-Kister equation using five parameters.	323
Table D.8. Comparison of the excess molar enthalpy obtained with the fitting of the experimental data with the Redlich-Kister equation using five parameters.	323

Table D.9. Summary of the parameters used in the fitting of the experimental data with the Redlich-Kister equation using six parameters.	324
Table D.10. Comparison of the excess molar enthalpy obtained with the fitting of the experimental data with the Redlich-Kister equation using six parameters.	324
Table D.11. Summary of the parameters used in the fitting of the experimental data with the Redlich-Kister equation using seven parameters.	325
Table D.12. Comparison of the excess molar enthalpy obtained with the fitting of the experimental data with the Redlich-Kister equation using seven parameters.	325
Table E.1. Summary of the cost of the instrumentation.	331
Table E.2. Summary of the cost of the materials used in the injection system.	331
Table E.3. Summary of the cost of the materials and parts used in the construction.	332
Table E.4. Summary of the cost of the parts and instrumentation used in the temperature control.	333
Table E.5. Summary of the cost of the workforce involved in the design, construction and test.	333
Table E.6. Summary of the cost of the development of the μ FlowCal calorimeter prototype.	333

List of Figures

Chapter 1 – Introduction

Figure 1.1. Chemical structure of the common cations and anions that constitute the ionic liquids.	3
Figure 1.2. Schematic representation of the nanostructuration of the ionic liquids.	7
Figure 1.3. Schematic representation of the sphere of influence of the polar network and therefore of the critical alkyl size.	9
Figure 1.4. Schematic diagram of the interaction potentials present in the ionic liquids as a function of the cation alkyl chain size.	10
Figure 1.5. Schematic representation of the structure of the $[C_4C_1im]$ cation and the sites available for hydrogen bond interaction with a hypothetical anion.	11
Figure 1.6. Schematic representation of the spatial isodensity surface of the $[NTf_2]$ anion around the $[C_4C_1im]$ cation.	12
Figure 1.7. Molecular structure of the Reichardt's solvatochromic dye: betaine no. 30 (2,6-diphenyl-4-(2,4,6-triphenylpyridinium-1-yl)phenolate).	16
Figure 1.8. Molecular structure of the solvatochromic probes used to determine the Kamlet-Taft parameters α and π^* : 4-nitroaniline and N,N-diethyl-4-nitroaniline.	21
Figure 1.9. Scheme containing snapshots of simulation boxes of binary mixtures of $[C_4C_1im][NTf_2]$ with propanol and butanol.	27
Figure 1.10. Scheme containing snapshots of simulation boxes of binary mixtures of $[C_NC_1im][NTf_2]$ (N = 2, 4, 6, 8) with 1-butanol and 1-dodecanol with a ratio of 5:1 (IL : ROH).	29
Figure 1.11. Schematic representation of the dependence of the electrical conductivity of a binary mixture constituted by an IL and an alcohol upon the composition of the mixture.	31
Figure 1.12. Excess molar volume of binary mixtures constituted by linear alcohols (from 1-methanol to 1-pentanol) and $[C_NC_1im][NTf_2]$ ionic liquids (N = 3, 6 and 8) as a function of the molar fraction of alcohol.	34
Figure 1.13. Excess molar volume of binary mixtures constituted by ethanol / propanol and ionic liquids composed by different cations ($[C_3C_1im][NTf_2]$, $[C_3C_1pyrr][NTf_2]$, $[C_4C_1pyrr][NTf_2]$ and $[C_4C_1py][NTf_2]$) as a function of the molar fraction of alcohol.	35
Figure 1.14. Excess molar volume of binary mixtures constituted by linear alcohols (methanol, ethanol and propanol) and imidazolium-based ILs with different anions ($[NTf_2]$, $[BF_4]$ and Cl) as a function of the molar fraction of alcohol.	36
Figure 1.15. Excess molar enthalpy of mixing at equimolar composition of binary mixtures constituted by linear alcohols and ionic liquids composed by different cations and anions. The excess molar enthalpy of the mixture is represented as a function of the number of carbons in alcohol's alkyl chain, N_{ROH} .	38

Figure 1.16. Enthalpy of solution at infinite dilution of alcohols in ionic liquids as a function of the number of carbons in the alkyl chain of the alcohol, N_{ROH} .	40
Figure 1.17. Schematic diagram of the solvation process and its dissection in two hypothetical steps: cavitation of the solvent and establishment of solute-solvent interactions.	43
Figure 1.18. Schematic diagram of the solution process and its dissection in two hypothetical steps: vaporization of the solute and its solvation.	46
Figure 1.19. Schematic diagram of the contribution of the three hypothetical steps for the endothermic / exothermic enthalpy of solution and solvation.	47
Figure 1.20. Schematic diagram of the excess molar enthalpy of mixing of a binary mixture. The diagrams correspondent to a hypothetical ideal, endothermic or exothermic mixture are presented, as well as, a simplistic scheme on the endothermic contribution of the breakage of the intermolecular interactions of the pure components and the exothermic contribution of the establishment of component 1 – component 2 intermolecular interactions to the final endothermic / exothermic enthalpy.	50
Figure 1.21. Schematic illustration of the use of alcohols as molecular probes in ionic liquids.	56
Figure 1.22. Schematic illustration of the strategy used to study the solvation of alcohols in ionic liquids.	58

Chapter 2 – Materials and Sample Preparation

Figure 2.1. Schematic representation of the <i>Schlenk</i> flask and of the drying/degassing tube.	75
Figure 2.2. Figure of the temperature-controlled aluminium blocks of the drying system.	76
Figure 2.3. Figure of the degassing and drying system of molecular solutes that will be used in μ FlowCal calorimeter and of the laboratory bottle of 10 mL with specially modified GL25 DURAN® cap.	77

Chapter 3 – Experimental Methodologies...Calorimetry

Figure 3.1. Schematic representation of a simplistic model of the heat flow in a calorimeter.	87
Figure 3.2. Schematic representation of a section through an adiabatic calorimeter.	88
Figure 3.3. Schematic curves of the temperature variation in the system along time in an ideal adiabatic calorimeter and in a semi-adiabatic calorimeter.	89
Figure 3.4. Schematic representation of a section through a heat / power compensation calorimeter.	91
Figure 3.5. Schematic representation of a section through a heat conduction / flow calorimeter.	92
Figure 3.6. Schematic representation of heat transfer from the sample to the heat sink, through heat flow sensors, in a heat flow calorimeter.	93
Figure 3.7. Schematic representation of a differential (isothermal) heat flow calorimeter.	94

Figure 3.8. Schematic representation of a thermoelectric couple – Seebeck effect.	96
Figure 3.9. Schematic representation of a thermoelectric couple and a thermopile constituted by metals and semiconductors.	97
Figure 3.10. Schematic representation of two calorimeters, which heat flow sensors are based in thermopiles made from metallic conductor couples and semiconductor materials.	99
Figure 3.11. Schematic curves of potential-time, $U = f(t)$, in a heat flow calorimeter.	102
Figure 3.12. Schematic representation of the Calvet type calorimeter SETARAM (model HT1000D).	109
Figure 3.13. Schematic representation of the Calvet-Tian drop method assembly constituted by a HT1000D SETARAM calorimeter and a vacuum line.	110
Figure 3.14. Schematic representation of the top of the calorimetric cell with the tunnelling tube and the bottom of the calorimetric cell with the Pyrex® glass tube and the Kanthal® hollow cylinder.	111
Figure 3.15. Schematic representation of the typical “heat flow over time” obtained in a vaporization experiment in DropCalvet calorimeter.	112
Figure 3.16. Thermochemical cycle which describes the determination of the molar enthalpy of vaporization, at 298 K, in a vaporization experiment, in the DropCalvet calorimeter.	113
Figure 3.17. Schematic representation of the ITC calorimeter and its working principle.	115
Figure 3.18. Schematic representation of the ITC calorimetric system.	116
Figure 3.19. Schematic representation of the calorimetric channel on three dimensions and of a horizontal and vertical cut, in the calorimetric section, in two dimensions.	117
Figure 3.20. Schematic representation of a vertical cut of the calorimetric channel with the insertion vessel.	119
Figure 3.21. Real and schematic picture of the titration insertion vessel used.	120
Figure 3.22. Picture of the screen with the software LABTERMO during an experiment of ITC.	123
Figure 3.23. Typical data set of an ITC experiment.	124
Figure 3.24. Data representation of a typical ITC experiment. Representation of the calorimetric data as obtained $U = f(t)$ and after smoothing the data and correction to the time constant of the calorimeter.	125
Figure 3.25. Schematic representation of the working principle of μ FlowCal.	128
Figure 3.26. Schematic representation of the μ FlowCal calorimetric principle.	129
Figure 3.27. Schematic representation and picture of the borosilicate glass microreactor/micromixer (model LTF-MX of the MR-Lab Series of the Little Things Factory) of 200 mm ³ (μ L).	130
Figure 3.28. Schematic representation in three dimensions and a real picture of the calorimetric core, with discrimination of its constitution: the reactor, the aluminium blocks, the Peltier sensors and the aligner.	133
Figure 3.29. Schematic drawing of the top/bottom and front views of the calorimeter core.	133
Figure 3.30. Schematic representation and real picture of the calorimetric core enclosed by aluminium blocks.	134

Figure 3.31. Picture of the assembling of the calorimetric core in the heat sink and schematic representation of the final calorimetric assembly (reactor, heat flow sensors and heat sink).	134
Figure 3.32. Lateral view of the schematic representation of the calorimetric assembly (reactor, heat flow sensors and heat sink).	135
Figure 3.33. Upper view of the schematic representation of the calorimetric assembly (reactor, heat flow sensors and heat sink).	135
Figure 3.34. Down view of the schematic representation of the calorimetric assembly (reactor, heat flow sensors and heat sink).	135
Figure 3.35. Front and back view of the schematic representation of the calorimetric assembly (reactor, heat flow sensors and heat sink).	136
Figure 3.36. Photograph of the interior of the aluminium box with six PVC spacer support parts without the calorimetric assembly and with the calorimetric assembly.	137
Figure 3.37. Photograph of the exterior of the aluminium box with the copper plate heat exchangers.	137
Figure 3.38. Photograph of the upper view of the structure (open) that contains the calorimeter.	138
Figure 3.39. Schematic representation of the flow system of the apparatus.	139
Figure 3.40. Schematic representation of the flangeless 1/4 inch-28 tube end fittings with collapsible ferrules and stainless steel reducing unions 1/4 inch-28 to 10-32 with a bore of 0.030 inch.	141
Figure 3.41. Schematic representation of the steel tube inserted inside the micromixer.	141
Figure 3.42. Picture of the monitor with the software “Nemesys User Interface” provided by CETONI working in “Direct Mode”.	143
Figure 3.43. Picture of the monitor with the software “Nemesys User Interface” provided by CETONI working in “Flow Profile Mode”.	143
Figure 3.44. Schematic representation and real picture of the system used to thermostate the syringes and sewer of the μ FlowCal.	144
Figure 3.45. Picture of the external face of the aluminium blocks that constitute part of the heat sink of the μ FlowCal.	145
Figure 3.46. Picture of the thermal anchoring region of the flow system in the heat sink.	146
Figure 3.47. Scheme of the localization of the Peltier elements towards the micromixer and illustration of the location, in the calorimeter, of the origin of the calorimetric output “signal 1” and “signal 2” of μ FlowCal.	147
Figure 3.48. Scheme of the heat transfer that originates the signal 1 and signal 2 of μ FlowCal.	148
Figure 3.49. Graphical representation of the calorimetric output data “signal 1”, “signal 2” and its sum “signal 1+2”.	149
Figure 3.50. Graphical representation of the calorimetric output data “signal 1”, “signal 2” and its sum “signal 1+2” as obtained from μ FlowCal and of the calorimetric output “signal 1”, “signal 2” and its sum “signal 1+2” corrected to the thermal inertia of the calorimeter.	150

Figure 3.51. Schematic representation of a constant thermal power dissipated by the electrical heater and the perturbation, caused by the thermal power dissipated, on the heat flow signal of the calorimeter.	157
Figure 3.52. Picture of the interior the calorimetric vessel, equipped with the electrical heater and the Teflon® propeller, and schematic representation of the electrical heater developed.	158
Figure 3.53. Representation of the electrical circuit used in the experiments of electrical calibration of ITC.	159
Figure 3.54. Graphical representation of the typical heat flow signal obtained, before and after dynamic correction for the time constant of the calorimeter, as a function of the experimental time, in the electrical calibration experiments, generically denominated as "A", "B", "C" and "D".	160
Figure 3.55. Chronological graphical representation of the calibration constant. The calibration constant obtained in each experiment is plotted in its chronological order.	161
Figure 3.56. Picture of the calibration heaters of μ FlowCal before and after insertion in the aluminium blocks.	164
Figure 3.57. Representation of the electrical circuit used in the experiments of electrical calibration of μ FlowCal.	165
Figure 3.58. Schematic representation of the electrical calibration experiments performed in μ FlowCal.	166
Figure 3.59. Graphical representation of the average calibration constant, obtained in each set of experiments, as a function of the thermal power, dissipated (in average) by the built-in heaters.	169
Figure 3.60. Graphical representation of the uncertainty of the calibration constant, obtained in each experimental set, at a confidence level of 95%, as a function of the thermal power level used in the experiments.	170
Figure 3.61. Graphical representation of the average calibration constant, obtained in each set of experiments, as a function of the total thermal energy dissipated (in average) by the built-in heaters.	171
Figure 3.62. Graphical representation of the uncertainty of the calibration constant, obtained in each experimental set, at a confidence level of 95%, as a function of the total thermal energy dissipated (in average) by the built-in heaters.	172
Figure 3.63. Graphical representation of the average calibration constant, obtained in each set of experiments, as a function of the thermal power dissipated (in average) by the built-in heaters.	173
Figure 3.64. Graphical representation of the area of the peaks associated to the injection of 1-octanol and n-decane, at equimolar composition, in μ FlowCal prototype calorimeter.	176
Figure 3.65. Graphical representation of the typical heat flow signal, obtained in an ITC experiment, consisting in the stepwise injection of PrOH in water.	178
Figure 3.66. Graphical representation of the partial molar excess enthalpy of 1-propanol, obtained experimentally, and of the data existent in the literature, as a function of the molar fraction of 1-propanol.	179
Figure 3.67. Graphical representation of the enthalpy of dilution of an aqueous sucrose solution, from 1.0 mol·kg ⁻¹ to 0.1 mol·kg ⁻¹ , obtained in μ FlowCal calorimeter, with a total flow of 2.45 mm ³ ·s ⁻¹ (μL·s ⁻¹), as a function of the volume injected into the micromixer. Together with this representation, it is presented the proportion of volume injected into the reactor and the heat involved in each experiment.	184

Figure 3.68. Graphical representation of the enthalpy of dilution of aqueous sucrose solution, from 1.0 mol·kg ⁻¹ to 0.1 mol·kg ⁻¹ , obtained in μ FlowCal calorimeter, with a total flow of 10.00 mm ³ ·s ⁻¹ (μ L·s ⁻¹), as a function of the volume injected into the micromixer. Together with this representation, it is presented the proportion of volume injected into the reactor and the heat involved in each experiment.	185
Figure 3.69. Graphical representation of the enthalpy of dilution of aqueous sucrose solution, from 1.0 mol·kg ⁻¹ to 0.1 mol·kg ⁻¹ , obtained in μ FlowCal calorimeter, with a total injection volume of 200 mm ³ (μ L), in the chronological order of the experiments performed.	188
Figure 3.70. Graphical representation of the relative deviation of the average of the enthalpy of dilution of aqueous sucrose solution, obtained in μ FlowCal calorimeter, as a function of the fluid flow used in the experiments.	191
Figure 3.71. Graphical representation of the relative deviation of the average of the enthalpy of dilution of aqueous sucrose solution, obtained in μ FlowCal calorimeter, as a function of the fluid flow used in the experiments.	192
Figure 3.72. Graphical representation of the methodology II used in μ FlowCal calorimeter, to measure the heat of mixing of the binary mixture decane-octanol.	195
Figure 3.73. Graphical representation of the area of integration of peaks originated by mixtures decane-octanol, at equimolar composition, performed using the two different experimental methodologies (I and II).	196
Figure 3.74. Graphical representation of the excess molar enthalpy, obtained in μ FlowCal calorimeter, as a function of the molar fraction of octanol.	197

Chapter 4 – Results and Discussion... *Solvation of Alcohols in Ionic Liquids*

Figure 4.1. Schematic representation of the strategy used in this thesis to study the solvation of alcohols in ionic liquids.	203
Figure 4.2. Scheme of the strategy used to evaluate the effect of the basicity of the anion and the nature of the cation in the solution / solvation of alcohols in ionic liquids.	205
Figure 4.3. Scheme of the pair alcohol-anion (PrOH-DCA) in the gas phase, which interaction energy was evaluated by quantum chemical calculations.	206
Figure 4.4. Graphical representation of the standard molar enthalpy of solvation, at infinite dilution, of PrOH in different ionic liquids, at the reference temperature ($T = 298.15$ K), as a function of the IL cation.	209
Figure 4.5. Graphical representation of the standard molar enthalpy of solvation, at infinite dilution, of PrOH in [cation][NTf ₂] ionic liquid series, at the reference temperature ($T = 298.15$ K), as a function of the hydrogen bond acidity of the ionic liquids.	211
Figure 4.6. Graphical representation of the standard molar enthalpy of solvation, at infinite dilution, of PrOH in [C ₄ C ₁ im][Anion] ionic liquid series, at the reference temperature ($T = 298.15$ K), as a function of the IL anion.	213

- Figure 4.7.** Graphical representation of the standard molar enthalpy of solvation, at infinite dilution, of PrOH in $[C_4C_1im][Anion]$ ILs, at the reference temperature ($T = 298.15$ K), as a function of the hydrogen-bond interaction energy in an equimolar cation–anion mixture (obtained by COSMO-RS), and Kamlet–Taft β parameters obtained with N,N-diethyl-4-nitroaniline and 4-nitroaniline solvatochromic dyes. 214
- Figure 4.8.** Graphical representation of the standard molar enthalpy of solvation, at infinite dilution, of PrOH in $[C_4C_1im][Anion]$ ILs, at the reference temperature ($T = 298.15$ K), as a function of the energy of interaction between the alcohol and the anion in the gas phase. 215
- Figure 4.9.** (I) Graphical representation of the standard molar enthalpy of solvation, at infinite dilution, of PrOH in ILs of the series $[C_4C_1im][Anion]$, obtained experimentally, against the same values obtained by MD simulations. (II) Plot of the histogram analysis of the 576 values of the standard molar enthalpy of solvation, at infinite dilution, of PrOH in $[C_4C_1im][TfA]$, obtained by MD simulations. 217
- Figure 4.10.** Radial distribution functions, RDFs: a) between the centre of charge of the cation and the hydrogen atom of the hydroxyl group of PrOH; b) between the hydrogen atom of the hydroxyl group of PrOH and the most electronegative atoms in the anions; c) superposition of the solute–cation and solute–anion RDFs for $[C_4C_1im][NTf_2]$; d) between the most acidic hydrogen atom in the imidazolium ring (HR) and the oxygen atom of the solute. 219
- Figure 4.11.** Plot of the number of cations/anions surrounding the hydrogen atom of the hydroxyl group of 1-propanol, against the standard molar enthalpy of solvation, at infinite dilution, obtained experimentally. 220
- Figure 4.12.** Scheme of the solution of BuOH, *t*-BuOH and PrOH in ionic liquids, highlighting the number of groups accessible for intermolecular interactions: 4 in BuOH, 3 in *t*-BuOH and PrOH. 222
- Figure 4.13.** Scheme of the strategy used to determine the effect of the acidity of the alcohol (by fluorination) in the solution / solvation of alcohols in ionic liquids. 223
- Figure 4.14.** Plot of the standard molar enthalpy of solution, at infinite dilution, of different alcohols in $[C_4C_1im][NTf_2]$, obtained experimentally by ITC, at the reference temperature ($T = 298.15$ K), as a function of the number of fluorinated groups “>CF₃” / “-CF₂” of the alcohol. 226
- Figure 4.15.** Plot of the standard molar enthalpy of solvation, at infinite dilution, of different in $[C_4C_1im][NTf_2]$, obtained experimentally by ITC, at the reference temperature ($T = 298.15$ K), as a function of the number of fluorinated groups “>CF₃” / “-CF₂” of the alcohol. 227
- Figure 4.16.** (I) Plot of the binding energy of the electron (1s) of the oxygen atom of the alcohol against the level of fluorination of the alcohols (number of “>CF₂” / “-CF₃” groups of the alcohol). (II) Plot of the enthalpy of solvation, at infinite dilution, of *tert*-butyl-alcohol with different degrees of fluorination in $[C_4C_1im][NTf_2]$, against the electron (1s) binding energy of the oxygen atom. 228
- Figure 4.17.** (I) Plot of the acidity of the alcohol (pKa) against the level of fluorination of the alcohols (number of “>CF₂” / “-CF₃” groups of the alcohol). (II) Plot of the enthalpy of solvation, at infinite dilution, of *tert*-butanol with different degrees of fluorination in $[C_4C_1im][NTf_2]$, against the acidity of the alcohols (pKa). 229
- Figure 4.18.** Plot of the standard molar enthalpy of solvation at infinite dilution of BuOH, *t*-BuOH and its fluorinated derivatives and PrOH and its fluorinated derivatives in $[C_4C_1im][NTf_2]$, at the reference temperature ($T = 298.15$ K), as well as, the symmetric of the standard molar enthalpy of vaporization of the same alcohols, at the reference temperature ($T = 298.15$ K), as a function of the number of fluorinated groups “>CF₃” / “-CF₂” of the alcohol alkyl chain. 231
- Figure 4.19.** Thermochemical cycle which describes the solution/solvation process. 232

- Figure 4.20.** Graphical representation of the standard molar enthalpy of solvation, at infinite dilution, of alcohols in ILs, at the reference temperature ($T = 298.15$ K), as a function of the energy of interaction between the alcohol and the anion of the IL, in the gas phase. 234
- Figure 4.21.** Graphical representation of the standard molar enthalpy of solvation, at infinite dilution, of alcohols in ILs, at the reference temperature ($T = 298.15$ K), as a function of the energy of interaction between the alcohol and the anion of the IL, in the gas phase. 235
- Figure 4.22.** Schematic representation of the preferential location of the hydroxyl group of the alcohol in ionic liquids forming alcohol - anion hydrogen bond. 236
- Figure 4.23.** Scheme of the strategy used to determine the effect of the alkyl chain length, of both alcohol and cation, in the solvation of alcohols in ILs. 238
- Figure 4.24.** Graphical representation of the standard molar enthalpy of solution, at infinite dilution, of PrOH, ButOH, PentOH, HexOH, HeptOH and OctOH in $[C_N C_1 \text{im}][\text{NTf}_2]$ IL series, at the reference temperature ($T = 298.15$ K), as a function of the number N of carbons in the alkyl side chain of the cation. 243
- Figure 4.25.** Graphical representation of the standard molar enthalpy of solution, at infinite dilution, of PrOH, ButOH, PentOH, HexOH, HeptOH and OctOH in $[C_N C_1 \text{im}][\text{NTf}_2]$ IL series, at the reference temperature ($T = 298.15$ K), as a function of the variable Z , that relates the number of carbons in the alcohol alkyl chain with the number of carbons in the cation alkyl chain. 244
- Figure 4.26.** Graphical representation of the standard molar enthalpy of solution, at infinite dilution, of PrOH, ButOH, PentOH, HexOH, HeptOH and OctOH in $[C_N C_1 \text{im}][\text{NTf}_2]$ and $[C_N C_1 \text{im}][\text{PF}_6]$ IL series, at the reference temperature ($T = 298.15$ K), as a function of the number N of carbons in the alkyl side chain of the cation. 245
- Figure 4.27.** Graphical representation of the standard molar enthalpy of solution, at infinite dilution, of PrOH, ButOH, PentOH, HexOH, HeptOH and OctOH in $[C_N C_1 \text{im}][\text{NTf}_2]$ and $[C_N C_1 \text{im}][\text{PF}_6]$ IL series, at the reference temperature ($T = 298.15$ K) as a function of the variable Z , that relates the number of carbons in the alcohol alkyl chain with the number of carbons in the cation alkyl chain. 245
- Figure 4.28.** Graphical representation of the standard molar enthalpy of solvation, at infinite dilution, of PrOH, ButOH, PentOH, HexOH, HeptOH and OctOH in $[C_8 C_1 \text{im}][\text{NTf}_2]$ and $[C_8 C_1 \text{im}][\text{PF}_6]$ IL series, as well as, the symmetric of the enthalpy of vaporization of the referred alcohols, at the reference temperature ($T = 298.15$ K), as a function of the number of carbons in the alcohol alkyl chain. 247
- Figure 4.29.** Graphical representations of the standard molar enthalpy of solvation, at infinite dilution, of PrOH, ButOH, PentOH, HexOH, HeptOH and OctOH in $[C_N C_1 \text{im}][\text{NTf}_2]$ IL series, at the reference temperature ($T = 298.15$ K), as a function of the variable Z , that relates the number of carbons in the alcohol alkyl chain with the number of carbons in the cation alkyl chain. 249
- Figure 4.30.** Graphical representations of the standard molar enthalpy of solvation, at infinite dilution, of PrOH, HexOH and OctOH in $[C_N C_1 \text{im}][\text{PF}_6]$ IL series, at the reference temperature ($T = 298.15$ K), as a function of the variable Z , that relates the number of carbons in the alcohol alkyl chain with the number of carbons in the cation alkyl chain. 250
- Figure 4.31.** Representative scheme of the preferential location of the alcohol in ionic liquids, interacting with the nonpolar domains through " $>\text{CH}_2$ " to " $>\text{CH}_2$ " interactions and forming an alcohol - anion hydrogen bond. 251

- Figure 4.32.** Graphical representation of the heat flow signal obtained in μ FlowCal calorimeter, corrected to the time constant of the calorimeter, in a binary mixture BuOH + [C₆C₁im][NTf₂] as a function of the experimental time and of a magnification on the heat flow signal axis. 254
- Figure 4.33.** Graphical representation of the excess molar enthalpy of the binary mixture BuOH + [C₆C₁im][NTf₂], determined experimentally in this work using μ FlowCal calorimeter, at the reference temperature ($T = 298.15$ K), as a function of the molar fraction of 1-butanol in [C₆C₁im][NTf₂]. 256
- Figure 4.34.** Graphical representation of the excess molar enthalpy of the binary mixture BuOH + [C₆C₁im][NTf₂] (right axis), determined experimentally using μ FlowCal, with the correspondent fitting of the data using the Redlich-Kister equation with 6 parameters, and of the partial molar excess enthalpy of BuOH and [C₆C₁im][NTf₂] (left axis), derived using the Redlich-Kister equations, as a function of the molar fraction of BuOH. 257
- Figure 4.35.** Graphical representation of the excess molar enthalpy of the binary mixtures BuOH + [C₆C₁im][NTf₂] and BuOH + [C₄C₁pyrr][DCA] (right axis), as well as, the correspondent partial molar excess enthalpy of BuOH and IL, as a function of the molar fraction of BuOH. 258
- Figure 4.36.** Graphical representation of the excess molar enthalpy of the binary mixtures BuOH + [C₆C₁im][NTf₂] and PrOH + [C₆C₁pip][NTf₂] (right axis), as well as, the correspondent partial molar excess enthalpy of ROH (PrOH / BuOH) and IL (in the left axis), as a function of the molar fraction of ROH. 260
- Figure 4.37.** Graphical representation of the partial molar excess enthalpy of the ionic liquid in several binary mixtures as a function of the alcohol molar fraction. 262
- Figure 4.38.** Graphical representation of the excess molar enthalpy of the binary mixtures of BuOH + [C₆C₁im][NTf₂] and BuOH + HexOH (on the left) and of the partial molar excess enthalpy of BuOH / IL / HexOH in referred binary mixtures (on the right) as a function of the BuOH molar fraction. 264
- Figure 4.39.** Scheme of the partial molar excess enthalpy of the binary mixture BuOH + [C₆C₁im][NTf₂] as a function of the BuOH molar fraction (upper representation) and BuOH volume fraction (bottom representation), with division of the diagrams into different regimes illustrated with representative simulation boxes. 267
- Figure 4.40.** Scheme of the excess molar volume of the binary mixture BuOH + [C₆C₁im][NTf₂] as a function of the BuOH molar fraction with division of the diagram into the different regimes. 271

Chapter 5 – Conclusions and Achievements

- Figure 5.1.** Graphical representation of the baseline stability of the μ FlowCal calorimeter, over a period of 15 hours, with respective magnifications on the axis of the heat flow signal, demonstrating the magnitude of medium and short-time noise. Data represented as obtained, without filtration or smoothing. 282

Appendix

Figure A.1. Graphical representation of the temperature in the calorimeter, in the aluminium box and in the thermostated bath over time.	293
Figure A.2. Schematic representation of the calorimeter, inside the aluminium box, with an air gap in between.	294
Figure A.3. Graphical representation of the " $\ln(T_{\infty} - T_s)$ " over time.	296
Figure A.4. Graphical representation of the temperature in the calorimeter over time and of the calculated temperature of the calorimeter, using the coefficients obtained from the fitting of the logarithm of the temperature difference.	296
Figure A.5. Graphical representation of the long-time temperature oscillation (40 000 s) and inset, representing the medium-time temperature oscillation (10 000 s) over time, in the aluminium box and the estimated temperature oscillation in the calorimeter, considering the inertia of the heat sink, $\tau = (2.009 \pm 0.092) \times 10^4$ s.	298
Figure A.6. Graphical representation of the fitting of a first order exponential to "signal 1+2".	300
Figure A.7. Graphical representation of the calorimetric output "signal 1", "signal 2" and its sum "signal 1+2" corrected to the calorimeter time constant.	300
Figure A.8. Graphical representation of the calorimetric output "signal 1+2" corrected to the thermal inertia of the calorimeter using two different methods.	301
Figure B.1. Block diagram of the Data Acquisition Software, developed in HPVÉE, to acquire, log and visualize in real-time the calorimetric output signals of μ FlowCal.	304
Figure B.2. Screenshot of the front panel of the Data Acquisition Software, developed in HPVÉE, to acquire, log and visualize in real-time the calorimetric output signals of μ FlowCal.	305
Figure B.3. Block diagram of the Data Treatment Software, developed in HPVÉE, to integrate the peaks obtained in the experiments performed in μ FlowCal calorimeter.	306
Figure B.4. Screenshot of the front panel of the Data Treatment Software, developed in HPVÉE, to integrate the peaks obtained in the calorimetric experiments performed in μ FlowCal.	308
Figure B.5. Block diagram of the Temperature Monitor Software, developed in HPVÉE, to monitor the thermostatzation of the μ FlowCal.	310
Figure B.6. Screenshot of the front panel of the Temperature Monitor Software, developed in HPVÉE, to monitor the thermostatzation of the μ FlowCal.	312
Figure D.1. Graphical representation of the excess molar enthalpy of mixing of the binary mixture BuOH + [C ₆ C ₁ im][NTf ₂], determined experimentally in this work using μ FlowCal, at the reference temperature ($T = 298.15$ K), as a function of the molar fraction of 1-butanol in [C ₆ C ₁ im][NTf ₂].	319
Figure D.2. Graphical representation of the excess molar enthalpy of mixing of the binary mixture BuOH + [C ₆ C ₁ im][NTf ₂], determined experimentally in this work using μ FlowCal, at the reference temperature ($T = 298.15$ K), as a function of the molar fraction of 1-butanol in [C ₆ C ₁ im][NTf ₂] and the fitting of the experimental data using the Redlich-Kister equation with 2 to 7 parameters.	326

Figure D.3. Graphical representation of the relative deviation of the excess molar enthalpy of mixing, calculated using the Redlich-Kister equation with 2 to 7 parameters, to the experimental data obtained in μ FlowCal calorimeter. 327

Figure D.4. Graphical representation of the partial molar excess enthalpy of mixing of $[\text{C}_6\text{C}_{1}\text{im}][\text{NTf}_2]$ calculated using the Redlich-Kister equation with 2 to 7 parameters. 328

Figure D.5. Graphical representation of the partial molar excess enthalpy of mixing of BuOH calculated using the Redlich-Kister equation with 2 to 7 parameters. 329

List of Symbols and Abbreviations

Symbols and Abbreviations associated to Physical Properties and Constants

A	Area of the isothermal surface, normal to the direction of the heat flow
A_k	Parameter / adjustable coefficient of the Redlich-Kister equation
A_s	Area of the surface "s"
A_T	Integration area, area under each peak
$\langle A \rangle$	Average of peak integration
α	Hydrogen bond donor ability / acidity
α	Thermal diffusivity
α_{pred}	Hydrogen bond acidity scale predicted by COSMO-RS
β	Hydrogen bond acceptor ability / basicity
C	Heat capacity
c	Specific heat capacity
c_l	Speed of light
ced	Cohesive energy density
γ	Electrical Conductivity
D	Diffusion coefficient
δ	Deviation
$\Delta_{\text{dil}} H_m$	Molar enthalpy of dilution (refers to the total enthalpy change upon dilution)
ΔH_{corr}	Enthalpic blank correction
ΔH_{total}	Enthalpy of vaporization measured in <i>DropCalvet</i> (raw value, before applying enthalpic blank correction)
$\Delta_l^g H_m$	Molar enthalpy of vaporization (refers to the total enthalpy change upon vaporization)
$\Delta_l^g H_m^o$	Standard molar enthalpy of vaporization (refers to the total enthalpy change upon vaporization)
$\Delta_{\text{mix}} H$	Enthalpy of Mixing (refers to the total enthalpy change upon mixing)
$\Delta_{\text{mix}} H_m$	Molar enthalpy of mixing (refers to the total enthalpy change upon mixing)
$\Delta_{\text{soln}} H_m$	Molar enthalpy of solution (refers to the total enthalpy change upon solution)
$\Delta_{\text{soln}} H_m^\infty$	Molar enthalpy of solution at infinite dilution (refers to the total enthalpy change upon solution)

$\Delta_{\text{soln}} H_{\text{m}}^{0,\infty}$	Standard molar enthalpy of solution at infinite dilution (refers to the total enthalpy change upon solution)
$\Delta_{\text{solv}} H_{\text{m}}$	Molar enthalpy of solvation (refers to the total enthalpy change upon solvation)
$\Delta_{\text{solv}} H_{\text{m}}^{\infty}$	Molar enthalpy of solvation at infinite dilution (refers to the total enthalpy change upon solvation)
$\Delta_{\text{solv}} H_{\text{m}}^{0,\infty}$	Standard molar enthalpy of solvation at infinite dilution (refers to the total enthalpy change upon solvation)
$\Delta_{298.15\text{ K}}^T H_{\text{m}}^0$	heat stored by variation of temperature from 298.15 K to temperature “ T ”
$\Delta_{\text{l}, 298.15\text{ K}}^{g, T} H_{\text{m}}^0$	Standard molar enthalpy of vaporization and temperature variation from 298.15 K to temperature “ T ”
Δt	Time interval
ΔT	Temperature variation
ΔT_{ad}	Temperature variation in adiabatic conditions
E	Internal energy
e_{c}	Seebeck coefficient of a thermocouple
$E_{\text{cfg}}(\text{sol})$	Internal molar configurational energies of the solution
$E_{\text{cfg}}(\text{IL}, \text{l})$	Internal molar configurational energies of the pure IL in its liquid phase
$E_{\text{cfg}}(\text{PrOH}, \text{g})$	internal molar configurational energies of the pure 1-propanol in its gaseous phase
E_{HB}	Hydrogen bonding interaction energy of ILs in equimolar cation–anion mixture / hydrogen bond basicity scale predicted by COSMO-RS
E_{int}	Energy of interaction
$E_{\text{T}}(30)$	Solvent polarity scale based in the UV-Vis spectra of the Reichardt’s zwitterion dye betaine no. 30
$E_{\text{T}}^{\text{N}}(30)$	Solvent polarity scale based in the UV-Vis spectra of the Reichardt’s zwitterion dye betaine no. 30 normalized
e_{TP}	Seebeck coefficient of a thermopile
ε	Static dielectric permittivity / dielectric constant
ε_0	Vacuum dielectric permittivity
ε_{s}	Emissivity of a surface “s”
ε_{cal}	Calibration constant
f	Fraction of heat loss
$f(x)$	Function of variable x
G	Thermal conductance

G_c	Thermal conductance of a thermocouple
h	Relative deviation of the enthalpy obtained towards the literature reported value
h	Planck's constant
h	Convection heat transfer coefficient
H	Enthalpy
H_i^*	Enthalpy of the component "i" in its pure state
$H_{i,m}^*$	Molar enthalpy of the component "i" in its pure state
H_m^E	Excess molar enthalpy (refers to the total enthalpy change upon mixing)
H_{mix}	Enthalpy in the mixture
$H_{mix, m}$	Molar enthalpy in the mixture
$\bar{H}_{i,m}$	Partial molar enthalpy of the component "i" (refers to the total enthalpy change upon mixing)
$\bar{H}_{i,m}^E$	Partial excess molar enthalpy of the component "i" (refers to the total enthalpy change upon mixing)
$\bar{H}_{i,m}^{E, \infty}$	Partial excess molar enthalpy of the component "i" at infinite dilution (refers to the total enthalpy change upon mixing)
η	Viscosity
I	Intensity of electrical current
k	Thermal conductivity
k	Exponential decay constant
k_B	Boltzmann constant
K_ϵ	Proportionality factor of calibration
L	Length
M	Molar mass
m_{exp}	Weight of the glass capillary containing the sample
m_{ref}	Weight of the glass capillary used as reference
m_1	Molality of the initial solution
m_2	Molality of the solution after dilution
n	Number of couples in a thermopile
n	Molar quantity
n	Number of elements of the sample
n_i	Molar quantity of the component "i"
N_A	Avogadro's constant
P	Thermal power
Pe	Peclét number

P_i	Internal pressure
pKa	Logarithm of symmetric of the acid dissociation constant
π^*	Dipolarity/polarizability
q_i, q_j	Charge of the ions “i” and “j”
Q	Heat / Thermal energy
r	Intermolecular distance
r	Travelled distance
R	Gas constant
R	Molecule radius
R	Resistance
Re	Reynolds number
rt	Ratio between the internal pressure and the cohesive energy density
ru	Relative confidence limits
ρ	Density
S_{id}	Sensitivity of an ideal heat flow calorimeter
S_{exp}	Sensitivity of a calorimeter experimentally determined (real sensitivity)
σ	Stefan-Boltzmann constant
σ	Standard Deviation
t	Time
T	Temperature
τ	Time constant, thermal inertia of a calorimeter
U	Thermoelectric potential
U_{corr}	Thermoelectric potential corrected to the time constant of the calorimeter
$u(r)$	Potential energy of interaction as a function of the intermolecular distance “r”
v	Velocity
V	Volume
V_m^E	Excess molar volume
V_{inj}	Injected volume
V_m	Molar volume
$\tilde{\nu}$	Wavenumber
ϕ	Heat flux / heat flow
x_i	Molar fraction of the compound “i”
(XYZ)	Result of a solvent-dependent process

Ionic Liquids Abbreviation Nomenclature

C(2)	Carbon situated between the nitrogen atoms in imidazolium cation
C(2)-H	Acidic hydrogen, bonded to the carbon situated between the nitrogen atoms in imidazolium ring
C(4)-H, C(5)-H	Acidic hydrogens, bonded to carbon atoms of the imidazolium ring
H(C2)	Acidic hydrogen, bonded to the carbon situated between the nitrogen atoms in imidazolium ring
IL	Ionic Liquid
CAS	Critical Alkyl Size
<i>N</i>	Number of carbon atoms in the alkyl chain
<i>M</i>	Number of carbon atoms in the alkyl chain

Anions:

[BF ₄]	tetrafluoroborate
[DCA]	dicyanamide
[DMP]	dimethylphosphate
[FAP]	tris(pentafluoroethyl)trifluorophosphate
[NTf ₂]	bis(trifluoromethanesulfonyl)imide
[PF ₆]	hexafluorophosphate
[RSO ₄]	alkylsulfate
[EtSO ₄]	ethylsulfate
[OctSO ₄]	octylsulfate
[SCN]	thiocyanate
[TFA]	trifluoroacetate
Br	bromide
Cl	chloride
I	iodide

Cations:

[C _{<i>N</i>} C ₁ im]	1-alkyl-3-methylimidazolium with <i>N</i> + 1 carbon atoms in the alkyl chain
[C _{<i>N</i>} C _{<i>N</i>} im]	1,3-dialkylimidazolium with <i>N</i> + <i>N</i> carbon atoms in the alkyl chain
[C _{<i>N</i>} C _{<i>M</i>} im]	1,3-dialkylimidazolium with <i>N</i> + <i>M</i> carbon atoms in the alkyl chain
[C ₁ C ₁ im]	1,3-dimethylimidazolium
[C ₂ C ₁ im]	1-ethyl-3-methylimidazolium
[C ₃ C ₁ C ₁ im]	1-butyl-2,3-dimethylimidazolium
[C ₃ C ₃ im]	1,3-dipropylimidazolium
[C ₄ C ₁ im]	1-butyl-3-methylimidazolium
[C ₅ C ₁ im]	1-pentyl-3-methylimidazolium
[C ₆ C ₁ im]	1-hexyl-3-methylimidazolium
[C ₇ C ₁ im]	1-heptyl-3-methylimidazolium
[C ₈ C ₁ im]	1-octyl-3-methylimidazolium

[C ₉ C ₁ im]	1-nonyl-3-methylimidazolium
[C ₁₀ C ₁ im]	1-decyl-3-methylimidazolium
[C ₁₁ C ₁ im]	1-undecyl-3-methylimidazolium
[C _N C _N pip]	n,n-dialkylpiperidinium with <i>N</i> + <i>N</i> carbon atoms in the alkyl chain
[C _N C ₁ pip]	1-alkyl-1-methylpiperidinium
[C ₄ C ₁ pip]	1-butyl-1-methylpiperidinium cation
[C ₆ C ₁ pip]	1-hexyl-1-methylpiperidinium cation
[C _N C _N pyrr]	n,n-dialkylpyrrolidinium with <i>N</i> + <i>N</i> carbon atoms in the alkyl chain
[C ₃ C ₁ pyrr]	1-methyl-1-propylpyrrolidinium
[C ₄ C ₁ pyrr]	1-butyl-1-methylpyrrolidinium
[C _N py]	n-alkylpyridinium with <i>N</i> carbon atoms in the alkyl chain
[C ₄ py]	1-butylpyridinium
[C ₄ (n)C ₁ py]	1-butyl-n-methylpyridinium
[C ₄ (2)C ₁ py]	1-butyl-2-methylpyridinium
[C ₄ (3)C ₁ py]	1-butyl-3-methylpyridinium
[C ₄ (4)C ₁ py]	1-butyl-4-methylpyridinium
[N _{NNNN}]	tetraalkylammonium with <i>N</i> + <i>N</i> + <i>N</i> + <i>N</i> carbon atoms in the alkyl chain
[P _{NNNN}]	tetraalkylphosphonium with <i>N</i> + <i>N</i> + <i>N</i> + <i>N</i> carbon atoms in the alkyl chain

Alcohols Abbreviation Nomenclature

>CH ₂	methylene group
>CF ₂	difluoromethylene group
-CF ₃	trifluoromethyl group
N _{ROH}	Number of Carbons in the alcohol alkyl chain
ROH	alcohol
MeOH	methanol
EtOH	ethanol
PrOH	1-propanol
BuOH	1-butanol
PentOH	1-pentanol
HexOH	1-hexanol
HeptOH	1-heptanol
OctOH	1-octanol
NonOH	1-nonanol
DecOH	1-decanol
UdecOH	1-undecanol

DdecOH	1-dodecanol
TFPrOH	3,3,3-trifluoro-1-propanol
PFPrOH	2,2,3,3,3-pentafluoropropan-1-ol
<i>t</i> -BuOH	<i>tert</i> -butyl-alcohol
TF <i>t</i> -BuOH	2-trifluoromethyl-2-propanol
HF <i>t</i> -BuOH	1,1,1,3,3,3-Hexafluoro-2-methyl-2-propanol
PF <i>t</i> -BuOH	perfluoro- <i>tert</i> -butyl alcohol

Others

BSSE	Basis set superposition error
B3LYP	Hybrid functional with three parameters from Becke and the correlational functional of Lee, Yang and Parr
Celeron	Composite material constituted by cotton and phenolic resins
COSMO-RS	COnductor-like Screening MOdel for Real Solvents Theory (i.e. a set of equations) to calculate the chemical potential differences of molecules in liquids; it uses quantum chemically generated charge density surfaces to describe each molecule and its interactions with other molecules
CTFE	Chlorotrifluoroethylene plastic material
DFT	Density Functional Theory
<i>DropCalvet</i>	Calorimetric methodology based in a drop method assembly constituted by a microcalorimeter SETARAM HT1000D equipped with a vacuum line and dropping system
FTIR	Fourier-transform infrared spectroscopy
HOESY	Heteronuclear Overhauser effect spectroscopy
HPVEE	Visual programming language from Hewlett Packard
ITC	Isothermal Titration Calorimetry
Kanthal	Alloy constituted by iron, chromium and aluminium
Manganin	Alloy constituted by copper, manganese and nickel
MD	Molecular dynamics
NaCl	Sodium chloride
NOESY	Nuclear Overhauser effect spectroscopy
N ₂	Gaseous nitrogen
PE	Polyethylene plastic material
PEEK	Polyether ether ketone plastic material
PID	Proportional integral derivative
Pt	Platinum
PTFE / teflon	Polytetrafluoroethylene plastic material

Pyrex	Low thermal expansion borosilicate glass
RDF	Radial distribution function
ref.	Reference
rpm	Rotations per minute
RS232C	Recommended standard 232, version "c"... standard for serial communication and transmission of data
Ryton	Composite material constituted by glass fiber and mineral filled Polyphenylene sulphide
UNF	Unified fine thread, standard designation to identify the standard in threaded objects... it generally follows the major diameter (in inch) and the number of threads per inch of threaded objects
UV-VIS	Ultraviolet–visible spectroscopy
Viton	Fluoroelastomer
Z	Variable that correlates the alkyl size of the alcohol and cation
μ FlowCal	Flow twin microcalorimeter of the heat conduction type based in a micromixer
\varnothing_{ext}	External diameter
\varnothing_{int}	Internal diameter
3D	Three-dimensional

Units, Conversion Factors and Constants

This thesis follows the International System of Units (SI)^a defined for the based physical quantities, as follows:

SI Unit	Physical quantity
s	Time
m	Length
kg	Mass
A	Electric current
K	Temperature
mol	Amount of substance
cd	Luminous intensity

All other physical quantities are derived from these seven base quantities, either by multiplication or division. Some of the SI derived units, have special symbols:

Derived SI Unit	Physical quantity
J $\text{m}^2 \cdot \text{kg} \cdot \text{s}^{-2}$	Energy, Work, Heat
W $\text{J} \cdot \text{s}^{-1}$	Power, Heat Flow
Pa $\text{kg} \cdot \text{m}^{-1} \cdot \text{s}^{-2}$	Pressure
V $\text{J} \cdot \text{s}^{-1} \cdot \text{A}^{-1}$	electric potential difference
Ω $\text{J} \cdot \text{s}^{-1} \cdot \text{A}^{-2}$	Electric resistance
S $\text{s} \cdot \text{A}^2 \cdot \text{J}^{-1}$	Electric conductance

Whenever is pertinent, multiples and submultiples of the SI units are used.

Multiple/ Submultiple	Factor
k	$\times 10^3$
n	$\times 10^{-9}$
μ	$\times 10^{-6}$
m	$\times 10^{-3}$
c	$\times 10^{-2}$
d	$\times 10^{-1}$

In cases where the units commonly used do not correspond to the SI units (or derived SI units), the SI unit is adopted and the common used unit is indicated in parenthesis. The conversion factors of different units to the SI units are now presented.

Unit	Value in SI Unit
Å	10^{-10} m
atm	101325 Pa
bar	10^5 Pa
°C	$T / ^\circ\text{C} + 273.15$ K
Cal	4.184 J
eV	$1.60217657 \times 10^{-19}$ J
E_h (Hartree)	$2625500 \text{ J}\cdot\text{mol}^{-1}$
L	10^{-3} m^3

The relative atomic masses used in this work are those recommended by the IUPAC Commission in 2007^b. The fundamental constants used for the calculations are the recommended values from CODATA^c, which are now presented in its concise form.

R	Molar Gas Constant	$8.314462618... \text{ J}\cdot\text{mol}^{-1}\cdot\text{K}^{-1}$
N_A	Avogadro constant	$6.02214076 \times 10^{23} \text{ mol}^{-1}$
ϵ_0	Electric permittivity in vacuum	$8.8541878128(13) \times 10^{-12} \text{ m}^3\cdot\text{kg}^{-1}\cdot\text{s}^4\cdot\text{A}^2$
k_B	Boltzmann constant	$1.380649 \times 10^{-23} \text{ J}\cdot\text{K}^{-1}$
σ	Stefan-Boltzmann constant	$5.670374419... \times 10^{-8} \text{ J}\cdot\text{s}^{-1}\cdot\text{m}^{-2}\cdot\text{K}^{-4}$
h	Planck constant	$6.62607015 \times 10^{-34} \text{ J}\cdot\text{s}$
c	Speed of light in vacuum	$299792458 \text{ m}\cdot\text{s}^{-1}$

^a NIST. The NIST Reference on Constants, Units and Uncertainty. International System Units (SI): <https://physics.nist.gov/cuu/Units/index.html>

^b M. Wieser, M. Berglund, Atomic Weights of the Elements 2007 (IUPAC Technical Report), *Pure and Applied Chemistry*, 81 (2009), p.2131-2156.

^c NIST. The NIST Reference on Constants, Units and Uncertainty. CODATA: <https://physics.nist.gov/cuu/Constants/index.html>

Organization of the Thesis

The work performed in this project, aiming to study the solvation of alcohols in ionic liquids, is described in this thesis along five chapters, which are structured as follows:

Chapter 1 – Introduction

A brief introduction is provided on the state of the art of ILs, solvation in ILs and particularly, its binary mixtures with alcohols. The main concepts and the thermodynamic formalism regarding the enthalpic properties of mixing are presented along with its relevance from the point of view of the aim of this thesis. The aim of this thesis and the strategy followed is briefly explained.

Chapter 2 – Materials and Sample Preparation

This chapter presents a list of the ionic liquids and alcohols studied. It also describes the purification process of the samples and some procedures regarding the handling of samples. Details on additional materials used as calibrants or test materials are also provided.

Chapter 3 – Experimental Methodologies... *Calorimetry*

Given the strong methodological character of the work conducted in this thesis and the importance of accurate calorimetric determinations to the results presented, adding to the fact that the experimental techniques used were of calorimetric type, this chapter is dedicated to calorimetry. This chapter includes the description, calibration and test of the three calorimeters used in this thesis. Different levels of detail were used in the three calorimeters, depending on its relevance to the final work presented in this thesis. The most detailed description was done to μ FlowCal, as the calorimeter was designed, constructed and tested in the context of this thesis.

Important general concepts in calorimetry are introduced in the beginning of the chapter to contextualize and facilitate the reading.

Chapter 4 – Results and Discussion... *Solvation of Alcohols in Ionic Liquids*

This chapter is dedicated to the presentation of the experimental results regarding the solvation of alcohols in ionic liquids and its discussion. This chapter is divided in four sub-chapters, each one exploring a different effect:

- the effect of the cation nature and the anion hydrogen bond basicity;
- the effect of the alcohol acidity/fluorination;
- the effect of the alkyl chain length of both alcohols and cations;
- the effect of the alcohol concentration.

In each subchapter, a brief introduction is done explaining the aim and the strategy used, followed by the presentation and discussion of the results.

Chapter 5 – Conclusions and Achievements

The main accomplishments and conclusions of this work are outlined in this chapter. The relevance of the work performed and some future work is also included.

CHAPTER 1

Introduction

-
- 1.1. State of Art
 - 1.2. Concepts on the Enthalpic Properties of Mixing
 - 1.3. Aim and Strategy
- References
-

1. Introduction

Ionic Liquids (ILs) have been generically defined as compounds constituted by ions which melting point is smaller than 373 K (100 °C). This temperature corresponds to the boiling point of water and has no physical meaning related with the ionic liquids. This temperature limit is used generically to distinguish the ionic liquids from the molten salts. By that reason, it should not be applied strictly^[1]. Ionic liquids, as well as molten salts, are compounds typically constituted entirely by ions which melting point is inferior to its decomposition temperature. Nevertheless, while molten salts are characteristically constituted by spherical and symmetrical inorganic ions, ionic liquids are usually constituted by large, highly asymmetric and diffusely charged organic cations, as well as, generally poor coordinating anions. The chemical structure of the main cations and anions which constitute the ILs are depicted in figure 1.1. In general, the cations are of organic nature and are constituted by a polar region where is localized the positive charge and by an alkyl region which is typically nonpolar. This nonpolar part is indicated in figure 1.1 by “R” and may be constituted by purely alkyl chains, fluorinated alkyl chains or functionalized with different functional groups.

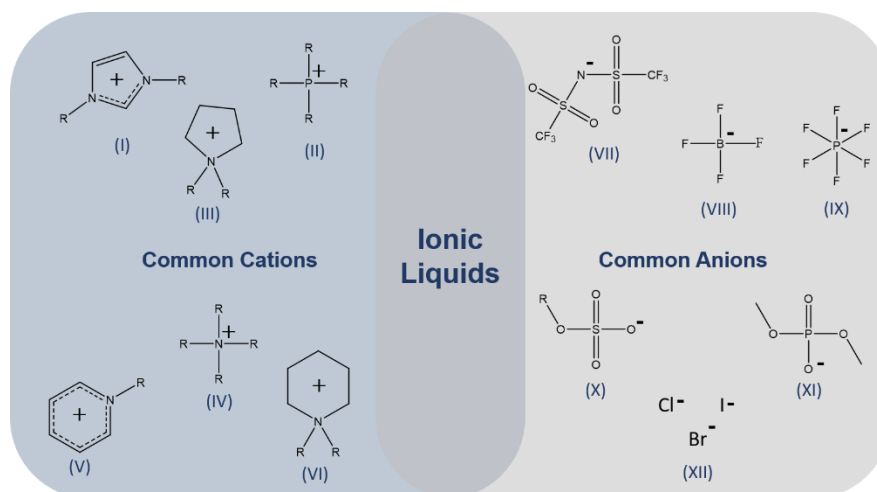


Figure 1.1. Chemical structure of the common cations and anions that constitute the ionic liquids. (I), 1,3-dialkylimidazolium ([C_NC_Nim]); (II), tetraalkylphosphonium ([P_{NNNN}]); (III), n,n-dialkylpyrrolidinium ([C_NC_Npyrr]); (IV), tetraalkylammonium ([N_{NNNN}]); (V), n-alkylpyridinium ([C_Npy]); (VI), n,n-dialkylpiperidinium ([C_NC_Npip]); (VII), bis(trifluoromethanesulfonyl)imide ([NTf₂]); (VIII), tetrafluoroborate ([BF₄]); (IX), hexafluorophosphate ([PF₆]); (X), alkylsulfate ([RSO₄]); (XI), dimethylphosphate ([DMP]); (XII), halides: chloride (Cl), bromide (Br), iodide (I).

The possibility of combining different anions and cations creates an enormous list of possible ionic liquids. As a result, it is possible to tailor their chemical composition and structure and thus, fine tune the IL properties to meet the requirements of a certain application, making in theory possible the design of a “task-specific ionic liquid”.

Overall, the possibility of the design of task-specific ILs together with the existence of accessible ionic liquids on the market and the existence of successful applications have raised interest from a high diversity of areas in the study of ionic liquids. The history of the ionic liquids and the crescent interest on them until today, when they represent a major subject of study in modern chemistry, was addressed by Tom Welton^[1] in 2018.

As ionic liquids are constituted by ions, have an amphiphilic nature and many times possess aromatic moieties, these compounds have the capability to dissolve a wide variety of compounds, from inorganic to organic polar and nonpolar solutes. Furthermore, the solubility of such a wide range of compounds allows ionic liquids to be used as reaction media and catalysts for several applications^[2, 3]. Naturally, the miscibility of the ILs will depend on the cation/anion combination. Nonetheless, the immiscibility of some substances with ionic liquids is not a drawback but an opportunity for its application in extraction and separation processes.

These characteristics combined with their low vapour pressures and to the possibility of a wide liquid phase (up to 400 °C) and high temperature stability provides the ILs with a portfolio of properties difficult to beat, which puts them in a very competitive position towards the volatile organic solvents.

The possibility of combining different anions and cations, or even mix ILs with other compounds, fine-tuning the solvent properties have granted them the designation of “designer solvents”. Nevertheless, the wide range of possibilities makes difficult to choose the best IL-based solvent for a given application. With such a vast range of possibilities of choice amongst the chemical composition of the ionic liquids, is not an easy task to describe a set of shared properties that go much further than what was already written and the inherent properties of its own definition^[4] :

- significant ionic conductivity, as they are constituted by ions;
- liquid at mild temperatures (their melting temperature or glass transition is inferior to 373 K).

All other properties will depend on the pair of cation and anion that constitutes the ionic liquid. Vapour pressures are generally low but they are not inexistent. In fact, the group where this thesis was conducted has been involved in the first determination of the enthalpy of vaporization of ILs, in which was shown that ionic liquids maintain the integrity of the ion pair

upon vaporization^[5]. Since then, the group has been reporting the vapour pressures of several ionic liquid families measured by a Knudsen effusion apparatus combined with a quartz crystal microbalance^[6], as well as, determining the standard molar enthalpies of vaporization of these compounds^[7-9]. Additionally, the generally low volatilities of the ionic liquids have led to the idea of “environmentally benign solvents”. Nevertheless, many ionic liquids are toxic. Thus, an analysis of the toxicity, biodegradation and recyclability is imposed when “green” or “sustainability” concepts are being discussed.^[2, 4]

The supposed high temperature stability of the ionic liquids also does not hold for all the compounds and furthermore, ionic liquids can undergo slow, but real, temperature dependent decomposition reactions^[2, 4].

The description of the IL properties is thus a non-trivial topic. The understanding of the IL properties must always be related with its composition, structure and intermolecular interactions. Only a complete analysis which includes and relates these topics may conduct to the understanding of structure-property or composition-property relationship and to the possibility of the design of a “task-specific IL” or a “designer solvent”.

In a work reported by Tom Welton and collaborators^[10] it is stated that “the key characteristics of a liquid that is to be used as a solvent are those that determine how it will interact with potential solutes”. The work presented in this PhD thesis is in absolute agreement with this line of thought, as in this work, alcohols were used as molecular probes to study the solvation properties of ionic liquids.

In this chapter, the state of the art on the subject, as well as, the scientific concepts necessary to understand this work are presented. This chapter aims only to introduce the key subjects and concepts necessary to understand the work presented in the thesis. To a deeper understanding of the topics mentioned, the reader is invited to look into the literature that is cited throughout the text.

At the end of this chapter, the aim and purpose of this work are briefly described. The strategy used to accomplish these scientific goals is succinctly explained.

1.1. State of art

In this section, the state of art on the solvation in ionic liquids is going to be presented, summarizing the most relevant publications available at the time of writing this thesis.

Following the idea of Tom Welton's publication^[10], according to which the essential characteristics of a liquid are the ones that determine how it will interact with solutes, a broad picture will be first provided on the self-organization, the intermolecular (including interionic and ionic-molecular) interactions and the polarity of the ionic liquids. These characteristics have major effects on their macroscopic properties, namely on their behaviour as solvents.

After this, a brief description of the mechanism of the solvation in ILs is provided, followed by a summary of the current knowledge on the binary mixtures constituted by alcohols and ionic liquids.

1.1.1. Structural Organization of Ionic Liquids

As discussed, ionic liquids are typically constituted by organic cations and inorganic/organic anions. To maintain the electroneutrality, some sort of short range organization concerning the cation and anion need to be present in the condensed phase. The structural complexity of these compounds leads to the existence of microphase separation in the nanometer scale.

In 2006, Canongia Lopes and Pádua^[11], using atomistic simulation studied the structuration of 1-alkyl-3-methylimidazolium hexafluorophosphate $[C_N\text{C}_1\text{im}][\text{PF}_6]$ ionic liquids with the length of the alkyl side chain of the imidazolium cation varying from $N = 2$ to $N = 12$. From the obtained results, they reported the structuration of the liquid phase to be analogous to the existence of microphase separation between polar and nonpolar domains. Additionally, it was reported that the charged domains constitute a three-dimensional continuous network of ionic channels, coexisting with the nonpolar domains which form, dispersed microphases in ionic liquids of small alkyl chain length or, continuous nonpolar microphases in ionic liquids of higher alkyl chain length. In figure 1.2, the snapshots of the simulation boxes of $[C_N\text{C}_1\text{im}][\text{PF}_6]$ ionic liquids obtained by Canongia Lopes and Pádua^[11] are depicted evidencing the nanostructuration of ionic liquids. The code colouring used by the authors enables a clear identification of the polar (coloured in red) and nonpolar domains (coloured in green) that constitute the ionic

liquids. From the observation of the snapshots of the simulation boxes of $[C_N C_1 \text{im}][\text{PF}_6]$ ionic liquids, it is evident the existence of ionic channels coexisting with nonpolar domains. The analysis of the snapshots along the increase in the length of alkyl chain of the imidazolium cation evidences the increase in size of the nonpolar domains from isolated “islands” dispersed in the ionic network (at small chain lengths) to large nonpolar domains coexisting with the polar domains. The analysis of the snapshots of the simulation boxes that represent only the nonpolar domains gives further visual insight into the topology of these domains.

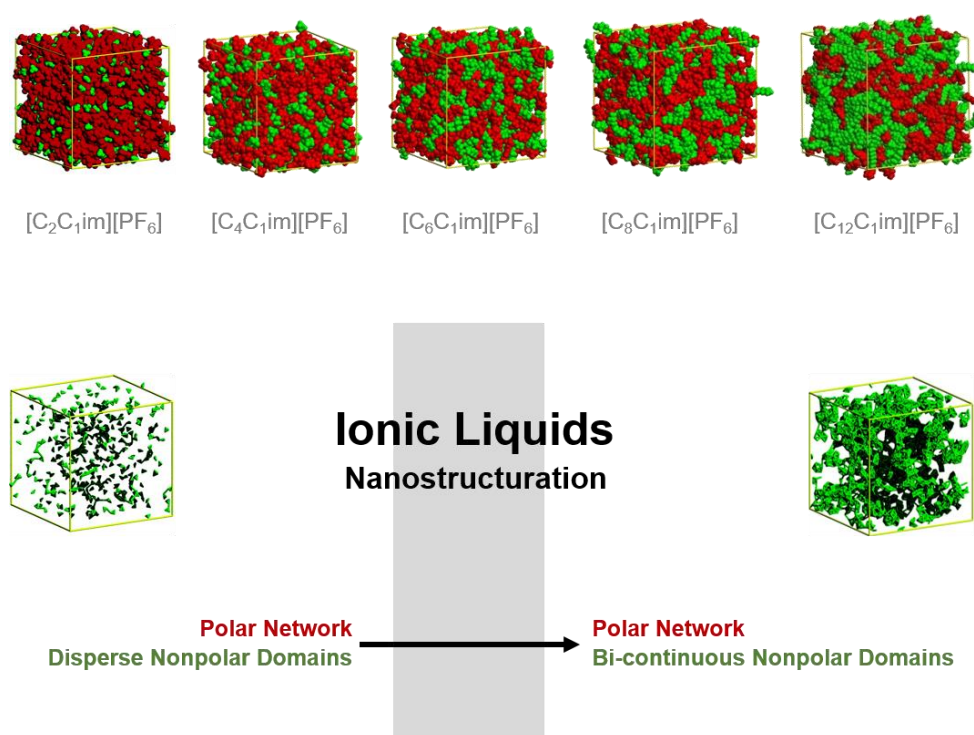


Figure 1.2. Schematic representation of the nanostructuration of the ionic liquids. The code colouring represents the polar (red) and nonpolar domains (green) of the ionic liquids. Figure adapted from the original figures presented by Canongia Lopes and Pádua [11].

The work of Canongia Lopes and co-workers^[12, 13] has extended the understanding on the mesoscopic segregation and nanostructuration of ionic liquids. The authors have studied ionic liquids based in 1-alkyl-3-methylimidazolium cations ($[C_N C_1 \text{im}]$) and 1,3-dialkylimidazolium cations ($[C_N C_M \text{im}]$) symmetric ($N = M$) and asymmetric ($N = M - 1$ and $N = M - 2$) using molecular dynamics and have reported similar conclusions for all series.

The authors have found that as the number of carbons in the cation's alkyl chain increases, the initial small and disperse alkyl chain aggregates percolate into bigger nonpolar domains that end up forming a bi-continuous mesoscopic phase when the number of carbons in the cation's alkyl chain is bigger than 6.

In parallel, as the number of carbons in the cation's alkyl chain increases, causing an increase of the nonpolar domains size, the ionic polar network stretches, accommodating the bigger nonpolar domains. When the number of carbons in the cation's alkyl chain equals 6, the polar network is fully stretched. In accordance, as the nonpolar bi-continuous domain continues to increase, the three-dimensional ionic network persists by losing part of its connectivity (becoming string like) and by increasing the distance between its different strands.

Furthermore, the authors have found that the distance from the centroid of the imidazolium ring until the carbon 6 of the alkyl chain, which acts as a critical alkyl size (CAS) beyond which bi-continuous nonpolar domains are formed, is approximately 0.7-0.8 nm. In addition, they report the characteristic length of the stretched polar network to be 0.77 nm (distance between ions of the same charge in direct space). Accordingly, they surmise that only when the alkyl side chains grow longer than the sphere of influence of the polar network, they are able to cause separation of the polar network strands instead of just sheath between them.

This was quite a straightforward insight into the understanding of nanostructuration in imidazolium based ionic liquids. In figure 1.3 is depicted a scheme, on a molecular scale, of the sphere of influence of the polar network. This scheme evidences the critical alkyl size of the ionic liquid and thus, the threshold beyond which the strings of the polar network are separated in space. It is also represented the equal distance between ions of the same charge in direct space (dashed line "a") and the distance from the centroid of the imidazolium ring until the CAS (dashed line "b").

It is thus understandable that the existence of large and flexible anions such as the bis(trifluoromethanesulfonyl)imide ([NTf₂]), used in these studies, or cations with charge delocalized rings as imidazolium cation can play an important role in the ability of stretch of the ionic channel, and thus modify the critical alkyl size. Regarding the critical alkyl size, it was detected in this work that the volumes of the nonpolar phase constitute an important factor. (Similar structuration phenomena was found, for example, for [C₃C₃im][NTf₂] and [C₅C₁im][NTf₂] ionic liquids.)

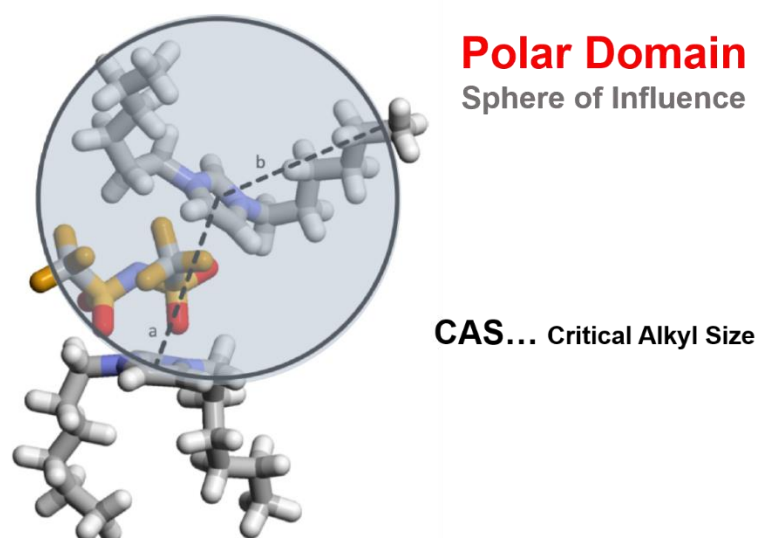


Figure 1.3. Schematic representation of the sphere of influence of the polar network and therefore of the critical alkyl size. The “a” dashed line represents the distance between ions of the same charge in direct space and the “b” dashed line represents the distance from the centroid of the imidazolium ring until the CAS. Figure adapted from ref.[13].

Evidences of the existence of this nanostructuration have been reported in multiple ionic liquids by structural characterization methodologies as X-ray scattering ^[14-18].

In different thermophysical properties a trendshift has been found which was interpreted as an evidence of nanostructuration ^[7, 8, 19-24]. The research group where this thesis work was conducted has been responsible for many of those studies and has proposed^[7] a model that explains the existence of the trendshift in a very simple and straightforward way as a superposition of the van der Waals and electrostatic interaction potentials along the alkyl chain length of the imidazolium cation as is represented in figure 1.4. As observed in the schematic diagram depicted in figure 1.4, the electrostatic interaction potential decreases initially until a stationary value at the sixth carbon (C₆) that is maintained despite of the further increase of the alkyl chain size of the imidazolium cation. This model is in accordance with the existence of an increase in the cation-anion distance as the size of the alkyl chain increases until reaching a critical alkyl size, the carbon 6, after which the cation-anion distance remains constant. This interaction potential is overlapped with the van der Waals interaction functional (non-electrostatic interaction potential) that increases linearly with the increase in the alkyl side chain of the imidazolium cation, describing the trendshift found. This model is in perfect accordance with the nanostructuration model for the ionic liquids described.

Although some details still challenge the understanding of the scientific community, the study of the nanostructuration of simple and most common ionic liquids has reached a robust level of interpretation ^[25-29].

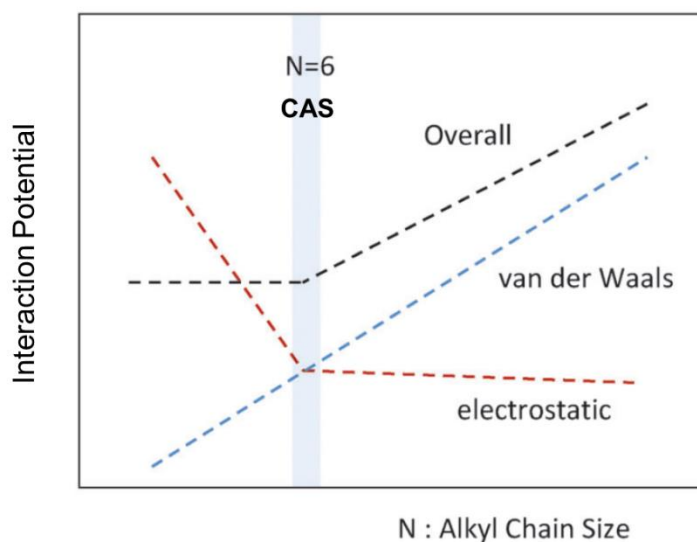


Figure 1.4. Schematic diagram of the interaction potentials present in the ionic liquids as a function of the cation alkyl chain size. Figure from ref [7].

1.1.2. Intermolecular Interactions in Ionic Liquids

Ionic liquids are composed by ions, which implicates the presence of electrostatic interactions. Nevertheless, the asymmetry and size of these ions leads to smaller coulombic forces, highly directional and of shorter range (in comparison to typical salts as NaCl) ^[30]. The intermolecular potential energy between two ions (of charge q_i and q_j), in vacuum, can be described as a function of the intermolecular distance r :

$$u(r) = \frac{q_i \cdot q_j}{4 \cdot \pi \cdot \epsilon_0 \cdot r}, \quad (1.1)$$

in which ϵ_0 is the vacuum dielectric permittivity. In ionic liquids the intermolecular potential energy should not be described simply as a function of two charges but taking into

account that the charge is dispersed through the ions, which are more complex than typical salts, as NaCl. Therefore, the electrostatic term of interaction in ionic liquids should be represented by partial charges at each interaction site of the molecule.

Other electrostatic interactions like ion–dipole interactions may be present in ionic liquids, especially if molecular solutes are added. In this case, the intermolecular potential energy is inversely proportional to r^4 [31].

Apart from these electrostatic interactions, anions and cations can also interact through other types of quite specific (and relatively strong) interactions like hydrogen bonding or π - π stacking [25, 32].

Regarding the hydrogen-bond type interactions, they depend upon the specific pair of cation and anion that constitutes the ionic liquid. The relative hydrogen bonding ability of both anions and cations will be addressed in the section of the ionic liquids polarity. Typically, cations are the hydrogen bond donors while anions are hydrogen bond acceptors. However, single hydrogen bonds are generally not formed. Instead, anions can interact simultaneously with multiple hydrogen atoms, either in the same cation or from different cations. In figure 1.5, the structure of an imidazolium cation is depicted, evidencing possible hydrogen bond interacting sites for the anion. Normally, the anions orientate over the cation maximizing the overall hydrogen bonding. This can happen through a single direct and strong hydrogen bond interaction or through multiple (normally up to three) moderate hydrogen bonds. [32]

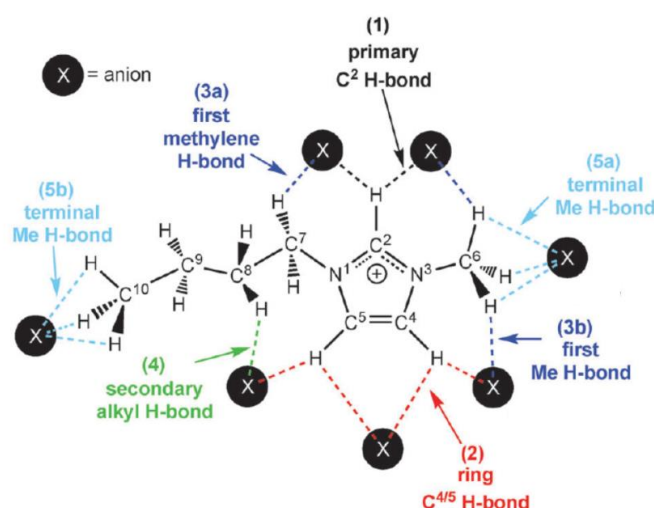


Figure 1.5. Schematic representation of the structure of the [C₄C₁im] cation and the sites available for hydrogen bond interaction with a hypothetical anion. The anion is represented as a black circle containing a white "X". The different types of hydrogen bond possible are coloured differently. Figure adapted from ref.[32].

The topic of hydrogen bonding in ILs has been reviewed by Patricia Hunt and collaborators^[32]. Generally, halide anions interact preferentially with C(2)-H, which is the most acidic hydrogen of the imidazolium cation. This hydrogen bond is not linear, which positions the anion in a favourable location to a weaker secondary hydrogen-bond interaction to one of the C(6) or C(7) alkyl groups. Alternative hydrogen bonding can be established to the less acidic hydrogens C(4)-H and C(5)-H. The high number of positions available in the cation for the anion to hydrogen bond are considered to be very relevant. The access of the anion to the mentioned positions can be restricted temporarily by steric hindrance or rotation of long alkyl chains. In this case, the anion may establish hydrogen bond interactions with the alkyl chain which will maintain the anion in the vicinity and allow for the stronger hydrogen bond to re-establish. Anions like $[\text{BF}_4]$ and $[\text{PF}_6]$ which are highly symmetric interact similar to halide anions, except for the higher distances which imply weaker interactions. Less symmetric anions as $[\text{DCA}]$, $[\text{TFA}]$ may interact with multiple and sometimes not adjacent hydrogen bond sites. The flexible $[\text{NTf}_2]$ anion is capable of torsional motion which facilitates the interaction to multiple cation sites or multiple cations.^[32] The main positions of interaction of $[\text{NTf}_2]$ anion and $[\text{C}_4\text{C}_1\text{im}]$ cation are illustrated in figure 1.6.

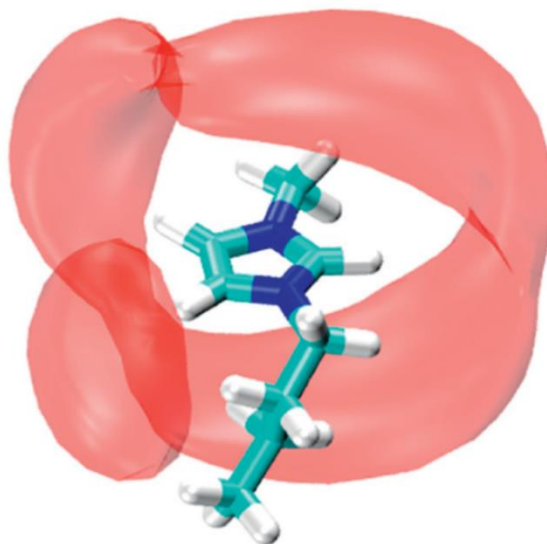


Figure 1.6. Schematic representation of the spatial isodensity surface of the $[\text{NTf}_2]$ anion around the $[\text{C}_4\text{C}_1\text{im}]$ cation. Figure adapted from ref.[33].

In summary, in ILs a high diversity of hydrogen bonding (weak, moderate and strong) can be found. This contrasts to the simple molecular liquids where the hydrogen bonds are generally of identical nature and established within the same atoms (e.g. alcohols or water). Nonetheless, the density of hydrogen bonding present in ionic liquids is typically high, promoting the existence of a network, as in simple molecular liquids, which is reflected in their physical properties. This network is expected to be maximum when similar number of donor and acceptor sites are present in ILs, creating “rigid networks”. On the contrary, a miss-match in the number of donor and acceptor sites is expected to create a “loose” network.^[32] In accordance, the existence of vacant acceptor or donor sites is expected to increase the fluidity of the IL. The addition of molecular solutes with both donor and/or acceptor sites is also expected to interfere with the IL hydrogen bond network, modifying its physical properties.

Despite of the strong repulsive electrostatic forces existent between ions of the same charge, π - π stacking is also present in ionic liquids. However, the energy of this type of interactions is typically small ($<10 \text{ kJ}\cdot\text{mol}^{-1}$) and competes with hydrogen bonding. As it was referred, big anions with multiple hydrogen bond acceptors, like $[\text{NTf}_2]$, form hydrogen bond interactions at various positions of the cation. Furthermore, it was demonstrated in figure 1.6 that this anion prefers configurations above and below the imidazolium ring, in addition to the positions close to the acidic hydrogens C(2)-H, C(4)-H and C(5)-H. This preferential location of the $[\text{NTf}_2]$ anion over the imidazolium cation prevents or at least weakens π - π stacking. Small anions, as Cl anion or $[\text{SCN}]$, do not hinder π - π stacking. It has been suggested that the balance between hydrogen bonding and π - π stacking could be optimized if anions have planar rings.^[25]

Overall, the intermolecular interactions described are limited to the polar domains of the ionic liquids. On the nonpolar domains the dispersive interactions are dominant. A great picture of the role of these interactions can be obtained from the analysis of the figure 1.4 which depicts the increasing of the van der Waals interaction with the increase of the alkyl chain in the imidazolium cation.

1.1.3. Characterization of the Polarity of Ionic Liquids

In order to accomplish the ideal of “designer solvent” it is essential to understand how the chemical composition of a given ionic liquid will affect the interaction with potential solutes. In other words, it is important to comprehend, the key features which an ionic liquid should possess to be used as a solvent. This understanding would allow to discern which parameters are flexible and thus, can be fine-tuned, and which should be fixed. Ultimately the design of the optimum ionic liquid would be determined by how it should interact with its potential solutes.

Regarding molecular liquids, this understanding have been based in the polarity of the liquid, which commonly was evaluated based in its dielectric permittivity^[34]. Measurements of the static dielectric permittivity (dielectric constants) of the ionic liquids have also been reported^[35]. However, this is a bulk property and therefore this approach consider the solvents as a non-structured homogeneous continuum.

Ionic liquids are mesostructured liquids and a high diversity of solute–solvent interactions may take place on a molecular level. Depending on the solutes, they may establish nonspecific interactions, act as hydrogen-bond donor or hydrogen-bond acceptor, electron-pair donor or electron-pair acceptor or stablsh specific interaction forces as π - π stacking or ionic interactions. In the case of amphiphilic solutes the system may be even more complex. Because of this multitude of solute–solvent interactions, macroscopic physical solvent parameters as the dielectric permittivity may fail in correlating different solvents.

In 1994, the IUPAC commission responsible for the edition of the Glossary of Terms Used in Physical Organic Chemistry has accepted a definition on the solvent polarity that considers that the polarity of a solvent is the sum of all possible specific and non-specific intermolecular interactions that may occur between the solvent and any potential solute, excluding interactions that lead to chemical transformation of the solute^[36, 37].

There are some polarity scales which are in line with this polarity definition. They are based in solvent-dependent processes which reflect the multitude of possible solute–solvent interactions and have been used to characterize both ionic liquids and molecular solvents. The multitude of polarity scales available will not be reviewed in the context of this thesis. (Some reviews can be consulted on the topic^[30, 38].)

However, there are two noteworthy scales that have been used in the field of ionic liquids and are worth mention and further exploration in the context of this thesis. Both these methods are based in the use of solvatochromic probes. In essence, the change in position (wavenumber) of an electronic absorption or emission band, caused by a

change in the polarity of the solvent is evaluated. In simpler words, solutes which UV-VIS / FTIR spectra is sensitive to the solute-solvent intermolecular interactions established are used.

The Reichardt's zwitterion dye betaine no. 30 (2,6-diphenyl-4-(2,4,6-triphenylpyridinium-1-yl)phenolate), which structure is depicted in figure 1.7, has been widely employed. As Reichardt explains in its work^[36], the molecular structure of this dye exhibits a large permanent dipole moment and therefore it has the potential to establish dipole/dipole and dipole/induced dipole interactions. Moreover, it possesses a large polarizable π -electron system which makes the dye apt for dispersion interactions. Finally, the phenolate oxygen atom exhibits a highly basic electron pair donating centre, and so it can interact with hydrogen-bond donors (H-bonding interaction) and Lewis acids. These interactions cause shifts of the bands in the UV-Vis spectra of the probe. The molar electronic transition energy of betaine dye No 30, $E_T(30)$, can thus be used empirically as a solvent polarity scale. This scale, E_T (usually expressed in $\text{kcal}\cdot\text{mol}^{-1}$), is obtained by using the referred dye as solute in solvents of different polarity at 298 K and 100 kPa (1 bar) and analysing the respective UV-VIS spectrum. The E_T value is obtained from the wavenumber, $\tilde{\nu}$, of the maximum of the long-wavelength, solvatochromic, intramolecular charge transfer absorption band of the dye, using the following equation:

$$E_T(30) = h \cdot c_l \cdot \tilde{\nu} \cdot N_A , \quad (1.2)$$

where, h is the Planck's constant, c_l is the speed of light and N_A is the Avogadro's constant. Higher $E_T(30)$ values reflect solvents of higher polarity. This scale was later normalized using water, $E_T^N = 1$, and tetramethylsilane, $E_T^N = 0$, as reference solvents, becoming dimensionless.

Despite of the fact of this scale being built with one unique parameter, the dye used is sensitive to multiple types of interactions which are reflected in the final $E_T^N(30)$ value obtained, thus it reflects the potential of the solvent for a multitude of interactions and is not only a bulk property as the static dielectric permittivity.

However, it should be noted that as the positive charge is delocalised and somewhat sterically shielded, interactions with electron pair donating solvents (Lewis bases) are practically inexistent. The solute is also not able to act as a hydrogen bond donor. In addition, in acidic solvents, the betaine dye is (reversibly) protonated and the long-wavelength solvatochromic visible absorption band disappears. To access the

polarity of the solvent regarding this aspect, other solvatochromic solutes have to be used.

Nevertheless, $E_T^N(30)$ scale has been widely used to evaluate the polarity of many solvents and therefore it allows the comparison of the polarity of the ionic liquids with these compounds.

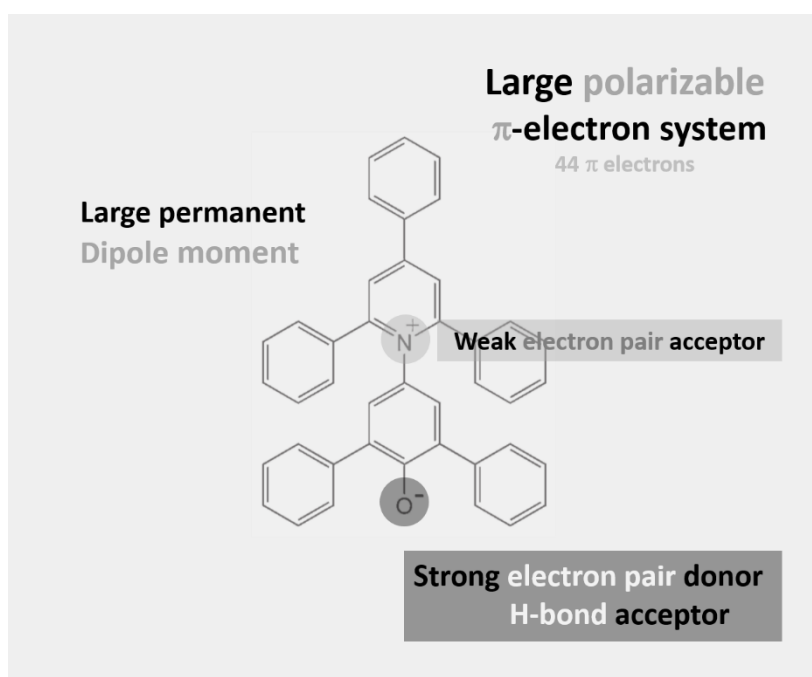


Figure 1.7. Molecular structure of the Reichardt's solvatochromic dye: betaine no. 30 (2,6-diphenyl-4-(2,4,6-triphenylpyridinium-1-yl)phenolate). Figure adapted from ref. [36].

Regarding the application of this scale to ILs, nearly 210 $E_T(30)$ values have been experimentally determined for these compounds^[34]. It should be noted that many times the $E_T^N(30)$ values obtained for ionic liquids are determined at temperatures higher than 298 K due to the melting point of the IL. The $E_T^N(30)$ values obtained from higher temperatures are not directly comparable because of the strong thermochromism of the Reichardt's dye.

Overall, the $E_T(30) / E_T^N(30)$ scale is a solvent dipolarity/polarizability scale which also reflects the hydrogen bond donor ability of the solvent. A different approach and

perhaps more adequate for the study of the ionic liquids in many cases is the application of the three-parameter polarity scale suggested by Kamlet, Taft and co-workers^[39].

The authors have proposed a methodology based on the comparison of effects on the UV-VIS spectra of closely related dyes, selected to probe separately the hydrogen bond donor/acceptor ability (acidity/basicity) of the solvent, as well as, its dipolarity/polarizability. This three-parameter polarity scale can be combined in a, also called “linear solvation energy relationship” which can be written, in its simplified form, as the following equation:

$$(XYZ) = (XYZ)_0 + a \cdot \alpha + b \cdot \beta + s \cdot \pi^*, \quad (1.3)$$

in which (XYZ) is the result of the solvent-dependent process, $(XYZ)_0$ is the value for the reference system (e.g. gas phase/nonpolar solvent), α is the parameter related with the hydrogen bond donor ability (acidity) of the solvent, β is the parameter related with the hydrogen bond acceptor ability (basicity) of the solvent and π^* is the parameter related with the dipolarity/polarizability of the solvent. The parameters a , b and s are solvent-independent correlation coefficients, which reflect predictions of the influence of the polarity parameters on the result (XYZ) of the chemical process.

It is important to highlight that the polarity scales are solute-dependent and so, two similar probes can present different solvatochromic parameters for the same solvent.

The experimental data found in the literature^[10, 35, 40-50] regarding the static dielectric permittivity (dielectric constant), ϵ_{IL} , the normalized $E_T^N(30)$ scale and the Kamlet-Taft solvatochromic parameters (α , β and π^*) for the ILs studied in this work are presented in table 1.1. Together with these values are presented the correspondent values of the hydrogen bond basicity $E_{HB} / \text{kJ} \cdot \text{mol}^{-1}$ and acidity α_{pred} scale proposed by Freire, Coutinho and co-workers^[51, 52], derived by COSMO-RS.

The static dielectric permittivity (dielectric constant) values presented in table 1.1 vary between 7 and 15. The ILs constituted by small cations present dielectric constants, ϵ_{IL} , from 9 to 15, with different authors reporting different values. Despite of this variation, there is evidence of a decrease on the dielectric constants with the increase of the alkyl chain of the cation. These results seem to be in accordance with Mizoshiri et al.^[53] which has estimated that the local dielectric constant of the polar domains is of the order of $\epsilon_{IL} = 20 \pm 1$, compared to $\epsilon_{IL} = 2.5 \pm 0.3$ for nonpolar domains. Considering these values, the dielectric constant of the ILs polar domains is similar to the dielectric constant of 1-propanol ($\epsilon = 20$) whereas the

dielectric constant of the ILs nonpolar domains is similar to the dielectric constant of alkanes ($\epsilon \approx 1.9$), which is in accordance with the nanostructuration model of the ionic liquids.

The normalized $E_T^N(30)$ scale values^[36] presented in table.1.1 were obtained with the Reichardt's dye. The values presented are dispersed between 0.6 and 0.7. In comparison with conventional molecular organic solvents, it can generally be said that the polarity of these ionic liquids are comparable to that of short-chain primary and secondary alcohols, as well as, secondary amides such as N-methylformamide (water $E_T^N(30)=1.000$; ethanol $E_T^N(30)=0.654$; 1-propanol $E_T^N(30)=0.617$; 2-propanol $E_T^N(30)=0.546$; n-methylformamide $E_T^N(30)=0.722$)^[42]. Moreover, a small decrease in $E_T^N(30)$ values was noticed with the increase of the length of the cation alkyl chain of the imidazolium cation. No significant effect was found between ILs with different anion. Due to the inaptitude of the Reichardt's dye to probe the hydrogen bond basicity of the solvent, these results are not surprising.

The $E_T^N(30)$ scale can be considered equivalent to the combination of the Kamlet-Taft solvatochromic parameters dipolarity/polarizability, π^* , and hydrogen bond acidity, α . It should be noted that the dipolarity/polarizability parameter, π^* , methodology used in ILs is different from the original Kamlet-Taft methodology^[40]. In the original methodology 45 dyes were used to generate the dipolarity/polarizability π^* parameter for a large quantity of solvents. The final dipolarity/polarizability parameter consisted in the normalized (between 0 and 1) average of the result obtained for all these dyes (0 – cyclohexane; 1 – dimethylsulfoxide). To this date, only a few of these dyes have been used to determine dipolarity/polarizability parameter π^* ^[40]. As the obtained values are dependent on the solvatochromic dye used, a comparison of this parameter for different ionic liquids should always be based in the same dye and temperature conditions. The dipolarity/polarizability, π^* , values presented in table 1.1 were obtained by different authors^[40, 44, 47, 48, 50] with the dye N,N-diethyl-4-nitroaniline at approximately 298 K. The molecular structure of this probe is presented in figure 1.8.

Ab Rani et al.^[40] considered the dipolarity/polarizability of the ionic liquids generally high due to its ionic character. Furthermore, they found that this parameter value is increased by the presence of large permanent dipoles, often caused by the existence of functional groups and delocalized bonds. In opposition the increase in the alkyl size of the cation appears to decrease the π^* parameter, similar to what has been verified in the $E_T^N(30)$ scale and in the static dielectric permittivity, ϵ_{IL} .

Table 1.1. Summary of the literature data concerning the dielectric constant, ϵ_{IL} , the E_{T}^{N} (30) scale, the hydrogen bond acidity, α , the hydrogen bond basicity, β , and the dipolarity/polarizability, π^* , obtained experimentally as well as, the hydrogen bond basicity and acidity predicted by COSMO-RS

IL	ϵ_{IL}	E_{T}^{N} (30)	α	β	π^*	E_{HB} /kJ · mol ⁻¹	α_{pred}
[C ₄ C ₁ im][NTf ₂]	9.2 ^a 15.0 ^b	0.596 ^c ; 0.642 ^d ; 0.644 ^e ; 0.645 ^f	0.61 ^l ; 0.635 ^f ; 0.72 ^m	0.23 ^l ; 0.248 ^f ; 0.24 ^m	0.99 ^l ; 0.971 ^f ; 0.90 ^m	-9.86 ⁿ	0.692 ^o
[C ₄ C ₁ im][PF ₆]	x	0.667 ^d ; 0.669 ^e ; 0.67 ^g ; 0.675 ^f ; 0.68 ^h ; 0.69 ^j	0.63 ^l ; 0.654 ^f ; 0.68 ⁱ	0.19 ^l ; 0.246 ^f ; 0.21 ⁱ	1.04 ^l ; 1.015 ^f ; 1.02 ⁱ	-2.88 ⁿ	x
[C ₄ C ₁ im][FAP]	x	x	x	x	x	-0.74 ⁿ	x
[C ₄ C ₁ im][DCA]	10.3 ^a	x	0.54 ^l	0.60 ^l	1.05 ^l	-22.60 ⁿ	x
[C ₄ C ₁ im][TFA]	x	0.63 ^g	x	0.84 ⁿ	x	-24.38 ⁿ	x
[C ₄ C ₁ pyrr][NTf ₂]	14.7 ^b	0.672 ^j	0.43 ^l ; 0.57 ^m ; 0.734 ^j	0.24 ^l ; 0.23 ^m ; -0.108 ^j	0.95 ^l ; 0.87 ^m ; 0.890 ^j	x	0.433 ^o
[C ₄ py][NTf ₂]	15.3 ^b	0.648 ^c ; 0.613 ^f	0.539 ^f ; 0.643 ^j	0.214 ^f ; 0.123 ^j	1.009 ^f ; 0.816 ^j	x	0.680 ^o
[C ₄ C ₁ pip][NTf ₂]	x	x	x	x	x	x	0.415 ^o
[C ₃ C ₁ C ₁ im][NTf ₂]	x	x	x	x	x	x	0.519 ^o
[C ₂ C ₁ im][NTf ₂]	12.0 ^b ; 13.8 ^a	0.676 ^c ; 0.685 ^f ; 0.690 ^c	0.42 ^m ; 0.63 ^l ; 0.705 ^f	0.10 ^m ; 0.23 ^l ; 0.233 ^f	1.02 ^m ; 1.00 ^l ; 0.980 ^f	-10.38 ⁿ	0.750 ^o
[C ₃ C ₁ im][NTf ₂]	9.3 ^a ; 13.3 ^b ; 14.0 ^b	0.654 ^k	x	x	x	x	0.727 ^o
[C ₅ C ₁ im][NTf ₂]	12.8 ^b		0.63 ^l	0.26 ^l	0.97 ^l	-9.65 ⁿ	0.677 ^o
[C ₆ C ₁ im][NTf ₂]	8.5 ^a	0.653 ^f	0.59 ^l ; 0.650 ^f	0.25 ^l ; 0.259 ^f	0.98 ^l ; 0.971 ^f	-9.50 ⁿ	0.659 ^o
[C ₇ C ₁ im][NTf ₂]	x	x	x	x	x	x	0.643 ^o
[C ₈ C ₁ im][NTf ₂]	6.9 ^a	0.629 ^d ; 0.630 ^c	0.60 ^l	0.29 ^l	0.96 ^l	-9.22 ⁿ	0.624 ^o
[C ₉ C ₁ im][NTf ₂]	x	x	x	x	x	x	0.615 ^o
[C ₁₀ C ₁ im][NTf ₂]	x	0.627 ^c	x	x	x	-8.90 ⁿ	0.593 ^o
[C ₆ C ₁ im][PF ₆]	7.1 ^a	0.66 ^j	0.63 ⁱ	0.24 ⁱ	1.02 ⁱ	-2.71 ⁿ	x
[C ₈ C ₁ im][PF ₆]	x	0.633 ^d	x	x	x	-2.57 ⁿ	x

a – ref.[41] b – ref. [35]; c – ref. [42]; d – ref. [43]; e – ref. [10]; f – ref. [44]; g – ref.[45]; h – ref. [46]; i – ref. [47]; j – ref. [48]; k – ref. [49]; l – ref. [40]; m – ref. [50]; n – ref. [51]; o – ref.[52]; x – not found.

The Kamlet-Taft α parameter, which describes the hydrogen bond acidity of the solvent, has generated great controversy regarding its application to ILs. Originally, this parameter was estimated directly using the solvatochromic comparison method. However, in ILs the α parameter has been obtained from the Reichardt's $E_T(30)$ scale and the Kamlet-Taft π^* parameter. The Kamlet-Taft α parameter reported in table 1.1 was determined using this methodology.

Regarding this parameter, it is considered^[40] that the cation nature plays a significant role with the values of the hydrogen bond acidity of ionic liquids constituted by the same anion varying in the following way: imidazolium > pyridinium > pyrrolidinium. The hydrogen bond acidity scale derived by COSMO-RS^[52] is in absolute agreement and further indicates that piperidinium α parameter is lower than the previous ones.

From values reported in literature regarding α parameter obtained using solvatochromic methodology^[40] and COSMO-RS methodology^[52] it is also notorious that the methylation in the C(2) position (carbon situated between the nitrogen atoms) of the imidazolium ring decreases the acidity of the imidazolium based ionic liquids.

From the literature data regarding α parameter using the solvatochromic methodology^[40] is also noticeable a secondary effect played by the IL anion. The increase in the IL hydrogen bond basicity, β , follows up the decrease of the hydrogen bond donor ability, α , of the ionic liquid. This effect is attributed^[40] to a competition between the Reichardt's dye probe and the anion for the hydrogen bond donor site of the cation. It was further noticed that the increase in the basicity of the anion led to lower α values of the ionic liquid until a minimum of $\alpha = 0.45$ (1-butyl-3-methylimidazolium dimethylphosphate [C_4C_{1im}][DMP]; $\beta = 1.13$) which is similar to the hydrogen bond acidity of the ionic liquid when the C(2) position of the imidazolium cation is methylated $\alpha = 0.38$.

As it was already discussed, each probe may lead to different solvatochromic parameters values. Indeed, some authors have argued on the ability of the ionic liquids to act as hydrogen bond donors, as their α parameter are not sensitive to the effects discussed here. Rani et al.^[40] propose that Reichardt's dye hydrogen bond interaction with the cation has a Coulombic contribution which is not present in hydrogen bond interaction of a common neutral probe with the cation and therefore the Reichardt's dye will experiment a greater effect.

The Kamlet-Taft β parameter which describes the hydrogen bond basicity of the solvent was generated by the original comparison method with the probe pair

N,N-diethyl-4-nitroaniline/4-nitroaniline^[40]. The molecular structure of these probes is presented in figure 1.8. In this methodology, probes are selected so that they are very similar but one of them is capable of hydrogen bonding and the other is not. In addition their spectra has to present a very good correlation in non-hydrogen bond acceptor solvents (non-basic), as the hydrogen bond basicity scale constructed will depend on the difference between the spectra of the probes in the basic solvents and these ones. Regarding the application of the Kamlet-Taft parameters to the ILs, this scale is the most robust. In the literature^[40], results obtained with other probes can be found. Despite of the different β values obtained, the β scales obtained are very similar. Furthermore, good correlations were verified between the Kamlet-Taft β parameter and the hydrogen bond basicity scale determined by COSMO-RS^[51].

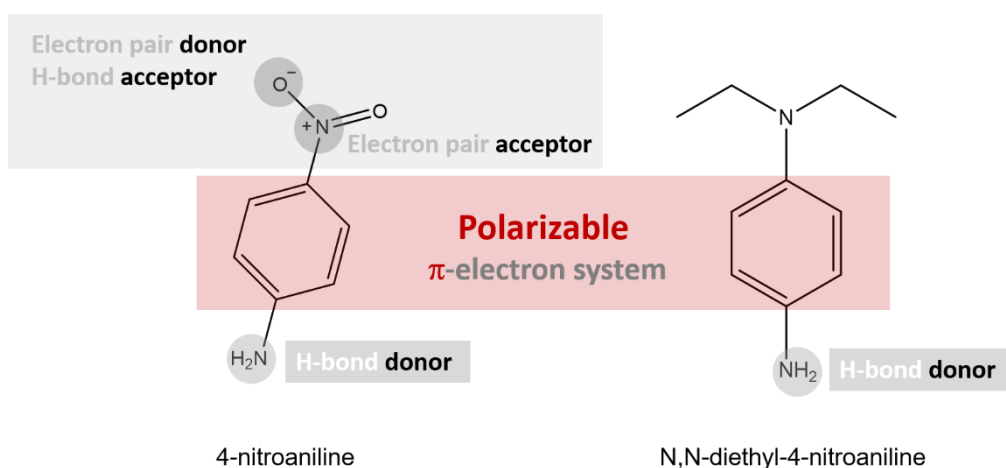


Figure 1.8. Molecular structure of the solvatochromic probes used to determine the Kamlet-Taft parameters α and π^* : 4-nitroaniline and N,N-diethyl-4-nitroaniline.

1.1.4. Solvation in Ionic Liquids

Given the promising solvent behaviour of ionic liquids, the research on the ILs solvation has become a hot topic in the last years ^[10, 36, 54-58]. Solutes of different types have been studied in ionic liquids. The solvation of the different solutes studied tends to obey to a “nanostructured solvation paradigm”, which has been proposed by Varela and collaborators^[59, 60]. According to this paradigm, the nanostructuring of the ionic liquids and its diverse nature influence the solvation of the different solutes. Depending on the

nature of each solute, it will be preferentially located/solvated in the nanodomain of the same nature. This is a generic description which provides a universal mechanism of solvation in ILs. More detailed understanding of solvation of the different solutes, regarding the intermolecular interactions established, as well as, the existence of aggregation and modification of the IL structures and characteristics is an ongoing area of study. Complete understanding of different IL containing mixtures is essential to establish composition dependent relations.

Regarding the mixtures of ionic liquids containing simple molecular solutes, water has been the most studied compound once that it constitutes a common contaminant in ionic liquids [18, 25, 28, 61, 62]. Its solubility, structuration, energetics of mixing, effect on the transport properties, etc has been studied in numerous ionic liquids. Overall, water tends to form clusters in non-hydrogen bonded ionic liquids, which increase and coalesce as the water content in the mixture increases. At a certain concentration of water, continuous water network appears in the bulk mixture, percolating the IL structure. On the contrary, in protic ionic liquids, which possess hydrogen bonded networks, water tends to be more homogeneously distributed, forming an extended hydrogen bond network with the ions^[60].

After water, alcohols have been the most studied compounds. In fact, the number of publications related to binary mixtures constituted by alcohols and ILs has been growing in the last years. In this section, the current knowledge on the binary mixtures constituted by alcohols and ionic liquids will be reviewed.

1.1.4.1. Liquid – Liquid Equilibria

Several works have been done studying the factors that govern the liquid-liquid behaviour of binary mixtures constituted by imidazolium based ionic liquids and alcohols. Considering the amount of data available on the topic, only the most relevant works in the context of this thesis will be reviewed.

Rathke and collaborators^[63-67] have done a systematic characterization of liquid-liquid phase diagrams of $[C_NC_{1im}][NTf_2]$ ($N = 1, 2, 3, 4, 6, 8, 10$ and 12) and simple linear alcohols (from 1-propanol to 1-icosanol). Brenecke et al.^[68] studied the effect of different characteristics (anion, alkyl chain size, and isomerization) of the components on the liquid–liquid equilibrium of a binary mixture of ILs and alcohol. Rebelo et al.^[69] have studied the liquid–liquid equilibrium of binary mixtures constituted by the

[C₆C₁im][NTf₂] and linear alcohols of different alkyl size (ethanol to 1-octanol). Domańska and Marciniak^[70] have studied the liquid–liquid equilibrium of binary mixtures constituted by the [C₂C₁im][PF₆] and a few alcohols (linear and branched). Maurer et al.^[71] have studied the liquid–liquid equilibrium of binary mixtures constituted by the [C₄C₁im][PF₆] and linear alcohols of different alkyl size (from ethanol to 1-butanol).

A summary containing the miscibility, at 298.15 K, of the relevant IL + alcohols systems, in the context of this thesis, was constructed based in these publications (table 1.2). In cases which the upper critical solution temperature was inferior to 298.15 K, the IL and alcohol are miscible in the full concentration range. These systems are indicated in table 1.2 as “Miscible”. In cases which the upper critical solution temperature is superior to 298.15 K, the range of miscibility was expressed in table 1.2 whenever was possible. In the cases which no indication of miscibility at 298.15 K exists, the indication of “Not miscible” was used and the concentration range studied is indicated.

Overall, it was verified that the miscibility range of the binary mixtures of ionic liquids and alcohols increases with the increase in the IL alkyl chain length of the cation. Furthermore, the increase in the alkyl side chain of the alcohol decreases the miscibility of the system. These conclusions seem to be transversal to the IL families analysed.

Comparing the alcohol-IL miscibility in ILs composed by different anions ([NTf₂], [BF₄] and [PF₆]) it is verified that miscibility decreases in the following order: [NTf₂] > [BF₄] > [PF₆].

Table 1.2. Summary of the miscibility of binary mixtures constituted by $[C_N C_1 \text{im}][\text{Anion}]$ and linear alcohols (1-propanol – PrOH, 1-butanol – BuOH, 1-pentanol – PentOH, 1-hexanol – HexOH, 1-heptanol – HeptOH and 1-octanol – OctOH), at 298.15 K

	PrOH	BuOH	PentOH	HexOH	HeptOH	OctOH
[C₁C₁im] [NTf₂]	$x_{\text{ROH}} < 0.6517^a$ $x_{\text{ROH}} > 0.9650^a$	Not miscible ^a 0.5085-0.9780	Not miscible ^a 0.5150-0.9803	Not miscible ^a 0.5014-0.9805	Not miscible ^a 0.5121-0.9783	Not miscible ^a 0.4945-0.9837
[C₂C₁im] [NTf₂]	Miscible ^b	Not miscible ^b 0.504-0.981	Not miscible ^b 0.507-0.981	Not miscible ^b 0.512-0.979	Not miscible ^b 0.505-0.983	Not miscible ^b 0.505-0.979
[C₃C₁im] [NTf₂]	Miscible ^a	$x_{\text{ROH}} < 0.5994^a$ $x_{\text{ROH}} > 0.9798^a$	-	Not miscible ^a 0.4939-0.9598	-	Not miscible ^a 0.5009-0.9799
[C₄C₁im] [NTf₂]	-	Miscible ^c $x_{\text{ROH}} < 0.7055^d$ $x_{\text{ROH}} > 0.9600^d$	Not miscible ^c 0.547-0.920	Not miscible ^{c, d} 0.540-0.970 0.4017-0.9875	Not miscible ^c 0.545-0.970	Not miscible ^c 0.537-0.970
[C₆C₁im] [NTf₂]	-	Miscible ^e	Miscible ^e	$x_{\text{ROH}} < 0.59452^e$ $x_{\text{ROH}} < 0.600^f$ $x_{\text{ROH}} > 0.97511^e$ $x_{\text{ROH}} > 0.981^f$	Not miscible ^f 0.499 - 0.981	Not miscible ^f 0.560 - 0.982
[C₈C₁im] [NTf₂]	-	-	-	-	-	$x_{\text{ROH}} < 0.560^g$ $x_{\text{ROH}} > 0.985^g$
[C₂C₁im] [PF₆]	Not miscible ^h 0.0000-0.9952	Not miscible ^h 0.0000-0.9974	-	-	-	-
[C₄C₁im] [PF₆]	$x_{\text{ROH}} < 0.0016^i$ $x_{\text{ROH}} > 0.7279^i$	$x_{\text{ROH}} < 0.0007^i$ $x_{\text{ROH}} > 0.8245^i$	-	-	-	-
[C₄C₁im] [BF₄]	$x_{\text{ROH}} < 0.4725^d$	$x_{\text{ROH}} < 0.2513^d$	-	Not miscible ^d 0.0849-0.9886	-	-
[C₆C₁im] [BF₄]	-	$x_{\text{ROH}} < 0.6513^d$ $x_{\text{ROH}} > 0.9187^d$	-	Not miscible ^d 0.3955-0.9878	-	Not miscible ^d 0.2673-0.9891

a – ref. [63]; b – ref.[64]; c – ref. [65]; d – ref.[68]; e – ref.[69]; f –ref.[66]; g – ref.[67]; h – ref. [70]; i – ref.[71].

1.1.4.2. Structuration of Mixtures

The structuration of the binary mixtures of alcohols and ionic liquids depends on the pair cation/anion, on the size of the ionic liquid and on the concentration of both components.

Varela and co-workers^[72] have published in 2011 a work regarding molecular dynamics simulations in mixtures of methanol and ethanol with ionic liquids constituted by the $[C_6C_{1im}]$ cation and three different anions: Cl, $[BF_4]$ and $[PF_6]$. The authors concluded that alcohol molecules are preferentially interacting with anions and that the strength of these interactions increase in the following order: $[PF_6] < [BF_4] < Cl$. Furthermore, the results indicated that both alcohols were “homogeneously” distributed in the structure of $[C_6C_{1im}]Cl$. The existence of significant hydrogen bonding between alcohol molecules was only verified in this ionic liquid at high concentrations of alcohol ($x_{ROH} \geq 0.8$). In opposition, in mixtures with $[C_6C_{1im}][PF_6]$ the results indicate that the studied alcohols tend to form clusters that increase in size with increasing concentration of the alcohol. The increase of the clusters size cause its percolation, probably forming a network which breaks the polar IL network. The mixtures of methanol and ethanol with $[C_6C_{1im}][BF_4]$ present similar effect to the mixtures with $[C_6C_{1im}][PF_6]$, with less pronounced clustering of the alcohols.

More recently (2018), Sharma and Ghorai^[73] have studied binary mixtures of $[C_4C_{1im}][PF_6]$ with methanol and ethanol by molecular dynamics simulation. The authors have noticed that at low alcohol molar fractions, $x_{ROH} = 0.2$, approximately 30 % of the alcohol molecules were completely dispersed as monomers. The number of monomers of alcohol decreases with the increase in the alcohol content, indicating that alcohol clusters are increasing. Indeed, at moderate alcohol content, $x_{ROH} = 0.4$ and $x_{ROH} = 0.6$, alcohol clusters of different sizes are present. At higher alcohol contents, $x_{ROH} = 0.8$ and $x_{ROH} = 0.9$, all the alcohol molecules seem to be aggregated in one cluster (there is no evidence of the presence of monomers or small clusters).

Agrawal and Kashyap^[33] have studied binary mixtures of $[C_4C_{1im}][NTf_2]$ with propanol and butanol, also by molecular dynamic simulations. The authors found evidences of the existence of an alcohol–anion hydrogen bond interaction established through the oxygen atoms of the anion. It was observed that the polar part of the alcohol is located near the head of the cation and the anion whereas, the nonpolar part of the alcohol is mainly localized near the alkyl chain of the cation. This preferential

location/interaction was maintained despite of the increase of the concentration of the alcohol in the mixture.

Regarding the structuration of the mixtures, in this study is reported the maintenance of the IL neat structure from $0 < x_{\text{ROH}} < 0.2$, as well as, the existence of transitional structural changes from $0.2 < x_{\text{ROH}} < 0.7$. In figure 1.9, snapshots of the simulation boxes regarding these binary mixtures at the molar fractions $x_{\text{ROH}} = 0.1, 0.3, 0.5, 0.7$ and 0.9 are presented. By visual analysis of the simulation snapshots reported, it is visible at $x_{\text{ROH}} = 0.1$, the existence of alcohol molecules dispersed throughout the nanostructure, with no visual evidence of alcohol aggregation. At $x_{\text{ROH}} = 0.3$, some aggregation of the alcohol molecules becomes noticeable embed into the IL nanostructure. At $x_{\text{ROH}} = 0.5$, the aggregation of the alcohol molecules is very clear with percolation of (at least some of) the isolated aggregates. At $x_{\text{ROH}} = 0.7$, the presence of big alcohol aggregates is visible as well as the presence of what could be an ionic network or at least, ionic liquid aggregates. At $x_{\text{ROH}} = 0.9$, alcohol molecules occupy most of the volume of the simulation box and the IL nanostructure seems to be broken. Still, the integrity of the ion pair seems to be present, as well as, some aggregation of the IL.

Using Raman spectroscopy, Yoshimura et al.^[74] have recently studied binary mixtures of $[\text{C}_4\text{C}_1\text{im}][\text{NTf}_2]$ with the following alcohols: methanol, ethanol, 1-propanol, 1-butanol, 1-pentanol, 1-hexanol, 1-heptanol, 1-octanol, 1-nonanol, 1-decanol, 1-undecanol and 1-dodecanol. They report that despite of the different size of the alcohols studied, even the long alcohol molecules could fit into the “nanoconfined space” of the $[\text{C}_4\text{C}_1\text{im}][\text{NTf}_2]$. Nevertheless, different aggregation behaviour of the alcohols was reported, depending on its length and concentration.

For methanol, ethanol, 1-propanol and 1-butanol the authors report the existence of all kinds of aggregation in the mixture, monomers, dimers, small and large clusters, depending on the alcohol concentration. At $x_{\text{ROH}} = 0.1$, all alcohol molecules seem to be dispersed into the IL as monomers. At $x_{\text{ROH}} = 0.2$, some dimers are noticed. However, the majority of the alcohol molecules is still dispersed as monomers. As the content of alcohol in the mixture increases, the number of alcohol molecules associated in dimers increases, while the number of monomers decrease. At $x_{\text{ROH}} = 0.6$, the presence of small clusters is noticed. As before, these clusters increase with the increase of the mixture in the alcohol content. Bigger clusters start to be noticed between $x_{\text{ROH}} = 0.7$ and $x_{\text{ROH}} = 0.8$.

Structuration of the Binary Mixture $[C_4C_1im][NTf_2] + ROH$

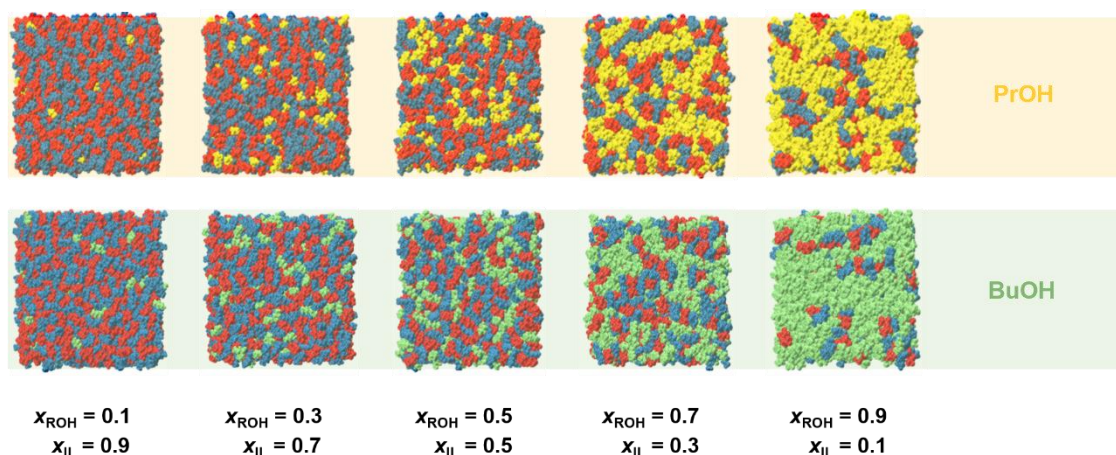


Figure 1.9. Scheme containing snapshots of simulation boxes of binary mixtures of $[C_4C_1im][NTf_2]$ with propanol and butanol. $[C_4C_1im]$ is coloured in red, $[NTf_2]$ is coloured in blue, 1-propanol (PrOH) is coloured in yellow and 1-butanol (BuOH) is coloured in green. Figure was adapted from ref.[33].

The simulated x-ray scattering static structure functions of PrOH-PrOH and BuOH-BuOH of Agrawal and Kashyap^[33] evidences the presence of a peak at $q = 1.47 \text{ \AA}^{-1}$, characteristic of the structure of the neat alcohol, to mixtures of alcohol molar fraction $x_{ROH} \geq 0.7$, in agreement with the results of Yoshimura et al.^[74].

Yoshimura et al.^[75] have also studied, using Raman spectroscopy, binary mixtures of $[C_4C_1im][BF_4]$ with the following alcohols: methanol, ethanol, 1-propanol, 1-butanol, 1-pentanol, 1-hexanol, 1-heptanol and 1-octanol. The results of this study contrast with the ones obtained for the binary mixtures containing $[C_4C_1im][NTf_2]$.

In methanol and ethanol solutions, the authors report the existence of all kinds of aggregation in the mixture, monomers, dimers, small and large clusters, depending on the alcohol concentration. At $x_{ROH} = 0.1$ and $x_{ROH} = 0.2$, methanol and ethanol molecules seem to be dispersed into the IL as monomers. At $x_{ROH} = 0.3$, some dimers are noticed. However, the majority of the alcohol molecules is still dispersed as monomers. As the content of alcohol in the mixture increases, the number of alcohol molecules associated in dimers increases, while the number of monomers decrease. At $x_{ROH} = 0.5$ in methanol solutions and $x_{ROH} > 0.6$ in ethanol solutions, the presence of small clusters is noticed. As before, these clusters increase with the increase of the mixture in the alcohol content. Bigger clusters start to be noticed between $x_{ROH} = 0.7$ and $x_{ROH} = 0.8$.

In longer alcohols solutions (from 1-propanol to 1-octanol) the majority of the alcohols is present as monomers. Furthermore, only monomers and dimers were detected. The presence of clusters was not detected.

The authors^[75] have associated the structuration difference of the binary mixtures of alcohols with the $[\text{C}_4\text{C}_1\text{im}][\text{BF}_4]$ and $[\text{C}_4\text{C}_1\text{im}][\text{NTf}_2]$ to the free volume existent in the neat IL. Krossing et al.^[76] have determined the free volume existent in a collection of ionic liquids which included $[\text{C}_4\text{C}_1\text{im}][\text{BF}_4]$ ($150 \pm 5 \text{ \AA}^3$) and $[\text{C}_4\text{C}_1\text{im}][\text{NTf}_2]$ ($240 \pm 5 \text{ \AA}^3$). Yoshimura et al.^[74] relate the ability of formation of clusters of bigger alcohol molecules, as well as the solution of bigger alcohols, in $[\text{C}_4\text{C}_1\text{im}][\text{NTf}_2]$ to the higher free volume of this IL. Nevertheless, they do not exclude the contribution of other factors as the hydrophilic/hydrophobic environment.

Another significant work on the topic has been performed by Kirchner et al.^[56]. They have studied, by molecular dynamic simulations, binary mixtures of $[\text{C}_N\text{C}_1\text{im}][\text{NTf}_2]$ ($N = 2, 4, 6, 8$) with 1-butanol and 1-dodecanol. They have analysed snapshots of the simulation boxes obtained by colouring differently the polar and nonpolar parts of both ILs and alcohols. The analysis of the simulation boxes in these terms provided very insightful information on the system, similarly to what has been observed in pure ILs by Canongia Lopes and Pádua^[11]. In figure 1.10, snapshots of their simulation boxes obtained with a ratio of five ion pairs to each alcohol molecule are presented.

From the analysis of the snapshots presented in figure 1.10, is visible that the polar units of the alcohols (coloured in yellow) are always connected to the polar domains of the ILs (coloured in red). Furthermore, the self-aggregation of 1-dodecanol is evident in $[\text{C}_2\text{C}_1\text{im}][\text{NTf}_2]$ (visible blue clusters). However, for higher side chains of the imidazolium cation, the blue units are dispersed, interacting with nonpolar domains of the IL (coloured in green). Snapshots of the simulation boxes containing 1-butanol did not show evidences of self-aggregation of the alcohol.

From further analysis, the authors^[56] report that in $[\text{C}_2\text{C}_1\text{im}][\text{NTf}_2]$, the polar parts of alcohols and ionic liquids form a unique domain, evidencing the interaction of the alcohol hydroxyl group with the polar domains of the IL. On the contrary, the nonpolar parts exist in a high number of domains. As the imidazolium side chain increases, the number of nonpolar domains decreases rapidly in accordance with the model of the nanostructuration of these ILs. In $[\text{C}_8\text{C}_1\text{im}][\text{NTf}_2]$, a unique nonpolar domain exists.

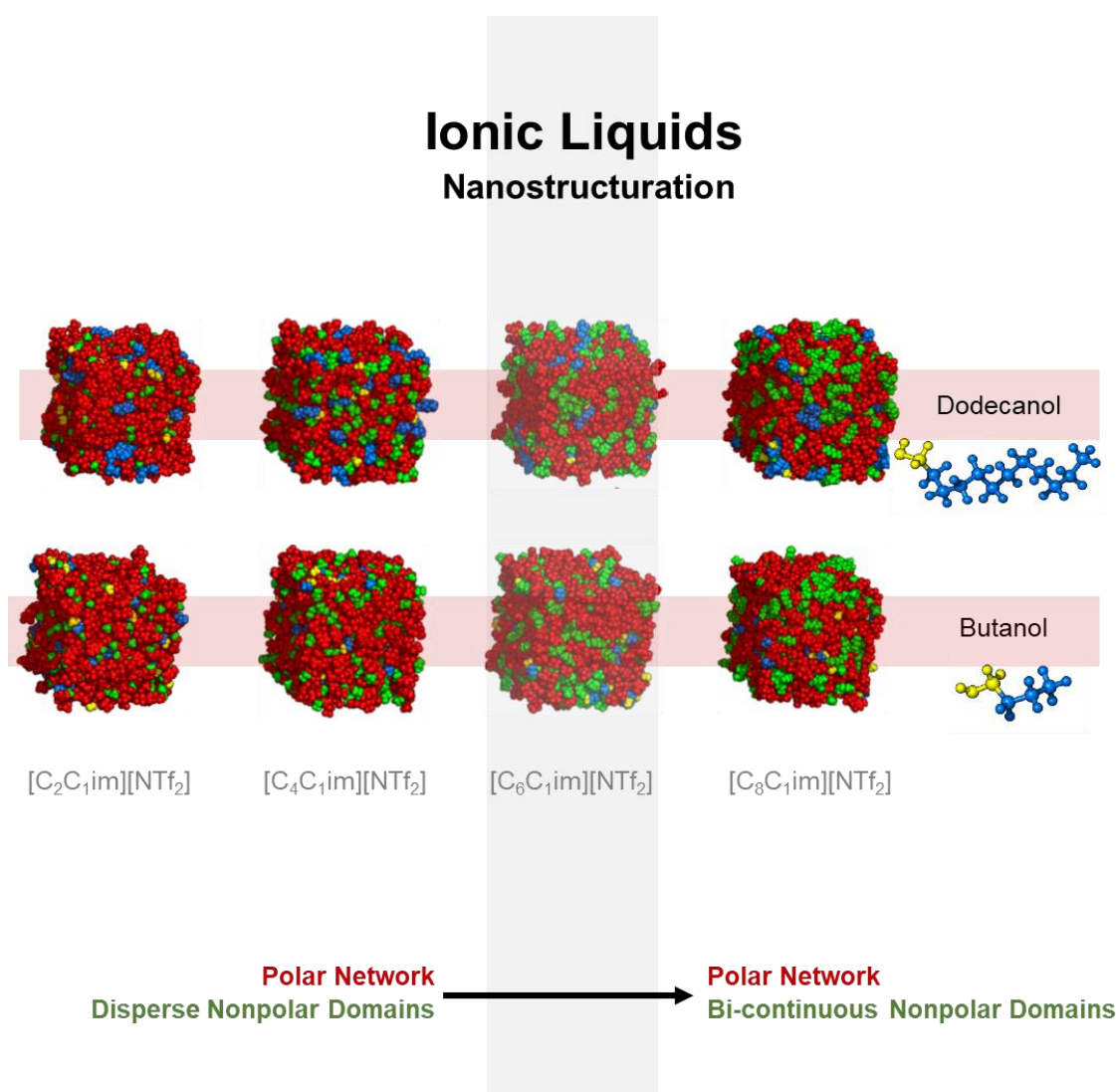


Figure 1.10. Scheme containing snapshots of simulation boxes of binary mixtures of $[C_NC_1im][NTf_2]$ ($N = 2, 4, 6, 8$) with 1-butanol and 1-dodecanol with a ratio of 5:1 (IL : ROH). The polar unit of the IL is coloured in red, the nonpolar unit of the IL is coloured in green, the polar unit of the alcohol is coloured in yellow and the nonpolar unit of the alcohol is coloured in blue. Figure was adapted from ref.[56].

Furthermore, it has been noticed that the majority of the polar part of both alcohols is interacting with the polar domains of the ionic liquids and not with other alcohol molecules. This proportion of monomers was not altered with the increase of the alkyl side chain of the cation.

Nevertheless, while the alkyl part of the alcohols tend to aggregate in $[C_2C_1im][NTf_2]$, in ILs of higher alkyl chain, the nonpolar part of the alcohols tend to dissolve into the nonpolar domain of the IL.

By last, the authors have noticed that the nanostructuration of the alcohols influences not only the association of the alcohols but also their orientation. Using the words of the authors, the IL “serves as a highly structured template for the orientation of the solutes”. This apparent ability of ILs to manipulate the orientation of its solutes is of an enormous importance from an application perspective.

1.1.4.3. Dynamics and Transport Properties

It is common knowledge, that the presence of molecular solutes, even in small quantities, decreases the viscosity of ionic liquids. For example, the presence of 1% methanol (in mass fraction) in $[C_4C_{1im}][NTf_2]$ causes a drop superior to 30% in the viscosity of this IL ^[77]. Thus, it is vital to get a molecular understanding of the effect of the molecular solute/solvent into the macroscopic properties of the fluid. Only in that way is possible to rationalize the composition-structure-property relation which would make possible the concretization of the “designer solvent” concept.

Furthermore, the understanding of the transport properties of ILs and the effect of the molecular solutes/solvents on these properties is of major importance from an application perspective.

It has been suggested that molecular solutes/solvents with high dielectric constant are the most effectives in the reduction of the viscosity of ILs^[77]. To this condition it should be added the consideration of the different size/volume of the molecules. Therefore, the interpretation should not be done only based on the molar composition of the binary system but also on the volume fraction. Finally, it should be taken into account that ionic liquids are structured into domains of different nature at the nanoscale. The molecular solute will thus, be distributed into these domains.^[77] The interpretation of the viscosity can thus give important information on the ionic movement and on the structuration of the liquid media. Furthermore, the information on the viscosity is important for interpretation of the electrical conductivities and the diffusion coefficients of IL based systems.

The electrical conductivity of ILs is originated by the mobility and orientation of cations and anions upon imposition of an electric potential difference^[78]. Therefore, the ILs conductivity depend on their mobility and number of charge carriers. Typically in IL-alcohol systems the electrical conductivity increases with a temperature increase, as the mobility of the ions increase with temperature. In addition, the electrical conductivity

of IL-alcohol binary mixtures displays a typical dependence on the composition of the system, as displayed in figure 1.11. Starting from the rich-IL to the poor-IL mixture, the electrical conductivity presents the following trend ^[77, 79]:

- low conductivity at high ionic liquid content due to the large viscosity of ILs;
- increase in the electrical conductivity with the increase in alcohol content due to the drop on the viscosity and thus, increase on the mobility of the ions;
- a maximum in electrical conductivity will be reached, which positioning will depend on the interplay between the increase of the mobility of the ions and decrease in the number of ions;
- at low IL content the ionic conductivity decreases due to the reduction in the number of ions.

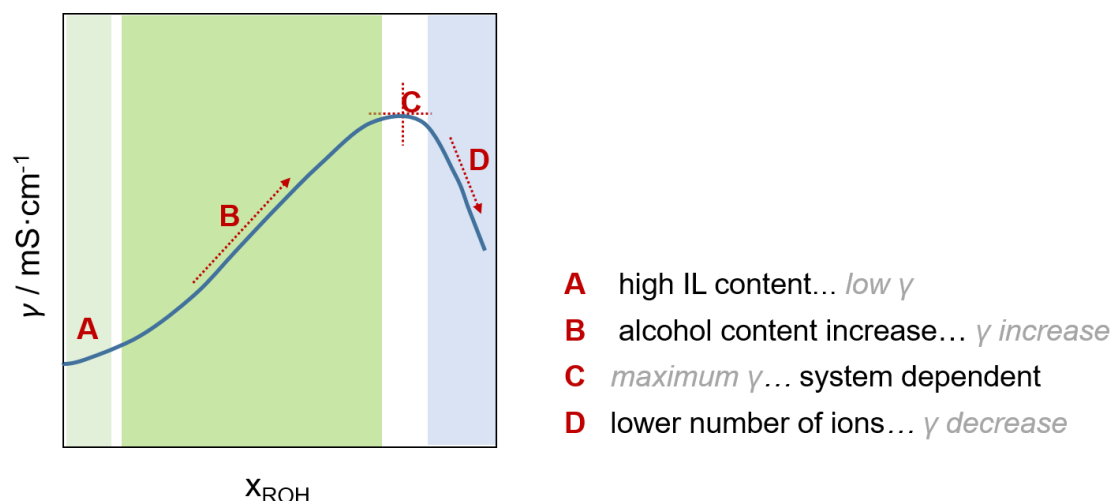


Figure 1.11. Schematic representation of the dependence of the electrical conductivity of a binary mixture constituted by an IL and an alcohol upon the composition of the mixture.

The absolute value of the maximum, as well as its positioning will depend on the structuration of the mixture and on the intermolecular interactions established. In binary mixtures constituted by ethanol and ionic liquids based in the cation $[\text{C}_2\text{C}_1\text{im}]$ and the alkylsulfate anion $[\text{RSO}_4]$ with different alkyl chain size, at 298.15 K, the maximum variate between $X_{ROH} = 0.78$ ($\gamma = 18.70 \text{ mS} \cdot \text{cm}^{-1}$, ethylsulfate $[\text{EtSO}_4]$) and $X_{ROH} = 0.87$ ($\gamma = 9.30 \text{ mS} \cdot \text{cm}^{-1}$, octylsulfate $[\text{OctSO}_4]$) ^[80]. In binary mixtures constituted by ethanol and $[\text{C}_N\text{C}_1\text{im}][\text{BF}_4]$, at 298.15 K, the maximum electric conductivity varied between

$x_{\text{ROH}} = 0.72$ ($\gamma = 18.74 \text{ mS}\cdot\text{cm}^{-1}$, $[\text{C}_4\text{C}_1\text{im}][\text{BF}_4]$), $x_{\text{ROH}} = 0.79$ ($\gamma = 12.50 \text{ mS}\cdot\text{cm}^{-1}$, $[\text{C}_6\text{C}_1\text{im}][\text{BF}_4]$) and $x_{\text{ROH}} = 0.79$ ($\gamma = 9.26 \text{ mS}\cdot\text{cm}^{-1}$, $[\text{C}_8\text{C}_1\text{im}][\text{BF}_4]$)^[81]. In binary mixtures constituted by alcohols and $[\text{C}_4\text{C}_1\text{im}][\text{NTf}_2]$, the maximum electric conductivity occurs at $x_{\text{ROH}} = 0.5$ ($\gamma = 6.77 \text{ mS}\cdot\text{cm}^{-1}$, 1-butanol) and $x_{\text{ROH}} = 0.88$ ($\gamma = 25.8 \text{ mS}\cdot\text{cm}^{-1}$, methanol)^[77].

These values reported in the literature have been associated to the structure regimes explained before. At low alcohol content, alcohol molecules are solvated into the IL according to its nanostructuration. As the alcohol content increases, alcohol molecules associate themselves in dimers and small clusters, swelling the IL structure. The continuous increase of alcohol content, leads to the percolation of the small alcohol domains which eventually ends-up breaking the IL polar network. The electric conductivity of the mixture will depend on the percolation of the domains and on the strength of the alcohol-IL, and cation-anion interaction.

The transport properties into ILs-alcohol mixtures are perhaps best explained from the analysis of the diffusive behaviour of the components of the mixture, which can be predicted using molecular dynamics, providing a molecular understanding on the dynamic of the components in the mixture.

On this topic, the works of Aparicio et al.^[82] and Varela et al.^[83] provide a good understanding into the relationship between the constitution of the mixture, the structure of the liquid phase, the intermolecular interactions and its influence on the dynamics of the components of the mixture and thus, on the macroscopic properties of transport.

The diffusivities of all components of the mixture increase with increasing alcohol concentrations. At very low alcohol concentrations, diffusion coefficients of alcohols are identical to the low diffusion coefficients of the ions. This phenomena is justified by the entrapment of the alcohol molecules into the IL structure. The increase in alcohols concentration leads to a progressive increase of the alcohols diffusion coefficient. This increase in the diffusivity is, nevertheless, considered to be slow until $x_{\text{ROH}} = 0.7$ (methanol and ethanol in $[\text{C}_6\text{C}_1\text{im}][\text{BF}_4]$ and $[\text{C}_6\text{C}_1\text{im}][\text{PF}_6]$), $x_{\text{ROH}} = 0.8$ (ethanol in $[\text{C}_4\text{C}_1\text{im}][\text{NTf}_2]$) and $x_{\text{ROH}} = 0.9$ (methanol and ethanol in $[\text{C}_6\text{C}_1\text{im}]\text{Cl}$). In accordance, the increase in the diffusivity of alcohols in ILs is rather moderate until high alcohol concentrations. These results evidence the increase in the alcohol fluidity, despite of the entrapment of the molecules into the IL structure. These results indicate the existence of aggregation of the alcohol molecules and enlargement of the IL structure possibly by separation of the polar network strands. At high alcohol concentrations, the diffusion coefficients of alcohols increases rapidly, which is related to the percolation of alcohol domains and breakage of the IL polar networks.

Regarding the diffusivity of the ions, they both follow an almost parallel trend along the composition range. Furthermore, at high IL content, the diffusion coefficient of the alcohol is identical to the diffusion coefficient of the ions. As the alcohol content increases, the diffusion coefficient of the ions increase. This increase is much more modest than the increase in the diffusivity of the alcohol. In addition, in all the reported systems the cation presents higher diffusivity than the anion, evidencing the existence of alcohol-anion interactions. In addition, the diffusivity of the alcohols seems to be higher in the ILs constituted by polyatomic anions than with the chloride anion, evidencing stronger interaction of the alcohols with the halide anion.

1.1.4.4. Excess Volume

Generally, the magnitude of the excess molar volumes of the binary mixtures constituted by alcohols and ionic liquids are less than 1% (typically less than $1 \text{ cm}^3 \cdot \text{mol}^{-1}$) of the molar volumes of the pure components (typically in the order of $100 \text{ cm}^3 \cdot \text{mol}^{-1}$, e.g. 1-butanol, and $300 \text{ cm}^3 \cdot \text{mol}^{-1}$, e.g. $[\text{C}_6\text{C}_1\text{im}][\text{NTf}_2]^{[69]}$). This phenomenon is indicative of the proximity of this behaviour to the ideality.

Nevertheless, the structuration of the alcohol-IL mixtures depends on its constituents and its concentration. Different molecular shapes, sizes and potentials for intermolecular interactions lead to different “packing effects” of the species in the mixture.

Binary mixtures based in imidazolium cations and linear alcohols commonly present an “S shape” dependence of its excess molar volume on the concentration, as depicted in figure 1.12. In mixtures containing small alcohols, the maximum excess volume occurs at low alcohol content. As the size of the alcohol increases, the maximum excess molar volume seem to be positioned at higher alcohol contents. In all mixtures, the minimum in excess molar volume was located at high alcohol concentrations. Furthermore, the excess molar volume of the binary mixtures constituted by methanol/ethanol and $[\text{C}_3\text{C}_1\text{im}][\text{NTf}_2]^{[84]}$ / $[\text{C}_6\text{C}_1\text{im}][\text{NTf}_2]^{[69, 85]}$ seems to be identical in all concentration range. Nonetheless, the binary mixture constituted by methanol and $[\text{C}_8\text{C}_1\text{im}][\text{NTf}_2]^{[86]}$ presents significantly different excess molar volumes. The excess molar volumes of the binary mixtures constituted by 1-propanol and $[\text{C}_3\text{C}_1\text{im}][\text{NTf}_2]^{[84]}$ / $[\text{C}_6\text{C}_1\text{im}][\text{NTf}_2]^{[69, 85]}$ also present significant differences. In these particular mixtures, the increase in the alkyl size of the cation seems to conduct to a behaviour closer to the ideality. Overall, regarding binary mixtures constituted by alcohols and

imidazolium-based ILs with $[\text{NTf}_2]$ anion, the increase in the alkyl chain of the alcohol seem to contribute to a less contractive behaviour of the mixture.

In figure 1.13 is depicted the excess molar volume of binary mixtures constituted by ethanol/1-propanol and ionic liquids based in pyrrolidinium^[87, 88], pyridinium^[88] and imidazolium^[84] cations, as well as, $[\text{NTf}_2]$ anions. The analysis of this figure evidences that the cation did not present significant effect on the excess molar volumes of mixtures containing ethanol. In mixtures containing 1-propanol, significant differences were found between the different cations pyridinium, pyrrolidinium and imidazolium. Mixtures with imidazolium-based cation present the most expansive behaviour.

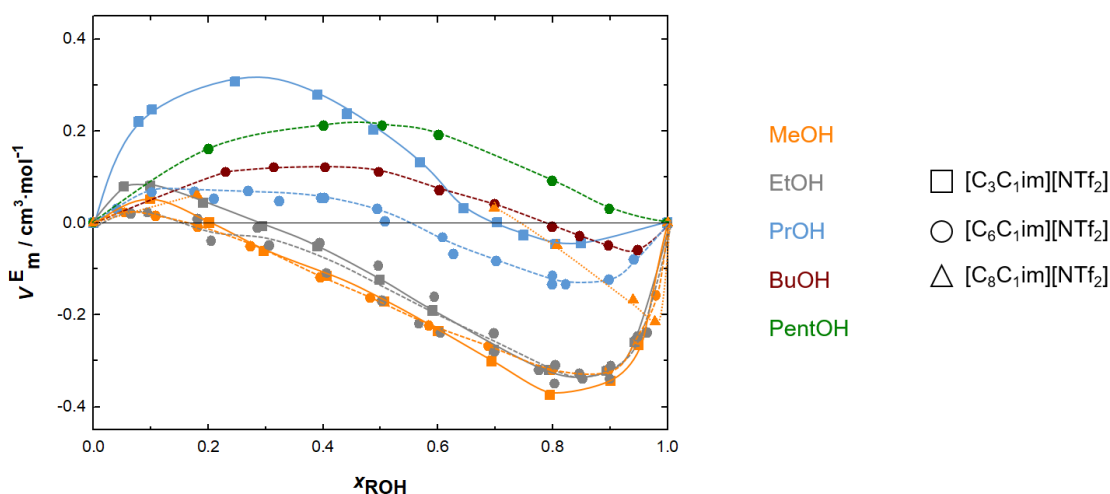


Figure 1.12. Excess molar volume of binary mixtures constituted by linear alcohols (from 1-methanol to 1-pentanol) and $[\text{C}_N\text{C}_1\text{im}][\text{NTf}_2]$ ionic liquids ($N = 3, 6$ and 8) as a function of the molar fraction of alcohol. The different colours of the data points are associated to the different alcohols that constitute the mixture and the different shape refer to the ionic liquids. The lines are just guide lines to the eyes. Data from refs. [69, 84-86].

Regarding the effect of the anion in alcohol-ILs binary mixtures, alcohol- $[\text{C}_8\text{C}_1\text{im}][\text{BF}_4]$ ^[89] mixtures present identical volumetric behaviour to the alcohol- $[\text{C}_6\text{C}_1\text{im}][\text{NTf}_2]$ ^[69, 85] mixtures, as depicted in figure 1.14. However, mixtures containing $[\text{C}_6\text{C}_1\text{im}][\text{NTf}_2]$ systematically evidenced less contractive behaviour. In opposition, binary mixtures of methanol, ethanol and 1-propanol with $[\text{C}_8\text{C}_1\text{im}]\text{Cl}$ ^[90] present negative excess molar volume in all concentration range. The negative excess molar volume indicates that the species are efficiently packed in the mixture and/or strong attractive interactions are present.

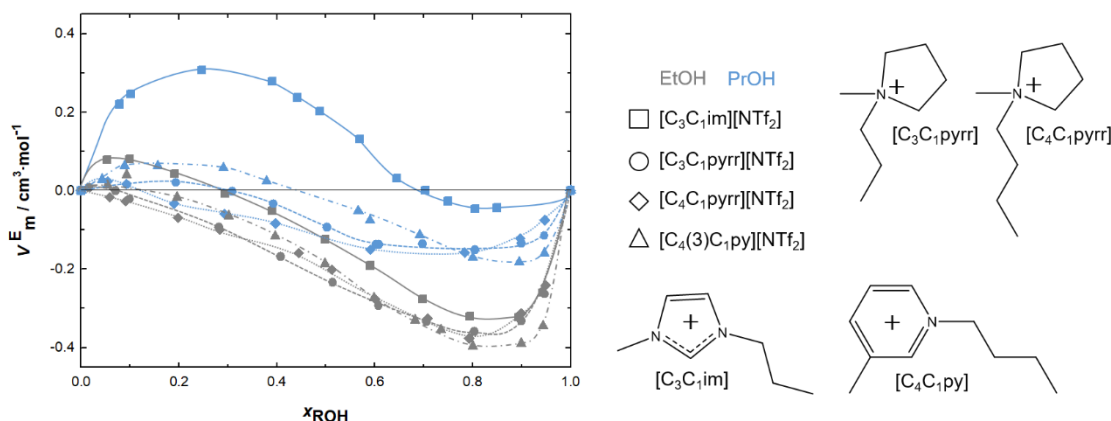


Figure 1.13. Excess molar volume of binary mixtures constituted by ethanol / propanol and ionic liquids composed by different cations ($[\text{C}_3\text{C}_1\text{im}][\text{NTf}_2]$, $[\text{C}_3\text{C}_1\text{pyrr}][\text{NTf}_2]$, $[\text{C}_4\text{C}_1\text{pyrr}][\text{NTf}_2]$ and $[\text{C}_4\text{C}_1\text{py}][\text{NTf}_2]$) as a function of the molar fraction of alcohol. The different colours of the data points are associated to the different alcohols that constitute the mixture and the different shape refer to the different ionic liquids. The lines are just guide lines to the eyes. Data from refs. [84, 87, 88].

In summary, binary mixtures containing small ILs and small alcohols tend to have negative excess molar volumes. Different anions can cause an enhancement of this contraction effect on the mixture.

The increase in the alkyl chain of alcohols seem to cause an expansive effect on the mixing, which is translated in an “S shaped” diagram of the dependence of the excess molar volume upon the concentration of the mixture. Further increase on the alkyl chain of alcohol increase this expansive effect, resulting in a positive excess molar volumes in all the compositions of the mixture. This effect is clear in figure 1.12, where the excess molar volume of the binary mixture of 1-pentanol and $[\text{C}_6\text{C}_1\text{im}][\text{NTf}_2]$ is represented.

Costa Gomes et al.^[86] have studied the effect of the alkyl chain of the alcohol on the volumetric properties of alcohol-IL mixtures by plotting the excess molar volume at equimolar composition of mixtures of alcohols with five ionic liquids as a function of the number of carbon atoms in the alcohol alkyl chain. The authors^[86] have also observed an increase in the excess molar volumes of the mixtures with the increase in the size of the alcohol that constitute the mixture.

As demonstrated, the nature of the cation and anion, as well as, the size of both ions and alcohols lead to different “packing” and interactions of the species in the mixture. This phenomena results in different volumetric behaviour of the mixture.

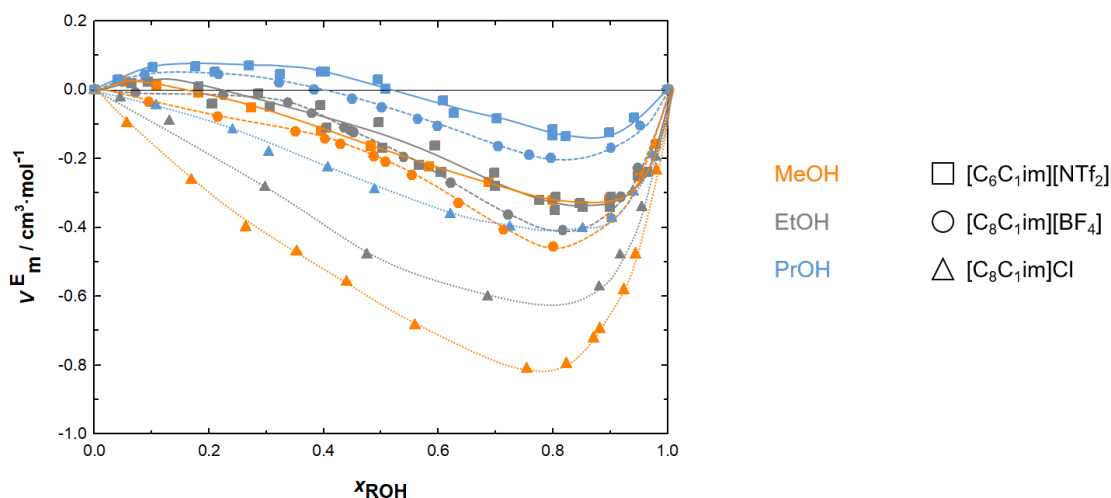


Figure 1.14. Excess molar volume of binary mixtures constituted by linear alcohols (methanol, ethanol and propanol) and imidazolium-based ILs with different anions ([NTf₂], [BF₄] and Cl) as a function of the molar fraction of alcohol. The different colours of the data points are associated to the different alcohols that constitute the mixture and the different shape refer to the different ionic liquids. The lines are just guide lines to the eyes. Data from refs. [85, 89, 90].

In accordance, the full understanding of the effects governing the volumetric behaviour of alcohol-IL binary mixtures would give important insights on the structuration and interactions present in these mixtures.

Despite of the growing number of volumetric studies conducted in binary mixtures constituted by alcohol and ILs, no work has been found reporting the full understanding of the structuration and composition of the mixture in its volumetric behaviour. The full understanding would thus require a systematic overview of the alcohol-IL mixtures studied in literature (and perhaps some still missing) and complementarity with results from other techniques which could provide insight into the structuration and interactions. (Systematization of the volumetric behaviour of ILs-water binary mixtures has been already published.^[61])

1.1.4.5. Enthalpic Properties of Mixing

As stated in the review of Costa Gomes et al.^[62] “the enthalpic quantities of mixing are closely related to the nature of molecular or ionic interactions and to the microscopic structure of mixtures”. Therefore, they constitute an excellent strategy to obtain further information on the molecular understanding and establishment of relations composition-structuration-properties in IL mixtures.

Considerable amount of data, regarding the energetic properties of mixing of alcohols and ILs, has already been reported in the literature. Contrarily to what was verified for alcohols-ILs volumetric behaviour, some work was already done regarding the systematization of the enthalpic data existent in the literature.

Kurnia and Coutinho^[91] have presented an overview into the excess enthalpies of binary mixtures composed by molecular solvents and ionic liquids and proposed the utilization of COSMO-RS as a predictive tool to be used as an initial screening method, capable of selecting significant combinations molecular compound-IL for a given application.

More recently, Costa Gomes et al.^[62] have published a very complete review on the enthalpic quantities of mixing involving ionic liquids published until May 2015. This review had related, through the utilization of the appropriate thermodynamic formalism, the enthalpy of mixing, the enthalpy of solution, the excess enthalpy and its partial molar quantities. The creation of a reliable and systematized “database” for these properties is very important in the perspective of systematization of the systems studied and establishment of relations between the results and the composition and structuration of the mixture. Nevertheless, the systematic conversion and relation between these mixing properties, allowing comparison between data obtained by different authors and methodologies, is of paramount importance given the high dispersion of the results commonly found between different authors^[62, 86, 92].

Regarding the excess molar enthalpy of mixing of binary mixtures constituted by alcohol and ILs, only a few systems have been studied in the whole composition region. Furthermore, for proper comparison, the data must be analysed at the same temperature. Considering the data available in literature, in figure 1.15 is summarized the excess molar enthalpy of mixing of some alcohol-IL binary mixtures, at equimolar composition, at 298.15 K. The data represented in figure 1.15 refers to the systems studied in the literature which included the equimolar composition. The only extrapolation considered refers to the $[C_4py][BF_4]$ / $[C_4(2)C_1py][BF_4]$ and 1-propanol, which mixing behaviour was studied in the concentration range $0 < x_{ROH} < 0.46$ ^[62, 93, 94].

From the analysis of the figure 1.15 is visible that for all binary systems represented (with one exception), the excess molar enthalpy, at equimolar composition, increase with the increase of the alcohol size. Between the represented data, it was found a unique exception, in binary mixtures constituted by alcohols and 1-butylpyridinium tetrafluoroborate, $[C_4py][BF_4]$ ^[62, 93], the excess molar volume at equimolar composition is smaller for mixtures containing alcohols of bigger alkyl chain.

Furthermore, the excess molar enthalpy at equimolar composition is endothermic for the majority of the systems. The two exceptions are the binary mixtures composed by ionic liquids 1-alkyl-3-methylimidazolium dimethylphosphate, $[C_N C_1 im][DMP]$ ^[62, 95, 96] and the mixture of 1-propanol and $[C_1 C_6 im][BF_4]$ ^[97].

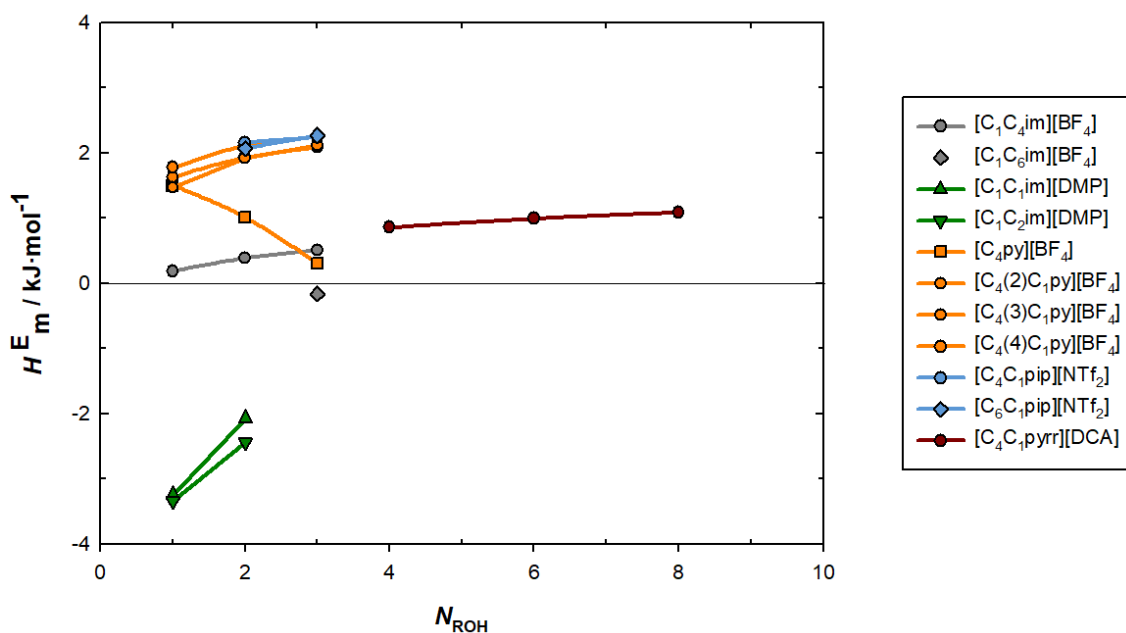


Figure 1.15. Excess molar enthalpy of mixing at equimolar composition of binary mixtures constituted by linear alcohols (methanol, ethanol, 1-propanol, 1-butanol, 1-hexanol and 1-octanol) and ionic liquids composed by different cations (imidazolium [im], pyridinium [py], piperidinium [pip] and pyrrolidinium [pyrr]) and anions (tetrafluoroborate $[BF_4]$, bis(trifluoromethanesulfonyl)imide $[NTf_2]$, dimethylphosphate [DMP]). The excess molar enthalpy of the mixture is represented as a function of the number of carbons in alcohol's alkyl chain, N_{ROH} . The different colours of the data points are associated to the different alcohol-IL binary systems and the different shape refer to the different alkyl size of the ionic liquids. The lines are just guide lines to the eyes. Data from refs.[62, 93-101].

Overall, it's notorious that the majority of the binary mixtures studied refer to small alcohols (methanol, ethanol and 1-propanol). This may be partially explained by the decrease of the solubility with the increase in alcohol alkyl chain. Nevertheless, as shown before, the increase of the alkyl chain of the IL, increase the solubility of the alcohols. Unfortunately, the increase in the alkyl chain of the ILs usually increases the viscosity of the IL, creating experimental difficulties.

From the analysis of the figure 1.15 is notorious that the existent results suggest the existence of an anion and cation differentiation effect. The amount of data collected do not allow to take more insightful conclusions.

Regarding the partial excess molar enthalpy of the alcohol at infinite dilution, also called, enthalpy of solution at infinite dilution, the data published in the literature was collected and summarized in figure 1.16. It must be highlighted that the measurements at infinite dilution are not experimentally feasible. Instead, experimental measurements are desirably made as close as possible to the infinite dilution of the alcohols and the partial excess molar enthalpy at infinite dilution is extrapolated afterwards. Therefore, the accuracy of this value is, between other factors, dependent on the distance of the experimental measurements to the infinite dilution. Furthermore, it is unfortunately common that partial excess molar enthalpy at infinite dilution reported in the literature by different authors present high deviations [62, 86, 92]. Accordingly, conclusions obtained by comparing data of different systems, obtained by different authors and techniques must be cautious. Differences reported between different authors could be of the same magnitude of differences found between different alcohol-IL systems.

Regarding the data collected, the enthalpy of solution at infinite dilution of alcohols in 1-alkyl-3-methylimidazolium ethylsulfate $[C_N C_1 im][EtSO_4]$ ^[102], 1-alkyl-3-methylimidazolium hexafluorophosphate $[C_N C_1 im][PF_6]$ ^[103] and 1-alkyl-3-methylimidazolium bis(trifluoromethanesulfonyl)imide $[C_N C_1 im][NTf_2]$ ^[86, 104, 105] was obtained from the extrapolation of the partial molar excess enthalpy to infinite dilution. The partial molar excess enthalpy of alcohols in the mentioned ILs was determined by isothermal titration calorimetry, at low alcohol concentration.

The enthalpy of solution at infinite dilution of alcohols in 1-alkyl-1-methylpyrrolidinium dicyanamide $[C_4 C_1 pyr][DCA]$ ^[101], and 1-alkyl-1-methylpiperidinium bis(trifluoromethanesulfonyl)imide $[C_N C_1 pip][NTf_2]$ ^[100] was derived from the measurement of the heat of mixing, in all composition range, using isothermal titration calorimetry. However, several measurements have been done in low concentrations of

alcohol, which should allow to extrapolate the partial excess molar enthalpy with accuracy.

The same methodology has been applied to the determination of the enthalpy of solution at infinite dilution of methanol/ethanol in 1-alkyl-3-methylimidazolium dimethylphosphate, $[C_N C_1 \text{im}][\text{DMP}]$ ^[95, 96]. Unfortunately, the enthalpy of mixing of these binary systems has been determined only at five compositions. No alcohol concentration inferior to $x_{\text{ROH}} < 0.2$ was studied. Therefore, it's possible that the enthalpy of solution of methanol/ethanol in $[C_N C_1 \text{im}][\text{DMP}]$ present deviations from real value.

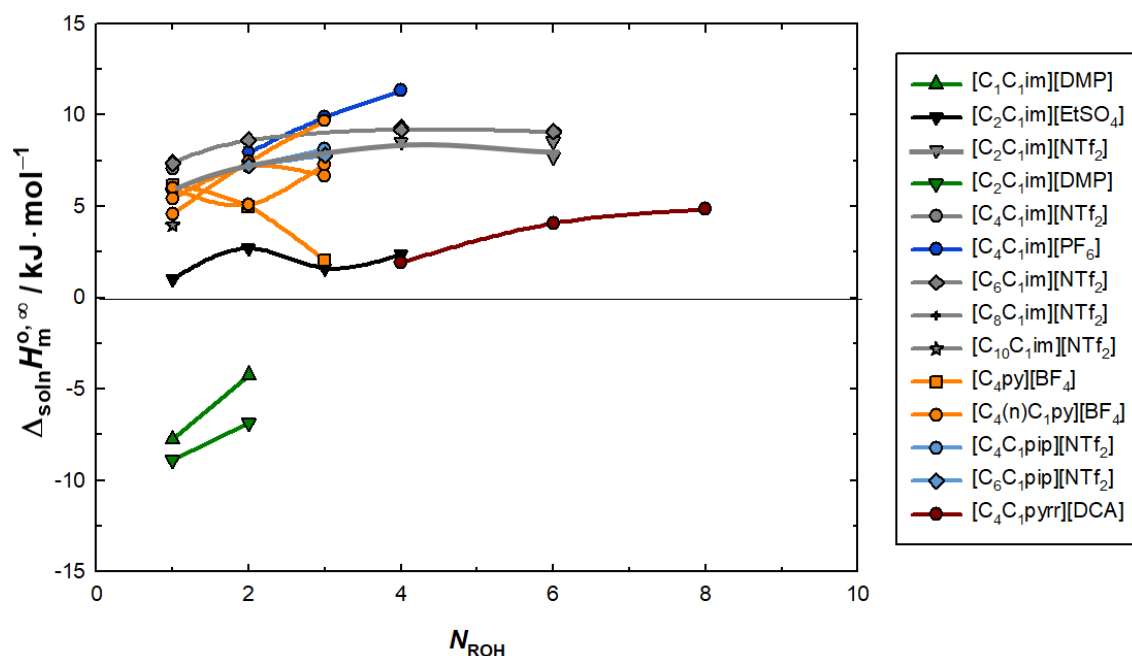


Figure 1.16. Enthalpy of solution at infinite dilution of alcohols in ionic liquids as a function of the number of carbons in the alkyl chain of the alcohol, N_{ROH} . The different colours of the data points are associated to ILs constituted by different cations (imidazolium [im], pyridinium [py], piperidinium [pip] and pyrrolidinium [pyrr]) and anions (tetrafluoroborate $[\text{BF}_4]$, bis(trifluoromethanesulfonyl)imide $[\text{NTf}_2]$, dimethylphosphate $[\text{DMP}]$, hexafluorophosphate $[\text{PF}_6]$, dicyanamide $[\text{DCA}]$, ethylsulfate $[\text{EtSO}_4]$) and the shape refers to the different alkyl size of the ionic liquids. The lines are just guide lines to the eyes. Data from ref. [62, 86, 93-96, 98-105].

From the analysis of figure 1.16, is notorious that the solution of alcohols is endothermic in all the ionic liquids represented, with exception of ionic liquids 1-alkyl-3-methylimidazolium dimethylphosphate, $[C_N C_1 \text{im}][\text{DMP}]$. In addition, the increase in the length of the alcohol seem to lead to a most endothermic enthalpy of

solution at infinite dilution, at least for the smaller alcohols (methanol, ethanol, 1-propanol). The solution of 1-butanol and 1-hexanol in $[\text{C}_2\text{C}_{1\text{im}}][\text{NTf}_2]$ and $[\text{C}_6\text{C}_{1\text{im}}][\text{NTf}_2]$ seems to generate identical amounts of heat.

Additionally, the enthalpy of solution of alcohols in ionic liquids constituted by different anions seem to follow the trend: $[\text{PF}_6] > [\text{BF}_4] \sim [\text{NTf}_2] > [\text{DCA}] \sim [\text{EtSO}_4] > [\text{DMP}]$. No systematic behaviour was found, regarding the effect of the alkyl chain of the IL cation.

As demonstrated, the nature of the cation and anion, as well as, the size of the alkyl chain of both ions and alcohols affect the mixing behaviour of alcohols-ILs mixtures. The enthalpic quantities of mixing are related to the microscopic structure of mixtures, as well as, the interactions present. Hence, the understanding of the effects governing the enthalpic behaviour of alcohol-IL binary mixtures, in infinite dilution and in all the range of concentrations, would give important insights on the structuration and interactions present in these mixtures.

As shown, some work have been done on the enthalpic quantities of mixing of alcohol-IL binary systems. Overall, the existence of some anion differentiation effect seem to be determinant. Nevertheless, some effects related to the cation nature and size of the alkyl chain are also suggested.

No work was found relating the mixing enthalpy to the relative effect of each component present. The full enthalpic characterization of the alcohol-IL systems from the infinite dilution of alcohols in ILs, to the ILs in alcohols, passing through mixtures of alcohol and IL at different compositions could provide insightful understanding of the alcohol-IL systems. The recognition of the influence of that systematic characterization over the enthalpic/energetic quantities of mixing was already expressed in the review of Costa Gomes et al.^[62]. Their revision of the mixtures involving ionic liquids is a valuable tool to recognize the state of the art on the topic (from the point of view of enthalpic quantities) and to understand the work that could be done to expand the knowledge on the subject.

1.2. Concepts on the Enthalpic Properties of Mixing

In this section an overview on the energetic (enthalpic) properties of mixing will be presented, focusing in the presentation of the main thermodynamic concepts that will be used in this thesis, as well as, the adopted terminology and formalism.

To understand how insightful the enthalpic quantities of mixing can be, regarding the solvation in ILs, is first necessary to comprehend the relative importance of the solute-solvent and solvent-solvent interactions, as well as, how they contribute to the enthalpic quantities of mixing and what is the effect of the solute concentration.

1.2.1. Solvation

Solvation is the designation attributed to the transference of a solute in its gaseous phase to a solvent in its liquid phase. Accordingly, in this thesis, the term enthalpy of solvation always refer to the heat absorbed or released upon the transference of a solute, in the gas phase, to a solvent, in its liquid phase, at constant pressure and temperature. Furthermore, according to this definition, condensation can be interpreted as a solvation process, in which the solute and the solvent have the same chemical composition.

The solvation process is commonly interpreted as a hypothetical sum of two main steps: the creation of a cavity into the solvent and the transference of the solute into this cavity. A scheme on the solvation process and its dissection in the two hypothetical steps is depicted in figure 1.17.

In this thesis, the enthalpy of solvation was studied at (hypothetical) infinite dilution conditions. At infinite dilution, is considered a model in which a unique solute molecule is transferred from the gaseous phase to the solvent. Therefore, in the final state, a unique solute molecule will be present, surrounded by solvent.

Considering this model, solute-solute interactions are absent in the whole solvation process. Furthermore, as a unique molecule is present in the solvent, it is considered that the solvent will maintain the structure, interactions and properties. Nevertheless, in some cases, significant local alteration may be present in the vicinity of the solute molecule. As it is a unique solute molecule, it will not affect further the structuration of the solvent.

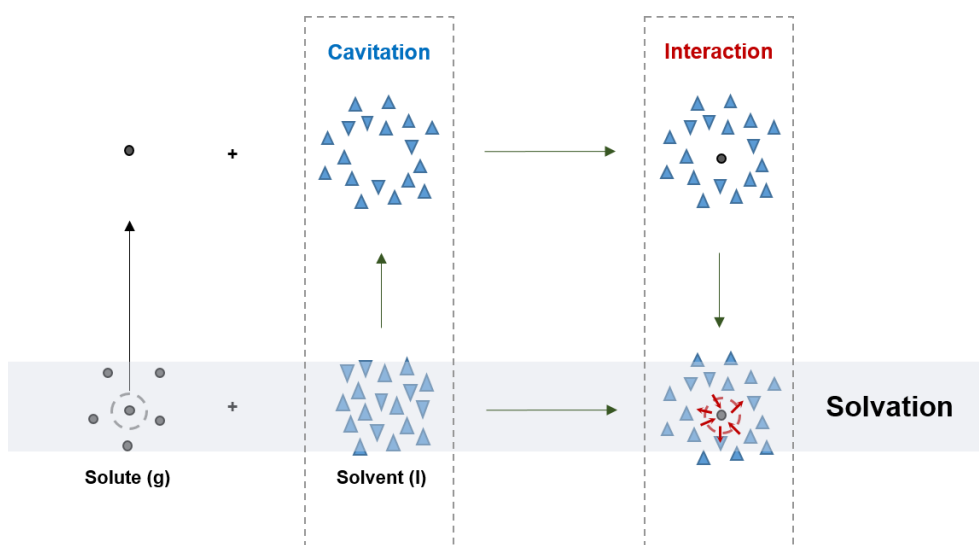


Figure 1.17. Schematic diagram of the solvation process and its dissection in two hypothetical steps: cavitation of the solvent and establishment of solute-solvent interactions.

Cavitation

The creation of a cavity into the solvent will depend on the interplay between the cohesive energy density of the solvent and its internal pressure. The cohesive energy density of the solvent (*ced*) is the energy required to disrupt the intermolecular interactions established between the solvent molecules, per unit of volume. The cohesive energy density can be calculated based in the enthalpy of vaporization of the solvent, as follows:

$$ced = \frac{\Delta_l^g H_m^o - R \cdot T}{V_m}, \quad (1.4)$$

where R is the gas constant, T is the temperature and V_m is the molar volume of the solvent. The internal pressure of the solvent (P_i) is related with the capacity of the solvent to reorganize its molecules to create a cavity without the breakage of the intermolecular interactions. In other words, the internal pressure of the solvent describes the change in its internal energy when the intermolecular distance between the molecules of the solvent increase, without disruption of the intermolecular interactions present. In accordance, this concept may be described in the form of an equation, as the effect on

the internal energy (E) of the solvent caused by a small modification in its volume (V), at constant temperature (T):

$$P_i = \left(\frac{\Delta E}{\Delta V} \right)_T. \quad (1.5)$$

The interplay between the cohesive energy density of the solvent and its internal pressure may be evaluated as the ratio:

$$rt = \frac{P_i}{ced}, \quad (1.6)$$

in which solvents which ratio is small, $rt \leq 0.80$, are denominated as “stiff” or “tight” solvents once that its cohesive energy density is superior that its internal pressure ^[106]. On the contrary, solvents which internal pressure is superior to its cohesive energy density, $rt \geq 1.20$, are considered “loose” solvents ^[106]. Given the uncertainties associated, deviations of the ratio in the order of $rt \pm 0.05$ are generally considered to be non-significant ^[106].

The solvation of a small solute in water (solute $< 3 \text{ \AA}$) allow to better understand the interplay between ced and P_i . Water presents a much higher ced than P_i , which results in a ratio $rt = 0.07$. Therefore, the solvation of a small molecule in water, which will involve the creation of a cavity, will preferentially occur through re-orientation of the solvent molecules without sacrificing the intermolecular interactions. Otto^[107] suggests that as long as the radius of the solute is inferior to 10 \AA , the water hydrogen bonds may be maintained. To bigger solutes, these intermolecular interactions have to be sacrificed for the creation of the cavity.

Nonpolar solvents, as alkanes, present similar values of cohesive energy density and internal pressure, $rt = 1$ ^[107]. Alcohols, in comparison, could be considered “tight” solvents as the ratio between internal pressure and cohesive energy density is smaller than 0.8 (from 1-propanol to 1-nonanol, $0.5 < rt < 0.8$) ^[108, 109]. According to the results obtained by Kumar and Singh^[108] for the most common ionic liquids, the ratio of these compounds is in the range: $0.6 < rt < 1.0$.

Solute-solvent Interaction

After the creation of a cavity in the solvent, the step of the transference of the solute from its gaseous phase to the solvent must be considered. Upon the transference of the solute to the cavity formed in the solvent, solvent repositioning and reorientation around the solute may occur, as well as, a possible adjustment of the solute structure and the establishment of concomitant solute–solvent interactions. Contrarily to the endothermic character of the cavitation process, the establishment of solute-solvent interactions play an exothermic contribution to the solvation process. Therefore, the magnitude of the solute-solvent interactions established and its capacity to overcome the energetic cost of the cavity creation in the solvent, will determine the exothermic/endothermic character and magnitude of the solvation process.

In accordance, the enthalpy of solvation must always be interpreted as an interplay between the endothermic contribution of the cavitation process and the exothermic contribution of the solute-solvent interactions established.

1.2.2. Solution

Solution is the designation attributed to the transference of a solute in its liquid, pure phase, to a solvent, also in its liquid phase. In this thesis, the term enthalpy of solution refers to the heat absorbed or released upon the transference of a solute to a solvent, both in its liquid phase, at constant pressure and temperature. In this thesis, the enthalpy of solution was studied at (hypothetical) infinite dilution conditions, in which a unique solute molecule is transferred to the solvent. Accordingly, solute-solute interactions are absent of the final solution.

This process is commonly interpreted as a hypothetical sum of three main steps: breaking of solute–solute interactions (in its initial liquid state), creation of a cavity in the solvent and transference of a solute molecule to the cavity accompanied by the repositioning and reorientation of the solvent molecules around the solute, possible adjustment of the structure of solute molecule and establishment of concomitant solute–solvent interactions. As a result, the enthalpy of solution can be dissected in the sum of the vaporization of the solute with its solvation in the solvent, as depicted in figure 1.18.

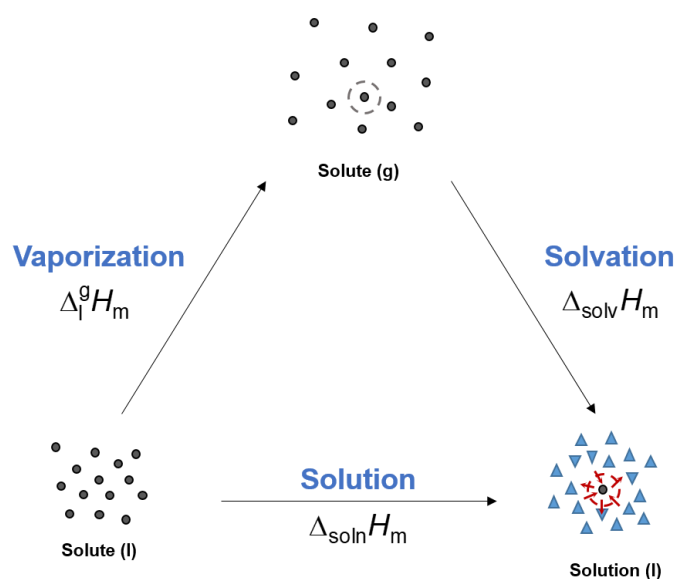


Figure 1.18. Schematic diagram of the solution process and its dissection in two hypothetical steps: vaporization of the solute and its solvation.

It should be noted that the vaporization of the solute will play an endothermic contribution to the enthalpy of solution, as well as the cavitation of the solvent. Both endothermic contributions will be opposed by the exothermic contribution of the solute-solvent interactions established. The endothermic/exothermic contribution of each of the three hypothetical steps which constitute the enthalpy of solution are schematized in figure 1.19. As represented in this figure, depending on the magnitude of the energy associated to each of the three processes, the enthalpy of solution will be 0 (ideal solution), endothermic or exothermic.

In the case of an ideal solution, the solute-solvent interactions established equalize the cost of breaking the solute-solute and solvent-solvent interactions. The solution of water in water is an excellent example of an ideal solution. As the solute and the solvent are constituted by the same molecules, the interactions broken will be re-established upon addition of the solute to the solvent.

In an endothermic solution the solute-solvent interactions established are not enough to compensate for the endothermic contribution of the vaporization of the solute and the cavitation of the solvent. Although, the enthalpy of solvation may be exothermic as long as the exothermic contribution of the solute-solvent interactions surpass the endothermic contribution of the cavitation of the solvent.

In the case of an exothermic enthalpy of solution, the solute-solvent interactions established compensate and surpass the magnitude of the endothermic contribution of the vaporization of the solute and the cavitation of the solvent and consequently, the referent enthalpy of solvation is always exothermic.

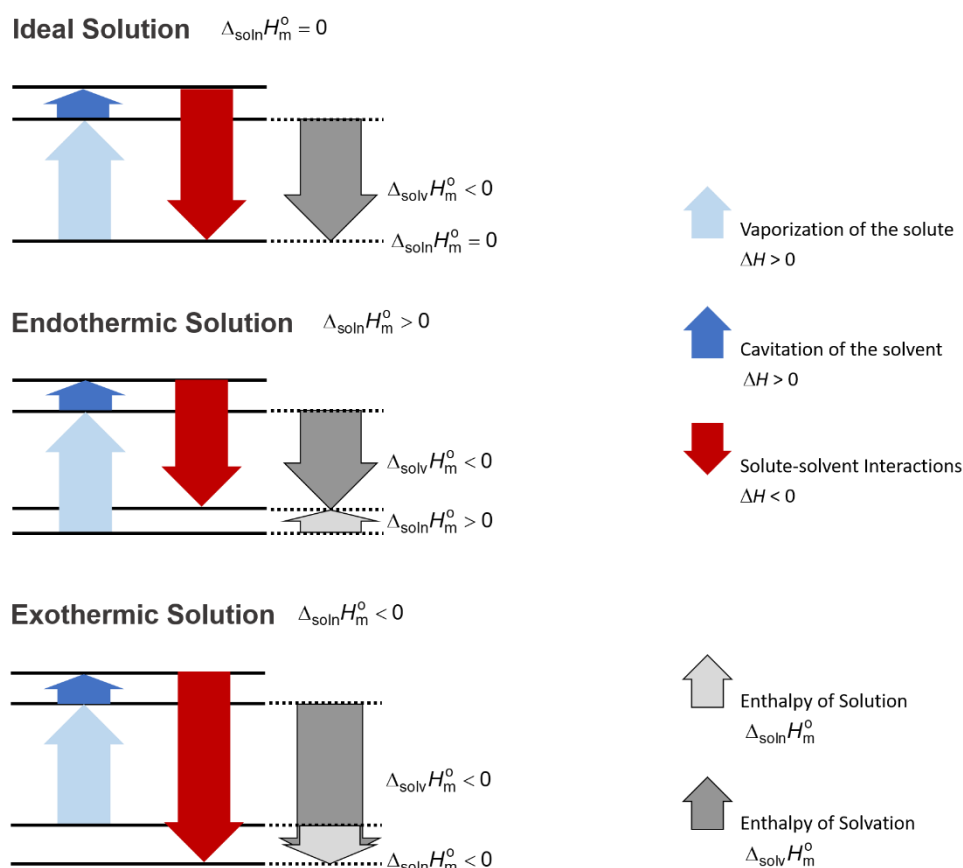


Figure 1.19. Schematic diagram of the contribution of the three hypothetical steps for the endothermic / exothermic enthalpy of solution and solvation.

The interpretation models described apply for solutions in infinite dilution conditions. In other words, these interpretation models are valid as long as solute molecules are completely surrounded by solvent molecules in a way that solvent properties are not modified and solute-solute interactions do not exist.

However, the logic of interpretation of these models can be applied to binary mixtures, as long as, the possible presence of solute-solute interactions and possible existence of structural modifications is considered and taken into account.

1.2.3. Excess Enthalpy of Mixing

The enthalpy of mixing refers to the total enthalpy change (heat released or absorbed at constant pressure and temperature) upon mixing of two pure compounds, in the same physical state. This quantity can be expressed as:

$$\Delta_{\text{mix}} H = H_{\text{mix}} - \sum_i n_i \cdot H_i^* \quad (1.7)$$

in which $\Delta_{\text{mix}} H$ is the total enthalpy exchange upon mixing, expressed as an extensive property, H_{mix} and H_i^* are the enthalpy in the mixture and the enthalpy of the component “i” in its pure state. The molar quantity is expressed as n , which represents the amount of substance present in the mixture:

$$n = \sum_i n_i . \quad (1.8)$$

In this thesis, the enthalpy is going to be expressed as a molar quantity:

$$\Delta_{\text{mix}} H_m = H_{\text{mix}, m} - \sum_i (x_i \cdot H_{i, m}^*), \quad (1.9)$$

where x_i is the mole fraction of the component “i”. As there is no absolute reference for enthalpy, to simplify the equation, the enthalpy of the pure components is considered to be 0. In accordance, equation 1.9 is simplified as follows:

$$\Delta_{\text{mix}} H_m = H_{\text{mix}, m} . \quad (1.10)$$

In the thermodynamics of mixing, the knowledge of the excess properties is relevant as it provides a measure of the distance of the mixture to the ideal behaviour. Nevertheless, in an ideal mixture, the $\Delta_{\text{mix}} H = 0$. In consequence, the excess enthalpy of mixing is numerically equivalent to the enthalpy of mixing:

$$H_m^E = \Delta_{\text{mix}} H_m (\text{real mixture}) - \Delta_{\text{mix}} H_m (\text{ideal mixture}) = \Delta_{\text{mix}} H_m (\text{real mixture}) \quad (1.11)$$

It should be referred that the enthalpy of solution refers to the same process as the enthalpy of mixing (mixing of two pure compounds, in the same physical state, at constant pressure and temperature). However, the enthalpy of solution refers to the transference of the solute to a solvent. In accordance, the composition of the solvent is fixed from the initial to the final state and only the solute composition alters.

In this thesis, the concept of enthalpy of solution (and solvation) will be addressed to discuss infinite dilution conditions. In opposition, the enthalpy of mixing and excess enthalpy of mixing will be used to refer to binary mixtures where the composition may change from infinitely dilute to infinitely concentrate, from $x_i = 0$ to $x_i = 1$, in all ranges of composition (or as allowed by the mutual solubility of the components).

Similarly to the solution and solvation models, it is possible to imagine a simplified general process of mixing of two components by two steps: breaking the intermolecular interactions of the two components in its pure state followed by the establishment of new interactions upon mixing of the components. Depending on the structuration and composition of the mixture formed, intermolecular interactions component 1 - component 2, component 1 – component 1 and component 2 – component 2 are possible. For simplification of the interpretation, it is considered than when component 1 – component 1 and component 2 – component 2 intermolecular interactions are established in the mixture, they equal the ones that have been broken in its pure state.

In an ideal mixture, the enthalpy of mixing or the excess molar enthalpy is 0. Therefore, the intermolecular interactions component 1 – component 1, component 2 – component 2 and component 1 – component 2, are balanced.

If the excess enthalpy of mixing is different from 0, the mixture is not ideal and the magnitude of the intermolecular interactions established between the mixed components, component 1 – component 2, do not equalize the cost of breaking the component 1 – component 1 and component 2 – component 2 interactions in its pure state. The deviation of the excess enthalpy of mixing from ideality can be indicative of the magnitude of the component 1 – component 2 intermolecular interactions established, if the relative composition of the mixture is taken into account.

As schematically depicted in figure 1.20, the deviation from ideality may be positive or negative, leading to endothermic or exothermic excess molar enthalpy of mixing. The endothermic excess molar enthalpy of mixing indicates that the intermolecular interactions established into the pure substances are stronger than the intermolecular interactions established between component 1 – component 2, upon mixing. On the contrary, exothermic excess molar enthalpy of mixing indicates that the intermolecular

interactions established between component 1 – component 2, upon mixing, are stronger than the intermolecular interactions established into the pure substances.

This is a very simplistic interpretation of the (excess) enthalpy of mixing. To start, the relative composition of the mixture has to be taken into account. Furthermore, in mixtures of compounds which structure and intermolecular interactions differ significantly from simple molecules and homogeneous media, (as ILs) the intermolecular interactions established may depend on the local composition of the mixture.

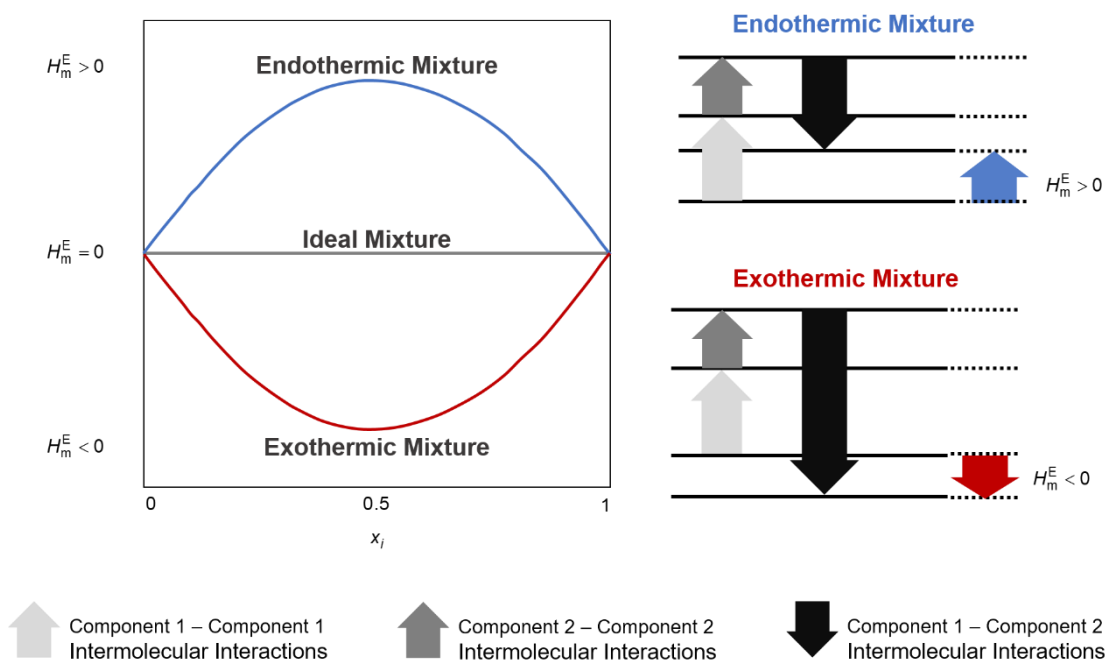


Figure 1.20. Schematic diagram of the excess molar enthalpy of mixing of a binary mixture. The diagrams correspondent to a hypothetical ideal, endothermic or exothermic mixture are presented, as well as, a simplistic scheme on the endothermic contribution of the breakage of the intermolecular interactions of the pure components and the exothermic contribution of the establishment of component 1 – component 2 intermolecular interactions to the final endothermic / exothermic enthalpy.

1.2.4. Partial Excess Enthalpy of Mixing

As referred, the enthalpy is an extensive property. When we consider the molar enthalpy, this property becomes intensive. However, it does not reflect the relative composition of the mixture. As a result, to interpret and understand the (excess) molar enthalpy of mixture from a molecular point of view, it is useful and perhaps indispensable to consider its dependence on the relative composition of the mixture. To access the effect of the composition of the mixture on the (excess) molar enthalpy of mixing, the partial molar quantities are determined.

The partial molar (excess) enthalpy of a component “*i*” in the mixture is the enthalpy change upon addition of an amount of that component to the system, at constant temperature, pressure and quantity of component “*j*”:

$$\bar{H}_{i,m} = \bar{H}_{i,m}^E = \left(\frac{d(n \cdot H)}{dn_i} \right)_{n_j, T, p} . \quad (1.12)$$

The (excess) molar enthalpy of mixture (and consequently, the enthalpy of mixing) is the sum of the partial molar enthalpy of its components:

$$\Delta_{\text{mix}} H_m = H_m^E = \sum_i (x_i \cdot \bar{H}_{i,m}^E) . \quad (1.13)$$

The enthalpy of the pure state is usually considered to be zero, $H_i^* = 0$. Nevertheless, the partial molar enthalpy of mixing is numerically equal to the partial excess molar enthalpy, at any reference state of the enthalpy of the pure substance, as expressed in the following equation:

$$\bar{H}_{i,m} + H_{i,m}^* = \bar{H}_{i,m}^E + H_{i,m}^* . \quad (1.14)$$

Moreover, the enthalpy of solution has the same physical significance of a partial molar enthalpy of mixing (and not of enthalpy of mixing, which is expressed per total quantity of solution/mixture). In accordance, the extrapolation of the partial molar enthalpy of the component “*i*” to $x_i = 0$, $\bar{H}_{i,m}^\infty$ is physically and numerically equivalent to the enthalpy of solution of “*i*” at infinite dilution, $\Delta_{\text{soln}} H_m^\infty$.

1.2.5. Redlich-Kister Equations

The Redlich-Kister equation^[110] (eq. 1.15) was used, along this thesis, to describe the dependence of the excess molar enthalpy of mixing on the molar composition of the components “1” and “2” (molar fraction, x_1 and x_2) of the mixture. This equation is a power series of the difference between the molar fractions of the two components ($x_1 - x_2$), in which A_k are adjustable coefficients of the polynomial of order 0 to k .

$$\Delta_{\text{mix}} H_m = H_m^E = x_1 \cdot x_2 \cdot \sum_k A_k \cdot (x_1 - x_2)^k. \quad (1.15)$$

As $(x_1 + x_2) = 1$, then $x_1 = (1 + (x_1 - x_2))/2$ and $x_2 = (1 - (x_1 - x_2))/2$. In the same way, $(x_1 - x_2) = (2x_1 - 1) = (1 - 2x_2)$. Therefore, equation 1.15 can be re-written in the form of equation 1.16, which is mathematically equivalent:

$$\Delta_{\text{mix}} H_m = H_m^E = (1 - x_1) \cdot x_1 \cdot \sum_k (A_k (2x_1 - 1)^k) = (1 - x_2) \cdot x_2 \cdot \sum_k (A_k (1 - 2x_2)^k). \quad (1.16)$$

From the derivatives of this equation, the partial excess molar enthalpy of both components “1” and “2” can be obtained, as expressed in equations 1.17 and 1.18:

$$\begin{aligned} \bar{H}_{1,m}^E &= \Delta_{\text{mix}} H_m + (1 - x_1) \cdot \left(\frac{d\Delta_{\text{mix}} H_m}{dx_1} \right) \\ &= (x_1 - 1)^2 \cdot \left(x_1 \cdot \sum_k (2 \cdot k \cdot A_k (2 \cdot x_1 - 1)^{-1+k}) + \sum_k (A_k (2 \cdot x_1 - 1)^k) \right) \end{aligned} \quad (1.17)$$

$$\begin{aligned} \bar{H}_{2,m}^E &= \Delta_{\text{mix}} H_m + (1 - x_2) \cdot \left(\frac{d\Delta_{\text{mix}} H_m}{dx_2} \right) \\ &= (x_2 - 1)^2 \cdot \left(x_2 \cdot \sum_k (-2 \cdot k \cdot A_k (1 - 2 \cdot x_2)^{-1+k}) + \sum_k (A_k (1 - 2 \cdot x_2)^k) \right) \end{aligned} \quad (1.18)$$

The capacity to obtain both properties, excess molar enthalpy of mixing and partial excess molar enthalpy of its components allow to analyse, discuss and understand the excess molar enthalpy of mixture taking into account the effect of the composition of the mixture.

To interconvert the mentioned properties, one of the equations 1.15 to 1.18 is fitted to the experimental data, using the minimum parameters A_k possible while reproducing closely the experimental data available, without introducing artefacts into the correlation of the results. Having determined the A_k parameters, the calculation of any of the mentioned properties is possible by utilization of the equations 1.15 to 1.18. In all cases, the number of fitting parameters A_k has to be kept smaller than the degree of freedom of the experimental data points.

From the equations 1.17 and 1.18, it is possible to obtain the extrapolation of the partial molar enthalpy of the components “1” or “2” of the binary mixture to $x_1 = 0$ or $x_2 = 0$, as follows:

$$\bar{H}_{1,m}^{E,\infty} = \lim_{x_1 \rightarrow 0} \bar{H}_{1,m}^E = \sum_k A_k \cdot (-1)^k, \quad (1.19)$$

$$\bar{H}_{2,m}^{E,\infty} = \lim_{x_2 \rightarrow 0} \bar{H}_{2,m}^E = \sum_k A_k. \quad (1.20)$$

As indicated before, the partial molar (excess) enthalpy of mixing at infinite dilution is equivalent to the enthalpy of solution at infinite dilution.

1.2.6. Relevance of the Enthalpic Properties of Mixing

The enthalpic properties of mixing can provide valuable information on a fundamental level. As stated in the review of Costa Gomes et al.^[62] these properties are related to the microscopic structure of mixtures and the nature of the interactions present.

The model of interpretation of the enthalpy of solution and solvation at infinite dilution, for example, is based in a final state constituted by a solute molecule surrounded by solvent. Depending on the experimental strategy adopted, the solute can thus, be used as a molecular probe which can provide valuable unique information on the structuration of the solvent and its ability to establish intermolecular interactions.

The molar enthalpy of solvation in particular, which is the balance between the endothermic contribution of the cavitation process and the exothermic contribution of the solute-solvent interactions, can provide information on the cohesive energy density of

the solvent and on the “ability” of the solvent to establish intermolecular interactions with a solute.

Nevertheless, the enthalpy of solution at infinite dilution can be interpreted as a measure of the enthalpic stability difference between a solute molecule solvated by equal molecules or by solvent. This interpretation can provide insights into the difference between both substances in its pure phase.

The (excess) enthalpy of mixing and its partial derivatives, give information on the effect of the concentration of the solute and its ability to modify the properties of the solvent. While, at infinite dilution the structuration and characteristics of the solvent are maintained and the solute can act as a molecular probe of the solvent characteristics, when the concentration of the solute increases, the structure, and the intermolecular interactions, between other characteristics, may be altered. The comprehension of the effect of the concentration on these characteristics is vital to understand the mixture at a molecular level. Only by understanding mixtures at the molecular level, the modification of the physical properties (viscosity, conductance, surface tension,...) can be understood.

Despite of the high relevance of the insights provided by the enthalpic quantities, they do not replace, other techniques, like spectroscopy or diffraction for example, which provide detailed structural information, or molecular dynamics simulations which often provide unambiguous molecular interpretation. On the contrary, the energetics of mixing complement these techniques.

1.3. Aim and Strategy

After a brief introduction on the state of the art of ILs and its binary mixtures with alcohols, as well as, understanding the relevance of the enthalpic properties of mixture, the motivation and aim of this work are presented.

1.3.1. Motivation and Aim

Over the previous pages it was shown that ionic liquids are solvents of great interest and utility. The great number of cations and anions that can be combined to create different ionic liquids, plus the possibility of addition of other compounds, lead to the possibility of creation of a tuneable solvent, which could be designed with excellent characteristics to a certain application. This hypothetical possibility created the desire of using ILs as “Designer Solvents”.

This project, which was initially titled “Ionic Liquids for the Sustainable Solvent Design and Functional Materials Application” was focused in the understanding of the solvent behaviour of ionic liquids, increasing the molecular knowledge on this field and thus, contribute to the rational development and use of ILs as “Designer Solvents”.

Because it is almost impossible to experimentally investigate a reasonable fraction of the potential cation–anion combinations, not to mention the possibility of adding other compounds to obtain the best solvent for a given application, a molecular-based understanding of the key characteristics of ionic liquids that determine how a given compound is solvated, is crucial to develop a rational design.

In line with this idea, in this work, the solvation properties (solvent characteristics) of ionic liquids were explored, using alcohols as molecular probes.

Due to alcohols and ILs similarities, the selection of alcohols as molecular probes is seen as an excellent approach to understand how ionic liquids will interact with different solutes. Different combination of alcohols and ILs were selected exploring the ability of the alcohol's hydroxyl group to interact with the IL by dispersive or hydrogen bond interactions, as well as, of the nonpolar tail to interact with the nonpolar moieties of the IL, as suggested in the schematic illustration depicted in figure 1.21.

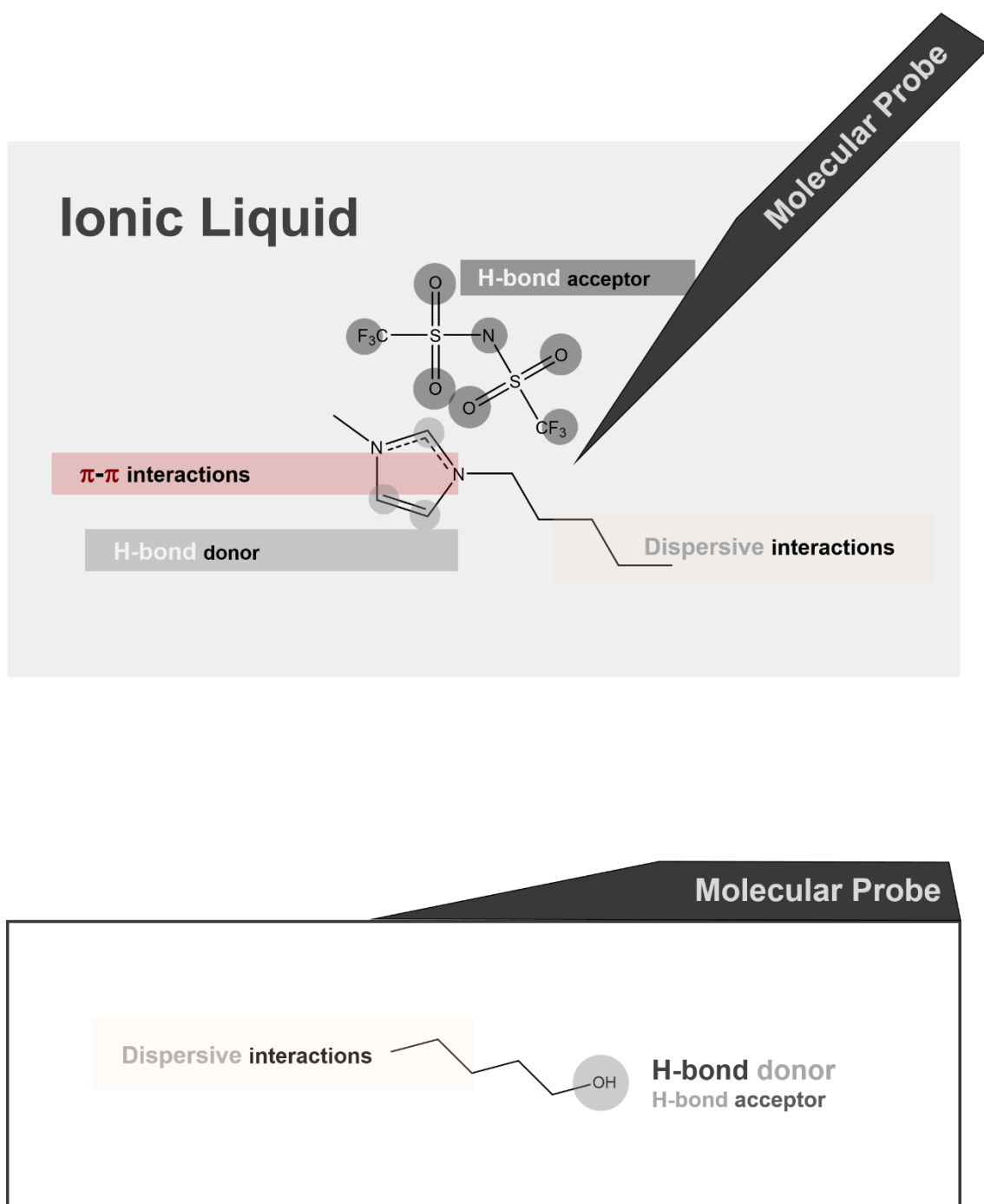


Figure 1.21. Schematic illustration of the use of alcohols as molecular probes in ionic liquids. On the top of the figure, the chemical structure of $[\text{C}_5\text{C}_1\text{im}][\text{NTf}_2]$ is presented as a model of an ionic liquid and the many possibilities of intermolecular interactions which can be established to potential solutes are indicated. On the bottom of the figure the chemical structure of 1-pentanol is presented, as a model alcohol, evidencing the ability of the hydroxyl group to act as a hydrogen bond donor or acceptor, as well as, the nonpolar alkyl chain to establish dispersive interactions.

1.3.2. Strategy

To accomplish the goal of this thesis and understand how ionic liquids interact with potential solutes using alcohols as molecular probes, the strategy schematized in figure 1.22 was followed and is now explained.

In a first approach, infinite dilution conditions were experimentally simulated. In these conditions, it is assumed that alcohol molecules are completely surrounded by ions and that ionic liquids maintain its properties and structuration as if the alcohol was absent. The preferential location of alcohols into ionic liquids and the predominant alcohol-ionic liquid interactions established are then investigated.

To this initial study, the standard molar enthalpy of solution at infinite dilution of alcohols in ionic liquids was measured by isothermal titration calorimetry (ITC). The respective standard molar enthalpy of solvation at infinite dilution was determined, based in these measurements and in the standard molar enthalpy of vaporization of the studied alcohols. Different combination of alcohols and ionic liquids were studied, exploring the solvation characteristics of the ionic liquids.

To explore the effect of the different anions and cations into the solvation process, the solution/solvation of simple and small alcohols in ILs constituted by different cations and anions was studied. Overall, it was investigated the difference into the solution/solvation of an alcohol in ionic liquids constituted by a common anion and the cations: imidazolium, pyridinium, pyrrolidinium and piperidinium. The same approach was followed by solvating the same alcohol in ionic liquids constituted by a common cation and anions of different hydrogen bond basicity. To complement this study, the effect of the alcohol acidity in the solvation of alcohols in ionic liquids was also evaluated. The study of these three effects allow to explore the capability of the ionic liquids to establish hydrogen bond interactions to a potential solute.

To access the interactions in the nonpolar domains and the interplay between polar and nonpolar domains, alcohols of several alkyl chain length were solvated in ILs with different alkyl chain length. This study was conducted in two IL series in order to check for the applicability of the results to other IL series.

In these studies, conducted at infinite dilution conditions, the effect of the anion, cation, acidity of the alcohol and nanostructuration of the IL on the preferential location of the alcohol (into the IL structure) along with the intermolecular interactions established was explored.

In a second approach, after having insights of the main effects ruling the solvation of the alcohols in ionic liquids, it was explored the effect of the concentration of the

alcohol into the ionic liquid. The main purpose of this study is to relate the enthalpic quantities to the different structuration regimes present in alcohol-IL binary mixtures.

To this purpose, a new high precision flow microcalorimeter based in a micromixer/microreactor has been designed, constructed and tested in the context of this PhD project, the μ FlowCal calorimeter. This microcalorimeter allow to broad the concentration range of the previous study and the expansion of the scientific equipment of the group, filling a gap for a calorimeter that would allow to explore wide concentration range in absence of gas phase.

Preliminary results of the excess molar enthalpy of a binary mixture constituted by a model alcohol and ionic liquid were obtained in this calorimeter in a wide concentration range. The enthalpic results obtained were related to the different structuration regimes which have been described in the literature for these alcohol-IL binary mixtures.

Solvation of Alcohols in Ionic Liquids

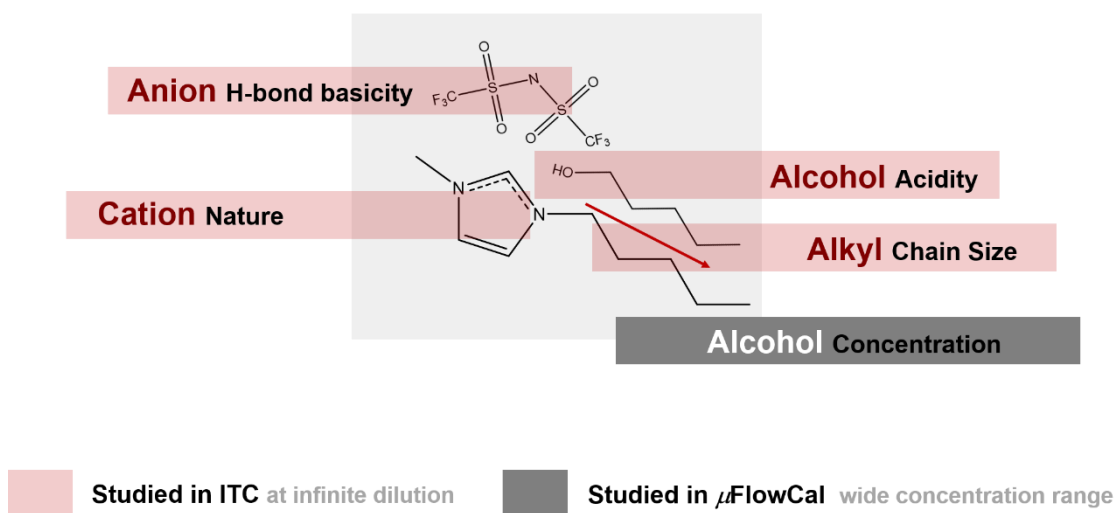


Figure 1.22. Schematic illustration of the strategy used to study the solvation of alcohols in ionic liquids.

References:

- [1] T. Welton, Ionic liquids: a brief history, *Biophysical Reviews*, 10 (2018) p. 691-706. DOI:10.1007/s12551-018-0419-2.
- [2] J. P. Hallett and T. Welton, Room-Temperature Ionic Liquids: Solvents for Synthesis and Catalysis. 2, *Chemical Reviews*, 111 (2011) p. 3508-3576. DOI:10.1021/cr1003248.
- [3] S. Subbiah, I. C. Cathy and C. Yen-Ho, Ionic Liquids for Green Organic Synthesis, *Current Organic Synthesis*, 9 (2012) p. 74-95. DOI:10.2174/157017912798889116.
- [4] D. R. MacFarlane and K. R. Seddon, Ionic Liquids - Progress on the Fundamental Issues, *Australian Journal of Chemistry*, 60 (2007) p. 3-5. DOI:10.1071/CH06478.
- [5] L. M. N. B. F. Santos, J. N. Canongia Lopes, J. A. P. Coutinho, J. M. S. S. Esperança, L. R. Gomes, I. M. Marrucho and L. P. N. Rebelo, Ionic Liquids: First Direct Determination of their Cohesive Energy, *Journal of the American Chemical Society*, 129 (2007) p. 284-285. DOI:10.1021/ja067427b.
- [6] L. M. N. B. F. Santos, L. M. S. S. Lima, C. F. R. A. C. Lima, F. D. Magalhães, M. C. Torres, B. Schröder and M. A. V. Ribeiro da Silva, New Knudsen effusion apparatus with simultaneous gravimetric and quartz crystal microbalance mass loss detection, *The Journal of Chemical Thermodynamics*, 43 (2011) p. 834-843. DOI:10.1016/j.jct.2010.12.022.
- [7] M. Vilas, M. A. A. Rocha, A. M. Fernandes, E. Tojo and L. M. N. B. F. Santos, Novel 2-Alkyl-1-ethylpyridinium Ionic Liquids: Synthesis, Dissociation Energies and Volatility, *Physical Chemistry Chemical Physics*, 17 (2015) p. 2560-2572. DOI:10.1039/C4CP05191B.
- [8] M. A. A. Rocha, J. A. P. Coutinho and L. M. N. B. F. Santos, Vapor pressures of 1,3-dialkylimidazolium bis(trifluoromethylsulfonyl)imide ionic liquids with long alkyl chains, *The Journal of Chemical Physics*, 141 (2014) p. 134502. DOI:10.1063/1.4896704.
- [9] A. S. M. C. Rodrigues, A. M. Fernandes, J. Dévemy, M. Costa Gomes and L. M. N. B. F. Santos, Fluorination effect in the volatility of imidazolium-based ionic liquids, *Journal of Molecular Liquids*, 282 (2019) p. 385-391. DOI:10.1016/j.molliq.2019.03.024.
- [10] L. Crowhurst, P. R. Mawdsley, J. M. Perez-Arlandis, P. A. Salter and T. Welton, Solvent-solute interactions in ionic liquids, *Physical Chemistry Chemical Physics*, 5 (2003) p. 2790-2794. DOI:10.1039/B303095D.
- [11] J. N. A. Canongia Lopes and A. A. H. Pádua, Nanostructural Organization in Ionic Liquids, *The Journal of Physical Chemistry B*, 110 (2006) p. 3330-3335. DOI:10.1021/jp056006y.
- [12] K. Shimizu, C. E. S. Bernardes and J. N. Canongia Lopes, Structure and Aggregation in the 1-Alkyl-3-Methylimidazolium Bis(trifluoromethylsulfonyl)imide Ionic Liquid Homologous Series, *The Journal of Physical Chemistry B*, 118 (2014) p. 567-576. DOI:10.1021/jp409987d.
- [13] C. E. S. Bernardes, K. Shimizu, A. I. M. C. Lobo Ferreira, L. M. N. B. F. Santos and J. N. C. Lopes, Structure and Aggregation in the 1,3-Dialkyl-imidazolium Bis(trifluoromethylsulfonyl)imide Ionic Liquid Family: 2. From Single to Double Long Alkyl Side Chains, *The Journal of Physical Chemistry B*, 118 (2014) p. 6885-6895. DOI:10.1021/jp502968u.
- [14] A. Triolo, O. Russina, H.-J. Bleif and E. Di Cola, Nanoscale Segregation in Room Temperature Ionic Liquids, *The Journal of Physical Chemistry B*, 111 (2007) p. 4641-4644. DOI:10.1021/jp067705t.
- [15] A. Triolo, O. Russina, B. Fazio, G. B. Appetecchi, M. Carewska and S. Passerini, Nanoscale organization in piperidinium-based room temperature ionic liquids, *The Journal of Chemical Physics*, 130 (2009) p. 164521. DOI:10.1063/1.3119977.

- [16] O. Russina, A. Triolo, L. Gontrani, R. Caminiti, D. Xiao, L. G. Hines Jr, R. A. Bartsch, E. L. Quitevis, N. Plechkova and K. R. Seddon, Morphology and intermolecular dynamics of 1-alkyl-3-methylimidazolium bis((trifluoromethane)sulfonyl)amide ionic liquids: structural and dynamic evidence of nanoscale segregation, *Journal of Physics: Condensed Matter*, 21 (2009) p. 424121. DOI:10.1088/0953-8984/21/42/424121.
- [17] O. Russina and A. Triolo, New experimental evidence supporting the mesoscopic segregation model in room temperature ionic liquids, *Faraday Discussions*, 154 (2012) p. 97-109. DOI:10.1039/C1FD00073J.
- [18] O. Russina, B. Fazio, G. Di Marco, R. Caminiti and A. Triolo, Chapter 2 - Structural Organization in Neat Ionic Liquids and in Their Mixtures, *The Structure of Ionic Liquids*, Springer International Publishing, Cham, 2014, p. 39-61. DOI:10.1007/978-3-319-01698-6_2.
- [19] P. B. P. Serra, F. M. S. Ribeiro, M. A. A. Rocha, M. Fulem, K. Růžicka, J. A. P. Coutinho and L. M. N. B. F. Santos, Solid-liquid equilibrium and heat capacity trend in the alkylimidazolium PF6 series, *Journal of Molecular Liquids*, 248 (2017) p. 678-687. DOI:10.1016/j.molliq.2017.10.042.
- [20] A. S. M. C. Rodrigues and L. M. N. B. F. Santos, Nanostructuration Effect on the Thermal Behavior of Ionic Liquids, *ChemPhysChem*, 17 (2016) p. 1512-1517. DOI:10.1002/cphc.201501128.
- [21] M. A. A. Rocha, M. Vilas, A. S. M. C. Rodrigues, E. Tojo and L. M. N. B. F. Santos, Physicochemical properties of 2-alkyl-1-ethylpyridinium based ionic liquids, *Fluid Phase Equilibria*, 428 (2016) p. 112-120. DOI:10.1016/j.fluid.2016.05.030.
- [22] H. F. D. Almeida, M. G. Freire, A. M. Fernandes, J. A. Lopes-da-Silva, P. Morgado, K. Shimizu, E. J. M. Filipe, J. N. Canongia Lopes, L. M. N. B. F. Santos and J. A. P. Coutinho, Cation Alkyl Side Chain Length and Symmetry Effects on the Surface Tension of Ionic Liquids, *Langmuir*, 30 (2014) p. 6408-6418. DOI:10.1021/la501308q.
- [23] M. A. A. Rocha, J. A. P. Coutinho and L. M. N. B. F. Santos, Evidence of nanostructuration from the heat capacities of the 1,3-dialkylimidazolium bis(trifluoromethylsulfonyl)imide ionic liquid series, *The Journal of Chemical Physics*, 139 (2013) p. 104502. DOI:10.1063/1.4820825.
- [24] M. A. A. Rocha, C. M. S. S. Neves, M. G. Freire, O. Russina, A. Triolo, J. A. P. Coutinho and L. M. N. B. F. Santos, Alkylimidazolium Based Ionic Liquids: Impact of Cation Symmetry on Their Nanoscale Structural Organization, *The Journal of Physical Chemistry B*, 117 (2013) p. 10889-10897. DOI:10.1021/jp406374a.
- [25] Y.-L. Wang, B. Li, S. Sarman, F. Mocci, Z.-Y. Lu, J. Yuan, A. Laaksonen and M. D. Fayer, Microstructural and Dynamical Heterogeneities in Ionic Liquids, *Chemical Reviews*, (2020) p. DOI:10.1021/acs.chemrev.9b00693.
- [26] R. Hayes, G. G. Warr and R. Atkin, Structure and Nanostructure in Ionic Liquids, *Chemical Reviews*, 115 (2015) p. 6357-6426. DOI:10.1021/cr500411q.
- [27] K. Shimizu, M. Tariq, A. A. Freitas, A. A. H. Pádua and J. N. C. Lopes, Self-Organization in Ionic Liquids: From Bulk to Interfaces and Films, *Journal of the Brazilian Chemical Society*, 27 (2016) p. 349-362. DOI:10.5935/0103-5053.20150274.
- [28] H. J. Jiang, R. Atkin and G. G. Warr, Nanostructured ionic liquids and their solutions: Recent advances and emerging challenges, *Current Opinion in Green and Sustainable Chemistry*, 12 (2018) p. 27-32. DOI:10.1016/j.cogsc.2018.05.003.
- [29] O. Russina, F. Lo Celso, N. V. Plechkova and A. Triolo, Emerging Evidences of Mesoscopic-Scale Complexity in Neat Ionic Liquids and Their Mixtures, *The Journal of Physical Chemistry Letters*, 8 (2017) p. 1197-1204. DOI:10.1021/acs.jpclett.6b02811.
- [30] H. Weingärtner, Understanding Ionic Liquids at the Molecular Level: Facts, Problems, and Controversies, *Angewandte Chemie International Edition*, 47 (2008) p. 654-670. DOI:10.1002/anie.200604951.
- [31] E. G. Azevedo, *Termodinâmica Aplicada*, 3ª ed., Escolar Editora, Lisboa, Portugal, 2011. ISBN: 978-972-592-315-3.

- [32] P. A. Hunt, C. R. Ashworth and R. P. Matthews, Hydrogen bonding in ionic liquids, *Chemical Society Reviews*, 44 (2015) p. 1257-1288. DOI:10.1039/C4CS00278D.
- [33] S. Agrawal and H. K. Kashyap, Structures of binary mixtures of ionic liquid 1-butyl-3-methylimidazolium bis(trifluoromethylsulfonyl)imide with primary alcohols: The role of hydrogen-bonding, *Journal of Molecular Liquids*, 261 (2018) p. 337-349. DOI:10.1016/j.molliq.2018.03.124.
- [34] X. Wang, S. Zhang, J. Yao and H. Li, The Polarity of Ionic Liquids: Relationship between Relative Permittivity and Spectroscopic Parameters of Probe, *Industrial & Engineering Chemistry Research*, 58 (2019) p. 7352-7361. DOI:10.1021/acs.iecr.9b00485.
- [35] H. Weingärtner, The static dielectric permittivity of ionic liquids, *Journal of Molecular Liquids*, 192 (2014) p. 185-190. DOI:10.1016/j.molliq.2013.07.020.
- [36] C. Reichardt, Polarity of ionic liquids determined empirically by means of solvatochromic pyridinium N-phenolate betaine dyes, *Green Chemistry*, 7 (2005) p. 339-351. DOI:10.1039/B500106B.
- [37] P. Muller, Glossary of terms used in physical organic chemistry (IUPAC Recommendations 1994), *Pure and Applied Chemistry*, 66 (1994) p. 1077-1184. DOI:10.1351/pac199466051077.
- [38] C. Chiappe and D. Pieraccini, Ionic liquids: solvent properties and organic reactivity, *Journal of Physical Organic Chemistry*, 18 (2005) p. 275-297. DOI:10.1002/poc.863.
- [39] M. J. Kamlet, J. L. M. Abboud, M. H. Abraham and R. W. Taft, Linear solvation energy relationships. 23. A comprehensive collection of the solvatochromic parameters, π^* , α , and β , and some methods for simplifying the generalized solvatochromic equation, *The Journal of Organic Chemistry*, 48 (1983) p. 2877-2887. DOI:10.1021/jo00165a018.
- [40] M. A. Ab Rani, A. Brant, L. Crowhurst, A. Dolan, M. Lui, N. H. Hassan, J. P. Hallett, P. A. Hunt, H. Niedermeyer, J. M. Perez-Arlandis, M. Schrems, T. Welton and R. Wilding, Understanding the polarity of ionic liquids, *Physical Chemistry Chemical Physics*, 13 (2011) p. 16831-16840. DOI:10.1039/C1CP21262A.
- [41] E. L. Bennett, C. Song, Y. Huang and J. Xiao, Measured relative complex permittivities for multiple series of ionic liquids, *Journal of Molecular Liquids*, 294 (2019) p. 111571. DOI:10.1016/j.molliq.2019.111571.
- [42] C. Reichardt, Solvatochromic Dyes as Solvent Polarity Indicators, *Chemical Reviews*, 94 (1994) p. 2319-2358. DOI:10.1021/cr00032a005.
- [43] M. J. Muldoon, C. M. Gordon and I. R. Dunkin, Investigations of solvent-solute interactions in room temperature ionic liquids using solvatochromic dyes, *Journal of the Chemical Society, Perkin Transactions 2*, (2001) p. 433-435. DOI:10.1039/B101449H.
- [44] C. Chiappe and D. Pieraccini, Determination of Ionic Liquids Solvent Properties Using an Unusual Probe: The Electron Donor-Acceptor Complex between 4,4'-bis(Dimethylamino)-benzophenone and Tetracyanoethene, *The Journal of Physical Chemistry A*, 110 (2006) p. 4937-4941. DOI:10.1021/jp057236f.
- [45] J. L. Kaar, A. M. Jesionowski, J. A. Berberich, R. Moulton and A. J. Russell, Impact of Ionic Liquid Physical Properties on Lipase Activity and Stability, *Journal of the American Chemical Society*, 125 (2003) p. 4125-4131. DOI:10.1021/ja028557x.
- [46] S. Park and R. J. Kazlauskas, Improved Preparation and Use of Room-Temperature Ionic Liquids in Lipase-Catalyzed Enantio- and Regioselective Acylations, *The Journal of Organic Chemistry*, 66 (2001) p. 8395-8401. DOI:10.1021/jo015761e.
- [47] A. Jeličić, N. García, H.-G. Löhmansröben and S. Beuermann, Prediction of the Ionic Liquid Influence on Propagation Rate Coefficients in Methyl Methacrylate Radical Polymerizations Based on Kamlet-Taft Solvatochromic Parameters, *Macromolecules*, 42 (2009) p. 8801-8808. DOI:10.1021/ma9017907.

- [48] N. D. Khupse and A. Kumar, Contrasting Thermosolvatochromic Trends in Pyridinium-, Pyrrolidinium-, and Phosphonium-Based Ionic Liquids, *The Journal of Physical Chemistry B*, 114 (2010) p. 376-381. DOI:10.1021/jp908498p.
- [49] S. V. Dzyuba and R. A. Bartsch, Expanding the polarity range of ionic liquids, *Tetrahedron Letters*, 43 (2002) p. 4657-4659. DOI:10.1016/S0040-4039(02)00858-4.
- [50] S. Coleman, R. Byrne, S. Minkovska and D. Diamond, Thermal reversion of spirooxazine in ionic liquids containing the [NTf₂]⁻ anion, *Physical Chemistry Chemical Physics*, 11 (2009) p. 5608-5614. DOI:10.1039/B901417A.
- [51] A. F. M. Claudio, L. Swift, J. P. Hallett, T. Welton, J. A. P. Coutinho and M. G. Freire, Extended Scale for the Hydrogen-Bond Basicity of Ionic Liquids, *Physical Chemistry Chemical Physics*, 16 (2014) p. 6593-6601. DOI:10.1039/C3CP55285C.
- [52] K. A. Kurnia, F. Lima, A. F. M. Claudio, J. A. P. Coutinho and M. G. Freire, Hydrogen-bond acidity of ionic liquids: an extended scale, *Physical Chemistry Chemical Physics*, 17 (2015) p. 18980-18990. DOI:10.1039/C5CP03094C.
- [53] M. Mizoshiri, T. Nagao, Y. Mizoguchi and M. Yao, Dielectric permittivity of room temperature ionic liquids: A relation to the polar and nonpolar domain structures, *The Journal of Chemical Physics*, 132 (2010) p. 164510. DOI:10.1063/1.3419906.
- [54] A. A. H. Pádua, M. F. Costa Gomes and J. N. A. Canongia Lopes, Molecular Solutes in Ionic Liquids: A Structural Perspective, *Accounts of Chemical Research*, 40 (2007) p. 1087-1096. DOI:10.1021/ar700050q.
- [55] J. N. Canongia Lopes, M. F. Costa Gomes and A. A. H. Pádua, Nonpolar, Polar, and Associating Solutes in Ionic Liquids, *The Journal of Physical Chemistry B*, 110 (2006) p. 16816-16818. DOI:10.1021/jp063603r.
- [56] R. Elfgén, O. Hollóczki and B. Kirchner, A Molecular Level Understanding of Template Effects in Ionic Liquids, *Accounts of Chemical Research*, 50 (2017) p. 2949-2957. DOI:10.1021/acs.accounts.7b00436.
- [57] C. Hardacre, J. D. Holbrey, M. Nieuwenhuysen and T. G. A. Youngs, Structure and Solvation in Ionic Liquids, *Accounts of Chemical Research*, 40 (2007) p. 1146-1155. DOI:10.1021/ar700068x.
- [58] C. Chiappe, M. Malvaldi and C. S. Pomelli, Ionic liquids_ Solvation ability and polarity, 81 (2009) p. 767. DOI:10.1351/PAC-CON-08-09-08.
- [59] T. Méndez-Morales, J. Carrete, Ó. Cabeza, O. Russina, A. Triolo, L. J. Gallego and L. M. Varela, Solvation of Lithium Salts in Protic Ionic Liquids: A Molecular Dynamics Study, *The Journal of Physical Chemistry B*, 118 (2014) p. 761-770. DOI:10.1021/jp410090f.
- [60] L. M. Varela, T. Méndez-Morales, J. Carrete, V. Gómez-González, B. Docampo-Álvarez, L. J. Gallego, O. Cabeza and O. Russina, Solvation of molecular cosolvents and inorganic salts in ionic liquids: A review of molecular dynamics simulations, *Journal of Molecular Liquids*, 210 (2015) p. 178-188. DOI:10.1016/j.molliq.2015.06.036.
- [61] I. Bahadur, T. M. Letcher, S. Singh, G. G. Redhi, P. Venkatesu and D. Ramjugernath, Excess molar volumes of binary mixtures (an ionic liquid+water): A review, *The Journal of Chemical Thermodynamics*, 82 (2015) p. 34-46. DOI:10.1016/j.jct.2014.10.003.
- [62] A. Podgoršek, J. Jacquemin, A. A. H. Pádua and M. F. Costa Gomes, Mixing Enthalpy for Binary Mixtures Containing Ionic Liquids, *Chemical Reviews*, 116 (2016) p. 6075-6106. DOI:10.1021/acs.chemrev.5b00379.
- [63] X. Shao, W. Schröer and B. Rathke, Liquid-Liquid Phase Behavior of Solutions of 1,3-Dimethylimidazolium- and 1-Methyl-3-propylimidazolium Bis[(trifluoromethyl)sulfonyl]amide (C1,3mimNTf₂) in n-Alkyl Alcohols, *Journal of Chemical & Engineering Data*, 59 (2014) p. 225-233. DOI:10.1021/je400253e.
- [64] V. R. Vale, S. Will, W. Schröer and B. Rathke, The General Phase Behavior of Mixtures of 1-Alkyl-3-Methylimidazolium Bis[(trifluoromethyl)sulfonyl]amide Ionic Liquids with n-Alkyl Alcohols, *ChemPhysChem*, 13 (2012) p. 1860-1867. DOI:10.1002/cphc.201100911.

- [65] V. R. Vale, B. Rathke, S. Will and W. Schröer, Liquid–Liquid Phase Behavior of Solutions of 1-Butyl-3-methylimidazolium Bis((trifluoromethyl)sulfonyl)amide (C4mimNTf2) in n-Alkyl Alcohols, *Journal of Chemical & Engineering Data*, 56 (2011) p. 4829-4839. DOI:10.1021/jc200792v.
- [66] V. R. Vale, B. Rathke, S. Will and W. Schröer, Liquid–Liquid Phase Behavior of Solutions of 1-Hexyl-3-methylimidazolium Bis((trifluoromethyl)sulfonyl)amide (C6mimNTf2) in n-Alkyl Alcohols, *Journal of Chemical & Engineering Data*, 56 (2011) p. 1330-1340. DOI:10.1021/jc2011357.
- [67] V. R. Vale, B. Rathke, S. Will and W. Schröer, Liquid–Liquid Phase Behavior of Solutions of 1-Octyl- and 1-Decyl-3-methylimidazolium Bis(trifluoromethylsulfonyl)imide (C8,10mimNTf2) in n-Alkyl Alcohols, *Journal of Chemical & Engineering Data*, 55 (2010) p. 2030-2038. DOI:10.1021/jc900988a.
- [68] J. M. Crosthwaite, S. N. V. K. Aki, E. J. Maginn and J. F. Brennecke, Liquid Phase Behavior of Imidazolium-Based Ionic Liquids with Alcohols, *The Journal of Physical Chemistry B*, 108 (2004) p. 5113-5119. DOI:10.1021/jp037774x.
- [69] J. Łachwa, P. Morgado, J. M. S. S. Esperança, H. J. R. Guedes, J. N. Canongia Lopes and L. P. N. Rebelo, Fluid-Phase Behavior of {1-Hexyl-3-methylimidazolium Bis(trifluoromethylsulfonyl) Imide, [C6mim][NTf2], + C2–C8 n-Alcohol} Mixtures: Liquid–Liquid Equilibrium and Excess Volumes, *Journal of Chemical & Engineering Data*, 51 (2006) p. 2215-2221. DOI:10.1021/jc060307z.
- [70] U. Domańska and A. Marciniak, Solubility of Ionic Liquid [emim][PF6] in Alcohols, *The Journal of Physical Chemistry B*, 108 (2004) p. 2376-2382. DOI:10.1021/jp030582h.
- [71] K. Sahandzhieva, D. Tuma, S. Breyer, Á. Pérez-Salado Kamps and G. Maurer, Liquid–Liquid Equilibrium in Mixtures of the Ionic Liquid 1-n-Butyl-3-methylimidazolium Hexafluorophosphate and an Alkanol, *Journal of Chemical & Engineering Data*, 51 (2006) p. 1516-1525. DOI:10.1021/jc050474j.
- [72] T. Méndez-Morales, J. Carrete, O. Cabeza, L. J. Gallego and L. M. Varela, Molecular Dynamics Simulations of the Structural and Thermodynamic Properties of Imidazolium-Based Ionic Liquid Mixtures, *The Journal of Physical Chemistry B*, 115 (2011) p. 11170-11182. DOI:10.1021/jp206341z.
- [73] A. Sharma and P. K. Ghorai, Effect of alcohols on the structure and dynamics of [BMIM][PF6] ionic liquid: A combined molecular dynamics simulation and Voronoi tessellation investigation, *The Journal of Chemical Physics*, 148 (2018) p. 204514. DOI:10.1063/1.5008439.
- [74] Y. Yoshimura, S. Hattori, T. Mori, K. Kaneko, J. Ueda, T. Takekiyo, Y. Masuda and A. Shimizu, An insight into the filling of the nanoheterogeneous structures of 1-butyl-3-methylimidazolium bis(trifluoromethanesulfonyl)amide by primary alcohols, *Journal of Molecular Liquids*, 300 (2020) p. 112351. DOI:10.1016/j.molliq.2019.112351.
- [75] Y. Yoshimura, T. Mori, K. Kaneko, S. Hattori, T. Takekiyo, Y. Masuda and A. Shimizu, Raman investigation on the local structure of alcohols in 1-butyl-3-methylimidazolium tetrafluoroborate, *Journal of Molecular Liquids*, 293 (2019) p. 111508. DOI:10.1016/j.molliq.2019.111508.
- [76] W. Beichel, Y. Yu, G. Dlubek, R. Krause-Rehberg, J. Pionteck, D. Pfeifferkorn, S. Bulut, D. Bejan, C. Friedrich and I. Krossing, Free volume in ionic liquids: a connection of experimentally accessible observables from PALS and PVT experiments with the molecular structure from XRD data, *Physical Chemistry Chemical Physics*, 15 (2013) p. 8821-8830. DOI:10.1039/C3CP43306D.
- [77] J. N. Canongia Lopes, M. F. Costa Gomes, P. Husson, A. A. H. Pádua, L. P. N. Rebelo, S. Sarraute and M. Tariq, Polarity, Viscosity, and Ionic Conductivity of Liquid Mixtures Containing [C4C1im][Ntf2] and a Molecular Component, *The Journal of Physical Chemistry B*, 115 (2011) p. 6088-6099. DOI:10.1021/jp2012254.
- [78] W.-L. Yuan, X. Yang, L. He, Y. Xue, S. Qin and G.-H. Tao, Viscosity, Conductivity, and Electrochemical Property of Dicyanamide Ionic Liquids, *Frontiers in Chemistry*, 6 (2018) p. DOI:10.3389/fchem.2018.00059.
- [79] M. García-Mardones, H. M. Osorio, C. Lafuente and I. Gascón, Ionic Conductivities of Binary Mixtures Containing Pyridinium-Based Ionic Liquids and Alkanols, *Journal of Chemical & Engineering Data*, 58 (2013) p. 1613-1620. DOI:10.1021/jc301347v.

- [80] E. Rilo, J. Vila, S. García-Garabal, L. M. Varela and O. Cabeza, Electrical Conductivity of Seven Binary Systems Containing 1-Ethyl-3-methyl Imidazolium Alkyl Sulfate Ionic Liquids with Water or Ethanol at Four Temperatures, *The Journal of Physical Chemistry B*, 117 (2013) p. 1411-1418. DOI:10.1021/jp309891j.
- [81] E. Rilo, J. Vila, M. García, L. M. Varela and O. Cabeza, Viscosity and Electrical Conductivity of Binary Mixtures of CnMIM-BF₄ with Ethanol at 288 K, 298 K, 308 K, and 318 K, *Journal of Chemical & Engineering Data*, 55 (2010) p. 5156-5163. DOI:10.1021/jc100687x.
- [82] R. Alcalde, M. Atilhan and S. Aparicio, Insights on 1-Butyl-3-methylimidazolium Bis(trifluoromethylsulfonyl)imide + Ethanol Liquid Mixtures: A Molecular Dynamics Approach, *Journal of Chemical & Engineering Data*, 61 (2016) p. 2729-2737. DOI:10.1021/acs.jced.6b00132.
- [83] T. Méndez-Morales, J. Carrete, M. García, O. Cabeza, L. J. Gallego and L. M. Varela, Dynamical Properties of Alcohol + 1-Hexyl-3-methylimidazolium Ionic Liquid Mixtures: A Computer Simulation Study, *J. Phys. Chem. B*, 115 (2011) p. 15313-15322. DOI:10.1021/jp209563b.
- [84] E. Gómez, N. Calvar, E. A. Macedo and Á. Domínguez, Effect of the temperature on the physical properties of pure 1-propyl 3-methylimidazolium bis(trifluoromethylsulfonyl)imide and characterization of its binary mixtures with alcohols, *The Journal of Chemical Thermodynamics*, 45 (2012) p. 9-15. DOI:10.1016/j.jct.2011.08.028.
- [85] E. J. González, Á. Domínguez and E. A. Macedo, Excess properties of binary mixtures containing 1-hexyl-3-methylimidazolium bis(trifluoromethylsulfonyl)imide ionic liquid and polar organic compounds, *The Journal of Chemical Thermodynamics*, 47 (2012) p. 300-311. DOI:doi.org/10.1016/j.jct.2011.11.007.
- [86] Y. Deng, P. Husson, J. Jacquemin, T. G. A. Youngs, V. L. Kett, C. Hardacre and M. F. Costa Gomes, Volumetric Properties and Enthalpies of Solution of Alcohols C_kH_{2k+1}OH (k=1, 2, 6) in 1-Methyl-3-alkylimidazolium Bis(trifluoromethylsulfonyl)imide {[C₁C_nIm][NTf₂] n=2, 4, 6, 8, 10} Ionic Liquids, *The Journal of Chemical Thermodynamics*, 43 (2011) p. 1708-1718. DOI:10.1016/j.jct.2011.05.033.
- [87] B. González and E. J. González, Physical properties of the pure 1-methyl-1-propylpyrrolidinium bis(trifluoromethylsulfonyl)imide ionic liquid and its binary mixtures with alcohols, *The Journal of Chemical Thermodynamics*, 68 (2014) p. 109-116. DOI:10.1016/j.jct.2013.08.021.
- [88] E. J. González, P. F. Requejo, Á. Domínguez and E. A. Macedo, Physical Properties of Binary Alcohol + Ionic Liquid Mixtures at Several Temperatures and Atmospheric Pressure, *Journal of Solution Chemistry*, 42 (2013) p. 746-763. DOI:10.1007/s10953-013-9990-0.
- [89] A. Arce, E. Rodil and A. Soto, Physical and Excess Properties for Binary Mixtures of 1-Methyl-3-Octylimidazolium Tetrafluoroborate, [Omim][BF₄], Ionic Liquid with Different Alcohols, *Journal of Solution Chemistry*, 35 (2006) p. 63-78. DOI:10.1007/s10953-006-8939-y.
- [90] E. J. González, L. Alonso and Á. Domínguez, Physical Properties of Binary Mixtures of the Ionic Liquid 1-Methyl-3-octylimidazolium Chloride with Methanol, Ethanol, and 1-Propanol at T = (298.15, 313.15, and 328.15) K and at P = 0.1 MPa, *Journal of Chemical & Engineering Data*, 51 (2006) p. 1446-1452. DOI:10.1021/jc060123k.
- [91] K. A. Kurnia and J. A. P. Coutinho, Overview of the Excess Enthalpies of the Binary Mixtures Composed of Molecular Solvents and Ionic Liquids and Their Modeling Using COSMO-RS, *Industrial & Engineering Chemistry Research*, 52 (2013) p. 13862-13874. DOI:10.1021/ie4017682.
- [92] I. C. M. Vaz, A. Bhattacharjee, M. A. A. Rocha, J. A. P. Coutinho, M. Bastos and L. M. N. B. F. Santos, Alcohols as molecular probes in ionic liquids: evidence for nanostructuration, *Physical Chemistry Chemical Physics*, 18 (2016) p. 19267-19275. DOI:10.1039/C6CP03616C.
- [93] R. Vreekamp, D. Castellano, J. Palomar, J. Ortega, F. Espiau, L. Fernández and E. Penco, Thermodynamic Behavior of the Binaries 1-Butylpyridinium Tetrafluoroborate with Water and Alkanols: Their Interpretation Using ¹H NMR Spectroscopy and Quantum-Chemistry Calculations, *The Journal of Physical Chemistry B*, 115 (2011) p. 8763-8774. DOI:10.1021/jp202828z.
- [94] A. Navas, J. Ortega, R. Vreekamp, E. Marrero and J. Palomar, Experimental Thermodynamic Properties of 1-Butyl-2-methylpyridinium Tetrafluoroborate [b2mpy][BF₄] with Water and with Alkan-1-ol and Their Interpretation with the

COSMO-RS Methodology, *Industrial & Engineering Chemistry Research*, 48 (2009) p. 2678-2690. DOI:10.1021/ie8009878.

[95] Z. He, Z. Zhao, X. Zhang and H. Feng, Thermodynamic properties of new heat pump working pairs: 1,3-Dimethylimidazolium dimethylphosphate and water, ethanol and methanol, *Fluid Phase Equilibria*, 298 (2010) p. 83-91. DOI:10.1016/j.fluid.2010.07.005.

[96] J. Ren, Z. Zhao and X. Zhang, Vapor pressures, excess enthalpies, and specific heat capacities of the binary working pairs containing the ionic liquid 1-ethyl-3-methylimidazolium dimethylphosphate, *The Journal of Chemical Thermodynamics*, 43 (2011) p. 576-583. DOI:10.1016/j.jct.2010.11.014.

[97] G. Rai and A. Kumar, An enthalpic approach to delineate the interactions of cations of imidazolium-based ionic liquids with molecular solvents, *Physical Chemistry Chemical Physics*, 13 (2011) p. 14715-14722. DOI:10.1039/C1CP20888H.

[98] J. Ortega, R. Vreekamp, E. Marrero and E. Penco, Thermodynamic Properties of 1-Butyl-3-methylpyridinium Tetrafluoroborate and Its Mixtures with Water and Alkanols, *Journal of Chemical & Engineering Data*, 52 (2007) p. 2269-2276. DOI:10.1021/jc700294p.

[99] J. Ortega, R. Vreekamp, E. Penco and E. Marrero, Mixing thermodynamic properties of 1-butyl-4-methylpyridinium tetrafluoroborate [b4mpy][BF₄] with water and with an alkan-1ol (methanol to pentanol), *The Journal of Chemical Thermodynamics*, 40 (2008) p. 1087-1094. DOI:10.1016/j.jct.2008.02.019.

[100] K. Padaszyński, M. Królikowski and U. Domańska, Excess Enthalpies of Mixing of Piperidinium Ionic Liquids with Short-Chain Alcohols: Measurements and PC-SAFT Modeling, *The Journal of Physical Chemistry B*, 117 (2013) p. 3884-3891. DOI:10.1021/jp401253r.

[101] K. Padaszyński, E. V. Lukoshko, M. Królikowski, U. Domańska and J. Szydłowski, Thermodynamic Study of Binary Mixtures of 1-Butyl-1-methylpyrrolidinium Dicyanamide Ionic Liquid with Molecular Solvents: New Experimental Data and Modeling with PC-SAFT Equation of State, *The Journal of Physical Chemistry B*, 119 (2015) p. 543-551. DOI:10.1021/jp511621j.

[102] E. Balantseva, J. K. Lehmann and H. Andreas, Enthalpies of Solution of Organic Solutes in the Ionic Liquids [Me₃BuN][NTf₂] and [EMIM][EtSO₄], *Zeitschrift für Physikalische Chemie*, 220 (2006) p. 1499-1550. DOI:10.1524/zpch.2006.220.10.1499.

[103] S. Li, W. Yan and H. Dong, Determination of partial molar excess enthalpies at infinite dilution for the systems four alcohols+[bmim]PF₆ at different temperatures by isothermal titration calorimeter, *Fluid Phase Equilibria*, 261 (2007) p. 444-448. DOI:10.1016/j.fluid.2007.06.007.

[104] W. Marczak, S. P. Verevkin and A. Heintz, Enthalpies of Solution of Organic Solutes in the Ionic Liquid 1-Methyl-3-ethyl-imidazolium Bis-(trifluoromethyl-sulfonyl) Amide, *Journal of Solution Chemistry*, 32 (2003) p. 519-526. DOI:10.1023/A:1025361832209.

[105] A. Heintz, S. P. Verevkin, J. K. Lehmann, T. V. Vasiltsova and D. Ondo, Activity Coefficients at Infinite Dilution and Enthalpies of Solution of Methanol, 1-Butanol, and 1-Hexanol in 1-Hexyl-3-methyl-imidazolium Bis(trifluoromethyl-sulfonyl)imide, *The Journal of Chemical Thermodynamics*, 39 (2007) p. 268-274. DOI:10.1016/j.jct.2006.07.006.

[106] Y. Marcus, Internal Pressure of Liquids and Solutions, *Chemical Reviews*, 113 (2013) p. 6536-6551. DOI:10.1021/cr3004423.

[107] S. Otto, The role of solvent cohesion in nonpolar solvation, *Chemical Science*, 4 (2013) p. 2953-2959. DOI:10.1039/C3SC50740H.

[108] T. Singh and A. Kumar, Static Dielectric Constant of Room Temperature Ionic Liquids: Internal Pressure and Cohesive Energy Density Approach, *The Journal of Physical Chemistry B*, 112 (2008) p. 12968-12972. DOI:10.1021/jp8059618.

[109] D. Kulikov, S. P. Verevkin and A. Heintz, Enthalpies of vaporization of a series of aliphatic alcohols: Experimental results and values predicted by the ERAS-model, *Fluid Phase Equilibria*, 192 (**2001**) p. 187-207. DOI:10.1016/S0378-3812(01)00633-1.

[110] O. Redlich and A. T. Kister, Algebraic Representation of Thermodynamic Properties and the Classification of Solutions, *Industrial & Engineering Chemistry*, 40 (**1948**) p. 345-348. DOI:10.1021/ie50458a036.

CHAPTER 2

Materials and Sample Preparation

-
- 2.1. Compounds Studied
 - 2.2. Purification of Alcohols and Ionic Liquids
 - 2.3. Sample Handling
 - 2.4. Additional Materials
 - References
-

2. Materials and Sample Preparation

In this chapter, the compounds used will be summarized together with its purification procedure. One of the compounds used, *tert*-butyl-alcohol, crystallizes close to room temperature. For that reason, special care was taken handling those samples in order to prevent crystallization.

2.1. Compounds Studied

As explained previously in chapter 1, different combinations of alcohols and ionic liquids were used in this project, aiming to evaluate the effects of anion, cation and alcohol nature along with the size of the alkyl chain in the solvation of alcohols in ILs.

The list of ionic liquids and molecular probes (alcohols) used in this work will be logged in tables 2.1 and 2.2.

Table 2.1. Summary of the ionic liquids used in this work

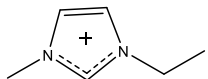
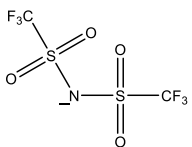
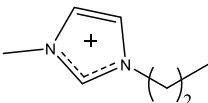
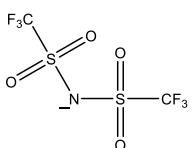
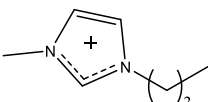
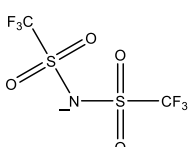
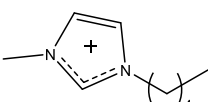
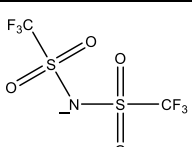
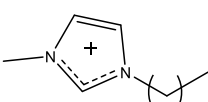
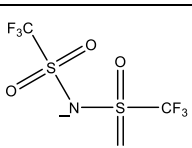
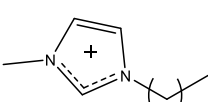
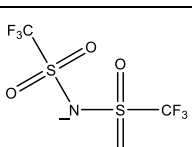
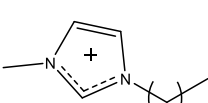
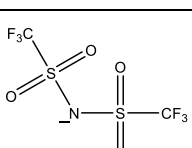
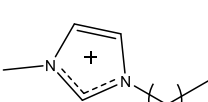
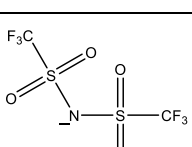
Name	Abbreviation	CAS	Molar Mass / g·mol ⁻¹	Purity / %	Supplier
1-Ethyl-3-methylimidazolium bis(trifluoromethylsulfonyl)imide	[C ₂ C ₁ im][NTf ₂]	174899-82-2	391.31	99.5	Io-li-tec
1-Butyl-3-methylimidazolium bis(trifluoromethylsulfonyl)imide	[C ₄ C ₁ im][NTf ₂]	174899-83-3	419.36	99	Io-li-tec
1-Hexyl-3-methylimidazolium bis(trifluoromethylsulfonyl)imide	[C ₆ C ₁ im][NTf ₂]	382150-50-7	447.42	99	Io-li-tec
1-Octyl-3-methylimidazolium bis(trifluoromethylsulfonyl)imide	[C ₈ C ₁ im][NTf ₂]	178631-04-4	475.47	99	Io-li-tec
1-Decyl-3-methylimidazolium bis(trifluoromethylsulfonyl)imide	[C ₁₀ C ₁ im][NTf ₂]	433337-23-6	503.53	>98	Io-li-tec
1-Butyl-3-methylimidazolium hexafluorophosphate	[C ₄ C ₁ im][PF ₆]	174501-64-5	284.18	99	Io-li-tec
1-Hexyl-3-methylimidazolium hexafluorophosphate	[C ₆ C ₁ im][PF ₆]	304680-35-1	312.24	99	Io-li-tec
1-Octyl-3-methylimidazolium hexafluorophosphate	[C ₈ C ₁ im][PF ₆]	304680-36-2	340.29	99	Io-li-tec

Table 2.2. Summary of the alcohols used in this work

Name	Abbreviation	CAS	Molar Mass / g·mol ⁻¹	Purity / %	Supplier
1-Butanol	BuOH	71-36-3	74.12	99.8	Sigma-Aldrich
				99.9	Sigma-Aldrich
1-Hexanol	HexOH	111-27-3	102.17	98	Sigma-Aldrich
				≥99	Sigma-Aldrich
1-Heptanol	HeptOH	111-70-6	116.20	99	Sigma-Aldrich
1-Octanol	OctOH	111-87-5	130.23	≥99.5	Fluka Analytical
<i>Tert</i> -butyl-alcohol	<i>t</i> -BuOH	75-65-0	74.12	99.3	Sigma-Aldrich
2-Trifluoromethyl-2-propanol	TF <i>t</i> -BuOH	507-52-8	128.09	98	Alfa Aesar
1,1,1,3,3,3-Hexafluoro-2-methyl-2-propanol	HF <i>t</i> -BuOH	1515-14-6	182.06	98	Alfa Aesar
Perfluoro- <i>tert</i> -butyl alcohol	PF <i>t</i> -BuOH	2378-02-1	236.04	99	Alfa Aesar
3,3,3-Trifluoro-1-propanol	TFPrOH	2240-88-2	114.07	97	Apollo Scientific
2,2,3,3,3-pentafluoropropan-1-ol	PFPrOH	422-05-9	150.05	98	Apollo Scientific

Beyond the ILs and alcohols listed in tables 2.1 and 2.2, solvation of other alcohols in ILs were studied by ITC, prior to the beginning of this PhD project. The tables 2.3 and 2.4 list the compounds, nomenclature and chemical structure of all alcohols and ionic liquids, which solution/solvation results are presented and discussed in this thesis.

Table 2.3. Summary of the ionic liquids studied in this thesis

Ionic Liquid	Abbreviation	Chemical Structure	
		Cation	Anion
1-Ethyl-3-methylimidazolium bis(trifluoromethylsulfonyl)imide	[C ₂ C ₁ im][NTf ₂]		
1-Propyl-3-methylimidazolium bis(trifluoromethylsulfonyl)imide	[C ₃ C ₁ im][NTf ₂]		
1-Butyl-3-methylimidazolium bis(trifluoromethylsulfonyl)imide	[C ₄ C ₁ im][NTf ₂]		
1-Pentyl-3-methylimidazolium bis(trifluoromethylsulfonyl)imide	[C ₅ C ₁ im][NTf ₂]		
1-Hexyl-3-methylimidazolium bis(trifluoromethylsulfonyl)imide	[C ₆ C ₁ im][NTf ₂]		
1-Heptyl-3-methylimidazolium bis(trifluoromethylsulfonyl)imide	[C ₇ C ₁ im][NTf ₂]		
1-Octyl-3-methylimidazolium bis(trifluoromethylsulfonyl)imide	[C ₈ C ₁ im][NTf ₂]		
1-Nonyl-3-methylimidazolium bis(trifluoromethylsulfonyl)imide	[C ₉ C ₁ im][NTf ₂]		

.../...

1-Decyl-3-methylimidazolium bis(trifluoromethylsulfonyl)imide	[C ₁₀ C ₁ im][NTf ₂]		
1-Undecyl-3-methylimidazolium bis(trifluoromethylsulfonyl)imide	[C ₁₁ C ₁ im][NTf ₂]		
1-Butyl-3-methylimidazolium hexafluorophosphate	[C ₄ C ₁ im][PF ₆]		
1-Pentyl-3-methylimidazolium hexafluorophosphate	[C ₅ C ₁ im][PF ₆]		
1-Hexyl-3-methylimidazolium hexafluorophosphate	[C ₆ C ₁ im][PF ₆]		
1-Heptyl-3-methylimidazolium hexafluorophosphate	[C ₇ C ₁ im][PF ₆]		
1-Octyl-3-methylimidazolium hexafluorophosphate	[C ₈ C ₁ im][PF ₆]		
1-Nonyl-3-methylimidazolium hexafluorophosphate	[C ₉ C ₁ im][PF ₆]		
1-Butyl-1-methylpyrrolidinium tris(pentafluoroethyl)trifluorophosphate	[C ₄ C ₁ pyrr][FAP]		
1-Butyl-3-methylimidazolium tris(pentafluoroethyl)trifluorophosphate	[C ₄ C ₁ im][FAP]		
1-Butyl-1-methylpyrrolidinium bis(trifluoromethylsulfonyl)imide	[C ₄ C ₁ pyrr][NTf ₂]		

.../...

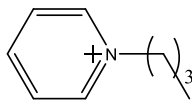
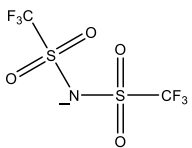
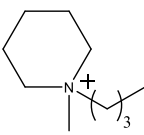
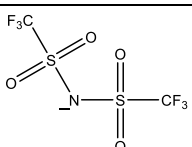
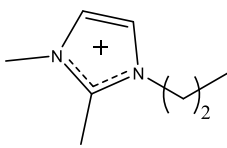
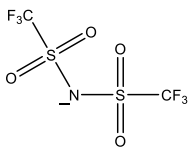
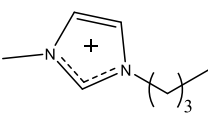
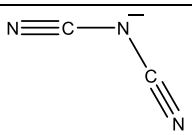
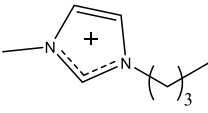
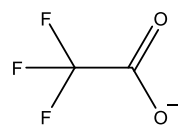
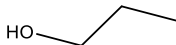




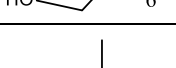
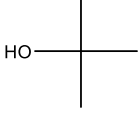
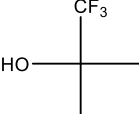
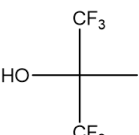
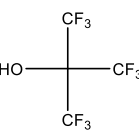
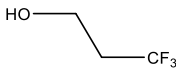
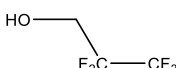
1-Butylpyridinium bis(trifluoromethylsulfonyl)imide	[C ₄ py][NTf ₂]		
1-Butyl-1-methylpiperidinium bis(trifluoromethylsulfonyl)imide	[C ₄ C ₁ pip][NTf ₂]		
1-Butyl-2,3-dimethylimidazolium bis(trifluoromethylsulfonyl)imide	[C ₃ C ₁ C ₁ im][NTf ₂]		
1-Butyl-3-methylimidazolium dicyanamide	[C ₄ C ₁ im][DCA]		
1-Butyl-3-methylimidazolium trifluoroacetate	[C ₄ C ₁ im][TFA]		

Table 2.4. Summary of the alcohols studied in this thesis

Alcohol	Abbreviation	Chemical Structure
1-Propanol	PrOH	
1-Butanol	BuOH	
1-Pentanol	PentOH	
1-Hexanol	HexOH	
1-Heptanol	HeptOH	
1-Octanol	OctOH	
<i>Tert</i> -butyl-alcohol	<i>t</i> -BuOH	
2-Trifluoromethyl-2-propanol	TF <i>t</i> -BuOH	
1,1,1,3,3,3-Hexafluoro-2-methyl-2-propanol	HF <i>t</i> -BuOH	
Perfluoro- <i>tert</i> -butyl alcohol	PF <i>t</i> -BuOH	
3,3,3-Trifluoro-1-propanol	TFPrOH	
2,2,3,3,3-Pentafluoropropan-1-ol	PFPrOH	

2.2. Purification of Alcohols and Ionic Liquids

Different procedures of purification were followed for ionic liquids and for molecular solutes used in ITC, in μ FlowCal or in *DropCalvet*. Details on the different procedures will be provided herein accompanied by a brief description of the vacuum drying/degassing methodologies used.

2.2.1. Purification of Ionic Liquids

The ionic liquids used were purified in a prototype vacuum drying/degassing installation used in our laboratory as a routine methodology in the purification of small samples.

The samples destined to be used in isothermal titration calorimetry, which had a volume of 2-3 cm³, were dried/degassed in a customized *Schlenk* flask that allows easier manipulation of the sample and avoids contamination with grease. This *Schlenk* flask, illustrated in figure 2.1, is based in a tube shape with 17 mm external diameter and 13 mm internal diameter fitted with a vacuum greaseless valve (J. Young Right Angel Taps) and a male joint B 19/26 (diameter = 19 mm and height = 26 mm) and covered with a female glass cap. A simplified version of the same system is illustrated also in figure 2.1 in which a Teflon® stopper is used for the vacuum line connection.



Figure 2.1. Schematic representation of the *Schlenk* flask (on the left) and of the drying/degassing tube (on the right). (Adapted from ref.[1]).

Schlenks are thermostated in an aluminium block (length = 21.7 cm, width = 13.7 cm, height = 6.0 cm), that allows the simultaneous thermostatzation of 15 *Schlenks* at a programmable temperature, which was always set to 60 °C. In its current version, this system does not allow the stirring of the samples. Alternatively, for drying of viscous samples, *Schlenks* were thermostated in a cylindrical aluminium block (diameter = 10.0 cm, height = 10.0 cm) on top of a magnetic stirring plate to enable constant stirring of the sample. This cylindrical aluminium block allows the simultaneous thermostatzation of 4 *Schlenks* at a programmable temperature, which was always set to 60°C. Both systems are illustrated in figure 2.2.

The samples of ionic liquids used in μ FlowCal calorimeter, were filtered with PTFE® filters (0.45 μ m, acquired from VWR™) and then dried in glass drying tubes (external diameter = 28 mm; height = 120 mm) containing a male joint 24/29 (diameter = 24 mm and height = 29 mm), which is used with a customized PTFE® “stopper” adapted to PE tubing (diameter = 6 mm), as illustrated in the right side of figure 2.1. These tubes are thermostated in cylindrical aluminium blocks identical to the ones described above, except for the fact that due to the diameter of the tubes, these aluminium blocks can only hold up to 3 tubes simultaneously.

All these systems are connected to a PE/stainless steel vacuum line existent in the laboratory. The vacuum of the line is maintained by a rotary vane vacuum pump (Edwards model RV5) reaching a final pressure lower than 10 Pa (0.1 mbar).



Figure 2.2. Figure of the temperature-controlled aluminium blocks of the drying system. On the left side the rectangular block that allows the simultaneous thermostatzation of 15 *Schlenks*. On the right side the cylindrical block that allows the simultaneous thermostatzation of 4 *Schlenks* on top of a magnetic stirring plate. (Adapted from ref. [1, 2]).

All the ionic liquids used in this work were purified as described for at least 48 hours prior to its utilization in order to minimize the amount of water, gases and volatile impurities. The methodology of drying of the ionic liquids was tested with a Karl Fischer from Metrohm (model 737 KF Coulometer using HYDRANAL™ - Coulomat AG from Riedel-de Haën) prior to the experiments with the content of water being lower than 100 ppm.

2.2.2. Purification of Molecular Solutes

The alcohols used have purities better than 99% (>97% in the case of fluorinated alcohols). Activated molecular sieves (pore size 0.3 nm with a humidity indicator), obtained from Metrohm AG, were used to ensure the dryness of the samples used in ITC and *DropCalvet*. In μ FlowCal calorimeter all the samples were filtrated with PTFE® filters (0.2 μ m, acquired from VWR™) and then degassed and dried at reduced pressure. The degassing and drying system, illustrated in figure 2.3 is held by a Vacuum Pump (BUCHI, model V-700 with vacuum controller V-850) able to reach final pressures in the range of 200-300 Pa (2-3 mbar). Laboratory bottles of 10 cm³ or 25 cm³ with specially modified GL25 DURAN® caps were used to hold the sample. The caps were obtained from DURAN® and modified in the laboratory in order to fit and seal in PE tubing (diameter = 4 mm). As illustrated in figure 2.3 the DURAN® glass bottles were used on top of a magnetic stirring plate.

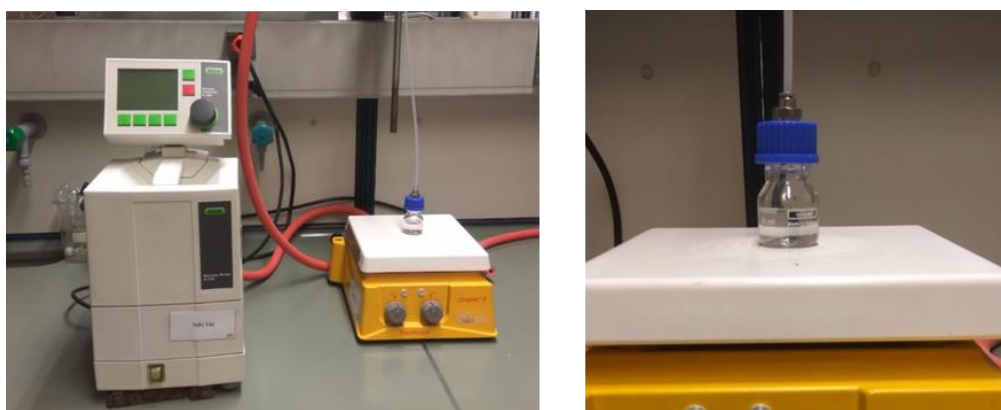


Figure 2.3. Figure of the degassing and drying system of molecular solutes that will be used in μ FlowCal calorimeter (on the left side) and of the laboratory bottle of 10 cm³ with specially modified GL25 DURAN® cap (on the right side).

2.3. Sample Handling

In the particular case of *tert*-butyl-alcohol, which crystallization occurs close to room temperature (around 290 K with melting at higher temperature 298-299 K)^[3, 4], special care was taken in the handling of the sample and preparation of the experiments in order to prevent crystallization of the alcohol.

For the preparation of the experiments in isothermal titration calorimetry, a thermostated box was constructed and used to maintain the alcohol sample and the syringe above room temperature and prevent crystallization during the filling of the Hamilton syringe. During the measurements in ITC, an external thermostated jacket was used to maintain the temperature of the alcohol at 298 K and prevent crystallization during the experiments.

To prepare the *tert*-butyl-alcohol samples for *DropCalvet* the thermostated box was used to maintain the alcohol stored above room temperature and special care was taken during the preparation of the capillary glass tubes with the sample and its manipulation until dropping of the capillary in the calorimeter, to avoid sample crystallization.

2.4. Additional Materials

The calorimetric techniques ITC and μ FlowCal were electrically calibrated and its performance and accuracy was tested with the mixture of test compounds. The *DropCalvet* Calorimeter was calibrated using calibrants which properties of interest were well documented in the literature and similar to the compounds in study. The summary of the calibrants and test compounds used in the calibration/ performance tests will be presented herein, in table 2.5, indicating the techniques where they were applied and its purpose (test/calibration). The water used was purified in Millipore Milli-Q® Gradient Water Purification System.

Table 2.5. Summary of the calibrants and test compounds used in calibration / performance tests and the techniques where they were used

Compound	CAS	Supplier	Purity	Technique	Purpose
1-Propanol	71-23-8	Sigma-Aldrich	≥99,9%	ITC ^a	Test
1-Butanol	71-36-3	Sigma-Aldrich	99.9%	DropCalvet	Calibrant
Water	7732-18-5	---	---	ITC ^a / μFlowCal	Test
1-Octanol	111-87-5	Fluka Analytical	≥99,5%	μFlowCal	Test
Decane	124-18-5	Sigma-Aldrich	>99%	μFlowCal	Test
<i>Tert</i> -butyl-alcohol	75-65-0	Sigma-Aldrich	99.3%	DropCalvet	Calibrant
Sucrose	57-50-1	Riedel-de Haën	Extra pure	μFlowCal	Test

^a ITC – Isothermal Titration Calorimetry

References

- [1] M. A. A. Rocha, PhD Thesis, Thermophysical Properties of Ionic Liquids, University of Porto, **2013**.
- [2] I. C. M. Vaz, MSc Thesis, Estudo da Solvatação de Álcoois em Líquidos Iónicos, University of Porto, **2015**.
- [3] E. S. Domalski and E. D. Hearing, Heat Capacities and Entropies of Organic Compounds in the Condensed Phase. Volume III, *Journal of Physical and Chemical Reference Data*, 25 (**1996**) p. 1-525. DOI:10.1063/1.555985.
- [4] I. C. M. Vaz, A. I. M. C. Lobo Ferreira and L. M. N. B. F. Santos, Fluorination effect on the phase behaviour and cohesive energy of alcohols, Manuscript in Preparation.

CHAPTER 3

Experimental Methodologies

Calorimetry

-
- 3.1. Concepts in Calorimetry
 - 3.2. Experimental Methodologies
 - 3.3. Calibration and Test of the Calorimetric Systems
 - References
-

3. Experimental Methodologies... *Calorimetry*

Along this project three different calorimetric techniques were used. Isothermal titration calorimetry was used to measure the heat of solution at infinite dilution of alcohols in ionic liquids. *DropCalvet* calorimetry was used to determine the heat of vaporization of some fluorinated alcohols. The knowledge of this property, together with the enthalpy of solution at infinite dilution allowed the determination of the enthalpy of solvation at infinite dilution of the alcohols in ionic liquids. μ FlowCal was designed, constructed and tested, in the context of this project, aiming to explore the mixing properties of alcohols in ionic liquids.

This chapter will thus concern calorimetry, with special focus in (isothermal) heat flow calorimetry. Some physical concepts on heat and its measurement will be first introduced. The three calorimeters will then be described and the calibration, testing and data treatment of the obtained results will be presented and discussed.

3.1. Concepts in Calorimetry

Calorimetry is the technique of measuring heat. The word itself derives from the word “*calor*”, the Latin word for heat, and “*metron*”, the Greek word for measure ^[1]. This technique/methodology is therefore appropriate to study any process which involves the absorption or release of heat, which is a description that fits in almost any physical, chemical or biological process that we may imagine. Despite its broad application range, the measurement of heat (heat flow) is a nontrivial subject. This section aims essentially to introduce the topic and to present some concepts which are important to understand and work in/with heat flow calorimetry.

3.1.1. Heat Transfer

Heat is associated with heat flow, which is the movement of energy caused by a gradient of temperature. Since a gradient of temperature must exist in order to exist heat transfer, the phenomena of heat transfer implies a thermodynamic non-equilibrium. According to zeroth law of thermodynamics, at thermodynamic equilibrium the heat transfer is zero.

Three kinds of heat transfer may be considered: heat transfer by conduction, heat transfer by convection and heat transfer by radiation.

3.1.1.1. Heat Transfer by Radiation

Heat transfer by radiation is energy emitted by matter, regardless of its state, and it can be attributed to changes in its electronic configuration. Moreover, it propagates in any kind of medium, including vacuum. For that reason, even in the absence of a contact medium, there is always present a net heat transfer by radiation, if two surfaces are at different temperatures (until thermal equilibrium is reached). Considering some simplifications/assumptions, the net rate of heat transfer by radiation, ϕ ($\text{J}\cdot\text{s}^{-1}$), from a surface "s", at a temperature T_s , which is completely surrounded by a larger isothermal surface, at a temperature $T_{\text{surroundings}}$, can be quantified by means of equation 3.1:

$$\phi = -\varepsilon_s \cdot \sigma \cdot A_s \cdot (T_s^4 - T_{\text{surroundings}}^4), \quad (3.1)$$

where ε_s is the emissivity of the surface, σ is the Stefan-Boltzmann constant and A_s (m^2) is the area of the surface "s". The net rate of heat transfer by radiation is obtained from the radiation emitted by surface "s" minus the radiation which is absorbed by the "s" surface. For this equation to be valid, it is considered that the surface "s" absorbs all radiation emitted by the larger isothermal surface, which is considered to emit radiation as a black body, at temperature $T_{\text{surroundings}}$, ($Q = \sigma \cdot T_{\text{surroundings}}^4$). Plus, the absorptivity of the "s" surface is considered to be equal to its emissivity " ε_s ".

3.1.1.2. Heat Transfer by Conduction

Heat transfer by conduction can be defined as heat being transferred by the excitement of the molecules that constitute a material in the absence of bulk motion of the molecules. In gases and liquids, the heat transfer by conduction happens due to the random motion of the molecules that end up colliding and transferring heat. Analogously, in solids, the heat is transferred by lattice vibration. Accordingly, due to the typical intermolecular space, a crystalline solid is typically a better thermal conductor than a liquid, which is typically a better conductor than a gas.

The heat transfer process can be quantified by means of an equation (equation 3.2) applicable for all matter regardless of its state,

$$\phi = -k \cdot A \cdot \frac{dT}{dx}, \quad (3.2)$$

where ϕ ($\text{J}\cdot\text{s}^{-1}$) is the heat flux, k ($\text{J}\cdot\text{s}^{-1}\cdot\text{m}^{-1}\cdot\text{K}^{-1}$) is the thermal conductivity, A (m^2) is the cross sectional area, which is the area of the isothermal surface, normal to the direction in which heat is being transferred. $-dT/dx$ is the gradient of temperature and is commonly negative, because it is considered the decreasing of the temperature.

Besides the thermal conductivity, there is another property which is very important when talking of heat transfer by conduction, the thermal diffusivity, α ($\text{m}^2\cdot\text{s}^{-1}$):

$$\alpha = \frac{k}{\rho \cdot c}, \quad (3.3)$$

where k ($\text{J}\cdot\text{s}^{-1}\cdot\text{m}^{-1}\cdot\text{K}^{-1}$) is the thermal conductivity, ρ is the density ($\text{kg}\cdot\text{m}^{-3}$) and c is the specific heat capacity ($\text{J}\cdot\text{K}^{-1}\cdot\text{kg}^{-1}$). Thus, the thermal diffusivity relates the ability of a material to conduct thermal energy to its ability to store thermal energy. Materials of high thermal diffusivity will respond quickly to thermal changes in their surroundings, whereas materials of smaller thermal diffusivity will take longer time to reach thermal equilibrium. As a result, thermal diffusivity can be interpreted as a measure of the speed of heat conduction. The thermal diffusivity and thermal conductivity are thus, very important properties in calorimetry.

3.1.1.3. Heat Transfer by Convection

Heat transfer by convection can be defined as heat transferred from a surface to a moving fluid. On the contrary of the heat transferred by conduction, where there was no bulk motion of the molecules and the heat was transferred due to their random motion, in heat transfer by convection, the heat is transferred by the bulk / “macro” motion of the fluid. As the molecules maintain its random motion, even if the bulk fluid is in motion, there is a contribution of heat transfer by conduction. Normally, the term convection is used to describe heat transferred by the bulk movement of the fluid plus the heat transferred by the random motion of the molecules, whereas the term advection refers only to heat transfer by the bulk movement of the fluid.

The characteristics of the fluid flow allow to distinguish between different types of convection. If the fluid flow is caused simply by density variations, caused by the existence of gradients of temperature, it can be named as free or natural convection. If the flow is caused by fans or pumps, it is named forced convection. However, both types of convection can coexist. Independently of the type of flow present, the heat transfer process can be quantified by means of equation:

$$\phi = -h \cdot A \cdot (T_f - T_\infty), \quad (3.4)$$

where ϕ ($\text{J}\cdot\text{s}^{-1}$) is the heat flux, h ($\text{J}\cdot\text{s}^{-1}\cdot\text{m}^{-2}\cdot\text{K}^{-1}$) is the convection heat transfer coefficient, that depends on the surface geometry, the nature of the fluid motion and on the transport properties of the fluid, A (m^2) is the cross sectional area, which is the area of the isothermal surface and $(T_f - T_\infty)$ is the difference between the temperature of the fluid T_f (K) and the temperature of the surface T_∞ (K).

3.1.2. Principle of Heat Measurement

Calorimeters can be classified in three different types, basing on the principle of measurement of its heat transfer.

In figure 3.1 a very simplistic model of the heat flowing in a calorimeter is presented. This model will be revisited and reformulated to present and discuss different concepts. A fundamental part of the calorimeter design, which is how the heat is measured, is missing in figure 3.1. In figures 3.2, 3.4 and 3.5, the present scheme is

reformulated in order to schematize a calorimeter which principle of operation is based in the principles of heat accumulation, heat compensation and heat conduction/flow. For this simplistic model, let's consider the compartment of the calorimeter which holds the sample to be the system in study, and that this sample holder is enclosed in an aluminium block of much higher heat capacity, designated by heat sink. This scheme represents only the sample, where the process under study will develop, the sample holder located in a cavity, which is enclosed in the heat sink, and the heat being transferred between them. The outside medium of the calorimeter is the surroundings. It is considered that the calorimeter is fully isolated and so, there is no heat being transferred from the surroundings to the calorimeter, or from the calorimeter to the surroundings. Considering this model, if an endothermic process occurs in the sample, energy will flow from the heat sink to the sample. If, on the contrary, an exothermic process takes place, the heat will flow from the sample to the heat sink.

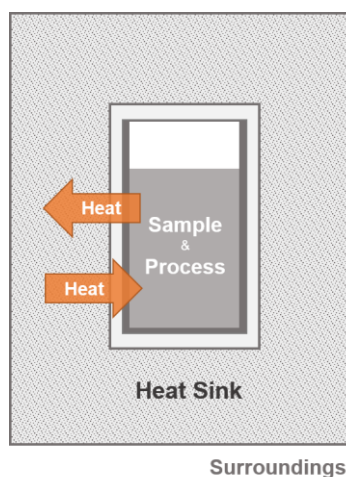


Figure 3.1. Schematic representation of a simplistic model of the heat flow in a calorimeter.

3.1.2.1. Heat Accumulation Calorimeters

Starting from the model proposed above, in a hypothetical scenario where the sample holder was fully isolated from the heat sink, no heat could be transferred between the sample and the heat sink. The increase/decrease of the thermal energy in the system, caused by the process being studied, would then lead to the increase/decrease of the temperature of the system. This is the principle of operation of a calorimeter based

in heat accumulation, also called adiabatic calorimeter or semi-adiabatic, which is schematized in figure 3.2.

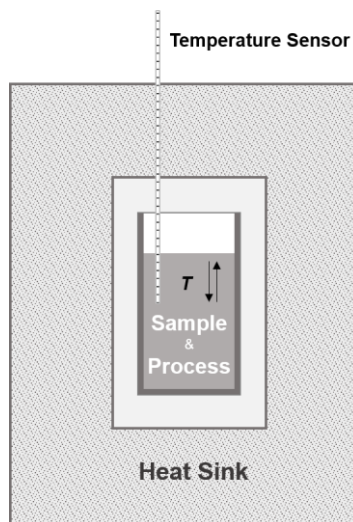


Figure 3.2. Schematic representation of a section through an adiabatic calorimeter.

In real calorimetric systems, the perfect isolation of the system from the heat sink is impossible, as there will always be some heat exchange when two surfaces are at different temperatures. Even in a hypothetical scenario in which the sample holder was separated in space, by a certain length, from the heat sink, and the medium between them was evacuated to prevent heat transfer from conduction and convection, heat transfer from radiation would still occur. To maintain ideal adiabatic conditions, the temperature of the calorimeter and the heat sink must be equalized to prevent net heat transfer. So, in practical cases is common to have semi-adiabatic calorimeters, also called isoperibol calorimeters.

In semi-adiabatic or isoperibol calorimeters there is some heat exchange between the vessel, where the process is occurring, and the thermostat/heat sink that remains at constant temperature, which is corrected afterwards.

In the left side of figure 3.3 is represented the schematic curve of the temperature variation in the system against time, $T = f(t)$, when an exothermal process takes place in the sample, in an ideal adiabatic calorimeter. The curves represent the difference between a very fast exothermic process (in orange), that “instantly” changes the temperature of the system, and a slower process, that increase the temperature for a period in time (in blue) at a constant heat production rate. In the right side of figure 3.3, the same curves are reproduced for a semi-adiabatic or isoperibol calorimeter. The

temperature of the system before and after the exothermic process are now in drift, converging to the temperature of the heat sink/thermostat in contrast to the constant temperature of an ideal adiabatic calorimeter.

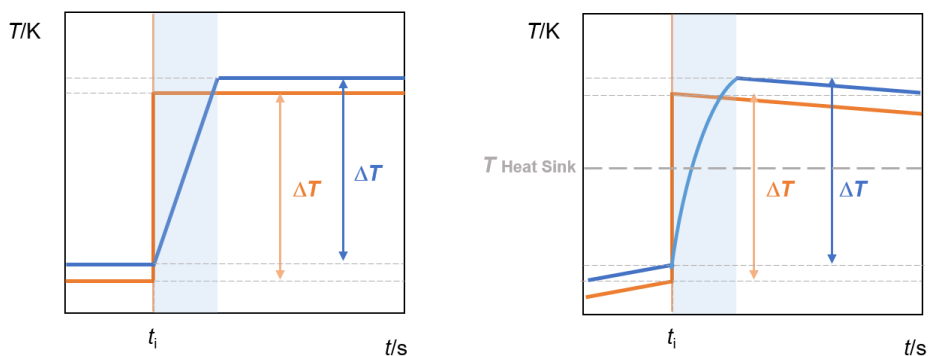


Figure 3.3. Schematic curves of the temperature variation in the system along time in an ideal adiabatic calorimeter (left side) and in a semi-adiabatic calorimeter (right side). Orange curve – instant exothermic process; blue curve – slow exothermic process.

In an ideal adiabatic calorimeter, the thermal energy absorbed/released by the process being studied can be described as,

$$Q = C \cdot \Delta T, \quad (3.5)$$

where Q (J) is the thermal energy involved in the process, C ($\text{J} \cdot \text{K}^{-1}$) is the capacity of the calorimetric vessel / sample holder and its content to store thermal energy and ΔT (K) is the temperature variation in the system. In a real calorimeter there is always a fraction of the heat being transferred to the surroundings. Thus, a calibration constant, ε_{cal} ($\text{J} \cdot \text{K}^{-1}$), must be derived by calibration in order to correct/include the hypothetical heat capacity associated with the fraction of the heat being transferred (heat leakage). The expression presented as equation 3.6 describes the thermal energy absorbed/released in the process in which " ε_{cal} " must always be higher than " C ".

$$Q = \varepsilon_{\text{cal}} \cdot \Delta T. \quad (3.6)$$

In semi-adiabatic or isoperibol calorimeters a correction must be performed to correct the temperature variation in the calorimeter ΔT (K) to the hypothetical temperature variation in the calorimeter if the process would have occurred under perfect adiabatic conditions ΔT_{ad} (K) ^[2]. Under these circumstances, the equation 3.6 should now be re-written as:

$$Q = \varepsilon_{cal} \cdot \Delta T_{ad}, \quad (3.7)$$

in which the calibration constant " ε_{cal} " should be very close to the heat capacity " C " of the system. The adiabatic and semi-adiabatic/isoperibol systems described here were simplified as the aim of this thesis is just to introduce the concept of the principle of heat measurement by accumulation. In figure 3.2, for example, a calibration heater, a stirrer and an adiabatic shield should be added for a more realistic scheme of an adiabatic calorimeter.

3.1.2.2. Heat Compensation Calorimeters

Another possibility of measuring the heat released or absorbed by the process under study is to compensate it, by electrically heating/cooling the system, maintaining it at the same temperature of the heat sink. The knowledge of the electrical input of power necessary to compensate the heat absorbed/released in the system gives information on the heat originated by the process. This is the principle of operation of a calorimeter based in heat/power compensation, as schematized in figure 3.4.

The mechanism of heating can be very easily accomplished by Joule effect (see section 3.3.2 for information on Joule effect). The simultaneous capacity of heating/ cooling the system can be based in a Peltier system, where the heating /cooling is based in a proportionality relation between the power input into the system and the electrical current, provided that on cooling, the Peltier effect surpasses the Joule effect.

Historically, these calorimeters were used with compensation of exothermic processes by melting a solid material.

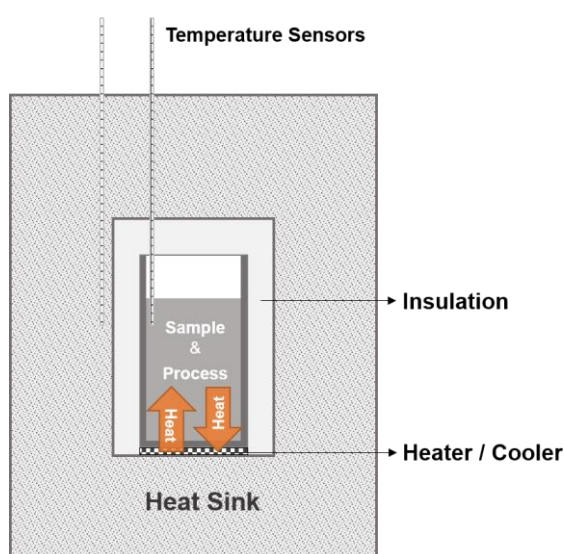


Figure 3.4. Schematic representation of a section through a heat / power compensation calorimeter.

3.1.2.3. Heat Conduction/Flow Calorimeters

In a heat flow calorimeter, the heat flows from the sample to the heat sink or from the heat sink to the sample, depending if a scanning temperature rate is applied and if the process is exothermic/endothermic. The heat sink has always a higher heat capacity, when compared to the sample, leading to a heat sink, ideally, with temperature uniformity despite of the magnitude of the heat exchange. In these calorimeters, there is heat transfer between the sample and the heat sink, through heat flow sensors (see figure 3.5), originating a potential difference across the sensor, due to the so-called Seebeck effect, a topic that will be explored further in section 3.1.3.

In an ideal heat flow calorimeter, and considering an exothermal process occurring in isothermal mode (with no imposed temperature scan), all the heat released in the sample would flow from the sample, through the wall of the sample holder, through the heat flow sensor, to the heat sink. The rate of the power release, P ($\text{J}\cdot\text{s}^{-1}$), can, in each instant, be described as,

$$P = \frac{dQ}{dt} + C \cdot \frac{d\Delta T}{dt}, \quad (3.8)$$

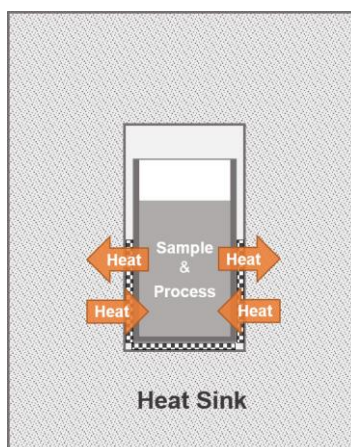


Figure 3.5. Schematic representation of a section through a heat conduction / flow calorimeter.

where dQ/dt , describes the heat flowing from the sample to the heat sink, through the heat flow sensor, and $C \cdot (d\Delta T/dt)$ the power accumulated or released by the calorimetric cell (including its content and half of the heat flow sensor), which is related with the local temperature change and the heat capacity C ($J \cdot K^{-1}$). In other words, the heat transferred through the heat flow sensor, at any moment in time, is a balance between the energy released/absorbed in the process and the heat stored by the sample and the calorimetric vessel.

In figure 3.6. is schematized the heat transfer from the sample to the heat sink, through heat flow sensors. In this scheme, for a better understanding, the sample, the sensor and the heat sink are separated in space to represent the heat flowing between them. In reality they are always in thermal contact ($d = 0$).

Heat flow calorimetry operates under the principles of heat conduction. So, the properties of heat conductivity and diffusivity of the different materials will be a fundamental issue in this kind of calorimetry. The concept of heat diffusivity, α ($m^2 \cdot s^{-1}$), was described in equation 3.3:

$$\alpha = \frac{k}{\rho \cdot c}, \quad (3.3)$$

where k ($J \cdot s^{-1} \cdot m^{-1} \cdot K^{-1}$) is the conductivity, ρ is the density ($kg \cdot m^{-3}$) and c is the specific heat capacity ($J \cdot K^{-1} \cdot kg^{-1}$). Therefore, the thermal diffusivity relates the ability of a material to conduct thermal energy to its ability to store thermal energy. In calorimetry we can

relate these properties with the thermal inertia of a calorimeter. The thermal inertia of a heat flow calorimeter, normally designated as the time constant of the calorimeter, τ (s), can be estimated from the conductance G ($\text{J}\cdot\text{s}^{-1}\cdot\text{K}^{-1}$) of the heat flow sensor and the total heat capacity of sample, the sample holder and half of the heat flow sensor C ($\text{J}\cdot\text{K}^{-1}$),

$$\tau = \frac{C}{G}. \quad (3.9)$$

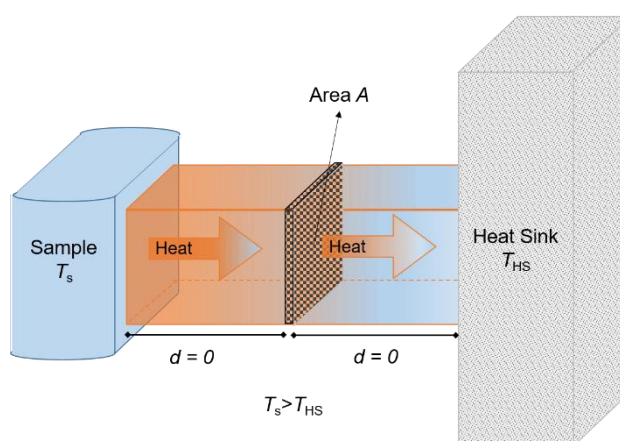


Figure 3.6. Schematic representation of heat transfer from the sample to the heat sink, through heat flow sensors, in a heat flow calorimeter.

Some of the characteristics of a heat flow calorimeter are related with the overall heat capacity of the calorimetric cell and its contents, as well as, to the thermal conductance of the heat flow sensor. If the heat flow sensor device has a very low conductance, the calorimeter will approach isolation conditions and heat will accumulate instead of flowing, maintaining no longer a low temperature gradient between the calorimetric cell and the heat sink (approaching the principle of a heat accumulation calorimeter). On the contrary, a high thermal conductance of the heat flow sensor device will lead to a very low temperature gradient and, in consequence, to a decrease of the heat flow device sensitivity.

The overall heat capacity of the calorimetric cell and its content do not affect directly the sensitivity of the calorimeter. However, it will have a strong effect on the thermal inertia of the calorimeter. An increase of the overall heat capacity of the calorimetric cell and its content leads to an increase of the thermal inertia of the

calorimeter. Hence, in order to optimize the sensitivity and the time-lag of the calorimetric signal, the thermal conductivity of the materials and the design of the heat flow sensor devices, as well as, the overall heat capacity (size) of the calorimetric cell must be balanced.

The Twin Design

Heat conduction calorimeters are usually constructed under the principle of the twin/differential design^[3], represented in figure 3.7, which is essential to achieve a long-time baseline stability, as well as, to have a direct cancelation of the heat capacity of the sample holder and heat flow device. The twin design strategy (differential type) is applied in other systems, which are not heat flow type calorimeters. However, this topic will not be addressed in this thesis.

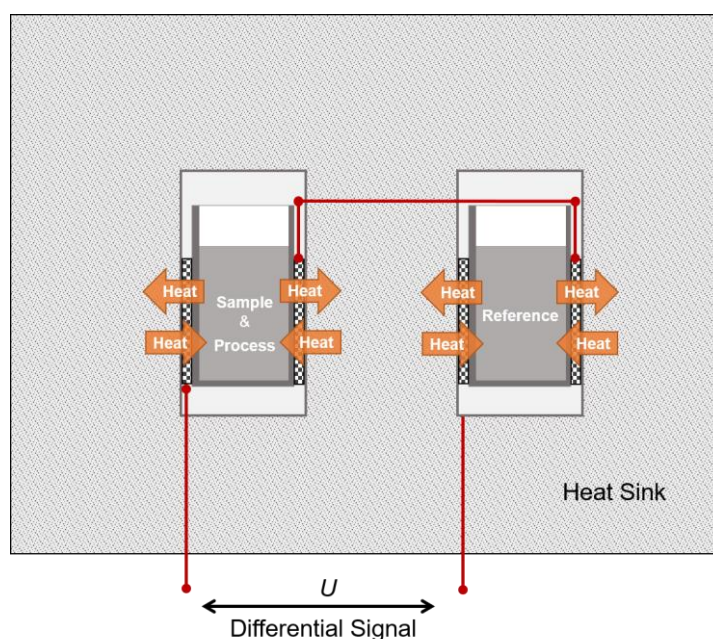


Figure 3.7. Schematic representation of a differential (isothermal) heat flow calorimeter.

As represented in figure 3.7, a differential (isothermal) heat flow calorimeter can be represented by two sample holders surrounded by thermopiles and sharing a

common heat sink. The term twin comes from the identical position and symmetrical arrangement of the sample and reference cells of the calorimeter, in addition to the use of identical heat flow sensors and sample holders. The heat flow sensors (sample and reference) are connected in opposition (differential mode) in order to have a noise cancelation arising from: the temperature fluctuation of the heat sink, electronic noise, environmental pressure, radiation, humidity, among others, which could arise from the complexity of the calorimetric methodology.

3.1.3. Measurement of Heat

Now that some introduction has been made on the transference of heat and on the main principles of heat measurement in calorimetry, it is important to understand how the heat flow is measured. The three calorimeters used in this work are of the isothermal heat flow type. So, this section will focus in the concepts of the measurement of heat in isothermal heat flow calorimeters.

3.1.3.1. Seebeck Effect and Heat Flow Sensor

As described before, in heat flow calorimeters, the heat transfers through heat flow sensors, generating an electrical potential across the sensor, which could be explained by the Seebeck effect. The Seebeck effect owes its name to the German physicist Thomas Johann Seebeck that in the beginning of 1820s ^[4] discovered that in an open circuit constituted by two wires of different conductor materials joined together, a thermoelectric voltage could be generated at the free wire ends, if the junctions of the materials were subjected to a gradient of temperature. This effect is illustrated in the left side of figure 3.8. In the figure, two different metals, represented by metal “A” and metal “B”, are joined together and are subjected to a gradient of temperature, $\Delta T = T_{\text{sense}} - T_{\text{ref}}$. A continuous current is then generated by the gradient of temperature created in the metallic wires. The thermoelectric potential generated in the circuit can be measured with a voltmeter, as represented.

As the generated thermoelectric potential (voltage) is dependent on the temperature gradient of the wires junction and the free (reference) ends, and this dependence is repeatable, the system can be used for the measurement of a temperature gradient. The sensors of temperature based in the Seebeck effect are

designated by thermocouples. In the right side of figure 3.8, a scheme of the principle of measurement of temperature with a thermocouple is presented.

Different thermocouples are possible depending on the pair of conductor materials that are combined. For the direct temperature measurement, one of the junctions must be at the reference temperature of 273 K (0 °C). The relation between the temperature gradient and the voltage generated is different for the different thermocouples. The Seebeck coefficient of a thermocouple, e_c ($\mu\text{V}\cdot\text{K}^{-1}$), which can also be designated by its temperature sensitivity, is determined by the ratio between the magnitude of the thermoelectric voltage, dU and the temperature difference dT , as follows:

$$e_c = \frac{dU}{dT} . \quad (3.10)$$

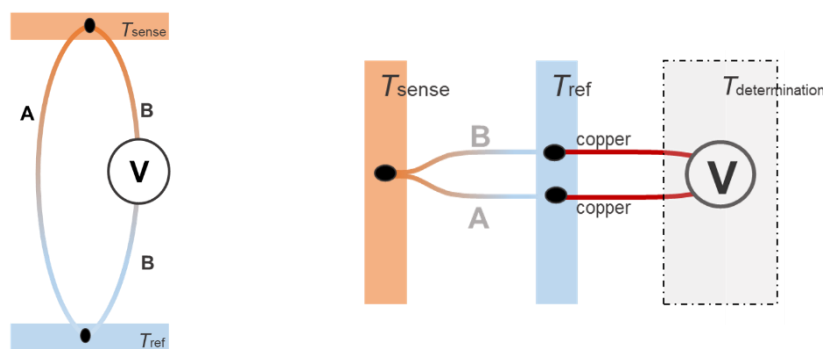


Figure 3.8. Schematic representation of a thermoelectric couple – Seebeck effect.

Thermocouples can be joined in series originating a thermopile (see figure 3.9), which allows the increase of the thermoelectric voltage to the same temperature gradient increasing thus the sensitivity. When gradients of temperature are very small, as in isothermal calorimeters, the Seebeck coefficient can be considered constant. In such conditions the potential difference, U (μV), originated across a thermopile of n couples can be expressed as,

$$U = n \cdot e_c \cdot \Delta T , \quad (3.11)$$

where ΔT (K) is the temperature difference, in the defined space, generated by the temperature gradient. The Seebeck coefficient of a thermopile, e_{TP} ($\mu V \cdot K^{-1}$), may be defined as,

$$e_{TP} = n \cdot e_c, \quad (3.12)$$

where, n is the number of thermocouples and e_c ($\mu V \cdot K^{-1}$) is its Seebeck coefficient. This means that the junction of n thermocouples in series, generates a thermopile whose temperature sensitivity is increased by a factor on n (in comparison to a single thermocouple).

Thermopiles can be used as very sensitive sensors of temperature and heat flow. Nevertheless, in heat flow calorimetry the sample holder is not in thermal equilibrium, so its temperature is not uniform. Plus, the temperature of the thermoelectric junctions does not correspond exactly to the temperature of the sample and the heat sink [5]. For those reasons, in this type of calorimetry, thermopiles are used as heat flow sensors instead of temperature sensors.

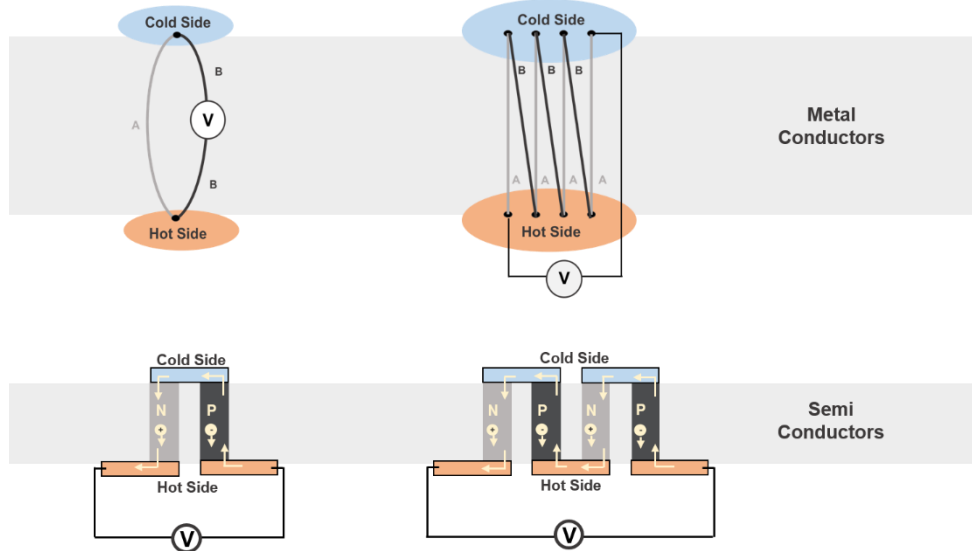


Figure 3.9. Schematic representation of a thermoelectric couple and a thermopile constituted by metals and semiconductors.

To be used as heat flow sensors in calorimetry, in general, the thermoelectric materials (thermocouples and thermopiles) should comply with the following requirements:

- to have high Seebeck coefficient / temperature sensitivity;
- to have high electrical conductivity (so that the heating by Joule effect is minimum);
- to have a “balanced” thermal conductivity (low enough to maintain a temperature gradient, but not approaching the behaviour of an insulator).

The choice of the right thermoelectric material will depend on the requirements of the application/working range of the calorimeter. To meet these requirements thermocouples and thermopiles can be constituted by metallic conductors or semi-conductors. In figure 3.9 is represented a scheme of thermocouples and thermopiles constituted by metallic conductors and semi-conductors.

Metallic thermocouples are used in calorimeters that operate in wide temperature range or at high or very low temperature. Thermopiles made from metallic conductor couples as iron-constantan (J type), chromel-constantan (E type) or platinum – platinum–10% rhodium alloy (S type) are usually applied in these conditions. Heat flow sensors based in semiconductors like Peltier elements are limited by working temperature range of the semiconductors materials (typical - 50 to 200 °C) as well as, of the materials used as solder connections. In contrast, the sensitivity of the semiconductors based couples are usually two orders of magnitude higher than the typical metallic conductors couples.

The number, size and geometry arrangement of the couples (metallic or semiconductor) is typically used/balanced in the optimization of the efficiency and thermal inertia of the calorimeter.

The Calvet drop calorimeter HT1000D from SETARAM, used in this thesis, is a heat flow differential calorimeter, designed to operate from ambient temperature to 1273 K (1000 °C). This calorimeter is based in a twin arrangement of a pair of cylindrical three dimensional thermopile heat flow sensor, constituted by 496 thermocouples of type S (pure platinum and platinum–10% rhodium alloy). This type of metallic thermocouple present a very low Seebeck coefficient ($10 \mu\text{V}\cdot\text{K}^{-1}$)^[6], in the other hand, this thermocouple has the highest physical and chemical stabilities. The combinations of number, size and geometry arrangement of the couples of 16 sheets of 31 type S thermocouples result in a calorimeter sensitivity of $3 \mu\text{V}/(\text{mJ}\cdot\text{s}^{-1})$.

More sensitive microcalorimeters are achieved using heat flow sensors based in semiconductor materials instead of metallic couples, as is the case of prototype microcalorimeters constructed by Ingemar Wadsö and co-workers^[7]. The isothermal titration calorimeter used in this work is identical to the described by Ingemar Wadsö “ITC-A”^[7]. This calorimeter is a twin heat flow isothermal calorimeter, in where the heat flow of each calorimetric cell is measured by two semiconductor thermocouple plates from MELCOR (reference FC 0.45-66-05) with 66 thermocouples per plate and with a Seebeck coefficient of $397 \mu\text{V}\cdot\text{K}^{-1}$ per thermocouple. The sensitivity coefficient of this calorimeter is $370 \mu\text{V}/(\text{mJ}\cdot\text{s}^{-1})$, far superior than the sensitivity of the Calvet HT1000D calorimeter, which essentially reflects the effect of the Seebeck coefficients on the sensitivity of the calorimeter. Nonetheless, these values should be compared with caution since the calorimeters have a quite different design.

In $\mu\text{FlowCal}$, the heat flow sensors are semiconductor thermocouple plates (Peltier elements), identical to the ones used in the ITC. The Peltier elements (Laird, model HT4-6-F2-2143) used in $\mu\text{FlowCal}$ prototype calorimeter are based in bismuth telluride semiconductor couples and thermally conductive aluminium oxide ceramics coated by a non-corrosive silicone adhesive.

In figure 3.10 is represented a scheme of two calorimeters which heat flow sensors are based in thermopiles made from metallic conductor couples (on the left), as the *DropCalvet* calorimeter, and semiconductor materials (on the right), as ITC or $\mu\text{FlowCal}$.

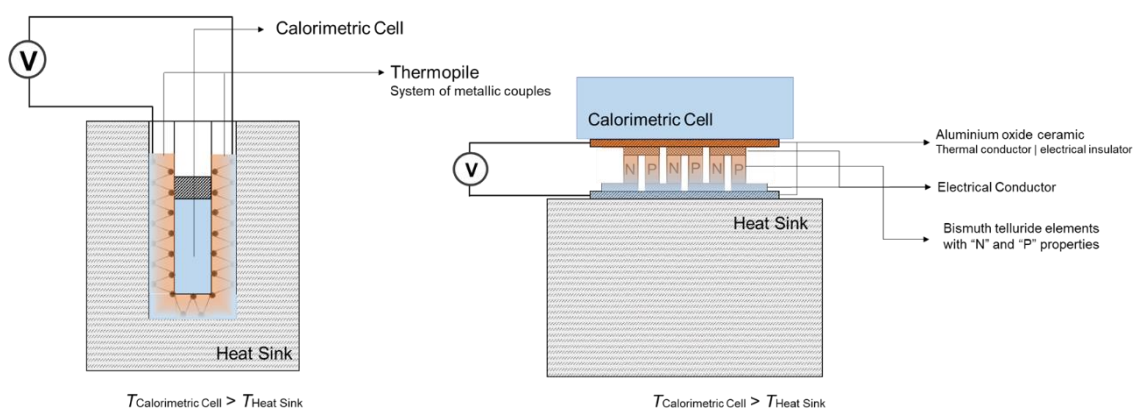


Figure 3.10. Schematic representation of two calorimeters, which heat flow sensors are based in thermopiles made from metallic conductor couples (on the left) and semiconductor materials (on the right). In the representation, heat is transferring from the calorimetric cell to the heat sink.

3.1.3.2. Fraction of Heat Measured - Sensitivity

In an ideal heat flow calorimeter, where all heat flows through the thermopile and there are no heat losses, the heat flow, ϕ ($\text{J}\cdot\text{s}^{-1}$), can be related to the thermal conductance of each thermocouple, G_c ($\text{J}\cdot\text{s}^{-1}\cdot\text{K}^{-1}$), multiplied by the number n of thermocouples in the thermopile and the difference of temperature across the thermopile:

$$\phi = \frac{dQ}{dt} = G_c \cdot n \cdot \Delta T. \quad (3.13)$$

The sensitivity of an ideal heat flow calorimeter, S_{id} ($\mu\text{V}\cdot\text{s}\cdot\text{J}^{-1}$), can be thus calculated from the relation between the thermoelectric potential generated and the heat flow that generated it, by combining equations 3.11 and 3.13,

$$S_{id} = \frac{U}{\phi} = \frac{n \cdot e_c \cdot \Delta T}{G_c \cdot n \cdot \Delta T} = \frac{e_c}{G_c}, \quad (3.14)$$

which clearly shows that for an ideal heat flow calorimeter, its sensitivity only depends on the Seebeck coefficient of the thermocouples, e_c ($\mu\text{V}\cdot\text{K}^{-1}$), and on its thermal conductance, G_c ($\text{J}\cdot\text{s}^{-1}\cdot\text{K}^{-1}$).

The sensitivity of an ideal heat flow calorimeter is thus independent of the number of thermocouples present in the sensor and of the heat capacity of the sample and sample holder. Moreover, from this relation it is clear that the increase of the thermal conductance of the thermopile will decrease the sensitivity of the heat flow calorimeter. Accordingly, in heat flow calorimetry there will always be a compromise between sensitivity and the time constant.

As seen before, in equation 3.9, the time constant of the calorimeter depends on the thermal capacity of the sample, sample holder and half of the thermopile and on the inverse of the thermal conductance of the thermopile. Therefore, in order to decrease the time constant of a heat flow calorimeter only the heat capacity can be minimized without losing sensitivity.

In a real heat flow calorimeter, part of the heat of the process under study is always lost by conduction, convection or radiation and does not flow through the sensor. By that reason, the sensitivity of the instrument must be determined experimentally,

S_{exp} ($\mu\text{V}/(\text{J}\cdot\text{s}^{-1})$). The fraction of the heat, which is not captured by the heat flow sensor, may be estimated by the ratio of the ideal sensitivity and the one experimentally obtained,

$$f = \frac{(S_{\text{id}} - S_{\text{exp}})}{S_{\text{id}}} . \quad (3.15)$$

The fraction of heat loss varies from calorimeter to calorimeter, depending on the particularities of its design. However, it has been showed^[7] that the fraction of heat loss is minimized when the sample holders were almost completely covered by thermocouple plates. This detail is more easily accomplished if the sample holder has a cylindrical shape with small radius relative to its height. This way, the thermocouples can be regularly distributed around the holder and the heat will flow uniformly. This design optimization was merit of Calvet^[5].

This does not mean however, that a calorimeter with a considerable fraction of heat lost can not be very accurate. The accuracy of such a calorimeter will essentially depend on the repeatability of the heat flow capture and of the calibration procedure used. In order to not have considerable systematic deviations, the calibration procedure chosen should mimic the heat flow path of a normal experiment of the process being investigated.

For convenience, the inverse of the experimental sensitivity is used as a calibration constant, ε_{cal} ($\text{J}\cdot\text{s}^{-1}/\mu\text{V}$),

$$\varepsilon_{\text{cal}} = \frac{1}{S_{\text{exp}}} . \quad (3.16)$$

It should be noted that this calibration constant is just the inverse of the real calorimeter sensitivity and therefore, has no relation with the heat capacity of the calorimeter. By knowing the calibration constant, the heat released or absorbed by the calorimeter can be obtained by the integration of the thermoelectric potential over time and application of the calibration constant as follows,

$$Q = \varepsilon_{\text{cal}} \cdot \int U dt . \quad (3.17)$$

3.1.3.3. Heat Flow Signal

As already described, in heat flow calorimetry, the thermal effect of the process under study is measured as a thermoelectric potential (voltage). Moreover, it represents not exactly the heat of the process flowing through the thermopiles, but the balance between the heat stored and the heat transferred as described in equation 3.8. Thus, for the same process, the voltage output may differ, depending on the calorimeter where the process is being studied. This difference can be minimized by correction of the thermal inertia of the calorimeter.

In figure 3.11 is represented the schematic potential-time curve, $U = f(t)$, typical of a heat flow calorimeter, when an exothermal process takes place in the sample. The curves represent the difference between a very fast exothermic process that “instantly” changes the thermal energy of the system (in orange) and a slower exothermic process with a constant heat production rate (in blue). For both curves, the time represented in the scheme is superior to the time of the process (shaded area on the figure) due to the inertia of the calorimeter, described by its time constant (equations 3.8 and 3.9).

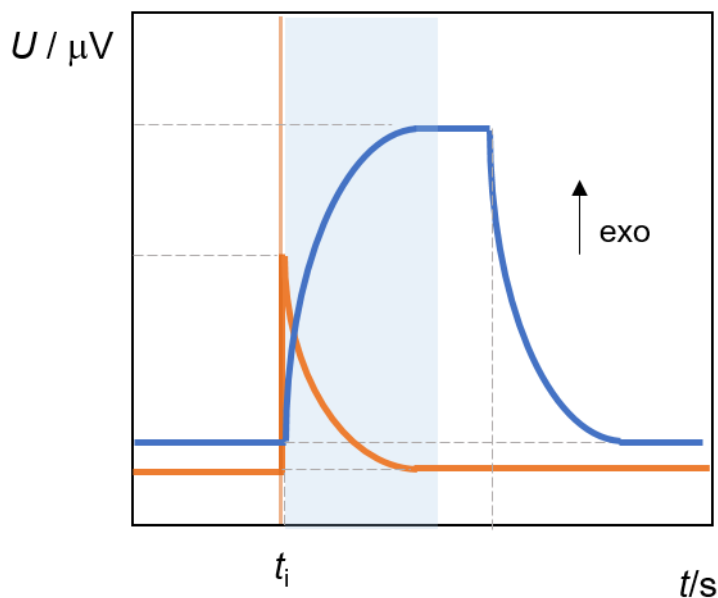


Figure 3.11. Schematic curves of potential-time, $U = f(t)$, in a heat flow calorimeter. Orange curve – instant exothermic process; blue curve – slow exothermic process. The shaded areas correspond to the time of the process.

The rate of the power release, P ($\text{J}\cdot\text{s}^{-1}$) in each instant, described in equation 3.8, may be combined with equations 3.11 and 3.13 as follows,

$$P = \frac{dQ}{dt} + C \left(\frac{d\Delta T}{dt} \right) = G_c \cdot n \cdot \frac{U}{n \cdot e_c} + \frac{C_p}{n \cdot e_c} \cdot \frac{dU}{dt}, \quad (3.18)$$

which may be simplified to,

$$P = G_c \cdot \frac{U}{e_c} + \frac{C}{n \cdot e_c} \cdot \frac{dU}{dt}. \quad (3.19)$$

Applying now the equations for the constant of calibration (equations 3.14 and 3.16) and the time constant of the calorimeter (equation 3.9), and considering the real (experimental) conditions, the usually called equation of Tian is derived:

$$P = \varepsilon_{\text{cal}} \cdot U + \varepsilon_{\text{cal}} \frac{C}{G_c \cdot n} \cdot \frac{dU}{dt} = \varepsilon_{\text{cal}} \left(U + \tau \left(\frac{dU}{dt} \right) \right). \quad (3.20)$$

Tian equation (3.20) is used to derive the instantaneous thermal power, P ($\text{J}\cdot\text{s}^{-1}$), originated by a real process, from the output sign of a heat flow calorimeter and in this way correct the effect of the thermal inertia of the calorimeter. For that purpose, it is necessary to know the time constant, τ (s), of the calorimeter and additionally include the information about the first derivative of the output signal, as shown in equation 3.20.

The total heat associated with the process under investigation can be obtained by the integration of the output voltage of the calorimeter directly or after correction to the time constant of the calorimeter using Tian's equation. Provided that the potential at the beginning and at the end of the integration are the same, the numerical value obtained directly from the calorimetric output data or after correction with Tian's equation, will be the same. Effectively, the integration of the Tian's equation is mathematically equivalent to the integration of the direct signal output.

It is worth of notice that the correction of the calorimetric data with the Tian equation will increase the noise of the output calorimetric signal by a factor equal to the time constant of the calorimeter. However, this noise does not affect the calculation of the

heat involved in process under investigation, as during integration the derivative will be cancelled.

Application of the Tian's equation allows to convert the output calorimetric data of the calorimeter in the instantaneous thermal power originated by the process under study. The analysis of the data in this form can give important thermokinetic information. Nonetheless, if considerable gradients of temperature are present in the sample compartment / calorimetric vessel, two or more time constants should be added to properly describe the power released by the process. In that case, the Tian's equation, derived in equation 3.20,

$$P = \varepsilon_{\text{cal}} \cdot \left(U + \tau \cdot \left(\frac{dU}{dt} \right) \right), \quad (3.20)$$

can be transformed to include two or more time constants, in the case of more complex temperature gradients. Calorimeters are usually designed in such a way that the existence of temperature gradients in calorimetric vessel are minimized. Therefore, in most situations, the use of first order equation (Tian's equation) is good enough to describe the heat flow in the system. However, a second order equation (3.21), is sometimes used, when there is the need to describe more complex processes. Higher order equations can be also used, but usually there is no need to. First and second order equations are usually enough to correct the output calorimetric data.

$$P = \varepsilon_{\text{cal}} \cdot \left(U + (\tau_1 + \tau_2) \cdot \left(\frac{dU}{dt} \right) + (\tau_1 \cdot \tau_2) \cdot \left(\frac{d^2U}{dt^2} \right) \right). \quad (3.21)$$

3.1.4. Other concepts

In this chapter, different topics concerning heat transfer and its measurement in calorimetry, along with some design principles have been discussed. Other topics like mass transfer or temperature scanning will now be briefly introduced.

3.1.4.1. Closed or Open Calorimetry

It has been discussed that in a calorimeter, the sample can exchange heat with the heat sink, as in heat flow calorimetry or it can be thermally isolated as in adiabatic calorimetry. It has not been discussed yet the difference between open and close calorimeters.

Calorimeters working as closed systems are typically bomb combustion calorimeters. In this type of calorimeters the combustion process occurs at constant volume. As the change in the internal energy of a system can be described as a sum of the heat and work, if the process in the sample occurs at constant volume, no expansion work can be done, and if in addition any other kind of work is possible, then the change in internal energy will be equivalent to the heat exchange,

$$dE = dQ. \quad (3.22)$$

This is only true to processes occurring at constant volume. It should be noted that E , in this section (Section 3.1.4.1), will represent the internal energy of the system as U represents the thermoelectric potential.

The majority of the calorimeters are “open calorimeters”, as μ FlowCal or ITC, in which the calorimetric vessel is maintained at constant pressure, many times at ambient pressure. As in the calorimetric vessels of these calorimeters the volume is not constant, the internal energy of the system cannot be considered equal to the heat transferred. If the process occurs at constant pressure, some of the heat may escape as expansion work reducing the internal energy of the system. Thus, the heat transfer at constant pressure will not equal the internal energy but the enthalpy,

$$dH = dQ. \quad (3.23)$$

The calorimetric systems ITC and μ FlowCal, used in this thesis, work at constant pressure, so the heat quantities measured will be equal to the enthalpy. The *DropCalvet* calorimeter used do not work at constant volume or constant pressure. However, it is considered that the heat quantities measured will also be equal to the enthalpy.

3.1.4.2. Batch or Flow Calorimetry

In open calorimeters, particularly in reaction or solution calorimetry, there are different configurations and designs that allow two or more components of the system to be joined, initiating thus a solution, a reaction, etc. The terms batch and flow calorimetry define respectively methodologies in which the fluids are mixed in a closed vessel or in a flow-through system.

In a batch calorimeter one or more components of the system are initially in the sample holder. The components can be separated in different compartments, some can be added by step-wise addition through a syringe or by breaking of ampoules previously installed. Either way, after each process the components remain in the sample holder, more component could be added as in the case of step-wise addition, but the system will only increase in the content of that component. Furthermore, in the majority of the calorimeters, the sample will be in contact with a gas phase and phenomena like evaporation or condensation may happen causing systematic deviations on the calorimetric results.

In flow calorimetry, different configurations exist but in all cases the components are going to flow through a certain path, passing through the section of the calorimeter where the heat flow is being measured and they will then continue its path to outside of the sensible zone. In the more common case, in continuous flow, the components will flow at a certain flux continuously. It is therefore, essential that the duration of the process being studied is shorter in time than the retaining time of the components in the sensible zone of the calorimeter to prevent important heat losses by mass transfer. For lent processes, there is the possibility of pulsation of the flow, also designated by stopped-flow. In this case, the components are allowed to flow to the sensible zone of the calorimeter, with subsequent stop of the flow, retaining the components on the calorimeter until the end of the process in study. At the end of the process, the flow can be initiated again, pushing to outside of the sensible zone the previous components. In this methodology care must be taken with the diffusion of the compounds.

3.1.4.3. Scanning or Isothermal Calorimetry

Another classification of the calorimeters is related to its temperature working range. In scanning calorimeters the temperature of the sample will change at a certain heating/cooling rate during an experiment and different processes temperature dependent can be studied.

For non-scanning temperature, in which the experiments are carried at a fixed temperature, the usual terminology is isothermal calorimetry. Heats of solution, dissolution, reaction, etc, are usually measured in isothermal calorimeters. The use of the term isothermal can be discussed as adiabatic calorimeters are based in the principle of heat accumulation and so temperature will vary during the evolution of a process and in heat flow calorimeters there is generated a temperature gradient across the thermopile that is responsible for the generation of the calorimetric signal. Though, and despite of the fact that usually very small temperature differences are involved making the experiments essentially isothermal, there is some discussion concerning the use of this term. The use of the term isothermal should not be understood as “perfectly isothermal” but as “essential isothermal” since the temperature differences are generally in the order of 10 mK ^[8].

Lars Wadsö proposes the following practical definition that will be considered in this thesis: “an isothermal measurement takes place at conditions where the temperature changes are so small so that the result of the measurement is the same as if there had been perfectly constant temperature conditions” ^[9].

3.2. Experimental Methodologies

Three twin heat flow microcalorimeters have been used in this thesis: isothermal titration calorimetry (ITC), μ FlowCal and *DropCalvet*. Their apparatuses are now described. A more detailed description was made to μ FlowCal as it was constructed in the context of this work.

3.2.1. *DropCalvet* – Drop Type Calvet Calorimetry

R. B. Kemp has stated in his chapter concerning non-scanning calorimetry that “Calvet’s great contribution was to constitute a twin calorimetric system from two Tian microcalorimetric vessels” ^[10] originating the twin calorimeters. Tian had first constructed a calorimeter based in the heat flow principle with one single cell and already with a set of thermocouples surrounding the sample holder. Calvet have converted this first design in a twin calorimeter along with other optimizations ^[5, 10]. It was indeed a great accomplishment for calorimetry. In fact, the french company SETARAM (first DAM) had developed several calorimeters that are still available on the market based in these first calorimeters of Tian-Calvet design.

In the laboratory where the work for this thesis was done a Tian-Calvet design calorimeter (SETARAM, model HT 1000D) is available. This calorimeter operates in a wide range of temperatures, from ambient temperature until 1273 K (1000 °C). It has been operated in isothermal mode, using the drop calorimetric methodology to the determination of enthalpies of vaporization, developed initially by Skinner et al.^[11]. More recently, a new system, with the same methodologic principle but with improvements of the vacuum system and in the temperature measurement inside the cell have been implemented and adapted in our group by Santos et al.^[12, 13], leading to more accurate values. Using this system and methodology, the *DropCalvet* calorimeter was used to measure the enthalpy of vaporization of some of the alcohols used in this work. This property was needed for the determination of the enthalpy of solvation of alcohols in ionic liquids.

3.2.1.1. The *DropCalvet* Calorimeter

The microcalorimeter SETARAM HT1000D is constituted by a metal block of high heat capacity, the heat sink, contained inside a refractory ceramic material. The heat sink contains two identical cavities in which the calorimetric cell and the reference are introduced. Each one of the cavities is surrounded by a thermopile composed of 496 radially arranged thermocouples (type S, 10% rhodium-Pt / Pt) connected in series. A schematic representation of the calorimeter is present in figure 3.12.

The temperature of the heat sink is regulated by a SETARAM G11 control system, which also amplifies and registers the electronic potential from the thermopiles. The temperature is programmed through the SETARAM 3.20 software, which is installed in a computer that also performs the data acquisition, graphical representation of the calorimetric signal curve in real time, the integration of the area ($\mu\text{V}\cdot\text{s}$) and its multiplication by the calibration constant of the calorimeter ($\text{J}\cdot\text{s}^{-1}/\mu\text{V}$).

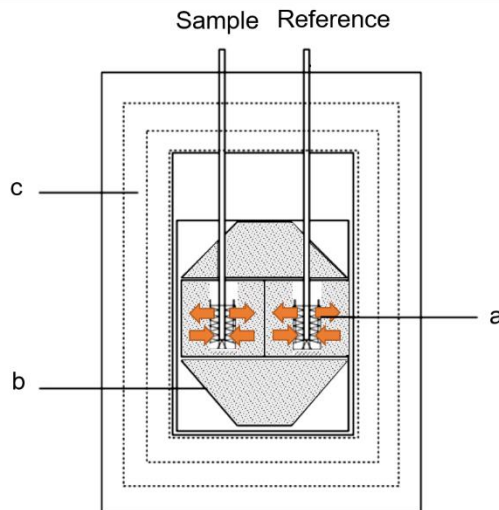


Figure 3.12. Schematic representation of the Calvet type calorimeter SETARAM (model HT1000D); a, heat flow sensor / thermopile; b, heat sink; c, ceramic. Picture adapted from ref. [14].

Given the purpose of the *DropCalvet*, in addition to the calorimeter, a vacuum pumping system and a glass vacuum line are included in the apparatus design (schematic picture on figure 3.13.).

The cells of the calorimeter are connected to a glass vacuum line, through long glass tubes, that includes a nitrogen trap to condense the evaporated sample, two vacuum pumps that evacuate the system, pressure gauges and two valves. The valves are installed between the trap and the calorimeter. One of the valves admit gas (air or N₂) into the system, restoring the atmospheric pressure and the other one isolates the pumping system.

The vacuum pumping system is composed by a rotary pump (Edwards, model RV5) that is responsible for pre-evacuating the system until approximately 40 Pa (0.4 mbar) and an oil diffusion pump (Edwards, model Diffstak 63), which can attain a vacuum level of approximately 10⁻⁴ Pa (10⁻⁶ mbar). A pirani type gauge (Edwards, model APG-M) and a penning type gauge (Edwards, model AIM-S) are used for the pressure measurement.

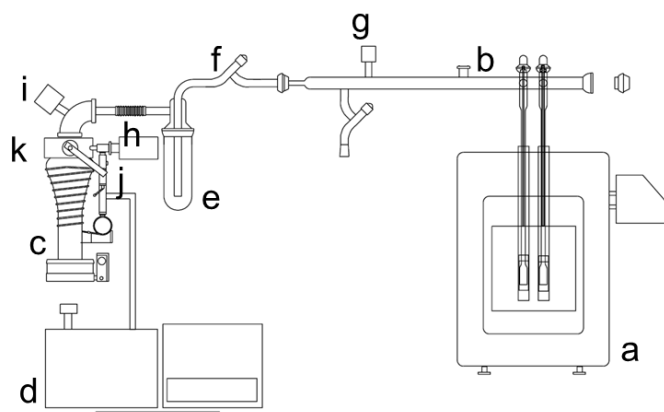


Figure 3.13. Schematic representation of the Calvet-Tian drop method assembly constituted by a HT1000D SETARAM calorimeter and a vacuum line; a, microcalorimeter SETARAM HT1000D; b, vacuum pumping system; c, diffusion pump; d, rotary pump; e, liquid nitrogen trap; f, valve that isolates the pumping system; g, air inlet valve; h, Pirani gauge; i, Penning gauge; j, commutation valve; k, butterfly valve. Image adapted from ref. [13].

3.2.1.2. Calorimetric Cells

The calorimetric cells (figure 3.14) are Pyrex® glass tubes embed in hollow Kanthal® cylinders. Prolongations of these glass tubes leave the hot zone of the calorimeter and connect to the vacuum line. Tunnelling tubes are inserted into these prolongations and allow the execution of repeating measurements without removing the cells, as its removal, to clean, does not disturb the thermal equilibrium of the cells.

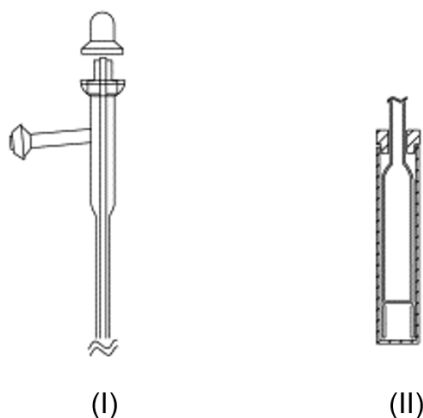


Figure 3.14. Schematic representation of the (I) top of the calorimetric cell with the tunnelling tube and (II) the bottom of the calorimetric cell with the Pyrex® glass tube and the Kanthal® hollow cylinder. Picture adapted from ref. [13].

3.2.1.3. Heat of Vaporization Measurement

In a normal experiment, a small glass capillary with a known mass of sample, initially at 298 K, is dropped into the sample side of the calorimeter. To compensate the thermal disturbance produced by dropping a glass capillary into the sample side, an identic empty capillary is dropped simultaneously into the reference side. Assuming that the temperature of the furnace is superior to the initial temperature (298 K), heat will flow from the heat sink to the capillaries, through the thermopile. To measure the heat of vaporization, the sample is then evacuated, leading to its complete vaporization at the calorimeter temperature. This phenomena is an endothermic process. Thus, heat will again flow from the heat sink to the sample. A typical calorimetric curve of the described process is represented in figure 3.15. The first peak of this curve is associated with the heat stored by the sample due to its heating from the initial temperature (typically 298 K) to the temperature T of the calorimeter cell (the same as the temperature of the heat sink) $\Delta_{298.15\text{ K}}^T H_m^o$, assuming that capillaries have identical mass and thus will cancel each other and its contribution can be despised. The second peak can be interpreted as the phase transition, $\Delta_l^g H_m^o(T)$, from the liquid to the gas phase at the temperature T . A *DropCalvet* vaporization experiment can thus be described by the upper triangle of the thermochemical cycle represented in figure 3.16.

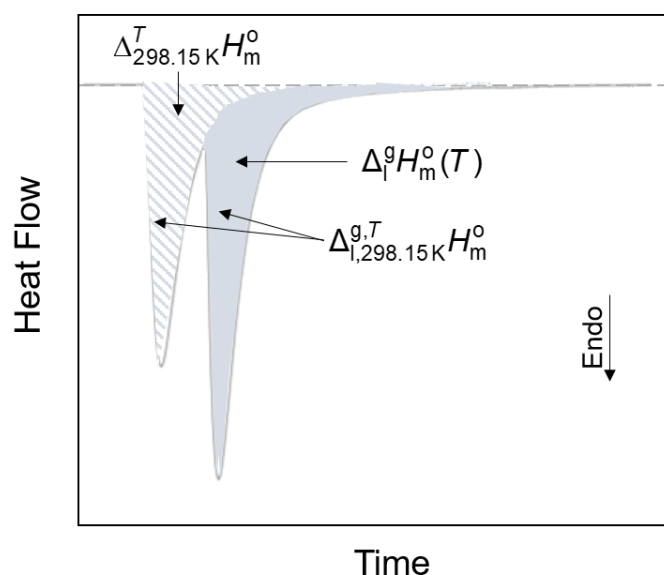


Figure 3.15. Schematic representation of the typical “heat flow over time” obtained in a vaporization experiment in DropCalvet calorimeter.

As evidenced in the thermochemical cycle, the sum of the heat stored by the sample due to its heating from 298.15 K to the T temperature, $\Delta_{298.15\text{ K}}^T H_m^o$, and the heat absorbed due to the phase transition from the liquid to the gas phase, at T temperature, $\Delta_l^g H_m^o(T)$, originate $\Delta_{l, 298.15\text{ K}}^{g,T} H_m^o$, which can be experimentally obtained by the joint integration of the two calorimetric peaks represented at figure 3.15. Therefore, and considering the lower triangle of the thermochemical cycle represented in figure 3.16, the standard enthalpy of vaporization can be derived from the following expression:

$$\Delta_l^g H_m^o(298.15\text{ K}) = \Delta_{l, 298.15\text{ K}}^{g,T} H_m^o - \Delta_{298.15\text{ K}}^T H_m^o = \Delta_{l, 298.15\text{ K}}^{g,T} H_m^o - C \cdot (T - 298.15), \quad (3.24)$$

where $\Delta_{298.15\text{ K}}^T H_m^o$ corresponds to the heat capacity correction determined to the sample in its gaseous phase, when is heated from 298.15 K to the temperature T of the calorimeter.

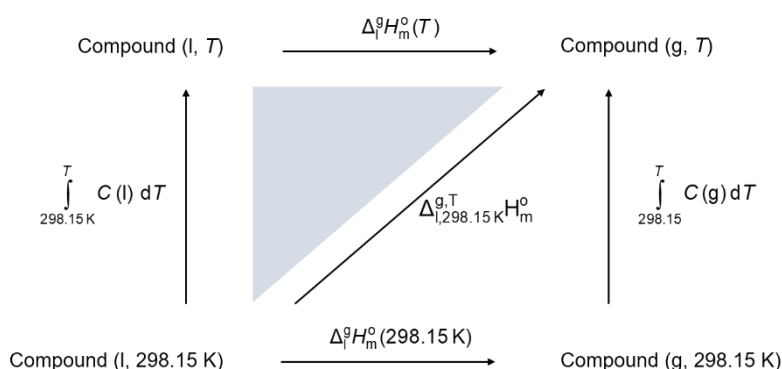


Figure 3.16. Thermochemical cycle which describes the determination of the molar enthalpy of vaporization, at 298 K, in a vaporization experiment, in the *DropCalvet* calorimeter.

3.2.1.4. Summary of the Measurements

A list of the compounds, which enthalpy of vaporization was determined using the Calvet type calorimeter SETARAM (model HT1000D) in the context of this thesis, is presented in table 3.1.

For the determination of the enthalpy of vaporization of these compounds glass capillary tubes of 27-28 mg were sealed at one end. In each experiment, two identical capillary tubes (one tube containing 6-10 mm³ of sample and one blank tube as reference) were simultaneously dropped from 298 K to the reaction zone of the calorimeter. Two sets of experiments were performed for each sample (except for perfluoro-*tert*-butyl alcohol): one with the reaction zone of the calorimeter at 303 K (30 °C) and another at 315 K (42 °C). Due to the high volatilities of the studied compounds, the mass of the sample tubes was measured just before the dropping procedure. A small mass loss correction was taken into account, based in the mass loss rate, which was previously evaluated, and in the time gap between the sample weighting and dropping.

Due to the high volatility of the PF*t*-BuOH sample, the top of the capillaries containing this sample were covered with a polymeric film (Parafilm®) to prevent the uncontrolled vaporization of the sample, before the beginning of the measurements. The enthalpy of vaporization of this compound was measured only at 303 K.

Table 3.1. List of the alcohols studied in *DropCalvet* calorimeter

Alcohols Abbreviation	Furnace Temperature/ K	
	303	315
TFt-BuOH	✓	✓
HFt-BuOH	✓	✓
PFt-BuOH	✓	×
TFPrOH	✓	✓
PFPrOH	✓	✓

✓ - measured; × - not measured.

3.2.2. ITC – Isothermal Titration Calorimetry

The enthalpy of solution of alcohols in ionic liquids at infinite dilution was measured by Isothermal Titration Calorimetry (ITC). The calorimetric system used is a multichannel system identical to the prototype multichannel system built by Ingemar Wadsö and Jaak Suurkuusk in Lund, Sweden ^[15].

A scheme of the isothermal titration calorimetry working principle is presented in figure 3.17. In the sample holder there is a liquid sample, which can be either a pure liquid or a solution. Small injections of a fluid are made into the sample, through a syringe.

Each addition leads to the release or absorbance of heat in the sample, depending if the mixture of both liquids is exothermic or endothermic. If the mixture is exothermic, heat will flow from the sample, to the sample holder, through the thermopile to the heat sink. If the mixture is endothermic, heat will flow in the opposite direction. As already explained, the heat flow across the thermopile is proportional to the temperature difference between its both walls, which is proportional to the thermoelectric potential (voltage) generated. As the ITC is a differential calorimeter, the observed thermoelectric potential is the differential signal between the sample and the reference cells. The difference between both thermoelectric potentials is proportional to the difference between both heat flows. The output differential signal is amplified, filtered and converted to digital by a 7½ nanovoltmeter (HP/Agilent, model 34420A) and recorded in a computer as function of the time, $U = f(t)$.

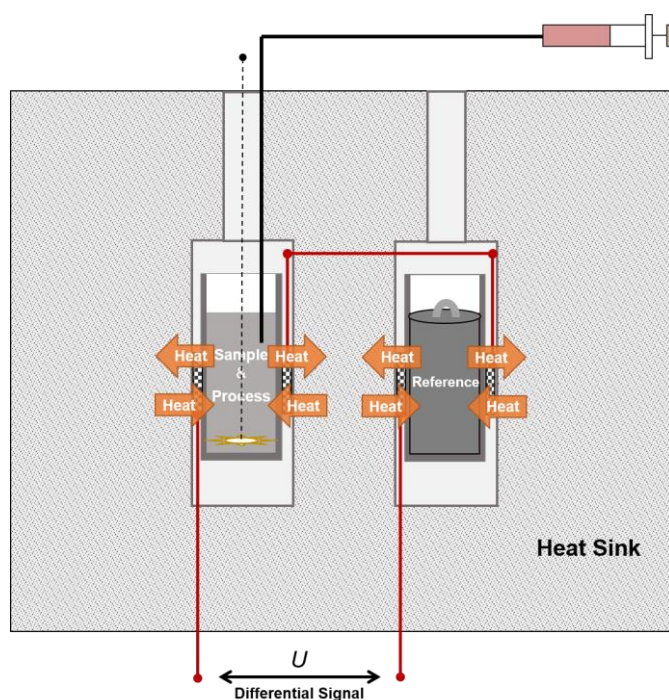


Figure 3.17. Schematic representation of the ITC calorimeter and its working principle.

To the accurate measurement of the heat of mixture of both liquids is necessary that the sample, the reference, the heat sink and the injected liquid are in thermal equilibria and that the heat fluctuations coming from the surroundings are small enough to provide long time baseline stability. Different peripherals are used with the calorimetric system in order to maintain these conditions: the temperature control, the control of the injection system, the acquirement of the data, etc. A scheme of the calorimetric system and all peripherals is presented in figure 3.18.

In summary, the system is constituted by two twin heat conduction calorimeters acquired from Thermometrics AB/TA, which are immersed in a precisely thermostated ($\sim 10^{-4}$ K) water bath, constructed in Lund University, in Sweden. Insertion vessels with stainless steel ampoules, acquired from Thermometrics AB/TA, were used. To perform the titration experiments, modified gastight® Hamilton syringes were used, together with high resolution step motors syringe pumps and control units developed in Lund University, which are programmable by software. The calorimetric signal (voltage, V) is monitored by 7½ nanovoltmeters (HP/Agilent, model 34420A) and recorded in a computer that performs both data acquisition and system control using a customized version of the LABTERMO software package, developed by Santos^[2, 18] (LABTERMO 3.0).

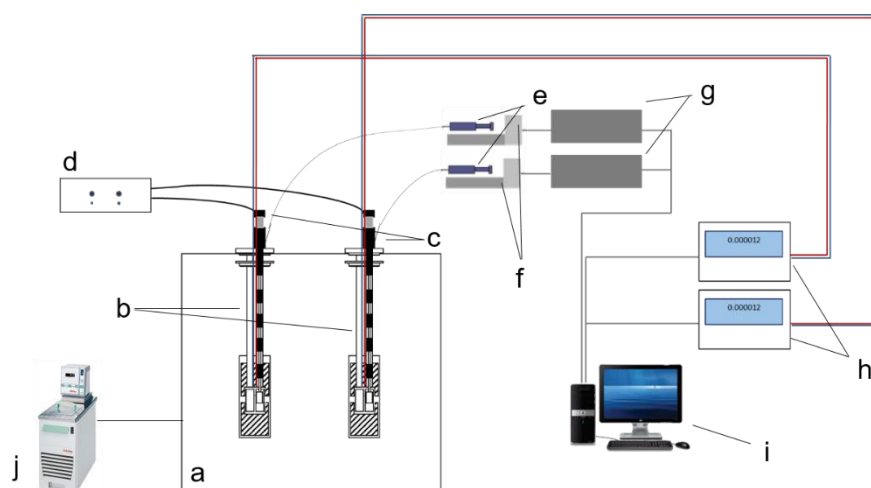


Figure 3.18. Schematic representation of the ITC calorimetric system: a, water bath; b, calorimetric channels; c, insertion vessels; d, stirring controller; e, modified gastight® Hamilton microsyringes; f, syringe pumps; g, controllers of the injection system; h, nanovoltmeters 7½ digits HP/Agilent (model 34420A); i, computer PC for data acquisition and system control; j, water bath (Julabo F12-EC). Picture adapted from ref.[16].

3.2.2.1. The Calorimetric Channel

The laboratory is equipped with two twin calorimetric channels, which are commercial versions, acquired from Thermometrics AB/ TA, of the calorimeter designed by Ingemar Wadsö and Jaak Suurkuusk^[15]. These calorimetric channels work as two calorimeters operating independently of each other. In this work, only one of these calorimetric channels was used.

The calorimetric channels are calorimeters of heat conduction type. Therefore, as schematized in figure 3.17, the core of the calorimeter is constituted by heat flow sensors, Peltier elements, which bridge the place where the solution process is occurring to aluminium blocks that work as heat sinks. In figures 3.19 and 3.20 the detailed design of the ITC calorimetric channels is depicted.

The solution process occurs into stainless steel ampoules which are assembled in insertion vessels, described in section 3.2.2.2., and inserted in the calorimetric channel through two suspended tube cavities that work as close-fitting holders for the insertion vessels. The ampoules assembled in the insertion vessel are stainless steel ampoules of 1 cm³ (mL) or 3 cm³ (mL) and are inserted through the tube cavities until reaching the calorimetric core of the channel. In this work, only 1 cm³ ampoule was used. Therefore,

a hollow inverted aluminium cylinder was inserted into the cavities to lift the ampoule and put it at the same height as the Peltier elements (see figure 3.20). The insertion vessel slides easily into the tube cavity, making possible to be inserted and removed in the beginning and end of each experiment, so that the charging with the sample and the cleaning process are made outside of the calorimeter.

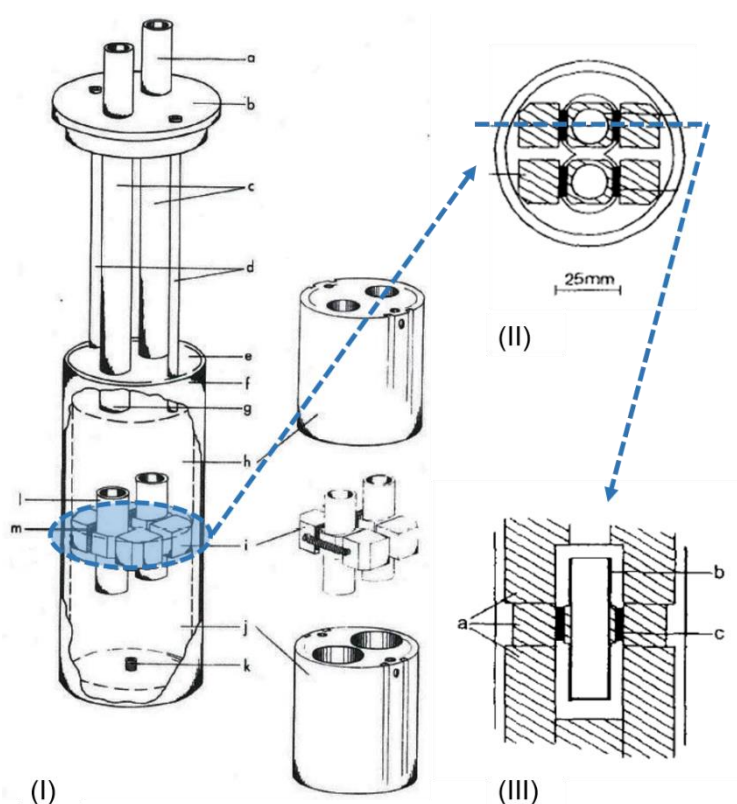


Figure 3.19. Schematic representation (I) of the calorimetric channel on three dimensions and (II) of a horizontal and (III) vertical cut, in the calorimetric section, in two dimensions; a, Ryton® tubes; b, steel lid covered with Ryton®; c, steel tubes that house and thermostat the insertion vessel; d, 6 mm steel tubes that house the electrical wires; e, steel lid of the canister; f, steel canister; g, Ryton® tubes; h, cylindrical top aluminium block; i, small (close to) cubic aluminium block; j, cylindrical bottom aluminium block; k, steel spring; l, tube cavity – ampoule holder; m, Peltier element / thermopile. Pictures (I), (II) e (III) adapted from ref.[7, 15].

To ensure good thermal contact between the suspended tube cavities and the Peltier elements, the external part of the cavity, the one that is in contact with the heat

flow sensors, is nearly cubic. The wall thickness of the cavity is 1 mm so that the heat flows easily from the insertion vessel, through the cavity and through the heat flow sensor to the heat sink, which is essential to maintain isothermal conditions ^[9]. Peltier elements (which dimensions are 14.3 x 11.3 x 2.8 mm, with 66 thermocouples per thermopile, MELCOR supplier) surrounding the same tube cavity are electrically connected in series and in opposition to Peltier elements of the other cavity, resulting in the measurement of the heat flow in differential mode. Therefore, one of the cavities works as a reference and in the other cavity occurs the solution process, inside a stainless steel ampoule. In total, 4 thermopiles are used, 2 in the sides of each vessel with a Seebeck coefficient of $26.2 \text{ mV}\cdot\text{K}^{-1}$ per thermopile ($397 \text{ }\mu\text{V}\cdot\text{K}^{-1}$ per thermocouple) ^[7].

The heat sink is very important to maintain the isothermal conditions and is mainly constituted by two large cylindrical aluminium blocks which maintain the position of the calorimetric core by holding (and being in thermal contact with) the four small aluminium blocks that are in thermal contact with the Peltier elements. This four small nearly cubic aluminium blocks positioned between the blocks “h” and “j” maintain the position of the Peltier elements and the tube cavities, forming a package that is hold together only by steel pins and springs. The cylindrical aluminium blocks have cylindrical bores with a 25 mm diameter, so they are not in thermal contact with the tube holders of the insertion vessels. Above the holder, this bore is narrowed to a diameter of 14 mm to fit the insertion vessel and ensure it is thermostated.

A cylindrical stainless steel canister contains all the assembly described above. In the bottom of the canister interior is fastened a plastic insulated steel pin that supports a spring which is holding the bottom aluminium cylindrical block suspended in an air box.

On the top of the canister there is a sealed lid of stainless steel with an O-ring and a circular locking spring. The lid of the canister is connected to the cylindrical aluminium block “h” through two thin-walled composite tubes (glass fiber and mineral filled polyphenylene sulphide, Ryton®) with an external diameter of 16 mm. From this stainless steel lid, two identical stainless steel tubes and two 6 mm tubes that house the electrical wires extend to a superior lid of steel covered with Ryton®. This last lid is sealed to the thermostatic bath by a rubber ring and houses two short Ryton® tubes through which the insertion vessels are inserted.

This last lid houses a steel coil tube, not shown in the figures 3.19 and 3.20, used to pump a slow stream of dry air to the calorimeter and prevent condensation effects when the calorimeter works under low temperatures. In this work, the experiments were performed at 298.15 K, so it was not used.

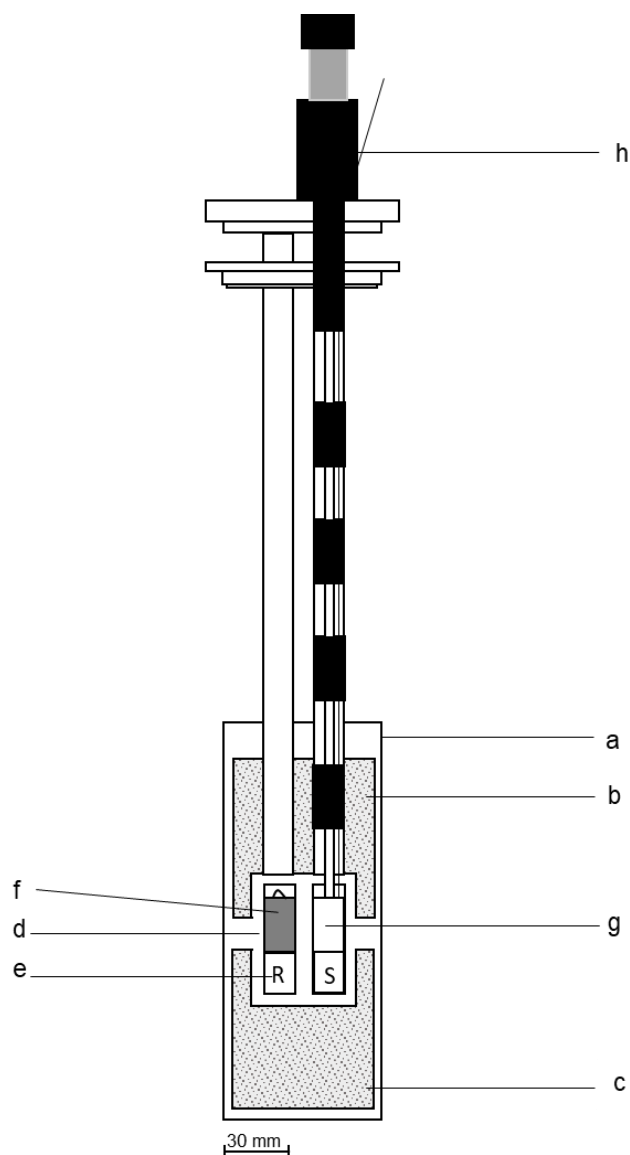


Figure 3.20. Schematic representation of a vertical cut of the calorimetric channel with the insertion vessel; a, stainless steel canister; b, cylindrical top aluminium block; c, cylindrical top aluminium block; d, tube cavity; e, inverted aluminium cylinder; f, solid cell; g) stainless steel ampoule; h, insertion vessel equipped with 1 cm³ stainless steel ampoule; S, sample; R, reference. Picture adapted from ref.[16].

3.2.2.2. The Insertion Vessel

The insertion vessel used in this work is a commercial version, acquired from Thermometric AB/TA, of the concept for titration vessel developed in Lund ^[15, 17]. A real picture and a schematic representation of the insertion cell used is shown in figure 3.21.

The sample container is a stainless steel ampoule of 1 or 3 cm³. In this thesis it was used the steel ampoule of 1 cm³. The lid of this ampoule is sealed by use of a nitrile or Viton® O-ring and a Teflon® ring (see figure 3.21). From the lid, a 40 cm long thin-walled steel tube extends until the support for the stirrer motor. Inside this steel tube there is a shaft, in all the extension, from the stirrer motor to the stirrer, inside the stainless steel ampoule.

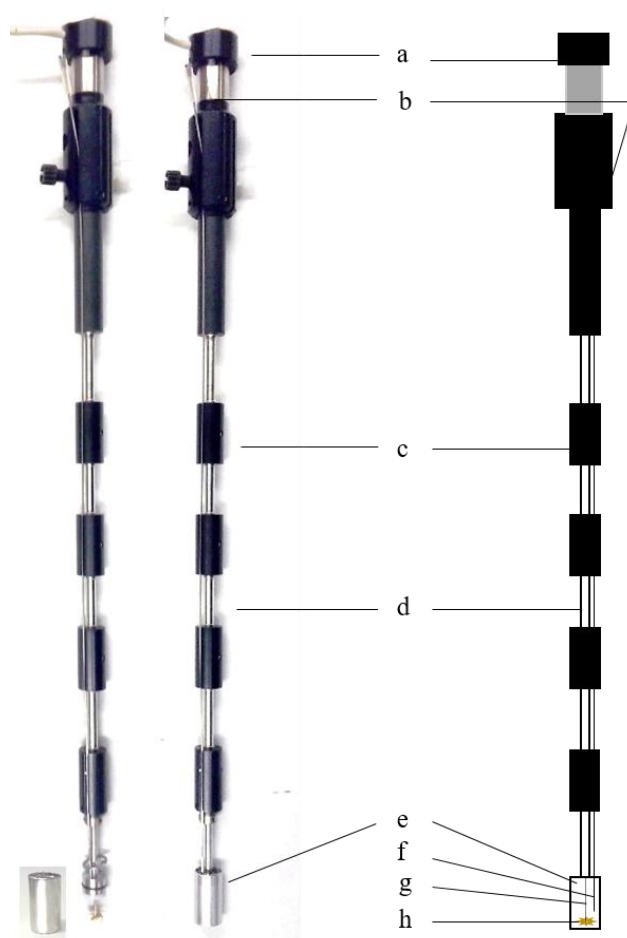


Figure 3.21. Real and schematic picture of the titration insertion vessel used. A, stirrer motor; b, guide tube for the injection needle; c, heat exchange bolt; d, steel tube that contains the shaft; e, sample container – stainless steel ampoule; f, injection needle; g, shaft; h, gold propeller. Picture adapted from ref.[16].

The injection of the titrant is made by a gastight® Hamilton syringe, whose needle has been modified to fit the requirements of this instrument. The needle, permanently coupled with this syringe, is a long steel injection needle with an internal diameter of 0.15 mm and an external diameter of 0.40 mm. The long injection needle enters in the stainless steel ampoule through a slightly larger tube from the exterior of the calorimeter. The path from the exterior of the calorimeter to the sample container allows the titrant to be in the same temperature as the calorimeter and thus, the sample. Four heat exchange bolts, positioned around the tube with the shaft, allow this thermal equilibration, as the tube that conducts the needle is in thermal contact with them. This heat exchange bolts, as well as the ampoule, define the external diameter of the insertion vessel, 14 mm. Thus, they are in thermal contact with the tube cavities of the calorimetric vessel. The gaps between the exchange bolts minimize the heat exchange between the calorimetric core of the calorimeter and its superior and exterior areas.

The position of all elements inside of the sample container is demonstrated in figure 3.21. The tip of the needle is positioned above the stirrer but immersed in the sample and the stirrer is positioned near the bottom of the ampoule. The stirrer is a gold three blade propeller and rotates with a speed of 100 rpm (in this work).

3.2.2.3. Multichannel Thermostat System

The calorimetric channels are immersed in a multichannel thermostated water bath constructed by Ingemar Wadsö in Lund, Sweden. The temperature of the water bath is controlled locally and then circulated through the bath by a built stainless steel stirrer/propeller. A thermistor, enclosed in a stainless steel tube, measures the temperature of the water continuously. This thermistor is connected to a proportional integral derivative (PID) temperature controller developed in Lund University, which regulates the temperature of the water bath. A stable cold source is provided by thermostated bath (Julabo, model F12-EC) programed to 295.6 K (22.4 °C). Temperature fluctuations in the water bath are within $\pm 1 \times 10^{-4}$ K in 24h. During this work, the temperature of the water bath was set to 298.15 K (25.00 °C).

3.2.2.4. Injection System

The injection system is constituted by three main components: a modified gastight® Hamilton syringe of 100 mm³ (μL), which needle consists in a long stainless steel capillary ($\varnothing_{\text{ext}} = 0.40$ mm and $\varnothing_{\text{int}} = 0.15$ mm), a syringe pump built in Lund, which contains a stepping motor Japan Servo type KP6M2-071 (1.8 deg/step) combined to a micrometer screw, which moves precisely the syringe piston, and a controller to the syringe pump.

The injections are programmable by the software LABTERMO^[2, 18] and the syringe controller. The injected volume is programmed by defining the number of turns in the micrometer screw and the injection speed by the screw rotation speed. The syringe was calibrated gravimetrically using water as calibration fluid.

In the experiments performed in this thesis, the maximum volume by injection was 1.6 mm³ (μL), independently of the alcohol injected. The amount of liquid being thermostated before injection is approximately 5.83 mm³ which we can consider to be approximately three times the maximum volume injected. Injections of water in water were also performed and no detectable thermal effect was observed.

3.2.2.5. Data Acquisition and System Control

The thermoelectric potential generated by the heat flow sensors of the calorimeter is measured by a nanovoltmeter at each 5 seconds with a 7^{1/2} digits resolution. The nanovoltmeter is connected via a RS232C serial interface to a computer that performs the acquisition and display of the thermoelectric potential, U as a function of the time, t , using a modified version of the LABTERMO^[2, 18] software.

This software performs real time monitoring of the calorimetric signal, as well as, the control of the microinjection syringe system. The injection syringe system allows to perform automatic injections, in which the number of injections, the injected volume, the injection speed and the time between injections can be programmed by the user. Alternatively, “manual” injection can be also executed which is quite useful for the optimization of the initial setup. Figure 3.22 depicts a “screenshot” of the LABTERMO software display output during a typical experiment (injection of HF*t*-BuOH in [C₄C₁im][NTf₂]).

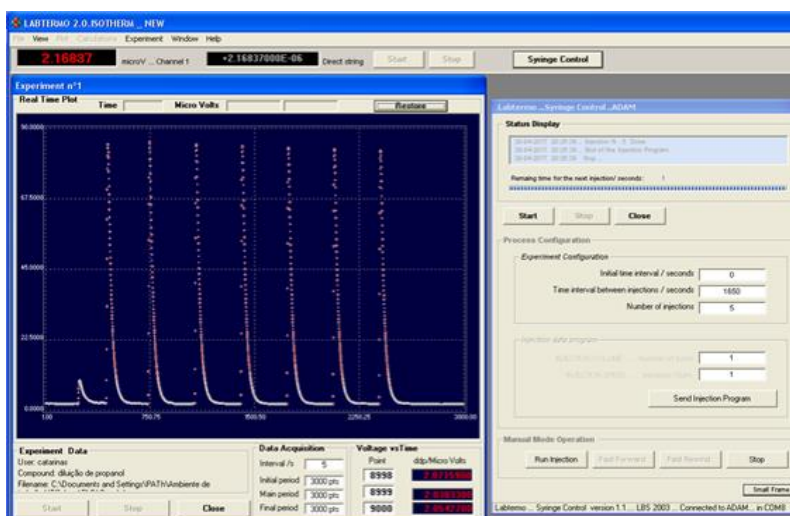


Figure 3.22. Picture of the screen with the software LABTERMO during an experiment of ITC, injections of HF \dagger -BuOH in [C₄C₁im][NTf₂].

3.2.2.6. Calorimetric Data Analysis

The typical calorimetric data set, $U = f(t)$, is represented in figure 3.23. This curve represents the differential thermoelectric potential generated in the thermopiles for the heat released/absorbed during an injection. Thus, this data does not represent directly the heat released in the process by mixing the two compounds. Instead, the signal is related with the heat flow generated and the heat capacity of the system. In order to access the real heat released/absorbed in the process the experimental thermoelectric signal must be corrected to the time constant of the calorimeter:

$$U_{\text{corr}} = U + \tau \cdot \left(\frac{dU}{dt} \right) \quad (3.25)$$

The application of this equation leads to a significant increase noise to signal ratio. Typically, the practical application of the Tian equation implies the use of smoothed or filtrated data, which in this case was done by application of a numerical smooth (moving average of 6 points). In figure 3.24, a graphical representation of the calorimetric signal is presented, before and after the application of the data smoothing function and the correction for the time constant of the instrument.

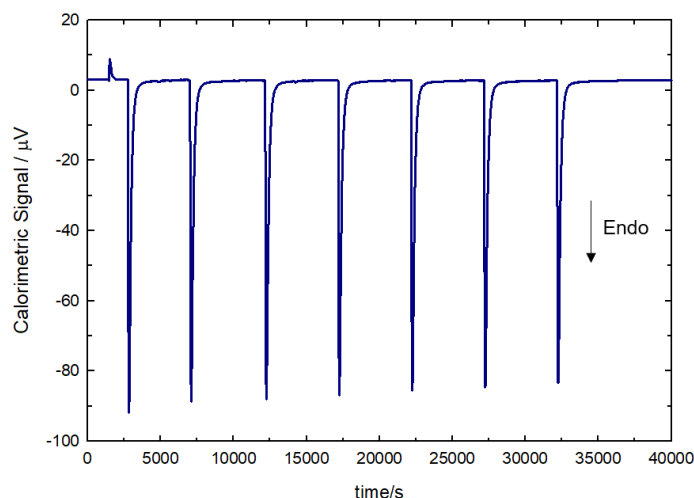


Figure 3.23. Typical data set of an ITC experiment (injection of HexOH in $[C_1C_8im][NTf_2]$). Representation of the calorimetric data as obtained $U = f(t)$.

As stated before, when presented the equation 3.17, the heat released or absorbed in an experiment can be obtained by the integration of the thermoelectric potential and application of the calibration constant. In ITC data treatment, the integration of the data is made from the corrected thermoelectric potential over time using the method of trapezoidal rule as follows,

$$A_T = \sum_a^b \left(\frac{(t_i - t_{i-1}) \cdot [U_{corr, t_i} + U_{corr, t_{i-1}}]}{2} \right), \quad (3.26)$$

where A_T represents the area under each peak, “ i ” represents each experimental point and “ a ” and “ b ” represent the beginning and the end points of the integration.

The enthalpy of solution at infinite dilution $\Delta_{soln} H_m^{0, \infty}$ ($J \cdot mol^{-1}$) is then calculated as,

$$\Delta_{soln} H_m^{0, \infty} = \frac{\langle A \rangle \times \varepsilon_{cal} \times M}{\rho \times V_{inj}}, \quad (3.27)$$

where $\langle A \rangle$ ($\mu V \cdot s$) is the average of the peak integration obtained in each experiment. The previous equation is applied if the concentration effect is negligible at this dilution level. If the concentration effect is found not to be negligible, the enthalpy of solution at

infinite dilution $\Delta_{\text{soln}} H_{\text{m}}^{0,\infty}$ is obtained by extrapolation to infinite dilution. ε_{cal} ($\text{J} \cdot \mu\text{V}^{-1} \cdot \text{s}^{-1}$) is the calibration constant or the inverse of the experimental sensitivity coefficient of the calorimeter, M ($\text{g} \cdot \text{mol}^{-1}$) is the molar mass of the injected alcohol, ρ ($\text{g} \cdot \text{mm}^{-3}$) is the density of the injected alcohol and V_{inj} (mm^3) is the injected volume.

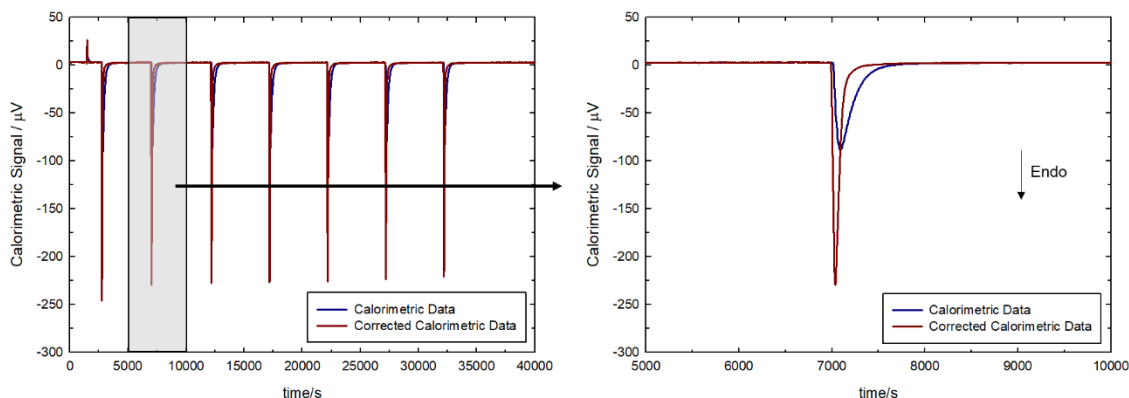


Figure 3.24. Data representation of a typical ITC experiment that consisted in the injection of HexOH in $[\text{C}_1\text{C}_8\text{im}][\text{NTf}_2]$. Representation of the calorimetric data as obtained $U = f(t)$ (in blue) and after smoothing the data and correction to the time constant of the calorimeter (dark red). On the right side a magnification on the time scale is showed, representing the data of a single injection.

3.2.2.7. Summary of the Experimental Procedure

For the measurement of the enthalpy of solution of alcohols in ionic liquids at infinite dilution, the insertion vessel was dried prior to its use, by passing a continuous flow of dry gaseous nitrogen, for at least 15 minutes, at approximately 10 kPa (0.1 bar), in both the guide tube for the injection needle and the steel tube that contains the shaft. Immediately after, the sample container is filled with 0.900 cm^3 of IL and the insertion vessel is closed.

The insertion vessel is then introduced by steps in the calorimetric vessel, in a total of three thermal stabilization positions, spaced in time and height, until its final position, where the stainless steel ampoule is at the same height as the thermopiles. These procedure guarantees that the stainless steel ampoule reaches a temperature identical to the calorimeter sensitive region before its final position, minimizing the thermal perturbation in the calorimetric channel and the time needed for the stabilization of the calorimetric signal.

The agitation of the system (at 100 rpm) is turned on after the stainless steel ampoule reaches its final position and the stabilization of the calorimetric signal. When a new thermal equilibrium of the calorimetric system is reached, the needle of the syringe may be inserted in its guide tube. The calorimetric experiment is ready to be initiated when the calorimetric heat flow signal reaches the baseline level.

Care was taken to avoid the existence of air bubbles in the syringe. Furthermore, before the insertion of the needle inside the guide tube of the insertion vessel, manual injections are made (outside of the vessel) to guarantee that the liquid at the end of the needle did not vaporize. Injections were made in slow mode, allowing for the calorimetric signal to return to the baseline prior to the next injection.

A compilation of the 27 systems (alcohol + ionic liquid) studied by ITC, in the context of this thesis, is presented in table 3.2. Some other systems will be presented and discussed in this thesis, as they are essential to the understanding of the solvation of alcohols in ionic liquids. Those systems are presented in table 3.3. They have been measured in ITC in the same conditions, using the calorimetric channel described here and another one with the exact same design and immersed in the same water thermostat. Some of those results were measured by the author of this thesis before the beginning of the work that has conducted to this thesis.

Table 3.2. List of the systems ionic liquid + alcohol studied, at the infinite dilution of the alcohol, by isothermal titration calorimetry, in the context of this thesis

Ionic Liquid Abbreviation	Alcohols Abbreviation								
	HexOH	HeptOH	OctOH	<i>t</i> -BuOH	TF <i>t</i> -BuOH	HF <i>t</i> -BuOH	PF <i>t</i> -BuOH	TFPrOH	PFPPrOH
[C ₂ C ₁ im][NTf ₂]	✓	✓	✓	×	×	×	×	×	×
[C ₄ C ₁ im][NTf ₂]	✓	✓	✓	✓	✓	✓	✓	✓	✓
[C ₆ C ₁ im][NTf ₂]	✓	✓	✓	×	×	×	×	×	×
[C ₈ C ₁ im][NTf ₂]	✓	✓	✓	×	×	×	×	×	×
[C ₁₀ C ₁ im][NTf ₂]	✓	✓	✓	×	×	×	×	×	×
[C ₄ C ₁ im][PF ₆]	✓	×	✓	×	×	×	×	×	×
[C ₆ C ₁ im][PF ₆]	✓	×	✓	×	×	×	×	×	×
[C ₈ C ₁ im][PF ₆]	✓	×	✓	×	×	×	×	×	×

✓ - measured in the context of this thesis; × - not measured.

Table 3.3. List of the systems ionic liquid + alcohol studied, at the infinite dilution of the alcohol, by isothermal titration calorimetry, before the beginning of the work that had conducted to this thesis, and of the experimentalist that have performed the measurements

Ionic Liquid Abbreviation	Alcohols Abbreviation			Experimentalist
	PrOH	BuOH	PentOH	
[C ₂ C ₁ im][NTf ₂]	✓	✓	✓	Arijit Bhattacharjee
[C ₃ C ₁ im][NTf ₂]	✓	✓	✓	Arijit Bhattacharjee
[C ₄ C ₁ im][NTf ₂]	✓	✓	✓	Inês C. M. Vaz; Arijit Bhattacharjee
[C ₅ C ₁ im][NTf ₂]	✓	✓	✓	Arijit Bhattacharjee
[C ₆ C ₁ im][NTf ₂]	✓	✓	✓	Inês C. M. Vaz; Arijit Bhattacharjee
[C ₇ C ₁ im][NTf ₂]	✓	✓	✓	Arijit Bhattacharjee
[C ₈ C ₁ im][NTf ₂]	✓	✓	✓	Arijit Bhattacharjee
[C ₉ C ₁ im][NTf ₂]	✓	✓	✓	Arijit Bhattacharjee
[C ₁₀ C ₁ im][NTf ₂]	✓	✓	✓	Arijit Bhattacharjee
[C ₁₁ C ₁ im][NTf ₂]	✓	✓	✓	Arijit Bhattacharjee
[C ₄ C ₁ im][PF ₆]	✓	×	×	Inês C. M. Vaz
[C ₅ C ₁ im][PF ₆]	✓	×	×	Inês C. M. Vaz
[C ₆ C ₁ im][PF ₆]	✓	×	×	Inês C. M. Vaz
[C ₇ C ₁ im][PF ₆]	✓	×	×	Inês C. M. Vaz
[C ₈ C ₁ im][PF ₆]	✓	×	×	Inês C. M. Vaz
[C ₉ C ₁ im][PF ₆]	✓	×	×	Inês C. M. Vaz
[C ₄ C ₁ pyrr][FAP]	✓	×	×	Inês C. M. Vaz
[C ₄ C ₁ im][FAP]	✓	×	×	Inês C. M. Vaz
[C ₄ C ₁ pyrr][NTf ₂]	✓	×	×	Inês C. M. Vaz
[C ₄ py][NTf ₂]	✓	×	×	Inês C. M. Vaz
[C ₄ C ₁ pip][NTf ₂]	✓	×	×	Inês C. M. Vaz
[C ₃ C ₁ C ₁ im][NTf ₂]	✓	×	×	Inês C. M. Vaz
[C ₄ C ₁ im][DCA]	✓	×	×	Inês C. M. Vaz
[C ₄ C ₁ im][TFA]	✓	×	×	Inês C. M. Vaz

✓ - measured before this thesis; × - not measured.

3.2.3. μ FlowCal – Isothermal Micromixer Calorimetry

The μ FlowCal is a flow twin microcalorimeter of the heat conduction type, designed to work in isothermal conditions. This calorimeter was designed to measure precisely and accurately the heat of mixing of two fluids (pure compounds or mixtures), in all ranges of composition, in isothermal mode and in a range of temperatures from 293 K to 308 K (20-35 °C). μ FlowCal calorimeter was designed, constructed and tested in the context of this thesis and so, it will be described in detail.

3.2.3.1. The Working Principle

The working principle of the μ FlowCal is schematized in figure 3.25, in a very simplistic form. Two fluids are injected in a borosilicate glass micromixer (model LTF-MX of the MR-Lab Series of the Little Things Factory) of 200 mm³ (μ L) assembled horizontally. The design of the micromixer allow the liquids to be mixed in a series of crossed channels and then, to flow through a unique channel for a certain path in the glass. As schematized, heat will develop in the mixing area, flowing in the reactor and to its surroundings.

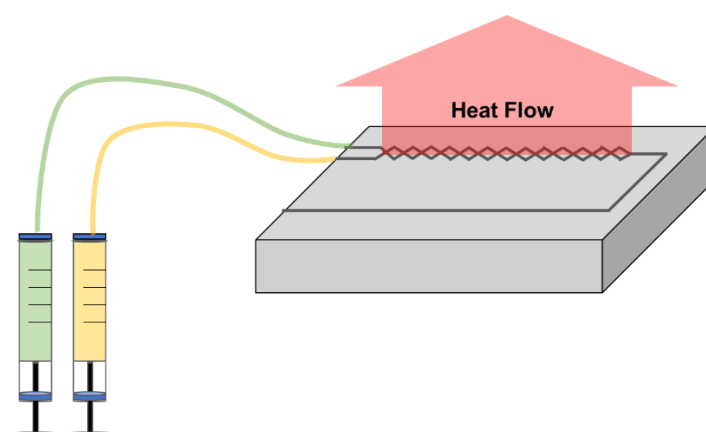


Figure 3.25. Schematic representation of the working principle of μ FlowCal.

To measure the heat flow originated in the mixture, four thermopile sensors made of multiple-junction bismuth-telluride thermocouples were used around the glass mixer. As the μ FlowCal was constructed under the principle of differential heat flow calorimetry, these thermopiles act as thermal bridges between the glass mixer and the heat sink. Due to the low thermal conductance of the glass micromixer, aluminium blocks were used between the glass micromixer and the heat flow sensors. Therefore, one face of the thermopiles is in contact with the heat sink and the other thermopile's face is in contact with aluminium blocks, which are in thermal contact with the micromixer glass.

In other words, four aluminium blocks conduct the heat from/to the mixer to/from the four thermopile sensors. These sensors are Peltier elements, through which the heat flows, from the mixer to the heat sink, or from the heat sink to the mixer, originating a voltage that is proportional to the temperature gradient and so, related with the heat flow across the sensitive device.

In one of the micromixers two fluids are mixed and the developed heat is measured. The other micromixer works as the calorimetric reference. The core of the calorimeter is then constituted by two glass micromixers, eight aluminium blocks (four for each mixer), that establish thermal contact between the mixers and the eight Peltier elements (four for each mixer), that constitute the frontier from the core of the calorimeter to the heat sink. The Peltier elements that are located above and below the reactor are connected in series and in parallel to the Peltier elements of the other reactor. This assembly is schematized in figure 3.26, where a scheme of the calorimetric principle behind the μ FlowCal is presented.

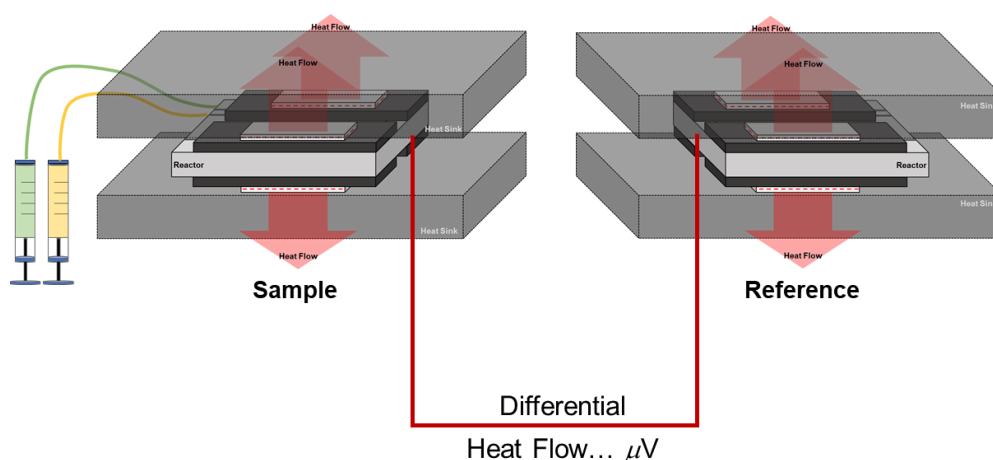


Figure 3.26. Schematic representation of the μ FlowCal calorimetric principle.

3.2.3.2. The Micromixer

This calorimeter measures the heat of mixing of two fluids, mixed in a micromixer (model LTF-MX of the MR-Lab Series of the Little Things Factory) of 200 mm³ (μL), with a channel diameter of 1 mm and pressure resistance up to 1500 kPa (15 bar). The microfluidic mixer is designed for intensive mixture, working with flows from 1.67 mm³ per second to 167 mm³ per second (0.1 to 10 cm³ per minute). The connections to the fluidic system are made by means of an aluminium connecting bar with 1/4" UNF fittings, on the front of the micromixer. More details on the fittings used and on the fluidic system are given in section 3.2.3.5. A schematic representation of the micromixer and a real picture of the microfluidic mixer with the connecting bar is presented in figure 3.27.

The micromixer is constituted by 2 borosilicate glasses bonded together by heat and pressure, each one with an imprinted 3D structure. The imprinted structure features a design that allows the split and recombination of the fluids along with the existence of two levels, which intensifies the mixture by repeated level change and crossflow. The mixture of both fluids relies thus, on the phenomena of diffusion and chaotic advection. The only external energy supplied that can help the achievement of a more efficient mixing is the pumping energy of the fluids, which means that the micromixer used can be classified as a micromixer of passive type.

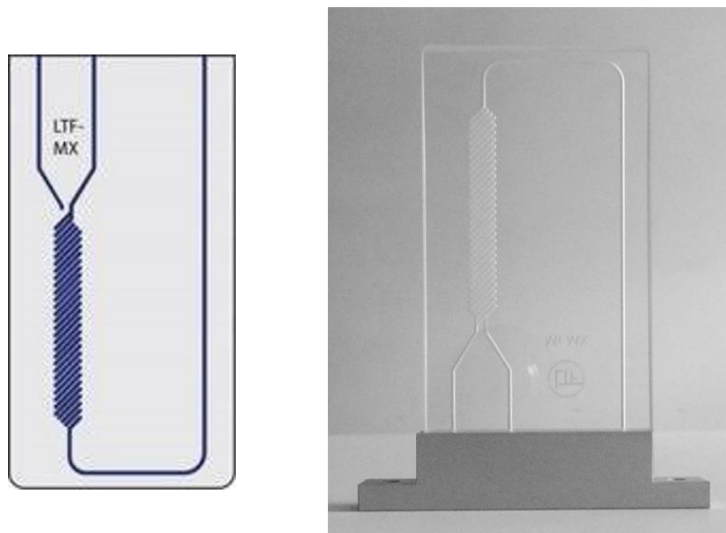


Figure 3.27. Schematic representation (on the left) and picture (on the right) of the borosilicate glass microreactor/micromixer (model LTF-MX of the MR-Lab Series of the Little Things Factory) of 200 mm³ (μL).

In the absence of any other external energy source that could increase the mixing efficiency, it is important to categorize the flow into one of the following regimes, laminar, turbulent or transitional and understand the factors which will be the mixture driving-force. The two regimes differ by the relative importance of the viscous and inertial forces, which can be accessed by the calculation of the Reynolds number (Re):

$$Re = \frac{\rho \cdot v \cdot L}{\eta}, \quad (3.28)$$

where ρ ($\text{kg}\cdot\text{m}^{-3}$) is the density of the fluid, v ($\text{m}\cdot\text{s}^{-1}$) is the velocity, L (m) is the length of the stream and η ($\text{kg}\cdot\text{m}^{-1}\cdot\text{s}^{-1}$) is the viscosity. At low Reynolds number, the viscous forces dominate over inertial forces and laminar flow occurs. In laminar flow the mass transfer occurs only in the direction of the fluid flow and mixing can be achieved only by diffusion. At high Reynolds number, inertial forces dominate over viscous forces, the motion of the fluid is random and so, mass transfer occurs randomly in all directions. Between laminar and turbulent flow there is a transitional regime.

In microfluidics, Reynolds number is usually inferior to 100 and so the flow is usually considered to be essentially laminar ^[19]. In all the experiments performed in this work, considering the diameter of the micromixer channel to be 1 mm, the Reynolds number was inferior to 10, being therefore in the domain of the laminar flow.

Knowing that in passive micromixers the efficiency of the mixture relies on the phenomena of diffusion and chaotic advection and that the flow of the fluid is mainly laminar, micromixers geometry is generally optimized in order to increase these two phenomena. For spherical simple particles diffusion coefficient, D ($\text{m}^2\cdot\text{s}^{-1}$), can be obtained from the Einstein-Stokes equation:

$$D = \frac{k_B \cdot T}{6 \cdot \pi \cdot \eta \cdot R}, \quad (3.29)$$

where k_B is the Boltzmann constant, T (K) is the temperature, η ($\text{kg}\cdot\text{m}^{-1}\cdot\text{s}^{-1}$) is the viscosity and R (m) is the radius of the molecule. Furthermore, the time, t , necessary for a molecule to diffuse increases quadratically with the travelled distance (r),

$$t = \frac{r^2}{2 \cdot D}. \quad (3.30)$$

Consequently, the mixture efficiency is beneficated in micromixers with narrow channels. The ratio between diffusion and chaotic advection can be accessed by the Peclet number (Pe),

$$Pe = \frac{L \cdot v}{D}, \quad (3.31)$$

where L (m) is the length of the stream and v ($\text{m}\cdot\text{s}^{-1}$) is the velocity of the flow.

In the used micromixer, the design takes advantage of the splitting of the stream into n laminae, which decreases the diffusion length. Moreover, the consecutive splitting and recombination of the flow benefit the mixing by increasing greatly the contact surface area. Additionally, the x-shape and the repeated level change alter the flow direction successively, creating mass transfer in other directions and having thus the ability to induce chaotic advection.

3.2.3.3. Calorimeter Design

As a heat flow calorimeter, the vital part of this calorimeter is the reactor, the heat flow sensors and the existence of a heat sink of a virtually infinite heat capacity.

In figures 3.28 and 3.29, pictures of the assembly of the calorimetric core are presented. Starting from the inside to the outside, there is the reactor, the aluminium block, that establish thermal contact between the glass reactor and the Peltier type heat flow sensors (model HT4-6-F2-2143 of the ThermoTEC™ Series from Laird™ Thermal Systems). A small part (Celeron® composite) “aligner” was used to maintain the position of the Peltier sensors. Between the aluminium blocks and the reactor, as well as, between the aluminium blocks and the Peltier sensors, a thin layer of silicone heat sink compound (DOW CORNING® 340) was used to improve the thermal contact.

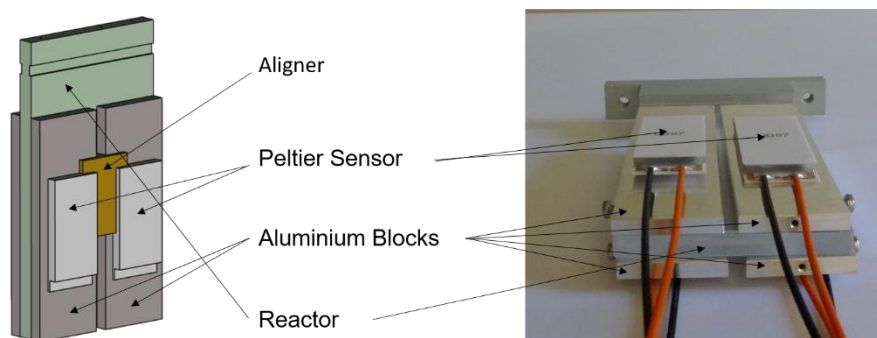


Figure 3.28. Schematic representation in three dimensions (on the left) and a real picture (on the right) of the calorimetric core, with discrimination of its constitution: the reactor, the aluminium blocks, the Peltier sensors and the aligner.

The calorimetric core is encapsulated by four aluminium blocks, which are in thermal contact with the Peltier sensors and cover the upper or lower side of the core (see picture 3.30). Other five aluminium blocks enclose the described system, as it can be seen in figures 3.31-3.35. In total, the heat sink is constituted by nine aluminium blocks in a total mass of 18 kg of aluminium 5083 (aluminium alloy with 3 to 5 % of manganese and chromium).

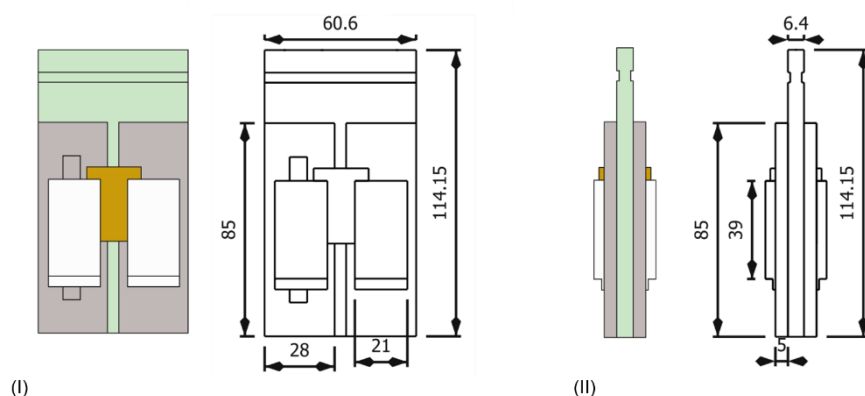


Figure 3.29. Schematic drawing of the top/bottom (I) and front (II) views of the calorimeter core. Dimensions in millimetres.

The glass micromixer, aluminium block and heat flow sensors are kept under controlled stress by means of a sandwich type assembly. The aluminium plates are spaced by four aluminium cylinders (see figure 3.30). The fixed stress and alignment

between these cylinders and the aluminium plates is guaranteed by eight cork disks (0.8 mm thickness).

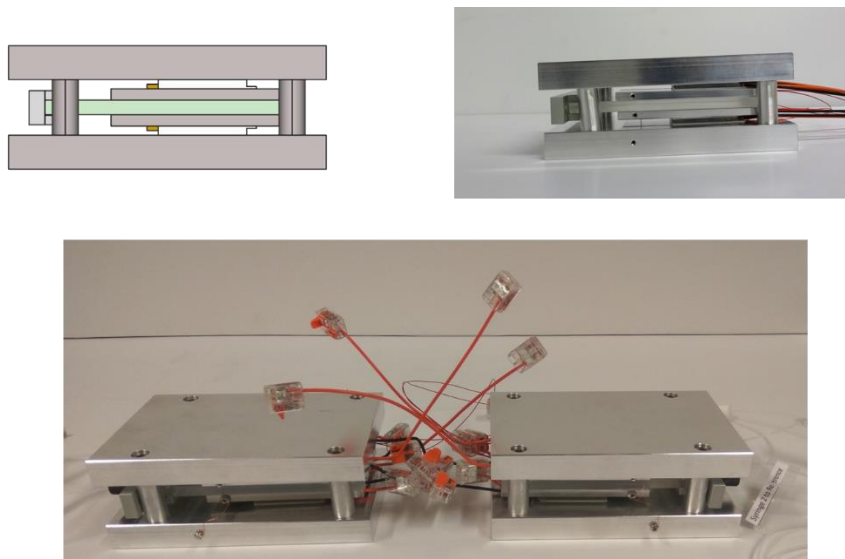


Figure 3.30. Schematic representation and real picture of the calorimetric core enclosed by aluminium blocks.

The aluminium block that constitutes the front view of the final assembly, depicted in figure 3.35, was modified to thermostat the fluid before entering the reactor. The modifications will be described in section 3.2.3.6.

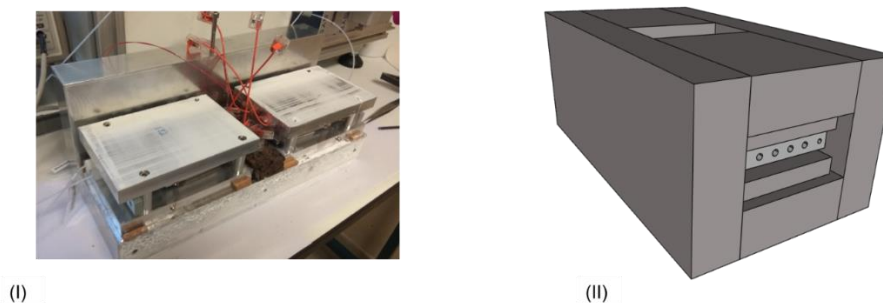


Figure 3.31. (I) Picture of the assembling of the calorimetric core in the heat sink and (II) schematic representation of the final calorimetric assembly (reactor, heat flow sensors and heat sink).

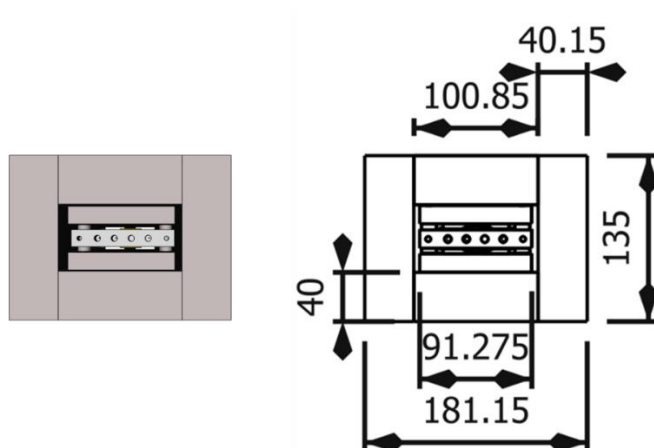


Figure 3.32. Lateral view of the schematic representation of the calorimetric assembly (reactor, heat flow sensors and heat sink). Dimensions in millimetres.

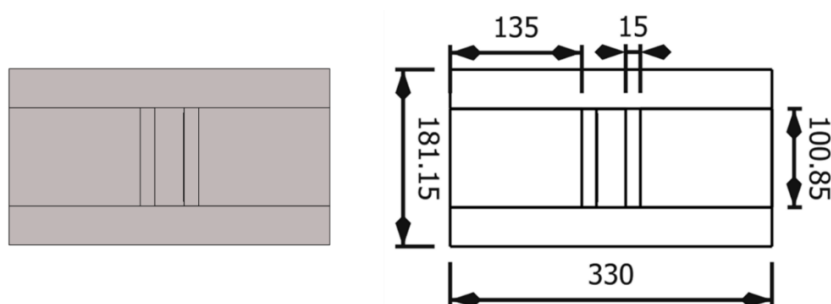


Figure 3.33. Upper view of the schematic representation of the calorimetric assembly (reactor, heat flow sensors and heat sink). Dimensions in millimetres.

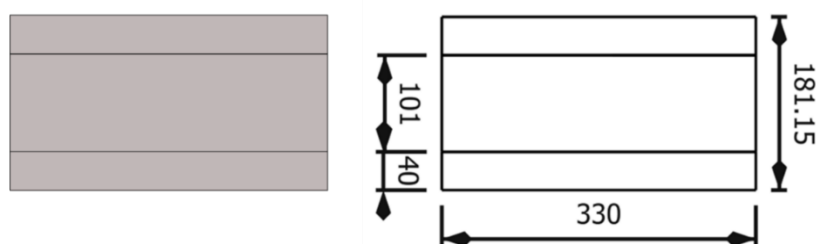


Figure 3.34. Down view of the schematic representation of the calorimetric assembly (reactor, heat flow sensors and heat sink). Dimensions in millimetres.

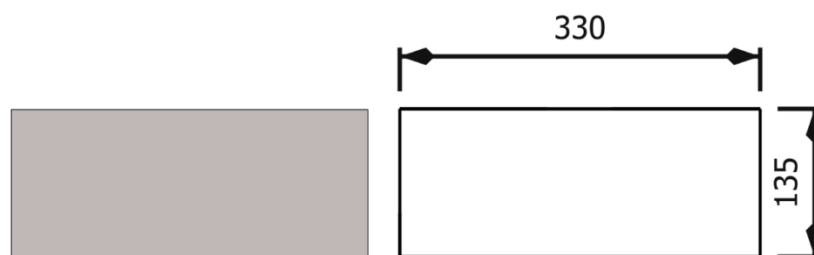


Figure 3.35. Front and back view of the schematic representation of the calorimetric assembly (reactor, heat flow sensors and heat sink). Dimensions in millimetres.

3.2.3.4. Calorimeter Thermostatization

The thermostatization of the calorimeter is of extreme importance as it will affect the baseline stability. The temperature of the laboratory was kept at 295 K (22 °C) whereas the temperature of the calorimeter was set to 298.15 K (25.00 °C). The higher temperature of the calorimeter when compared to the room temperature of the laboratory avoids condensation but it also means that heat exchanges will be present. The temperature of the calorimeter will always tend to the temperature of the laboratory and oscillation in laboratory temperature will affect the quality of the temperature control of the calorimeter. An elevated thermal inertia is then desirable for the sake of the quality and stability of the baseline.

The calorimetric assembly described previously (reactor, heat flow sensors and heat sink), which total dimensions were 181 mm x 330 mm x 135 mm, was inserted in an aluminium box of internal dimensions of 200 mm x 350 mm x 155 mm, as shown in figure 3.36. This external aluminium box was designed to maintain the calorimetric assembly inside an air box of 10 mm side, reducing the heat transfer by conduction and preventing the existence of significant heat transfer by convection. The external faces of the aluminium boxes were covered by copper plate heat exchangers. In figure 3.37 is depicted the aluminium box with the copper plate heat exchangers. An aqueous solution of ethylenoglycol 15 % (volume) is used as heat exchange fluid. This fluid is pumped from a high precision temperature controlled external bath. Silicone heat sink compound (Dow corning 340) was used as thermal contact between the copper plates and the aluminium box.

The aluminium box containing the calorimeter block is thermal isolated from the outside using 40 mm (thickness) extruded polystyrene. The empty spaces are filled with hydrophilic cotton as depicted in figure 3.38.



Figure 3.36. Photograph of the interior of the aluminium box with six PVC spacer support parts without the calorimetric assembly (on the left) and with the calorimetric assembly (on the right).

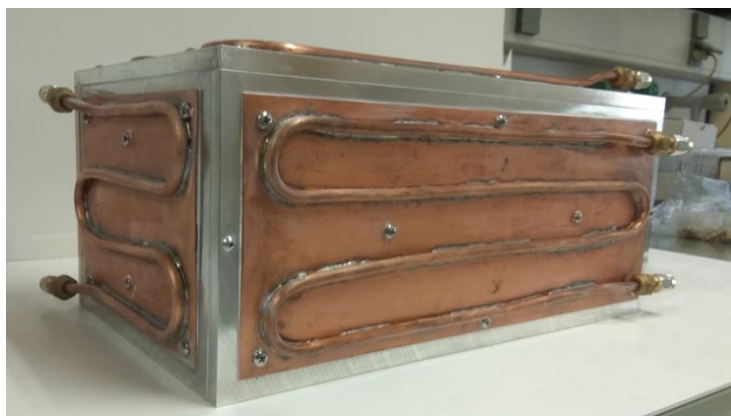


Figure 3.37. Photograph of the exterior of the aluminium box with the copper plate heat exchangers.

The temperature of the bath is controlled locally by means of a high precision proportional integral derivative (PID) temperature controller connected to a thermistor. A cold source is provided by a spiral serpentine, in which circulates a fluid at 293.2 K (20.0 °C), supplied by a Julabo F25-MP thermostat. The homogenization of the temperature in the water-ethylene glycol bath is provided by a stainless steel stirrer assembled in the zone of the temperature control. Immersed in the bath there is a pump (EHEIM universal 2400), that pumps the aqueous solution of 15 % (volume) ethylene glycol to the copper plate heat exchangers and back to the thermostated bath.

A hose brings the thermal fluid, pumped from the bath, until a metal splitter that distributes the mixture to 6 polyethylene tubes ($\varnothing = 10$ mm) which are connected in parallel to 6 independent heat exchange plates. The circulation of the thermal fluid is done in parallel through the faces of the aluminium box, thermostating the box and

consequently the calorimeter at 298.15 K. The exits of the copper heat exchangers are connected to 6 identic polyethylene tubes ($\varnothing = 10$ mm) that combine into a unique hose which transports the fluid back to the bath.



Figure 3.38. Photograph of the upper view of the structure (open) that contains the calorimeter.

To monitor the thermostatzation of the calorimeter and evaluate the temperature fluctuations, three identical thermistors ($2\text{ k}\Omega$ at $20\text{ }^{\circ}\text{C}$), reference GL23 (RS-stock No 151-029, glass bead type), were used. One thermistor was installed in the water / ethylene glycol bath, other in the exterior of the aluminium box and the other inside the calorimeter, between the sample and reference block. The resistance of each thermistor is acquired by a data logger (Agilent, LXI Data acquisition 34972A) and registered in a PC computer using a customized software application developed in HPVEE (described in the appendix B).

By simultaneous monitoring of the temperatures in the bath, aluminium box and calorimeter, the behaviour and time constant of the heat transfer for the heat sink was evaluated. This evaluation study of the μ FlowCal thermostatzation system and its inertia, is described in the appendix A.

3.2.3.5. The Flow System

The microinjection system is schematized in figure 3.39. It is constituted by two high precision syringe pumps, located in a thermostated air box, tubing channels, thermostatzation block and fittings, which interconnect the syringes to the micromixer. The mixing point is located in the micromixer and the outlet channel is connected to the sewer, which is located in the thermostated air box.

Two neMESYS (Brand CETONI, model low pressure pump neMESYS 290N) precision syringe pumps are used. The control system of these syringe pumps was designed to work with syringes from 10 mm³ (μL) to 50 cm³ (mL) and guarantees a pulsation free flow. The neMESYS syringe pumps constitute a modular system fully controllable by software, which makes possible to perform sequential, parallel or continuous injections, either using the same fluid or different fluids. The syringe pumps have an integrated 3-2 way valve that allows to perform an injection or to refill the syringe in an alternate way.

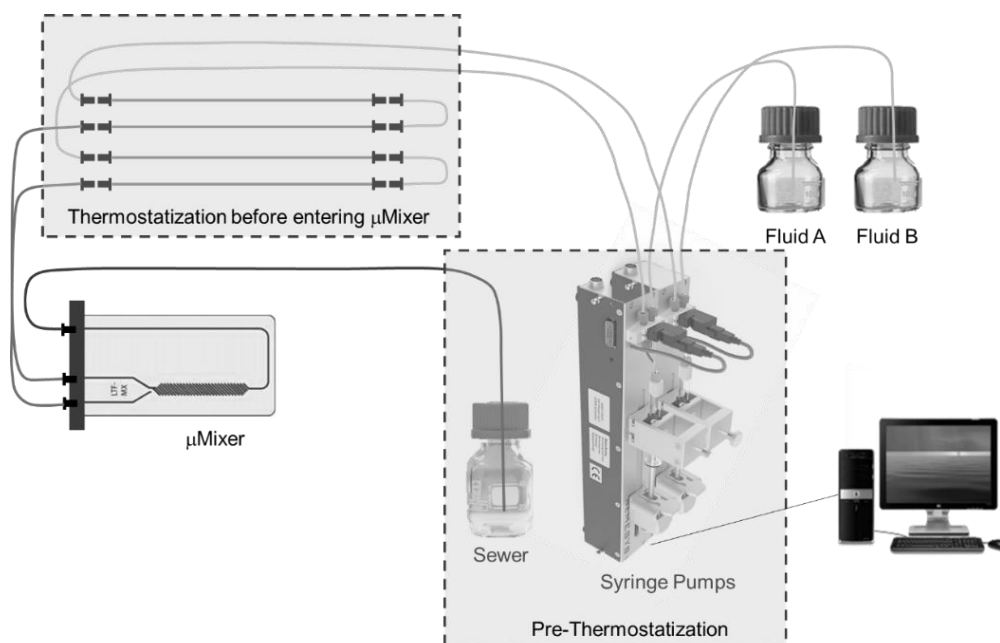


Figure 3.39. Schematic representation of the flow system of the apparatus.

In the syringe pumps are assembled high-precision gastight glass syringes (from SETonic GMBH) of 2.5 cm³ (mL) or 5.0 cm³ (mL). The syringes are equipped with a PEEK® (Polyetheretherketone) female tubing connector ¼ inch-28 fitting thread with a PTFE® (Polytetrafluoroethylene) plunger seal. These syringes are stable until pressures of 1700 kPa (17 bar, syringe of 5.0 cm³) and 2300 kPa (23 bar, syringe of 2.5 cm³). Flangeless ¼ inch-28 tube end fittings with collapsible ferrules and PTFE® tubing were used to connect the syringes to the 3-2 way valves of the neMESYS syringe pump. The (VICI) flangeless fittings used consist in propylene nuts with knurl geometry equipped with the VICI patented collapsible ferrule design. The knurl geometry allows to tight the fitting just using fingers, without the use of any wrench. The design of the ferrule consists in a one-piece ferrule designed to collapse as it is tightened resulting in a very effective seal with negligible distortion of the tubing inner diameter. Ferrules of PEEK®, and CTFE® (Chlorotrifluoroethylene) for 1/16 inch tube end fittings were used. The PTFE® tube has an outer diameter of 1/16 inch ($\varnothing_{\text{ext}} = 1.6$ mm) and an inner diameter of 0.030 inch ($\varnothing_{\text{int}} = 0.8$ mm).

From the 3-2 way valve of the syringe pumps, tube end fittings with the same specifications are connected to a PTFE® tube that extends to a flask containing the fluid that will be injected, making possible to refill the syringe at any time. The 3-2 way valve of the syringe pumps allows to alternate between injection in the calorimeter and refill of the syringe. Accordingly, tube end fittings with PTFE® tubing of the same specifications described are connected to the 3-2-way valve and extend to the interior of the calorimeter. In the other end of this tube, the same fittings already described connect to stainless steel reducing unions 1/4 inch-28 to 10-32 with a bore of 0.030 inch. On the other side of the union are connected stainless steel nuts 10-32, which were assembled in the end of a stainless steel tubing, 20 cm long, with an outer diameter of 1/16 inch and an inner diameter of 0.030 inch. On the other end of the stainless steel tube, the union and the assembled fittings are replicated, connecting to a PTFE® tube that act as a loop, to a new stainless steel tube through the unions and fittings described. At the end of this second stainless steel tube, a new union is used to connect the stainless steel tube to a PTFE® tube that connects to the micromixer, through a flangeless 1/4 inch-28 tube end fitting with a collapsible ferrule. The set described until now transports the fluids from the syringes to the mixer. The stainless steel tubes are used to thermostatize the fluid before injection in the micromixer. In figure 3.40 the connections used, fittings and unions are schematized.

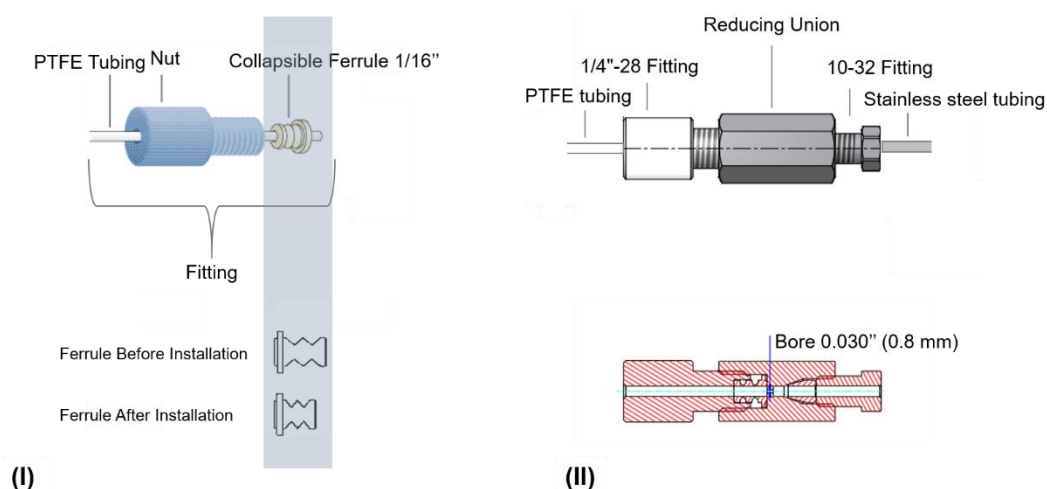


Figure 3.40. Schematic representation of the (I) flangeless 1/4 inch -28 tube end fittings with collapsible ferrules and (II) stainless steel reducing unions 1/4 inch-28 to 10-32 with a bore of 0.030 inch. Picture adapted from VICI catalog.

At the end of the mixer, a new flangeless 1/4 inch-28 tube end fitting with a collapsible ferrule is connected to a PTFE® tubing that transports the fluid, which exits the microfluidic mixer, to a flask in the exterior of the calorimeter, acting like a sewer.

The fittings used were chosen and connected in order to be flat and to face directly into the connecting port, fitting perfectly to the surface and avoiding leakages.

To reduce the back diffusion of the fluid at mixing point, a steel tube of 29 mm ($\varnothing_{\text{ext}} = 0.8 \text{ mm}$; $\varnothing_{\text{int}} = 0.45 \text{ mm}$) was inserted in the entrance of the glass mixer in order to reduce the channel section, as represented schematically in figure 3.41.

In table 3.4 some key dimensional information regarding the flow system is presented.

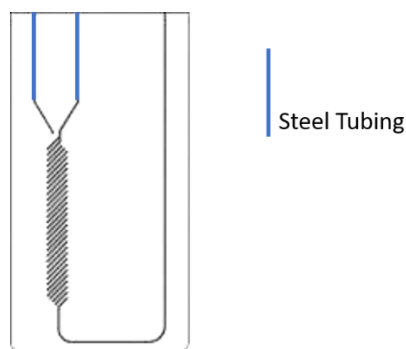


Figure 3.41. Schematic representation of the steel tube inserted inside the micromixer.

Table 3.4. Volume of the tubing and other parts that constitute the flow system of the μ FlowCal

Part	\varnothing_{int} / inch	\varnothing_{int} / cm	Length / cm	Volume / cm^3 (mL)	Volume / mm^3 (μL)
PTFE® Tubing from syringe	0.030	0.076	88.5	0.401	401
Stainless steel tubing	0.030	0.076	20	0.091	91
PTFE® Tubing loop	0.030	0.076	20	0.091	91
Stainless steel tubing	0.030	0.076	20	0.091	91
PTFE® Tubing to Micromixer	0.030	0.076	20	0.091	91
Micromixer	-	-	-	0.200	200
After Micromixer ^a	0.039	0.1	13	0.100	100
Drainage tubing	0.030	0.076	140	0.635	635
Total Volume				1.699	1699
Volume until reach micromixer				0.764	764
Volume per cm				0.005	5

a – estimated values.

The control and setup of the flow system is done by software, using the “Nemesys User Interface Program” provided by CETONI. The software allows to perform manual injections by using the “Direct Mode” and programmed injections by using the “Flow Profile Mode”. In the “Direct Mode” the volume (in mm^3) and the flow (in $\text{mm}^3\cdot\text{s}^{-1}$) is set and the injection can be initiated in one of the syringes, or simultaneously in all the installed syringes. In the “Flow Profile Mode” the flow (in $\text{mm}^3\cdot\text{s}^{-1}$), the injection time (in seconds) and the time between each injection is programmed. Each injection is individually programmed so, different volumes or injections speeds can be programmed. The software allows also to include, in the injection program, the commutation of the 3-2 way valve to refill the syringe. The injection programmes can be programmed directly on the software or using a script file, which is read by the software. In both modes the fluid can be injected or pushed back in the syringe direction. In figure 3.42 and 3.43 a “screenshot” of the software in the “Direct Mode” and in the “Flow Profile Mode” is presented.

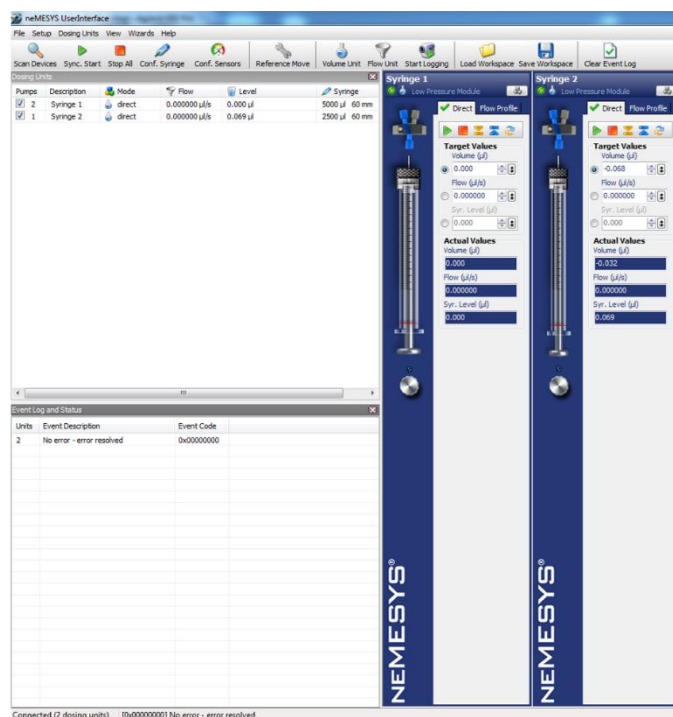


Figure 3.42. Picture of the monitor with the software “Nemesys User Interface” provided by CETONI working in “Direct Mode”.

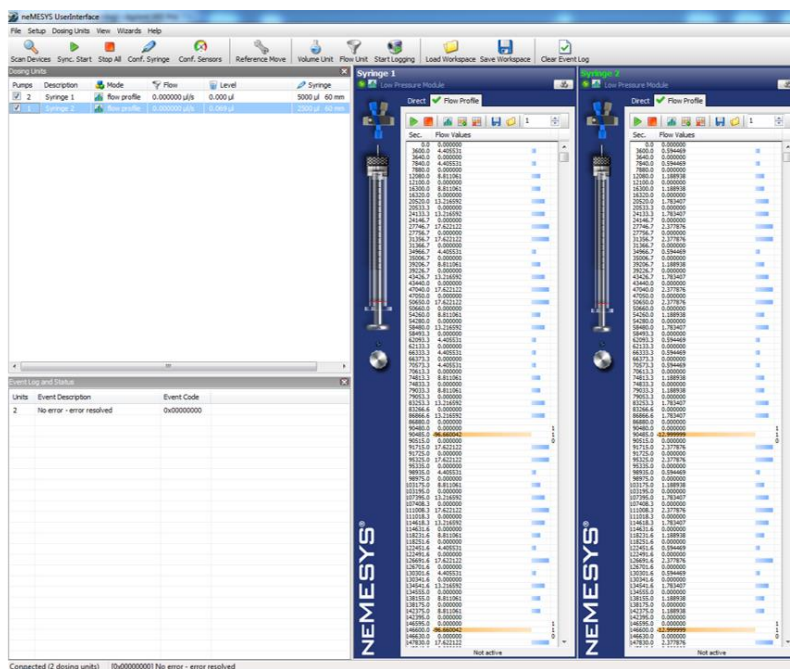


Figure 3.43. Picture of the monitor with the software “Nemesys User Interface” provided by CETONI working in “Flow Profile Mode”.

3.2.3.6. The Fluid Thermostatization

As described in figure 3.39, two thermostatization systems were used in the flow system of μ FlowCal.

A first pre-thermostatization system, depicted in figure 3.44, was build and installed in order to maintain the temperature of the syringes and sewer at 298 K. The thermostatization of all the flow system is essential to maintain the stability of the baseline of the calorimeter. The small fluctuations of the ambient temperature of the laboratory are enough to lead to significant thermal expansion and compression of the liquid, causing microinjections, which are enough to affect the baseline stability.

In the first pre-thermostatization system, the temperature is controlled locally and then air is circulated through all the system. The temperature sensor, a thermocouple type J (iron–constantan), is located at the fan, measuring the temperature of the air bath exiting the thermostatization area. The temperature sensor is connected to a PID temperature controller (Fuji, model PXR4) which regulates the power of a cartridge resistance of 50 W installed in a heat exchanger. An Air-to-Air Thermoelectric Assembly with a maximum cooling power of 33.5 W (Laird, Part Number AA-034-12-22-00-00) is used as cold source.

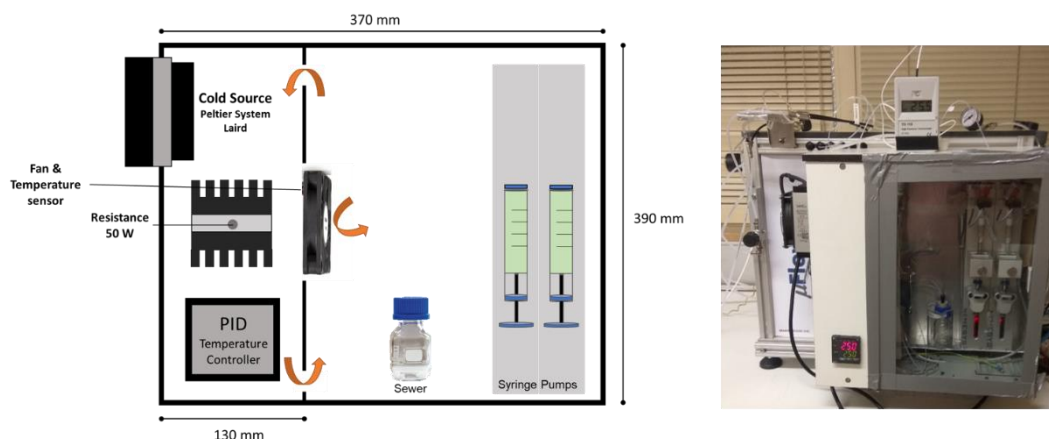


Figure 3.44. Schematic representation (on the left) and real picture (on the right) of the system used to thermostatize the syringes and sewer of the μ FlowCal.

The second thermostatzation system is based in the anchoring of part of the flow system in the exterior face region of the heat sink of the calorimeter. For this purpose, the aluminium block of the heat sink was machined as shown in figure 3.45. The thermal anchoring of the flow system in the heat sink is depicted in figure 3.46. Using this set-up, the injected fluid is thermostated at the temperature of the calorimeter before injection in the micromixer. As demonstrated in table 3.4, the volume of liquid thermostated is higher than the volume of the micromixer. The pre-thermostatzation system is responsible for the thermostatzation of the syringes and its content at 298 K, which decreases the residence time, in the second thermostatzation block, needed to ensure a proper temperature equality of the liquid in the injection channels and the mixer.

For thermal anchoring of the flow system, a stainless steel tubing channel was used, which was leaned towards the heat sink. A thin layer of silicone heat sink compound (DOW CORNING® 340) was used to guarantee good thermal contact between the stainless steel tubing and the heat sink block.

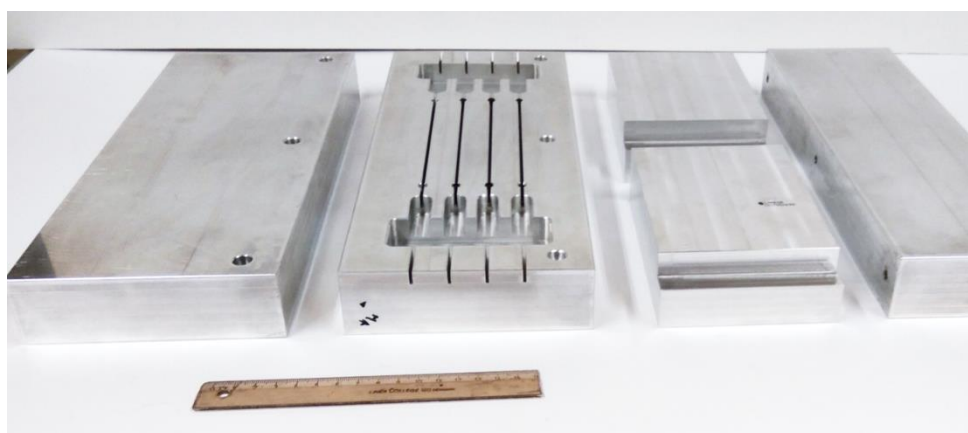


Figure 3.45. Picture of the external face of the aluminium blocks that constitute part of the heat sink of the μ FlowCal.



Figure 3.46. Picture of the thermal anchoring region of the flow system in the heat sink.

3.2.3.7. Nitrogen Line

The flow system of μ FlowCal was kept under positive pressure of nitrogen, avoiding the entrance of contaminants, like water, into the system. Furthermore, the pressurization of the sewage creates a backpressure into the system, which diminishes cavitation issues that are chiefly relevant with volatile fluids. The pressure of the system is adjustable between 100 – 600 kPa (1 to 6 bar).

If viscous fluids are used, like ionic liquids, its resistance to flow / viscosity is enough to create back pressure and prevent cavitation effects.

3.2.3.8. Heat Flow Signals

The borosilicate glass micromixer, where both fluids are mixed, is constituted by a series of cross channels, where the fluids are mixed and then, by a unique channel, as is showed in figure 3.27. The heat flow sensors, Peltier plates, are located above and below the glass micromixer, in the mixing area and after the mixing area.

The thermopiles, located above and below the mixing area, are connected in series and in opposition to the thermopiles of the mixing area of the glass micromixer used as reference, originating the signal 1. The thermopiles located above and below the unique channel after the mixing area are also connected in series and in opposition to the thermopiles of the glass micromixer used as reference, originating the signal 2. Accordingly, two thermoelectric signals are acquired in the μ FlowCal prototype

calorimeter, the signal originated in the Peltier elements located above and below the mixing area and the signal from the Peltier elements located above and below the unique channel after the mixing area. In figure 3.26, a scheme on the differential arrangement of the heat flow sensors is represented. In figure 3.47 is represented a simplistic scheme of the localization of the heat flow sensors towards the micromixer, illustrating the location in the calorimeter in which the calorimetric output “signal 1” and “signal 2” is originated.

These two calorimetric signals are acquired in a sequential mode by a nanovoltmeter (7 ½ Digit, Agilent/Keysight 34420A), connected via RS232C to a PC that performs data acquisition of the calorimetric data, as a function of the time of measurement, in a software developed in HPVEE. This software is described in the appendix B.

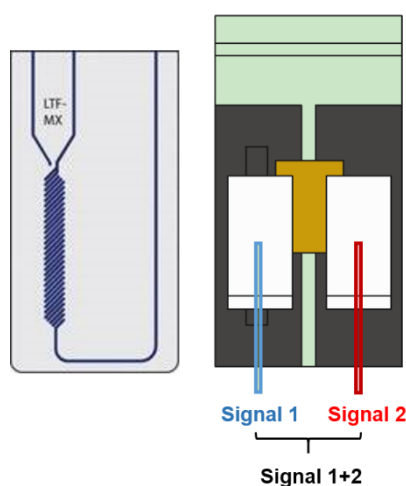


Figure 3.47. Scheme of the localization of the Peltier elements towards the micromixer and illustration of the location, in the calorimeter, of the origin of the calorimetric output “signal 1” and “signal 2” of μ FlowCal.

The thermoelectric signals recorded (“signal 1” and “signal 2”) are proportional to the differential heat transferred through the thermopiles located in the mixing area and after the mixing area.

The calorimetric output “signal 1” corresponds to the heat accumulated in the calorimetric cell (glass micromixer), exchanged through the glass and released to the heat sink, through the aluminium blocks and heat flow sensors, as demonstrated in the scheme presented in figure 3.48. The calorimetric output “signal 2” is measured after the

zone of mixing. Thus, it corresponds to the fraction of heat transferred through the glass micromixer (from the mixing area), accumulated in the glass mixer, aluminium blocks and heat flow sensors and released to the heat sink, through the aluminium blocks and heat flow sensors, as demonstrated in the scheme presented in figure 3.48.

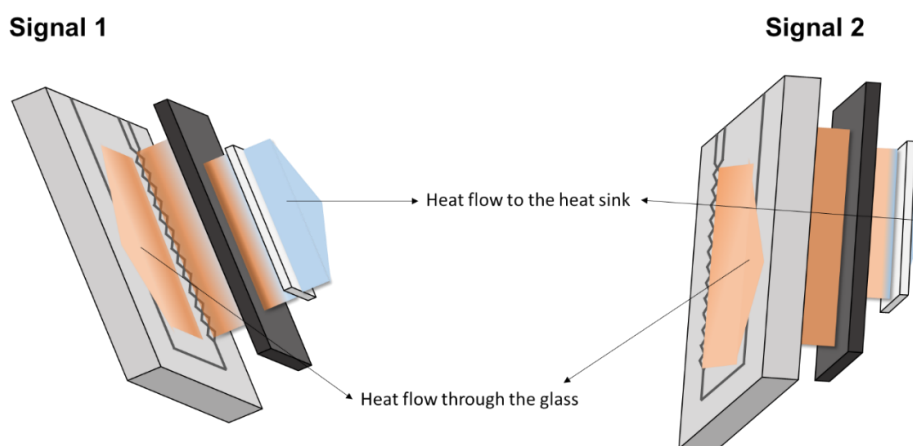


Figure 3.48. Scheme of the heat transfer that originates the signal 1 and signal 2 of μ FlowCal.

It should be noted that the schemes of heat transfer represented in figure 3.48 show the micromixer in a different position from the reality and show only one aluminium block and one heat flow sensor. However, the glass micromixer is assembled horizontally and the heat transfer occurs through the aluminium blocks and heat flow sensors that are both above and below the glass micromixer, as represented in figure 3.26. Plus, “signal 1” is originated in the Peltier elements located in the micromixer area, and “signal 2”, in the opposite area of the glass mixer, as represented in the scheme presented in figure 3.47. If the “signal 1” and “signal 2” are summed, the heat flow through the glass reactor is cancelled and so, the sum of two signals, in each instant, correspond to the balance between the heat accumulated in the glass micromixer, aluminium blocks and heat flow sensors and the heat that is flowing through the heat flow sensors.

Thus, if the sum of “signal 1” and “signal 2” is considered, the analysis of the calorimetric data is simpler, as we can consider a more simplistic heat path. In addition, we can consider that all the thermal energy originated by the process under investigation is captured, if both signals are summed. However, it should be noted that the noise is increased by the sum of two signals, as showed in the right side of figure 3.49. Figure 3.49 represents the calorimetric signal output “signal 1” and “signal 2”, as well as, the

sum “signal 1 + signal 2”, showing the typical results obtained in μ FlowCal. The calorimetric data represented in figure 3.49 is presented as obtained, without application of any filter, smooth or thermal inertia correction. The magnification of the baseline (in the right side of figure 3.49) evidences the level of noise/signal ratio in the two independent signal outputs, “signal 1” and “signal 2”, as well as, the expected nominal increase of the noise/signal ratio in the “signal 1+2”.

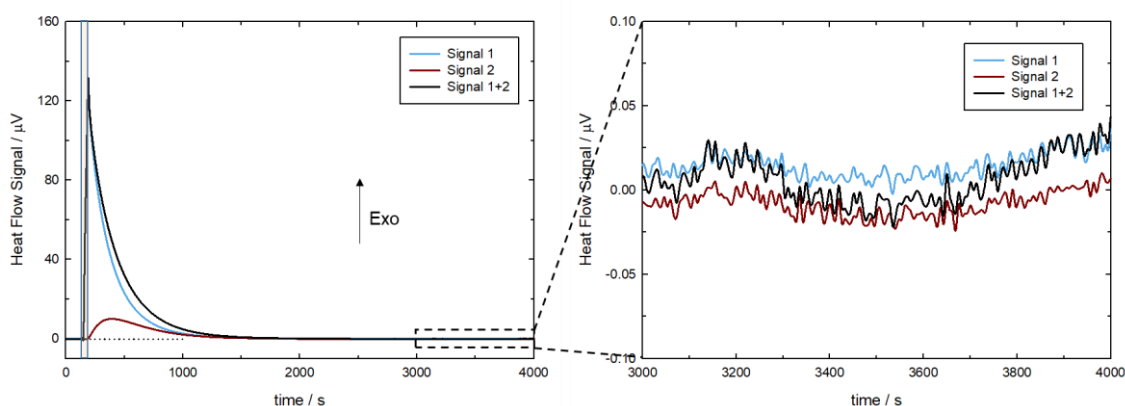


Figure 3.49. Graphical representation of the calorimetric output data “signal 1”, “signal 2” and its sum “signal 1+2”. On the left side is represented the output calorimetric data obtained by release of thermal energy into the mixing area by joule effect and on the right side a magnification of the calorimeter baseline evidencing the magnitude of the noise/signal ratio.

The fact that the sum of the thermoelectric potentials generated (signal 1+2) correspond to the balance between the heat accumulated and the heat that is flowing through the heat flow sensors indicates that the calorimetric output signal depends, not only of the process under investigation, but also on the thermal inertia of the calorimeter. Accordingly, the transformation of the obtained experimental signals in the different heat conduction phenomena occurring in the calorimeter is of major importance. Only in this way, it is possible to reconstruct the instantaneous thermal power originated by the process under investigation, which is essential to obtain thermokinetic information. The determination of the time constant of the calorimeter is detailed in the appendix A.2.

In figure 3.50 is presented the calorimetric output data “signal 1”, “signal 2” and its sum “signal 1+2”, resultant from the release of thermal energy, by Joule effect, during 40 seconds in the calorimeter. On the left side of figure 3.50, the calorimetric output data is represented as obtained from μ FlowCal calorimeter. On the right side are presented the respective curves, corrected to the thermal inertia of the calorimeter.

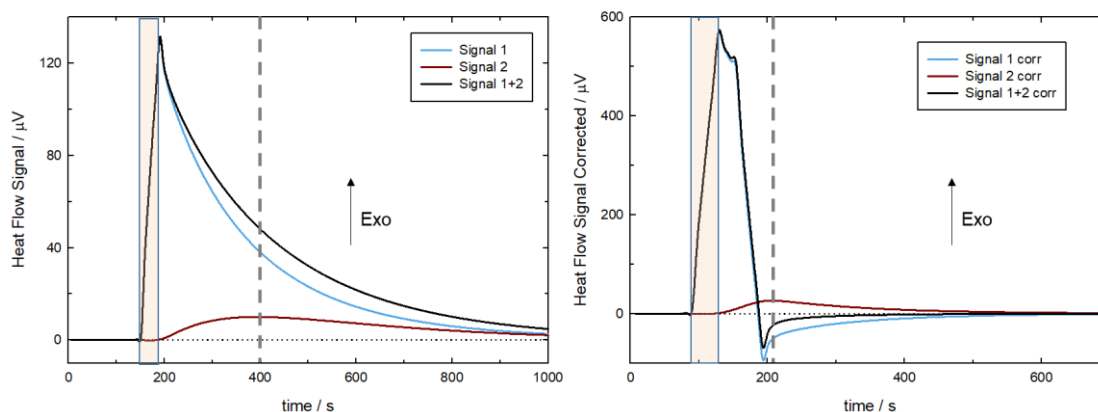


Figure 3.50. Graphical representation (on the left) of the calorimetric output data “signal 1”, “signal 2” and its sum “signal 1+2” as obtained from μ FlowCal and (on the right) of the calorimetric output “signal 1”, “signal 2” and its sum “signal 1+2” corrected to the thermal inertia of the calorimeter. The dash line marks the time where time derivative of the heat flow of signal 2 is zero.

As discussed in the Appendix A.2, the correction of the heat flow signal to the thermal inertia of the calorimeter, using one time constant, is not enough to correct the “signal 1” and the “signal 2”. However, to correct the calorimetric output “signal 1 + 2”, one time constant is enough, correcting the thermal inertia associated with the heat transfer from the glass mixer to the heat sink.

It is interesting to notice that during the 40 s that last the thermal energy release, represented in the figure as a light yellow shaded area, there seems to be present a linear increase of the heat flow signal in both curves. In the “raw” calorimetric signal, this linear increase is followed by a first order exponential decay. In the corrected signal “1+2”, it would be expected that at the stop of the calibration pulse, the signal would decay rapidly to the baseline. However, it was verified that the signal decay at a very small ratio for a small period in time, followed by a rapid decrease of the heat flow signal. This time lag was associated with the complex heat flow process present in the calorimeter, as the heat is being released in the aluminium blocks and not directly in the micromixer.

Another interesting point is the maximum heat flow of the “raw” output signal “2”. In this maximum (zero at the time derivative of the heat flow), the heat flow being transferred through the glass plate and the heat flow transferred through the Peltier plates is balanced. Therefore, from the heat flow signal at that point, in both “signal 1” and “signal 2”, we can estimate the proportion of heat flow conductance. Accordingly, it

was found that the conductance of heat through the glass plate is approximately $\frac{1}{4}$ of heat transferred through the Peltier plates.

Moreover, after the correction to the time constant of the calorimeter, when the heat flow of “signal 2” reaches its maximum, at approximately 200 s, the glass plate is in thermal equilibrium and both signal 1 and 2 are exchanging the same amount of heat. The heat flow “signal 1+2” corrected to the thermal inertia of the calorimeter, do not yet equals the baseline level at this point, but the observed description is quite reasonable, taking into account the complexity of the heat flow process.

3.2.3.9. Customized Software

Customized software was developed in HPVVEE, a visual programming language of Keysight, specifically to acquire μ FlowCal calorimetric output signal, treat calorimetric output data and monitor the thermostatzation of the calorimeter. To that effect, a software package of three customized programs was created.

The Data Acquisition Software allow real time visualization of the heat flow signal “signal 1”, “signal 2” and “signal 1+2” over time. This software corrects the acquired output calorimetric data to the thermal inertia of the calorimeter, allowing the visualization of the approximate thermokinetics of the process under study, along with the “raw” calorimetric output. The acquired data is also logged in an output file for posterior treatment. A detailed description on the developed software is provided on the Appendix B.1.

To read and treat the calorimetric output data was developed a program, Data Treatment Software, which reads the output file of the data acquisition software, smooths the data, corrects the calorimetric output data “signal 1” and “signal 2” and “signal 1+2” to the time constant of the calorimeter (which can be altered at any time), integrates each peak individually and registries the output of the individual integrations in a output file. A detailed description on the Data Treatment Software is provided on the Appendix B.2.

The Temperature Monitor Software was developed, as indicated in its name, to monitor the thermostatzation of the calorimeter. The software performs data acquisition and allows real time visualization of the temperature in the calorimeter, in the aluminium external box (calorimeter thermostat) and in the water / ethylene glycol thermostated bath. A detailed description on the Temperature Monitor Software is provided on the Appendix B.3.

3.2.3.10. Summary of the Experimental Procedure

μ FlowCal calorimeter was designed, constructed, calibrated and tested in the context of this thesis, aiming the development of a new experimental methodology, which could be used to explore the mixing properties of organic solvents (as alcohols) in ionic liquids at wide concentration range.

Due to the delay and workload involved in the development of the μ FlowCal prototype calorimeter, only the study of the excess enthalpy of BuOH in [C₆C₁im][NTf₂] was fully explored in this thesis. This study, to our knowledge, is the first one exploring the heat of mixing of these compounds in such a wide range of concentration. Despite the fact of being a preliminary study, it proves the utility and feasibility of the calorimeter to explore the mixing properties of alcohols in ionic liquids, in a wide concentration range.

The measurements performed in μ FlowCal were done in stopped-flow mode. It should be clear then, that this methodology does not consist in continuous flow. Instead, the micromixer is filled with 200 mm³ (μ L), in the appropriate proportion of the fluids injected, and then the injection is stopped for a period of time, retaining the components on the micromixer until the end of the process under investigation. After complete return of the heat flow signal to its initial state, the micromixer may be filled again, pushing the fluid that was before in the micromixer area to move forward in the flow system.

Ideally, there should be enough time between the successive injections for the heat flow to return to baseline signal. In systems of high diffusion rate, successive injections without complete return to the calorimetric baseline can be made provided that the rest of the curve can be estimated with sufficient accuracy. The amount of the diffusion can be qualitatively evaluated by the repeatability (or not) of successive injections.

At each concentration studied, the first injections are not considered as experiments, as they have the purpose of achieve the appropriate concentration in the micromixer.

Given the design of the micromixer and the inexistence of an external energy that could help achieving a more efficient mixing, it is important that the fluids, that will be mixed, are injected during equal periods of time with a flow as high as possible. The use of higher flows together with the simultaneous injection of both fluids will increase the fractionation of the fluid and thus, increase the contact area between the two fluids, improving the mixing efficiency.

3.3. Calibration and Test of the Calorimetric Systems

In the isothermal heat flow calorimeters used in this thesis, the thermoelectric signal (voltage) is related to the heat flow. Therefore, the integral of the signal obtained could be related to the energy/enthalpy of the process under investigation. Furthermore, in a real heat-flow calorimetric experiment there is always some fraction of the heat flow involved in the investigated process that is lost or is not captured by heat flow sensors. The calibration of the calorimeter allows to determine the experimental sensitivity of the calorimeter, S_{exp} ($\mu\text{V}/(\text{J}\cdot\text{s}^{-1})$), which relates the calorimetric signal to the power involved in the process under study. Therefore, to prevent the existence of systematic deviations of the results, the experimental sensitivity of the calorimeters must always be experimentally determined and its variation in time monitored. For convenience, the inverse of the experimental sensitivity is used as a proportionality factor, usually called, calibration constant, ε_{cal} ($(\text{J}\cdot\text{s}^{-1})/\mu\text{V}$).

Most of the time, heat flow isothermal calorimeters are calibrated electrically by release of a known amount of heat in an electrical heater positioned inside the calorimetric vessel or in its close proximity. As stated by Wadsö^[20], in electrical calibration, the electrical power and energy can easily be measured with higher accuracy than needed for most calorimetric experiments. Nevertheless, to prevent significant systematic deviations, it is essential that the heat flow pattern, caused by heat release in the electric heater, mimic the heat flow pattern originated in the calorimeter by the processes under investigation.

ITC and $\mu\text{FlowCal}$ calorimeters were electrically calibrated. The $\mu\text{FlowCal}$ prototype calorimeter was also calibrated using a mixing process well established in the literature. The results of the chemical and electrical calibration methods were compared and discussed.

The accuracy of the calibration and the performance of the calorimeters were tested using recommended procedures and chemical substances as reference materials. *DropCalvet* was already calibrated in the context of another work^[13]. Therefore, chemical substances with volatilities comparable to the ones of the compounds under investigation were used as calibrants / test compounds.

Details on the calibration procedures and testing of *DropCalvet*, ITC and $\mu\text{FlowCal}$ calorimeters will now be described.

3.3.1. Calibration of *DropCalvet*

The *DropCalvet* calorimeter was already calibrated in the context of a previous work^[13]. The results of this calibration are already embedded in the software used for treatment of the *DropCalvet* experimental data. For that reason, a proportionality factor K_{ε} , that relates the heat involved in the phase transition and the heat obtained from the integration of the calorimetric output signal, was determined as described in equation 3.32:

$$K_{\varepsilon} = \frac{\Delta_{l, 29815\text{ K}}^{g, T} H_m^o(\text{lit})}{\Delta_{l, 298.15\text{ K}}^{g, T} H_m^o(\text{exp})}. \quad (3.32)$$

In accordance, for the determination of the proportionality factor K_{ε} , it was determined the vaporization of 1-butanol and *tert*-butyl-alcohol, chemical compounds which the standard enthalpy of vaporization is well described in the literature^[21]. These experiments were performed under the same experimental conditions of the experiments of vaporization of the compounds under investigation. Thus, the proportionality factor K_{ε} was determined at both experimental temperatures used, $T = 303\text{ K}$ ($30\text{ }^{\circ}\text{C}$) and $T = 315\text{ K}$ ($42\text{ }^{\circ}\text{C}$). Furthermore, this factor was calculated from the average of at least six experimental results. The proportionality factor obtained, $K_{\varepsilon} = (1.022 \pm 0.004)$, was concordant for both compounds used as calibrants in the range of temperature studied. No dependence of the proportionality factor with temperature was found.

In addition, blank experiments have been performed once that:

- mass of the capillaries tubes could not be exactly the same for both sample and reference;
- in each experiment, the heat capacities of the capillary tubes cannot exactly be cancelled;
- the sensitivity of the heat flow sensors of both cells can differ slightly.

The blank experiments have been performed using the same capillary tubes which were used in the vaporization experiments. In each blank experiment, empty capillary tubes of similar weight were dropped simultaneously into both calorimetric cells. Then, the procedure of a vaporization experiment was followed and the calorimetric output signal was integrated. It was found out that, due to the small temperature difference involved in the dropping process, the enthalpic correction contribution of the blanks is

less than 1% of the heat related with the vaporization experiments. Nevertheless, an enthalpic correction was performed in the experimental results of vaporization using the following expression:

$$\Delta_{l, 298.15K}^{g, T} H = \Delta H_{\text{total}} - \Delta H_{\text{corr}}(\text{blank}) . \quad (3.33)$$

The enthalpic blank correction was determined as a function of temperature difference, ΔT (K) (between the temperature of the calorimetric cell and 298.15 K), and the mass of the reference capillary tube, m_{ref} (mg), and the sample capillary tube, m_{exp} (mg), as expressed in equation 3.34.

$$\Delta H_{\text{corr}}(\text{blank}) = a + (b \cdot m_{\text{exp}} + c \cdot m_{\text{ref}}) \cdot \Delta T + d \cdot \Delta T . \quad (3.34)$$

This equation was derived in another work^[13] performed in the *DropCalvet* calorimeter, using the same procedure described in this thesis. (The values of the coefficients of equation 3.34 are: $a = -20.3902$, $b = -0.88204$, $c = 0.816818$, $d = 1.814894$).

3.3.2. Electrical Calibration of ITC and μ FlowCal

The most used methodology to calibrate isothermal heat flow calorimeters is electrical calibration. This methodology consists in the release of a certain amount of thermal energy, by Joule effect, in an electrical heater, which can be positioned inside the calorimetric vessel or in its close proximity.

The thermal power, P ($\text{J} \cdot \text{s}^{-1}$), released by the electrical heater, with a resistance R (Ω), when a certain current I (A), is passed through the calibration circuit can be precisely obtained by the relation:

$$P = R \cdot I^2 . \quad (3.35)$$

If the calibration is performed by electrical pulses of a certain duration in time, Δt (s), the amount of heat, Q (J), dissipated by the electrical heater can be calculated using the following equation:

$$Q = R \cdot I^2 \cdot \Delta t . \quad (3.36)$$

The exact knowledge of the heat released by the electrical heater, allows the calculation of the calibration constant ε_{cal} ($\text{J} \cdot \text{s}^{-1} \cdot \mu\text{V}^{-1}$), as follows:

$$\varepsilon_{\text{cal}} = \frac{Q}{\int U dt} . \quad (3.37)$$

In the usual situations, in which, U (μV) is the thermoelectric potential developed in the thermopiles as a result of the small temperature gradient generated across the sensor, the calibration constant is the inverse of the experimental sensitivity coefficient, S_{exp} , of the instrument, $\varepsilon_{\text{cal}} = 1/S_{\text{exp}}$.

Due to the small temperature gradient generated across the heat flow sensor, linearity should exist between the thermal power dissipated by the electrical heater and the thermoelectric potential generated in the heat flow sensor and thus, the calibration constant should be independent of the thermal power. Nevertheless, the effect of the thermal power dissipated by the electrical heater on the calibration constant of ITC and $\mu\text{FlowCal}$ was investigated.

The release of a constant thermal power during a certain period of time could be schematized as a square function, as showed in figure 3.51. However, the thermal response of a heat flow calorimeter will not be a square function due to the thermal inertia of the calorimeter. Instead, the thermal response of a heat flow calorimeter could be described by an increase in the calorimetric signal until steady state, as demonstrated in the right side of figure 3.51. Therefore, the calibration of a calorimeter by electrical pulses of different duration allow to determine if there is a difference between pulse calibration or steady-state. Furthermore, the variation of time length of the calibration pulses together with the intensity of the electrical current allow to discern between the effect of the thermal energy dissipated and the effect of the thermal power.

For both calorimeters (ITC and $\mu\text{FlowCal}$), electrical calibration experiments were done by means of a calibration circuit, allowing for the electrical current to be permanently “ON”. The electrical current passing in the circuit was determined by measuring directly the intensity of the current with a multimeter or by using a voltmeter and a standard external resistor. The electrical heaters (constituted by Manganin® wire) used in both instruments were constructed in the workshop of the Faculty of Science of

the University of Porto. The resistance of the electrical heaters was measured at the calorimeter temperature (298.15 K), using the four wire methodology. The contribution of the prolongation wiring was taken into account in the calculation of the effective heater resistance.

A precision resistance box was used in both systems to maintain the electrical impedance as high as possible (from 1 to 10 k Ω). In the assembled circuits, the electrical heater is “intercalated” in the circuit by a switch only to perform the electrical pulses without interruption of the current and is then “removed” from the circuit. In this moment, to maintain the current stability, a “dummy”, resistance similar to the electrical heater, is “intercalated” in the circuit. In this way, the difference in the impedance is insignificant when compared to the impedance of the circuit.

In the following sections, the calibration circuits used to electrically calibrate both calorimetric systems will be described and the effect of the thermal power released, the duration of the electrical pulse and the level of energy used in the obtained calibration constants will be presented and discussed.

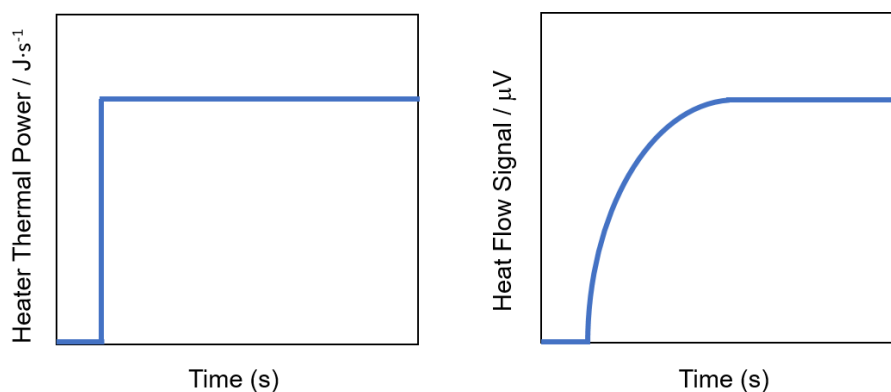


Figure 3.51. Schematic representation of a constant thermal power dissipated by the electrical heater (on the left) and the perturbation, caused by the thermal power dissipated, on the heat flow signal of the calorimeter (on the right).

3.3.2.1. Calibration of ITC

Insertion Heaters

The electrical calibration experiments were performed with the electrical heater assembled inside of the stainless steel ampoule of the calorimetric vessel in order to better reproduce the heat flow path of a typical ITC experiment. No commercially available heater was found that would fit the necessary requirements of the application. Therefore, an insertion heater was fabricated in the workshop of the Faculty of Science of the University of Porto. It was based in a ring-shaped Teflon® mould involved by a Manganin® wire with a total resistance of 50 Ω . The Manganin® ring was involved with an epoxy resin (Araldite®) which guarantees the electric isolation. The Manganin® wire ends were welded to two copper terminals. The resistance of the constructed heaters is $50.72 \pm 0.02 \Omega$ and $50.71 \pm 0.02 \Omega$.

Due to the low volume of the stainless steel ampoule of the calorimetric vessel used (1 cm³) the position of the different elements is very important. Thus, the heater is assembled right on the top of the propeller, with the wire ends ascending to the outside of the vessel by the guide tube for the injection needle. Due to the dimensional limitations, the propeller used is not the gold propeller used in the current ITC experiments but a Teflon® based propeller constructed for this purpose. In figure 3.52 is presented a picture of the interior the calorimetric vessel equipped with the electrical heater and the Teflon® propeller as well as, a schematic representation of the electrical heater.

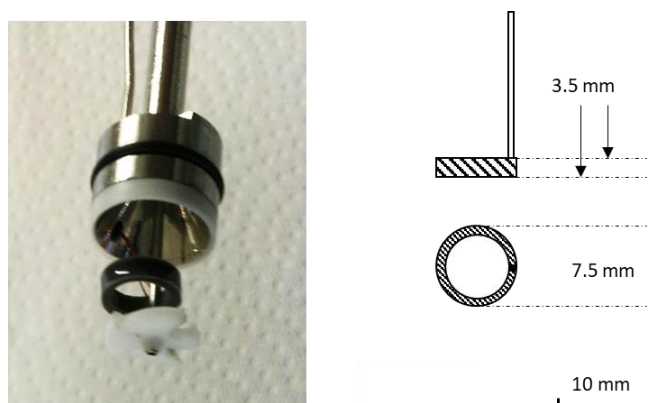


Figure 3.52. Picture of the interior the calorimetric vessel (on the left), equipped with the electrical heater and the Teflon® propeller, and schematic representation of the electrical heater developed. Picture from ref.[16].

Electrical Circuit

The electric heater constructed is intercalated in an electrical circuit designed to maintain a DC programmable power supply (Agilent, model E3631A; 0-25 VDC) permanently “ON” (during the electrical calibration pulses and in the time between them). For that purpose, a switch commutes the current from two parallel circuits in which is installed the electrical heater or a dummy of similar resistance. A precision resistance box (CROYDON, type RBB4) is shared by both circuits, providing higher electrical impedance (from 1 to 10 k Ω) to the circuits and making the difference of resistance between the electric heater or the dummy insignificant when compared to the impedance of the circuit. The time period of the electrical pulses is monitored by a digital timer which is activated and deactivated by the switch that commutes the circuits. In figure 3.53 is presented a figure of the electrical circuit used in the electrical calibration of ITC.

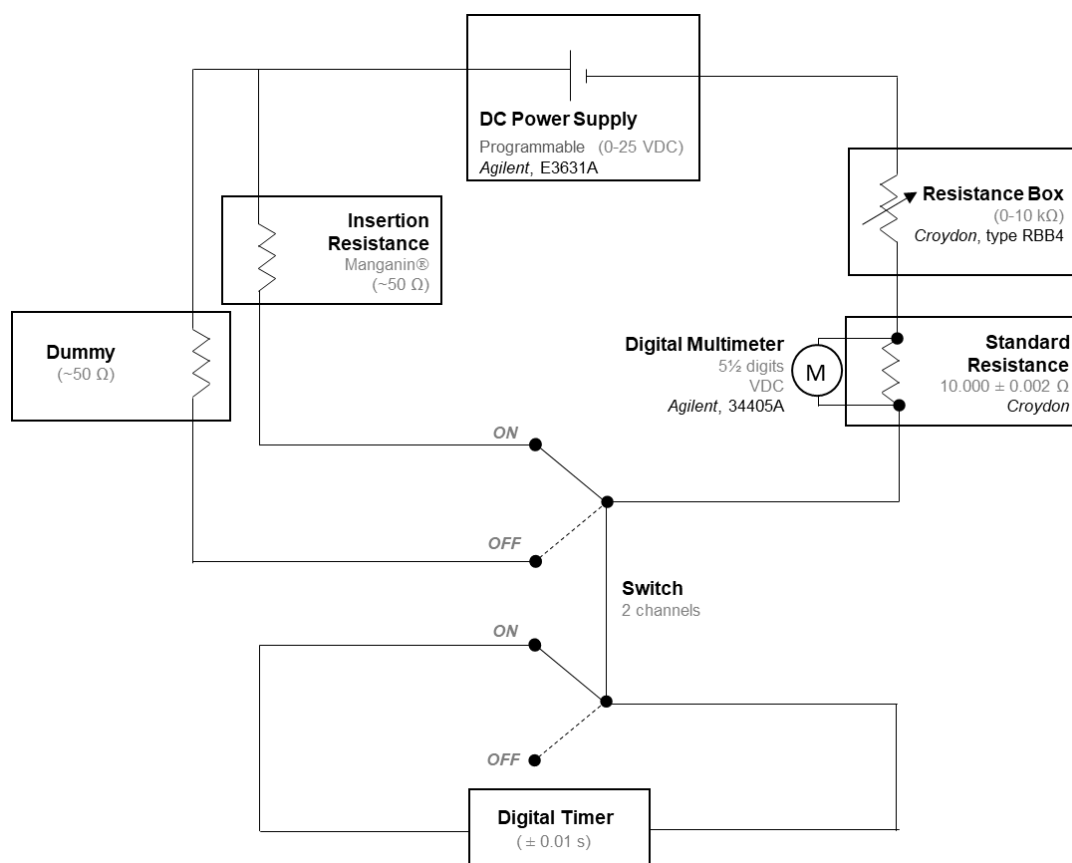


Figure 3.53. Representation of the electrical circuit used in the experiments of electrical calibration of ITC.

Thermal Power, Time and Energy Effect

To calibrate electrically ITC, the intensity of the current and the time length of the calibration pulses was varied. Two intensity levels were used, $I \approx 4$ mA and $I \approx 6$ mA, which results in a thermal power of $P \approx 0.83$ mJ·s⁻¹ and $P \approx 1.87$ mJ·s⁻¹. For both intensities the duration in time of the calibration pulses was $\Delta t \approx 50.00$ s and $\Delta t \approx 100.00$ s. In figure 3.54 the typical calorimetric output signal obtained for the different calibration pulses effectuated is presented together with its correction using Tian equation.

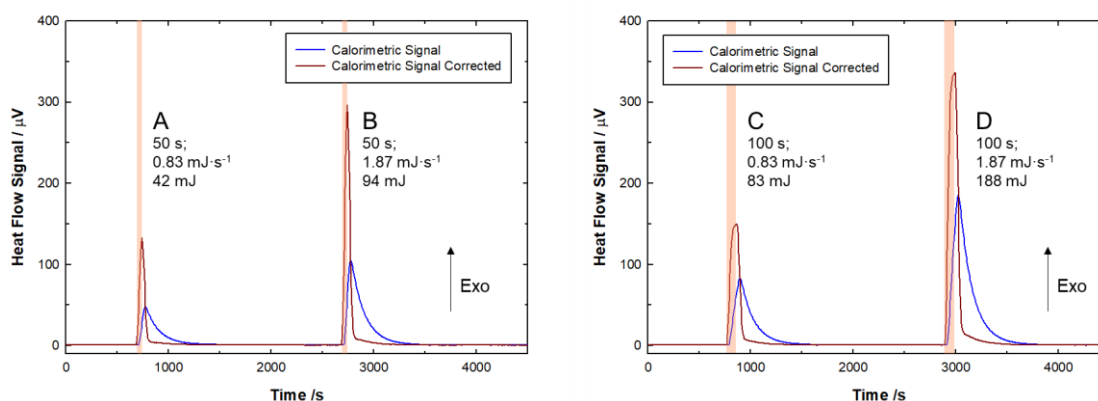


Figure 3.54. Graphical representation of the typical heat flow signal obtained, before (blue line) and after dynamic correction for the time constant of the calorimeter (dark red line), as a function of the experimental time, in the electrical calibration experiments, generically denominated as “A”, “B”, “C” and “D”.

In table 3.5 is presented a summary of the experiments. Within the conditions tested, no dependence of the constant of calibration was found on the calibration time, the thermal power or the energy. Nevertheless, the confidence interval of the constant of calibration decreases with the increase of the energy level. In figure 3.55 all experiments were represented in the sequence of its measurement. No dependence in time was found.

As the time, thermal power and energy did not show to influence the constant of the calibration of the ITC, the calibration constant was determined as a weighted average (on the confidence interval) of all the experiments. In accordance, the calibration constant of the ITC was found to be, $\varepsilon_{\text{cal}} = (5.168 \pm 0.019) \times 10^{-6} \text{ J} \cdot \text{s}^{-1} \cdot \mu\text{V}^{-1}$.

Three months later, some of the experiments were repeated with a new insertion heater and the results were in accordance with the ones presented here, within a

confidence level of 95%. During the time period of the experiments performed in ITC the calibration was tested periodically using a recommended chemical test.

Table 3.5. Summary of the nomenclature, the average of the results obtained for the calibration constant ($\langle \varepsilon_{cal} \rangle$) and the conditions associated to the electrical calibrations performed in ITC: number of experiments (#N), average of the intensity of the electrical current ($\langle I \rangle$), average of the time length of the calibration pulses ($\langle \Delta t \rangle$), average of the thermal power ($\langle P \rangle$) and thermal energy ($\langle Q \rangle$) dissipated by the insertion heater

Nomenclature	#N	$\langle I \rangle$ /mA	$\langle \Delta t \rangle$ /s	$\langle P \rangle$ / mJ·s ⁻¹	$\langle Q \rangle$ / mJ	$\langle \varepsilon_{cal} \rangle^a$ / J·s ⁻¹ ·V ⁻¹
A	7	4.0463	50.25	0.8304	41.73	5.169 ± 0.024
B	7	6.0694	50.32	1.8684	94.03	5.163 ± 0.011
C	7	4.0463	100.31	0.8304	83.30	5.158 ± 0.017
D	7	6.0693	100.38	1.8684	187.55	5.175 ± 0.006

a - The uncertainty is the confidence interval of the (average) calibration constant obtained in each set of experiments, at a confidence level of 95% ($\pm 2 \cdot \sigma \cdot n^{-1/2}$).

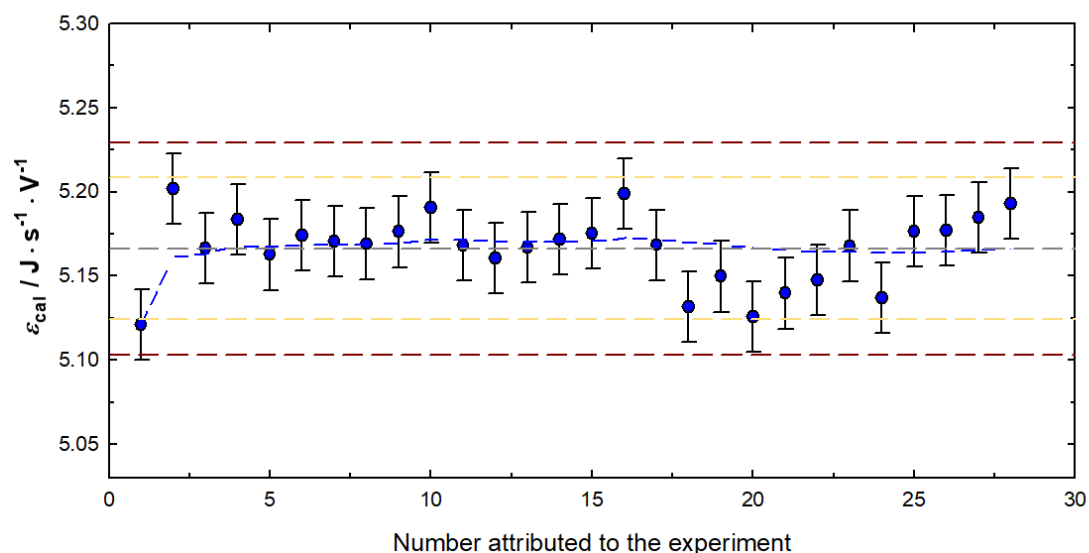


Figure 3.55. Chronological graphical representation of the calibration constant. The calibration constant obtained in each experiment is plotted, as blue circles, in its chronological order. The error bars represent the standard deviation of the sample ($\pm \sigma$). The blue dashed line represents the cumulative average of the calibration constant, whereas the final average is represented by the grey dashed line. The lines parallel to the grey dashed line represent the limits of the sample dispersion ($\pm 2 \cdot \sigma$ and $\pm 3 \cdot \sigma$) within 95 % (in yellow) and 99 % (in red) confidence levels.

Comment on the Calibration Results

As referred in the description of ITC, two identical calorimetric channels were used in the laboratory. The constant of calibration obtained for the ITC channel used in this thesis, $\varepsilon_{cal} = (5.168 \pm 0.019) \times 10^{-6} \text{ (J}\cdot\text{s}^{-1})/\mu\text{V}$, is about half of the one obtained for the other calorimetric channel, already reported in another work^[16] to be $\varepsilon_{cal} = (2.502 \pm 0.007) \times 10^{-6} \text{ (J}\cdot\text{s}^{-1})/\mu\text{V}$.

These values are the inverse of the experimental sensitivities of the referred instruments, which are respectively $S_{exp} = 193 \text{ mV}/(\text{J}\cdot\text{s}^{-1})$ (determined for ITC in this work) and $S_{exp} = 400 \text{ mV}/(\text{J}\cdot\text{s}^{-1})$ (for the other calorimetric channel existent in the lab). Wadsö has also reported in his work^[7], for an identical calorimeter, an experimental sensitivity of $S_{exp} = 376 \text{ mV}/(\text{J}\cdot\text{s}^{-1})$.

Furthermore, the time constant obtained for the calorimetric channel used in this thesis is $\tau = 115 \text{ s}$, whereas for the other calorimetric channel existent in the lab, the reported time constant is $\tau = 200 \text{ s}$ ^[16], and the one reported in Wadsö's work is $\tau = 190 \text{ s}$ ^[7].

Therefore, and given the fact that sensitivity depends on the Seebeck coefficient and on the thermal conductance of the heat flow sensors and that the time constant depends on the conductance of the heat flow sensor and the heat capacity of the sample, sample holder and half of the sensor, it becomes evident that the conductance has increased by some reason, by a factor close to 2.

Despite of the decrease in the sensitivity and the increase of the time constant, the behaviour of the calorimeter seems to be stable in time.

3.3.2.2. Calibration of μ FlowCal Prototype Calorimeter

Built-in Heaters

Given the micromixer design, it is not feasible to use an insertion heater or to install a built-in heater into the micromixer. Instead, a built-in heater was created in order to be installed in the aluminium blocks that are located immediately above and below the microreactor/mixer.

In accordance, four electrical heaters were fabricated in the workshop of the Faculty of Science of the University of Porto based in a coated Manganin® wire rolled around a fiberglass small rod that act as a mould. The coating of the Manganin® wire provided electrical insulation. The heaters were inserted in a close-fitting cavity of the aluminium blocks filled with silicone heat sink compound (DOW CORNING® 340).

In figure 3.56 a picture of the four electrical heaters is presented together with a picture of the heaters inserted in the aluminium blocks, which were later used in the construction of μ FlowCal. The built-in heaters located inside the aluminium blocks were located on the top and on the bottom of the micromixer and were connected in series. In this way, when electrical current is passed in the electrical heaters, heat is released by Joule effect in the aluminium blocks, on the top and below the area in the micromixer in which the mixing of the fluids occurs. In this way, the heat released by the mixing of two fluids is simulated, as close as possible, by electrical calibration. This assembly was made for the calorimetric system used as sample and repeated for the calorimetric system used as reference. With the resistances connected in series (2 in the sample calorimetric system and 2 in the reference calorimetric system). The determined resistance of the sample side is $R = 101.55 \pm 0.02 \, \Omega$ and of the reference side $R = 101.87 \pm 0.02 \, \Omega$.

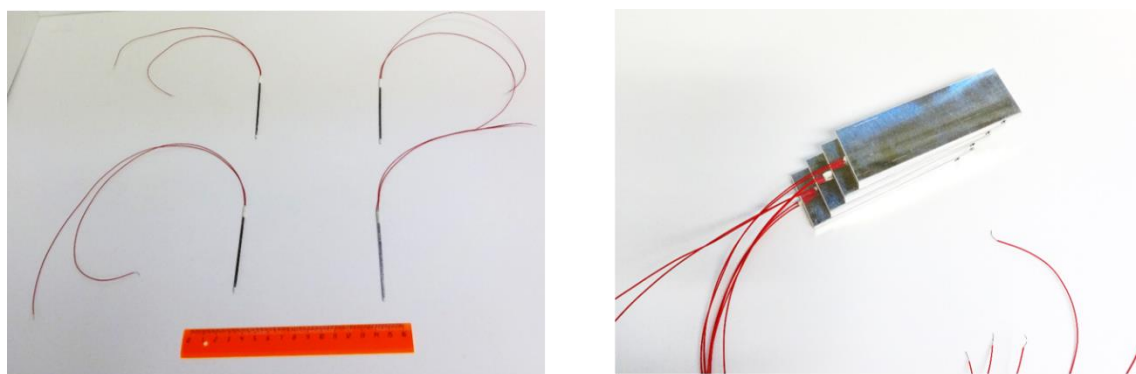


Figure 3.56. Picture of the calibration heaters of μ FlowCal before (on the left) and after (on the right) insertion in the aluminium blocks.

Electrical Circuit

The electric heaters constructed are permanently inside the μ FlowCal as they were assembled in aluminium blocks that were used in the construction of the calorimeter, in between the micromixer and the Peltier heat flow sensors, in the same area where the fluids are mixed, simulating as close as possible the heat release during mixing.

An electrical circuit (figure 3.57) similar to the one used in ITC calibration was used to electrically calibrate μ FlowCal calorimeter. As in the ITC circuit, a switch commutes the current from parallel circuits, in which is installed the electrical heater or a dummy of similar resistance. This circuit differs as there are built-in heaters located in the aluminium blocks of the glass micromixers that constitute the sample and the reference. In accordance, an extra switch provides the possibility of commutation between heat release in the sample side or in the reference side. In the time between calibration pulses, the electrical current passes in the dummy resistance instead of the built-in heaters.

The switch that provides commutation between the built-in heaters mounted in the sample or in the reference is installed in a box created for the calibration of the instrument. This “calibration box” contains also a stable 9 V power source and a switch that commutes between the dummy and the electrical built-in heaters. The switch that commutes between the dummy and the electrical built-in heaters is connected to an OMRON timer, in which the time interval of the electrical pulse and the time interval between electrical pulses is programmable. In figure 3.57 is presented a scheme of the electrical circuit used in the electrical calibration of μ FlowCal prototype calorimeter.

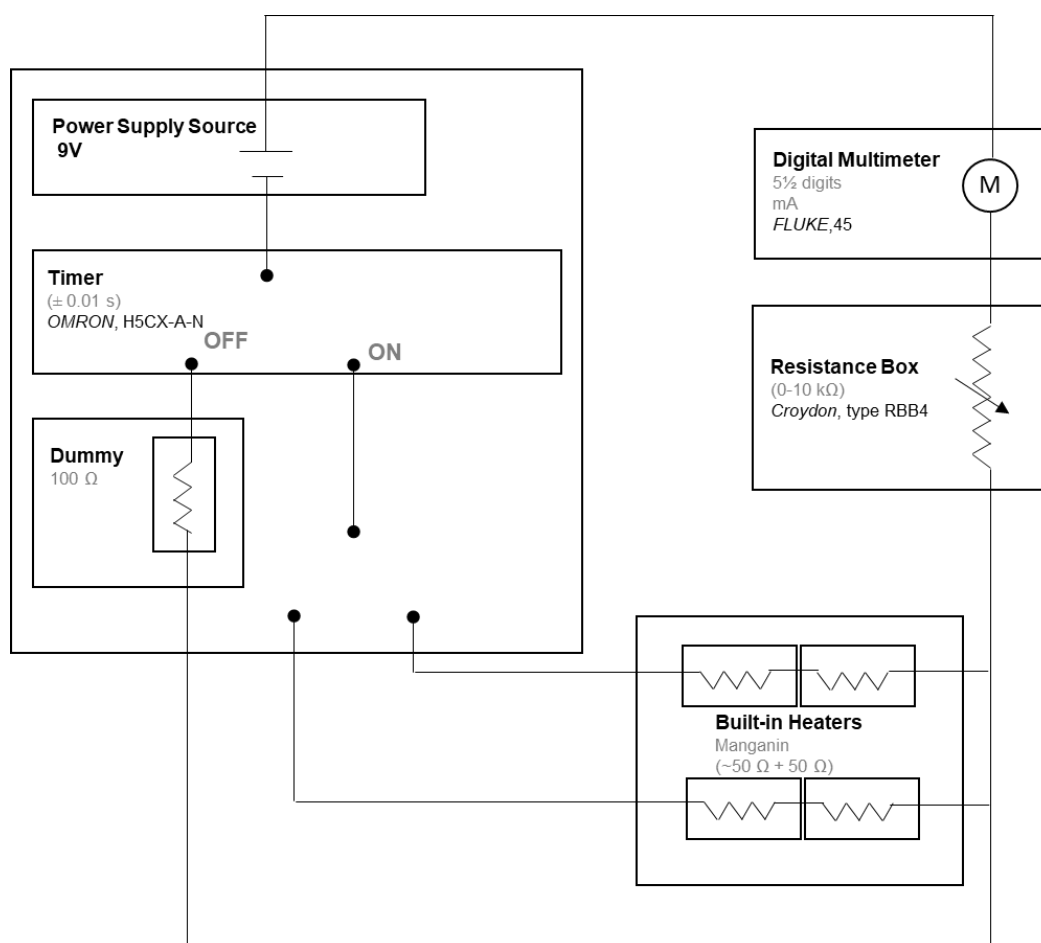


Figure 3.57. Representation of the electrical circuit used in the experiments of electrical calibration of μ FlowCal.

Summary of the Experiments

As the μ FlowCal was constructed in the context of this thesis, the electrical calibration here described is the first calibration of this calorimeter. Both sides of the calorimeter, sample and reference, were electrically calibrated. The calibration was done by varying the time intervals (20 s to 150 s) and the intensity of the electrical current (2 mA to 8 mA) of the calibration pulses.

For a better understanding of the effect of the calibration parameters (intensity of the current and time interval of the calibration pulses), in figure 3.58 is schematically

represented a matrix summarizing the experiments performed in both systems (sample and reference). Together with this representation is presented a matrix displaying the effect of changing those parameters (intensity of the current and time interval of the calibration pulses) in the associated thermal power and in the energy dissipated by the heaters. In tables 3.6 and 3.7, the electrical calibration experiments performed in μ FlowCal calorimeter are summarized.

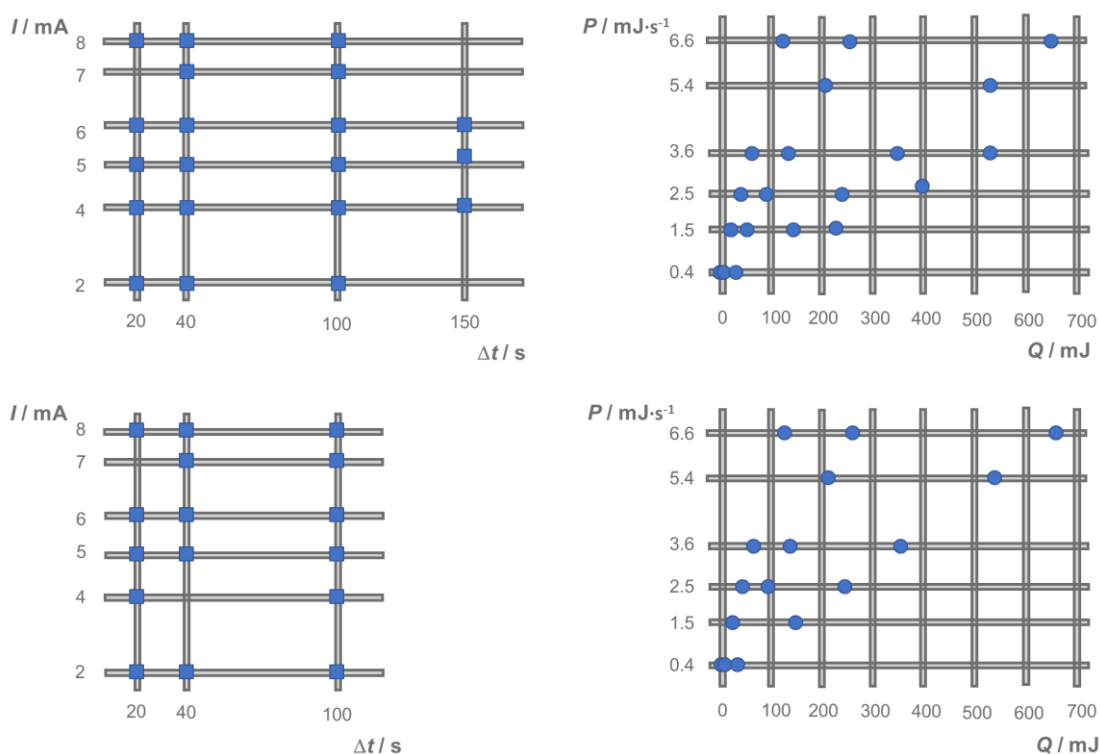


Figure 3.58. Schematic representation of the electrical calibration experiments performed in μ FlowCal. In the left side are represented matrixes of the variables: intensity of the electrical current and the time interval of the calibration pulses. In the right side are represented matrixes of the thermal power and total energy dissipated in the μ FlowCal, caused by the variation of the intensity of the electrical current and the time interval of the calibration pulses. The top matrixes refer to the calibration of the sample side and the bottom matrixes refer to the calibration of the reference side.

Table 3.6. Summary of the nomenclature, the average of the results obtained for the calibration constant ($\langle \mathcal{E}_{cal} \rangle$) and the conditions associated to the electrical calibrations performed in the sample side of μ FlowCal: number of experiments (#N), average of the intensity of the electrical current ($\langle I \rangle$), average of the time interval of the calibration pulses ($\langle \Delta t \rangle$), average of the thermal power ($\langle P \rangle$) and thermal energy ($\langle Q \rangle$) dissipated by the insertion heater

Nomenclature	#N	$\langle I \rangle$ /mA	$\langle \Delta t \rangle$ /s	$\langle P \rangle$ / mJ·s ⁻¹	$\langle Q \rangle$ / mJ	$\langle \mathcal{E}_{cal} \rangle^a$ / J·s ⁻¹ ·V ⁻¹
A	11	1.9892	20.00	0.4018	8.04	8.424 ± 0.326
B	9	3.8795	20.00	1.5283	30.57	8.191 ± 0.059
C	5	5.9281	20.00	3.5686	71.37	8.123 ± 0.106
D	5	1.9891	40.00	0.4018	16.07	8.499 ± 0.714
E	5	3.8793	40.00	1.5282	61.13	8.162 ± 0.173
F	11	5.9273	40.00	3.5677	142.71	8.162 ± 0.013
G	5	1.9890	100.00	0.4017	40.17	8.248 ± 0.166
H	5	3.8790	100.00	1.5280	152.80	8.116 ± 0.059
I	4	5.9273	100.00	3.5677	356.77	8.102 ± 0.005
J	11	4.9476	20.00	2.4858	49.72	8.193 ± 0.042
K	5	4.9469	40.00	2.4851	99.40	8.166 ± 0.043
L	5	4.9473	100.00	2.4855	248.55	8.125 ± 0.015
M	8	3.9348	150.00	1.5722	235.83	8.139 ± 0.009
N	9	5.1569	150.00	2.7006	405.09	8.099 ± 0.033
O	8	5.9466	150.00	3.5911	538.66	8.133 ± 0.007
P	9	8.0498	20.00	6.5803	131.61	8.186 ± 0.082
Q	10	8.0493	40.00	6.5795	263.18	8.263 ± 0.021
R	10	8.0499	100.00	6.5805	658.05	8.268 ± 0.007
S	9	7.2817	40.00	5.3845	215.38	8.242 ± 0.009
T	10	7.2833	100.00	5.3868	538.68	8.238 ± 0.011

a - The uncertainty is the confidence interval of the (average) calibration constant obtained in each set of experiments, at a confidence level of 95% ($\pm 2 \cdot \sigma \cdot n^{-1/2}$).

Table 3.7. Summary of the nomenclature, the average of the results obtained for the calibration constant ($\langle \mathcal{E}_{cal} \rangle$) and the conditions associated to the electrical calibrations performed in the reference side of μ FlowCal: number of experiments ($\#N$), average of the intensity of the electrical current ($\langle I \rangle$), average of the time interval of the calibration pulses ($\langle \Delta t \rangle$), average of the thermal power ($\langle P \rangle$) and thermal energy ($\langle Q \rangle$) dissipated by the insertion heater

Nomenclature	#N	$\langle I \rangle$ / mA	$\langle \Delta t \rangle$ / s	$\langle P \rangle$ / mJ·s ⁻¹	$\langle Q \rangle$ / mJ	$\langle \mathcal{E}_{cal} \rangle^a$ / J·s ⁻¹ ·V ⁻¹
A	9	1.9885	20.00	0.4028	8.06	8.206 ± 0.208
B	9	3.8764	20.00	1.5307	30.61	8.288 ± 0.060
C	8	5.9222	20.00	3.5728	71.46	8.269 ± 0.242
D	5	1.9885	40.00	0.4028	16.11	8.382 ± 0.103
F	4	5.9234	40.00	3.5742	142.97	8.287 ± 0.029
G	5	1.9883	100.00	0.4027	40.27	8.323 ± 0.079
H	5	3.8767	100.00	1.5310	153.10	8.276 ± 0.050
I	4	5.9210	100.00	3.5714	357.14	8.208 ± 0.045
J	10	4.9440	20.00	2.4900	49.80	8.308 ± 0.047
K	4	4.9447	40.00	2.4907	99.63	8.312 ± 0.022
L	4	4.9433	100.00	2.4893	248.93	8.285 ± 0.018
P	10	8.0494	20.00	6.6004	132.01	8.265 ± 0.091
Q	10	8.0487	40.00	6.5992	263.97	8.248 ± 0.045
R	9	8.0491	100.00	6.5999	659.99	8.201 ± 0.029
S	8	7.2829	40.00	5.4033	216.13	8.313 ± 0.009
T	8	7.2834	100.00	5.4039	540.39	8.275 ± 0.003

a - The uncertainty is the confidence interval of the (average) calibration constant obtained in each set of experiments, at a confidence level of 95% ($\pm 2 \cdot \sigma \cdot n^{-1/2}$).

Thermal Power Effect

The change of the intensity of the electrical current allow to evaluate the effect of the thermal power dissipated by the electrical heater. Given the small temperature differences originated in heat flow calorimeters, it is not expected the occurrence of any significant change of the Seebeck coefficient of the thermocouples that constitute the heat flow sensor. Accordingly, the calorimetric output signal should be proportional to the thermal power dissipated by the heaters and consequently, the calibration constant / sensitivity of the calorimeter should be independent of the thermal power.

Nevertheless, the effect of the thermal power dissipated by the electric heaters on the calibration constant and thus, on the sensitivity of the calorimeter was evaluated. In figure 3.59, the average calibration constant obtained in each set of experiments (“A”, “B”, ... , “T”) is presented, as a function of the thermal power dissipated by the electrical heater, in average, in that experimental set.

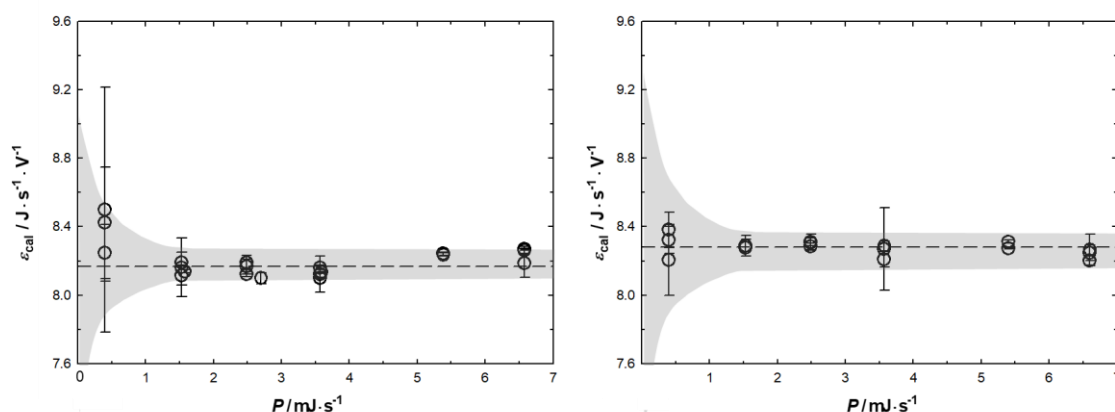


Figure 3.59. Graphical representation of the average calibration constant, ε_{cal} , obtained in each set of experiments, as a function of the thermal power, P , dissipated (in average) by the built-in heaters. In the left side is represented the data relative to the calibration of the sample system and in the right side is represented the data relative to the calibration of the reference system. The error bars represent the confidence intervals of the calibration constant obtained in each set, at a confidence level of 95% ($\pm 2 \cdot \sigma \cdot n^{-1/2}$). The shaded area is just a guide to the eyes.

In figure 3.59 is observable that the constant of calibration is independent of the thermal power level used in the experiments. However, at the lowest levels of thermal power tested, the graphical representation on the left side of figure 3.59, regarding the sample calorimetric system, evidences a deviation of the constant of calibration. A

weaker deviation can also be noticed in the graphical representation of the right side, which refers to the reference calorimetric system. Similar results were found by L. Wadsö^[8] in TAM Air calorimeters. The author reported the occurrence of significant deviations in the calibration constants determined in experiments in which the thermal powers dissipated were inferior to $3 \text{ mJ}\cdot\text{s}^{-1}$. The author initially attributes these results to two possibilities: higher calibration uncertainties at low thermal powers or non-linear electronics; after, he comes to the conclusion that the deviations found are fully explained by the uncertainties.

The results found in the electrical calibration of $\mu\text{FlowCal}$ are in line with this idea. In figure 3.60 graphical representation of the uncertainty ($2\cdot\sigma\cdot n^{-1/2}$) of the calibration constant obtained in each experimental set, at a confidence level of 95%, is represented as a function of the thermal power level used in the experiments. In the left side are presented the results obtained in the sample calorimetric system and in the right side are presented the results obtained in the reference calorimetric system. In both systems there is a higher uncertainty at low thermal powers which decrease to lower uncertainties at higher thermal powers.

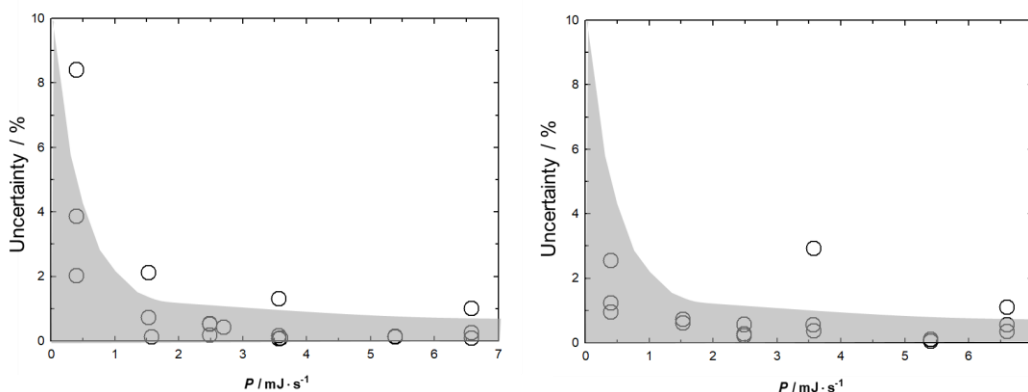


Figure 3.60. Graphical representation of the uncertainty ($2\cdot\sigma\cdot n^{-1/2}$) of the calibration constant, obtained in each experimental set, at a confidence level of 95%, as a function of the thermal power level, P , used in the experiments. The shaded area is just a guide to the eyes.

A clear exception is visible in the graphical representation of the reference calorimetric system, in figure 3.60, where at a thermal power of approximately $P \approx 3.6 \text{ mJ}\cdot\text{s}^{-1}$, a higher uncertainty occurs. Despite of this higher uncertainty, no deviation of the experimental value was found. As it is a single occurrence and there is

no deviation of the calibration constant, this higher uncertainty could be attributed to some artefact resulting from an environmental perturbation which may have caused some increase in the noise.

Energy Effect

The variation of the time interval of the electrical pulses together with the intensity of the electrical current allow to discern between the thermal power effect and the energy effect on the calibration constant and so, on the sensitivity of the calorimeter.

In order to discern between the two effects, the previous representations regarding the average calibration constant, obtained in each set of experiments, and its uncertainty are repeated in figures 3.61 and 3.62, now as a function of the different energy levels studied. The graphical representations presented in figure 3.61 highlight the existence of some deviations of the constant of calibration together with higher uncertainties at lower energy levels. At energy levels higher than 200 mJ the constant of calibration is apparently constant and equally dispersed, independently of the energy level tested.

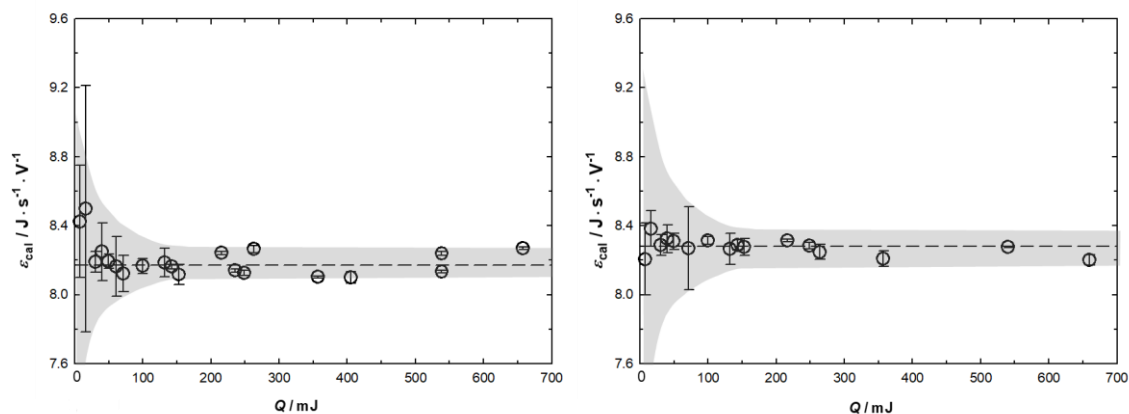


Figure 3.61. Graphical representation of the average calibration constant, ε_{cal} , obtained in each set of experiments, as a function of the total thermal energy, Q , dissipated (in average) by the built-in heaters. In the left side is represented the data relative to the calibration of the sample system and in the right side is represented the data relative to the calibration of the reference system. The error bars represent the confidence intervals of the calibration constant, obtained in each set, at a confidence level of 95% ($\pm 2 \cdot \sigma \cdot n^{-1/2}$). The shaded area is just a guide to the eyes.

In addition, figure 3.62 evidences the existence of a better correlation between the decrease in the uncertainty along with the increase in the thermal energy level, when compared to the possible correlation with the thermal power. The small discrepancies found in the previous analysis are now fully described by considering the different energy levels. Moreover, the higher uncertainty value found at the power level $P = 3.6 \text{ mJ}\cdot\text{s}^{-1}$ is now more coherent with the rest of the values.

Taking this into account, it seems that the uncertainty of the calibration constant is related with the energy level rather than the thermal power level. The deviations found at lower thermal powers are thus justifiable with the higher uncertainties existent at low energy.

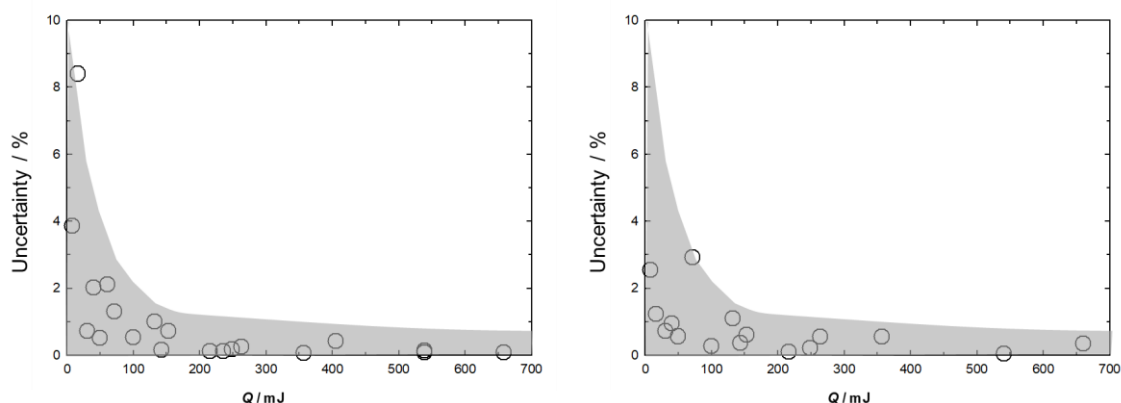


Figure 3.62. Graphical representation of the uncertainty ($2\cdot\sigma\cdot n^{-1/2}$) of the calibration constant, obtained in each experimental set, at a confidence level of 95%, as a function of the total thermal energy, Q , dissipated (in average) by the built-in heaters. The shaded area is just a guide to the eyes.

Time Effect

As the increase in the thermal power increase the dissipated energy, some correlation would always exist between the uncertainty of the calibration constant and the thermal power level. The use of different time intervals in the calibration pulses discerns however the real effect.

At this point, is interesting to remake figure 3.59, but now discerning between the different time intervals of the experiments. In figure 3.63 is now evidenced that, at low thermal powers, the deviations are higher in the experiments with smaller time intervals

of the calibration pulse. As the thermal power increase there is no time effect differentiation into the calibration results.

Thus, this figure highlights the fact that it is indifferent to use pulse calibration or steady-state calibration, as long as considerable thermal powers are used. For posterior electrical calibrations, it is indifferent to the accuracy of the instrument the thermal power or time intervals chosen, as long as the thermal power is at least higher than $P = 2.5 \text{ mJ}\cdot\text{s}^{-1}$.

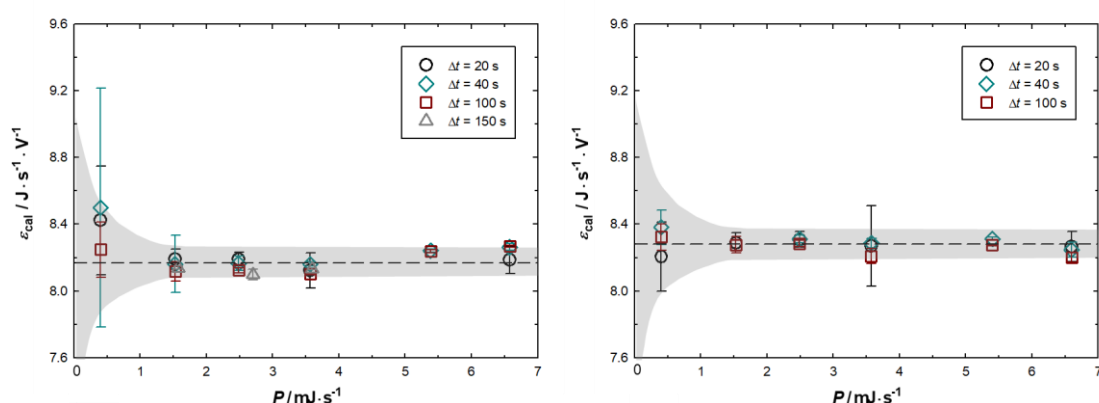


Figure 3.63. Graphical representation of the average calibration constant, ϵ_{cal} , obtained in each set of experiments, as a function of the thermal power, P , dissipated (in average) by the built-in heaters. In the left side is represented the data relative to the calibration of the sample system and in the right side is represented the data relative to the calibration of the reference system. The error bars represent the confidence intervals of the calibration constant, obtained in each set, at a confidence level of 95% ($\pm 2\cdot\sigma\cdot n^{-1/2}$). The different colours and symbols are represent the time period of the calibration pulses. The shaded area is just a guide to the eyes.

Relatively to the stability in time of the calibration constant of the calorimeter, in 10 months no variation was found.

Comment on the Calibration Results

Given that the calibration constant was seen to be independent of the power level and of the time intervals chosen, the calibration constant of the calorimeter was determined from the weighted (on the uncertainty) average of all experiment sets. The confidence interval of the calibration constant was determined as the average of the confidence interval of all experimental sets, with exception of “A” and “D” experimental sets (the ones that correspond to lower thermal energies dissipated by the heaters). In

accordance, the calibration constant obtained for the sample calorimetric system is $\varepsilon_{\text{cal}} = (8.17 \pm 0.05) \times 10^{-6} \text{ (J}\cdot\text{s}^{-1})/\mu\text{V}$ and for the reference calorimetric system is $\varepsilon_{\text{cal}} = (8.28 \pm 0.05) \times 10^{-6} \text{ (J}\cdot\text{s}^{-1})/\mu\text{V}$.

As the calibration constant is just the inverse of the experimental sensitivity of the instrument, the sample calorimetric system has an experimental sensitivity of $S_{\text{exp}} = (122.3 \pm 0.7) \text{ (mV/(J}\cdot\text{s}^{-1})\text{)}$ and the reference calorimetric system has an experimental sensitivity of $S_{\text{exp}} = (120.8 \pm 0.8) \text{ (mV/(J}\cdot\text{s}^{-1})\text{)}$. Therefore, the experimental sensitivity of the sample calorimetric system and of the reference calorimetric system are quite similar.

It should be noted that the electric heaters used to electrically calibrate the $\mu\text{Flowcal}$ are positioned in aluminium blocks between the place in the glass micromixer where both fluids are mixed and the heat flow sensors. Therefore, the heat flow path can be different from a normal mixing calorimetric experiment and so, the calibration constant and the experimental sensitivities determined may present some deviation from the true value in a normal mixing experiment.

3.3.3. Chemical Calibration of $\mu\text{FlowCal}$ with a Mixing Process

Both ITC and $\mu\text{FlowCal}$ calorimeters were electrically calibrated. However, the calibration heaters used to calibrate $\mu\text{FlowCal}$ were not insertion / mobile heaters inserted into the sample container, but fixed heaters built-in the aluminium blocks, which are located between the micromixer and the heat flow sensors. Given the positioning of the heat flow sensors in the $\mu\text{Flowcal}$, there is the possibility of the existence of a systematic deviation due to the different heat flow path associated to the electrical calibration towards a typical mixing experiment.

Therefore, a calibration of the system was performed using a reference mixing process. In accordance, the $\mu\text{FlowCal}$ calorimeter was chemically calibrated by studying the mixture of n-decane and 1-octanol, at equimolar composition.

The heat of mixing of these compounds has been studied by different research groups, in the whole composition range. Featherstone and Dickinson^[22] have been the firsts to determine the excess enthalpies of 1-octanol and n-decane at 293.15 K, 298.15 K, 308.15 K and 313.15 K in an isothermal dilution calorimeter. Two years later, Christensen and co-workers^[23] have reported the same property at 298.15 K in a high pressure isothermal flow calorimeter (170 kPa) using both continuous run and

fixed-composition methods, without evidences of significant differences between them. Later, Paz-Andrade and co-workers^[24] have reported the molar excess enthalpies of the decane-octanol mixture at 298.15 K and 308.15 K, determined using a Calvet microcalorimeter in the absence of gas phase. The data reported at 298.15 K by both Christensen^[23] and Paz-Andrade^[24] research groups, which are considered as world-wide reference laboratories on the field, are in excellent agreement and will be used as a reference in this thesis.

The choice of the equimolar concentration as a procedure to the chemical calibration is related to two factors:

- the injection of both fluids in similar flows;
- the existence of small dependence of the enthalpy upon small differences in composition, over that concentration range.

The heat (Q) associated to the mixture of n-decane with 1-octanol at equimolar composition is calculated as indicated in equation 3.38:

$$Q = \Delta_{\text{mix}} H_m \cdot (n_{\text{OctOH}} + n_{\text{Dec}}), \quad (3.38)$$

in which, n_{OctOH} and n_{Dec} is the molar quantity of 1-octanol and n-decane injected into the system. The enthalpy of mixing ($\Delta_{\text{mix}} H_m = 595 \pm 13 \text{ J} \cdot \text{mol}^{-1}$), at equimolar concentration, was determined from the fitting of the data of Christensen^[23] and Paz-Andrade^[24] research groups with Redlich-Kister equation: $A_0 = (2.381 \pm 0.015) \times 10^3 \text{ J} \cdot \text{mol}^{-1}$; $A_1 = (1.027 \pm 0.065) \times 10^3 \text{ J} \cdot \text{mol}^{-1}$; $A_2 = (-0.24 \pm 0.11) \times 10^3 \text{ J} \cdot \text{mol}^{-1}$; $A_3 = (-0.30 \pm 0.31) \times 10^3 \text{ J} \cdot \text{mol}^{-1}$; $A_4 = (3.487 \pm 0.146) \times 10^3 \text{ J} \cdot \text{mol}^{-1}$; $A_5 = (3.752 \pm 0.323) \times 10^3 \text{ J} \cdot \text{mol}^{-1}$. From this value and the molar quantity of 1-octanol and n-decane injected, the heat involved in the mixture was calculated: $Q = 0.669 \pm 0.015 \text{ J}$.

The real sensitivity of the $\mu\text{FlowCal}$ (S_{exp}) was calculated by the relation between the integration of the calorimetric signal ($A_T / \mu\text{V} \cdot \text{s}$) and the heat involved in the process (Q / J), as described in equation 3.39. The uncertainty of the sensitivity was calculated from the propagation of the uncertainty associated to the heat involved in the mixing process and the uncertainty associated to the (average) of the integration of the calorimetric signal ($\pm 2 \cdot \sigma \cdot n^{-1/2}$). The obtained result is presented in table 3.8.

$$S_{\text{exp}} = \frac{1}{\varepsilon_{\text{cal}}} = \frac{A_T}{Q}. \quad (3.39)$$

The chemical calibration measurements were performed by injecting 200 mm^3 (μL) of the fluids at $20.00 \text{ mm}^3 \cdot \text{s}^{-1}$ ($\mu\text{L} \cdot \text{s}^{-1}$). The particular flow of each component injected was balanced in order to inject both components simultaneously, in the right proportions, to accomplish the equimolar composition, and equalize a total flow of $20.00 \text{ mm}^3 \cdot \text{s}^{-1}$ ($\mu\text{L} \cdot \text{s}^{-1}$). Accordingly, n-decane was injected at $11.00 \text{ mm}^3 \cdot \text{s}^{-1}$ and 1-octanol was injected at $9.00 \text{ mm}^3 \cdot \text{s}^{-1}$. As 200 mm^3 of total fluid were injected at $20.00 \text{ mm}^3 \cdot \text{s}^{-1}$ ($\mu\text{L} \cdot \text{s}^{-1}$), both injections last for 10 s.

A few injections of pure 1-octanol and n-decane are performed, as indicated, to fill the micromixer with the desired molar fraction. When the peaks obtained become reproducible, it is considered that the desired molar fraction was accomplished and the following peaks are integrated. The value associated to the integrated calorimetric signal was determined from the average of the integration of seven concordant injections, represented in figure 3.64.

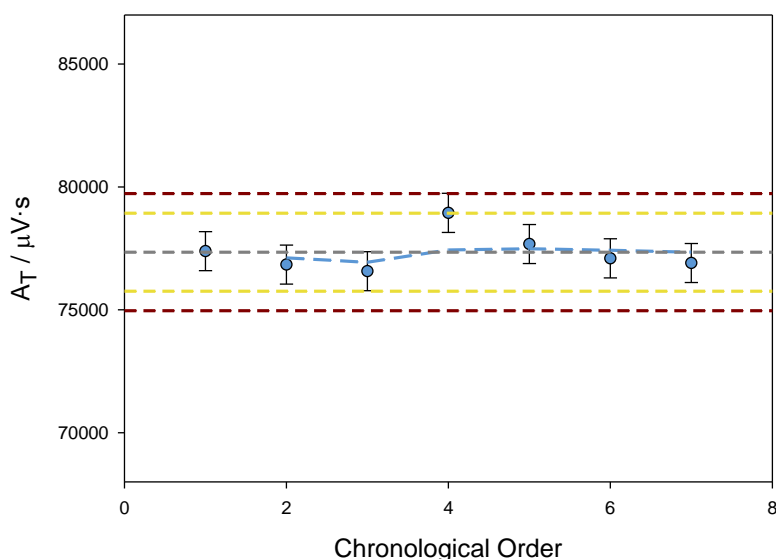


Figure 3.64. Graphical representation of the area of the peaks associated to the injection of 1-octanol and n-decane, at equimolar composition, in $\mu\text{FlowCal}$ prototype calorimeter. The area obtained in each experiment is plotted, as blue circles, in its chronological order. The error bars represent the standard deviation of the sample ($\pm \sigma$). The blue dashed line represents the cumulative average, whereas the final average is represented by the grey dashed line. The lines parallel to the grey dashed line represent the limits of the sample dispersion ($\pm 2 \cdot \sigma$ and $\pm 3 \cdot \sigma$) within 95 % (in yellow) and 99 % (in red) confidence levels.

In table 3.8 is summarized the constant of calibration and experimental sensitivity of μ FlowCal, determined by chemical (mixing process) and electrical calibration (Joule effect). A difference of about 6 % was found between both calibration methods. It is also observable that the uncertainty associated to the chemical calibration results is one order of magnitude higher than the electrical calibration. This higher uncertainty of the chemical calibration is inherent to the different processes in study. The repeatability of the heat release by Joule effect is better than the repeatability of a mixing process.

Table 3.8. Summary of the experimental sensitivity and constant of calibration of μ FlowCal determined by electrical calibration and chemical calibration

	Electrical Calibration	Chemical Calibration
$S_{\text{exp}} / (\text{mV}/(\text{J}\cdot\text{s}^{-1}))$	122.3 ± 0.7	115.6 ± 2.7
$\varepsilon_{\text{cal}} / ((\text{J}\cdot\text{s}^{-1})/\text{V})$	8.17 ± 0.05	8.65 ± 0.20

The deviation found between the two methods may be explained by the non-ideal position of the heaters used in the electrical calibration towards the “sample cell”, which in this calorimeter is the micromixer, and to the heat flow sensors. We estimate that a systematic deviation occurs in the electrical calibration method due to the different heat path generated (in an electrical calibration experiment and in a normal mixing experiment).

These effects are common, depending on the calorimeter design. Electrical calibration techniques are precise and convenient, as stated by Wadsö^[20]. Nevertheless, it is recognized that this technique can origin significant systematic deviations, especially in microcalorimeters^[8, 20]. It was found to be the case for μ FlowCal prototype calorimeter. Accordingly, chemical calibration will be considered from now on.

3.3.4. Performance and Accuracy Test of ITC

The ITC performance and the accuracy of the electrical calibration was verified by stepwise addition 1-propanol to water at 298.15 K until the molar fraction $x_{\text{PrOH}} = 0.08$. The partial molar excess enthalpy of 1-propanol in water, $\bar{H}_{\text{PrOH,m}}^{\text{E}}$ ($\text{kJ}\cdot\text{mol}^{-1}$), was determined in the molar fraction range $x_{\text{PrOH}} = 0.00$ to $x_{\text{PrOH}} = 0.08$. The results obtained were compared with the results existent in the literature^[25, 26]. In parallel, the partial molar excess enthalpy was extrapolated to infinite dilution from the obtained results ($\bar{H}_{\text{PrOH,m}}^{\text{E}}$ when $x_{\text{PrOH}} = 0.00$) and the values were compared with the standard molar enthalpy of solution at infinite dilution of 1-propanol in water at 298.15 K proposed by Wadsö^[20].

The stepwise injection of propanol in water in the molar fraction range $x_{\text{PrOH}} = 0.00$ to $x_{\text{PrOH}} = 0.08$, allows the evaluation of the calorimeter performance using different thermal power levels as demonstrated in figure 3.65 where the experimental results of one experiment are represented. The heat flow signal represented in figure 3.65 refers to an experiment where 7 injections of 8.3 mm^3 (μL) of 1-propanol were made, followed by 6 injections of 20.8 mm^3 (μL). The molar fraction of 1-propanol in that experience has thus, variated from $x_{\text{PrOH}} = 0.00$ to $x_{\text{PrOH}} = 0.08$. Some experiments of stepwise injection of 5.8 mm^3 (μL) of 1-propanol were also performed exploring a smaller range of molar fraction, but having higher resolution into the obtained curve.

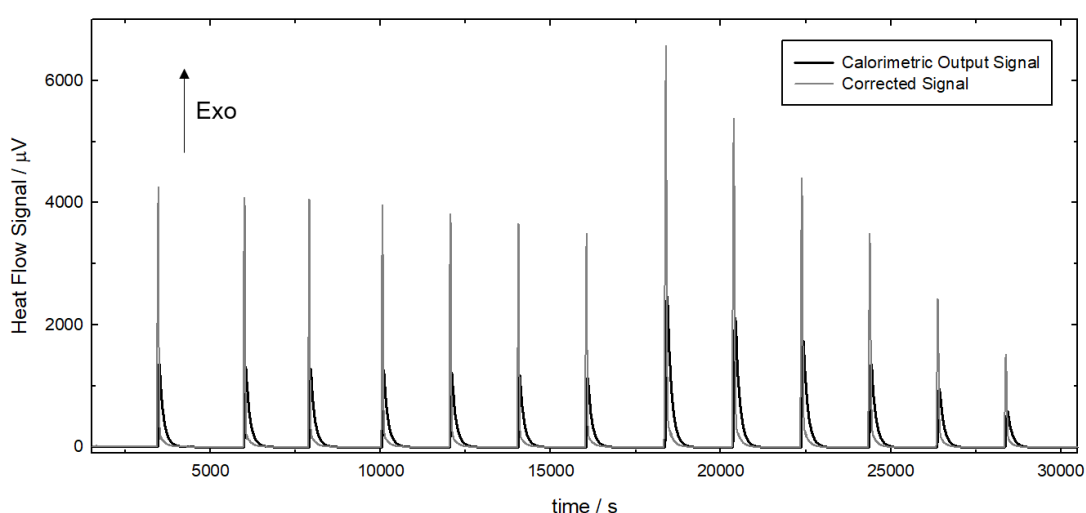


Figure 3.65. Graphical representation of the typical heat flow signal, obtained in an ITC experiment, consisting in the stepwise injection ($7 \times 8.3 \text{ mm}^3 + 6 \times 20.8 \text{ mm}^3$) of PrOH in water (0.8 cm^3). The heat flow signal is presented, before and after correction to the time constant of the calorimeter.

Along time several experiments were performed, in a first approach evaluating the accuracy of the electrical calibration but also monitoring in time, the stability of the experimental sensitivity of the calorimeter and the performance of ITC. In figure 3.66, the curve of partial molar excess enthalpy of 1-propanol in water obtained at 298.15 K as a function of the 1-propanol molar fraction are presented and compared with the data existent in the literature.

Tanaka and co-workers^[25] have measured the partial molar excess enthalpy of 1-propanol in water and thus, the data can be compared directly. However, Davis and Ham^[26] have measured the excess molar enthalpy of 1-propanol in water. Their experimental data was fitted (in the molar fraction interval $x_{\text{PrOH}} = 0.00$ to $x_{\text{PrOH}} = 0.09$) using the Redlich-Kister equation to access the parameters “ A_k ” and hence calculate the partial molar excess enthalpy. The parameters “ A_k ” obtained in the fitting and used in the calculation of the partial molar excess enthalpy were: $A_0 = -9.60 \times 10^2 \text{ kJ}\cdot\text{mol}^{-1}$, $A_1 = -3.34 \times 10^3 \text{ kJ}\cdot\text{mol}^{-1}$; $A_2 = -3.84 \times 10^3 \text{ kJ}\cdot\text{mol}^{-1}$; $A_3 = -1.45 \times 10^3 \text{ kJ}\cdot\text{mol}^{-1}$. The partial molar excess enthalpy data obtained is represented in figure 3.66 together with the literature data and the experimental data obtained in this work in ITC.

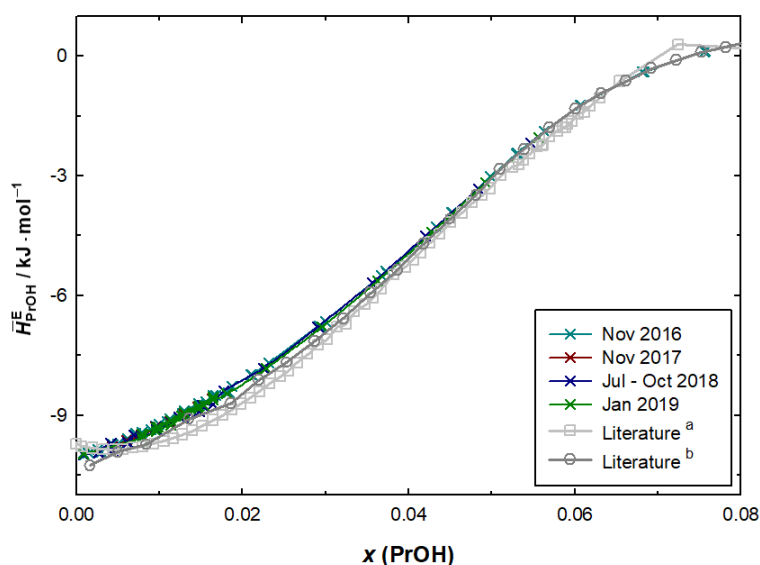


Figure 3.66. Graphical representation of the partial molar excess enthalpy of 1-propanol, obtained experimentally, and of the data existent in the literature, as a function of the molar fraction of 1-propanol. a - ref [26]; b - [25].

From the analysis of the data presented in figure 3.66, the results obtained in ITC from 2016 to 2019 seem to be reproducible in time and doesn't show evidences of any change of the sensitivity or performance of the calorimeter along time. Furthermore, the data obtained in ITC is in agreement with the data reported in the literature with exception of the partial molar excess enthalpy values obtained in the molar fraction interval from $x_{\text{PrOH}} = 0.01$ and $x_{\text{PrOH}} = 0.03$. In this molar fraction interval the data obtained in ITC is more endothermic than the data reported in the literature. It is admitted that the data obtained in ITC may present some endothermic deviation caused by some vaporization of 1-propanol, given the fact that ITC experiments are performed in the presence of a gaseous phase and that the volume of sample used in the beginning of the experiment is smaller than the typical volumes used in ITC experiments, increasing the gaseous phase present in the calorimetric cell.

The partial molar excess enthalpy of 1-propanol at infinite dilution, $\bar{H}_{\text{PrOH},m}^{E,\infty}$ ($\text{kJ}\cdot\text{mol}^{-1}$), was extrapolated from linear regression of the obtained data of partial molar excess enthalpy of propanol in the molar fraction interval $x_{\text{PrOH}} = 0.000$ to $x_{\text{PrOH}} = 0.015$. The obtained results concerning the partial molar excess enthalpy of propanol at infinite dilution and the value reported in the literature by Wadsö^[20] are summarized in table 3.9. Given the obtained results, it is considered that there is excellent agreement between the data obtained in ITC and data reported in the literature.

Table 3.9. Summary of the standard molar enthalpy of solution, at infinite dilution, of propanol in water, at 298 K, reported in the literature and obtained experimentally in ITC, in the context of this thesis

	$\bar{H}_{\text{PrOH},m}^{E,\infty} / \text{kJ}\cdot\text{mol}^{-1}$
Nov 2016	-10.14 ± 0.02
Nov 2017	-10.16 ± 0.04
Jul-Oct 2018	-10.16 ± 0.04
Jan 2019	-10.17 ± 0.06
Literature ^b	-10.16 ± 0.02

a - The uncertainty is the standard deviation associated to the intercept of the linear fitting of the partial molar excess enthalpy of 1-propanol in water, in the molar fraction interval $x_{\text{PrOH}} = 0.000$ to $x_{\text{PrOH}} = 0.015$;

b – ref. [20].

The dilution of pure propanol in water had already been proposed by Wadsö^[20] as “a convenient and safe calibration and test reaction for experiments where small volumes of liquid are injected into a larger volume of solvent”. In this thesis the test was taken further, determining not only the enthalpy of solution at infinite dilution and comparing the results with the value proposed by Wadsö but exploring the enthalpies of mixing in a wider mole fraction range, allowing to explore in a single experiment different thermal power and thermal energy levels and compare the results with the ones reported in the literature.

The dilution of pure propanol in water was chosen as a performance and accuracy test as it allows to compare the enthalpy of solution at infinite dilution of 1-propanol in water with reliable values reported in the literature and in addition, is a compound similar to the compounds that will be studied in ITC in both viscosity, diffusion and volatility. In fact it is one of the studied compounds!

The detail of increasing the molar fraction range of the test is very important in this work as the mixture of alcohols and ionic liquids may involve significant heat effects, even in very small quantities. As it was seen in the electrical calibration, smaller thermal energies may lead to significant deviations due to the higher uncertainty involved. This test allows to test the ITC performance to several thermal powers and thermal energies in the same experiment, in conditions very similar of the ones that will be used in the study of alcohols-ILs mixtures.

3.3.5. Performance and Accuracy Test of μ FlowCal

It is known that the location of the calibration heaters can lead to significant systematic deviations^[8, 20]. It was found to be the case of μ FlowCal calorimeter prototype. The evaluation of the accuracy of the calibration performed is thus, important. Furthermore, μ FlowCal was constructed in the context of this thesis. Therefore, standard tests were used to test and evaluate the calorimetric system accuracy, the mixing efficiency, as well as, allow the establishment of a correct methodology to the reliable measurement of the heat of mixing of alcohols and ionic liquids.

To fulfil the described requirements, two different tests were performed. The first test consisted in the dilution of aqueous sucrose solutions. Concentrated sucrose solutions are quite viscous and difficult to mix with water. The dilution of these solutions is thus, an optimum test to the efficiency of mixing in flow calorimeters, which do not involve stirring of the fluids. The second test was the measurement of the excess molar enthalpy of mixing of the decane-octanol binary mixture, in a wide concentration range. The test of a broad concentration range provided a good test of the flow system and of the mixing efficiency, once that the enthalpy is dependent on the concentration.

3.3.5.1. Dilution of Aqueous Sucrose Solutions

The enthalpy of dilution of aqueous sucrose solutions has been recommended as a standard test to detect possible systematic errors in calibration and when solutions of moderate viscosity are going to be studied^[20, 27, 28]. Gucker and Pickard^[26] have measured the enthalpy of dilution of aqueous solutions of sucrose at the temperatures 293.15 K, 298.15 K, and 303.15 K. Wadsö^[20, 27] have confirmed the obtained results, at 298.15 K and 310.15 K. From those measurements, the following equation has been proposed to describe the enthalpy of dilution $\Delta_{\text{dil}}H_m$ ($\text{J}\cdot\text{mol}^{-1}$) of aqueous sucrose solutions:

$$\Delta_{\text{dil}}H_m = A \cdot (m_2 - m_1) - B \cdot (m_2^2 - m_1^2) \quad (3.40)$$

where m_1 is the initial molality and m_2 the final molality of the aqueous sucrose solution. At 298.15 K, the parameters “A” and “B”, are: $A = 572.0 \text{ J}\cdot\text{kg}\cdot\text{mol}^{-2}$ and $B = 29.4 \text{ J}\cdot\text{kg}^2\cdot\text{mol}^{-3}$. Using the equation 3.38 and the parameters “A” and “B” indicated, the enthalpy of dilution of aqueous sucrose solutions is judged, by Wadsö^[20], to be

accurate to about $\pm 1\%$, provided that the initial molality is in the range (0.1 to 2.0) $\text{mol}\cdot\text{kg}^{-1}$ and the final molality in the range (0.01 to 0.2) $\text{mol}\cdot\text{kg}^{-1}$.

As this test is well documented in the literature and recommended to test the mixture efficiency of a flow calorimeter, the test was used first to establish a measurement procedure and after to verify the accuracy of the calibration procedure. The detailed description of all the tests performed in the calorimeter is out of the scope of the thesis. However, the central aspects of the testing and methodology definition will be briefly described.

Dependence on the Injected Volume

The volume injected was one of the first tests. The total volume of the micromixer is 200 mm^3 (μL). However, the glass plate in which the micromixer is embedded has a superior volume.

The syringes of the $\mu\text{FlowCal}$ were programmed to inject pure water and an aqueous sucrose solution of 1.0 $\text{mol}\cdot\text{kg}^{-1}$, in order to obtain its dilution to 0.1 $\text{mol}\cdot\text{kg}^{-1}$. The injection of both fluids was made simultaneously, in the right proportion, to obtain the desired dilution, using two different (total) flow levels: 2.45 $\text{mm}^3\cdot\text{s}^{-1}$ ($\mu\text{L}\cdot\text{s}^{-1}$) and 10.00 $\text{mm}^3\cdot\text{s}^{-1}$ ($\mu\text{L}\cdot\text{s}^{-1}$). The total volumes injected were variated from 50 mm^3 (μL) to 250 mm^3 (μL). In figures 3.67 and 3.68, the obtained results are presented together with a representation of the heat involved and the volume injected.

From the analysis of figures 3.67 and 3.68, it is observable that for both flows tested, 2.45 $\text{mm}^3\cdot\text{s}^{-1}$ ($\mu\text{L}\cdot\text{s}^{-1}$) and 10.00 $\text{mm}^3\cdot\text{s}^{-1}$ ($\mu\text{L}\cdot\text{s}^{-1}$), the increase of the injected volumes decreases the dispersion of the results and increases their accuracy. The grey dashed line, which represents the average value of the enthalpy of dilution of aqueous sucrose solution from 1.0 $\text{mol}\cdot\text{kg}^{-1}$ to 0.1 $\text{mol}\cdot\text{kg}^{-1}$, is becoming closer to the black full line with the increase in the injected volume, which evidences the improvement of the accuracy of the results. The decrease in the dispersion of the results can be seen by the decrease in size of the error bars of the sample dispersion ($\pm 2\cdot\sigma$), within 95 % of confidence level.

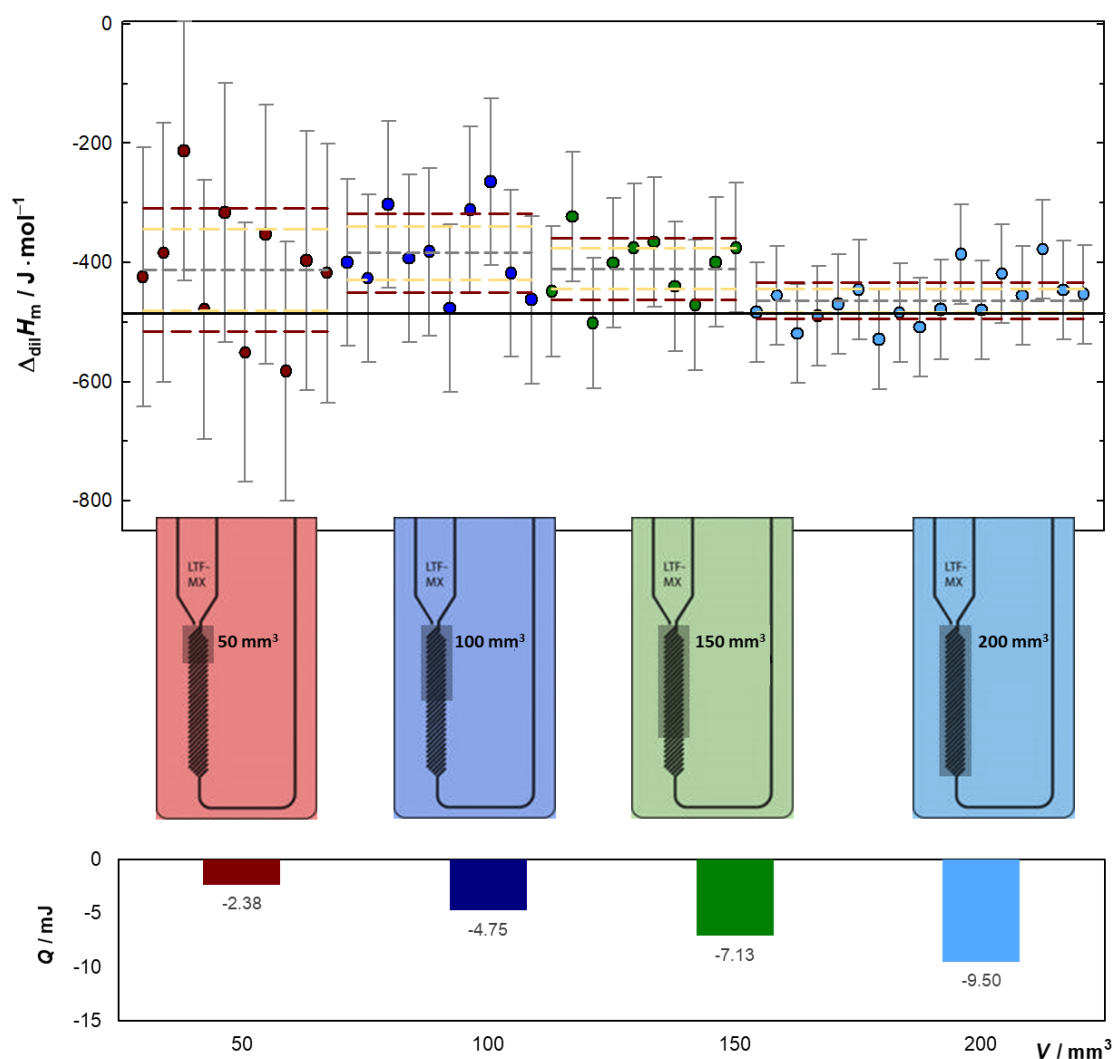


Figure 3.67. Graphical representation of the enthalpy of dilution of aqueous sucrose solution, from 1.0 $\text{mol} \cdot \text{kg}^{-1}$ to 0.1 $\text{mol} \cdot \text{kg}^{-1}$, obtained in $\mu\text{FlowCal}$ calorimeter, with a total flow of $2.45 \text{ mm}^3 \cdot \text{s}^{-1}$ ($\mu\text{L} \cdot \text{s}^{-1}$), as a function of the volume injected into the micromixer. The coloured circles represent the obtained enthalpy of dilution by injection of different volumes: • 50 mm^3 (μL), • 100 mm^3 (μL), • 150 mm^3 (μL), • 200 mm^3 (μL). The error bars represent the dispersion of the sample ($\pm 2 \cdot \sigma$) within 95 % confidence level. The grey dashed line represents the average of the enthalpy of dilution of the aqueous sucrose solution in each set of experiments, whereas the lines parallel to the grey dashed line represent its limits of uncertainty ($\pm 2 \cdot \sigma \cdot n^{-1/2}$ and $\pm 3 \cdot \sigma \cdot n^{-1/2}$) within 95 % (in yellow) and 99 % (in red) confidence levels. The black solid line represents the literature value for the enthalpy of dilution of aqueous sucrose solution, from 1.0 $\text{mol} \cdot \text{kg}^{-1}$ to 0.1 $\text{mol} \cdot \text{kg}^{-1}$, obtained from equation 3.38. Together with this representation, it is presented the proportion of volume injected into the reactor and the heat involved in each experiment. The constant of calibration obtained by the chemical methodology was used: $(8.65 \pm 0.21) \times 10^{-6} (\text{J} \cdot \text{s}^{-1}) / \mu\text{V}$.

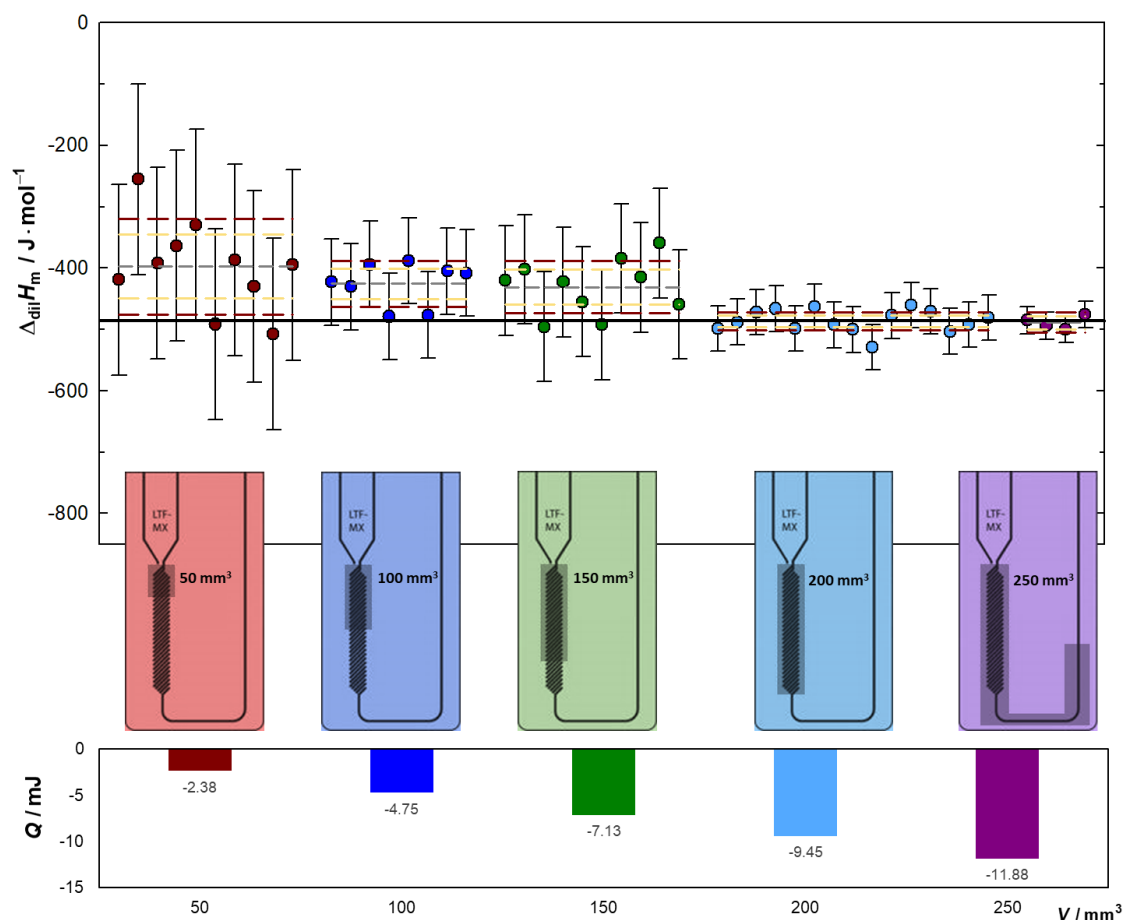


Figure 3.68. Graphical representation of the enthalpy of dilution of aqueous sucrose solution, from $1.0 \text{ mol} \cdot \text{kg}^{-1}$ to $0.1 \text{ mol} \cdot \text{kg}^{-1}$, obtained in $\mu\text{FlowCal}$ calorimeter, with a total flow of $10.00 \text{ mm}^3 \cdot \text{s}^{-1}$ ($\mu\text{L} \cdot \text{s}^{-1}$), as a function of the volume injected into the micromixer. The coloured circles represent the obtained enthalpy of dilution, by injection of different volumes: \bullet 50 mm^3 (μL), \bullet 100 mm^3 (μL), \bullet 150 mm^3 (μL), \bullet 200 mm^3 (μL), \bullet 250 mm^3 (μL). The error bars represent the dispersion of the sample ($\pm 2 \cdot \sigma$) within 95 % confidence level. The grey dashed line represents the average of the enthalpy of dilution of the aqueous sucrose solution, in each set of experiments, whereas the lines parallel to the grey dashed line represent its limits of uncertainty ($\pm 2 \cdot \sigma \cdot n^{-1/2}$ and $\pm 3 \cdot \sigma \cdot n^{-1/2}$) within 95 % (in yellow) and 99 % (in red) confidence levels. The black solid line represents the literature value for the enthalpy of dilution of aqueous sucrose solution, from $1.0 \text{ mol} \cdot \text{kg}^{-1}$ to $0.1 \text{ mol} \cdot \text{kg}^{-1}$, obtained from equation 3.38. Together with this representation, it is presented the proportion of volume injected into the reactor and the heat involved in each experiment. The constant of calibration obtained by the chemical methodology was used: $(8.65 \pm 0.21) \times 10^{-6} (\text{J} \cdot \text{s}^{-1}) / \mu\text{V}$.

The results obtained were as expected due to the design of the micromixer. The design of the micromixer used promotes the mixing of the fluids injected by split and recombination of the fluids, together with the repeated level change and crossflow, due to the existence of two levels. Is then easy to conceive that if the fluids flow through all the micromixer channels, they will experience a much more efficient mixing then if they flow only through a section of it. That's exactly what happens when the volume injected is shorter than the volume of the micromixer. If only $50 \text{ mm}^3 (\mu\text{L})$ are injected, the fluid will only fill a quarter of the mixer. Furthermore, it has to be considered that prior to the injection, the micromixer is not empty. Therefore, if the injected volume is smaller than the volume of the mixer, the fluids injected are going to be mixed also with the previous filling of the mixer. Is thus, easy to understand why the complete filling of the micromixer gives more reliable results.

The injection of a volume above to the capacity of the micromixer, $250 \text{ mm}^3 (\mu\text{L})$, has also showed very good results, despite of the short number of experiments performed. This is easy to understand, as what was said about filling the capacity of the micromixer also applies, taking advantage of the full length of split and recombination of the fluids together with the repeated level change and crossflow and thus, increasing mixing efficiency. Due to the design of the calorimeter, the $250 \text{ mm}^3 (\mu\text{L})$ injected, although are higher than the capacity of the micromixer, are not bigger than the capacity of the all glass device. Accordingly, the part of the fluid that has exceeded the volume of the micromixer will remain in the following channel, in the same glass device, and the heat of the mixture will still be captured by the heat flow sensors localized in that area.

The small amounts of energy involved in this test, which are indicated in the figures 3.67 and 3.68, should be noted, as they are in the range of the lower energies tested in the electrical calibration and that showed higher uncertainties associated with the obtained results. Therefore, the uncertainties obtained here may be related not only with the volumes injected, the fluid flow chosen, the efficiency of the mixture and the viscosity of the fluids but also with the lower energy levels involved in the process.

However, regarding the presented results, it was seen, as expected, that the filling of the micromixer with $200 \text{ mm}^3 (\mu\text{L})$ is the best approach. Therefore, the following tests and experiments will always be performed using injections of both fluids of $200 \text{ mm}^3 (\mu\text{L})$ (in total). Higher volumes will not be used as, it is believed that to the efficiency of the mixture and reduction of concentration gradients it is important that the fluids remain in the micromixer for a certain time after the end of the injections, giving time for the diffusion of the species and for the homogenization to be improved by this effect.

From the analysis of figures 3.67 and 3.68, is also observable that the increase in the fluid flow from $2.45 \text{ mm}^3\cdot\text{s}^{-1}$ ($\mu\text{L}\cdot\text{s}^{-1}$) to $10.00 \text{ mm}^3\cdot\text{s}^{-1}$ ($\mu\text{L}\cdot\text{s}^{-1}$) caused a decrease of the dispersion of the obtained results and an increase in the accuracy of the measurements. Therefore the flow effect is now going to be discussed.

Dependence on the Magnitude of the Flow

In addition to the previous results, there is no stirring of the mixture or any external source of energy that could increase the efficiency of the mixture. The only driving force, that could act as a source of energy to improve the mixing efficiency is the pumping energy of the fluid injection. Therefore, the effect of the fluid flow was tested.

As a first approach, the dilution of an aqueous sucrose solution of $1.0 \text{ mol}\cdot\text{kg}^{-1}$ to $0.1 \text{ mol}\cdot\text{kg}^{-1}$ was studied. The fluid total flow was changed from $2.45 \text{ mm}^3\cdot\text{s}^{-1}$ ($\mu\text{L}\cdot\text{s}^{-1}$) to $20.00 \text{ mm}^3\cdot\text{s}^{-1}$ ($\mu\text{L}\cdot\text{s}^{-1}$), maintaining the correct flow proportion between the pure water injected and aqueous sucrose solution of $1.0 \text{ mol}\cdot\text{kg}^{-1}$, in order for both fluids to be injected simultaneously and to obtain the dilution of the aqueous sucrose solution to $0.1 \text{ mol}\cdot\text{kg}^{-1}$. The heat involved in the mixture was 9.50 mJ . The results obtained are represented in figure 3.69.

From the analysis of figure 3.69, it is observable that as the fluid flow increases, the size of the error bars is decreasing, which evidences a decrease in the dispersion of the results. The grey dashed line, which represents the average value of the enthalpy of dilution of aqueous sucrose solution from $1.0 \text{ mol}\cdot\text{kg}^{-1}$ to $0.1 \text{ mol}\cdot\text{kg}^{-1}$, is becoming more exothermic. Nevertheless, no heat effect related to the increase of the flow was observed upon injection of the pure fluids.

The results obtained are thus in line with previous findings, evidencing that the increase in the fluid flow decreases the dispersion of the results. This effect suggests that the increase of the fluid flow, which increases the pumping energy of the fluid injection, consists in a driving force to increase the mixing efficiency, improving the repeatability of the mixing process.

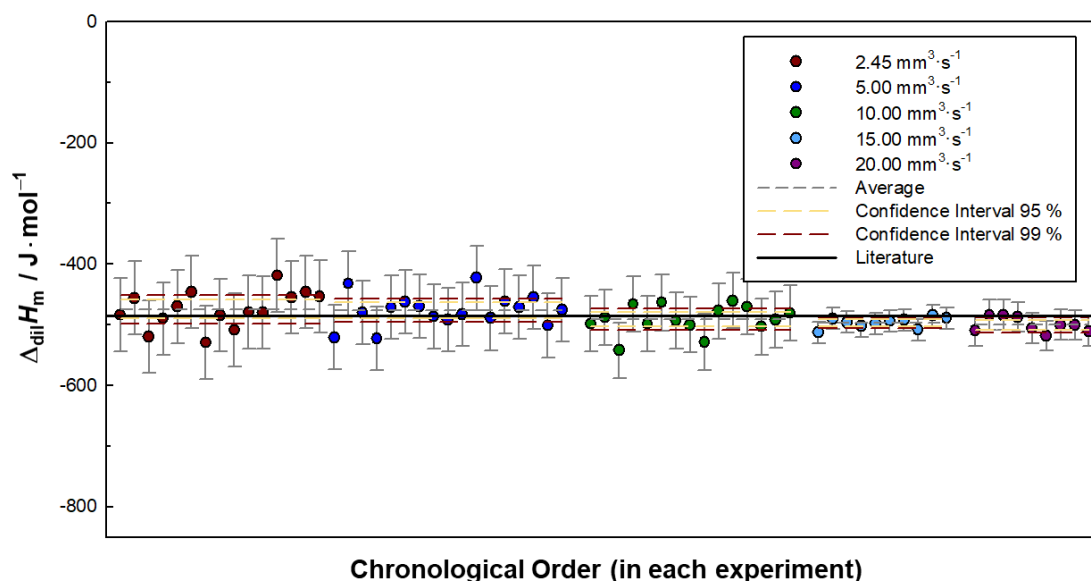


Figure 3.69. Graphical representation of the enthalpy of dilution of aqueous sucrose solution, from $1.0 \text{ mol}\cdot\text{kg}^{-1}$ to $0.1 \text{ mol}\cdot\text{kg}^{-1}$, obtained in $\mu\text{FlowCal}$ calorimeter, with a total injection volume of 200 mm^3 (μL), in the chronological order of the experiments performed. The chronological order is just valid inside each set of experiments, as the experiments were performed with alternation of the flow. The coloured circles represent the enthalpy of dilution obtained in the experiments performed with the different fluid flows tested: \bullet $2.45 \text{ mm}^3\cdot\text{s}^{-1}$ ($\mu\text{L}\cdot\text{s}^{-1}$), \bullet $5.00 \text{ mm}^3\cdot\text{s}^{-1}$ ($\mu\text{L}\cdot\text{s}^{-1}$), \bullet $10.00 \text{ mm}^3\cdot\text{s}^{-1}$ ($\mu\text{L}\cdot\text{s}^{-1}$), \bullet $15.00 \text{ mm}^3\cdot\text{s}^{-1}$ ($\mu\text{L}\cdot\text{s}^{-1}$), \bullet $20.00 \text{ mm}^3\cdot\text{s}^{-1}$ ($\mu\text{L}\cdot\text{s}^{-1}$). The error bars represent the dispersion of the sample ($\pm 2\cdot\sigma$) within 95 % confidence level. The grey dashed line represents the average of the enthalpy of dilution of the aqueous sucrose solution, in each set of experiments, whereas the lines parallel to the grey dashed line represent its limits of uncertainty ($\pm 2\cdot\sigma\cdot n^{-1/2}$ and $\pm 3\cdot\sigma\cdot n^{-1/2}$) within 95 % (in yellow) and 99 % (in red) confidence levels. The black solid line represents the literature value for the enthalpy of dilution of aqueous sucrose solution, from $1.0 \text{ mol}\cdot\text{kg}^{-1}$ to $0.1 \text{ mol}\cdot\text{kg}^{-1}$, obtained from equation 3.38. The constant of calibration obtained by the chemical methodology was used: $(8.65 \pm 0.21) \times 10^{-6} (\text{J}\cdot\text{s}^{-1})/\mu\text{V}$.

Dependence on the Flow Effect & Viscosity of the Fluid

One of the questions that still remained after the previous testing was which was the actual effect of the viscosity of the fluid and what would be the effect of the fluid flow in higher viscosity fluids.

The complexity of the previous study was thus increased in order to gain more information on the effect of the fluid flow. The exact same fluid flows used in the previous experiment were repeated now with the exception of the $2.45 \text{ mm}^3\cdot\text{s}^{-1}$ ($\mu\text{L}\cdot\text{s}^{-1}$), that was taken out of the study. To clarify, not only the total fluid flows were repeated but also the

individual flows of the pure water and the aqueous sucrose solution. The only change performed to the experiment was the change of the concentration of the sucrose in the initial sucrose solution, which resulted in solutions with different viscosity. The details of the experiments were summarized in the following table 3.10. Details on the viscosity of the initial solution, as well as the sucrose weight percentage and the molar fraction are indicated in table 3.11.

Table 3.10. Summary of the details associated with the study of the flow effect on the experiments of dilution of aqueous sucrose solution, performed in μ FlowCal calorimeter: the initial molality of the aqueous sucrose solution (m_1), the final molality of the aqueous sucrose solution (m_2 , after the dilution process), the fluid flow of the injections performed, the enthalpy of dilution of the aqueous sucrose solution obtained, the literature recommended value[20], and the heat (Q) involved in the dilution process.

$m_1 /$ mol·kg ⁻¹	$m_2 /$ mol·kg ⁻¹	Total Flow / mm ³ ·s ⁻¹	H ₂ O Flow / mm ³ ·s ⁻¹	Sucrose Sol. Flow / mm ³ ·s ⁻¹	$\Delta_{\text{dil}}H_m^{a,b}/$ J·mol ⁻¹	Lit. c/ J·mol ⁻¹	Q / mJ
1.0004	0.10020				-476 ± 13	-486 ± 5	9.50
1.4998	0.13915	5.000000	4.405531	0.594469	-678 ± 14	-713 ± 7	19.18
2.0001	0.17289				-914 ± 14	-928 ± 9	30.87
1.0004	0.10020				-491 ± 12	-486 ± 5	9.50
1.4998	0.13915	9.999999	8.811061	1.188938	-686 ± 11	-713 ± 7	19.18
2.0001	0.17289				-918 ± 26	-928 ± 9	30.87
1.0004	0.10020				-497 ± 6	-486 ± 5	9.50
1.4998	0.13915	14.999999	13.216592	1.783407	-701 ± 13	-713 ± 7	19.18
2.0001	0.17289				-909 ± 23	-928 ± 9	30.87
1.0004	0.10020				-500 ± 8	-486 ± 5	9.50
1.4998	0.13915	19.999998	17.622122	2.377876	-698 ± 17	-713 ± 7	19.18
2.0001	0.17289				-915 ± 22	-928 ± 9	30.87

a - The constant of calibration obtained by the chemical methodology was used: $(8.65 \pm 0.21) \times 10^{-6} \text{ (J·s}^{-1}\text{)}/\mu\text{V}$;

b - The uncertainty is the confidence interval of the (average) enthalpy of dilution obtained in each set of experiments, at a confidence level of 95% ($\pm 2 \cdot \sigma \cdot n^{-1/2}$);

c - The uncertainty is estimated to be 1% of the magnitude of the enthalpy of dilution (ref. [20]).

Table 3.11. Summary of the details associated to the concentration and viscosity of the aqueous sucrose solutions before dilution experiments: molality of the aqueous sucrose solution (m_1), percentage in weight of sucrose (% (w/w)), molar fraction of sucrose (x) and viscosity (η)

m_1 / mol·kg ⁻¹	% (w/w)	x (sucrose)	η (298 K) ^{a/} mPa·s
1.0004	25.51	0.017703	2.203
1.4998	33.92	0.026308	3.510
2.0001	40.64	0.034779	5.488

a – ref.[29].

To a better visualization of the obtained results, the relative deviation (h) of the average enthalpy of dilution obtained to the literature proposed value is represented as a function of the total flow in figure 3.70. In the error bars, it is presented the relative confidence limits (ru) of the enthalpy of dilution obtained to a confidence level of 95 % ($\pm 2 \cdot \sigma \cdot n^{-1/2}$). The calculations of the two values are demonstrated in the following equations:

$$h = \frac{\Delta_{\text{dil}} H_{m, \text{exp}} - \Delta_{\text{dil}} H_{m, \text{lit}}}{\Delta_{\text{dil}} H_{m, \text{lit}}} \quad (3.41)$$

$$ru = \frac{2 \cdot \sigma \cdot \sqrt{n}}{\Delta_{\text{dil}} H_{m, \text{lit}}} \quad (3.42)$$

From the analysis of figure 3.70, it stands out that the experimental results of the enthalpy of dilution of sucrose solutions is within 5% deviation from the literature, independently of the flow level tested.

The increase of the viscosity and fluid flow seems to present a non-regular behaviour. In the case of the aqueous sucrose solution which initial molality is 1.0 mol·kg⁻¹ and 1.5 mol·kg⁻¹, the increase of the fluid flow increases the exothermic character of the enthalpy of dilution. Unexpectedly, the results regarding the 2.0 mol·kg⁻¹ solution indicate a smaller deviation than the 1.5 mol·kg⁻¹ sucrose solution at both 5.00 mm³·s⁻¹ (μL·s⁻¹) and 10.00 mm³·s⁻¹ (μL·s⁻¹). Furthermore, in the specific case

of this solution, the increase of the flow to $15.00 \text{ mm}^3 \cdot \text{s}^{-1}$ ($\mu\text{L} \cdot \text{s}^{-1}$) seems to increase the deviation of the final result, although given the uncertainty of the value, there is not enough resolution to be certain. The non-regular effect together with the small deviations found towards the literature data (both positive and negative) may suggest that the deviations found are within the dispersion of the results. In order words, the dilution process may not have enough resolution (both due to the heat involved and mixing process), to distinguish clearly amongst viscosity and flow effects in the studied systems. Nonetheless, in a general way, it seems that the increase in the viscosity cause positive deviations to the literature value which may be indicative of less efficient mixing. On the other side, the increase of the flow seems to have a small exothermic effect.

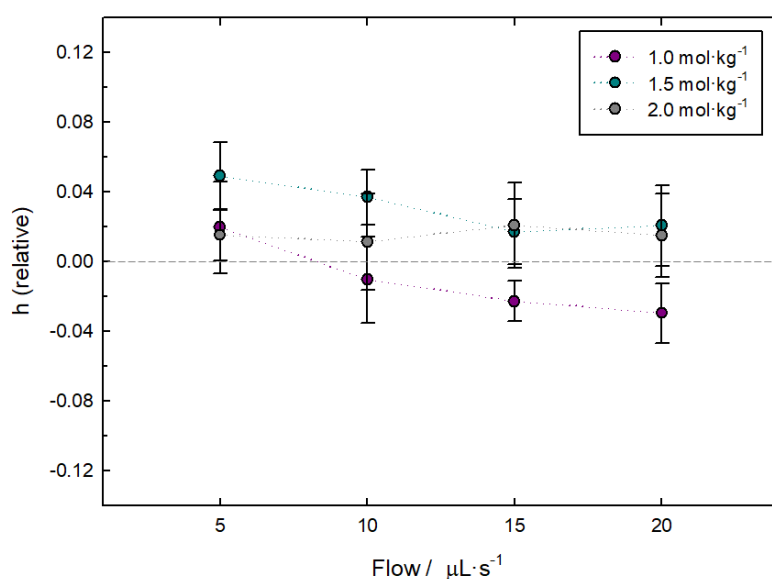


Figure 3.70. Graphical representation of the relative deviation of the average of the enthalpy of dilution of aqueous sucrose solution, obtained in $\mu\text{FlowCal}$ calorimeter, as a function of the fluid flow used in the experiments. The coloured circles represent the initial molality of the aqueous sucrose solution. The error bars represent the limits of the relative confidence limits within 95 % confidence level. The dotted lines are just a guide line to the eyes. The constant of calibration obtained by the chemical methodology was used: $(8.65 \pm 0.21) \times 10^{-6} (\text{J} \cdot \text{s}^{-1})/\mu\text{V}$.

An extra dilution was performed using the four levels of total fluid flow already used: $5.00 \text{ mm}^3\cdot\text{s}^{-1}$ ($\mu\text{L}\cdot\text{s}^{-1}$), $10.00 \text{ mm}^3\cdot\text{s}^{-1}$ ($\mu\text{L}\cdot\text{s}^{-1}$), $15.00 \text{ mm}^3\cdot\text{s}^{-1}$ ($\mu\text{L}\cdot\text{s}^{-1}$) and $20.00 \text{ mm}^3\cdot\text{s}^{-1}$ ($\mu\text{L}\cdot\text{s}^{-1}$). This time, the particular flows of water and aqueous sucrose solution were adjusted in order to accomplish the desired dilution and maintain the total flow levels. Using the described procedure, the enthalpy of dilution of an aqueous solution of $1.5 \text{ mol}\cdot\text{kg}^{-1}$ to $0.05 \text{ mol}\cdot\text{kg}^{-1}$ was measured in $\mu\text{FlowCal}$ prototype calorimeter. The obtained results are presented in figure 3.71. For comparison purposes, the results already presented in figure 3.70 are repeated in this representation.

As showed in figure 3.71, the enthalpy of dilution of aqueous sucrose solution, from $1.5 \text{ mol}\cdot\text{kg}^{-1}$ to $0.05 \text{ mol}\cdot\text{kg}^{-1}$, is approximately 20 % deviated from the literature value, independently of the fluid flow level used. In addition, the dispersion of the results is significantly higher than the previous ones. These results are probably associated with two facts: lack of efficient mixing of the fluids, conducting to different enthalpy values in each experiment performed and on the low energy of the dilution process (7.5 mJ). Despite of the higher uncertainty, it is still visible that the increase of the fluid flow decreases the dispersion of the results.

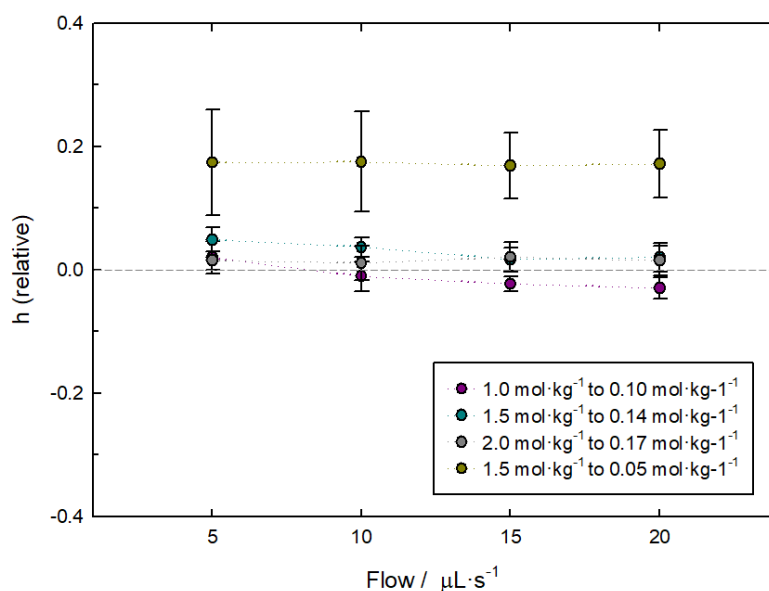


Figure 3.71. Graphical representation of the relative deviation of the average of the enthalpy of dilution of aqueous sucrose solution, obtained in $\mu\text{FlowCal}$ calorimeter, as a function of the fluid flow used in the experiments. The different coloured circles represent the different initial and final molality of the aqueous sucrose solution dilution. The error bars represent the limits of the relative confidence limits within 95 % confidence level. The dotted lines are just a guide line to the eyes. The constant of calibration obtained by the chemical methodology was used: $(8.65 \pm 0.21) \times 10^{-6} \text{ (J}\cdot\text{s}^{-1})/\mu\text{V}$.

Comment on the Obtained Results

The flow levels tested do not cause significant heat release due to the friction of the fluid on the glass channels. The weight of the solutions stock was controlled during the experiments. There was no evidence of alteration on the concentration of the solutions during the testing of the calorimeter. In some of the tests performed, different solutions with the same concentrations were prepared and used.

From the obtained results, some procedures and precautions were taken for future measurements in μ FlowCal calorimeter. It was seen that injections should have enough volume to fill the micromixer. Generally, the increase of the flow seems to increase the efficiency of the mixing. Furthermore, despite of viscosity differences on the initial solutions (up to 2.5 times the less viscous solution), the enthalpy of dilution of the sucrose solution was within 5% deviation from the literature recommended values, independently of the fluid flow level used.

The only exception was the dilution of the sucrose solution from $1.5 \text{ mol}\cdot\text{kg}^{-1}$ to $0.05 \text{ mol}\cdot\text{kg}^{-1}$ ($\approx 20\%$ deviation towards literature recommended data), which is probably due to the inefficient mixing given the dilution level involved, the low flow of the sucrose solution used (between ≈ 0.2 and $0.9 \text{ mm}^3\cdot\text{s}^{-1}$) and the low level of heat involved in the process ($\approx 7.5 \text{ mJ}$).

It should be noted that the energy levels involved in the dilution of the sucrose solution (highest energy tested was $\approx 30 \text{ mJ}$) are comparable to the lower energy levels tested in the electrical calibration. Therefore, if we consider the possibility of the uncertainty and deviations found in the electrical calibration to be related with the calorimeter performance at low energy levels and not with the electrical / electronic components used in the calibration, then, some of the deviations and uncertainties found in this chemical test could be partially attributed to the lower levels of energy tested. The high viscosity of the sucrose solutions is an additional difficulty.

In summary, the tests executed evidenced a good performance of the mixing and calorimetric system. Despite of the low energy levels, no evidence of systematic deviations was found. The dilution of solutions of different viscosities (with the same fluid flow conditions) was successfully performed without significant deviations from recommended values, evidencing the mixing efficiency. Nonetheless, some results suggested that inefficient mixing may occur if higher dilutions are attempted. This is inherent to the calorimeter design. This calorimeter should not be used to perform high dilutions as it will imply that one of the fluid flows has to be very low. A very low fluid flow

will decrease the precision of the injection and enhance the existence of concentration gradients into the micromixer.

3.3.5.2. Binary Mixtures Decane-Octanol

To complement the previous test of the performance and accuracy of μ FlowCal prototype calorimeter, the excess molar enthalpy of the decane-octanol mixture, in wide concentration range, was measured. As shown previously, the enthalpy of mixing of these compounds have been well established in the literature^[23, 24].

The decane-octanol mixtures were chosen as a test system to the μ FlowCal as they constitute an approximation to the systems that are going to be studied in the μ FlowCal calorimeter (alcohols + ionic liquids). Moreover, the excess enthalpy is strongly dependent on the concentration of both solvents and has been well studied by two reference groups on the field ^[23, 24]. Therefore, it constitutes an excellent way to test the performance of the flow system, the existence of diffusion, the efficiency of the mixing and the accuracy of the calibration performed. On the contrary of the previous test, the study of the enthalpy of mixing of 1-octanol and n-decane, in wide concentration ranges, involve the absorption of energies in μ FlowCal ranging from 300-700 mJ.

The excess molar enthalpy of the decane-octanol binary mixtures was measured in the molar fraction range $0.06 < x_{\text{OctOH}} < 0.83$. All the measurements were performed by injecting 200 mm^3 (μL) of the fluids at $20.00 \text{ mm}^3 \cdot \text{s}^{-1}$ ($\mu\text{L} \cdot \text{s}^{-1}$). The particular flow of each component injected was defined individually for each molar fraction studied, in such a way, that both components were injected simultaneously, in the right proportions, to accomplish the desired molar fraction under study, and equalizing a total flow of $20.00 \text{ mm}^3 \cdot \text{s}^{-1}$ ($\mu\text{L} \cdot \text{s}^{-1}$). As 200 mm^3 (μL) were injected at $20.00 \text{ mm}^3 \cdot \text{s}^{-1}$ ($\mu\text{L} \cdot \text{s}^{-1}$), each injection lasted for 10 s.

Initially, the experimental procedure used in the chemical calibration was followed (methodology I):

- i) a few injections of pure 1-octanol and n-decane were performed, at the right proportions, to fill the micromixer with the desired molar fraction;
- ii) when the peaks obtained become reproducible, it was considered that the molar fraction desired was accomplished;
- iii) the following peaks were considered as experiments. In agreement, they were integrated and considered for the determination of the heat

involved in the process. The excess molar enthalpy of the decane-octanol binary mixture was determined from the average heat absorbed in at least five concordant injections.

However, for some of the molar fractions, $x_{\text{OctOH}} > 0.55$, the mixing turned out to be very slow and the period between injections had to be increased. With long periods between injections (several hours) the back diffusion of the solvents became problematic and the described methodology had to be adapted.

To overcome the back diffusion problem and still allow for the mixture to be complete, prior to each measurement, two injections are performed, filling the micromixer with the desired molar fraction of octanol-decane mixture, as schematized in figure 3.72 (methodology II).

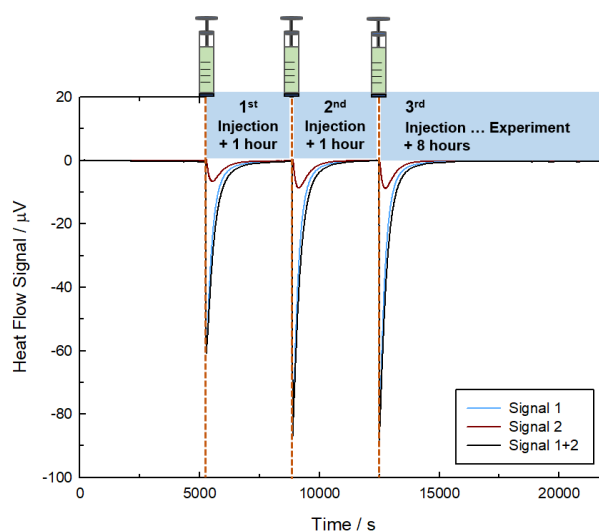


Figure 3.72. Graphical representation of the experimental methodology II used in μ FlowCal calorimeter, to measure the heat of mixing of the binary mixture decane-octanol. Graphical representation of the heat flow signal obtained in μ FlowCal, in a decane-octanol mixture ($x_{\text{OctOH}} = 0.83$), as a function of the experimental time and schematic representation of the three injections performed, exemplifying the methodology used. In each injection both n-decane and 1-octanol are injected simultaneously.

The time spacing between the two injections and between the last injection and the experiment is one hour. This hour is not enough for the mixture to be complete but it is enough for a great part of it. Furthermore, the following injection pushes forward the content of the micromixer. As the content of the calorimeter which was absorbing heat at a certain thermal power is pushed forward, from a methodological point of view, we

can interpret as if there was a sudden jump of the heat flow back to the baseline in the moment of the following injection. In this way, after performing the injection considered “the experiment”, the calorimeter waits for eight hours allowing for the heat flow to return to the baseline. This methodology (methodology II) is considered to be valid, if the integration of this last peak is done considering as baseline only the final part of the curve.

After eight hours, the calorimeter repeats the described cycle (1 injection, 1 hour waiting, 1 injection, 1 hour waiting, 1 injection and eight hours waiting). The heat flow signal and the integrations obtained in these cycles were found to be reproducible. Moreover, this methodology was applied also to some of the lower molar fractions of octanol and the results were similar to the ones obtained using the first methodology. In figure 3.73, the area of integration obtained for the experiments performed using this methodology at $x_{\text{OctOH}} = 0.5$ are compared with the ones obtained with the first methodology, in the chemical calibration experiments. For better comparison, the figure 3.64 is repeated in figure 3.73, displaying also the integration of the peaks related to experiments performed using the experimental methodology II. As depicted in figure 3.73, no significant difference was found between the two methodologies I and II.

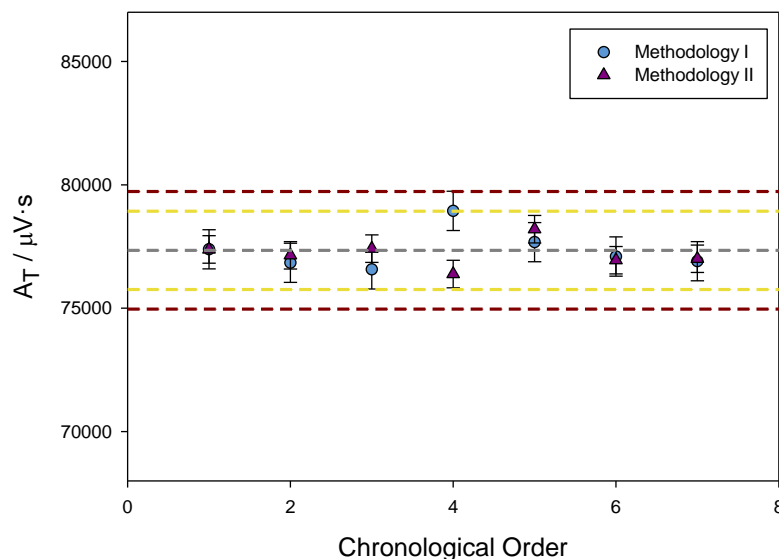


Figure 3.73. Graphical representation of the area of integration of peaks originated by mixtures decane-octanol, at equimolar composition, performed using the two different experimental methodologies (I and II). The error bars represent the standard deviation of the sample ($\pm \sigma$). The grey dashed line represents the average of the experimental data obtained using methodology (I). The lines parallel to the grey dashed line represent the limits of the sample dispersion ($\pm 2 \cdot \sigma$ and $\pm 3 \cdot \sigma$) within 95 % (in yellow) and 99 % (in red) confidence levels (relative to the data obtained using methodology I).

The excess molar enthalpy results of the decane-octanol mixture measured in μ FlowCal calorimeter, at the molar fraction interval $0.06 < x_{\text{OctOH}} < 0.83$, is presented in figure 3.74 as a function of 1-octanol molar fraction. As depicted in figure 3.74, a very good description of the excess molar enthalpy curve is obtained in the molar fractions interval $0.25 < x_{\text{OctOH}} < 0.75$ (in comparison to the experimental data of Christensen and Paz-Andrade research groups [23, 24]). Out of this interval some deviations are present. This is probably due to the fact that in this molar fractions, we are approaching the extremes of the concentration and therefore, methodologically it means that one of the solvent flows is necessarily very low. In addition, it is precisely in this area that there is higher variation of the enthalpy with the molar fraction of the solvents.

In figure 3.74 is also presented the excess molar enthalpy of the decane-octanol binary mixture reported by Featherstone and Dickinson [22]. As already discussed, this data is systematically deviated from the measurements reported by Christensen and Paz-Andrade research groups [23, 24].

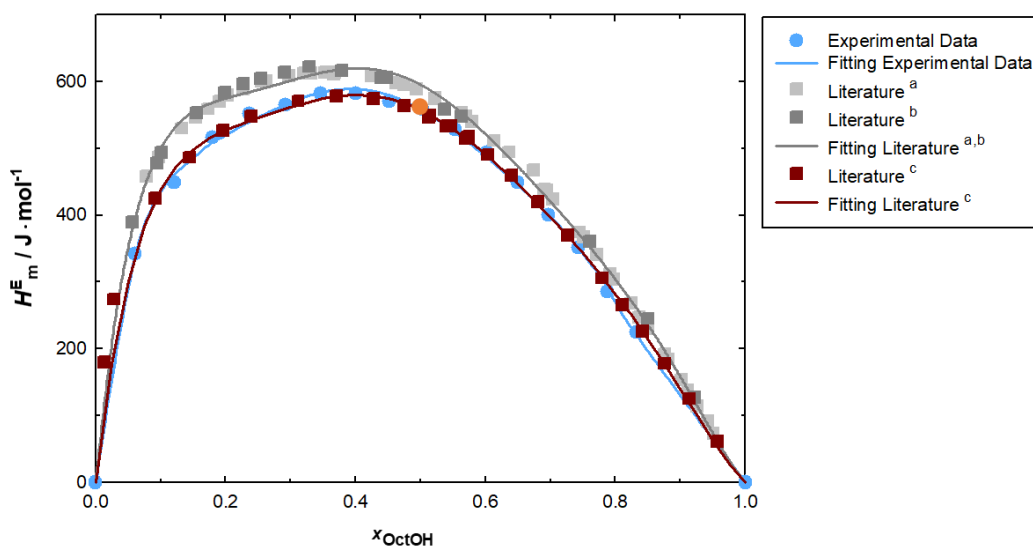


Figure 3.74. Graphical representation of the excess molar enthalpy, obtained in μ FlowCal calorimeter, as a function of the molar fraction of octanol. The constant of calibration obtained by the chemical methodology was used: $(8.65 \pm 0.21) \times 10^{-6} (\text{J} \cdot \text{s}^{-1})/\mu\text{V}$. The calibration point is represented (\bullet). The data existent in the literature is also represented for comparison purposes: a – Christensen and co-workers [23]; b - Paz-Andrade and co-workers [24]; c - Featherstone and Dickinson [22].

3.3.5.3. Comments on the Test Results

Overall, μ FlowCal prototype calorimeter demonstrated a good performance. The determination of the enthalpy of mixing / excess enthalpy of the binary mixture decane-octanol has proven the efficiency of the flow system and of the mixing efficiency of the calorimeter. Some deviations have been found in systems which require very low flows of one component, showing that ideally the calorimeter should not work with very low flows. To work at small concentrations, other calorimetric systems should be used.

Furthermore, an effective methodology has been created to overcome the existence of back-diffusion.

References:

- [1] B. Fegley and R. Osborne, Chapter 4 - An Overview of Calorimetry, Practical Chemical Thermodynamics For Geoscientists, Academic Press, Elsevier, **2013**, p. 87-101.
- [2] L. M. N. B. F. Santos, M. T. Silva, B. Schröder and L. Gomes, Labtermo: Methodologies for the calculation of the corrected temperature rise in isoperibol calorimetry, *J Therm Anal Calorim*, 89 (**2007**) p. 175-180. DOI:10.1007/s10973-006-7509-2.
- [3] J. Suurkuusk, M. Suurkuusk and P. Viikari, Chapter 4 - An Odyssey in Calorimetric Development From Past to Future, Biocalorimetry Foundations and Contemporary Approaches, CRC Press, Taylor & Francis Group, Boca Raton, **2016**, p. 63-78. DOI:10.1201/b20161.
- [4] B. S. Finn, Chapter 3 - Thermoelectricity, Advances in Electronics and Electron Physics, 50, Academic Press, Elsevier, **1980**, p. 175-240. DOI:10.1016/S0065-2539(08)61063-X.
- [5] Calvet and Prat, Recent Progress in Microcalorimetry, First Edition, Pergamon Press, **1963**. ISBN:9781483280134.
- [6] A. S. Morris and R. Langari, Chapter 14 - Temperature Measurement, Measurement and Instrumentation, Academic Press, Elsevier, Boston, **2016**, p. 407-461. DOI:10.1016/B978-0-12-800884-3.00014-9.
- [7] P. Bäckman, M. Bastos, D. Hallén, P. Lönnbro and I. Wadsö, Heat conduction calorimeters: time constants, sensitivity and fast titration experiments, *Journal of Biochemical and Biophysical Methods*, 28 (**1994**) p. 85-100. DOI:10.1016/0165-022X(94)90023-X.
- [8] L. Wadsö, Operational issues in isothermal calorimetry, *Cement and Concrete Research*, 40 (**2010**) p. 1129-1137. DOI:10.1016/j.cemconres.2010.03.017.
- [9] L. Wadsö, Temperature changes within samples in heat conduction calorimeters, *Thermochimica Acta*, 366 (**2001**) p. 121-127. DOI:10.1016/S0040-6031(00)00738-3.
- [10] R. B. Kemp, Chapter 14 - Nonscanning Calorimetry, Handbook of Thermal Analysis and Calorimetry, Vol. 1, Elsevier Science B.V., **1998**, p. 577-675. DOI:10.1016/S1573-4374(98)80017-4.
- [11] F. A. Adediji, D. Lalage, S. Brown, J. A. Connor, M. L. Leung, I. M. Paz-Andrade and H. A. Skinner, Thermochemistry of arene chromium tricarbonyls and the strenghts of arene-chromium bonds, *Journal of Organometallic Chemistry*, 97 (**1975**) p. 221-228. DOI:10.1016/S0022-328X(00)89468-1.
- [12] M. A. V. Ribeiro da Silva, M. A. R. Matos and L. M. P. F. Amaral, Thermochemical study of 2-, 4-, 6-, and 8-methylquinoline, *The Journal of Chemical Thermodynamics*, 27 (**1995**) p. 565-574. DOI:10.1006/jcht.1995.0058.
- [13] L. M. N. B. F. Santos, B. Schröder, O. O. P. Fernandes and M. A. V. Ribeiro da Silva, Measurement of enthalpies of sublimation by drop method in a Calvet type calorimeter: design and test of a new system, *Thermochimica Acta*, 415 (**2004**) p. 15-20. DOI:10.1016/j.tca.2003.07.016.
- [14] L. M. N. B. F. Santos, PhD Thesis, Estudo termodinâmico de algumas β -dicetonas, monotio- β -dicetonas e respetivos complexos metálicos, Universidade do Porto, **1995**.
- [15] J. Suurkuusk and I. Wadsö, A Multichannel Microcalorimetry System, *Chemica Scripta*, 20 (**1982**) p. 155-163.
- [16] I. C. M. Vaz, MSc Thesis, Estudo da Solvatação de Álcoois em Líquidos Iónicos, University of Porto, **2015**.
- [17] M. Görman Nordmark, J. Laynez, A. Schön, J. Suurkuusk and I. Wadsö, Design and testing of a new microcalorimetric vessel for use with living cellular systems and in titration experiments, *Journal of Biochemical and Biophysical Methods*, 10 (**1984**) p. 187-202. DOI:10.1016/0165-022X(84)90039-3.

- [18] G. Bai, L. M. N. B. F. Santos, M. Nichifor, A. Lopes and M. Bastos, Thermodynamics of the Interaction between a Hydrophobically Modified Polyelectrolyte and Sodium Dodecyl Sulfate in Aqueous Solution, *The Journal of Physical Chemistry B*, 108 (2004) p. 405-413. DOI:10.1021/jp036377j.
- [19] L. Capretto, W. Cheng, M. Hill and X. Zhang, Chapter 2 - Micromixing Within Microfluidic Devices, *Microfluidics: Technologies and Applications*, Springer Berlin Heidelberg, Berlin, Heidelberg, 2011, p. 27-68. DOI:10.1007/128_2011_150.
- [20] I. Wadsö and R. N. Goldberg, Standards in Isothermal Microcalorimetry, *Pure Appl. Chem.*, 73 (2001) p. 14. DOI:10.1351/pac200173101625.
- [21] I. Wadsö, Heats of Vaporization for a Number of Organic Compounds at 25°C, *Acta Chemica Scandinavica*, 20 (1966) p. 9. DOI:10.3891/acta.chem.scand.20-0544.
- [22] J. D. B. Featherstone and N. A. Dickinson, Excess enthalpy of n-octanol + n-decane at 293.15, 298.15, 308.15, and 313.15 K, *The Journal of Chemical Thermodynamics*, 9 (1977) p. 75-77. DOI:10.1016/0021-9614(77)90200-2.
- [23] J. J. Christensen, R. M. Izatt, B. D. Stitt, R. W. Hanks and K. D. Williamson, The excess enthalpies of seven n-nonane + alcohol mixtures at 298.15 K, *The Journal of Chemical Thermodynamics*, 11 (1979) p. 1029-1034. DOI:10.1016/0021-9614(79)90133-2.
- [24] A. Amigo, J. L. Legido, R. Bravo and M. I. Paz-Andrade, Excess molar enthalpies of (n-octan-1-ol + an n-alkane) at 298.15 K and 308.15 K, *The Journal of Chemical Thermodynamics*, 22 (1990) p. 633-638. DOI:10.1016/0021-9614(90)90016-J.
- [25] S. H. Tanaka, H. I. Yoshihara, A. W.-C. Ho, F. W. Lau, P. Westh and Y. Koga, Excess partial molar enthalpies of alkane-mono-ols in aqueous solutions, *Canadian Journal of Chemistry*, 74 (1996) p. 713-721. DOI:10.1139/v96-077.
- [26] M. I. Davis and E. S. Ham, Analysis and interpretation of excess molar properties of amphiphile + water systems: Part 2. Comparisons of the propanol isomers in their aqueous mixtures, *Thermochimica Acta*, 190 (1991) p. 251-258. DOI:10.1016/0040-6031(91)85251-C.
- [27] L.-E. Briggner and I. Wadsö, Test and Calibration Processes for Microcalorimeters with Special Reference to Heat Conduction Instruments Used with Aqueous Systems, *Journal of Biochemical and Biophysical Methods* 22 (1991) p. 101-118. DOI:10.1016/0165-022X(91)90023-P.
- [28] R. Sabbah, A. Xu-wu, J. S. Chickos, M. L. P. Leitão, M. V. Roux and L. A. Torres, Reference materials for calorimetry and differential thermal analysis, *Thermochimica Acta*, 331 (1999) p. 93-204. DOI:10.1016/S0040-6031(99)00009-X.
- [29] Reiser, Birch and Mathlouthi, Chapter 8 - Physical Properties, *Sucrose Properties and Applications* Springer-Science + Business Media, BV, 1995, p. 186-221. DOI:10.1007/978-1-4615-2676-6.

CHAPTER 4

Results and Discussion

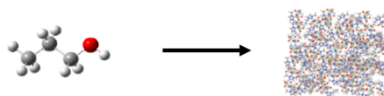
Solvation of Alcohols in Ionic Liquids

-
- 4.1. Study of the Anion and Cation Effect on the Solvation of Alcohols in Ionic Liquids
 - 4.2. Exploration of the Fluorination / Acidity Effect of the Alcohol in Ionic Liquids
 - 4.3. The Effect of the Alkyl Chain Length on the Solvation of Alcohols in Ionic Liquids
 - 4.4. Enthalpy of Mixing of a Binary Mixture of Alcohol – IL
- References
-

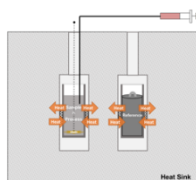
4. Results and Discussion

This section presents an overview of the main results and achievements of this PhD, regarding the study of ionic liquids and particularly its solvation using alcohols as molecular probes. The presented results and discussion will be presented in different subchapters highlighting the role of the anion and the cation, the effect of the alcohol acidity/fluorination in the solvation of alcohols in ionic liquids and the effect of the alkyl chain length of the alcohols and the cation. By last, a preliminary study of a binary mixture alcohol-IL made in μ FlowCal will be presented together with literature data on the topic aiming to show the feasibility of the μ FlowCal to explore the effect of the concentration of the alcohol and thus, access the structuration and energetics of binary mixtures containing ionic liquids.

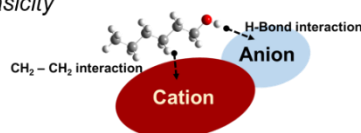
Solvation of Alcohols in Ionic Liquids



Infinite Dilution Conditions



1. Effect of the Cation Nature and Anion Basicity
2. Effect of the Alcohol Acidity
3. Effect of the Alkyl Chain Length



4. Effect of the Alcohol Concentration

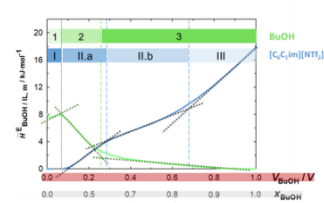
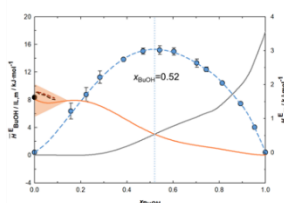
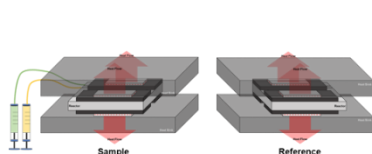


Figure 4.1. Schematic representation of the strategy used in this thesis to study the solvation of alcohols in ionic liquids.

4.1. Study of the Anion and Cation Effect on the Solvation of Alcohols in Ionic Liquids

In this section is presented the study of the effect of the nature of the cation and anion basicity, in the solvation properties of ionic liquids. The standard molar enthalpy of solution of 1-propanol (PrOH) in ionic liquids constituted by different cations and anions will be presented and discussed. In the context of this PhD thesis, some results which have been obtained previously will be revisited and complemented with quantum chemical calculations allowing a deeper interpretation of the results.

In addition, some results obtained by molecular dynamics simulations, in a collaboration with José N. Canongia Lopes and Carlos E. S. Bernardes, were used in the analysis of the results aiming to gain further molecular insights into the alcohol-anion interaction and its effect on the solvation of alcohols in ionic liquids.

In summary, the results presented in this subchapter reveal the work performed by the author and some collaborative work. The author of this thesis has done the experimental determinations, the quantum chemical calculations and contributed to the data analysis, discussion of the results and writing of a manuscript, on the topic, under the name “Solvation of alcohols in ionic liquids – understanding the effect of the anion and cation” which has been already published^[1].

The strategy used to determine the effect of the anion and cation in the solvation properties of ionic liquids, using alcohols as molecular probes will be addressed. The main results obtained in the topic will be presented and discussed.

4.1.1. Strategy

To study the effect of the anion basicity and the cation nature in the solvation of alcohols in ionic liquids, a simple alcohol, PrOH was used as a molecular probe for the study of solvation in ionic liquids. The purpose of this study is to unveil the potentials of interaction existent in the polar domains of the ionic liquids to interact with a polar and hydrogen donor/acceptor group, as the hydroxyl group of an alcohol.

To accomplish that purpose, a group of different ILs, constituted by different cations and anions was studied, maintaining the number of carbons in the cation alkyl chain not bigger than 4 carbons and by doing so, restraining the alcohols-ILs interactions to the sphere of influence of the polar network, schematically represented in figure 1.3 on the Introduction of this thesis.

Aiming to study the effect of the cation nature, ionic liquids constituted by the [NTf₂] anion and the following different cations were studied: [C₄C₁im], [C₄py], [C₄C₁pip], [C₄C₁pyrr] and [C₃C₁C₁im]. In addition, ionic liquids constituted by the [FAP] anion and two different cations, [C₄C₁pyrr] and [C₄C₁im] were also studied complementing the study of the cation nature effect. Regarding the study of the anion effect, ionic liquids constituted by the [C₄C₁im] cation and the following different anions were studied: [NTf₂], [PF₆], [FAP], [DCA] and [TFA].

Using isothermal titration calorimetry (ITC), the standard molar enthalpy of solution of PrOH at infinite dilution in different ionic liquids was determined. From the calculation of standard molar enthalpy of solution of PrOH at infinite dilution and the standard molar enthalpy of vaporization of PrOH^[2], the standard molar enthalpy of solvation at infinite dilution was determined. In figure 4.2 is presented a schematic overview of the alcohol-IL systems studied / strategy followed, in the context of this work.

Solution & Solvation in Ionic Liquids

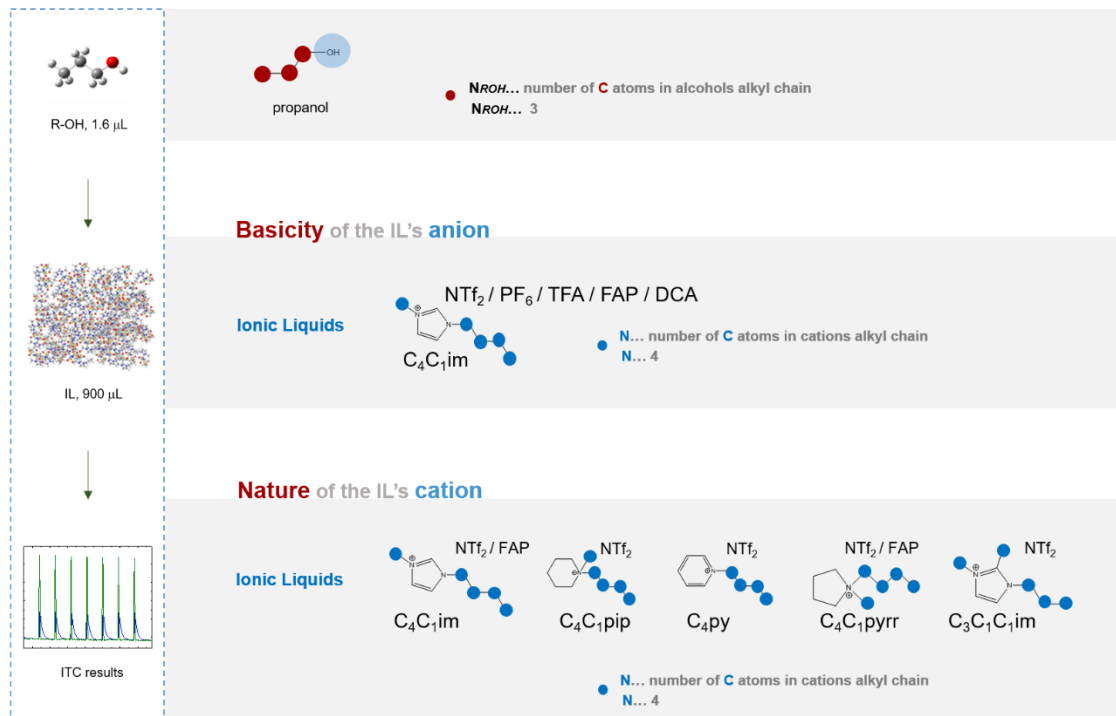


Figure 4.2. Scheme of the strategy used to evaluate the effect of the basicity of the anion and the nature of the cation in the solution / solvation of alcohols in ionic liquids.

For a better interpretation of the enthalpy of solvation results, the energy of interaction in the gas phase between the PrOH and the different anions (figure 4.3) was evaluated using quantum chemical calculation (Gaussian 09 software package^[3]) and correlated with the correspondent enthalpy of solvation. The quantum chemical calculations were performed using the density functional theory (DFT)^[4, 5] with the hybrid exchange correlation functional B3LYP and the 6-311++G(d,p) basis set. The obtained energy of interaction have been corrected to basis set superposition error (BSSE) by the counterpoise method^[6, 7] and the modification in the optimized geometry by the formation of the dimer was considered.

Molecular dynamics simulations of an infinite-dilution solution of PrOH in ionic liquids constituted by different anions were done. The simulation boxes contained 90 ion pairs and 1 molecule of alcohol. The detailed description of the simulations performed is reported in the literature ^[1].

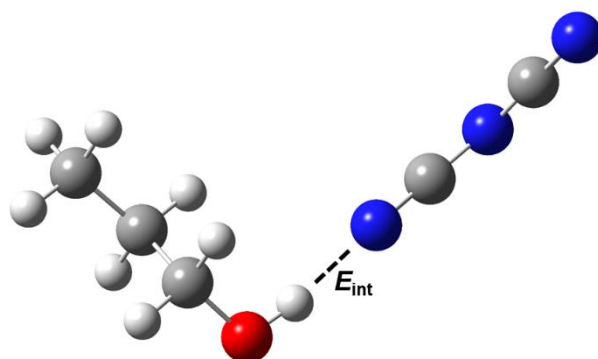


Figure 4.3. Scheme of the pair alcohol-anion (PrOH-DCA) in the gas phase, which interaction energy was evaluated by quantum chemical calculations.

4.1.2. Results and Discussion

The experimental results of the standard ($p^0 = 0.1$ MPa) molar enthalpy of solution of 1-propanol, at infinite dilution, in the ionic liquids studied, at the reference temperature ($T = 298.15$ K), are listed in table 4.1. The uncertainty of the results was calculated from the propagation of the uncertainty associated to the calibration constant, to the injected volume and to the integration of the peaks of the experiments ($\pm 2 \cdot \sigma \cdot n^{-1/2}$). Together with these results, are provided the derived standard molar enthalpies of solvation of 1-propanol in ILs at infinite dilution. The uncertainty of the results was calculated from the propagation of the uncertainty associated to the enthalpy of solution and the enthalpy of vaporization. The same results will be presented in graphical representations in figures 4.4 and 4.6.

Table 4.1. Summary of the standard molar enthalpy of solution and solvation, at infinite dilution, of PrOH in ILs constituted by different cations and anions, at the reference temperature ($T = 298.15$ K), obtained experimentally in ITC, and comparison with correspondent data reported in the literature

Ionic Liquid	$\Delta_{\text{soln}} H_{\text{m, exp}}^{0, \infty} / \text{kJ} \cdot \text{mol}^{-1}$	$\Delta_{\text{solv}} H_{\text{m, exp}}^{0, \infty} / \text{kJ} \cdot \text{mol}^{-1}$	$\Delta_{\text{soln}} H_{\text{m, lit}}^{0, \infty} / \text{kJ} \cdot \text{mol}^{-1}$
[C ₄ C ₁ im][NTf ₂]	8.37 ± 0.24	-39.08 ± 0.27	12.6^a ,
[C ₄ py][NTf ₂]	8.56 ± 0.26	-38.89 ± 0.28	
[C ₄ C ₁ pip][NTf ₂]	8.71 ± 0.26	-38.74 ± 0.29	8.04^b ; 8.11^c
[C ₄ C ₁ pyrr][NTf ₂]	8.57 ± 0.26	-38.88 ± 0.28	
[C ₃ C ₁ C ₁ im][NTf ₂]	9.67 ± 0.19	-37.78 ± 0.23	
[C ₄ C ₁ im][FAP]	10.78 ± 0.42	-36.67 ± 0.44	
[C ₄ C ₁ pyrr][FAP]	12.46 ± 0.81	-34.99 ± 0.82	
[C ₄ C ₁ im][TFA]	-0.42 ± 0.11	-47.87 ± 0.16	
[C ₄ C ₁ im][DCA]	2.80 ± 0.13	-44.65 ± 0.18	
[C ₄ C ₁ im][PF ₆]	11.02 ± 0.22	-36.43 ± 0.25	9.875^d ; 11.6^e ; 6.2385^f ; 10.81^g

a – obtained from activity coefficients (312 to 385 K), ref [8];

b – obtained from activity coefficients (308 to 358 K), ref [9];

c – determined by ITC (298.15 K), ref [10];

d – determined by ITC (298.15 K), ref [11];

e – obtained from activity coefficients (293 to 353 K), ref [12];

f – obtained from activity coefficients (313 to 333 K), ref [13];

g – obtained from activity coefficients (316 to 335 K), ref.[14].

In table 4.1 is also presented the data reported in the literature regarding the molar enthalpy of solution of 1-propanol, at infinite dilution, in the studied ILs. The results of the enthalpy of solution derived from activity coefficients were based on the measurements at different temperatures and do not correspond to a direct measurement (like calorimetry). For that reason they are listed but were not used for direct comparison. Regarding the enthalpy of solution measured by calorimetry, at 298.15 K, reported in the literature, it was found out that the data previously reported^[10, 11] seems to be slightly lower than our experimental results. The results were obtained using the ITC described in this thesis, using the same calibration, testing and experimental procedures. It is worth of notice that large dispersion of the enthalpy of solution at infinite dilution in ILs can be found amongst different authors and methods^[15, 16]. As it will be shown later, in other measurements performed in ITC, large deviations, both positive and negative were found towards our results.

The discussion and analysis of the results of solvation of propanol in the different ionic liquids will be based in the enthalpy of solvation or solution. In these systems, the difference between the enthalpy of solution or solvation is just a scale effect caused by the subtraction of the enthalpy of vaporization of the 1-propanol.

4.1.2.1. Effect of the Cation Nature

In figure 4.4 the enthalpy of solvation of 1-propanol in different ionic liquids is presented as a function of the IL cation. Regarding the standard molar enthalpy of solvation, at infinite dilution of 1-propanol in the [cation][NTf₂] IL series, no significant dependence of the solvation enthalpy with the cations imidazolium (im), pyridinium (py), piperidinium (pip) and pyrrolidinium (pyrr) was found. An exception was found for the standard molar enthalpy of solvation at infinite dilution of 1-propanol in [C₃C₁C₁im][NTf₂] which behaves like an outlier in this IL series.

In opposition to the results found in the [cation][NTf₂] IL series, the standard molar enthalpy of solvation at infinite dilution of 1-propanol in [C₄C₁pyrr][FAP] is significantly higher than the standard molar enthalpy of solvation at infinite dilution of 1-propanol in [C₄C₁im][FAP], as is evident in figure 4.4. Furthermore, it was found that the enthalpy of solvation of 1-propanol at infinite dilution in the [cation][FAP] IL series is less exothermic than in the [cation][NTf₂] IL series.

These results could be interpreted considering the model of solvation described in the introduction of this thesis. Accordingly, the enthalpy of solvation at infinite dilution

could be interpreted as an interplay between the energetics involved in two processes: i) cavitation of the ionic liquid (endothermic); ii) interactions established between the alcohol and the ionic liquids (exothermic). In accordance, the increase in the exothermic character of the enthalpy of solvation from the [cation][FAP] IL series to the [cation][NTf₂] IL series could be interpreted as a consequence of the decrease in the cavitation energy, an increase in the alcohol–IL interactions or a combination of both.

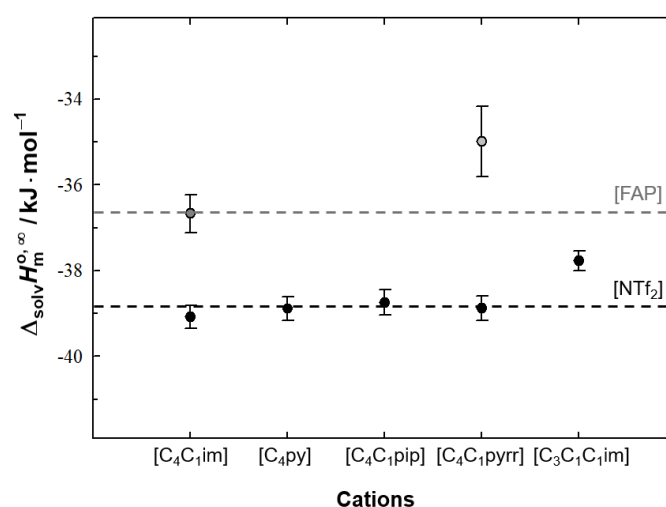


Figure 4.4. Graphical representation of the standard molar enthalpy of solvation, at infinite dilution, of PrOH in different ionic liquids, at the reference temperature ($T = 298.15$ K), as a function of the IL cation. The standard molar enthalpy of solvation of PrOH in the two different IL families is differentiated by colour: • [cation][FAP] and • [cation][NTf₂]. The dashed lines represented are just a guide line to the eyes.

As the solute is the same, the volume of the cavitation of the IL necessary to accommodate the alcohol is near the same. As a result, the cavitation energy should be similar in both IL families, differing only due to the differences in the cohesive energies / internal pressure of both ILs. Nevertheless, slightly higher cohesive energies are expected for the [cation][NTf₂] IL series ($\Delta^9 H_m^0$ [C₄C₁im][NTf₂] = 139 kJ · mol⁻¹)^[17] in comparison to the [cation][FAP] IL series ($\Delta^9 H_m^0$ [C₄C₁im][FAP] = 134 kJ · mol⁻¹)^[18]. This phenomena could lead to a weakly higher cavitation energy in the [cation][NTf₂] IL series, which would cause a less exothermic enthalpy of solvation in this series. As the opposite was verified (enthalpy of solvation of PrOH is more exothermic in the [cation][NTf₂] IL

series), it is assumed that the magnitude of the alcohol-IL interactions is higher in the [cation][NTf₂] IL series.

This is not surprising as the [NTf₂] anion has a higher hydrogen bond basicity than the [FAP] anion and thus, is a better hydrogen bond acceptor and may be interacting with the hydroxyl group of the alcohol by hydrogen bond. The higher hydrogen bond basicity of this anion is evidenced in the results of the hydrogen-bond interaction energy reported by Freire et al.^[19] in equimolar cation–anion mixtures obtained by COSMO-RS. The authors reported a hydrogen-bond interaction energy of $E_{\text{HB}} = -0.74 \text{ kJ}\cdot\text{mol}^{-1}$ for [C₄C₁im][FAP] and a hydrogen-bond interaction energy of $E_{\text{HB}} = -9.86 \text{ kJ}\cdot\text{mol}^{-1}$ for [C₄C₁im][NTf₂]. The effect of the cation nature verified in the [cation][FAP] / [cation][NTf₂] IL series may also be explained in the light of these results reported by Freire et al.^[19].

As described in the Introduction of this thesis, the acidity of ionic liquids constituted by the same anion, depends on the nature of the cation and follows the trend imidazolium > pyridinium > pyrrolidinium > piperidinium. Therefore, the higher exothermic enthalpy of solvation found in the [C₄C₁im][FAP], when compared to the [C₄C₁pyrr][FAP], may be explained by a stronger alcohol-cation interaction in the case of the imidazolium (im) cation. This higher interaction alcohol-imidazolium is not evident in the [cation][NTf₂] IL series. However, regarding the intermolecular interactions in the net IL, Caudio et al.^[19] have estimated a hydrogen-bond interaction energy of $E_{\text{HB}} = -9.86 \text{ kJ}\cdot\text{mol}^{-1}$ for [C₄C₁im][NTf₂], which is almost negligible in the case of the [C₄C₁im][FAP]. Therefore, we propose that either the [NTf₂] anion competes with the hydroxyl group of the alcohol for hydrogen-bond interactions with the cation or the hydroxyl group of the alcohol is preferentially interacting with the anion by hydrogen bond interaction and its interactions with the cation are negligible.

Welton et al.^[20] have already reported a decrease in the Kamlet-Taft α parameter, which describes the hydrogen bond acidity of the solvent, accompanied by the increase of the β parameter, which describes the hydrogen bond basicity of the solvent. The author had attributed these results to the existence of a competition between the probe and the anion for the hydrogen bond donor site of the cation, which had already been suggested also in a previous paper^[21]. Furthermore, trying to explain some differences found in the literature, verified using different probes, the authors have proposed that common molecular solutes would be less apt for probe these small differences in the acidity of the ionic liquids than the zwitterionic betaine no. 30. In accordance, it is expectable that, even though the [NTf₂] anions does not belong to the group of the most

basic anions, it is basic enough to compete with the hydroxyl group of the PrOH for the hydrogen bond donor site of the cation.

The literature data regarding the Kamlet-Taft α parameter obtained using the solvatochromic methodology^[20], as well as, using the COSMO-RS methodology^[22] evidence a decrease in the hydrogen bond acidity of the ionic liquid caused by the methylation in the C(2) position (carbon situated between the nitrogen atoms) of the imidazolium ring. This decrease in the acidity of the cation may lead to a decrease in the cation – alcohol interaction, leading to a less exothermic enthalpy of solvation of PrOH in [C₃C₁C₁im][NTf₂] in comparison to [C₄C₁im][NTf₂]. However, this cannot be the only explanation as the hydrogen bond acidity of pyrrolidinium and piperidinium is lower and the enthalpy of solvation of PrOH in ionic liquids constituted by these cations was in the same magnitude of the [C₄C₁im] imidazolium cation, as depicted in figure 4.5.

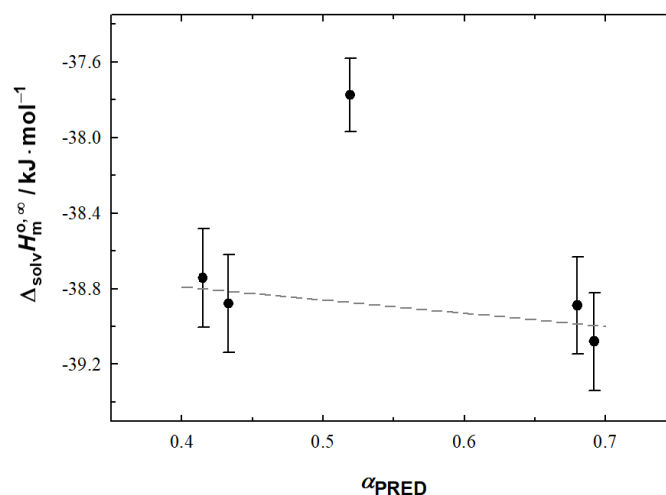


Figure 4.5. Graphical representation of the standard molar enthalpy of solvation, at infinite dilution, of PrOH in [cation][NTf₂] ionic liquid series, at the reference temperature ($T = 298.15 \text{ K}$), as a function of the hydrogen bond acidity of the ionic liquids predicted by COSMO-RS by Freire et al.^[22]. The line is just a guide line to the eyes.

The effect of the methylation in the C(2) position of the imidazolium cation into the properties of the ionic liquid has been object of discussion^[23-25]. The group where this thesis has been conducted has proved that the decrease of the hydrogen bond interaction, did not alter significantly the cohesive energy of the IL ($\Delta_l^0H_m^0$ [C₃C₁C₁im][NTf₂] = 140 kJ·mol⁻¹). It has been reported that the methylation in the

C(2) position of the imidazolium cation decreases the number of possible positions of the anion around the cation ^[23-25], directly affecting the anion–cation dynamics. We estimate that this effect indirectly decreases the alcohol to cation / anion interaction by reducing the number of possible conformers for the alcohol–anion and alcohol-cation interaction, reducing the overall alcohol–IL interaction.

4.1.2.2. Effect of the IL Anion Nature

In the analysis of the effect of the cation in the solvation of alcohols in ionic liquids, a predominant effect of the anion over the cation was suggested. The analysis of the effect of the anion nature and in particular, the effect of the anion basicity brings light into the subject, giving insights into the solvation phenomena and allowing the understanding of the obtained results.

In figure 4.6 is represented the standard molar enthalpy of solvation at infinite dilution of 1-propanol in [C₄C₁im][anion] ionic liquids as a function of the IL anion, which are ordered in function of its basicity: [FAP] < [PF₆] < [NTf₂] < [DCA] < [TFA], following the scale for the hydrogen-bond basicity of ionic liquids proposed by Freire et al.^[19]. This graphical representation highlights the existence of an increasingly exothermic enthalpy of solvation of 1-propanol in the following order: [FAP] ~ [PF₆] < [NTf₂] < [DCA] < [TFA], which is in line with the increase of the hydrogen-bond basicity of the IL anion. At this point, is important to notice that this trend is in accordance with the difference found previously in the enthalpy of solvation of PrOH in [cation][NTf₂] and [cation][FAP] IL series.

Taking into account the model of the solvation already discussed, the increase in the exothermic character of the enthalpy of solvation as the hydrogen basicity of the anions increase could be interpreted as a consequence of the decrease in the cavitation energy, an increase in the alcohol–IL interactions or a combination of both.

To distinguish between these two factors, the standard molar enthalpy of solvation at infinite dilution of 1-propanol in the referred ILs was related with the hydrogen bond basicity of the ionic liquids using the hydrogen-bond interaction energy in an equimolar cation–anion mixture, reported by Freire et al.^[19], and Kamlet-Taft solvatochromic β parameters obtained with the pair of solvatochromic dyes: N,N-diethyl-4-nitroaniline / 4-nitroaniline^[19, 20, 26-28]. In figure 4.7, the relation between the standard molar enthalpy of solvation at infinite dilution of PrOH in [C₄C₁im][Anion] and the referred data is presented.

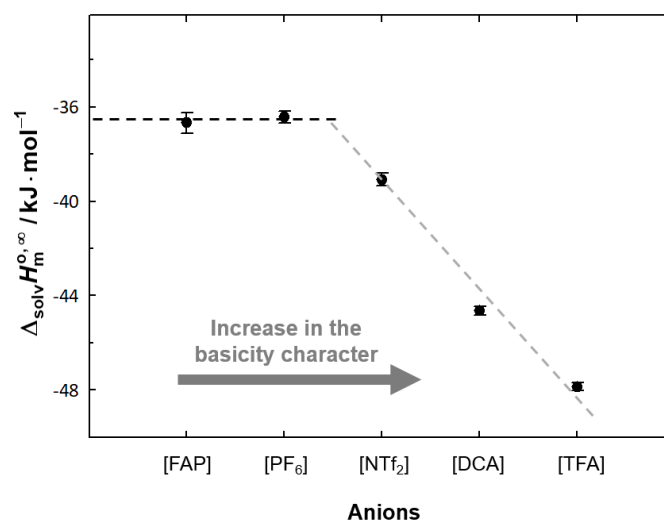


Figure 4.6. Graphical representation of the standard molar enthalpy of solvation, at infinite dilution, of PrOH in $[\text{C}_4\text{C}_{1\text{im}}][\text{Anion}]$ ionic liquid series, at the reference temperature ($T = 298.15 \text{ K}$), as a function of the IL anion. The anions are ordered in crescent hydrogen bond basicity following the scale for the hydrogen bond basicity of ionic liquids proposed by Freire et al.[19]. The lines are just a guide line to the eyes.

In figure 4.7, the existence of a good correlation between the standard molar enthalpy of solvation at infinite dilution of 1-propanol in the $[\text{C}_4\text{C}_{1\text{im}}][\text{anion}]$ IL series and the hydrogen bond basicity of the ionic liquid is evidenced. Therefore, the results obtained seem to suggest the existence of a significant hydrogen bond interaction between the anion and the alcohol studied (PrOH). To verify the existence of a relation between these two energies, quantum chemical calculations were performed to determine the energy of interaction, E_{int} ($\text{kJ} \cdot \text{mol}^{-1}$), in the gas phase, between the alcohol and the anion. The obtained results are summarized in the Appendix C of this thesis together with a picture of the geometry at the absolute minimum of the alcohol-anion energy potential, in the gas phase.

In figure 4.8, the standard molar enthalpy of solvation at infinite dilution of PrOH in $[\text{C}_4\text{C}_{1\text{im}}][\text{Anion}]$ is plotted against the energy of interaction between the alcohol and the anion in the gas phase, E_{int} . For comparison purposes, the interaction energy, E_{int} , of the molecules PrOH-PrOH and PrOH-propano, in the gas phase, was calculated using the same methodology used in anion-alcohol calculations and is also represented. Two indicative lines were included in the representation: the estimated value of the enthalpy of solvation of 1-propanol in 1-propanol (horizontal red dashed line) and the enthalpy of

solvation of 1-propanol in alkanes (horizontal grey dashed line). The enthalpy of solvation at infinite dilution of PrOH in alkanes was obtained from the enthalpy of solution at infinite dilution of 1-propanol in n-nonane and n-pentane, derived from the data reported by Christensen et al.^[29, 30]. To estimate, the enthalpy of solvation of 1-propanol in 1-propanol, its condensation from the vapour phase to the liquid 1-propanol phase, was considered. Therefore, the value used as the enthalpy of solvation of 1-propanol in 1-propanol is the symmetric of its enthalpy of vaporization (enthalpy of condensation)^[2].

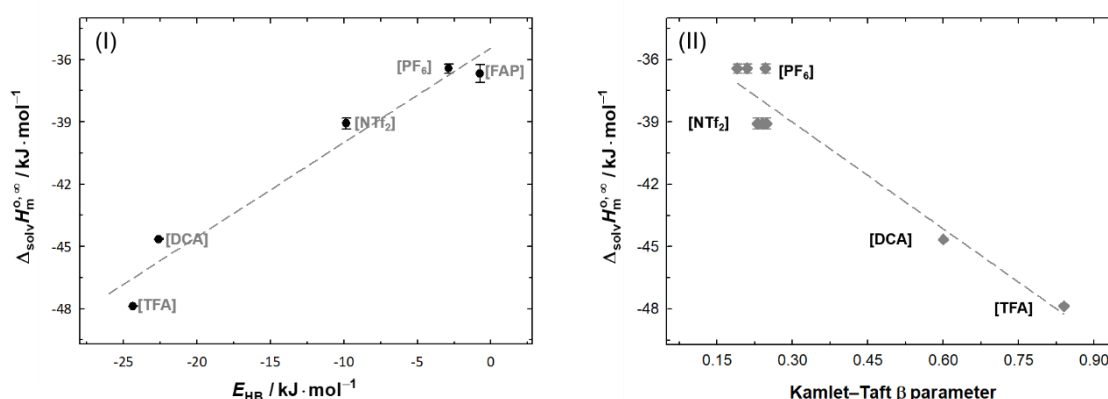


Figure 4.7. Graphical representation of the standard molar enthalpy of solvation, at infinite dilution, of PrOH in $[\text{C}_4\text{C}_{1\text{im}}][\text{Anion}]$ ILs, at the reference temperature ($T = 298.15 \text{ K}$), as a function (I) of the hydrogen-bond interaction energy in an equimolar cation–anion mixture (obtained by COSMO-RS), reported by Freire et al.^[19], and (II) Kamlet–Taft β parameters obtained with N,N-diethyl-4-nitroaniline and 4-nitroaniline solvatochromic dyes^[19, 20, 26–28]. The dashed lines correspond to the linear fitting of the represented data. (I) Fitting: $\Delta_{\text{solv}} H_m^{0,\infty} = 0.455 (\pm 0.056) \cdot E_{\text{HB}} - 35.44 (\pm 0.88)$; (II) Fitting: $\Delta_{\text{solv}} H_m^{0,\infty} = -17.1 (\pm 1.9) \cdot \beta - 33.88 (\pm 0.78)$.

Excluding the $[\text{PF}_6]$ anion, an excellent correlation ($R^2 = 0.996$) was found between the quantities represented. The complex geometry and location of the $[\text{PF}_6]$ anion was slightly deviated from the path of the absolute minimum of the energy potential, in order to minimize the contribution of the interaction between the $[\text{PF}_6]$ anion and the alkyl moieties of the alcohol. Nonetheless, the energy of interaction of the $[\text{PF}_6]$ anion with 1-propanol obtained was still higher than that predicted by the correlation. The linear fitting of the data (excluding the $[\text{PF}_6]$ anion) is given by the following equation:

$$\Delta_{\text{solv}} H_m^{0,\infty} (\text{kJ} \cdot \text{mol}^{-1}) = 0.242 \cdot E_{\text{int}} - 32.31. \quad (4.1)$$

The excellent correlation found between the enthalpies of solvation at infinite dilution and the interaction energy of the alcohol and the anion in the gas phase strongly suggests that the differences in the enthalpy of solvation of 1-propanol in these different ILs are ruled by the alcohol–IL interaction and that the cavitation energy caused by the solvation of this alcohol in the various ILs is nearly constant.

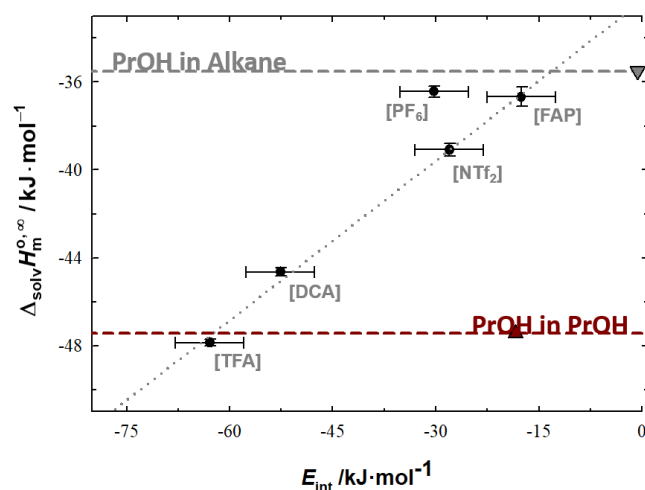


Figure 4.8. Graphical representation of the standard molar enthalpy of solvation, at infinite dilution, of PrOH in $[\text{C}_4\text{C}_1\text{im}][\text{Anion}]$ ILs, at the reference temperature ($T = 298.15 \text{ K}$), as a function of the energy of interaction between the alcohol and the anion in the gas phase. The grey dotted line is a linear fitting of the data excluding the $[\text{PF}_6]$ anion. Fitting: $\Delta_{solv} H_m^{0,\infty} = 0.242 (\pm 0.010) \cdot E_{\text{HB}} - 32.31 (\pm 0.45)$. The dashed horizontal lines represent the enthalpy of solvation of PrOH in itself (red) and in an alkane (grey). The up and down triangles represent the interaction energy in the gas phase between two PrOH molecules (\blacktriangle) and between PrOH and an alkane (\blacktriangledown).

At this point, it is interesting to consider the hypothetical scenario in which there is no hydrogen bond interaction between the anion and the alcohol. Considering the linear fitting presented in figure 4.8, equation 4.1, in a scenario of no interaction between the anion and the alcohol, $E_{\text{int}} = 0 \text{ kJ} \cdot \text{mol}^{-1}$. Accordingly, the estimated value for the enthalpy of solvation would be $\Delta_{solv} H_m^{0,\infty} = -32.31 \text{ kJ} \cdot \text{mol}^{-1}$. Curiously, this value is not far from the value estimated for the enthalpy of solvation of 1-propanol in an alkane, $\Delta_{solv} H_m^{0,\infty} = -35.5 \text{ kJ} \cdot \text{mol}^{-1}$. In our point of view, this means that considering this model, in a limiting situation where there is no significant hydrogen bond interaction between the anion and the alcohol, the ionic liquid would interact with 1-propanol similarly to an alkane, i.e., through dispersive interactions. This is an evidence of the preferential

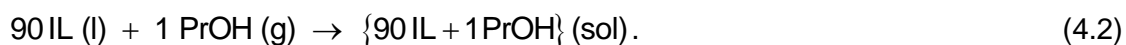
location of the alcohol close to the anion interacting preferentially with this specie by hydrogen bond.

To gain further molecular insights into the alcohol-anion interaction and its effect on the solvation of alcohols in ionic liquids, a series of molecular dynamics (MD) simulations were performed by Carlos E. S. Bernardes and José N. Canongia Lopes, in collaboration.

Similarly to the calorimetric experiments, the simulations were performed for solutions of 1-propanol in ionic liquids constituted by the cation [C₄C₁im] and different anions: [TFA], [DCA], [PF₆], [FAP] and [NTf₂]. Two types of analyses were conducted using the MD simulations:

- (i) the capability of the model to reproduce the trends in the experimental enthalpies of solvation of 1-propanol in different ionic liquids;
- (ii) the structural modifications that occurred when one 1-propanol molecule is solvated by different IL ions.

The standard ($p^\circ = 0.1$ MPa) molar enthalpy of solvation at infinite dilution of 1-propanol in ionic liquids was modelled using one alcohol molecule and 90 ion pairs, as described in the following reaction:



The standard molar enthalpy of solvation at infinite dilution is obtained from the difference of the following quantities, obtained from the MD simulation result: internal molar configurational energies of the solution, $E_{\text{cfg}}(\text{sol})$, internal molar configurational energies of the pure IL in its liquid phase, $E_{\text{cfg}}(\text{IL, l})$, and 1-propanol in the gas phase, $E_{\text{cfg}}(\text{PrOH, g})$, as expressed in the following equation:

$$\Delta_{\text{solv}} H_m^{\circ, \infty} = E_{\text{cfg}}(\text{sol}) - E_{\text{cfg}}(\text{IL, l}) - E_{\text{cfg}}(\text{PrOH, g}) - RT, \quad (4.3)$$

where $T = 298.15$ K is the temperature and R (J·mol⁻¹·K⁻¹) is the gas constant^[31]. As evidenced in equation 4.3 the standard molar enthalpy of solvation at infinite dilution obtained from the MD simulation is calculated from the subtraction of $E_{\text{cfg}}(\text{sol})$ and $E_{\text{cfg}}(\text{IL, l})$, which are very large quantities. These two values were calculated with standard deviations in the 0.1–1% range. However, due to the magnitude of the values involved, it results in standard deviation intervals, regarding the standard molar enthalpy

of solvation at infinite dilution obtained from the MD simulation, of around $50 \text{ kJ}\cdot\text{mol}^{-1}$ which are in the same order of magnitude of the values of enthalpy of solvation obtained. The intrinsic lack of precision of the MD results was partially compensated by the use of multiple independent simulation runs (24) that on aggregation terms allows the calculation of an average $\Delta_{\text{solv}}H_m^{0,\infty}$ value with relatively good resolution, as it can be seen in figure 4.9.

In this figure, the standard molar enthalpy of solvation at infinite dilution obtained from the MD simulation is represented against the experimental results. The figure evidences that the results of the two quantities present the same trend and are of the same order of magnitude. Together with this representation a plot of the histogram analysis of the values of the standard molar enthalpy of solvation at infinite dilution of PrOH in $[\text{C}_4\text{C}_1\text{im}][\text{TFA}]$ obtained by MD simulation is represented, evidencing a wide Gaussian distribution centred at approximately $-60 \text{ kJ}\cdot\text{mol}^{-1}$ with standard deviation intervals on the same magnitude ($61.1 \pm 59.6 \text{ kJ}\cdot\text{mol}^{-1}$).

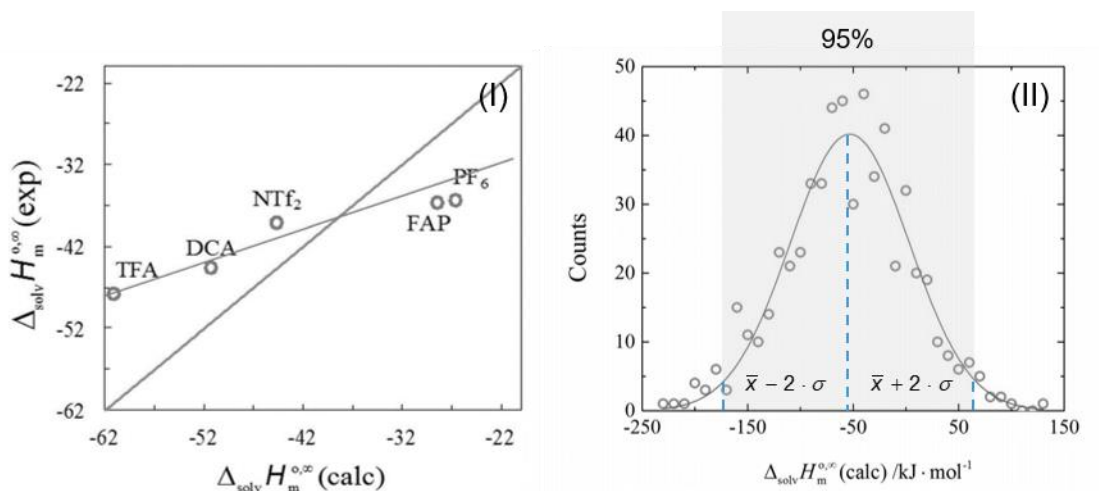


Figure 4.9. (I) Graphical representation of the standard molar enthalpy of solvation, at infinite dilution, of PrOH in ILs of the series $[\text{C}_4\text{C}_1\text{im}][\text{Anion}]$ obtained experimentally against the same values obtained by MD simulations. The line that correlates both quantities is represented, as well as, a hypothetical 1 to 1 correlation for comparison purposes. (II) Plot of the histogram analysis of the 576 values of the standard molar enthalpy of solvation, at infinite dilution, of PrOH in $[\text{C}_4\text{C}_1\text{im}][\text{TFA}]$, obtained by MD simulations.

As demonstrated, the precision of the MD simulations is poor but the accuracy seems to be meaningful and capturing the magnitude and trend of the experimental

results. Therefore, it is considered that the interactions and structural modifications that occur during the solvation of the alcohol molecule in the midst of the ionic liquid solvents are well captured by the simulations.

In figure 4.10 several radial distribution functions (RDFs) between the IL and the alcohol molecule are represented. Figure 4.10 a) shows the RDFs found between the centre of charge of the cation (defined as the centre of mass of the imidazolium ring) and the hydrogen atom of the hydroxyl group of 1-propanol. The figure suggests that in the different ionic liquids studied, the interactions established between the cation and the alcohol are apparently equivalent independently of the anion that constitutes the IL. The differences observed in the intensities of the peaks result from the dilution effects caused by the different molar volumes of the anions (in ILs with bulkier anions the numerical density of the cations is lower).

In opposition, from the analysis of figure 4.10 b), which shows the RDFs found between the hydrogen atom of the hydroxyl group of 1-propanol and the most electronegative atoms in the anions, is evident a dependence on the position of the first contact peak with the anions that constitute the IL. The intensity of the peaks also follow the order that was observed in the experimental enthalpy of solvation at infinite dilution: [TFA] > [DCA] > [NTf₂] > [FAP] > [PF₆], despite of the different density of the anions.

For comparison purposes, the number of cations and the number of anions surrounding the solute molecule were determined from the integration of the first contact peaks represented in figures 4.10. a) and b). In figure 4.11 these values are plotted against the standard molar enthalpy of solvation at infinite dilution obtained experimentally.

Regarding the relation between the number of cations surrounding the hydrogen atom of the hydroxyl group of 1-propanol number and the standard molar enthalpy of solvation at infinite dilution obtained experimentally, a poor correlation was found, indicating that the solute–cation interactions only contribute indirectly to the enthalpy of solvation values. On the contrary, excellent correlation was found between the number of anions surrounding the hydrogen atom of the hydroxyl group of 1-propanol and the standard molar enthalpy of solvation at infinite dilution obtained experimentally.

In addition, if we consider again the scenario of a hypothetical situation of nil interaction between the anion and the hydroxyl group of the alcohol, $N_{\text{anion}} / N_{\text{PrOH}} = 0$, the value of the enthalpy of solvation estimated from the linear correlation is - 34 kJ·mol⁻¹, which is in excellent agreement with the value derived from

the linear fitting represented in figure 4.8. ($-32.3 \text{ kJ}\cdot\text{mol}^{-1}$) and the estimated value of the enthalpy of solvation of propanol in an alkane, $-35.5 \text{ kJ}\cdot\text{mol}^{-1}$.

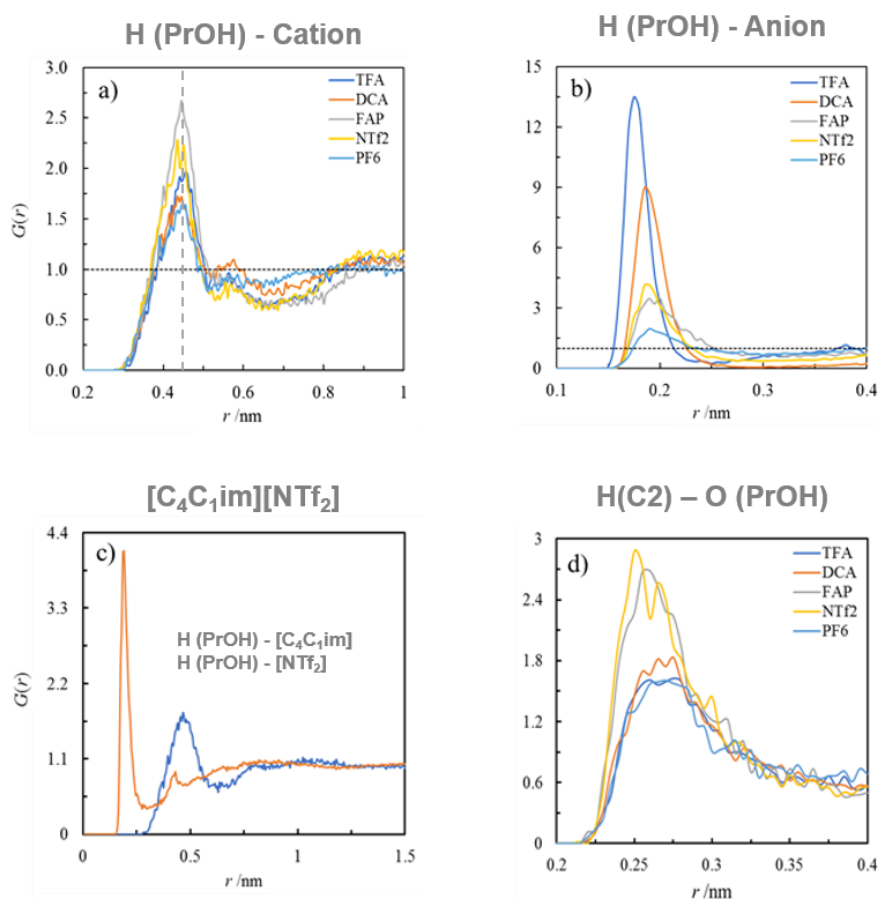


Figure 4.10. Radial distribution functions, RDFs: a) between the centre of charge of the cation (defined as the centre of mass of the imidazolium ring) and the hydrogen atom of the hydroxyl group of PrOH; b) between the hydrogen atom of the hydroxyl group of PrOH and the most electronegative atoms in the anions (oxygen atoms in [TFA] and [NTf₂], fluorine atoms attached to the phosphorus atom in [PF₆] and [FAP], and the terminal nitrogen atoms in [DCA]); c) superposition of the solute-cation and solute-anion RDFs for [C₄C₁im][NTf₂]; d) between the most acidic hydrogen atom in the imidazolium ring (HR) and the oxygen atom of the solute.

These findings, evidence the preferential interaction of the hydroxyl group of the alcohol with the anion. Extra evidence can be obtained from the analysis of the figure 4.10.c) in which the RDFs of the solute-cation and solute-anion, relative to the solvation of 1-propanol in [C₄C₁im][NTf₂], are superposed. This figure, together with figure 4.11 gives a very clear insight into the solvation shell around the solute, with one anion in the

first solvation shell close to the hydroxyl group of 1-propanol and the presence of two cations further away, in a second solvation shell. Furthermore, the representation of the RDFs between the most acidic hydrogen atom in the imidazolium ring “H(C2)” and the oxygen atom of the solute, in figure 4.10 d), evidences that the corresponding distances are centred at approximately 0.25 nm. The analogous hydrogen bond distances for solute–anion interactions are all below 0.20 nm. This suggests the absence of efficient hydrogen bonds between the cations and the alcohol molecules.

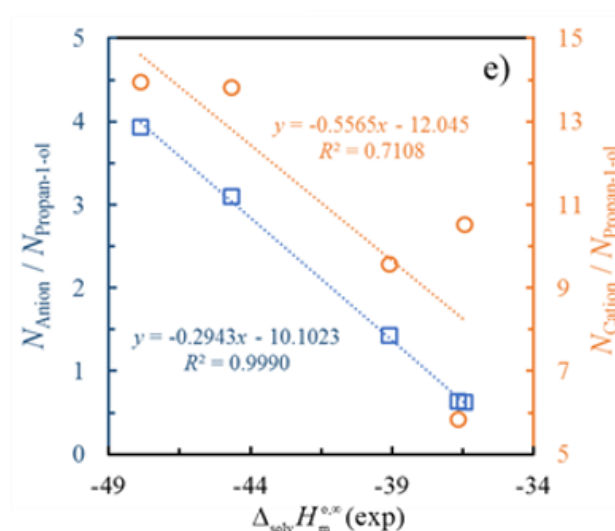


Figure 4.11. Plot of the number of cations/anions surrounding the hydrogen atom of the hydroxyl group of 1-propanol, against the standard molar enthalpy of solvation, at infinite dilution, obtained experimentally. The lines are the respective linear fittings of the data.

Even for the $[\text{C}_4\text{C}_1\text{im}][\text{FAP}]$ and $[\text{C}_4\text{C}_1\text{im}][\text{PF}_6]$, the results evidence the presence of the anion at close proximity to the hydroxyl group, than the cation. Accordingly, it is considered that the phenomena verified in the study of the cation effect, regarding the differentiation found in the enthalpies of solvation of $[\text{Cation}][\text{FAP}]$ IL series contrasting with the similarity in $[\text{Cation}][\text{NTf}_2]$ IL series, is attributed to a preferential interaction of the solute with the anion. The differentiation found in $[\text{Cation}][\text{FAP}]$ IL series is then explained by the inability of the $[\text{FAP}]$ anion to establish localized hydrogen bonding interactions with the solute, making possible the existence of interactions with the cation once that 1-propanol has both hydrogen bond acceptor and donor capabilities.

4.2. Exploration of the Fluorination / Acidity Effect of the Alcohol in Ionic Liquids

In the previous section, the effects of the cation nature and the hydrogen bond basicity of the anion in the solvation process were explored. The obtained results presented clear evidences of the location of the alcohol hydroxyl group in the polar domains of ionic liquids, interacting preferentially with basic anions. In the case of less basic anions, with lower capacity to interact with the hydroxyl group of the alcohol, the results exhibited a bigger role of the cation in the solvation process. Furthermore, the results also suggested that the introduction of substituent groups in the cation that modify the possible positions of the cation around the anion alters the IL/alcohol interaction and creates differentiation in the solvation properties.

In this section, the effect of the acidity of the solute / molecular probe in the solvation properties of ionic liquids is going to be presented.

Aiming to do that, in the context of this PhD thesis, the standard molar enthalpy of solution of alcohols with different levels of fluorination in a representative ionic liquid was determined by ITC. In order to determine the enthalpy of solvation at infinite dilution of the referred alcohols in ionic liquids, the enthalpy of vaporization of some of these alcohols was measured using the *DropCalvet* methodology. As in the previous study, complementary theoretical calculations were performed, allowing a most robust interpretation of the solvation thermodynamics.

In the following pages, the strategy used to determine the effect of the fluorination and acidity of the solute in the solvation properties of ionic liquids, using alcohols as molecular probes, will be addressed. The main results obtained in the topic will be presented and discussed.

4.2.1. Strategy

In this study, the effect of the acidity of the solute / molecular probe in the solvation in ionic liquids was explored. The modulation of the acidity of the alcohols was achieved by studying alcohols with different degrees of fluorination. For comparison purposes, linear and non-linear alcohols were studied:

- 1-propanol and its fluorinated derivatives TFPrOH and PFPrOH;
- *tert*-butyl-alcohol (*t*-BuOH) and its fluorinated derivatives, TF*t*-BuOH, HF*t*-BuOH, PF*t*-BuOH, with equivalent number of “superficial” interacting groups as 1-propanol.

In figure 4.12 is depicted a schematic illustration presenting the similarity in the “superficial” interacting groups of *t*-BuOH and PrOH.

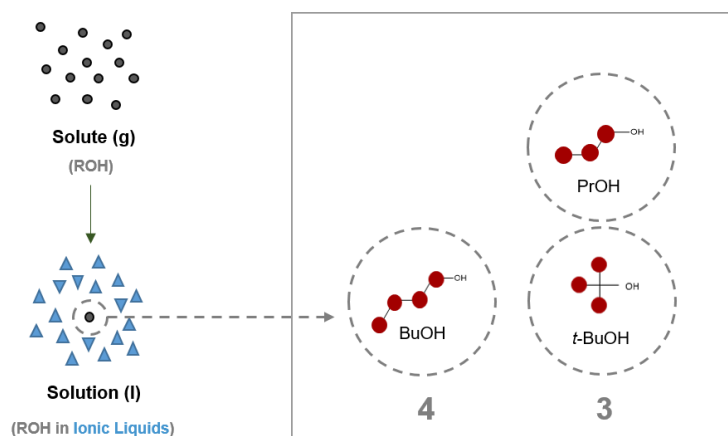


Figure 4.12. Scheme of the solution of BuOH, *t*-BuOH and PrOH in ionic liquids, highlighting the number of groups accessible for intermolecular interactions: 4 in BuOH, 3 in *t*-BuOH and PrOH.

The purpose of this study is to extend the previous investigation, regarding the ability of the polar domains of the ionic liquids to interact with a polar and hydrogen donor/acceptor group, as the hydroxyl group of an alcohol. In this work, the effect of the acidity of the alcohol is going to be evaluated.

To accomplish that purpose, the solution and solvation of the referred alcohols in an ionic liquid based in bis(trifluoromethylsulfonyl)imide ([NTf₂]) anion was evaluated, since it constitutes one of the most usual anions in ILs, and it was seen in the previous study, that it has the ability to interact with 1-propanol by hydrogen bond. The IL cation

chosen is based in an asymmetric imidazolium cation with 1 methyl group and 4 carbons in the other alkyl chain, $[C_4C_1\text{im}]$, restraining the alcohols-ILs interactions to the sphere of influence of the polar network, as schematically represented in figure 1.3 on the Introduction of this thesis.

In agreement, the standard molar enthalpy of solution at infinite dilution of the referred alcohols in $[C_4C_1\text{im}][\text{NTf}_2]$ ionic liquid, was determined by ITC, at 298.15 K. From the standard molar enthalpy of solution at infinite dilution and the standard molar enthalpy of vaporization (determined experimentally by *DropCalvet* methodology or reported in the literature ^[2, 32]), the standard molar enthalpy of solvation at infinite dilution was determined. This experimental strategy is depicted in figure 4.13

Similarly to the previous study, the energy of interaction in the gas phase between the studied alcohols and the $[\text{NTf}_2]$ anion was calculated and the obtained data was correlated with the enthalpy of solvation at infinite dilution. The quantum chemical calculations were performed using the same methodology described in the previous work.

Solution & Solvation in Ionic Liquids

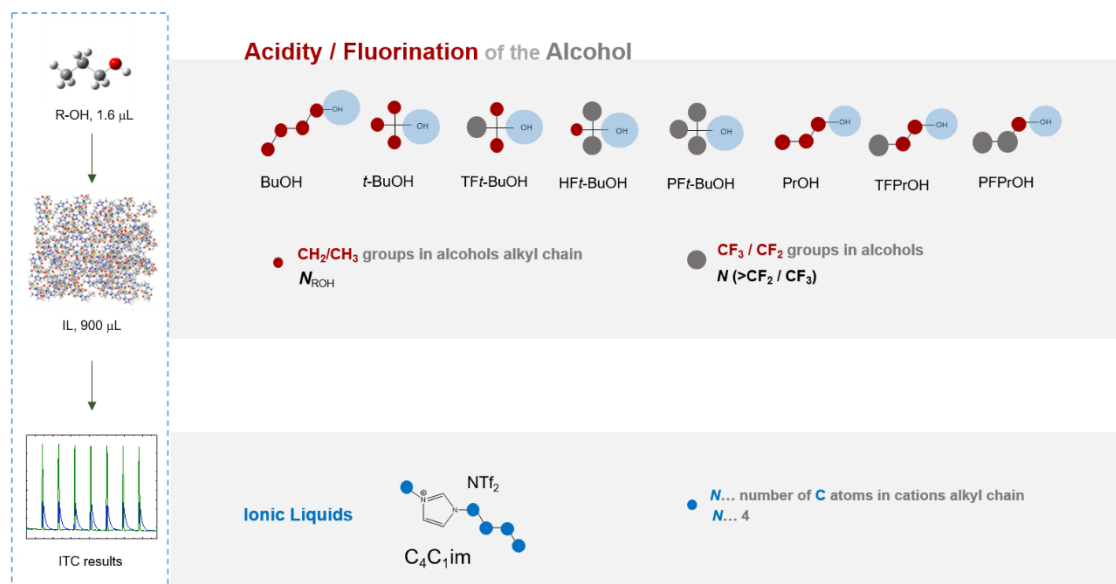


Figure 4.13. Scheme of the strategy used to determine the effect of the acidity of the alcohol (by fluorination) in the solution / solvation of alcohols in ionic liquids.

4.2.2. Results and Discussion

In table 4.2 is summarized the standard molar enthalpy of solution at infinite dilution of PrOH, TFPrOH, PFPrOH, BuOH, *t*-BuOH, TF*t*-BuOH, HF*t*-BuOH and PF*t*-BuOH in [C₄C₁im][NTf₂], at the standard temperature ($T = 298.15$ K), determined by ITC. Along with these results, is also presented the standard molar enthalpy of solvation at infinite dilution, calculated from the standard molar enthalpy of vaporization of the alcohol and the standard molar enthalpy of solution at infinite dilution.

Table 4.2. Summary of the standard molar enthalpy of solution and solvation, at infinite dilution, of different alcohols in [C₄C₁im][NTf₂] ionic liquid, at the reference temperature ($T = 298.15$ K)

Alcohol	$\Delta_{\text{soln}} H_m^{0, \infty} / \text{kJ} \cdot \text{mol}^{-1}$	$\Delta_{\text{solv}} H_m^{0, \infty} / \text{kJ} \cdot \text{mol}^{-1}$
PrOH	8.37 ± 0.24	-39.08 ± 0.27
TFPrOH	5.04 ± 0.11	-43.24 ± 0.39
PFPrOH	3.26 ± 0.09	-43.22 ± 0.37
BuOH	8.89 ± 0.25	-43.46 ± 1.08
<i>t</i> -BuOH	7.49 ± 0.26	-39.11 ± 0.28
TF <i>t</i> -BuOH	3.24 ± 0.22	-41.34 ± 0.43
HF <i>t</i> -BuOH	-4.84 ± 0.40	-43.94 ± 0.48
PF <i>t</i> -BuOH	-13.46 ± 0.39	-45.65 ± 0.61

In table 4.3 the values of the standard molar enthalpy of vaporization of the studied alcohols, at the reference temperature, $T = 298.15$ K, are summarized. Some of the presented values are well established in the literature^[2, 32]. The others were determined by *DropCalvet* calorimetry, in the context of this work.

The enthalpy of vaporization of PFPrOH has already been reported by some authors. Murto and Kivinen^[33] have been the firsts to report the standard molar enthalpy of vaporization of PFPrOH: $41.3 \text{ kJ} \cdot \text{mol}^{-1}$. In the same year, 1967, Meeks and Goldfarb^[34] have reported the vapour pressures of this alcohol at different temperatures. In 1973,

Rochester and Symonds^[35] have used this data along with their own vapour pressure measurements and derived the standard molar enthalpy of vaporization using the Clapeyron's equation, at $T = 298$ K, obtaining the following value: $44.38 \text{ kJ}\cdot\text{mol}^{-1}$. Filipe et al.^[36] calculated the enthalpy of vaporization derived from the Meeks and Goldfarb^[34] data, at the medium temperature $T = 285.7$ K: $46.9 \text{ kJ}\cdot\text{mol}^{-1}$. From their own measurements^[36], they report an enthalpy of vaporization of $45.1 \text{ kJ}\cdot\text{mol}^{-1}$ at the medium temperature $T = 313.01$ K. No calorimetric results were found. The value determined in this work ($46.48 \text{ kJ}\cdot\text{mol}^{-1}$), using *DropCalvet* calorimetry is not far from the values reported, taking into account the uncertainties associated to the experimental methodologies used.

Table 4.3. Summary of the standard molar enthalpy of vaporization, at the reference temperature ($T = 298.15$ K), obtained experimentally in *DropCalvet*, in the context of this work, and reported in literature by other authors

Alcohol	$\Delta_l^g H_m^{0,\infty} / \text{kJ}\cdot\text{mol}^{-1}$
PrOH	47.45^a
TFPrOH	48.28 ± 0.38^b
PFPrOH	46.48 ± 0.36^b
BuOH	52.35^a
<i>t</i> -BuOH	46.6^c
TF <i>t</i> -BuOH	44.58 ± 0.37^b
HF <i>t</i> -BuOH	39.10 ± 0.26^b
PF <i>t</i> -BuOH	32.19 ± 0.47^b

a – data from ref. [2];

b – this work;

c – data from ref. [32].

In figure 4.14 the standard molar enthalpy of solution at infinite dilution of several alcohols in $[\text{C}_4\text{C}_{1\text{im}}][\text{NTf}_2]$ is represented against the number of fluorinated groups “>CF₂” and “-CF₃” of the alcohol. Two different alcohol series are represented: one based in

1-propanol and its fluorinated derivatives (PrOH, TFPrOH and PFPrOH) and another one based in *tert*-butyl-alcohol and its fluorinated derivatives (*t*-BuOH, TF*t*-BuOH, HF*t*-BuOH and PF*t*-BuOH). For comparison purposes, the standard molar enthalpy of solution at infinite dilution of 1-butanol (BuOH) is also represented. From the representation, it is evident that PrOH series is more endothermic than *t*-BuOH series. Furthermore, it is notorious a decrease in the enthalpy of solution with the increase in the fluorination of the series. This decrease is more accentuated in the case of the fluorination of the *t*-BuOH series.

On the right side of the figure 4.14 a zoom-in in the axis of the enthalpy is depicted. This zoom-in highlights the less endothermic enthalpy of *t*-BuOH in [C₄C₁im][NTf₂], in comparison to the enthalpy of solution of both PrOH and BuOH in the same IL.

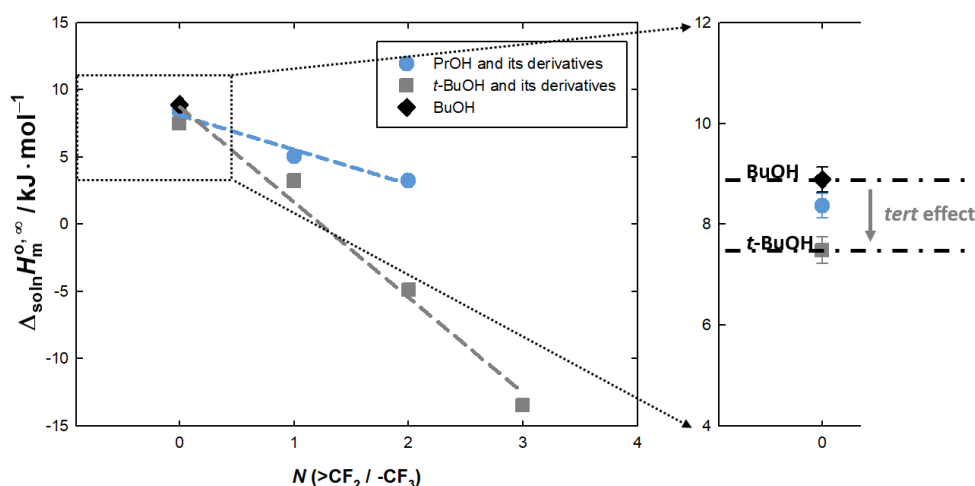


Figure 4.14. Plot of the standard molar enthalpy of solution, at infinite dilution, of different alcohols (BuOH, *t*-BuOH and its fluorinated derivatives, PrOH and its fluorinated derivatives) in [C₄C₁im][NTf₂], obtained experimentally by ITC, at the reference temperature ($T = 298.15$ K), as a function of the number of fluorinated groups ">CF₃" / "-CF₂" of the alcohol. The grey and blue dashed lines are linear fittings of the data: $\Delta_{\text{soln}}H_m^{0,\infty}(\text{PrOH}) = -2.56 (\pm 0.45) \cdot N(>\text{CF}_2 / -\text{CF}_3) + 8.11 (\pm 0.58)$; $\Delta_{\text{soln}}H_m^{0,\infty}(t\text{-BuOH}) = -7.09 (\pm 0.73) \cdot N(>\text{CF}_2 / -\text{CF}_3) + 8.7 (\pm 1.4)$. On the right is presented a magnification in the enthalpy of solution axis, highlighting the *tert* effect on the enthalpy of solution at infinite dilution in [C₄C₁im][NTf₂]. The black dashed lines are just guide lines to the eyes.

To a better interpretation of the results, in figure 4.15 the previous graphical representation is replicated, now displaying the standard molar enthalpy of solvation at infinite dilution instead of the standard molar enthalpy of solution at infinite dilution. In this representation, is notorious the similarity between the enthalpy of solvation of PrOH

and *t*-BuOH in [C₄C₁im][NTf₂], both less exothermic than the enthalpy of solvation of BuOH approximately 5 kJ·mol⁻¹. This value is very similar to the contribution to the enthalpy of vaporization of a linear alcohol by addition of a methylene group (“>CH₂”), 4.95 kJ·mol⁻¹, which is the same of the contribution by methylene group found for the enthalpy of vaporization of both alkylamines and alkanes and therefore, it indicates the magnitude of “>CH₂” to “>CH₂” interaction^[37].

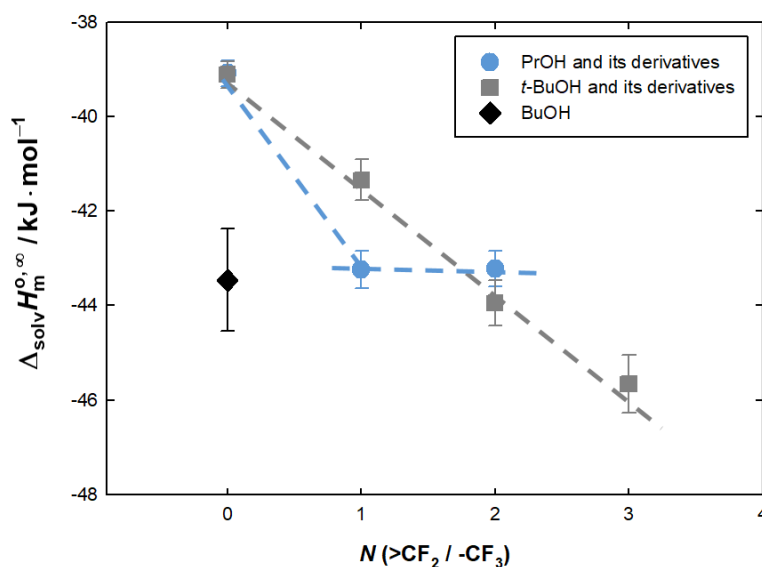


Figure 4.15. Plot of the standard molar enthalpy of solvation, at infinite dilution, of different alcohols (BuOH, *t*-BuOH and its fluorinated derivatives, PrOH and its fluorinated derivatives) in [C₄C₁im][NTf₂], obtained experimentally by ITC, at the reference temperature ($T = 298.15$ K), as a function of the number of fluorinated groups “>CF₃” / “-CF₂” of the alcohol. The blue dashed lines are just a guide line to the eyes. The grey dashed line is the linear fitting of *t*-BuOH and its fluorinated derivatives data. Fitting: $\Delta_{\text{sol}}H_m^{0,\infty} (t\text{-BuOH}) = -2.22 (\pm 0.12) \cdot N (>\text{CF}_2 / -\text{CF}_3) - 39.18 (\pm 0.23)$.

The similarity between the enthalpy of solvation at infinite dilution of *tert*-butyl-alcohol in [C₄C₁im][NTf₂] and 1-propanol in [C₄C₁im][NTf₂] may be explained by the similarities in the superficial interacting groups of both alcohols with the anion and cation of the IL: both alcohols have three “-CH₃” / “>CH₂” “superficial” interacting groups and an hydroxyl group. The 1-butanol has an additional “>CH₂” group, which leads to an additional exothermic contribution of 5 kJ·mol⁻¹.

Furthermore, from the analysis of the graphical representation it is notorious that the increase in the fluorination of the *tert*-butyl-alcohol seems to have a linear relation

with the increase in the exothermic character of the enthalpy of solvation at infinite dilution in $[\text{C}_4\text{C}_{1\text{im}}][\text{NTf}_2]$.

The increase of the exothermic character of the enthalpy of solvation at infinite dilution of the *tert*-butyl-alcohol alcohols series in the $[\text{C}_4\text{C}_{1\text{im}}][\text{NTf}_2]$ with the increase in the fluorination level of the alcohols may be explained by the negative inductive effect of the fluorine atoms, which increases the acidity of the hydrogen atom of the hydroxyl group and thus, enhances the ability of the hydrogen atom to form hydrogen bonds with the $[\text{NTf}_2]$ anion. This enhancement of the ability to hydrogen bond formation would increase the alcohol to IL interactions, which would result in an exothermic increment in the enthalpy of solvation.

To verify the effect of the fluorine negative inductive effect on the enthalpy of solvation, in figure 4.16 (I), the fluorination level of the *tert*-butyl-alcohol is related with the binding energy of the (1s) electrons of the oxygen of the hydroxyl group of the alcohol, reported by Hercules et al.^[38]. The graphical representation evidences the existence of a proportional relation between the level of fluorination of the alcohol and the increase in the binding energy of the electrons to the oxygen atom of the hydroxyl group. In this way, this plot evidences the negative inductive effect caused by the fluorine atoms into the oxygen-hydrogen bond.

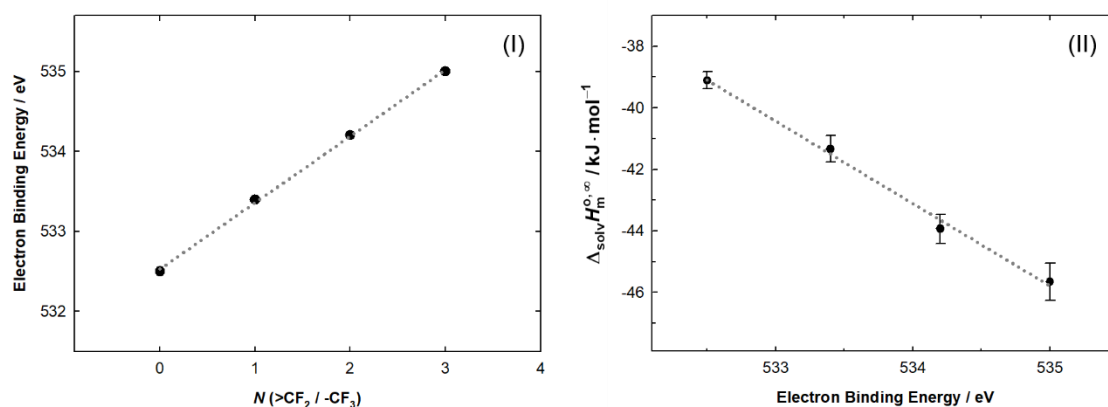


Figure 4.16. (I) Plot of the binding energy of the electron (1s) of the oxygen atom of the alcohol against the level of fluorination of the alcohols (number of “>CF₂” / “-CF₃” groups of the alcohol). (II) Plot of the enthalpy of solvation, at infinite dilution, of *tert*-butyl-alcohol with different degrees of fluorination in $[\text{C}_4\text{C}_{1\text{im}}][\text{NTf}_2]$, against the electron (1s) binding energy of the oxygen atom. The dotted lines represent the linear fittings of the represented data. (I) Fitting: Electron Binding Energy = $0.83 \cdot N(>\text{CF}_2 / -\text{CF}_3) + 532.53$; (II) Fitting: $\Delta_{\text{sol}}H_{\text{m}}^{0,\infty} = -2.68 \cdot \text{Electron Binding Energy} + 1386$. Data of the binding energy of the electron (1s) of the oxygen atom of the alcohol from ref. [38].

In figure 4.16 (II), a linear relation is presented between the oxygen electron binding energies and the enthalpy of solvation at infinite dilution of *t*-BuOH, TF*t*-BuOH, HF*t*-BuOH and PF*t*-BuOH in [C₄C₁im][NTf₂], showing the existence of a linear relation between the higher potential of the hydrogen atom to form hydrogen bonds and the increase in the exothermic character of the solvation.

In figure 4.17 (I), the acidity (pKa in water at 298 K or room temperature)^[38-44] is represented against the level of fluorination of the alcohol, showing that the increase in the number of fluorine atoms increases the acidity of the alcohol, in both *t*-BuOH and PrOH alcohol series, in accordance with the existence of a negative inductive effect caused by the fluorine atoms. Nevertheless, the increase in the acidity of the alcohol is higher in *t*-BuOH alcohol series than in PrOH alcohol series. This phenomenon may be caused by the geometry of both alcohols. The geometry of *tert*-butyl-alcohol favours the proximity in space of some of the fluorine atoms with the hydroxyl group. Therefore, in the case of this alcohol series some negative inductive effect may be occurring also through space and not only through the chemical bonds.

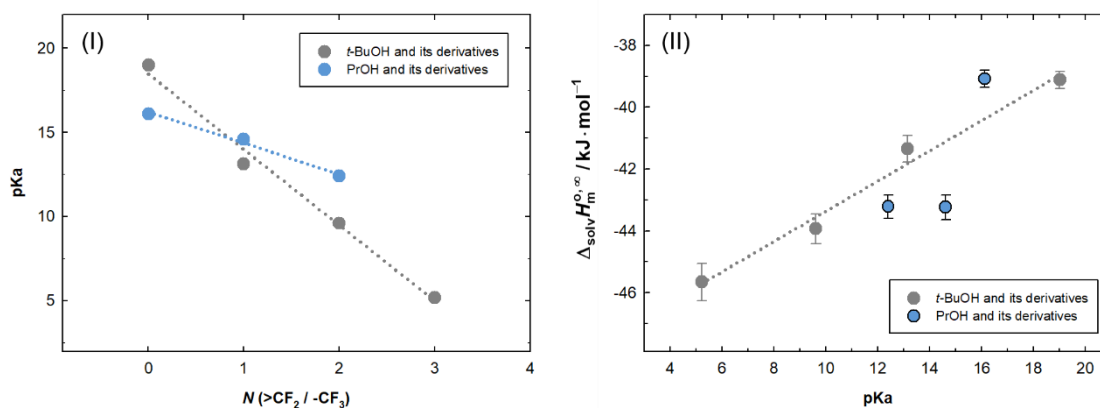


Figure 4.17. (I) Plot of the acidity of the alcohol (pKa) against the level of fluorination of the alcohols (number of “>CF₂” / “-CF₃” groups of the alcohol). (II) Plot of the enthalpy of solvation, at infinite dilution, of *tert*-butyl-alcohol with different degrees of fluorination in [C₄C₁im][NTf₂], against the acidity of the alcohols (pKa). The dotted lines represent the linear fittings of the represented data. (I) Fitting (*t*-BuOH): $pK_a = -4.49 (\pm 0.32) \cdot N(>CF_2 / -CF_3) + 18.47 (\pm 0.61)$; Fitting (PrOH): $pK_a = -1.86 (\pm 0.20) \cdot N(>CF_2 / -CF_3) + 16.22 (\pm 0.26)$; (II) Fitting (*t*-BuOH): $\Delta_{solv}H_m^{0,\infty} = 0.489 (\pm 0.045) \cdot pK_a - 48.25 (\pm 0.58)$. Acidity (pKa) of the alcohols from ref. [38-44].

In Figure 4.17 (II), it is plotted the relation between the acidity of the alcohol and the enthalpy of solvation at infinite dilution. In the figure, it is evident the existence of a linear relation between the acidity of *t*-BuOH alcohol series and its enthalpy of solvation at infinite dilution in [C₄C₁im][NTf₂]. The existence of this linear relation is in agreement with the explanation proposed: the increase in the fluorination of the alcohol, increases the acidity of the hydroxyl group of the alcohol due to the negative inductive effects of the fluorine atoms, increasing the hydrogen bond interaction between the alcohol and the anion and, in consequence, increasing the exothermic character of the enthalpy of solvation at infinite dilution.

In the case of the fluorination of the 1-propanol, as it can be seen in figure 4.15, there is an initial increase in the exothermic character of the enthalpy of solvation, which is bigger than in the case of *tert*-butyl-alcohol. However, the enthalpy of solvation at infinite dilution of PFPrOH is similar to the enthalpy of solvation of TFPrOH. No increase in the exothermic character of the enthalpy of solvation was observed by the increase in the fluorination of PrOH (from 3 to 5 fluorine atoms). The enthalpy of solvation at infinite dilution does not present a linear relation with the level of fluorination of the alcohol, contrary to what was verified in the enthalpy of solution at infinite dilution.

In figure 4.18, the enthalpy of solvation at infinite dilution of several alcohols in [C₄C₁im][NTf₂] and in itself is represented against the number of ">CF₂" and "-CF₃" groups of the alcohol. The enthalpy of solvation of the alcohols in itself is estimated considering the condensation of gaseous alcohol molecules, to its liquid phase. Accordingly, the enthalpy of solvation of the alcohols in itself was represented as the symmetric of the enthalpy of vaporization of the referred alcohols.

The enthalpy of solution at infinite dilution measured can be interpreted as a sum of three processes: the breaking of the alcohol-alcohol interactions (endothermic – given by the enthalpy of vaporization and related to the cohesive energy), creation of a cavity in the ionic liquid (endothermic – related to the volume of the cavity and the solvent cohesive energy) and relaxation of the ions around the alcohol with simultaneous establishment alcohol-IL interactions (exothermic). The enthalpy of solvation at infinite dilution can be viewed as the sum of the two last processes.

Considering this interpretation, and the thermochemical cycle depicted in figure 4.19, the enthalpy of solution at infinite dilution of an alcohol in an IL can be interpreted as the sum of the enthalpy of vaporization of the alcohol with the enthalpy of solvation of the alcohol in an IL:

$$\Delta_{\text{soln}} H_m^{\text{O}, \infty} = \Delta_l^g H_m^{\text{O}} + \Delta_{\text{solv}} H_m^{\text{O}, \infty}. \quad (4.4)$$

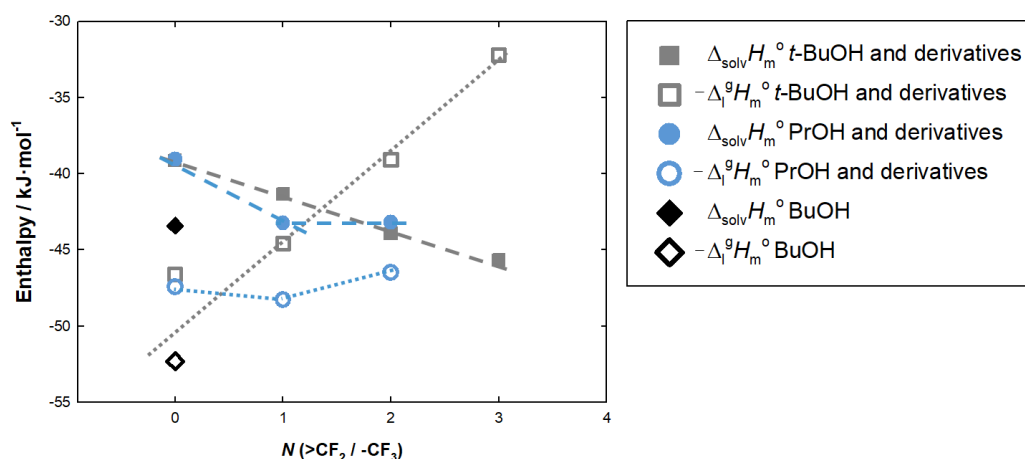


Figure 4.18. Plot of the standard molar enthalpy of solvation at infinite dilution of BuOH, *t*-BuOH and its fluorinated derivatives and PrOH and its fluorinated derivatives in [C₄C₁im][NTf₂], at the reference temperature ($T = 298.15$ K), as well as, the symmetric of the standard molar enthalpy of vaporization of the same alcohols, at the reference temperature ($T = 298.15$ K), as a function of the number of fluorinated groups “>CF₃” / “-CF₂” of the alcohol alkyl chain. The dashed and pointed lines are just a guide line for the eyes.

Accordingly with this interpretation, the graphical representation depicted in figure 4.17 helps interpreting the results of the enthalpy of solution and enthalpy of solvation from a molecular perspective. In this figure is represented:

- the enthalpy of solvation of the alcohol in itself, the symmetric of its vaporization enthalpy, which gives information on the cohesive energy of the solute;
- the enthalpy of solvation at infinite dilution of the alcohol in [C₄C₁im][NTf₂] which reflects the sum of the cavitation energy with the energy of the intermolecular interactions established;
- the enthalpy of solution which is the distance (in the Enthalpy axis) between the two properties.

From the analysis of figure 4.18, it stands out the similar behaviour of the enthalpy of solvation and vaporization of the PrOH alcohol series in comparison to the *t*-BuOH alcohol series. The increase in the fluorination of PrOH, from $N(“>CF_2” / “-CF_3”) = 0$ to $N(“>CF_2” / “-CF_3”) = 1$, increases slightly the enthalpy of vaporization of the alcohol,

indicating an increase in the cohesive energy of the alcohol. However, the increase of the fluorination, from $N(>\text{CF}_2 / -\text{CF}_3) = 1$ to $N(>\text{CF}_2 / -\text{CF}_3) = 2$, leads to a decrease in the cohesive energy of the alcohol. The magnitude of the enthalpy of solvation of the PrOH alcohol series is smaller than the enthalpy of vaporization. The increase in the fluorination of PrOH, from $N(>\text{CF}_2 / -\text{CF}_3) = 0$ to $N(>\text{CF}_2 / -\text{CF}_3) = 1$, increases the (magnitude) enthalpy of solvation of the alcohol. Furthermore, this increase is bigger than the increase verified in the enthalpy of vaporization of the alcohol. This phenomenon may indicate that the substitution of the $-\text{CH}_3$ for a $-\text{CF}_3$ group in PrOH intensifies the hydrogen bond between the alcohol and the anion more than the hydrogen bonds established between the alcohol molecules. This singularity may be due to the increase of the hydrogen bond acidity, and decrease in the hydrogen bond basicity of the alcohols originated by the fluorine inductive effect. Nevertheless, as the increase in the magnitude of the enthalpy of solvation is bigger than the enthalpy of vaporization, the “distance” between both properties is shortened and therefore, the enthalpy of solution of TFPrOH is smaller than PrOH as it can be seen in figure 4.14.

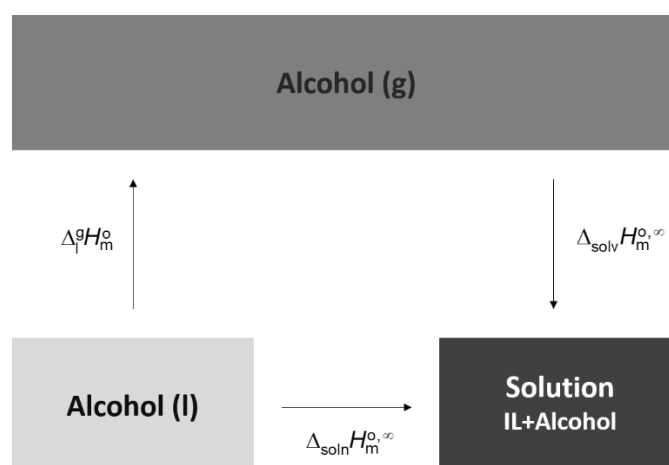


Figure 4.19. Thermochemical cycle which describes the solution/solvation process.

The increase in the fluorination of PrOH, from $N(>\text{CF}_2 / -\text{CF}_3) = 1$ to $N(>\text{CF}_2 / -\text{CF}_3) = 2$, does not present any effect in the enthalpy of solvation of the alcohol in $[\text{C}_4\text{C}_{1\text{im}}][\text{NTf}_2]$, which means that either there is no further increase in the hydrogen bond interactions or the increase in the interactions is of the same magnitude of an eventual increase in the cavitation energy.

In figure 4.17 (II), is observable that the enthalpy of solvation at infinite dilution of PrOH, TFPrOH and PFPrOH in $[C_4C_{1im}][NTf_2]$ is not proportional to the acidity of the alcohol. The initial increase in the acidity of the alcohol (decrease in pKa) is accompanied by a significant increase in the magnitude of the enthalpy of solvation. However, from $N(>CF_2 / -CF_3) = 1$ to $N(>CF_2 / -CF_3) = 2$, the acidity increase seems to have a minor effect in the enthalpy of solvation.

Regarding the enthalpy of solution, as the magnitude of the cohesive energy of this alcohol series decreases with the substitution of $>CH_2$ for $>CF_2$, the “distance” between both properties is again shortened, resulting in a smaller enthalpy of solution. By this reason, the enthalpy of solution decreases continuously, despite of the phenomenon verified at the enthalpy of solvation.

In *t*-BuOH alcohol series, there is a linear increase in the magnitude of the enthalpy of solvation with the increase of the alcohol fluorination, which was already related with the increase in the alcohol-anion hydrogen bond interaction.

The magnitude of the enthalpy of vaporization however, decreases with the increase of the alcohol fluorination. This phenomena is probably due to the steric hindrance on the hydroxyl group which hinders the interaction between the hydroxyl groups of both alcohols. We estimate that the interaction of the alcohol with the anion is less affected by the steric hindrance of the hydroxyl group, inherent to the structure of the alcohol.

In order to have more information on the topic, the enthalpy of solvation at infinite dilution of *t*-BuOH, TF*t*-BuOH, HF*t*-BuOH, PF*t*-BuOH, PrOH, TFPrOH and PFPrOH in $[C_4C_{1im}][NTf_2]$ was related with the energy of interaction between the alcohol and $[NTf_2]$ anion in the gas phase. For that purpose, in figure 4.20, the figure 4.8 is repeated to include the enthalpy of solvation at infinite dilution of *t*-BuOH, TF*t*-BuOH, HF*t*-BuOH, PF*t*-BuOH, PrOH, TFPrOH, HFPrOH and PFPrOH in $[C_4C_{1im}][NTf_2]$ and the respective energy of interaction, in the gas phase, between the alcohol and the anion, determined by quantum chemical calculations.

The results seem to follow the trend found before, when studying the effect of the basicity of the anion, despite of generally presenting higher dispersion of the results. Moreover, on the light of the present results, the solvation of PrOH in $[C_4C_{1im}][PF_6]$, that previously was considered an outlier seems now to be part of the normal dispersion of the results. Given the obtained results, a new linear fitting was done, in figure 4.21, including the results of all systems with exception of the solvation of BuOH and PFPrOH in $[C_4C_{1im}][NTf_2]$. The result of the enthalpy of solvation of PFPrOH in $[C_4C_{1im}][NTf_2]$ was

not considered due to the fact that it seems to not be governed only by the hydrogen bond interaction with the anion.

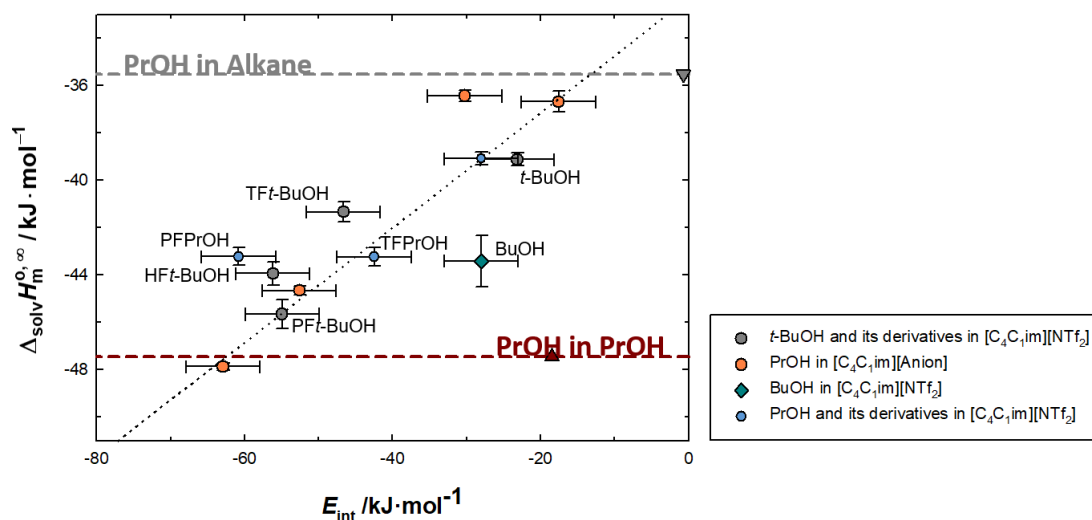


Figure 4.20. Graphical representation of the standard molar enthalpy of solvation, at infinite dilution, of alcohols in ILs, at the reference temperature ($T = 298.15$ K), as a function of the energy of interaction between the alcohol and the anion of the IL, in the gas phase: ● PrOH in $[C_4C_1im][TFA]$, ● PrOH in $[C_4C_1im][DCA]$, ● PrOH in $[C_4C_1im][FAP]$, ● PrOH in $[C_4C_1im][PF_6]$, ● PrOH in $[C_4C_1im][NTf_2]$, ● TFPrOH in $[C_4C_1im][NTf_2]$, ● PFPrOH in $[C_4C_1im].0[NTf_2]$, ● t -BuOH in $[C_4C_1im][NTf_2]$, ● TF t -BuOH in $[C_4C_1im][NTf_2]$, ● HF t -BuOH in $[C_4C_1im][NTf_2]$, ● PF t -BuOH in $[C_4C_1im][NTf_2]$, ◆ BuOH in $[C_4C_1im][NTf_2]$. The back dotted line is the linear fitting of the data regarding PrOH in $[C_4C_1im][Anion]$ excluding the $[PF_6]$ anion. The dashed horizontal lines represent the enthalpy of solvation of PrOH in itself (red) and in an alkane (grey). The up and down triangles represent the interaction energy in the gas phase between two PrOH molecules (▲) and between PrOH and an alkane (▼). Fitting (PrOH in $[C_4C_1im][Anion]$): $\Delta_{sol\nu}H_m^{0,\infty} = 0.242 (\pm 0.010) \cdot E_{int} - 32.31 (\pm 0.45)$.

The linear fitting of the data (excluding the BuOH and PFPrOH in $[C_4C_1im][NTf_2]$) is given by the following equation:

$$\Delta_{sol\nu}H_m^{0,\infty} (\text{kJ} \cdot \text{mol}^{-1}) = 0.229 \times E_{int} - 32.3 \quad (4.5)$$

This relation establishes that, for the studied alcohols, the enthalpy of solvation at infinite dilution is approximately 23 % of the energy of interaction between the alcohol and the anion in the gas phase, in addition to $-32.3 \text{ kJ} \cdot \text{mol}^{-1}$. This value ($-32.3 \text{ kJ} \cdot \text{mol}^{-1}$) represents the enthalpy of solvation of these alcohols when there is no preferential interaction between the anion and the hydroxyl group of the alcohol. This value is similar to the estimated value of the enthalpy of solvation at infinite dilution of

propanol in an alkane, $-35.5 \text{ kJ}\cdot\text{mol}^{-1}$, and the value estimated from the molecular simulations data, $-34 \text{ kJ}\cdot\text{mol}^{-1}$.

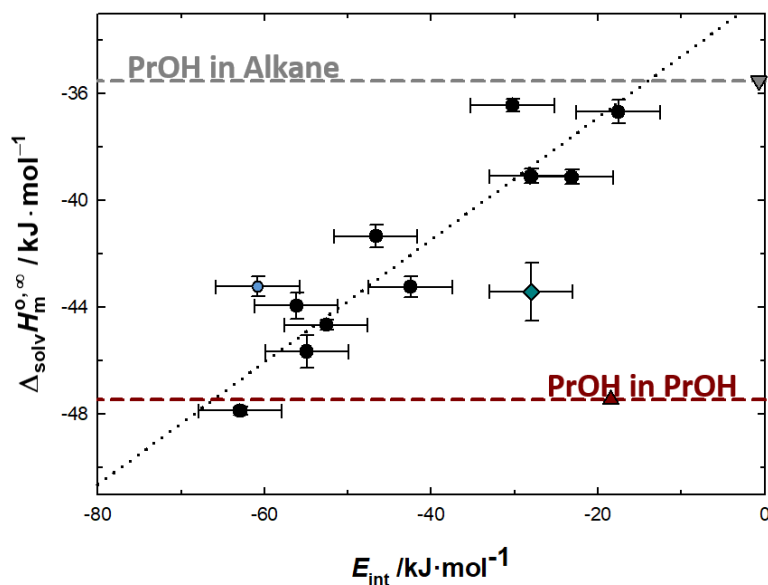


Figure 4.21. Graphical representation of the standard molar enthalpy of solvation, at infinite dilution, of alcohols in ILs, at the reference temperature ($T = 298.15 \text{ K}$), as a function of the energy of interaction between the alcohol and the anion of the IL, in the gas phase: ● ProOH in $[\text{C}_4\text{C}_1\text{im}][\text{TFA}]$, ● ProOH in $[\text{C}_4\text{C}_1\text{im}][\text{DCA}]$, ● ProOH in $[\text{C}_4\text{C}_1\text{im}][\text{FAP}]$, ● ProOH in $[\text{C}_4\text{C}_1\text{im}][\text{PF}_6]$, ● ProOH in $[\text{C}_4\text{C}_1\text{im}][\text{NTf}_2]$, ● TFPrOH in $[\text{C}_4\text{C}_1\text{im}][\text{NTf}_2]$, ● PFPrOH in $[\text{C}_4\text{C}_1\text{im}][\text{NTf}_2]$, ● *t*-BuOH in $[\text{C}_4\text{C}_1\text{im}][\text{NTf}_2]$, ● TF*t*-BuOH in $[\text{C}_4\text{C}_1\text{im}][\text{NTf}_2]$, ● HF*t*-BuOH in $[\text{C}_4\text{C}_1\text{im}][\text{NTf}_2]$, ● PF*t*-BuOH in $[\text{C}_4\text{C}_1\text{im}][\text{NTf}_2]$, ◆ BuOH in $[\text{C}_4\text{C}_1\text{im}][\text{NTf}_2]$. The back dotted line is the linear fitting of the data regarding ROH in $[\text{C}_4\text{C}_1\text{im}][\text{Anion}]$ excluding the solvation of BuOH and PFPrOH in $[\text{C}_4\text{C}_1\text{im}][\text{NTf}_2]$. The dashed horizontal lines represent the enthalpy of solvation of ProOH in itself (red) and in an alkane (grey). The up and down triangles represent the interaction energy in the gas phase between two ProOH molecules (▲) and between ProOH and an alkane (▼). Fitting (ROH in $[\text{C}_4\text{C}_1\text{im}][\text{Anion}]$): $\Delta_{\text{solv}}H_m^{0,\infty} = 0.229 (\pm 0.029) \cdot E_{\text{int}} - 32.3 (\pm 1.2)$.

Overall, the present results are in accordance with the solvation results obtained by variation of the hydrogen bond basicity of the anion. The increase of the hydrogen bond acidity of the alcohol, as well as, the increase of the hydrogen bond basicity of the anion, contribute to the increase of the hydrogen bond alcohol to anion interaction, leading to higher exothermic character of the enthalpy of solvation at infinite dilution. Furthermore, in the absence of local interactions between the alcohol and the anion, the alcohol seems to present an enthalpy of solvation similar to its solvation in an alkane. At this point, it should be noticed that, in the previous study, it has been also highlighted the

role of the cation in the solvation process, which could be relevant in the case of anions of lower basicity.

Summarizing, the obtained results present evidences of the preferential location of the alcohol hydroxyl group in the polar domains of ionic liquids, interacting preferentially with basic anions by hydrogen bond, as schematically represented in figure 4.22.

Nevertheless, enthalpy of solvation is a result of the interplay existent between the cavitation energy (endothermic) and the energy of the interactions established (exothermic). The linearity of the relations found regarding the solvation of *t*-BuOH, TF*t*-BuOH, HF*t*-BuOH, PF*t*-BuOH in [C₄C₁im][NTf₂], suggest that the cavitation energy is similar, despite of the level of fluorination of the *tert*-butyl-alcohol. Accordingly, the molecular volume of the alcohols (*t*-BuOH, TF*t*-BuOH, HF*t*-BuOH, PF*t*-BuOH) must be very similar despite of the level of fluorination.

However, small differences on the cavitation energies may contribute to the differences found in the results. Additionally, the discussion was based in the effect of the acidity of the alcohol and its effect in the hydrogen bond interaction with the anion. Furthermore, in solution, many species are present and the geometry and dynamics of the species has to be considered. The simple relation of the acidity and basicity with the enthalpy of solvation, gives a general and very important insight of the main phenomena present, but do not provide full description of the system.

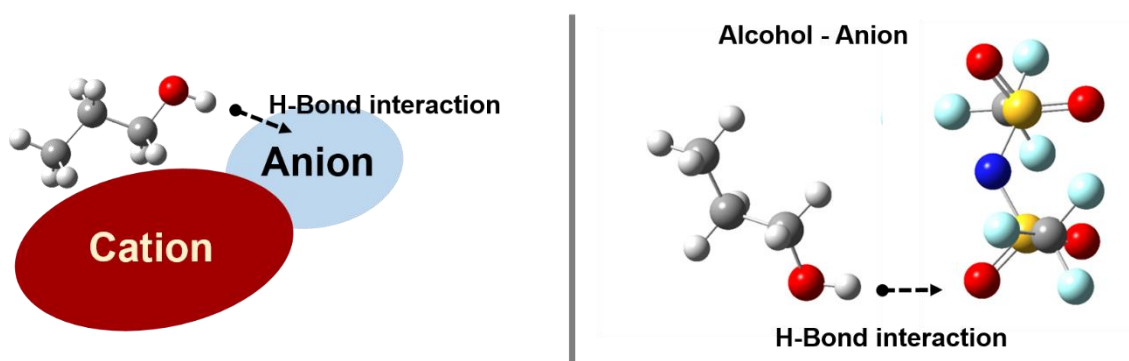


Figure 4.22. Schematic representation of the preferential location of the hydroxyl group of the alcohol in ionic liquids forming alcohol - anion hydrogen bond.

4.3. The Effect of the Alkyl Chain Length on the Solvation of Alcohols in Ionic Liquids

In the previous subchapters, the effects of the cation nature, the hydrogen bond basicity of the anion and the hydrogen bond acidity of the alcohol, in the solvation process, were explored. The obtained results presented evidences of the preferential location of the alcohol hydroxyl group in the polar domains of ionic liquids, interacting preferentially with basic anions. In the case of less basic anions, as $[PF_6]$ and $[FAP]$ anions, which possess lower ability to interact with the hydroxyl group of the alcohol by hydrogen bond, the results exhibited a bigger role of the cation in the solvation process.

In this section, the nonpolar domains of the ionic liquids will be explored. Aiming to study the potential for interaction existent in the nonpolar domains of the ionic liquids to interact with simple molecular solutes and access the interplay between polar and nonpolar domains, alcohols of several alkyl chain length were used as molecular probes, taking advantage of its amphiphilic nature. To accomplish that goal, the effect of the alkyl chain length of both the cation and the alcohol in the solvation properties of ionic liquids is going to be studied.

In a first approach, the standard molar enthalpy of solution of 1-propanol (PrOH), 1-butanol (BuOH) and 1-pentanol (PentOH) in ionic liquids of different alkyl chain length was measured by the author of this thesis and Arijit Bhattacharjee using ITC, as described in the chapter 3 of this thesis. This initial work has already been published in literature, under the name "Alcohols as molecular probes in ionic liquids: evidence for nanostructuration"^[15]. In the context of this PhD thesis, this data was revisited and the standard molar enthalpy of solution at infinite dilution of 1-hexanol (HexOH), 1-heptanol (HeptOH) and 1-octanol (OctOH) in two IL series ($[C_N C_1 im][NTf_2]$ and $[C_N C_1 im][PF_6]$) was measured using ITC.

In the following pages, the strategy used to determine the effect of the alkyl chain of both the alcohol and the cation in the solution / solvation in ionic liquids will be addressed. The main results obtained in the topic will be presented and discussed.

4.3.1. Strategy

Using linear alcohols as solutes, the ability of the nonpolar domains of the ionic liquids for interaction with alcohols of different molecular weight was studied, aiming to have insights about the localization of the alcohols, the intermolecular interactions established and evaluate the influence of the variation of the size of the alkyl moieties of both alcohols and ILs.

To accomplish this purpose, the standard molar enthalpy of solution at infinite dilution of PrOH, BuOH, PentOH, HexOH, HeptOH and OctOH in ILs, constituted by cations of different alkyl chain length, was analysed. The study was performed for $[C_N C_1 \text{im}][\text{NTf}_2]$ and $[C_N C_1 \text{im}][\text{PF}_6]$ IL series, comparing if the effect of the alkyl chain is the same for the different anions. In figure 4.23, the experimental strategy used is schematized.

From the standard molar enthalpy of solution at infinite dilution of the different alcohols in ILs and the standard molar enthalpy of vaporization of those alcohols^[2, 32, 45], the standard molar enthalpy of solvation at infinite dilution was determined. The analysis of the obtained results will be based in the interpretation of the obtained solution and solvation data.

Solution & Solvation in Ionic Liquids

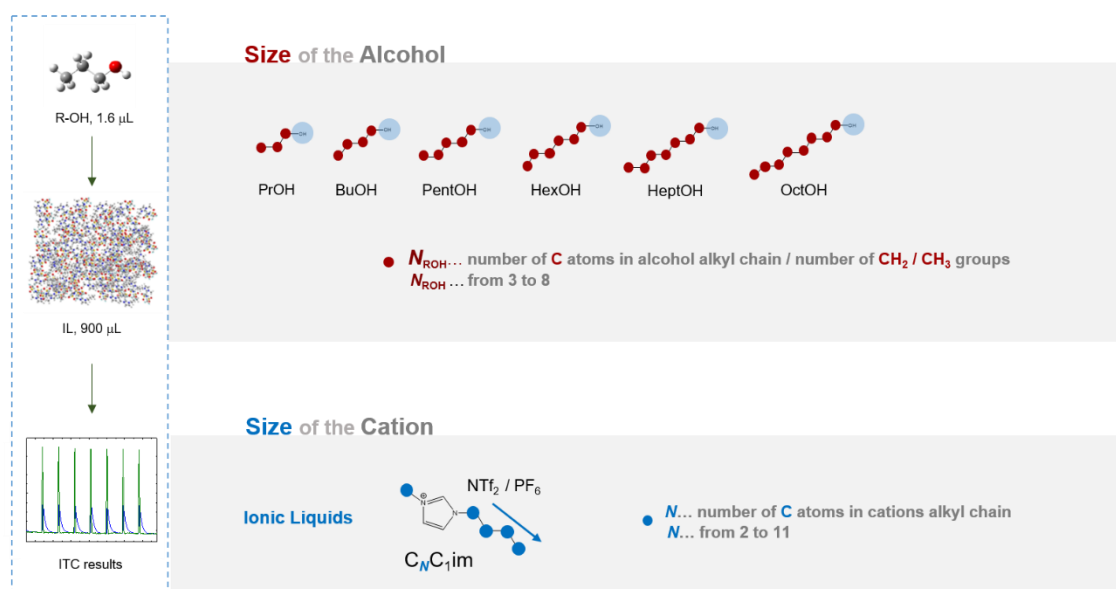


Figure 4.23. Scheme of the strategy used to determine the effect of the alkyl chain length, of both alcohol and cation, in the solvation of alcohols in ILs.

4.3.2. Results and Discussion

The experimental results of the standard ($p^\circ = 0.1$ MPa) molar enthalpy of solution at infinite dilution of the different alcohols in ILs, at the reference temperature ($T = 298.15$ K), are listed in tables 4.4 and 4.5. The respective standard molar enthalpy of solvation at infinite dilution of these systems is listed in tables 4.5 and 4.6. In tables 4.7 and 4.8, the values of the standard molar enthalpy of solution at infinite dilution were compared with the data existent in the literature [8, 11-14, 16, 46-52]. Together with these values, the deviations found between the literature data and our experimental results, which were calculated according to the equation 4.6, are presented in tables 4.7 and 4.8.

$$\delta / \% = 100 \times (\Delta_{\text{soln}} H_{\text{m, lit}}^{0, \infty} - \Delta_{\text{soln}} H_{\text{m, exp}}^{0, \infty}) / \Delta_{\text{soln}} H_{\text{m, exp}}^{0, \infty} \quad (4.6)$$

Table 4.4. Summary of the standard molar enthalpy of solution, at infinite dilution, of alcohols of different alkyl chain length in $[\text{C}_n\text{C}_1\text{im}][\text{NTf}_2]$ IL series, at the reference temperature ($T = 298.15$ K), obtained experimentally in ITC

Ionic Liquid	$\Delta_{\text{soln}} H_{\text{m}}^{0, \infty} / \text{kJ} \cdot \text{mol}^{-1}$					
	PrOH	BuOH	PentOH	HexOH	HeptOH	OctOH
$[\text{C}_2\text{C}_1\text{im}][\text{NTf}_2]$	8.72 ± 0.17	9.41 ± 0.19	9.86 ± 0.20	10.85 ± 0.10	11.82 ± 0.14	13.00 ± 0.67
$[\text{C}_3\text{C}_1\text{im}][\text{NTf}_2]$	8.58 ± 0.17	9.15 ± 0.18	9.44 ± 0.19	x	x	x
$[\text{C}_4\text{C}_1\text{im}][\text{NTf}_2]$	8.37 ± 0.24	8.89 ± 0.25	9.19 ± 0.25	9.54 ± 0.07	10.69 ± 0.12	11.11 ± 0.73
$[\text{C}_5\text{C}_1\text{im}][\text{NTf}_2]$	8.34 ± 0.17	8.70 ± 0.17	8.81 ± 0.18	x	x	x
$[\text{C}_6\text{C}_1\text{im}][\text{NTf}_2]$	8.13 ± 0.29	8.35 ± 0.24	8.53 ± 0.24	8.84 ± 0.14	9.38 ± 0.22	10.38 ± 0.60
$[\text{C}_7\text{C}_1\text{im}][\text{NTf}_2]$	8.38 ± 0.17	8.45 ± 0.17	8.32 ± 0.17	x	x	x
$[\text{C}_8\text{C}_1\text{im}][\text{NTf}_2]$	8.42 ± 0.17	8.53 ± 0.17	8.15 ± 0.16	8.49 ± 0.17	9.01 ± 0.47	9.45 ± 0.57
$[\text{C}_9\text{C}_1\text{im}][\text{NTf}_2]$	8.47 ± 0.17	8.50 ± 0.17	8.11 ± 0.16	x	x	x
$[\text{C}_{10}\text{C}_1\text{im}][\text{NTf}_2]$	8.45 ± 0.17	8.54 ± 0.17	8.18 ± 0.16	8.47 ± 0.18	8.68 ± 0.24	8.50 ± 0.34
$[\text{C}_{11}\text{C}_1\text{im}][\text{NTf}_2]$	8.57 ± 0.17	8.67 ± 0.17	8.10 ± 0.16	x	x	x

Table 4.5. Summary of the standard molar enthalpy of solution and solvation, at infinite dilution, of alcohols of different alkyl chain length in $[C_nC_1im][PF_6]$ IL series, at the reference temperature ($T = 298.15$ K), obtained experimentally in ITC

Ionic Liquid	$\Delta_{\text{soln}} H_m^{O, \infty} / \text{kJ} \cdot \text{mol}^{-1}$			$\Delta_{\text{solv}} H_m^{O, \infty} / \text{kJ} \cdot \text{mol}^{-1}$		
	PrOH	HexOH	OctOH	PrOH	HexOH	OctOH
$[C_4C_1im][PF_6]$	11.02 ± 0.22	14.23 ± 0.58	16.20 ± 1.86	-36.43 ± 0.97	-47.37 ± 1.36	-54.78 ± 2.34
$[C_5C_1im][PF_6]$	10.65 ± 0.15	x	x	-36.80 ± 0.96	x	x
$[C_6C_1im][PF_6]$	10.49 ± 0.21	11.24 ± 0.62	13.47 ± 1.06	-36.96 ± 0.97	-50.36 ± 1.38	-57.51 ± 1.77
$[C_7C_1im][PF_6]$	10.25 ± 0.38	x	x	-37.20 ± 1.02	x	x
$[C_8C_1im][PF_6]$	10.16 ± 0.36	11.46 ± 0.61	10.87 ± 0.62	-37.29 ± 1.01	-50.14 ± 1.37	-60.11 ± 1.55
$[C_9C_1im][PF_6]$	9.89 ± 0.35	x	x	-37.56 ± 1.01	x	x

Table 4.6. Summary of the standard molar enthalpy of solvation, at infinite dilution, of alcohols of different alkyl chain length in $[C_nC_1im][NTf_2]$ IL series, at the reference temperature ($T = 298.15$ K)

Ionic Liquid	$\Delta_{\text{solv}} H_m^{O, \infty} / \text{kJ} \cdot \text{mol}^{-1}$					
	PrOH	BuOH	PentOH	HexOH	HeptOH	OctOH
$[C_2C_1im][NTf_2]$	-38.73 ± 0.96	-42.94 ± 1.06	-47.16 ± 1.16	-50.75 ± 1.24	-54.98 ± 1.34	-57.98 ± 1.57
$[C_3C_1im][NTf_2]$	-38.87 ± 0.96	-43.20 ± 1.06	-47.58 ± 1.16	x	x	x
$[C_4C_1im][NTf_2]$	-39.08 ± 0.98	-43.46 ± 1.08	-47.83 ± 1.17	-52.06 ± 1.23	-56.11 ± 1.34	-59.87 ± 1.60
$[C_5C_1im][NTf_2]$	-39.11 ± 0.96	-43.65 ± 1.06	-48.21 ± 1.15	x	x	x
$[C_6C_1im][NTf_2]$	-39.32 ± 0.99	-44.00 ± 1.07	-48.49 ± 1.17	-52.76 ± 1.24	-57.42 ± 1.35	-60.60 ± 1.54
$[C_7C_1im][NTf_2]$	-39.07 ± 0.96	-43.90 ± 1.06	-48.70 ± 1.15	x	x	x
$[C_8C_1im][NTf_2]$	-39.03 ± 0.96	-43.82 ± 1.06	-48.87 ± 1.15	-53.11 ± 1.24	-57.79 ± 1.42	-61.53 ± 1.53
$[C_9C_1im][NTf_2]$	-38.98 ± 0.96	-43.85 ± 1.06	-48.91 ± 1.15	x	x	x
$[C_{10}C_1im][NTf_2]$	-39.00 ± 0.96	-43.81 ± 1.06	-48.84 ± 1.15	-53.13 ± 1.25	-58.12 ± 1.36	-62.48 ± 1.46
$[C_{11}C_1im][NTf_2]$	-38.88 ± 0.96	-43.68 ± 1.06	-48.92 ± 1.15	x	x	x

Table 4.7. Comparison of standard molar enthalpy of solution, at infinite dilution, of alcohols in [C_nC₁im][NTf₂] IL series obtained experimentally in ITC, at the reference temperature (*T* = 298.15 K), with literature data

System		$\Delta_{\text{soln}}H_{\text{m}}^{\text{o}} / \text{kJ}\cdot\text{mol}^{-1}$		
IL	Alcohol	This work	Literature	$\delta / \%$
[C ₂ C ₁ im][NTf ₂]	PrOH	8.72 (± 0.17)	7.946 (± 0.360) ^a	-8.9
			6.926 ^b	-21
	BuOH	9.41 (± 0.19)	9.307 (± 0.420) ^a	-1.1
			8.518 (± 0.140) ^c	-9.5
	PentOH	9.86 (± 0.20)	11.217 (± 0.480) ^a	14
	HexOH	10.85 (± 0.10)	10.812 (± 450) ^a	-0.4
7.702 (± 12.347) ^c			-29	
			10.100 (± 0.600) ^d	-6.9
[C ₄ C ₁ im][NTf ₂]	PrOH	8.37 (± 0.24)	12.6 ^e	50
	BuOH	8.89 (± 0.25)	9.8 ^e	10
			-3.2 (± 0.9) ^f	-136
	PentOH	9.19 (± 0.25)	9.7 ^e	5.5
	HexOH	9.54 (± 0.07)	9.9 ^e	3.8
	HeptOH	10.69 (± 0.12)	10.7 ^e	0.1
[C ₆ C ₁ im][NTf ₂]	PrOH	8.13 (± 0.29)	7.536 ^b	-7.3
			11.4 ^g	40.2
	BuOH	8.35 (± 0.24)	8.1 ^h	-0.4
			9.201 (± 0.125) ^c	10
	PentOH	8.53 (± 0.24)	9.0 ^g	7.8
			9.1 ^h	9.0
	HexOH	8.84 (± 0.14)	9.6 (± 0.8) ⁱ	15
			9.32 (± 0.01) ^j	12
	PentOH	8.53 (± 0.24)	9.4 ^g	10
	[C ₈ C ₁ im][NTf ₂]	PrOH	8.42 (± 0.17)	9.074 (± 0.230) ^c
9.3 ^g				5.2
BuOH		8.53 (± 0.17)	9.8 (± 0.8) ⁱ	11
			9.04 (± 0.07) ^j	2.3
[C ₈ C ₁ im][NTf ₂]	PrOH	8.42 (± 0.17)	8.445 ^b	0.3
	BuOH	8.53 (± 0.17)	-6.8 ± 0.1 ^f	-180

a – determined by Gas Chromatography (313 K – 343 K) ref. [46];
b – determined by Gas Chromatography (303 K – 333 K) ref [47];
c – determined by ITC (298.15 K), ref. [16];
d – determined by ITC (298.15 K), ref. [48];
e – determined by Gas Chromatography (312 – 385 K), ref. [8];
f – determined by Gas Chromatography (333 K – 363 K), ref. [49];
g – determined by Gas Chromatography (temperatures between 312.5 K and 396 K; different for each alcohol), ref. [50];
h – determined by the Dilutor Technique (293 K – 353 K), ref. [12];
i – determined by Gas Chromatography (298 K – 396 K), ref. [51];
j – determined by ITC (298.15 K), ref. [51].

Table 4.8. Comparison of standard molar enthalpy of solution, at infinite dilution, of alcohols in $[C_N C_1 \text{im}][\text{PF}_6]$ IL series obtained experimentally in ITC, at the reference temperature ($T = 298.15 \text{ K}$), with literature data

System		$\Delta_{\text{soln}} H_m^{0, \infty} / \text{kJ} \cdot \text{mol}^{-1}$		
IL	Alcohol	This work	Literature	$\delta / \%$
$[\text{C}_4 \text{C}_1 \text{im}][\text{PF}_6]$	PrOH	$11.02 (\pm 0.22)$	11.6 ^a	5.3
			6.2385 ^b	-43
			9.875 ^c	-10
			10.81 ^d	-1.9
$[\text{C}_6 \text{C}_1 \text{im}][\text{PF}_6]$	PrOH	10.49 ± 0.21	$2.212 (\pm 0.0033)$ ^e	-98
$[\text{C}_8 \text{C}_1 \text{im}][\text{PF}_6]$	PrOH	10.16 ± 0.36	$6.901 (\pm 0.0282)$ ^e	-96

a – determined by the Dilutor Technique (293 K – 353 K), ref. [12];

b – determined by Gas Chromatography (313 K – 333 K), ref. [13];

c – determined by ITC (298.15 K), ref. [11];

d – determined by Gas Chromatography (316 K – 335 K), ref. [14];

e – determined by Gas Chromatography (303 K – 363 K), ref. [52].

Most of our experimental values deviate from 5% to 15% from literature results. Positive and negative deviations were found and there is no indication of a systematic deviation in our values. Nevertheless, it is notorious the high dispersion of the data, with large deviations amongst different authors, even using similar methodologies. Furthermore, the data reported by Stark et al.^[49] is exothermic. However, to our knowledge any other author has reported exothermic enthalpy of solution regarding the systems under study. If the existence of some typing mistake is assumed and the correspondent data is assumed to be endothermic, the deviations to our values would be of 64 % and 20 %, which are much more reasonable deviations and are in the range of the deviations found in the experimental values of this property.

The large deviations found with regard to the enthalpy values obtained from activity coefficients may at a first approximation be explained by the range of temperatures used in the experiments. However, even amongst values obtained from calorimetric experiments, performed at the reference temperature ($T = 298.15 \text{ K}$), deviations in the order of 30 % may be found. These deviations in the enthalpy of solution highlight the sensitivity of the property to the sample purity. In the particular case of the calorimetric experiments, probably in addition to the sample purity, the experimental procedure used in both titration and calibration experiments also play a predominant role.

In figure 4.24 the standard molar enthalpy of solution at infinite dilution of PrOH, ButOH, PentOH, HexOH, HeptOH and OctOH in $[C_N C_1 \text{im} \text{NTf}_2]$ IL series is presented as a function of the number of carbons existent in the alkyl chain of the imidazolium cation.

At small sizes of the cation's alkyl chain, it is evident from figure 4.24, an increase to a more endothermic enthalpy of solution at infinite dilution, with the increase in the number of carbons of the alcohol alkyl chain. However, as the number of carbons in the cation's alkyl chain increases, the enthalpy of solution of all of the alcohols seems to converge to approximately $8.5 \text{ kJ} \cdot \text{mol}^{-1}$.

To a better interpretation of the results, a variable Z that correlates the size of both cations and alcohols is created:

$$Z = N - N_{\text{ROH}}, \quad (4.7)$$

where N is the number of carbons in the cation alkyl chain ($[C_N C_1 \text{im}][\text{Anion}]$) and N_{ROH} is the number of carbons in the alcohol alkyl chain ($\text{C}_{N_{\text{ROH}}} \text{H}_{2N_{\text{ROH}}+1} \text{OH}$).

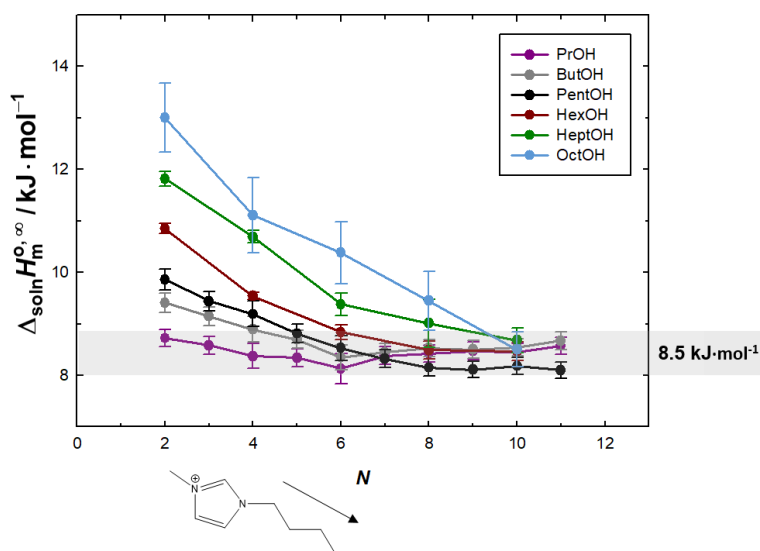


Figure 4.24. Graphical representation of the standard molar enthalpy of solution, at infinite dilution, of PrOH, ButOH, PentOH, HexOH, HeptOH and OctOH in $[C_N C_1 \text{im}][\text{NTf}_2]$ IL series, at the reference temperature ($T = 298.15 \text{ K}$), as a function of the number N of carbons in the alkyl side chain of the cation. The lines are just a guide line to the eyes.

In figure 4.25, the enthalpy of solution at infinite dilution of the alcohols studied is represented as a function of this Z variable. The analysis of the enthalpy of solution as a function of this variable gives very interesting results. It is clear from the analysis of the presented plot that when the alcohol has a bigger number of carbons in its alkyl chain than the cation, $Z < 0$, the enthalpy of solution is more endothermic. As the number of carbons of the cation alkyl chain increases, equalizing the number of carbons in the alcohols alkyl chain, from $Z \ll 0$ to $Z = 0$, the enthalpy of solution decreases. A minimum in the enthalpy of solution appears to be found when the cation has approximately more 2 to 3 atoms than the alcohol, $Z = 2$ or $Z = 3$. Beyond this size it seems that the enthalpy of solution is approximately $8.5 \text{ kJ} \cdot \text{mol}^{-1}$, independently of the size of the alcohol or the cation, as long as the cation has more 2 to 3 carbons than the alcohol.

In figures 4.26 and 4.27 the previous plots are repeated, now presenting the enthalpy of solution obtained in the $[\text{C}_n\text{C}_{1m}][\text{PF}_6]$ IL series. Overall, the solution in $[\text{C}_n\text{C}_{1m}][\text{PF}_6]$ IL series seems to follow the trend of the enthalpy of solution in $[\text{C}_n\text{C}_{1m}][\text{NTf}_2]$ IL series with the exception of the values converging for $10.2 \text{ kJ} \cdot \text{mol}^{-1}$, instead of $8.5 \text{ kJ} \cdot \text{mol}^{-1}$.

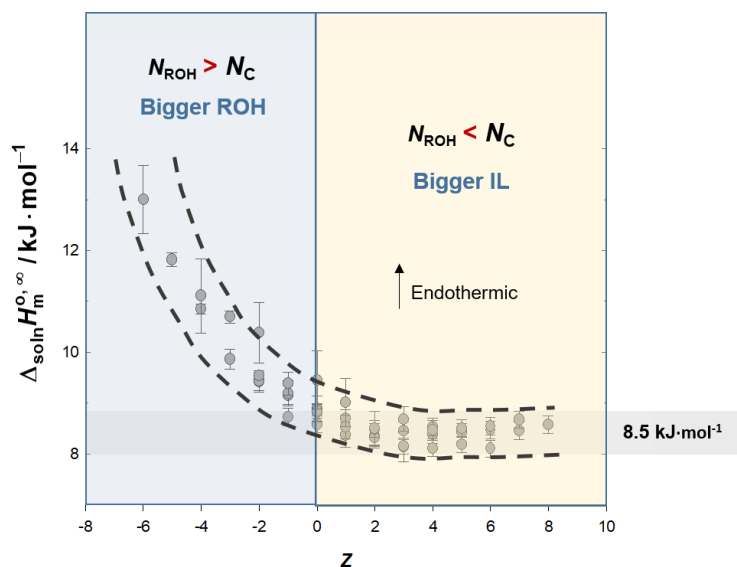


Figure 4.25. Graphical representation of the standard molar enthalpy of solution, at infinite dilution, of ProOH, ButOH, PentOH, HexOH, HeptOH and OctOH in $[\text{C}_n\text{C}_{1m}][\text{NTf}_2]$ IL series, at the reference temperature ($T = 298.15 \text{ K}$), as a function of the variable Z , that relates the number of carbons in the alcohol alkyl chain with the number of carbons in the cation alkyl chain.

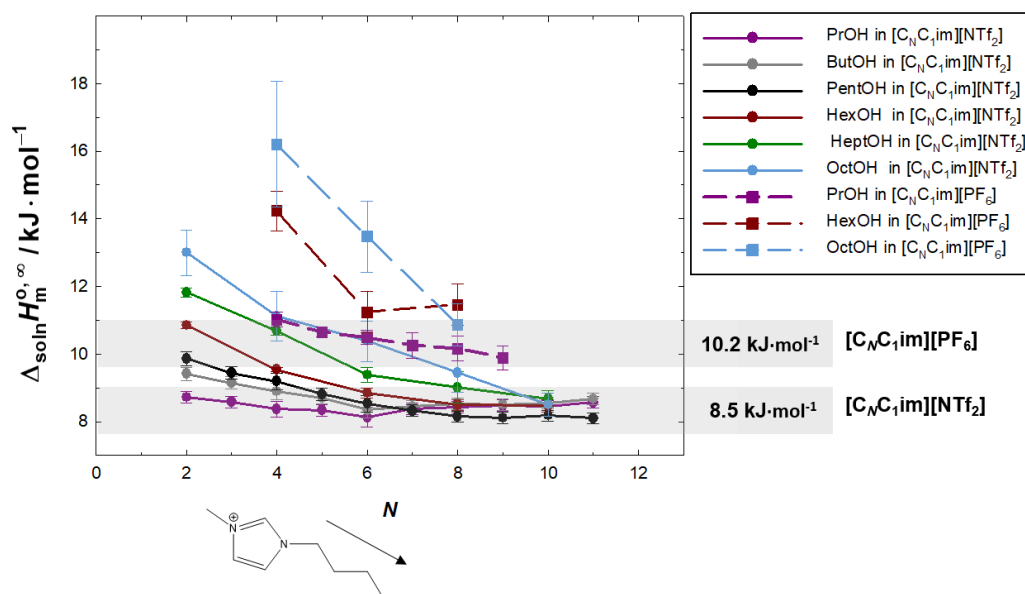


Figure 4.26. Graphical representation of the standard molar enthalpy of solution, at infinite dilution, of ProOH, ButOH, PentOH, HexOH, HeptOH and OctOH in $[\text{C}_N\text{C}_1\text{im}][\text{NTf}_2]$ and $[\text{C}_N\text{C}_1\text{im}][\text{PF}_6]$ IL series, at the reference temperature ($T = 298.15 \text{ K}$), as a function of the number N of carbons in the alkyl side chain of the cation. The lines are just guide lines to the eyes.

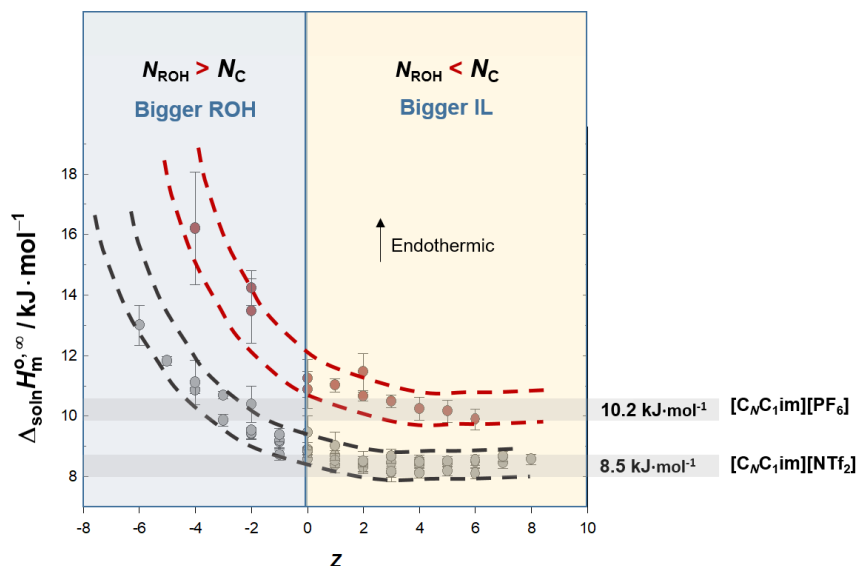


Figure 4.27. Graphical representation of the standard molar enthalpy of solution, at infinite dilution, of ProOH, ButOH, PentOH, HexOH, HeptOH and OctOH in $[\text{C}_N\text{C}_1\text{im}][\text{NTf}_2]$ and $[\text{C}_N\text{C}_1\text{im}][\text{PF}_6]$ IL series, at the reference temperature ($T = 298.15 \text{ K}$) as a function of the variable Z , that relates the number of carbons in the alcohol alkyl chain with the number of carbons in the cation alkyl chain.

The convergence of the enthalpy of solution of all the studied alcohols is an interesting achievement. Considering the thermochemical cycle depicted in figure 4.19, the enthalpy of solution of an alcohol in an IL can be interpreted as the sum of the enthalpy of vaporization of the alcohol with the enthalpy of solvation of the alcohol in an IL (equation 4.4). Accordingly, the convergence of the values of the enthalpy of solution, after $Z = 2$ or $Z = 3$, indicates that the increment in the enthalpy of solvation caused by the addition of a methylene group " $>\text{CH}_2$ " must be approximate to the increment in the enthalpy of vaporization. In figure 4.28, the enthalpy of solvation at infinite dilution of PrOH, ButOH, PentOH, HexOH, HeptOH and OctOH in $[\text{C}_8\text{C}_1\text{im}][\text{NTf}_2]$ and $[\text{C}_8\text{C}_1\text{im}][\text{PF}_6]$ are represented together with the symmetric of the vaporization enthalpy of these alcohols. Together with the data, a linear fitting is also represented. Indeed, the increment in the enthalpy of solvation by addition of a " $>\text{CH}_2$ " group to the alcohol alkyl chain is $-4.53 \text{ kJ}\cdot\text{mol}^{-1}$ ($[\text{C}_8\text{C}_1\text{im}][\text{NTf}_2]$) and $-4.54 \text{ kJ}\cdot\text{mol}^{-1}$ ($[\text{C}_8\text{C}_1\text{im}][\text{PF}_6]$). These values are very similar to the increment in the enthalpy of vaporization caused by addition of a " $>\text{CH}_2$ " group to the alcohol alkyl chain $4.73 \text{ kJ}\cdot\text{mol}^{-1}$. On its turn, this value is close to the value reported by Matulis^[37] regarding the contribution by methylene group for the enthalpy of vaporization of alcohols, alkanes and alkylamines, $4.95 \text{ kJ}\cdot\text{mol}^{-1}$.

The symmetric of the enthalpy of vaporization could be interpreted as the enthalpy of solvation of the alcohol in itself. The linear fittings of the data presented in figure 4.28 highlight the parallel behaviour of the fittings, evidencing a similar effect of the size of the alcohol in its solvation in itself and in the ionic liquids studied. In fact, the differentiation between the data seems to be in the enthalpy axis intercept, which is related with the energy of interaction of the hydroxyl group with the solvent.

Our interpretation is that the convergence value of the enthalpy of solution is originated by a balance between the interactions established by an alcohol molecule amongst alcohol molecules or by an alcohol molecule and the cations/anions of an ionic liquid. Moreover, as the interactions of the alkyl moieties, " $>\text{CH}_2$ " to " $>\text{CH}_2$ " are similar in both alcohols and ionic liquids, the difference in the convergence of the enthalpy of solution found for $[\text{C}_M\text{C}_1\text{im}][\text{NTf}_2]$ and $[\text{C}_M\text{C}_1\text{im}][\text{PF}_6]$ must arise from the polar domain of the ionic liquid and how it interacts with the hydroxyl group of the alcohol.

In fact, by the extrapolation of both enthalpy of solvation and enthalpy of vaporization of the alcohol to the number of carbon atoms "zero", a balance between the interactions established by the hydroxyl group of the alcohol with alcohol molecules and with the IL is obtained. By extrapolation of the linear fitting of the data presented in figure

4.28 to $N_{\text{ROH}} = 0$, it is possible to estimate the enthalpy of solution at the convergence in $[\text{C}_8\text{C}_1\text{im}][\text{NTf}_2]$ IL series :

$$\Delta_{\text{soln}} H_{\text{m}}^{0, \infty} = \Delta_{\text{l}}^{\text{g}} H_{\text{m}}^0 + \Delta_{\text{solv}} H_{\text{m}}^{0, \infty} = 33.3 - 25.8 = 7.5 \text{ kJ} \cdot \text{mol}^{-1}, \quad (4.8)$$

and in $[\text{C}_8\text{C}_1\text{im}][\text{PF}_6]$ IL series:

$$\Delta_{\text{soln}} H_{\text{m}}^{0, \infty} = \Delta_{\text{l}}^{\text{g}} H_{\text{m}}^0 + \Delta_{\text{solv}} H_{\text{m}}^{0, \infty} = 33.3 - 23.4 = 9.9 \text{ kJ} \cdot \text{mol}^{-1}. \quad (4.9)$$

The proximity of the estimated values to the ones experimentally obtained give strength to our interpretation. In accordance, providing that sufficient number of carbons are present in the IL alkyl chain to accommodate the alcohol, $Z = 2$ or $Z = 3$, the alkyl chain of the alcohol will interact in IL as it will interact amongst its own molecules. On the light of our results, the ability of the anion / cation to interact with the hydroxyl group of the alcohol will be the cause of the differentiation amongst the solution behaviour in different IL families.

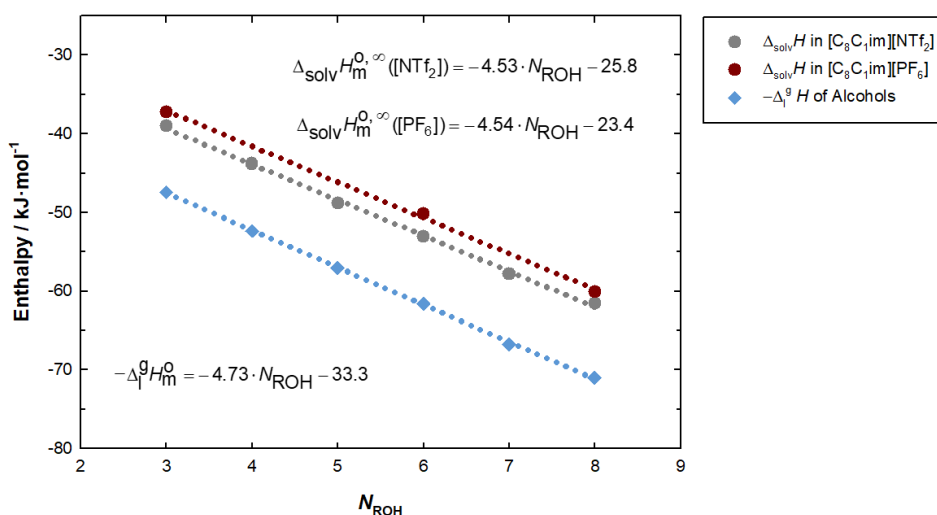


Figure 4.28. Graphical representation of the standard molar enthalpy of solvation, at infinite dilution, of PrOH, ButOH, PentOH, HexOH, HeptOH and OctOH in $[\text{C}_8\text{C}_1\text{im}][\text{NTf}_2]$ and $[\text{C}_8\text{C}_1\text{im}][\text{PF}_6]$ IL series, as well as, the symmetric of the enthalpy of vaporization of the referred alcohols, at the reference temperature ($T = 298.15 \text{ K}$), as a function of the number of carbons in the alcohol alkyl chain. The dotted lines constitute the linear fitting of the represented data.

Following this line, the increase in the enthalpy of solution in small ionic liquids with the increase of the alkyl chain of the alcohol may be interpreted as being caused by the increase of the cavitation energy (endothermic) along with the impossibility of the nonpolar moieties of the IL (due to its small size) to accommodate the size of the alkyl chain of the alcohol.

Accordingly, a long alcohol, as 1-octanol, is too big to be accommodated in a small IL as $[C_4C_{1im}][NTf_2]$ for example. The cavitation energy (endothermic contribution) is bigger than in the case of solution of 1-hexanol or 1-butanol and, in addition, the alkyl moieties of the IL are not long enough to interact with the " $>CH_2$ " groups as if the alcohol was between alike molecules. Therefore, enthalpy of solution is higher in this case. As the alkyl chain size of the IL cation increases, there are more " $>CH_2$ " groups of the IL available to interact with the " $>CH_2$ " groups of the alcohol. As the interaction has an exothermic contribution, the enthalpy of solution decreases with the increase of the alkyl chain of the IL cation. However, when the alkyl chain of the ionic liquid cation is bigger than the alkyl chain of the alcohol, we could say that the positions for " $>CH_2$ " to " $>CH_2$ " interaction are all occupied and no more " $>CH_2$ " positions of the alcohol are available for interaction with the new " $>CH_2$ " groups of the cation. Therefore, after a certain length of the cation, relatively to the alcohol, the size of the cation may increase but there will be no change in the enthalpy of the solution of the alcohol.

The interpretation presented was based in the enthalpy of solution. However, the enthalpy of solvation of these alcohols also reflect the effect of the stabilization of the enthalpy at a certain length of the cation relatively to the alcohol. In figure 4.29, the enthalpy of solvation of PrOH, BuOH, PentOH, HexOH, HeptOH and OctOH in $[C_N C_{1im}][NTf_2]$ IL series is represented as a function of the Z variable highlighting this phenomenon.

In figure 4.30, the graphical representations are replicated for the enthalpy of solvation at infinite dilution of PrOH, HexOH and OctOH in $[C_N C_{1im}][PF_6]$ IL series. The results seem to follow the trends of the solvation in $[C_N C_{1im}][NTf_2]$ IL series, despite of the smaller number of measurements. Overall, the results reflect a decrease in the enthalpy of solvation at infinite dilution until a certain value of Z , remaining approximately constant after this value, despite of the increase of the number of carbons in the alkyl side chain of the cation relatively to the alkyl chain of the alcohol. The initial decrease of the enthalpy of solvation reflects the increase in the " $>CH_2$ " to " $>CH_2$ " interactions between the alcohol and the alkyl side chain of the cation. The value of Z at which the decreasing trend of the enthalpy of solvation shifts to an approximately constant enthalpy

of solvation seem to be different depending on the system, varying between $Z = 0$ and $Z = 3$. The approximately constant enthalpy of solvation found can be explained by the “saturation” of the available positions of the alcohol to “>CH₂” to “>CH₂” alcohol-IL interaction. These results are in complete agreement with the interpretation model proposed.

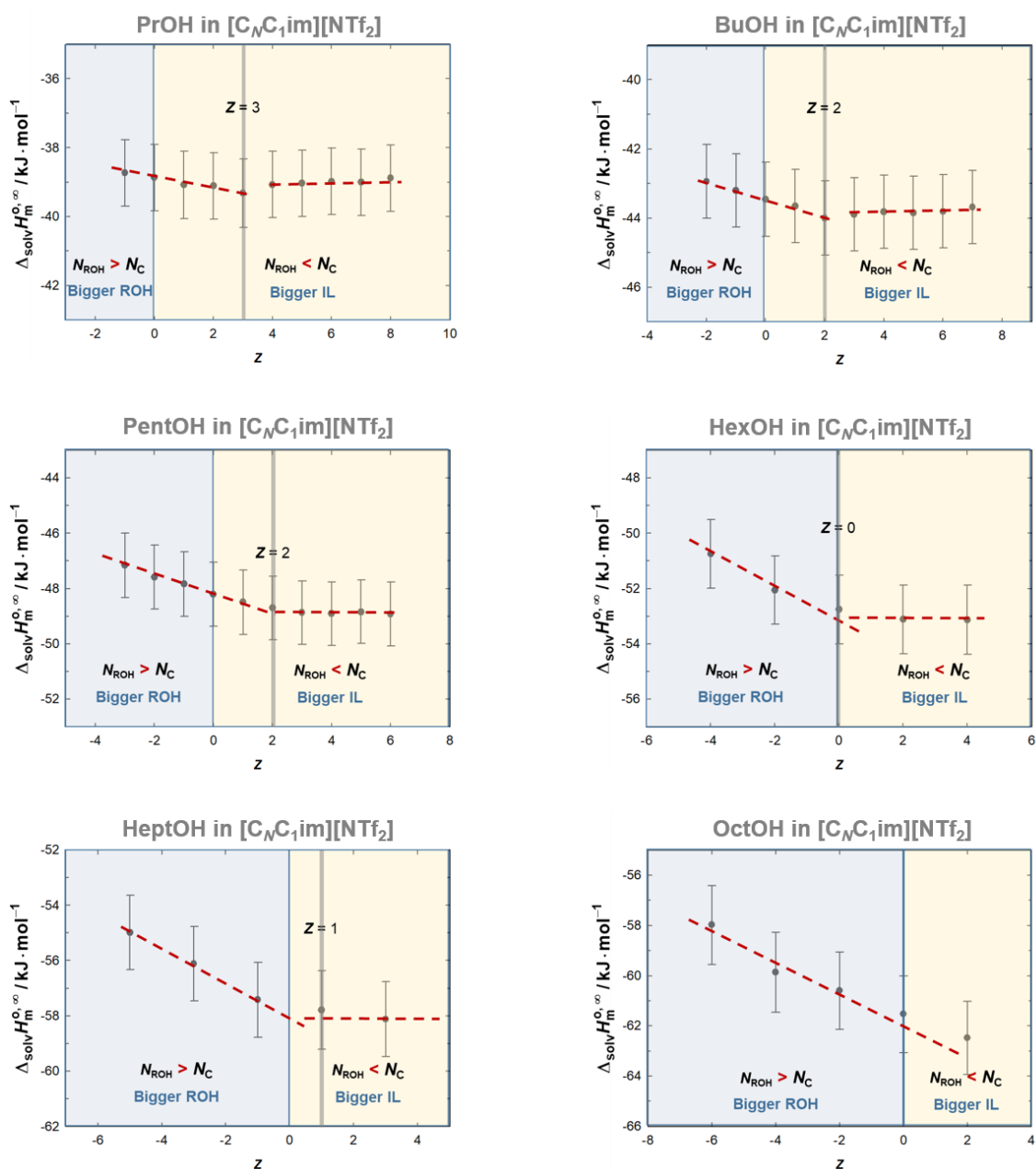


Figure 4.29. Graphical representations of the standard molar enthalpy of solvation, at infinite dilution, of PrOH, BuOH, PentOH, HexOH, HeptOH and OctOH in $[\text{C}_N \text{C}_1 \text{im}][\text{NTf}_2]$ IL series, at the reference temperature ($T = 298.15 \text{ K}$), as a function of the variable Z , that relates the number of carbons in the alcohol alkyl chain with the number of carbons in the cation alkyl chain. The lines are just guide lines for the eyes.

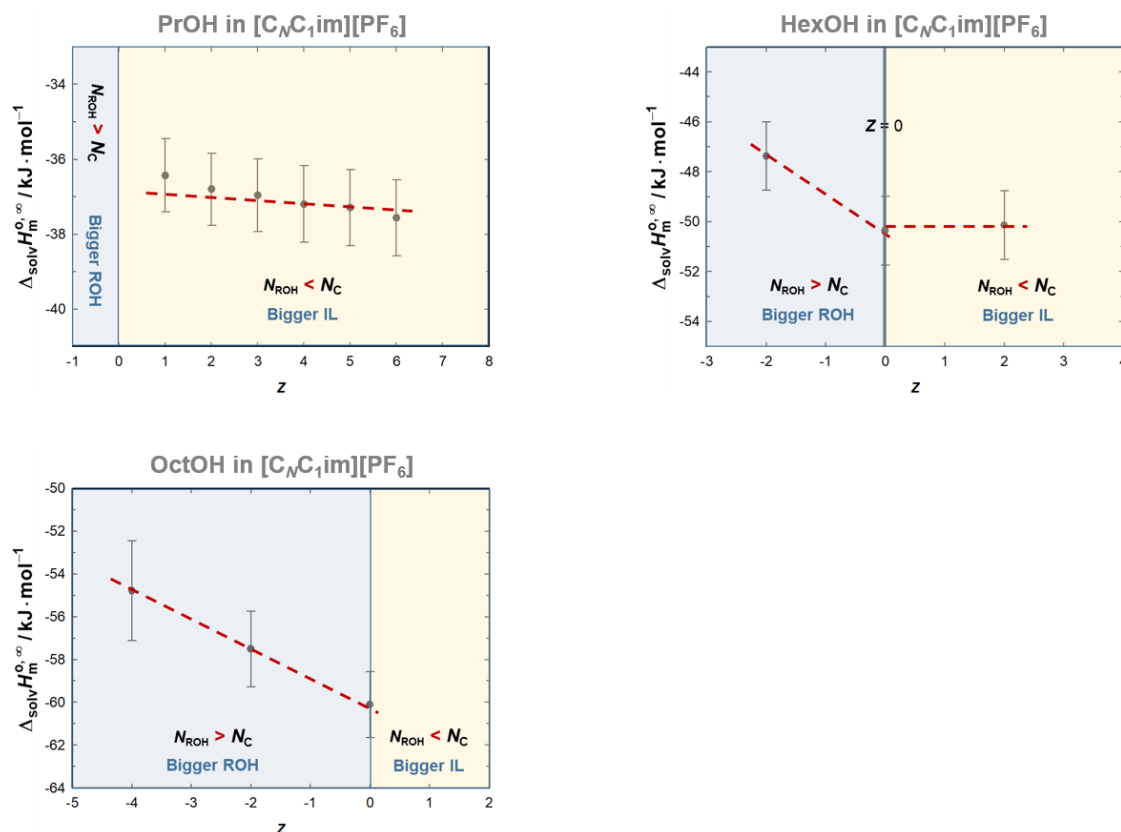


Figure 4.30. Graphical representations of the standard molar enthalpy of solvation, at infinite dilution, of ProOH, HexOH and OctOH in $[\text{C}_N \text{C}_1 \text{im}][\text{PF}_6]$ IL series, at the reference temperature ($T = 298.15 \text{ K}$), as a function of the variable Z , that relates the number of carbons in the alcohol alkyl chain with the number of carbons in the cation alkyl chain. The lines are just guide lines for the eyes.

Overall, the results suggest that alcohols are preferentially located both at the polar and nonpolar domains. The hydroxyl group seems to be preferentially located at the polar domain of the ionic liquid interacting with basic anions by hydrogen bond. The alkyl parts of the alcohol interact with the nonpolar domains of the ILs similarly to interactions established in bulk alkanes. These results are in accordance with the so called “solvation paradigm” described in the literature. This model defends that solutes will be preferentially located in the polar and nonpolar domains of the ionic liquids depending on their polar or nonpolar nature. In the specific case of alcohols, due to their amphiphilic nature, they are preferentially located in both polar and nonpolar domains: the alkyl chain in the nonpolar domain and the hydroxyl group in the polar domain interacting through hydrogen bonding, as schematized in the figure 4.31.

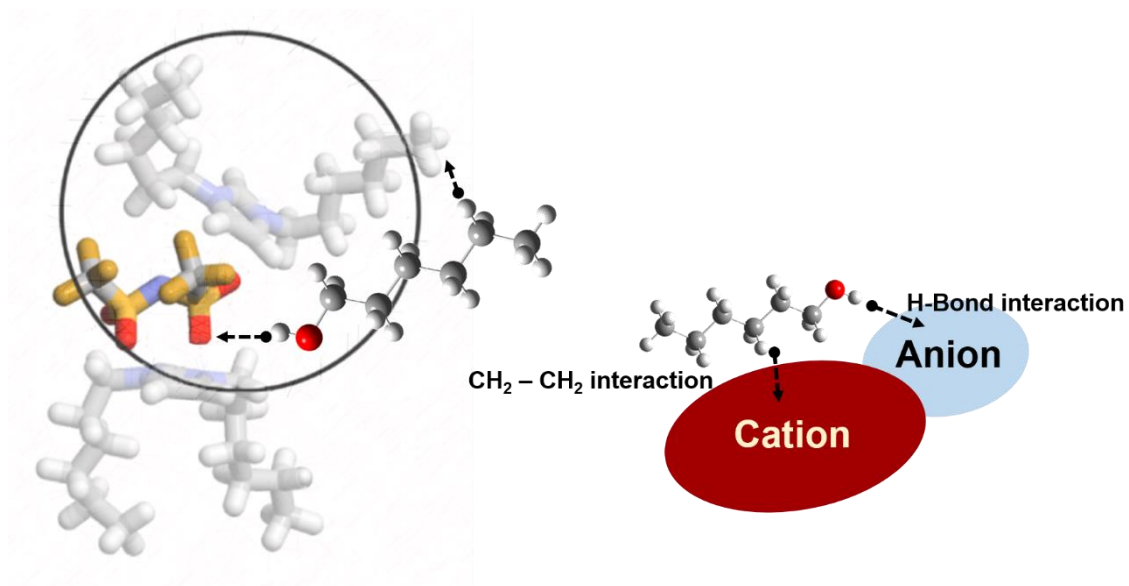


Figure 4.31. Representative scheme of the preferential location of the alcohol in ionic liquids interacting with the nonpolar domains through “>CH₂” to “>CH₂” interactions and forming an alcohol - anion hydrogen bond. Figure adapted from a configuration of a simulation run of [C₆C₆im][NTf₂] of ref.[53] in which the sphere of influence of the polar network is represented.

4.4. Enthalpy of Mixing of a Binary Mixture of Alcohol – IL

In the previous subchapters the study of solution and solvation of alcohols in ionic liquids, at infinite dilution was presented and discussed. That study encompassed the understanding of both the solution/solvation environment and energetics, as well as, the role of the polar and nonpolar domains of the ILs in the solvation phenomena. Over the previous pages, important insights into the topic, as the location of alcohols at both polar and nonpolar domains of the ionic liquids, have been found:

- preferential interaction by hydrogen bond of the hydroxyl group of the alcohol with IL anions;
- significant role of the cation on the solvation process in ionic liquids with poor basicity;
- similar magnitude of the alkyl chain interaction alcohol - ILs to the interactions established in the bulk of alkanes, locating alcohol alkyl moieties in IL nonpolar domains.

These insights are valid at infinite dilution conditions. As the content of the alcohol in the ionic liquid increases forming binary mixtures, from rich ionic liquid mixtures to rich alcohol mixtures, different structuration and interaction profiles are expected. The μ FlowCal calorimeter was designed and developed in order to explore the effect of the concentration of alcohols and other solutes in ionic liquids. It allows the measurement of the heat of mixing of binary mixtures in the full concentration range (or as the mutual solubility would allow).

In this subchapter, the results of the excess molar enthalpy of the binary mixture BuOH + [C₆C₁im][NTf₂], obtained in μ FlowCal, at the reference temperature ($T = 298.15$ K), are presented. The obtained results are discussed and compared with the available literature data. The results presented in this subchapter evidence the utility and feasibility of the μ FlowCal calorimeter to explore the structuration and energetics of the binary mixtures containing ILs.

Due to a problem in the sample side of the calorimeter, the reference calorimetric system was used to perform the BuOH + [C₆C₁im][NTf₂] mixtures and the “initial sample side” was used as a reference. Therefore, the electrical calibration constant of the “initial reference side” was used, with a 6% correction (systematic deviation found on the “initial sample side”): $8.78 \times 10^{-6} \text{ (J}\cdot\text{s}^{-1})/\mu\text{V}$.

4.4.1. Experimental Methodology

The μ FlowCal calorimeter was used in the measurement of the heat of mixing of the binary mixture BuOH + [C₆C₁im][NTf₂], at the reference temperature ($T = 298.15$ K), in the molar fraction range ($0.15 < x_{\text{BuOH}} < 0.95$).

The measurements were performed in stopped-flow mode, as described in the chapter 3 of the thesis. The fluids were injected simultaneously, in a total of 200 mm³ (μ L), with the mixture occurring at the mixing zone of the reactor. The complete mixing of the BuOH and [C₆C₁im][NTf₂] turned out to be a very slow process that could take a few hours. Accordingly, the slow mode injection methodology, which would involve the return of the calorimetric signal to the baseline level before each injection has been found to be an inefficient methodological procedure due to the existence of significant back diffusion. Therefore, in order to successfully decrease the back diffusion, the time interval between injections has been reduced to 30 minutes. This time interval is enough to observe more than 90% of the mixing process by in situ diffusion and is short enough to decrease the back diffusion to negligible levels. The evaluation of the heat fraction, which was not captured due to the reduction of the time interval between injections, was calculated from the integration of the decay of the calorimetric signal to the baseline, which was well fitted by an exponential decay (equation 4.10):

$$\phi(t) = (\phi_{\infty} - \phi_i) \cdot e^{-k(t-t_i)}, \quad (4.10)$$

where, ϕ is the heat flow signal, k is the exponential decay constant, which defines the rate of the decay, t is the time of the experiment and the subscripts “ ∞ ” and “ i ” are associated with the baseline level and the beginning of the exponential decay, respectively. It was verified that the exponential decay of the calorimetric signal ((associated to the in situ diffusion) had the same rate of decay (k), despite of the concentration tested.

Therefore, the integration of the peak associated to each injection was later corrected, to include the heat lost by doing a new injection before the complete return of the signal to the baseline level. In each set of experiments (for a certain concentration), the peaks associated with the first injections were discarded as the purpose of these first injections is to fill the micromixer with the desired BuOH / [C₆C₁im][NTf₂] molar fraction. In figure 4.32 is presented the corrected heat flow signal obtained in μ FlowCal calorimeter in a set of injections performed to determine the excess molar enthalpy of

the binary mixture BuOH / [C₆C₁im][NTf₂] at the molar fraction $x_{\text{BuOH}} = 0.54$, at the reference temperature, ($T = 298.15$ K).

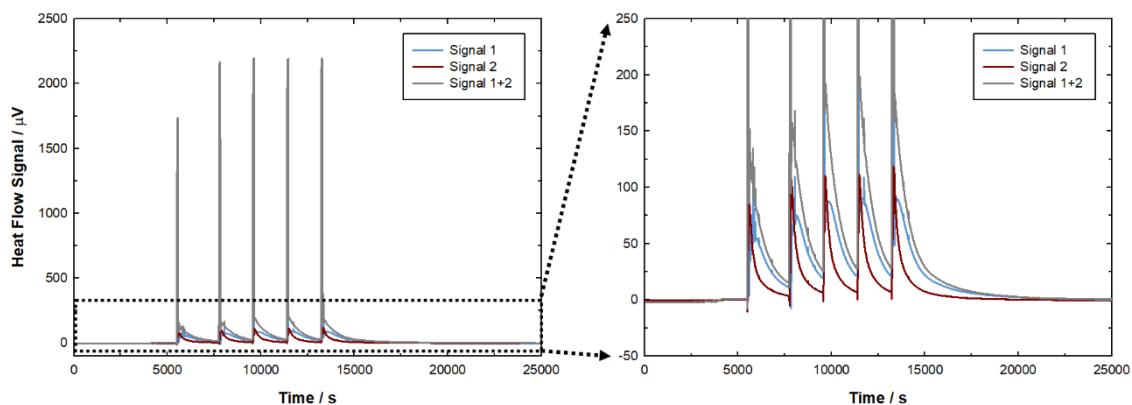


Figure 4.32. Graphical representation of the heat flow signal obtained in μ FlowCal calorimeter, corrected to the time constant of the calorimeter, in a binary mixture BuOH + [C₆C₁im][NTf₂] ($x_{\text{BuOH}} = 0.54$) as a function of the experimental time (on the left) and of a magnification on the heat flow signal axis (on the right).

4.4.2. Results and Discussion

In table 4.9, the preliminary results of the excess molar enthalpy of the binary mixture BuOH + [C₆C₁im][NTf₂], determined experimentally in μ FlowCal calorimeter, at the reference temperature ($T = 298.15$ K), are summarized. These results are graphically represented in figure 4.33 as a function of the molar fraction of 1-butanol. Together with the results is presented the fitting of the experimental data, determined with the Redlich-Kister equation using 6 parameters (in kJ·mol⁻¹): A_0 , (12.14 ± 0.14); A_1 , (1.182 ± 0.605); A_2 , (-3.116 ± 1.281); A_3 , (5.947 ± 3.167); A_4 , (3.952 ± 2.386); A_5 , (-2.218 ± 4.069). The shape of the curve of the excess enthalpy of mixing could be captured with 4 parameters. However, it was observed that the fitting with 6 parameters provided a better description of the data close to the infinite dilution of the alcohol. Care was taken not to induce artefacts in the results. Due to the variability of the excess molar enthalpy at some concentrations, the fitting was performed using all the experimental data and not the average of the excess molar enthalpy obtained at each experimental concentration. Further details are presented in the Appendix D.

Two research groups^[16, 51] have reported the partial molar excess enthalpy of BuOH in [C₆C₁im][NTf₂] in the molar fraction interval ($0.006 < x_{\text{BuOH}} < 0.08$). From this

data, the excess molar enthalpy was derived using the Redlich-Kister equations. These results are presented in figure 4.33 together with the experimental results determined in this work and its fitting. Unfortunately, the comparison of these results with the preliminary results reported in this thesis is very poor given the differences in the concentration range. Nevertheless, according to the graphical representation presented in figure 4.33, our results are in close agreement to the data derived from the literature^[16, 51].

The excess molar enthalpy at equimolar concentration, $x_{\text{BuOH}} = 0.5$, was calculated by extrapolation from the excess molar enthalpy results presented in the literature^[16, 51]. The obtained results are represented in the figure 4.33 (black and red circles). As depicted in figure 4.33, the extrapolated results are systematically lower than the one obtained in $\mu\text{FlowCal}$ calorimeter. Given the range of concentration studied in the literature, the difference found between the values extrapolated from the literature data towards the value determined in this work was considered to be acceptable.

Table 4.9. Summary of the excess molar enthalpy of the binary mixture BuOH + [C₆C₁im][NTf₂], determined experimentally in $\mu\text{FlowCal}$, at the reference temperature ($T = 298.15$ K), and of the correspondent BuOH molar fraction

x_{BuOH}	$H_m^E \text{ }^{a, b} / \text{kJ} \cdot \text{mol}^{-1}$	x_{BuOH}	$H_m^E \text{ }^{a, b} / \text{kJ} \cdot \text{mol}^{-1}$
0.1572	1.22 (\pm 0.23)	0.6031	2.98 (\pm 0.11)
0.2233	1.71 (\pm 0.20)	0.7027	2.64 (\pm 0.12)
0.2826	2.22 (\pm 0.18)	0.7436	2.45 (\pm 0.07)
0.3848	2.74 (\pm 0.03)	0.8125	2.05 (\pm 0.04)
0.4698	2.98 (\pm 0.09)	0.8921	1.43 (\pm 0.02)
0.5416	3.02 (\pm 0.13)	0.9526	0.74 (\pm 0.05)

a - Constant of calibration used: $8.78 \times 10^{-6} (\text{J} \cdot \text{s}^{-1}) / \mu\text{V}$;

b - The uncertainty is the dispersion of the enthalpy of mixing obtained in each set of experiments, at a confidence level of 95% ($\pm 2 \cdot \sigma$).

Using the fitting of the experimental data obtained in $\mu\text{FlowCal}$ with the Redlich-Kister equation, the partial molar excess enthalpy of BuOH and the partial molar excess enthalpy of [C₆C₁im][NTf₂] was derived. In figure 4.34 these properties are represented against the molar fraction of BuOH. For comparison, the partial molar

excess enthalpy of BuOH in $[\text{C}_6\text{C}_{1}\text{im}][\text{NTf}_2]$ reported in the literature^[16, 51] is also plotted, as well as, the enthalpy of solution at infinite dilution of BuOH in $[\text{C}_6\text{C}_{1}\text{im}][\text{NTf}_2]$ determined by ITC.

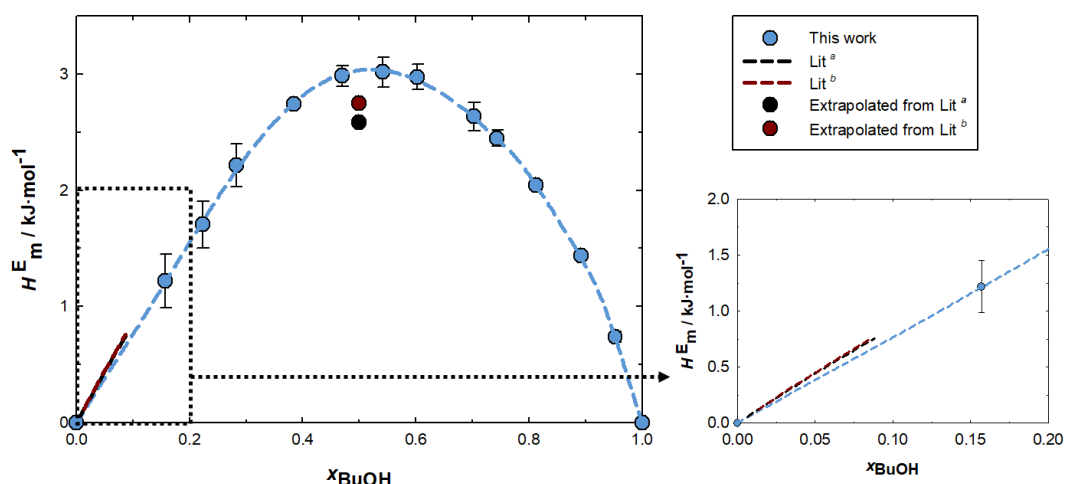


Figure 4.33. Graphical representation of the excess molar enthalpy of the binary mixture BuOH + $[\text{C}_6\text{C}_{1}\text{im}][\text{NTf}_2]$, determined experimentally in this work (●) using $\mu\text{FlowCal}$ calorimeter, at the reference temperature ($T = 298.15 \text{ K}$), as a function of the molar fraction of 1-butanol in $[\text{C}_6\text{C}_{1}\text{im}][\text{NTf}_2]$. The fitting of the experimental data, using Redlich-Kister equation, is also represented (— —). The excess molar enthalpy data, calculated from the partial molar excess enthalpy data of BuOH in $[\text{C}_6\text{C}_{1}\text{im}][\text{NTf}_2]$, existent in the literature are also represented, as well as the extrapolated values to the excess molar enthalpy at equimolar concentrations. Lit ^a (●, —) is the ref.[16]; Lit ^b (●, —) is the ref.[51].

Before the analysis of the graphical representation depicted in figure 4.34, it should be taken into account that, at high IL concentrations, the experimental measurements in $\mu\text{FlowCal}$ calorimeter presented higher uncertainty. This higher uncertainty of the results, in addition to the smallest concentration measured in $\mu\text{FlowCal}$ being $x_{\text{BuOH}} = 0.16$, lead to significant differences in the extrapolation of the partial molar excess enthalpy of BuOH in the approximation of the infinite dilution conditions. The higher uncertainty of the partial molar excess enthalpy of mixing close to the infinite dilution of BuOH is depicted in the figure 4.34 by a shaded area (coloured in orange).

Despite of the higher uncertainty, taking into consideration the comparison of the extrapolated value ($8.1 \pm 5.9 \text{ kJ}\cdot\text{mol}^{-1}$) with the value obtained in ITC ($8.35 \pm 0.24 \text{ kJ}\cdot\text{mol}^{-1}$) and the values reported in the literature ($9.20 \pm 0.13 \text{ kJ}\cdot\text{mol}^{-1}$ and $9.32 \pm 0.01 \text{ kJ}\cdot\text{mol}^{-1}$)^[16, 51], the magnitude of the results was considered to be meaningful. Moreover, at the two lowest concentrations (of BuOH) measured, $x_{\text{BuOH}} = 0.16$ and

$x_{\text{BuOH}} = 0.22$, the partial molar excess enthalpy of BuOH is approximately $8 \text{ kJ}\cdot\text{mol}^{-1}$ despite of the number of parameters used in the Redlich-Kister equation. This fact, suggests that between $0 < x_{\text{BuOH}} < 0.2$, the partial molar excess enthalpy of BuOH is around $8 \pm 2 \text{ kJ}\cdot\text{mol}^{-1}$.

In contrast to what was verified for the partial molar excess enthalpy of BuOH, very good reproducibility was found in the determination of the partial molar excess enthalpy of $[\text{C}_6\text{C}_{1\text{im}}][\text{NTf}_2]$ at infinite dilution, derived from the $\mu\text{FlowCal}$ calorimeter measurements ($17.9 \pm 5.9 \text{ kJ}\cdot\text{mol}^{-1}$) regardless of the number of parameters considered in the Redlich-Kister equation. No other experimental data was found in the literature.

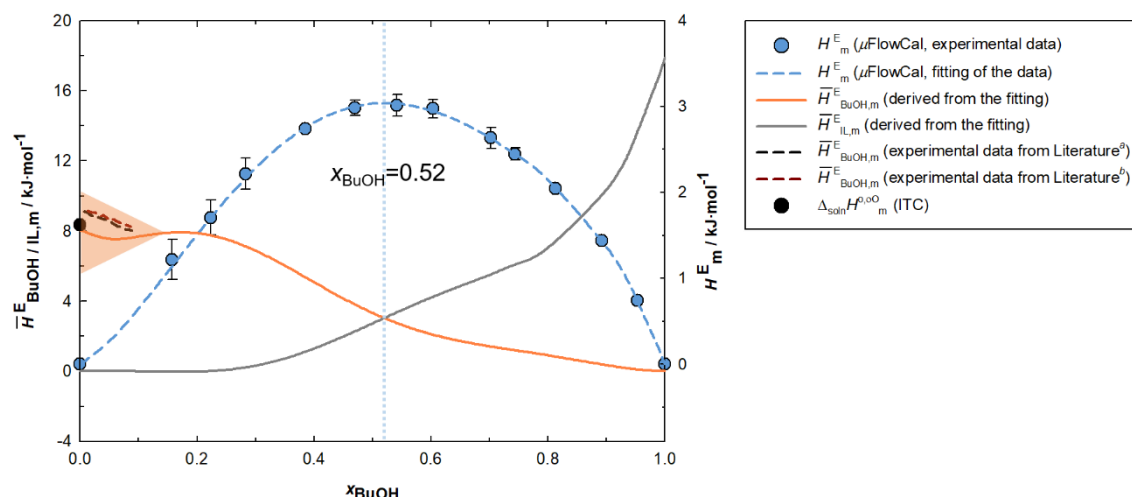


Figure 4.34. Graphical representation of the excess molar enthalpy of the binary mixture BuOH + $[\text{C}_6\text{C}_{1\text{im}}][\text{NTf}_2]$ (right axis), determined experimentally using $\mu\text{FlowCal}$ (●), with the correspondent fitting of the data using the Redlich-Kister equation with 6 parameters (— —), and of the partial molar excess enthalpy of BuOH (—) and $[\text{C}_6\text{C}_{1\text{im}}][\text{NTf}_2]$ (—) (left axis), derived using the Redlich-Kister equations, as a function of the molar fraction of BuOH, x_{BuOH} . The partial molar excess enthalpy data of BuOH in $[\text{C}_6\text{C}_{1\text{im}}][\text{NTf}_2]$, existent in the literature is also represented: Lit ^a (— —) is the ref.[16]; Lit ^b (— —) is the ref.[51], as well as the standard molar enthalpy of solution at infinite dilution, determined in ITC (●).

4.4.2.1. Comparison with other Binary Mixtures

The excess molar enthalpy of mixing of BuOH + $[\text{C}_6\text{C}_{1\text{im}}][\text{NTf}_2]$, measured in this work using the $\mu\text{FlowCal}$ calorimeter, as well as, the partial molar quantities of each component, was compared with similar binary systems.

To our knowledge, the only binary diagram of 1-butanol and ILs mixtures regarding its enthalpy of mixing / excess molar enthalpy, at 298.15 K, has been reported by Domańska et al.^[54] In this study, the excess enthalpy of the binary mixture BuOH + [C₄C₁pyrr][DCA] has been measured. Unfortunately, the hydrogen bond basicity of the [DCA] anion is very different of the [NTf₂] anion and, as it was observed before, the hydrogen bond acidity of the anion plays an important role in the solution/solvation properties. Therefore, it is predictable that it will also affect the binary diagram of the alcohol-IL mixtures.

Nevertheless, in figure 4.35 the excess molar enthalpy of the binary mixture BuOH + [C₆C₁im][NTf₂] is represented together with the data reported by Domańska et al.^[54] for the binary mixture of BuOH + [C₄C₁pyrr][DCA]. From the fitting of this data with the Redlich-Kister equation, the partial molar excess enthalpy of BuOH and of the IL was derived, for both binary mixtures and is also represented in figure 4.35. It was found that the excess molar enthalpy of the mixture BuOH + [C₄C₁pyrr][DCA] is less endothermic than the mixture BuOH + [C₆C₁im][NTf₂]. The less endothermic excess molar enthalpy of the binary mixture BuOH + [C₄C₁pyrr][DCA] is in line with the stronger hydrogen bond basicity of this anion.

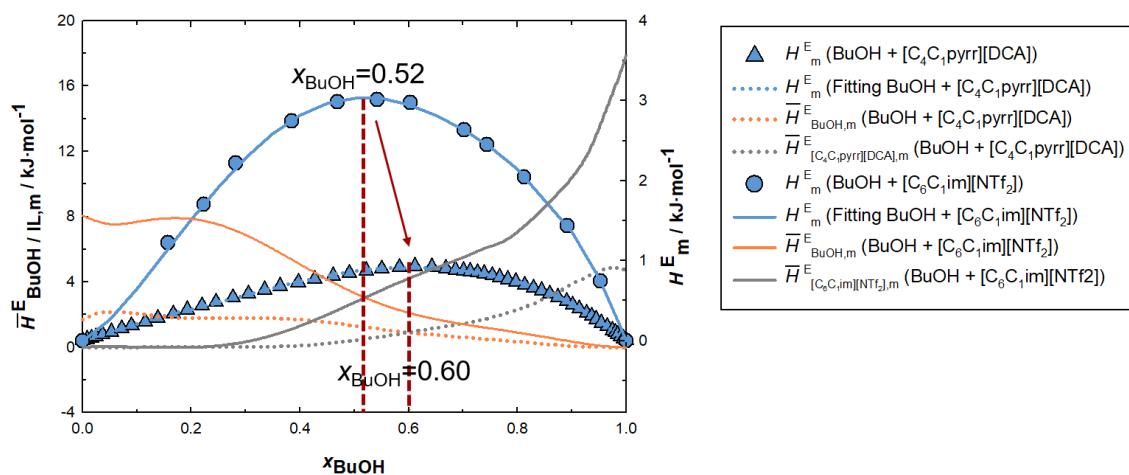


Figure 4.35. Graphical representation of the excess molar enthalpy of the binary mixtures (●) BuOH + [C₆C₁im][NTf₂] and (▲) BuOH + [C₄C₁pyrr][DCA] (right axis) with the correspondent fitting of the data using the Redlich-Kister equation, as well as, the correspondent partial molar excess enthalpy of BuOH and IL (left axis), derived using the Redlich-Kister equations, as a function of the molar fraction of BuOH, x_{BuOH} . Excess enthalpy data of BuOH in [C₄C₁pyrr][DCA] from ref.[54].

In fact, Ortega and collaborators^[55] have studied the enthalpy of mixture in binary mixtures of $[\text{C}_4\text{C}_1\text{py}][\text{BF}_4]$ + alcohols and have used COSMO-RS to get molecular understanding of the experimental results. They have reported that the major contribution to the endothermic enthalpy of mixtures found is related with the breakage of the hydrogen bond interactions of the alcohol. Furthermore, they estimate that in cases in which strong hydrogen bond interactions are possible between the alcohol and the anion, due to the higher exothermic contribution of the alcohol-IL interaction, the enthalpy of mixture would be considerably less endothermic and it could even be exothermic, depending on the interactions established. We estimate that most of the difference existent between the excess molar enthalpy of $\text{BuOH} + [\text{C}_6\text{C}_1\text{im}][\text{NTf}_2]$ and $\text{BuOH} + [\text{C}_4\text{C}_1\text{pyrr}][\text{DCA}]$, arises from the magnitude of the alcohol-IL interaction.

The maximum excess molar enthalpy, in the case of $\text{BuOH} + [\text{C}_6\text{C}_1\text{im}][\text{NTf}_2]$ binary mixture, occurs around the BuOH molar fraction $x_{\text{BuOH}} \approx 0.5$ (proportion $\text{BuOH} : [\text{C}_6\text{C}_1\text{im}][\text{NTf}_2]$ is 1:1). In the case of $\text{BuOH} + [\text{C}_4\text{C}_1\text{pyrr}][\text{DCA}]$ binary mixture, the maximum excess molar enthalpy occurs around the BuOH molar fraction $x_{\text{BuOH}} \approx 0.6$ (proportion $\text{BuOH} : [\text{C}_4\text{C}_1\text{pyrr}][\text{DCA}]$ is 3:2), which is slightly deviated to higher molar fraction/proportion of alcohol.

Regarding the partial molar excess enthalpy of both BuOH and the IL, the values of both properties at $x_{\text{BuOH}} = 0$ and $x_{\text{BuOH}} = 1$ can give additional information. The partial molar excess enthalpy of BuOH in the binary mixture $\text{BuOH} + [\text{C}_4\text{C}_1\text{pyrr}][\text{DCA}]$, at $x_{\text{BuOH}} = 0$ ($1.68 \pm 0.98 \text{ kJ}\cdot\text{mol}^{-1}$) is similar to the standard molar enthalpy of solution at infinite dilution of PrOH in $[\text{C}_4\text{C}_1\text{im}][\text{DCA}]$ ($2.80 \pm 0.13 \text{ kJ}\cdot\text{mol}^{-1}$), determined in ITC. The similarity of these values, despite of the different alkyl length of the alcohol evidence the high hydrogen bond basicity of the $[\text{DCA}]$ anion and the preferential interaction alcohol-anion, as it was demonstrated in the section 4.1 of this thesis.

The partial molar excess enthalpy of the IL at the molar fraction $x_{\text{BuOH}} = 1$ is equivalent to the molar enthalpy of solution of the IL in 1-butanol, at infinite dilution. Therefore, this property can be interpreted as a sum of three processes: the breaking of the IL-IL interactions (endothermic – associated to the enthalpy of vaporization of the IL, providing that the integrity of the ion pair is maintained), cavitation of the alcohol (endothermic – related to the volume of the cavity and the alcohol cohesive energy/internal pressure) and establishment of intermolecular interactions of alcohol molecules with ions / ion pair (alcohol-IL interactions, exothermic). The partial molar excess enthalpy of $[\text{C}_4\text{C}_1\text{pyrr}][\text{DCA}]$ in the binary mixture $\text{BuOH} + [\text{C}_4\text{C}_1\text{pyrr}][\text{DCA}]$, at $x_{\text{BuOH}} = 1$, is $4.75 \pm 0.98 \text{ kJ}\cdot\text{mol}^{-1}$. This value is around four times smaller than the enthalpy of

solution of partial molar excess enthalpy of $[\text{C}_6\text{C}_1\text{im}][\text{NTf}_2]$ in the mixture $\text{BuOH} + [\text{C}_6\text{C}_1\text{im}][\text{NTf}_2]$, at $x_{\text{BuOH}} = 1$, $17.9 \pm 5.9 \text{ kJ}\cdot\text{mol}^{-1}$, which could be related with the stronger alcohol-anion interaction.

Therefore, the results seem to indicate that the hydrogen bond interaction established between the alcohol and basic anions seems to play an important role in alcohol-IL mixtures, not only at infinite dilution conditions but also in all the concentration range of the binary mixtures.

The excess molar enthalpy of binary mixtures of $\text{PrOH} + [\text{C}_6\text{C}_1\text{pip}][\text{NTf}_2]$ has been reported in the literature by Domańska et al.^[10]. In figure 4.36, the excess molar enthalpy of this binary mixture is compared with the excess molar enthalpy of $\text{BuOH} + [\text{C}_6\text{C}_1\text{im}][\text{NTf}_2]$, obtained in this work using $\mu\text{FlowCal}$ calorimetry. It is observable that the excess molar enthalpy of the mixture $\text{PrOH} + [\text{C}_6\text{C}_1\text{pip}][\text{NTf}_2]$ is less endothermic than the mixture $\text{BuOH} + [\text{C}_6\text{C}_1\text{im}][\text{NTf}_2]$. The excess molar enthalpy maximum ($2.3 \text{ kJ}\cdot\text{mol}^{-1}$) occurs around the PrOH molar fraction $x_{\text{PrOH}} \approx 0.55$, very similar to the binary mixture $\text{BuOH} + [\text{C}_6\text{C}_1\text{im}][\text{NTf}_2]$, which maximum ($3.0 \text{ kJ}\cdot\text{mol}^{-1}$) occurs at the BuOH molar fraction $x_{\text{BuOH}} \approx 0.52$. Therefore, for both binary mixtures, the maximum excess molar enthalpy seems to occur close to the proportion alcohol : IL of 1:1.

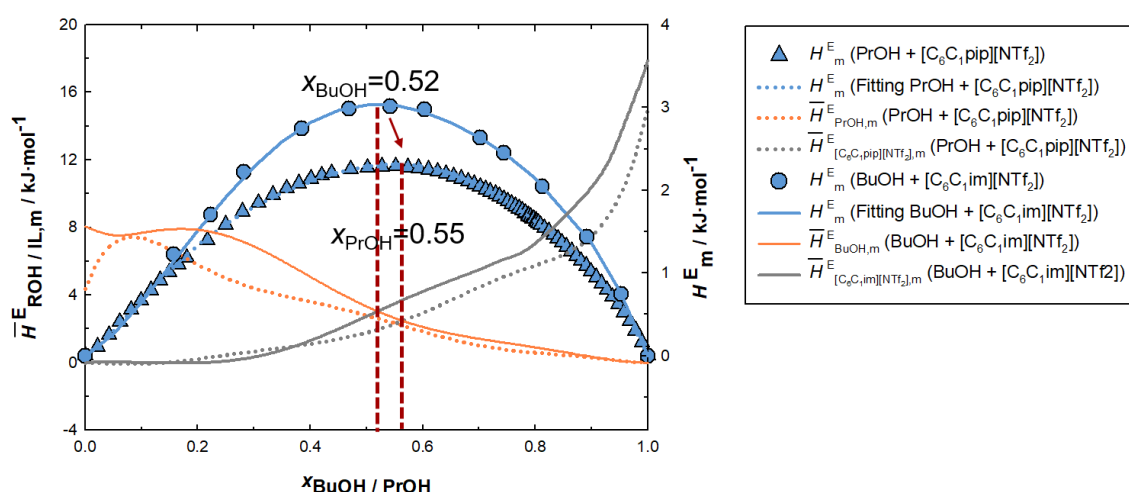


Figure 4.36. Graphical representation of the excess molar enthalpy of the binary mixtures (●) $\text{BuOH} + [\text{C}_6\text{C}_1\text{im}][\text{NTf}_2]$ and (▲) $\text{PrOH} + [\text{C}_6\text{C}_1\text{pip}][\text{NTf}_2]$ (right axis) with the correspondent fitting of the data using the Redlich-Kister equation, as well as, the correspondent partial molar excess enthalpy of ROH ($\text{PrOH} / \text{BuOH}$) and IL (in the left axis), derived using the Redlich-Kister equations, as a function of the molar fraction of ROH, $x_{\text{BuOH}} / \text{PrOH}$. Excess enthalpy data of PrOH in $[\text{C}_6\text{C}_1\text{pip}][\text{NTf}_2]$ from ref.[10].

Ortega and collaborators^[55] have reported, from their study regarding the enthalpy of mixture in binary mixtures of $[\text{C}_4\text{C}_1\text{py}][\text{BF}_4]$ + alcohols, that the increase in the alcohol alkyl chain causes an endothermic effect, which arises from a decrease of the balance between the IL-IL / alcohol-alcohol and the IL-alcohol interaction (increase in the repulsion between the IL charged domains and the alcohol). In addition, they also report a smaller endothermic contribution to the enthalpy of mixture arising from an increase in the cohesive energy of the alcohol. These verifications of the authors may help explain the difference in magnitude found in the excess molar enthalpy of the binary mixtures $\text{BuOH} + [\text{C}_6\text{C}_1\text{im}][\text{NTf}_2]$ and $\text{PrOH} + [\text{C}_6\text{C}_1\text{pip}][\text{NTf}_2]$.

Additionally, the comparison of the curves of the partial molar excess enthalpy show that the curves of the partial molar excess enthalpy of the IL (grey curves of the figure 4.36) have a similar profile, with the curve of the IL in BuOH being a little more endothermic than in PrOH. The values of the partial molar excess enthalpy of the IL at $x_{\text{BuOH} / \text{PrOH}} = 1$ seem to reflect this behaviour. The partial molar excess enthalpy of the $[\text{C}_6\text{C}_1\text{pip}][\text{NTf}_2]$, at $x_{\text{PrOH}} = 1$, is $15.0 \pm 0.9 \text{ kJ}\cdot\text{mol}^{-1}$, whereas the partial molar excess enthalpy of the $[\text{C}_6\text{C}_1\text{im}][\text{NTf}_2]$, at $x_{\text{BuOH}} = 1$, is $17.9 \pm 5.9 \text{ kJ}\cdot\text{mol}^{-1}$.

The partial molar excess enthalpy curves of the alcohol PrOH/BuOH (orange curves of the figure 4.36) present higher differentiation. The partial molar excess enthalpy of PrOH (orange dotted curve) is less endothermic than the partial molar excess enthalpy of BuOH in the molar fraction $0.1 < x_{\text{BuOH} / \text{PrOH}} < 0.5$. However, at $x_{\text{BuOH} / \text{PrOH}} = 0.1$, both partial molar excess enthalpy curves converge to approximately $8 \text{ kJ}\cdot\text{mol}^{-1}$. As the excess molar enthalpy curves superpose at low alcohol concentrations, we estimate that the partial molar excess enthalpy curves of the alcohol are not well defined in the proximity of the infinite dilution of the alcohol and that the real value of the partial molar excess enthalpy of the alcohol / enthalpy of solution, at infinite dilution, is approximately $8 \text{ kJ}\cdot\text{mol}^{-1}$, as determined in ITC.

Overall, the binary mixtures $\text{BuOH} + [\text{C}_6\text{C}_1\text{im}][\text{NTf}_2]$ and $\text{PrOH} + [\text{C}_6\text{C}_1\text{pip}][\text{NTf}_2]$ seem to present a similar mixing behaviour with the differences found being justified by the different size of the alcohol present in the mixture.

Nevertheless, given the insights acquired in the solution / solvation studies, it is considered that it would be interesting the comparison of the enthalpy of mixture of the binary mixture studied in the $\mu\text{FlowCal}$ calorimeter ($\text{BuOH} + [\text{C}_6\text{C}_1\text{im}][\text{NTf}_2]$) with similar systems composed by ILs with anions of similar hydrogen-bond basicity as the $[\text{NTf}_2]$ anion. According to the hydrogen bond basicity scale proposed by Freire et al.^[19], which

is based in the calculation, by COSMO-RS, of the hydrogen-bonding energy in equimolar cation-anion pairs, the $[\text{BF}_4]$ anion, for example, has a similar hydrogen bond basicity as $[\text{NTf}_2]$ anion (hydrogen-bonding energy in $[\text{C}_6\text{C}_1\text{im}][\text{BF}_4]$, $-9.35 \text{ kJ}\cdot\text{mol}^{-1}$, very similar to the $[\text{C}_6\text{C}_1\text{im}][\text{NTf}_2]$, $-9.50 \text{ kJ}\cdot\text{mol}^{-1}$).

Therefore, it is interesting to compare the partial molar excess enthalpy of the $[\text{C}_N\text{C}_1\text{im}][\text{BF}_4]$ IL in binary mixtures with alcohols of different alkyl chain length, and see how it relates with the partial molar excess enthalpy of $[\text{C}_6\text{C}_1\text{im}][\text{NTf}_2]$ in the $\text{BuOH} + [\text{C}_6\text{C}_1\text{im}][\text{NTf}_2]$ binary mixture. In figure 4.37 is represented the partial molar excess enthalpy of $[\text{C}_6\text{C}_1\text{im}][\text{NTf}_2]$ in the binary mixture $\text{BuOH} + [\text{C}_6\text{C}_1\text{im}][\text{NTf}_2]$ as a function of the BuOH molar fraction. Together with these results is presented the partial molar excess enthalpy of $[\text{C}_N\text{C}_1\text{im}][\text{BF}_4]$ (with $N = 2, 4, 6, 8$) in binary mixtures with MeOH , EtOH and PrOH , reported in the literature^[56].

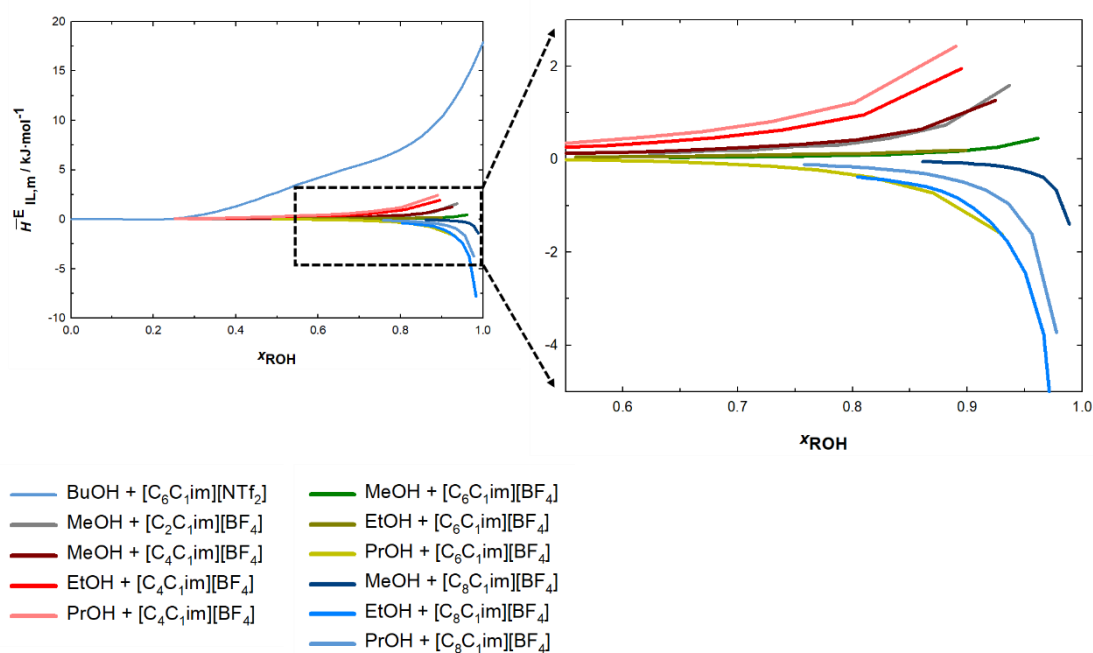


Figure 4.37. Graphical representation of the partial molar excess enthalpy of the ionic liquid in several binary mixtures as a function of the alcohol molar fraction. Data from the binary mixture $\text{BuOH} + [\text{C}_6\text{C}_1\text{im}][\text{NTf}_2]$ was derived from the $\mu\text{FlowCal}$ calorimetry measurements. Data regarding the other binary systems has been reported in ref. [56].

Figure 4.37 shows that the partial molar excess enthalpy of $[\text{C}_6\text{C}_1\text{im}][\text{NTf}_2]$ is much more endothermic than the partial molar excess enthalpy of the other ionic liquids (constituted by the $[\text{BF}_4]$ anion), despite of the alcohol it was mixed with. This observation shows that mixing behaviour is not only ruled by the hydrogen bond basicity of the IL. Instead, the role of other characteristics may have strong effect in the mixing properties, which unveils a new path for future studies in order to understand these effects at a molecular level.

Amongst the partial molar excess enthalpy of $[\text{C}_N\text{C}_1\text{im}][\text{BF}_4]$ (with $N = 2, 4, 6, 8$) in binary mixtures with MeOH, EtOH and PrOH it is observable that this property starts to differentiate in the “rich” alcohol area ($x_{\text{BuOH}} > 0.5$). The partial molar excess enthalpy of $[\text{C}_2\text{C}_1\text{im}][\text{BF}_4]$ in the binary mixture MeOH + $[\text{C}_2\text{C}_1\text{im}][\text{BF}_4]$ is similar to the partial molar excess enthalpy of $[\text{C}_4\text{C}_1\text{im}][\text{BF}_4]$ in the binary mixture MeOH + $[\text{C}_4\text{C}_1\text{im}][\text{BF}_4]$. However, the partial molar excess enthalpy of $[\text{C}_6\text{C}_1\text{im}][\text{BF}_4]$ in the binary mixture MeOH + $[\text{C}_6\text{C}_1\text{im}][\text{BF}_4]$ presents lower endothermic character and the partial molar excess enthalpy of $[\text{C}_8\text{C}_1\text{im}][\text{BF}_4]$ in the binary mixture MeOH + $[\text{C}_8\text{C}_1\text{im}][\text{BF}_4]$ is exothermic. Furthermore, the increase of the alkyl chain of the alcohol increases the endothermic character of the partial molar excess enthalpy of $[\text{C}_4\text{C}_1\text{im}][\text{BF}_4]$. Regarding the $[\text{C}_6\text{C}_1\text{im}][\text{BF}_4]$, the partial molar excess enthalpy of this IL in MeOH and EtOH is endothermic, despite of its low magnitude, and is similar in both alcohols. Nevertheless, in PrOH, the partial molar excess enthalpy of $[\text{C}_6\text{C}_1\text{im}][\text{BF}_4]$ is exothermic. Accordingly, the increase in the alkyl chain of the alcohol and the cation seems to play a non-uniform role in the mixture. The behaviour of the partial molar excess enthalpy of $[\text{C}_8\text{C}_1\text{im}][\text{BF}_4]$ reinforces this idea as it is more exothermic in EtOH than in MeOH or PrOH.

The authors^[56] suggest that the different nature of the ILs $[\text{C}_2\text{C}_1\text{im}][\text{BF}_4]$ and $[\text{C}_4\text{C}_1\text{im}][\text{BF}_4]$ in relation to the ILs $[\text{C}_6\text{C}_1\text{im}][\text{BF}_4]$ and $[\text{C}_8\text{C}_1\text{im}][\text{BF}_4]$ induce this differentiated effect. The mixture of the small ILs $[\text{C}_2\text{C}_1\text{im}][\text{BF}_4]$ and $[\text{C}_4\text{C}_1\text{im}][\text{BF}_4]$ with the alcohol molecules disturbs the hydrogen bond network of the alcohols. However, as these ILs have small alkyl chains the authors suggest that the alcohol molecules are able to re-orient and regain the lost network upon reorientation of the molecules. Thus, the breakage and reorientation of the alcohol molecules, solvating the small ILs $[\text{C}_2\text{C}_1\text{im}][\text{BF}_4]$ and $[\text{C}_4\text{C}_1\text{im}][\text{BF}_4]$, originates endothermic enthalpies. According to the authors, the long chains of the $[\text{C}_6\text{C}_1\text{im}][\text{BF}_4]$ and $[\text{C}_8\text{C}_1\text{im}][\text{BF}_4]$ ILs induce a solvophobic effect upon the hydroxyl groups, inducing a higher degree reorganization of the alcohol molecules around the cation, which causes a differentiation in the excess enthalpies.

The reason to explain why the $[\text{C}_6\text{C}_1\text{im}][\text{NTf}_2]$ in BuOH does not behave similarly than $[\text{C}_6\text{C}_1\text{im}][\text{BF}_4]$ or the reason why it is more endothermic could be related with the free volume existent in the different ILs and the different aggregation/structuration of the alcohol-IL mixture.

Given the similarities found between the alcohols and the ionic liquids, in figure 4.38, the excess molar enthalpy of mixing of the binary mixture BuOH + $[\text{C}_6\text{C}_1\text{im}][\text{NTf}_2]$, was compared with the excess molar enthalpy in the binary mixture BuOH + HexOH.

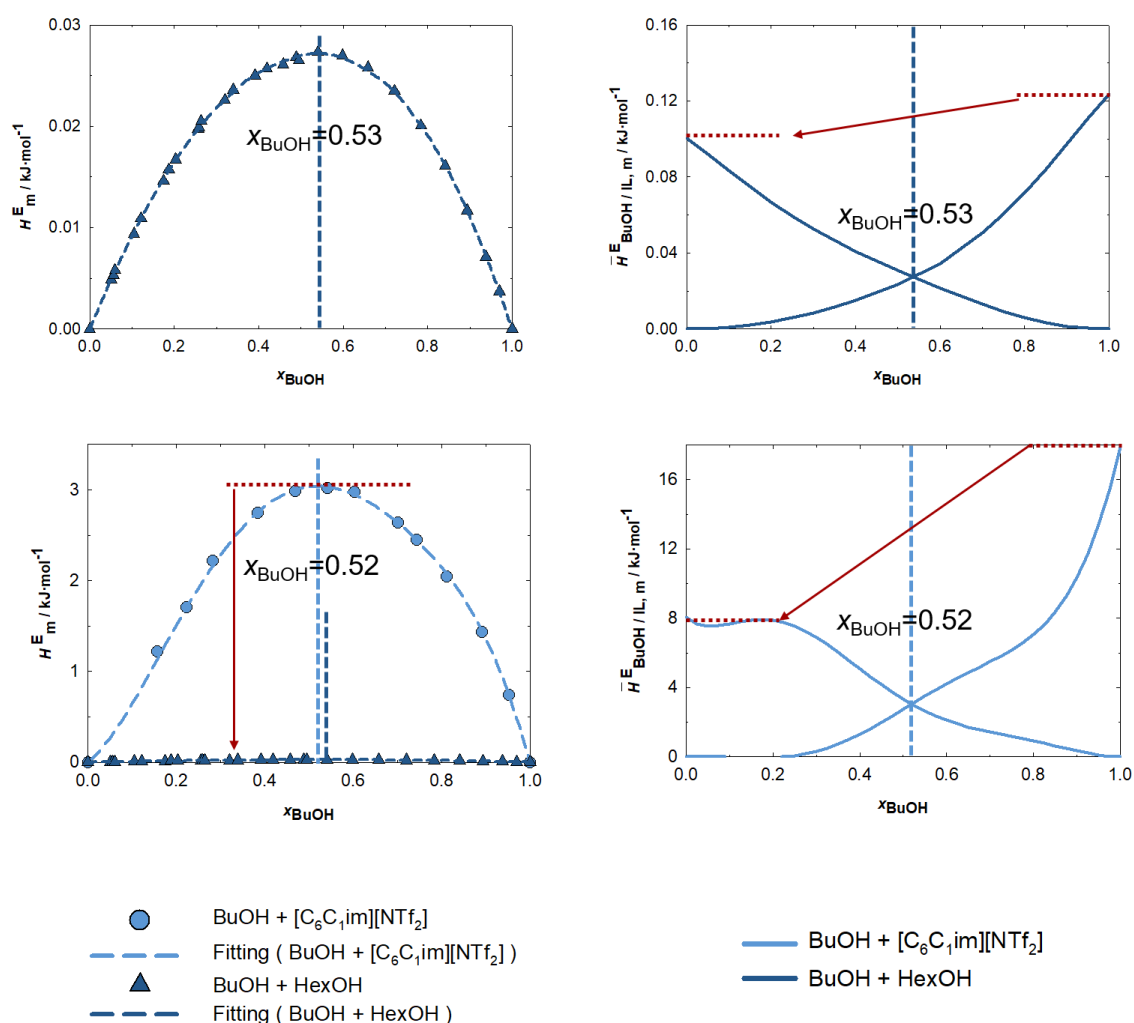


Figure 4.38. Graphical representation of the excess molar enthalpy of the binary mixtures of BuOH + $[\text{C}_6\text{C}_1\text{im}][\text{NTf}_2]$ and BuOH + HexOH (on the left) and of the partial molar excess enthalpy of BuOH / IL / HexOH in referred binary mixtures (on the right) as a function of the BuOH molar fraction. Data from the binary mixture BuOH + HexOH has been reported in ref. [57].

The two graphical representations on the top of the figure refer to the excess molar enthalpy of mixing (on the left) and the partial molar excess enthalpy of mixing (on the right) of the binary mixture BuOH + HexOH, as a function of the molar fraction of BuOH. In these representations stands out the quasi-symmetrical character of the excess molar enthalpy of mixing, as well as, the small magnitude of the enthalpy values. The partial molar excess enthalpy of mixing of BuOH and HexOH evidence a regular shape and a similar value of enthalpy at infinite dilution. These observations evidence the proximity of the binary mixture BuOH + HexOH to the ideal behaviour.

The two graphical representations on the bottom of the figure 4.38 depict the excess molar enthalpy of mixing of the binary mixture BuOH + [C₆C₁im][NTf₂] (on the left) and the partial molar excess enthalpy of mixing of BuOH and [C₆C₁im][NTf₂] (on the right). On the bottom-left representation, the excess molar enthalpy of mixing of BuOH + HexOH is also represented, evidencing the difference in the magnitude between the enthalpy in both mixtures (approximately 100 times). On the bottom-right representation, is evident the absence of a regular shape in the partial molar excess enthalpy of mixing of BuOH and [C₆C₁im][NTf₂], as well as, the existence of a high difference in both enthalpies at infinite dilution.

From the analysis of the graphical representations depicted in figure 4.38 it is evident that the excess molar enthalpy of the binary mixture BuOH + [C₆C₁im][NTf₂], measured in μ FlowCal calorimeter is much higher than the excess molar enthalpy of the binary mixture BuOH + HexOH. Interestingly, the shape of the curves of the partial molar excess enthalpy of BuOH is completely different in both mixtures. The curves of the partial molar excess enthalpy of the binary mixture BuOH + HexOH decay uniformly, which is not verified in the binary mixture BuOH + [C₆C₁im][NTf₂].

We propose that the 100 times difference in the enthalpy values is related with the different nature of the species and molecular interactions established, deviating the mixture from the ideality. In addition, we speculate that the different shape of the curves of partial molar excess enthalpy may be related to the effect of nanostructuration of the ionic liquids and to their ability to solvate the added alcohol molecules, until a certain amount, preserving its structure.

4.4.2.2. Structuration and Energetics of the BuOH + [C₆C₁im][NTf₂] Mixture

We found no report in the literature of structural experimental data on the binary mixture studied in the μ FlowCal calorimeter. Nevertheless, as referred in the Introduction, Agrawal and Kashyap^[58] have studied by molecular dynamics simulation, binary mixtures of [C₄C₁im][NTf₂] + BuOH / PrOH focusing into the structuration and the intermolecular interactions present.

In this study is reported the maintenance of the IL neat structure from $x_{\text{BuOH}} < 0.2$, as well as, the existence of transitional structural changes from $0.2 < x_{\text{BuOH}} < 0.7$. Complementarily, Yoshimura et al.^[59] have studied binary mixtures of [C₄C₁im][NTf₂] + MeOH/ EtOH/ PrOH/ BuOH/ PentOH/ HexOH/ HeptOH/ OctOH/ NonOH/ DecOH/ UdecOH/ DdecOH using Raman spectroscopy. For BuOH mixtures the authors^[59] reported the existence of all kinds of aggregation in the mixture, monomers, dimers, small and large clusters, depending on the alcohol concentration. At high dilution of BuOH, $x_{\text{ROH}} = 0.1$, all alcohol molecules seemed to be dispersed into the IL as monomers. At $x_{\text{ROH}} = 0.2$, some dimers were noticed despite of the majority of the alcohol molecules being still dispersed as monomers. As the content of alcohol in the mixture increases, the number of alcohol molecules associated in dimers increase, while the number of monomers decrease. The presence of small clusters has been detected at $x_{\text{ROH}} = 0.6$. As before, these clusters increase with the increase of the mixture in the alcohol content. Bigger clusters are noticed between $x_{\text{ROH}} = 0.7$ and $x_{\text{ROH}} = 0.8$.

In agreement with the results of these authors and having into account the curves of the partial molar excess enthalpy of mixing obtained, we venture to propose that the binary mixture BuOH + [C₆C₁im][NTf₂], studied in μ FlowCal calorimeter, is governed by different structuration regimes which are expressed in the partial molar enthalpy of both components. In figure 4.39, the partial molar excess enthalpy of mixing of BuOH (represented in green) and [C₆C₁im][NTf₂] (represented in blue), obtained in the context of this thesis, are presented, evidencing the different structuration regimes. Given the difference between the molar volume of the alcohol and IL ($V_{\text{m,BuOH}} = 92.0 \text{ cm}^3 \cdot \text{mol}^{-1}$ and $V_{\text{m,IL}} = 326.5 \text{ cm}^3 \cdot \text{mol}^{-1}$)^[60], the partial molar excess enthalpy of mixing is represented as a function of the molar fraction and volume fraction of BuOH.

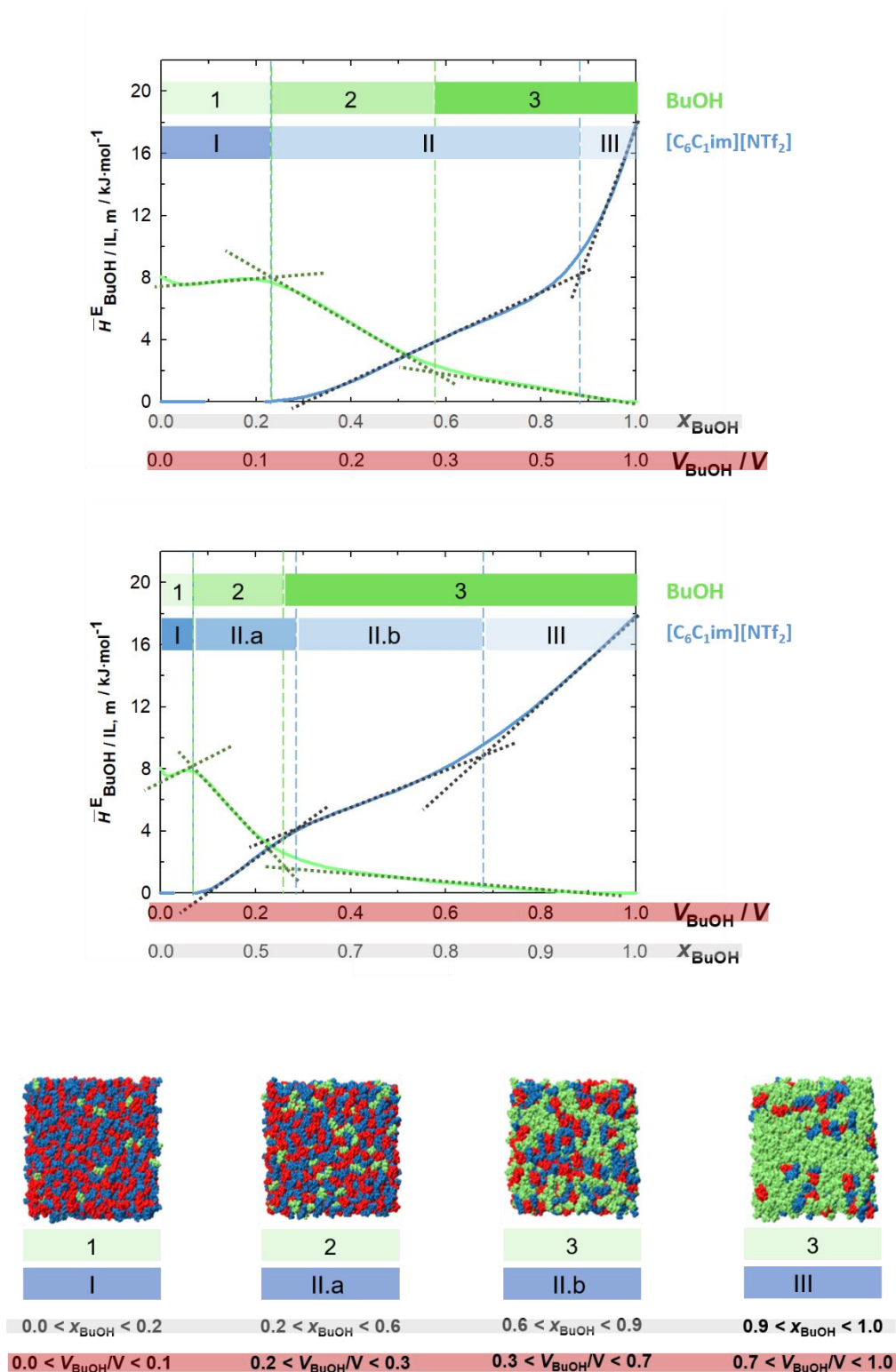


Figure 4.39. Scheme of the partial molar excess enthalpy of the binary mixture BuOH + [C₆C₁im][NTf₂] as a function of the BuOH molar fraction (upper representation) and BuOH volume fraction (bottom representation), with division of the diagrams into different regimes illustrated with representative simulation boxes. The figure was created using the simulation boxes of BuOH (coloured in green) in [C₄C₁im][NTf₂] (cation coloured in red, anion coloured in blue) used from the molecular dynamics simulations from ref. [58]. The dashed lines are just guide lines to the eyes.

In the top graphical representation, the partial molar excess enthalpy of mixing of BuOH and [C₆C₁im][NTf₂] is represented as a function of the molar fraction of BuOH. To facilitate the analysis of the results, the approximate volume fraction is represented below of the axis of the molar fraction. Looking to this graphical representation, it stands out the existence of three different regimes in the BuOH curve (1, 2, 3) and in the [C₆C₁im][NTf₂] curve (I, II, III).

The first regime of [C₆C₁im][NTf₂] ("I") co-exists with the first regime of BuOH ("1"). In this area, between $0.0 < x_{\text{BuOH}} < 0.2$, the partial molar excess enthalpy of mixing of the [C₆C₁im][NTf₂] is approximately zero over this concentration range and the partial molar excess enthalpy of BuOH is approximately 8 kJ·mol⁻¹ (despite of the existence of some uncertainty in this area), a value very similar to the enthalpy of solution of BuOH in [C₆C₁im][NTf₂], at infinite dilution.

At $x_{\text{BuOH}} = 0.2$, the partial molar excess enthalpy of the [C₆C₁im][NTf₂] increases linearly until approximately $x_{\text{BuOH}} = 0.8$, regime "II". During this range of concentration, $0.2 < x_{\text{BuOH}} < 0.9$, the partial molar excess enthalpy of BuOH decreases at two distinct rates, constituting the regimes "2" and "3" of the alcohol.

At approximately $x_{\text{BuOH}} = 0.9$, there is a modification of the curvature of the partial molar excess enthalpy of [C₆C₁im][NTf₂]. Beyond this concentration of BuOH, the partial molar excess enthalpy of BuOH increases linearly until its infinite dilution in BuOH, regime "III".

In the bottom graphical representation, the previous graphical representation is repeated, this time, as a function of the volume fraction of BuOH. As before, to facilitate the analysis of the results, below the axis of the volume fraction, the approximate mole fraction is indicated.

The first regime of BuOH ("1") and [C₆C₁im][NTf₂] ("I"), occupies now a very small area of the diagram, evidencing the low volume fraction of alcohol present in the mixture, in this regime. Moreover, in the upper representation, it seemed that the IL presented a unique regime ("II") in the molar fraction interval $0.2 < x_{\text{BuOH}} < 0.9$. Nonetheless, looking to the bottom graphical representation, it stands out that two domains are present: "II.a" which co-exists with the regime "2" of the alcohol and "II.b" which precedes the regime "III" of the IL and co-exists with the regime "3" of the alcohol. These regimes, "II.a" and "II.b" are not noticeable if the partial molar excess enthalpy of [C₆C₁im][NTf₂] is represented as a function of the molar fraction.

The increasing/decreasing rates of each regime identified in the partial molar excess enthalpy of the alcohol and IL are presented in table 4.10. The regimes identified

in the alcohol and IL may be explained on the light of the structural insights given by the works of Agrawal and Kashyap^[58] and Yoshimura et al.^[59].

In the first regime of [C₆C₁im][NTf₂] (“I”), which co-exists with the first regime of BuOH (“1”), a very small amount of alcohol is present in the mixture ($x_{\text{BuOH}} < 0.2$ and $V_{\text{BuOH}}/V < 0.1$). Therefore, we estimate that the IL has the ability to solvate the alcohol molecules in its nanostructure (as in neat IL). In accordance, it is our belief that between $0.0 < x_{\text{BuOH}} < 0.2$, the BuOH molecules are dispersed into the IL nanostructure. To illustrate the structuration in this regime, the simulation box of Agrawal and Kashyap^[58] was included in figure 4.39.

After $x_{\text{BuOH}} = 0.2$, there is a decrease in the partial molar excess enthalpy of BuOH (regime “2”). We propose that after $x_{\text{BuOH}} = 0.2$, the amount of the alcohol present in the mixture is too much to be dispersed into the neat IL structure and starts to aggregate, forming small clusters into the IL. The formation of alcohol clusters restores partially the alcohol-alcohol interactions, decreasing the partial molar excess enthalpy of BuOH. The regime differentiation is also visible in the excess molar volume, as it can be seen in figure 4.40.

The formation of these small clusters is accompanied by the enlargement of the structure of the neat IL to accommodate the small alcohol clusters, leading to the increase of the partial molar excess enthalpy of the [C₆C₁im][NTf₂] (regime “II”).

Table 4.10. Summary of the increasing/decreasing rates of each regime, in the partial molar excess enthalpy of BuOH and [C₆C₁im][NTf₂], in relation to the molar fraction and volume fraction of the alcohol

BuOH		[C ₆ C ₁ im][NTf ₂]		
Regime	$\overline{H}^E_{\text{BuOH},m}/x_{\text{BuOH}}$	Regime	$\overline{H}^E_{\text{IL},m}/x_{\text{BuOH}}$	$\overline{H}^E_{\text{IL},m}/V_{\text{BuOH}}$
1	$\sim 0 \text{ kJ}\cdot\text{mol}^{-1}$ ^a	I	$\sim 0 \text{ kJ}\cdot\text{mol}^{-1}$	$\sim 0 \text{ kJ}\cdot\text{mol}^{-1}$
2	$-18 \text{ kJ}\cdot\text{mol}^{-1}$	II.a	$14 \text{ kJ}\cdot\text{mol}^{-1}$	$22 \text{ kJ}\cdot\text{mol}^{-1}$
3	$-5 \text{ kJ}\cdot\text{mol}^{-1}$	II.b		$12 \text{ kJ}\cdot\text{mol}^{-1}$
		III	$82 \text{ kJ}\cdot\text{mol}^{-1}$	$28 \text{ kJ}\cdot\text{mol}^{-1}$

a – with a considerable degree of uncertainty.

We anticipate that at approximately $x_{\text{BuOH}} = 0.6$, the small aggregates of BuOH molecules coalesce into bigger aggregates, with some of the alcohol molecules solvated inside of the aggregates, re-establishing partially the neat alcohol structure. Consequently, as the BuOH content of the mixture increases, the shape of the partial molar excess enthalpy approaches the behaviour of BuOH in BuOH media (regime “3”). The distinction between regime “2” and “3” of the alcohol is also visible in the excess molar volume of the mixture (figure 4.40). While in regime “2” of the alcohol the excess molar volume of the mixture is approximately constant, it decreases continuously in regime “3”.

The model proposed is in accordance with the work of Yoshimura et al.^[59], in which the BuOH molecules were first dispersed as monomers in the $[\text{C}_4\text{C}_{1}\text{im}][\text{NTf}_2]$, forming dimers after $x_{\text{BuOH}} = 0.2$, small clusters after $x_{\text{BuOH}} = 0.6$ and bigger clusters at $x_{\text{BuOH}} = 0.7$.

Therefore, we propose that the decreasing rate of the partial molar excess enthalpy in the regime “2” is due to a balance between the alcohol molecules being solvated into the IL or a dimer of BuOH being solvated into the IL. In accordance, the decreasing rate $-18 \text{ kJ}\cdot\text{mol}^{-1}$ should be related to the energy of interaction of two BuOH molecules. Indeed, as indicated in the Appendix C, the energy of interaction between two PrOH molecules, in the gas phase is $-18.46 \text{ kJ}\cdot\text{mol}^{-1}$.

The decreasing rate in regime “3” of the alcohol, $-5 \text{ kJ}\cdot\text{mol}^{-1}$, is then, in our point of view, associated to the transference of a BuOH molecule from the “interface” alcohol-IL of the aggregate, to the bulk of the aggregate, interacting only with BuOH molecules.

It should be noted that the regime “II” of the ionic liquid is maintained until approximately $x_{\text{BuOH}} = 0.9$. Therefore, it encompasses the beginning of the formation of the alcohol aggregates (dimers) and its enlargement and coalescence into bigger aggregates where some of the alcohol molecules are solvated into the bulk of the aggregates. The continuous increase, first in the number of the small aggregates and after into the size of these aggregates swells the ionic structure until its maximum. We estimate that this maximum occur at the molar fraction interval $0.8 < x_{\text{BuOH}} < 0.9$, and causes the “breakage” of the IL swelled structure.

After this concentration, the IL structure is not present, instead there are aggregates of ion pairs which are becoming smaller and more dispersed as the alcohol concentration increases until the infinite dilution of the IL, at $x_{\text{BuOH}} = 1.00$, regime “III”. Based in this model, we associate the increasing rate of $82 \text{ kJ}\cdot\text{mol}^{-1}$ to the energy necessary to separate the ion pairs (from each other). The magnitude of the value

indicates that the integrity of the ion pair is maintained, as the energy necessary to separate the cation and anion is approximately $305 \text{ kJ}\cdot\text{mol}^{-1}$ (calculated by DFT with BSSE correction for $[\text{C}_4\text{C}_1\text{im}][\text{NTf}_2]$)^[61].

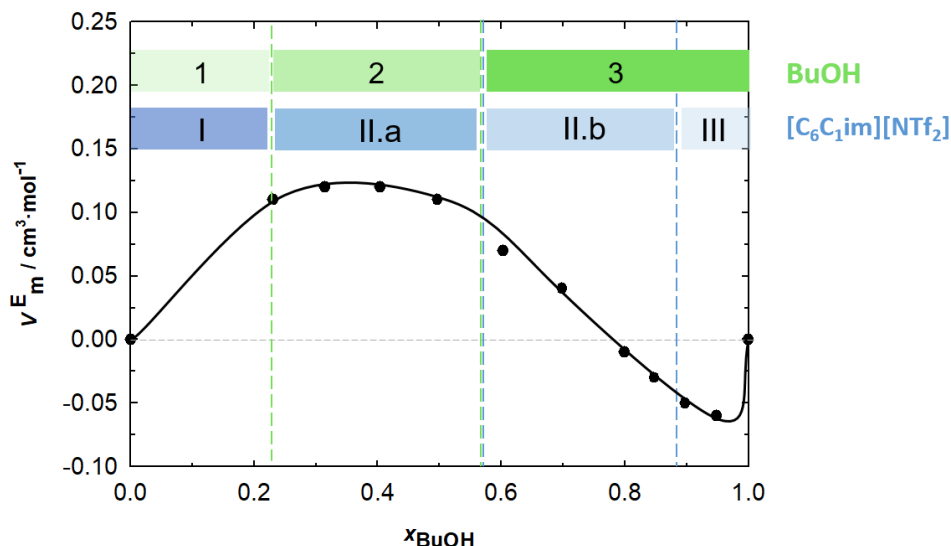


Figure 4.40. Scheme of the excess molar volume of the binary mixture BuOH + $[\text{C}_6\text{C}_1\text{im}][\text{NTf}_2]$ as a function of the BuOH molar fraction with division of the diagram into the different regimes. The black full line is just a guide line to the eyes. The excess molar volume data used in the graphical representation was consulted in ref. [60].

Furthermore, Canongia Lopes et al.^[62] have calculated, from molecular dynamics simulations, the contribution of the electrostatic and dispersive components to the cohesive molar energy of the $[\text{C}_6\text{C}_1\text{im}][\text{NTf}_2]$ IL. From this data, is possible to estimate the enthalpy of vaporization ($185 \text{ kJ}\cdot\text{mol}^{-1}$), as well as, the enthalpic contribution of the electrostatic ($78 \text{ kJ}\cdot\text{mol}^{-1}$) and dispersive ($110 \text{ kJ}\cdot\text{mol}^{-1}$) interactions. These calculations should not be far from the reality (up to 23 % deviation), as the reported^[17] enthalpy of vaporization of $[\text{C}_6\text{C}_1\text{im}][\text{NTf}_2]$, at $T = 298.15 \text{ K}$, is $150 \text{ kJ}\cdot\text{mol}^{-1}$.

The increase rate of the partial molar excess enthalpy at the regime “III” ($82 \text{ kJ}\cdot\text{mol}^{-1}$) is thus, similar to the electrostatic component of the vaporization enthalpy ($78 \text{ kJ}\cdot\text{mol}^{-1}$). This fact, gives strength to our interpretation model. In regime “III”, the structure of the alcohol approaches the one of the pure alcohol and the ionic aggregates are broken into ion pairs, which are dispersed through the alcohol, until the point of infinite dilution of the IL, in which a unique ion pair is solvated by BuOH molecules.

The continuous increase of the partial molar excess enthalpy of $[\text{C}_6\text{C}_{1\text{im}}][\text{NTf}_2]$, during the regime “II”, when represented as a function of the molar fraction of BuOH contrasts with the existence of two different regimes “II.a” and “II.b”, when represented as a function of the volume fraction of BuOH. The continuous increase found on the representation of the partial quantity upon the molar fraction may be associated to the transference of the ions from its bulk structure to the interface with the alcohol aggregates. We were not able to find an explanation for the distinction of the two domains in the volume fraction representation.

Nevertheless, the existence of different structuration regimes in the binary mixture BuOH + $[\text{C}_6\text{C}_{1\text{im}}][\text{NTf}_2]$ is visible in the partial molar excess enthalpy of the mixture components and in the excess volume. The full understanding of structuration phenomena involved in the identified regimes would benefit of complementary results of spectroscopy techniques or molecular dynamics.

References:

- [1] I. C. M. Vaz, M. Bastos, C. E. S. Bernardes, J. N. Canongia Lopes and L. M. N. B. F. Santos, Solvation of alcohols in ionic liquids – understanding the effect of the anion and cation, *Physical Chemistry Chemical Physics*, 20 (2018) p. 2536-2548. DOI:10.1039/C7CP07525A.
- [2] D. R. Lide, CRC Handbook of Chemistry and Physics, 82nd ed., CRC Press, Boca Raton, Florida, FL, 2001.
- [3] M. J. Frisch, G. W. Trucks, H. B. Schlegel, G. E. Scuseria, M. A. Robb, J. R. Cheeseman, G. Scalmani, V. Barone, B. Mennucci, G. A. Petersson, H. Nakatsuji, M. Caricato, X. Li, H. P. Hratchian, A. F. Izmaylov, J. Bloino, G. Zheng, J. L. Sonnenberg, M. Hada, M. Ehara, K. Toyota, R. Fukuda, J. Hasegawa, M. Ishida, T. Nakajima, Y. Honda, O. Kitao, H. Nakai, T. Vreven, J. A. Montgomery Jr., J. E. Peralta, F. Ogliaro, M. J. Bearpark, J. Heyd, E. N. Brothers, K. N. Kudin, V. N. Staroverov, R. Kobayashi, J. Normand, K. Raghavachari, A. P. Rendell, J. C. Burant, S. S. Iyengar, J. Tomasi, M. Cossi, N. Rega, N. J. Millam, M. Klene, J. E. Knox, J. B. Cross, V. Bakken, C. Adamo, J. Jaramillo, R. Gomperts, R. E. Stratmann, O. Yazyev, A. J. Austin, R. Cammi, C. Pomelli, J. W. Ochterski, R. L. Martin, K. Morokuma, V. G. Zakrzewski, G. A. Voth, P. Salvador, J. J. Dannenberg, S. Dapprich, A. D. Daniels, Ö. Farkas, J. B. Foresman, J. V. Ortiz, J. Cioslowski and D. J. Fox, Gaussian 09, Gaussian, Inc., Wallingford, CT, USA, 2013.
- [4] P. Hohenberg and W. Kohn, Inhomogeneous Electron Gas, *Physical Review*, 136 (1964) p. 864-871. DOI:10.1103/PhysRev.136.B864.
- [5] W. Kohn and L. J. Sham, Self-Consistent Equations Including Exchange and Correlation Effects, *Physical Review*, 140 (1965) p. A1133-A1138. DOI:10.1103/PhysRev.140.A1133.
- [6] S. F. Boys and F. Bernardi, The calculation of small molecular interactions by the differences of separate total energies. Some procedures with reduced errors, *Molecular Physics*, 19 (1970) p. 553-566. DOI:10.1080/00268977000101561.
- [7] F. B. van Duijneveldt, J. G. C. M. van Duijneveldt-van de Rijdt and J. H. van Lenthe, State of the Art in Counterpoise Theory, *Chemical Reviews*, 94 (1994) p. 1873-1885. DOI:10.1021/cr00031a007.
- [8] A. Heintz, L. M. Casás, I. A. Nesterov, V. N. Emel'yanenko and S. P. Verevkin, Thermodynamic Properties of Mixtures Containing Ionic Liquids. 5. Activity Coefficients at Infinite Dilution of Hydrocarbons, Alcohols, Esters, and Aldehydes in 1-Methyl-3-butyl-imidazolium Bis(trifluoromethyl-sulfonyl) Imide Using Gas-Liquid Chromatography, *Journal of Chemical & Engineering Data*, 50 (2005) p. 1510-1514. DOI:10.1021/je050125p.
- [9] K. Paduszyński and U. Domańska, Limiting Activity Coefficients and Gas-Liquid Partition Coefficients of Various Solutes in Piperidinium Ionic Liquids: Measurements and LSER Calculations, *The Journal of Physical Chemistry B*, 115 (2011) p. 8207-8215. DOI:10.1021/jp202010w.
- [10] K. Paduszyński, M. Królikowski and U. Domańska, Excess Enthalpies of Mixing of Piperidinium Ionic Liquids with Short-Chain Alcohols: Measurements and PC-SAFT Modeling, *The Journal of Physical Chemistry B*, 117 (2013) p. 3884-3891. DOI: 10.1021/jp401253r.
- [11] S. Li, W. Yan and H. Dong, Determination of partial molar excess enthalpies at infinite dilution for the systems four alcohols+[bmim]PF₆ at different temperatures by isothermal titration calorimeter, *Fluid Phase Equilibria*, 261 (2007) p. 444-448. DOI:10.1016/j.fluid.2007.06.007.
- [12] Y. G. Dobryakov, D. Tuma and G. Maurer, Activity Coefficients at Infinite Dilution of Alkanols in the Ionic Liquids 1-Butyl-3-methylimidazolium Hexafluorophosphate, 1-Butyl-3-methylimidazolium Methyl Sulfate, and 1-Hexyl-3-methylimidazolium Bis(trifluoromethylsulfonyl) Amide Using the Dilutor Technique, *Journal of Chemical & Engineering Data*, 53 (2008) p. 2154-2162. DOI:10.1021/je800355e.
- [13] F. Mutelet, V. Butet and J.-N. Jaubert, Application of Inverse Gas Chromatography and Regular Solution Theory for Characterization of Ionic Liquids, *Industrial & Engineering Chemistry Research*, 44 (2005) p. 4120-4127. DOI:10.1021/ie048806l.

- [14] Y. Shimoyama, T. Hirayama and Y. Iwai, Measurement of Infinite Dilution Activity Coefficients of Alcohols, Ketones, and Aromatic Hydrocarbons in 4-Methyl-N-butylpyridinium Tetrafluoroborate and 1-Butyl-3-methylimidazolium Hexafluorophosphate by Gas-Liquid Chromatography, *Journal of Chemical & Engineering Data*, 53 (2008) p. 2106-2111. DOI:10.1021/jc800246v.
- [15] I. C. M. Vaz, A. Bhattacharjee, M. A. A. Rocha, J. A. P. Coutinho, M. Bastos and L. M. N. B. F. Santos, Alcohols as molecular probes in ionic liquids: evidence for nanostructuration, *Physical Chemistry Chemical Physics*, 18 (2016) p. 19267-19275. DOI:10.1039/C6CP03616C.
- [16] Y. Deng, P. Husson, J. Jacquemin, T. G. A. Youngs, V. L. Kett, C. Hardacre and M. F. Costa Gomes, Volumetric Properties and Enthalpies of Solution of Alcohols $C_kH_{2k}+1OH$ ($k=1, 2, 6$) in 1-Methyl-3-alkylimidazolium Bis(trifluoromethylsulfonyl)imide $\{[C_1C_nIm][NTf_2] \text{ } n=2, 4, 6, 8, 10\}$ Ionic Liquids, *The Journal of Chemical Thermodynamics*, 43 (2011) p. 1708-1718. DOI:10.1016/j.jct.2011.05.033.
- [17] M. A. A. Rocha, C. F. R. A. C. Lima, L. R. Gomes, B. Schröder, J. A. P. Coutinho, I. M. Marrucho, J. M. S. S. Esperança, L. P. N. Rebelo, K. Shimizu, J. N. Canongia Lopes and L. M. N. B. F. Santos, High-Accuracy Vapor Pressure Data of the Extended $[C_nC_1im][NTf_2]$ Ionic Liquid Series: Trend Changes and Structural Shifts, *The Journal of Physical Chemistry B*, 115 (2011) p. 10919-10926. DOI:10.1021/jp2049316.
- [18] D. H. Zaitsau and S. P. Verevkin, Imidazolium-based ionic liquids containing FAP anion: Thermodynamic study, *Journal of Molecular Liquids*, 287 (2019) p. 110959. DOI:10.1016/j.molliq.2019.110959.
- [19] A. F. M. Claudio, L. Swift, J. P. Hallett, T. Welton, J. A. P. Coutinho and M. G. Freire, Extended Scale for the Hydrogen-Bond Basicity of Ionic Liquids, *Physical Chemistry Chemical Physics*, 16 (2014) p. 6593-6601. DOI:10.1039/C3CP55285C.
- [20] M. A. Ab Rani, A. Brant, L. Crowhurst, A. Dolan, M. Lui, N. H. Hassan, J. P. Hallett, P. A. Hunt, H. Niedermeyer, J. M. Perez-Arlandis, M. Schrems, T. Welton and R. Wilding, Understanding the polarity of ionic liquids, *Physical Chemistry Chemical Physics*, 13 (2011) p. 16831-16840. DOI:10.1039/C1CP21262A.
- [21] L. Crowhurst, P. R. Mawdsley, J. M. Perez-Arlandis, P. A. Salter and T. Welton, Solvent-solute interactions in ionic liquids, *Physical Chemistry Chemical Physics*, 5 (2003) p. 2790-2794. DOI:10.1039/B303095D.
- [22] K. A. Kurnia, F. Lima, A. F. M. Claudio, J. A. P. Coutinho and M. G. Freire, Hydrogen-bond acidity of ionic liquids: an extended scale, *Physical Chemistry Chemical Physics*, 17 (2015) p. 18980-18990. DOI:10.1039/C5CP03094C.
- [23] A. S. M. C. Rodrigues, M. A. A. Rocha, H. F. D. Almeida, C. M. S. S. Neves, J. A. Lopes-da-Silva, M. G. Freire, J. A. P. Coutinho and L. M. N. B. F. Santos, Effect of the Methylation and N-H Acidic Group on the Physicochemical Properties of Imidazolium-Based Ionic Liquids, *The Journal of Physical Chemistry B*, 119 (2015) p. 8781-8792. DOI:10.1021/acs.jpcc.5b05354.
- [24] K. Noack, P. S. Schulz, N. Paape, J. Kiefer, P. Wasserscheid and A. Leipertz, The role of the C2 position in interionic interactions of imidazolium based ionic liquids: a vibrational and NMR spectroscopic study, *Physical Chemistry Chemical Physics*, 12 (2010) p. 14153-14161. DOI:10.1039/C0CP00486C.
- [25] A. S. M. C. Rodrigues, C. F. R. A. C. Lima, J. A. P. Coutinho and L. M. N. B. F. Santos, Nature of the C2-methylation effect on the properties of imidazolium ionic liquids, *Physical Chemistry Chemical Physics*, 19 (2017) p. 5326-5332. DOI:10.1039/C6CP08451F.
- [26] C. Chiappe and D. Pieraccini, Determination of Ionic Liquids Solvent Properties Using an Unusual Probe: The Electron Donor-Acceptor Complex between 4,4'-bis(Dimethylamino)-benzophenone and Tetracyanoethene, *The Journal of Physical Chemistry A*, 110 (2006) p. 4937-4941. DOI:10.1021/jp057236f.
- [27] S. Coleman, R. Byrne, S. Minkovska and D. Diamond, Thermal reversion of spirooxazine in ionic liquids containing the $[NTf_2]^-$ anion, *Physical Chemistry Chemical Physics*, 11 (2009) p. 5608-5614. DOI:10.1039/B901417A.
- [28] A. Jeličić, N. García, H.-G. Löhmansröben and S. Beuermann, Prediction of the Ionic Liquid Influence on Propagation Rate Coefficients in Methyl Methacrylate Radical Polymerizations Based on Kamlet-Taft Solvatochromic Parameters, *Macromolecules*, 42 (2009) p. 8801-8808. DOI:10.1021/ma9017907.

[29] J. J. Christensen, R. M. Izatt, B. D. Stitt, R. W. Hanks and K. D. Williamson, The excess enthalpies of seven n-nonane + alcohol mixtures at 298.15 K, *The Journal of Chemical Thermodynamics*, 11 (1979) p. 1029-1034. DOI:10.1016/0021-9614(79)90133-2.

[30] S. G. Collins, J. J. Christensen, R. M. Izatt and R. W. Hanks, The excess enthalpies of 10 (n-pentane + and n-alkanol) mixtures at 298.15 K, *The Journal of Chemical Thermodynamics*, 12 (1980) p. 609-614. DOI:10.1016/0021-9614(80)90081-6.

[31] CODATA: <http://physics.nist.gov/constants>.

[32] I. Wadsö, Heats of Vaporization for a Number of Organic Compounds at 25°C, *Acta Chemica Scandinavica*, 20 (1966) p. 9. DOI:10.3891/acta.chem.scand.20-0544.

[33] J. Murto; and A. Kivinen, (unknown title), *Suomen Kemistil. B*, 40 (1967) p. 258. (Results consulted in NIST WebBook).

[34] A. C. Meeks and I. J. Goldfarb, Vapor pressure of fluoroalcohols, *Journal of Chemical & Engineering Data*, 12 (1967) p. 196-196. DOI:10.1021/je60033a010.

[35] C. H. Rochester and J. R. Symonds, Thermodynamic studies of fluoroalcohols. Part 1.—Vapour pressures and enthalpies of vaporization, *Journal of the Chemical Society, Faraday Transactions 1: Physical Chemistry in Condensed Phases*, 69 (1973) p. 1267-1273. DOI:10.1039/F19736901267.

[36] G. M. C. Silva, P. Morgado, J. D. Haley, V. M. T. Montoya, C. McCabe, L. F. G. Martins and E. J. M. Filipe, Vapor pressure and liquid density of fluorinated alcohols: Experimental, simulation and GC-SAFT-VR predictions, *Fluid Phase Equilibria*, 425 (2016) p. 297-304. DOI:10.1016/j.fluid.2016.06.011.

[37] D. Matulis, Thermodynamics of the hydrophobic effect. III. Condensation and aggregation of alkanes, alcohols, and alkylamines, *Biophysical Chemistry*, 93 (2001) p. 67-82. DOI:10.1016/S0301-4622(01)00209-5.

[38] J. C. Carver, R. C. Gray and D. M. Hercules, Remote inductive effects evaluated by x-ray photoelectron spectroscopy (ESCA), *Journal of the American Chemical Society*, 96 (1974) p. 6851-6856. DOI:10.1021/ja00829a007.

[39] R. Filler and R. M. Schure, Highly acidic perhalogenated alcohols. A new synthesis of perfluoro-tert-butyl alcohol, *The Journal of Organic Chemistry*, 32 (1967) p. 1217-1219. DOI:10.1021/jo01279a081.

[40] B. L. Dyatkin, E. P. Mochalina and I. L. Knunyants, The acidic properties of fluorine-containing alcohols, hydroxylamines and oximes, *Tetrahedron*, 21 (1965) p. 2991-2995. DOI:10.1016/S0040-4020(01)96918-2.

[41] W. K. McEwen, A Further Study of Extremely Weak Acids, *Journal of the American Chemical Society*, 58 (1936) p. 1124-1129. DOI:10.1021/ja01298a017.

[42] C. H. Arrowsmith, A. J. Kresge and Y. C. Tang, The base-catalyzed decomposition of nitramide: mechanism of the second reaction pathway, *Journal of the American Chemical Society*, 113 (1991) p. 179-182. DOI:10.1021/ja00001a026.

[43] E. P. Serjeant and B. Dempsey, Ionisation Constants of Organic Acids in Aqueous Solution, International Union of Pure and Applied Chemistry (IUPAC). IUPAC Chemical Data Series. No. 23, Pergamon Press, Inc., New York, 1979.

[44] P. Vollhardt and N. Schore, Organic Chemistry: Structure and Function, 8th ed., W.H. Freeman & Company, 2018. ISBN:1319079458.

[45] V. Majer and V. Svoboda, Enthalpies of Vaporization of Organic Compounds: A critical review and data compilation, 1st ed., Blackwell Scientific Publications, 1985. ISBN:0-632-01529-2.

[46] A. Heintz, D. V. Kulikov and S. P. Verevkin, Thermodynamic Properties of Mixtures Containing Ionic Liquids. 2. Activity Coefficients at Infinite Dilution of Hydrocarbons and Polar Solutes in 1-Methyl-3-ethyl-imidazolium Bis(trifluoromethyl-sulfonyl) Amide and in 1,2-Dimethyl-3-ethyl-imidazolium Bis(trifluoromethyl-sulfonyl) Amide Using Gas-Liquid Chromatography, *Journal of Chemical and Engineering Data*, 47 (2002) p. 894-899. DOI:10.1021/je0103115.

- [47] R. Kato and J. Gmehling, Systems with Ionic Liquids: Measurement of VLE and γ^∞ Data and Prediction of their Thermodynamic Behavior Using Original UNIFAC, mod. UNIFAC(DO) and COSMO-RS(OI), *The Journal of Chemical Thermodynamics*, 37 (2005) p. 603-619. DOI:10.1016/j.jct.2005.04.010.
- [48] W. Marczak, S. P. Verevkin and A. Heintz, Enthalpies of Solution of Organic Solutes in the Ionic Liquid 1-Methyl-3-ethyl-imidazolium Bis-(trifluoromethyl-sulfonyl) Amide, *Journal of Solution Chemistry*, 32 (2003) p. 519-526. DOI:10.1023/A:1025361832209.
- [49] A. Stark, B. Ondruschka, D. H. Zaitsau and S. P. Verevkin, Biomass-Derived Platform Chemicals: Thermodynamic Studies on the Extraction of 5-Hydroxymethylfurfural from Ionic Liquids, *Journal of Chemical & Engineering Data*, 57 (2012) p. 2985-2991. DOI:10.1021/jc300529j.
- [50] A. Heintz, S. P. Verevkin and D. Ondo, Thermodynamic Properties of Mixtures Containing Ionic Liquids. 8. Activity Coefficients at Infinite Dilution of Hydrocarbons, Alcohols, Esters, and Aldehydes in 1-Hexyl-3-methylimidazolium Bis(trifluoromethylsulfonyl) Imide Using Gas-Liquid Chromatography, *Journal of Chemical & Engineering Data*, 51 (2006) p. 434-437. DOI:10.1021/jc0503554.
- [51] A. Heintz, S. P. Verevkin, J. K. Lehmann, T. V. Vasiltsova and D. Ondo, Activity Coefficients at Infinite Dilution and Enthalpies of Solution of Methanol, 1-Butanol, and 1-Hexanol in 1-Hexyl-3-methyl-imidazolium Bis(trifluoromethyl-sulfonyl)imide, *The Journal of Chemical Thermodynamics*, 39 (2007) p. 268-274. DOI:10.1016/j.jct.2006.07.006.
- [52] Y. Li, L.-S. Wang, Y.-X. Feng and C.-Y. Zhang, Activity Coefficients of Organic Solutes at Infinite Dilution in Ionic Liquids. 1. 1-Hexyl-3-Methylimidazolium Hexafluorophosphate and 1-Octyl-3-Methylimidazolium Hexafluorophosphate and Their Application to Alkane/Aromatic and Aromatic/Aromatic Hydrocarbon Separation, *Industrial & Engineering Chemistry Research*, 50 (2011) p. 10755-10764. DOI:10.1021/ie102458k.
- [53] C. E. S. Bernardes, K. Shimizu, A. I. M. C. Lobo Ferreira, L. M. N. B. F. Santos and J. N. C. Lopes, Structure and Aggregation in the 1,3-Dialkyl-imidazolium Bis(trifluoromethylsulfonyl)imide Ionic Liquid Family: 2. From Single to Double Long Alkyl Side Chains, *The Journal of Physical Chemistry B*, 118 (2014) p. 6885-6895. DOI:10.1021/jp502968u.
- [54] K. Paduszyński, E. V. Lukoshko, M. Królikowski, U. Domańska and J. Szydłowski, Thermodynamic Study of Binary Mixtures of 1-Butyl-1-methylpyrrolidinium Dicyanamide Ionic Liquid with Molecular Solvents: New Experimental Data and Modeling with PC-SAFT Equation of State, *The Journal of Physical Chemistry B*, 119 (2015) p. 543-551. DOI:10.1021/jp511621j.
- [55] A. Navas, J. Ortega, R. Vreekamp, E. Marrero and J. Palomar, Experimental Thermodynamic Properties of 1-Butyl-2-methylpyridinium Tetrafluoroborate [b2mpy][BF₄] with Water and with Alkan-1-ol and Their Interpretation with the COSMO-RS Methodology, *Industrial & Engineering Chemistry Research*, 48 (2009) p. 2678-2690. DOI:10.1021/ie8009878.
- [56] G. Rai and A. Kumar, An enthalpic approach to delineate the interactions of cations of imidazolium-based ionic liquids with molecular solvents, *Physical Chemistry Chemical Physics*, 13 (2011) p. 14715-14722. DOI:10.1039/C1CP20888H.
- [57] A. E. Pope, H. D. Pflug, B. Dacre and G. C. Benson, Molar excess enthalpies of binary n-alcohol systems at 25 °C, *Canadian Journal of Chemistry*, 45 (1967) p. 2665-2674. DOI:10.1139/v67-436.
- [58] S. Agrawal and H. K. Kashyap, Structures of binary mixtures of ionic liquid 1-butyl-3-methylimidazolium bis(trifluoromethylsulfonyl)imide with primary alcohols: The role of hydrogen-bonding, *Journal of Molecular Liquids*, 261 (2018) p. 337-349. DOI:10.1016/j.molliq.2018.03.124.
- [59] Y. Yoshimura, S. Hattori, T. Mori, K. Kaneko, J. Ueda, T. Takekiyo, Y. Masuda and A. Shimizu, An insight into the filling of the nanoheterogeneous structures of 1-butyl-3-methylimidazolium bis(trifluoromethanesulfonyl)amide by primary alcohols, *Journal of Molecular Liquids*, 300 (2020) p. 112351. DOI:10.1016/j.molliq.2019.112351.
- [60] J. Łachwa, P. Morgado, J. M. S. S. Esperança, H. J. R. Guedes, J. N. Canongia Lopes and L. P. N. Rebelo, Fluid-Phase Behavior of {1-Hexyl-3-methylimidazolium Bis(trifluoromethylsulfonyl) Imide, [C6mim][NTf₂], + C₂-C₈ n-Alcohol} Mixtures: Liquid-Liquid Equilibrium and Excess Volumes, *Journal of Chemical & Engineering Data*, 51 (2006) p. 2215-2221. DOI:10.1021/jc060307z.

[61] A. M. Fernandes, M. A. A. Rocha, M. G. Freire, I. M. Marrucho, J. A. P. Coutinho and L. M. N. B. F. Santos, Evaluation of Cation–Anion Interaction Strength in Ionic Liquids, *The Journal of Physical Chemistry B*, 115 (2011) p. 4033-4041. DOI:10.1021/jp201084x.

[62] K. Shimizu, M. Tariq, M. F. C. Gomes, L. P. N. Rebelo and J. N. C. Lopes, Assessing the Dispersive and Electrostatic Components of the Cohesive Energy of Ionic Liquids Using Molecular Dynamics Simulations and Molar Refraction Data, *The Journal of Physical Chemistry B*, 114 (2010) p. 5831-5834. DOI:10.1021/jp101910c.

CHAPTER 5

Conclusions and Achievements

-
- 5.1. Overview
 - 5.2. Contribution and Relevance
 - 5.3. Still to be done
 - References
-

5. Conclusions and Achievements

The main conclusions and achievements of this work are outlined in this chapter, demonstrating their contribution to the field. At the end, some possibilities of future work are proposed.

5.1. Overview

According to the objectives of this work, the solution/solvation of alcohols in ionic liquids was studied close to infinite dilution by isothermal titration calorimetry, exploring which aspects most influence the solvation of alcohols in ionic liquids. To explore the effect of the concentration of the molecular solutes (as alcohols) in ionic liquids a new calorimeter, the μ FlowCal, was constructed in the context of this thesis. The feasibility of the constructed instrument to pursue this goal was demonstrated by the measurement of the excess molar enthalpy of a binary mixture constituted by a model alcohol and a model ionic liquid in a wide concentration range.

The main achievements of this work will now be outlined, subdividing them into two categories: methodological achievements and achievements on the understanding of the solvation in ionic liquids.

5.1.1. New Experimental Methodologies

In the context of this thesis, a new calorimeter was constructed, titled as μ FlowCal, based in the principle of heat conduction. The μ FlowCal is a flow twin microcalorimeter that works in stopped-flow mode, in isothermal conditions. The instrument is able to measure the heat of mixing of two fluids mixed in a micromixer of 200 mm³ (μ L) located in the sensitive zone of the calorimeter. The calorimeter evidence a high sensitivity $115.6 \pm 2.8 \text{ mV} \cdot \text{W}^{-1}$ together with a rather good baseline stability (see figure 5.1) with a short-time noise (6.4 s) of approximately 5 nV and a long time noise (4 to 5 h) of approximately 170 nV. Further specifications are summarized in table 5.1.

The calorimeter was electrically calibrated and tested using recommended procedures. Overall, μ FlowCal demonstrated a good performance on the testing of the calorimetric and mixing system, even using high viscosity fluids (sucrose solutions). The

determination of the enthalpy of mixing of the decane-octanol binary mixture, in a wide concentration range, has proven also the efficiency of the calorimetric and flow system. Nevertheless, higher deviations have been found at low flows, showing that the calorimeter has a lower sensitivity at the low concentrations, which is related with the efficiency of the mixing and the accuracy of low flow levels.

Due to the high workload associated to the construction and test of this new calorimeter, only the enthalpy of mixing of 1-butanol in $[\text{C}_6\text{C}_{1\text{im}}][\text{NTf}_2]$ was measured in this thesis. The enthalpic properties of mixing of this system have been reported in literature only in the rich-IL area of the diagram. Nevertheless, the magnitude of the data obtained in $\mu\text{FlowCal}$ calorimeter was found to be in close agreement with the data reported in the literature. The measurement of the enthalpy of mixing of this alcohol-IL binary mixture demonstrated the feasibility of the $\mu\text{FlowCal}$ calorimeter to explore the effect of the concentration of alcohols and other solutes in ionic liquids.

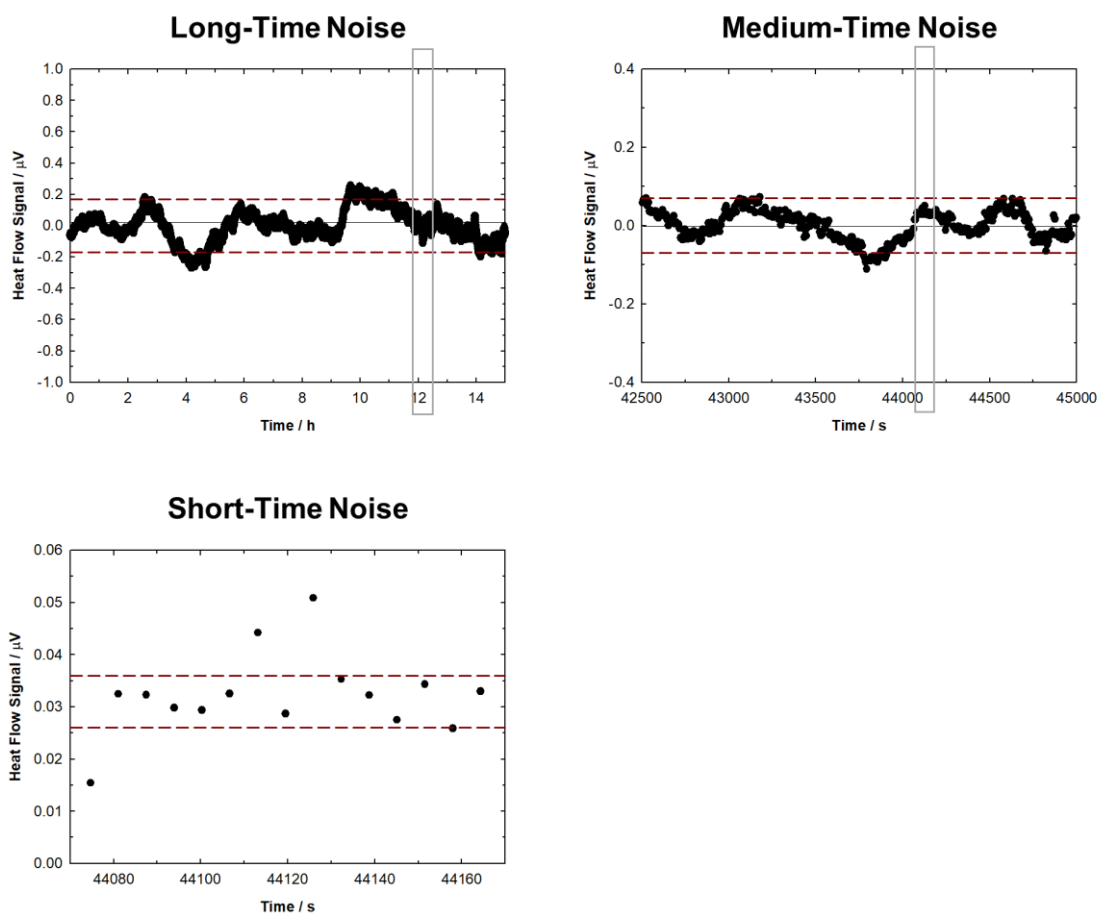


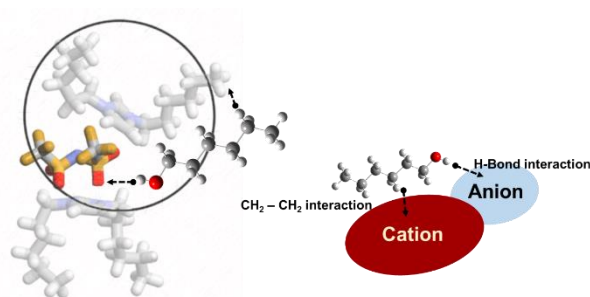
Figure 5.1. Graphical representation of the baseline stability of the $\mu\text{FlowCal}$ calorimeter, over a period of 15 hours, with respective magnifications on the axis of the heat flow signal, demonstrating the magnitude of medium and short-time noise. Data represented as obtained, without filtration or smoothing.

Table 5.1. Summary of the specifications of μ FlowCal prototype calorimeter

Baseline	
Short-time noise (6.4 s)	± 5 nV
Medium-time noise (1000 s)	± 70 nV
Long-time noise (4 - 5 h)	± 170 nV
Temperature	
Long-Time Oscillation calorimeter thermostat (external box) (40 000 s)	2.0 mK
Long-Time Oscillation Calorimeter (40 000 s)	up to 0.25 mK
Calorimetric System	
Time Constant	250 s
Sensitivity (Side A; Side B)	115.6 mV·W ⁻¹ ; 113.9 mV·W ⁻¹
Micromixer Volume	200 μ L
Micromixer Composition	Borosilicate glass
Flow System Composition	CTFE; PTFE;PEEK; Stainless Steel

5.1.2. Solvation of Alcohols in Ionic Liquids

At Infinite dilution



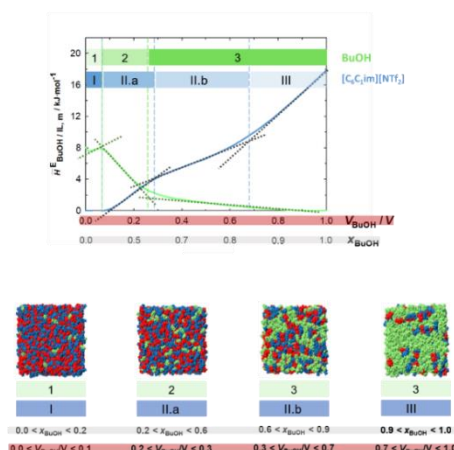
The effects of the cation nature, the hydrogen bond basicity of the anion and the hydrogen bond acidity of the alcohol on the solvation process, were explored in conditions close to the infinite dilution of the alcohol. The obtained results presented evidences of the location of the alcohol hydroxyl group in the polar domains of ionic liquids, interacting preferentially with basic anions. The strength of this interaction seems to be conditioned by the hydrogen bond acidity of the alcohol and the hydrogen bond basicity of the anion that constitutes the ionic liquid.

In the case of ionic liquids constituted by less basic anions, as $[\text{PF}_6]$ and $[\text{FAP}]$ anions, with lower ability to interact with the hydroxyl group of the alcohol, the results exhibited a bigger role of the cation in the solvation process. Furthermore, the results also suggested that the introduction of substituent groups in the cation, which cause the modification of the possible positions of the cation around the anion, changes the IL/alcohol interaction and leads to a differentiation in the solvation properties.

The effect of the alkyl chain length of both the cation and the alcohol in the solvation properties of ionic liquids, was also studied in experimental conditions close to the infinite dilution of the alcohol. In this way, the potential of the nonpolar domains of the ionic liquids to interact with simple molecular solutes was evaluated. The obtained results indicated that the alkyl chain of the alcohol interact with the nonpolar domains of the ILs similarly to the interactions established in bulk alkanes.

These results are in accordance with the so called “nanostructured solvation paradigm”^[1, 2] described in the literature. According to this model, solutes are preferentially solvated in the polar and nonpolar domains of the ionic liquids depending on their nature. In the specific case of alcohols, due to their amphiphilic nature, they are preferentially located in both polar and nonpolar domains: the hydroxyl group is preferentially in the polar domain, interacting with the anion through hydrogen bond, while the alkyl chain is preferentially solvated in the nonpolar domain.

At the Full Concentration Range



Overall, it was possible to see that the basicity of the IL anion plays an important role into the enthalpy of mixing of binary mixtures, as in the solvation at infinite dilution, due to the capacity of the basic anions to form hydrogen bond interactions with the alcohol. The hydrogen bond acidity of the anion is related with the strength of the alcohol–IL interaction established and determines the degree of compensation of the endothermic effect of the breakage of the solute and solvent interactions upon the mixture. Accordingly, the anion chosen, has the ability to decrease the endothermic character of the enthalpy of mixture or even causing it to become exothermic, depending on the strength of the hydrogen bond interaction it establishes with the alcohol.

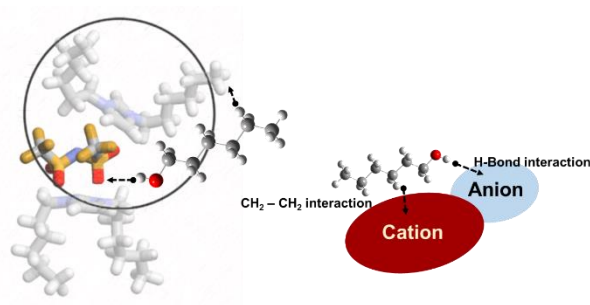
Furthermore, by comparing binary mixtures composed by ILs of similar hydrogen bond basicity and observing significant differences in the mixing properties, it was seen that although the hydrogen bond basicity plays an important role in the mixing process, the effect of other characteristics should be studied, as they may play an important part in the process. Additionally, the effect of the size of the alkyl chain of the alcohol and the cation was seen to modify the mixing properties.

Despite of the preliminary character of the calorimetric results obtained in μ FlowCal calorimeter, the existence of a relation with the structuration of the binary mixture is ventured, which is in line with the current understanding of structuration of similar mixtures^[3, 4]. The determination of the enthalpy of mixture provide important energetic information on the mixtures, which together with structural characterization studies and molecular dynamics simulation, consists in a powerful tool into the molecular understanding of the ILs and its characterization as a solvent, being a few steps closer to the possibility of rationally design IL based solvents specific for a given application.

5.2. Contribution and Relevance

In this section, the major achievements of this thesis will be evoked, outlining their contribution to the field and the relevance of this contribution.

Preferential Solvation in ILs

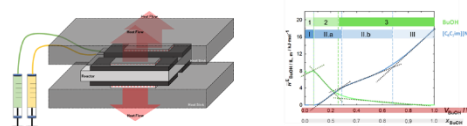


The characterization of ionic liquids solvation ability and the understanding of the interactions established with molecular solutes are of major importance to promote the functionality and applicability of IL-based solvents. The general mechanism of solvation in ionic liquids has already been established in the literature^[1, 2]. Nonetheless, detailed characterization of different systems is still necessary to fully understand the solvation in ILs and to rationalize the effects of the different cations/anions chosen in the IL solvent properties. This experimental work evaluates both the solvation environment and solvation energetics of a wide range of IL families, with an emphasis on a rational interpretation of the effects of the cation and anion on the solvation properties of ionic liquids.

The relevance of these systematic studies to the field can be seen by the inclusion and citation of the only two works published^[5, 6] on the topic in a very recent review of Wang and collaborators on ionic liquids^[7]. This review, which included a summarization on the state of art of binary mixtures constituted by alcohols and ionic liquids, had included the effect of the anion and cation in the process of solvation in ionic liquids, as well as, the rational interpretation of the solution/solvation model used in this thesis.

As mentioned, the development of the understanding of the solvation in ionic liquids from a molecular stand point is essential to develop the rational design of IL-based solvents. As an example, ionic liquids have been indicated as promising reaction media to promote different organic reactions^[8, 9]. To understand the role of the ionic liquids and its potential as reaction media in different organic reactions, it would be essential to understand the preferential location and solute-solvent interactions of the reactants, intermediates and products in ILs^[8]. The different solvation of these compounds may alter the equilibrium of the reaction^[8].

μ FlowCal and the Study of Mixtures



The successful construction and development of the methodology of μ FlowCal calorimeter, turns possible, together with the use of ITC, the study of the enthalpy of mixture of binary mixtures containing ionic liquids in the whole range of composition, from the pure ionic liquid to the infinitely dilute ionic liquid, or as the mutual solubility would allow. As it was demonstrated in this work, the combination of the results obtained in both calorimetric methodologies enables the measurement of the enthalpic contribution associated to the different mixing regimes in binary mixtures containing ionic liquids. The importance and relevance of the evaluation of the heat involved in the mixing of molecular solvents in ionic liquids had already been identified in a review regarding enthalpic quantities of binary mixtures containing ionic liquids of Costa Gomes and collaborators^[10]. Transcribing their words^[10]: “...the complexity of ionic liquids and the large differences between their pure fluid properties and those of the molecular compounds lead to complex mixtures. Our understanding of these requires a systematic overview of energetic properties of mixing...”. Their review is a relevant work to this endeavour of systematization of these properties, covering a wide range of systems, aiming to the characterization of solvation in ILs.

In summary, the construction and development of this new methodology expands the diversity of the available scientific equipment of the group, filling a gap for a calorimeter that would allow to explore the enthalpy of mixture in a wide concentration range for small sample size. The development and availability of this new experimental methodology will be a key tool for the research group to pursue one of its open investigation lines “Study of ionic liquids - based mixtures”. This expansion on the equipment of the group is essential to study the mixing properties of ionic liquids in a broad concentration range. As was shown in this thesis, the preliminary results of the binary mixture BuOH + [C₆C₁im][NTf₂] evidence the capacity of the results obtained in this instrument to provide new tools to answer to an ongoing challenge existent in the scientific community: the understanding of the different structuration regimes existent in IL containing mixtures.

5.3. Still to be done

Scientific research is a never ending process. Every time a question is answered, several others are raised. The time period involved on a PhD project is seldom sufficient to obtain all the answers we propose ourselves to...

According to the objectives of this PhD, the work performed in the scope of this project and the work which was not done due to time limitations, some future work is now going to be purposed. The future work is going to be divided in two topics: solvation of alcohols in ionic liquids at infinite dilution and μ FlowCal and the study of binary mixtures containing ionic liquids.

Solvation of Alcohols in Ionic Liquids at Infinite Dilution

As already referred the solution/solvation of alcohols in ionic liquids was studied close to infinite dilution by isothermal titration calorimetry, exploring which aspects most influence the solvation of alcohols in ionic liquids: the cation/anion nature, the alkyl chain length, the acidity/basicity.

A similar behaviour was found for the solution/solvation of alcohols in the ILs $[C_N C_{1im}][NTf_2]$ and $[C_N C_{1im}][PF_6]$ when exploring the effect of the alkyl chain length of both cation and alcohol, differing only by the strength of alcohol-anion interaction. The expansion of this study and confirmation of this trend in solvation could be checked by studying an ionic liquid of higher hydrogen bond acidity as [DCA] or [TFA]. Furthermore, the study with different cations, associated with anions of high and low hydrogen bond basicity could provide important insights on the effect of the cation.

A further step would be the study of the solution/solvation of alcohols in mixtures of ionic liquids. The study of the enthalpy of solution/solvation at infinite dilution of 1-propanol in binary mixtures of ionic liquids constituted, for example, by the ILs $[C_4 C_{1im}][NTf_2]$ and $[C_4 C_{1im}][PF_6]$ would allow to see if the alcohols have preferential location close to the anion of higher hydrogen bond basicity.

The calorimetric results/analysis could also be complemented using NOESY/HOESY (nuclear / heteronuclear Overhauser effect spectroscopy) as it was initially planned. Unfortunately the time was not long enough to perform both studies. These studies would allow to identify atoms in close proximity (through space) to each other, providing insights into the solvation sphere and the intermolecular interactions present, complementing the calorimetric results and conclusions.

μ FlowCal and the Study of Mixtures

There is not sufficient data in the literature regarding the enthalpy of mixing of the alcohol-IL binary system studied to fully validate the experimental results obtained in μ FlowCal calorimeter. For that reason, the values presented in this thesis regarding the binary mixture of $[\text{C}_6\text{C}_{1\text{im}}][\text{NTf}_2]$ and 1-butanol are taken as preliminary results. From our stand-point, a single measurement at equimolar composition, for example, in another calorimeter could allow to validate the obtained results.

Despite of the preliminary character of the results presented, and assuming that some small systematic deviation may exist, the results are nevertheless meaningful regarding the different structuration regimes. Accordingly, it would be extremely interesting to measure the enthalpy of mixing of binary mixtures containing ionic liquids, varying its components in a systematic fashion. The differential analysis of the results obtained in mixtures constituted by ILs of different cations/anions/alkyl chain length, as well as, different molecular or ionic compounds would certainly provide important information both on the enthalpic properties of mixing and on the structuration and molecular interactions present.

References:

- [1] T. Méndez-Morales, J. Carrete, Ó. Cabeza, O. Russina, A. Triolo, L. J. Gallego and L. M. Varela, Solvation of Lithium Salts in Protic Ionic Liquids: A Molecular Dynamics Study, *The Journal of Physical Chemistry B*, 118 (2014) p. 761-770. DOI:10.1021/jp410090f.
- [2] L. M. Varela, T. Méndez-Morales, J. Carrete, V. Gómez-González, B. Docampo-Álvarez, L. J. Gallego, O. Cabeza and O. Russina, Solvation of molecular cosolvents and inorganic salts in ionic liquids: A review of molecular dynamics simulations, *Journal of Molecular Liquids*, 210 (2015) p. 178-188. DOI:10.1016/j.molliq.2015.06.036.
- [3] S. Agrawal and H. K. Kashyap, Structures of binary mixtures of ionic liquid 1-butyl-3-methylimidazolium bis(trifluoromethylsulfonyl)imide with primary alcohols: The role of hydrogen-bonding, *Journal of Molecular Liquids*, 261 (2018) p. 337-349. DOI:10.1016/j.molliq.2018.03.124.
- [4] Y. Yoshimura, S. Hattori, T. Mori, K. Kaneko, J. Ueda, T. Takekiyo, Y. Masuda and A. Shimizu, An insight into the filling of the nanoheterogeneous structures of 1-butyl-3-methylimidazolium bis(trifluoromethanesulfonyl)amide by primary alcohols, *Journal of Molecular Liquids*, 300 (2020) p. 112351. DOI:10.1016/j.molliq.2019.112351.
- [5] I. C. M. Vaz, A. Bhattacharjee, M. A. A. Rocha, J. A. P. Coutinho, M. Bastos and L. M. N. B. F. Santos, Alcohols as molecular probes in ionic liquids: evidence for nanostructuration, *Physical Chemistry Chemical Physics*, 18 (2016) p. 19267-19275. DOI:10.1039/C6CP03616C.
- [6] I. C. M. Vaz, M. Bastos, C. E. S. Bernardes, J. N. Canongia Lopes and L. M. N. B. F. Santos, Solvation of alcohols in ionic liquids – understanding the effect of the anion and cation, *Physical Chemistry Chemical Physics*, 20 (2018) p. 2536-2548. DOI:10.1039/C7CP07525A.
- [7] Y.-L. Wang, B. Li, S. Sarman, F. Mocci, Z.-Y. Lu, J. Yuan, A. Laaksonen and M. D. Fayer, Microstructural and Dynamical Heterogeneities in Ionic Liquids, *Chemical Reviews*, (2020) p. DOI:10.1021/acs.chemrev.9b00693.
- [8] J. P. Hallett and T. Welton, Room-Temperature Ionic Liquids: Solvents for Synthesis and Catalysis. 2, *Chemical Reviews*, 111 (2011) p. 3508-3576. DOI:10.1021/cr1003248.
- [9] S. Subbiah, I. C. Cathy and C. Yen-Ho, Ionic Liquids for Green Organic Synthesis, *Current Organic Synthesis*, 9 (2012) p. 74-95. DOI:10.2174/157017912798889116.
- [10] A. Podgoršek, J. Jacquemin, A. A. H. Pádua and M. F. Costa Gomes, Mixing Enthalpy for Binary Mixtures Containing Ionic Liquids, *Chemical Reviews*, 116 (2016) p. 6075-6106. DOI:10.1021/acs.chemrev.5b00379.

Appendix

Appendix A

- A.1. Thermostatization of μ FlowCal Calorimeter
- A.2. Determination of the Time Constant of μ FlowCal Calorimeter

Appendix B

- B.1. Data Acquisition Software of μ FlowCal Calorimeter
- B.2. Data Treatment Software of μ FlowCal Calorimeter
- B.3. Temperature Monitor Software of μ FlowCal Calorimeter

Appendix C

- C.1. Quantum Chemical Calculation of Alcohol-Anion Interaction
- C.2. Quantum Chemical Calculation of Alcohol-[NTf₂] Interaction
- C.3. Quantum Chemical Calculation of Alcohol-Alcohol and Alcohol-Alkane Interaction

Appendix D

- D.1. Redlich-Kister Fittings of the Mixture BuOH and [C₆C₁im][NTf₂]

Appendix E

- E.1. Cost Evaluation of μ FlowCal Calorimeter Prototype
-

Appendix A

A.1. Thermostatization of μ FlowCal Calorimeter

The temperatures in the thermostated bath, aluminium box and calorimeter were simultaneous monitored to evaluate the behaviour and time constant of the heat transfer for the heat sink.

In figure A.1, the temperature in the three locations of the system over time is represented, starting from an initial condition, in which the calorimeter temperature was below the temperature of the surroundings (heat exchange fluid and external aluminium box), as schematically represented in figure A.2. As represented in figure A.1, the thermostated bath and the aluminium box are at thermal equilibrium, both their temperatures are at 298.15 K and the temperature of the calorimeter is rising to 298.15 K, following a heat exchange behaviour which could be described by a Newton's law of heat transfer between two bodies.

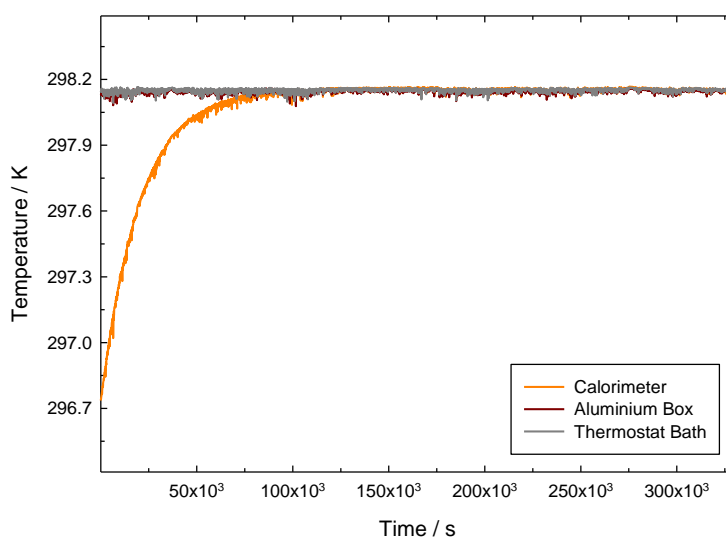


Figure A.1. Graphical representation of the temperature in the calorimeter (orange line —), in the aluminium box (dark red line —) and in the thermostated bath (gray line —) over time.

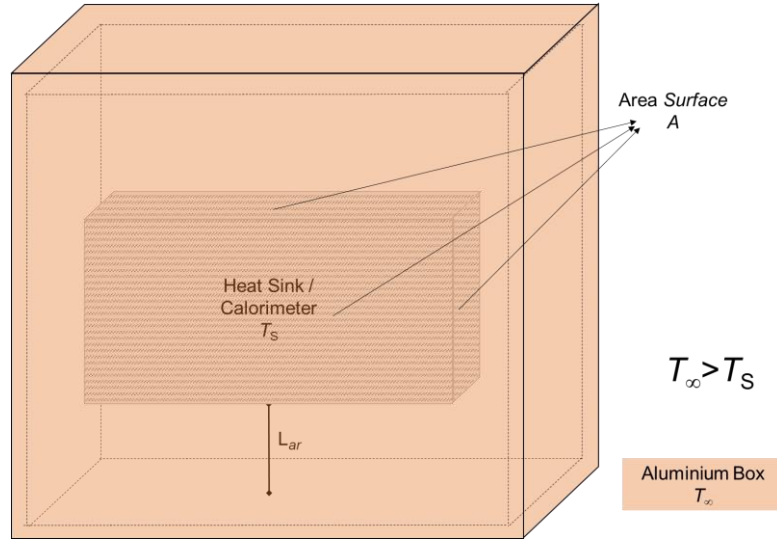


Figure A.2. Schematic representation of the calorimeter, inside the aluminium box, with an air gap in between. The dimensions in the scheme are not at real scale.

Starting from the application of Newton's law of cooling for heat transfer,

$$\phi = G(T_s - T_\infty) , \quad (\text{A.1})$$

where, in this system, G ($\text{J}\cdot\text{s}^{-1}\cdot\text{K}^{-1}$) is the conductance of the aluminium, T_∞ (K) is the temperature at thermal equilibrium, and T_s (K) is the temperature of the aluminium of the calorimetric block surface in each moment. It is possible to obtain the following expression,

$$\phi = \frac{dQ}{dt} = \frac{dQ}{dT} \cdot \frac{dT}{dt} = C \frac{dT}{dt} = G \cdot (T_s - T_\infty) , \quad (\text{A.2})$$

as the heat capacity C ($\text{J}\cdot\text{K}^{-1}$) may be defined by the amount of heat, ΔQ , added to an object to raise its temperature, ΔT . From the previous expression, the conductance of the aluminium, G ($\text{J}\cdot\text{s}^{-1}\cdot\text{K}^{-1}$) and the heat capacity of the calorimeter C ($\text{J}\cdot\text{K}^{-1}$), the time constant, τ (s) can be obtained:

$$\frac{dT}{dt} = \frac{G}{C} \cdot (T_s - T_\infty) = \frac{1}{\tau} \cdot (T_s - T_\infty) . \quad (\text{A.3})$$

This expression can be derived to time,

$$\frac{dT}{dt} dt = \frac{1}{\tau} \cdot (T_s - T_\infty) dt \quad (\text{A.4})$$

and then, its antiderivative may be applied,

$$\int \frac{1}{(T_s - T_\infty)} dT = \int \frac{1}{\tau} dt. \quad (\text{A.5})$$

Multiplying both sides by -1, as $(T_s - T_\infty) < 0$,

$$\ln(T_\infty - T_s) = -\frac{1}{\tau} \cdot t + b, \quad (\text{A.6})$$

in which “b” is a constant related with the initial state. From this expression, knowing that the temperature at thermal equilibrium, T_∞ , is very close to 298.15 K and that the temperature of the calorimeter block is being monitored over time, it's possible to obtain the time constant for the heat sink temperature change. In figure A.3, the “ $\ln(T_\infty - T_s)$ ” is represented as a function of the time of measurement together with its fitting (equation A.6). From the fitting of the experimental temperature versus time (figure A.3), the time constant of the heat transfer from the aluminium box to the heat sink of the calorimeter was determined, $\tau = (2.009 \pm 0.092) \times 10^4$ s.

From equation A.6, the following equations could be written:

$$e^{\ln(T_\infty - T_s)} = e^{-\frac{t}{\tau} + b}, \quad (\text{A.7})$$

$$(T_\infty - T_s) = e^b \cdot e^{-\frac{t}{\tau}}. \quad (\text{A.8})$$

From this equation, the time dependence of the temperature of the system, T_s is derived as:

$$T_s = T_\infty - e^b \cdot e^{-\frac{t}{\tau}}. \quad (\text{A.9})$$

In figure A.4, the fitting is compared with the experimental data, using equation A.9.

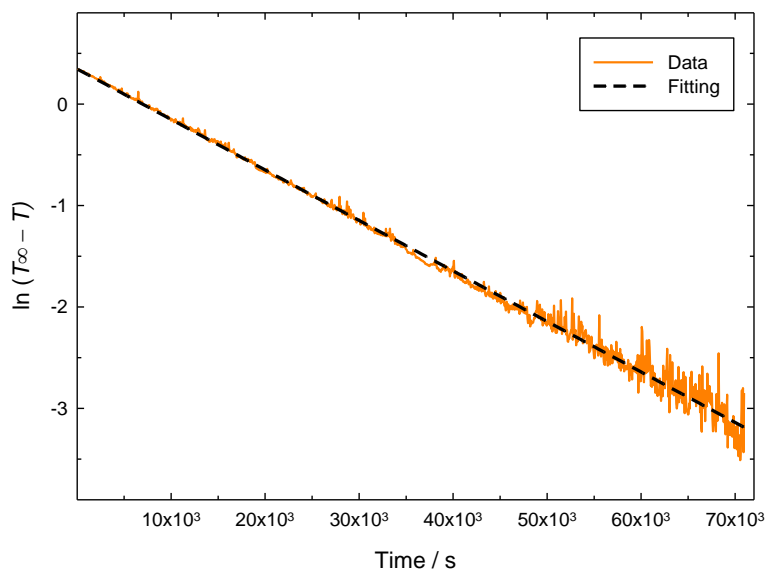


Figure A.3. Graphical representation of the “ $\ln(T_{\infty} - T_S)$ ” over time. Fitted data from equation A.6: $\ln(T_{\infty} - T_S) = -1/\tau \cdot t + b$; $1/\tau = (4.977 \pm 0.011) \times 10^{-5}$; $b = 0.3449 \pm 0.0045$; $R^2 = 0.994$.

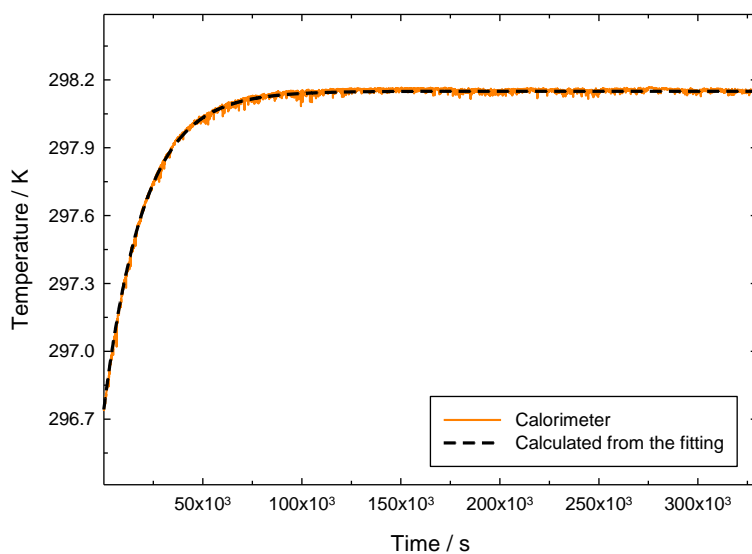


Figure A.4. Graphical representation of the temperature in the calorimeter (orange line \rightarrow) over time and of the calculated temperature of the calorimeter (black dashed line $-$), using the coefficients obtained from the fitting of the logarithm of the temperature difference.

Alternatively, the time constant of the heat sink block can be estimated considering that the heat is mainly transferred by conduction through the air gap between the heat sink and the aluminium box. Accordingly, the time constant can be calculated as,

$$\tau = \frac{C}{G} = \frac{m \cdot c \cdot L}{k \cdot A}, \quad (\text{A.10})$$

where m (kg) is the mass of aluminium in the calorimeter (18.9 kg), c ($\text{J} \cdot \text{K}^{-1} \cdot \text{kg}^{-1}$) is the specific heat capacity of the aluminium ($900 \text{ J} \cdot \text{K}^{-1} \cdot \text{kg}^{-1}$)^[1], k ($\text{J} \cdot \text{s}^{-1} \cdot \text{m}^{-1} \cdot \text{K}^{-1}$) is the thermal conductivity of the air ($0.0263 \text{ J} \cdot \text{s}^{-1} \cdot \text{m}^{-1} \cdot \text{K}^{-1}$)^[1], L (m) is the average length of the air gap (0.010 m) and A (m^2) is the total surface area of the calorimeter (0.250 m^2) through which the heat is being conducted. The estimated time constant, $\tau = 2.54 \times 10^4 \text{ s}$, is approximately 25% above the one derived from the fitting of the experimental data ($2.009 \times 10^4 \text{ s}$). The higher estimated value means that, in reality, the heat is being transferred faster than what was expected by the air gap conduction or the heat capacity is smaller than estimated. The difference may arise partially from inaccurate values used for the heat capacity of the aluminium for example or to some deficiencies in the accuracy of the model for the conductivity of the air gap. There is also a contribution of convection and the consideration of air being conducted only by random motion of the air molecules is an approximation, which is minimized by the small spacing of 10 mm between the two walls.

In figure A.5 is represented the temperature in the aluminium box after reaching thermal equilibrium for a period of approximately 11 hours. This representation demonstrates the long-time (40 000 s) temperature oscillation of the calorimeter thermostat. From the analysis of the data, it is clear that the temperature of the aluminium box is stable at 298.15 K and that the long-time noise level is of approximately $\pm 2.0 \text{ mK}$. The observed temperature oscillation was in the limit of the instrumentation resolution level. The actual temperature variation should be lower. In fact, the experimental temperature oscillation represented was filtered in order to overcome the instrumental noise of the measurement. In accordance, we were not able to measure the real variation in the temperature of the calorimeter after thermostatization, as it was lower than the instrumentation resolution.

The maximum variation of the temperature in the calorimeter was estimated from the experimental temperature of the aluminium box (filtered) and the thermal inertia of the heat sink calculated previously, $\tau = (2.009 \pm 0.092) \times 10^4 \text{ s}$. In figure A.5, is

represented the long-time (40 000 s) and medium-time (10 000 s) temperature oscillation of both the aluminium box and the estimated temperature in the calorimeter. It is observable that the average deviation of the temperature in the calorimeter should be smaller than ± 0.25 mK, which highlights the attenuation on the temperature oscillation (from ± 2.0 mK in the thermostat to ± 0.25 mK in the calorimeter block).

Due to the filtering of the experimental temperature to overcome the instrumental noise of the measurement, it is not possible to evaluate the short-time noise.

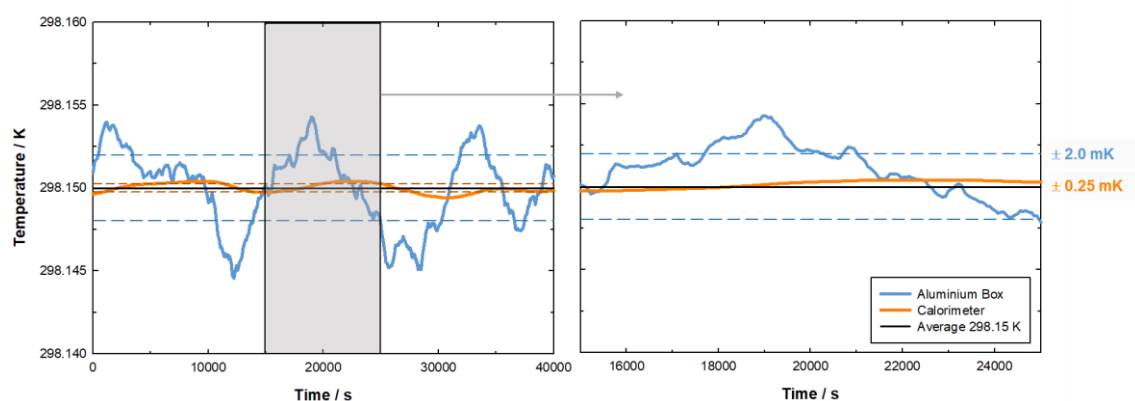


Figure A.5. Graphical representation (on the left) of the long-time temperature oscillation (40 000 s) and inset (on the right), representing the medium-time temperature oscillation (10 000 s) over time, in the aluminium box (full blue line —) and the estimated temperature oscillation in the calorimeter (full orange line —), considering the inertia of the heat sink, $\tau = (2.009 \pm 0.092) \times 10^4$ s. For guidance, the average of the temperatures, 298.15 K, is represented by a black line —, as well as, the average deviation of the temperature (coloured dashed lines).

A.2. Determination of the Time Constant of μ FlowCal Calorimeter

To obtain the time constant of the calorimeter, thermal energy was released, by joule effect, in two heaters which were incorporated inside the aluminium blocks that surround the mixing area, disturbing the thermal equilibrium of the calorimeter. The determination of the time constant, τ (s), was done by fitting a first order exponential to the “relaxation” of the calorimetric signal “signal 1+2” back to the initial state following the methodology (“time response technique”) described by Randzio and Suurkuusk ^[2] in “Interpretation of Calorimetric Thermograms and their Dynamic Corrections”.

The first order exponential used to fit the “relaxation” of the calorimetric sign can be written as,

$$U = A \cdot e^{-t/\tau}, \quad (\text{A.11})$$

which can be used also in its logarithmic form, to facilitate the manipulation of the data,

$$\ln U = -\frac{1}{\tau} \cdot t + \ln A. \quad (\text{A.12})$$

Using this methodology, the value obtained for the time constant is $\tau = (254 \pm 1)$ s. The fitting of the “signal 1+2” is represented in figure A.6. The parameters of the fitting presented correspond to the average values of the fitting of 5 exponential decays of the signal “1+2”.

It was later found out, that in typical experiments, the thermal inertia of the calorimeter is better described if the time constant is considered to be $\tau = 250$ s.

The calorimetric signals can now be corrected to the thermal inertia of the calorimeter. In figure A.7 are represented, as a function of time, the calorimetric output “signal 1”, “signal 2” and its sum “signal 1+2” corrected to the thermal inertia of the calorimeter, using the equation A.13 (already presented in the chapter 3 as equation 3.25):

$$P = U + \tau \left(\frac{dU}{dt} \right). \quad (\text{A.13})$$

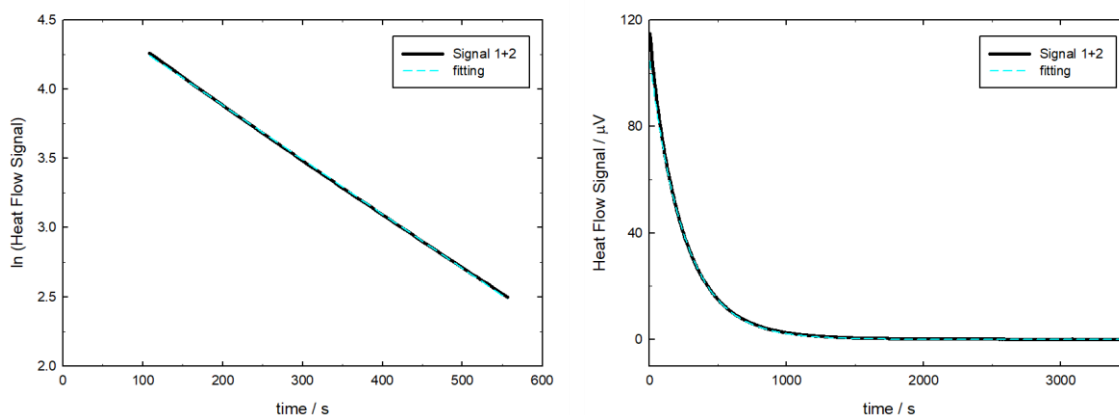


Figure A.6. Graphical representation of the fitting of a first order exponential to “signal 1+2”. On the left side is represented the fitting of the first exponential, made from the logarithm of the signal to facilitate the manipulation of the data; on the right, the exponential decay of the signal is represented together with the fitted exponential. Fitting parameters of equation A.12: $A = 107 \pm 2 \mu\text{V}$; $\tau = 254 \pm 1 \text{ s}$.

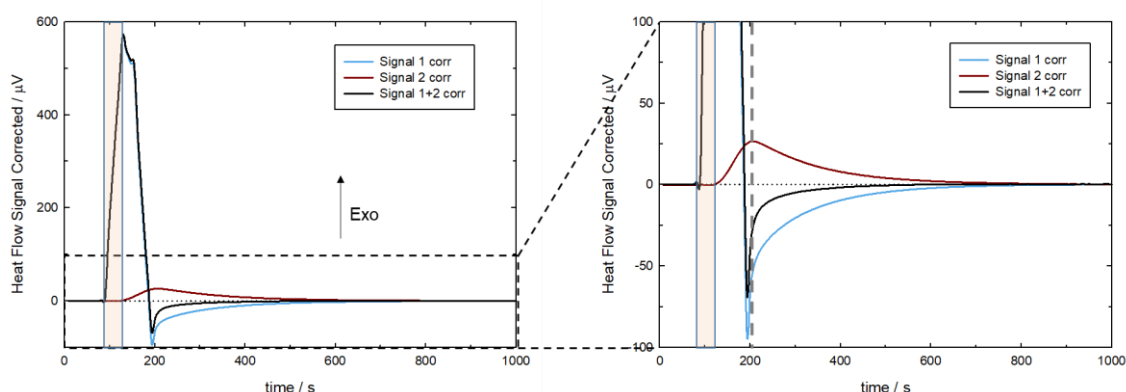


Figure A.7. Graphical representation of the calorimetric output “signal 1”, “signal 2” and its sum “signal 1+2” corrected to the calorimeter time constant. On the left side is represented the corrected output calorimetric data originated by thermal energy release during 40 s, by joule effect, in heaters incorporated inside the aluminium blocks that surround the mixing area; on the right, it is presented a magnification of the of the corrected output signal close to the baseline.

From the analysis of figure A.7 is evident that the correction with one time constant is not enough to correct the calorimetric output data “signal 1” and “signal 2” to the instantaneous thermal power originated by the process. When the signal resultant from the sum of the two signals “signal 1+2” returns to the baseline (Heat Flow Signal Corrected = 0 μV), the heat flow “signal 1” is negative, whereas the heat flow “signal 2”

is positive and symmetric in relation to the time axis. This fact reflects the heat exchanged through the glass micromixer, from the mixing area, where the thermal energy was released to the opposite area of the glass mixer. As “signal 1+2” is obtained from the sum of the calorimetric output “signal 1” and “signal 2”, and one side is releasing energy to the other side, the sum of the signals cancel this heat exchange. Therefore, to correct the calorimetric output “signal 1 + 2”, one time constant is enough, describing the thermal inertia related with the heat flow from the glass mixer to the heat sink.

Moreover, the sum of the “signal 1” to the “signal 2”, originating “signal 1+2” and posterior correction to the thermal inertia of the calorimeter, originating “signal 1+2 corr” is equivalent to the individual correction of “signal 1” and “signal 2” to “signal 1 corr” and “signal 2 corr” followed by its sum, originating “signal 1 corr + signal 2 corr”. In both methodologies the obtained signals will be equivalent as can be seen in figure A.8.

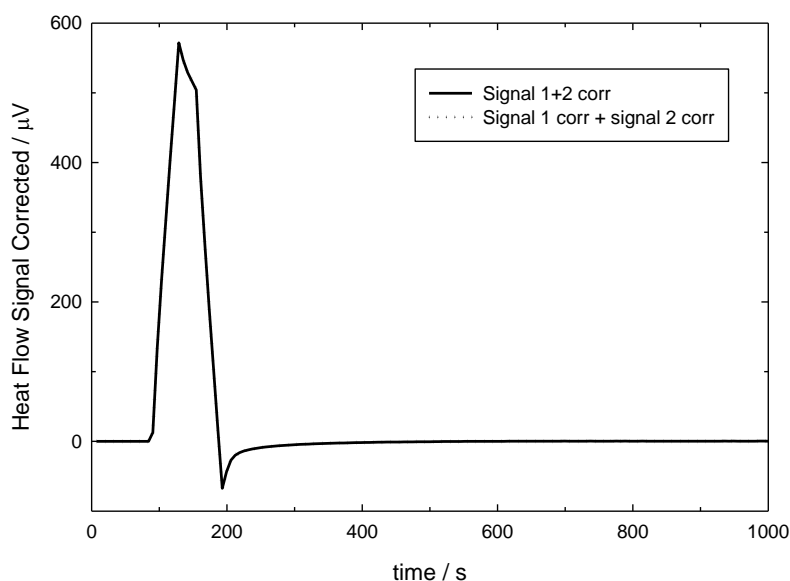


Figure A.8. Graphical representation of the calorimetric output “signal 1+2” corrected to the thermal inertia of the calorimeter using two different methods.

Appendix B

B.1. Data Acquisition Software of μ FlowCal Calorimeter

The acquisition of the calorimetric output data “signal 1” and “signal 2” is made in a software developed in HPVVEE, a visual programming language of Keysight. The software was developed specifically to perform the acquisition of the μ FlowCal calorimetric output signal, allowing real time visualization of the heat flow signal and logging the acquired data for posterior treatment. In figure B.1 is presented a block diagram which summarizes the software operation that could be described as follows:

Data acquisition

The software performs data acquisition from a nanovoltmeter of two channels of 7 ½ Digit (Agilent/Keysight 34420A), which is connected to the computer via RS232. When initiated, the software starts a timer and programs the nanovoltmeter to remote mode (“SYSTEM:REMOTE”), so it can be controlled by the software and resets the device to factory preset state (“*RST”). Then, the software configures the device to measure voltage in channel 1 with 20 NPLC (“SENS1:VOLT:DC:NPLC 20”), waits 1 second and configures the device to measure voltage in channel 2 with 20 NPLC (“SENS2:VOLT:DC:NPLC 20”). NPLC is the number of power line cycles performed to measure a single value. Higher NPLC values, decrease the instrumental noise of the readings and increase the accuracy of the voltage measurement. However, high NPLC values decrease the measurement speed and the time resolution of the calorimetric signal.

After setting the nanovoltmeter, the software selects the “channel 1” (“ROUT:TERM FRONT1”), waits 0.1 seconds and reads the value existent in the “channel 1” (“READ”). After, the software selects the “channel 2”, waits 0.1 seconds and reads the existent value in “channel 2”. Reading the signal in the channel 1 and in the channel 2 constitutes a cycle which is repeated at each 6 seconds.

Each time the channel 1 is read by the software, the software consults the timer initiated in the “start moment” and associates an experimental time in seconds to the voltage readings.

Real Time Calculations

The thermoelectric potential read from the “channel 1” and “channel 2” of the nanovoltmeters, is acquired in voltage. Therefore, the first step is to convert the thermoelectric potential from voltage to microvoltage. Then, the thermoelectric potential read from “channel 1” and “channel 2” of the nanovoltmeters are summed, creating the “signal 1+2”. The three signals are visualized in real time, in a graphical representation, as a function of the experimental time, and are also logged in a window.

Despite of the visualization in real time of the calorimetric output signals “signal 1”, “signal 2” and “signal 1+2”, the software calculates also the derivatives of the signals and corrects them to the time constant of the calorimeter using equation A.13. The time constant considered in the calculations was 250 s and not 254 s, as it was found that it described better the exponential decay of the heat flow signal, in a normal calorimetric experiment.

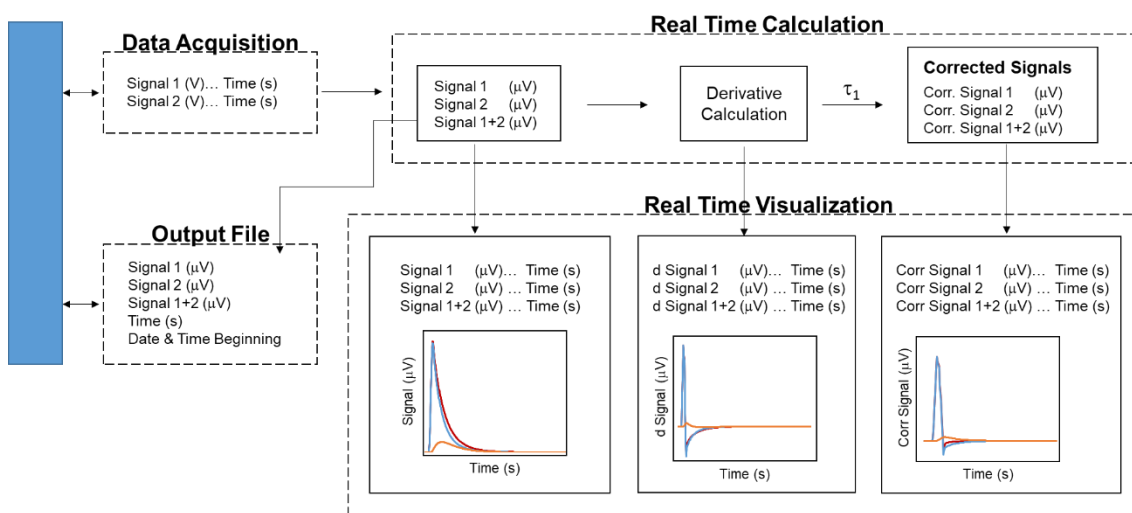


Figure B.1. Block diagram of the Data Acquisition Software, developed in HPVEE, to acquire, log and visualize in real-time the calorimetric output signals of μ FlowCal.

Real Time Visualization

During an experiment in μ FlowCal, the software shows in real time three graphical representations (picture of the front panel of the program in figure B.2). In the first one, the calorimetric output data “signal 1”, “signal 2” and “signal 1+2” are represented as a function of the experimental time. In the second one are presented, the previous signals,

corrected for the time constant of the calorimeter, allowing a visualization of the approximate thermokinetics of the process under study. In the third one, the derivative of the calorimetric output data “signal 1”, “signal 2” and “signal 1+2” is represented as a function of the experimental time. For detailed visualization, the zoom in and zoom out of the different regions of the graphical representations is possible, as well as, the use of markers to identify specific experimental points.

The individual values of the calorimeter thermoelectric potential read, as well as, its derivative and the correspondent time of measure are logged in windows, which the experimentalist can visualize in real time.

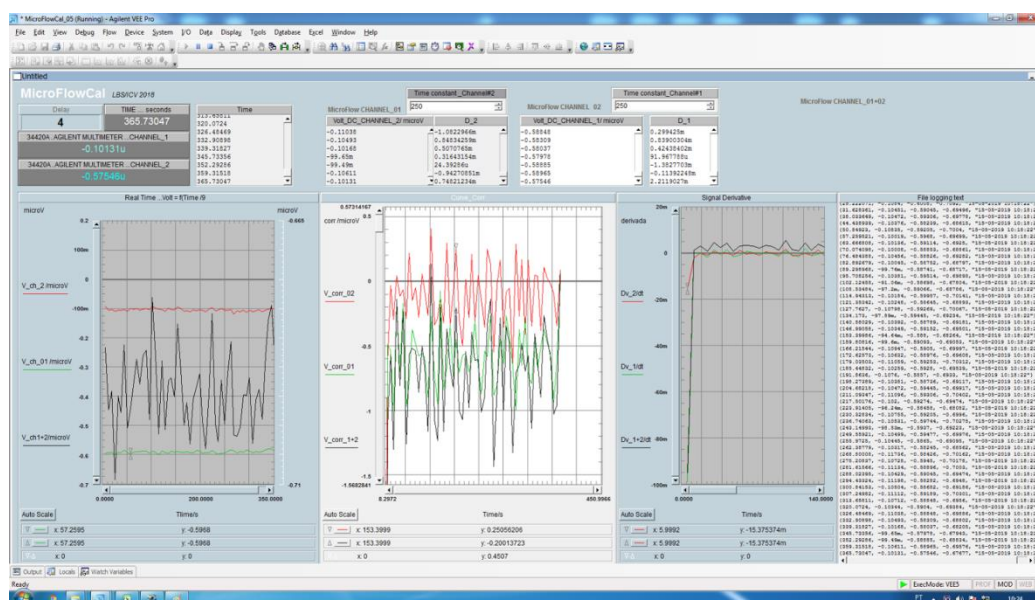


Figure B.2. Screenshot of the front panel of the Data Acquisition Software, developed in HPVee, to acquire, log and visualize in real-time the calorimetric output signals of μ FlowCal.

Output File

The software records the calorimetric output data “signal 1”, “signal 2” and “signal 1+2” in microvolts together with the experimental time in seconds and the date and time of the beginning of the experiment in a “.txt” file which allows the data to be read and analysed in commercial programs or in the Data Treatment Software developed for treating μ FlowCal data.

B.2. Data Treatment Software of μ FlowCal Calorimeter

In the context of this thesis a program was created in HPVEE to read the output files “.txt” created by the data acquisition software of the μ FlowCal. The data treatment software reads the output file of the data acquisition software, smooths the data, corrects the calorimetric output data “signal 1” and “signal 2” and “signal 1+2” to the time constant of the calorimeter, integrates each peak individually and registries the output of the individual integrations in a output “.intMFC” file. In figure B.3 is presented a block diagram which summarizes the software operation that could be described as follows:

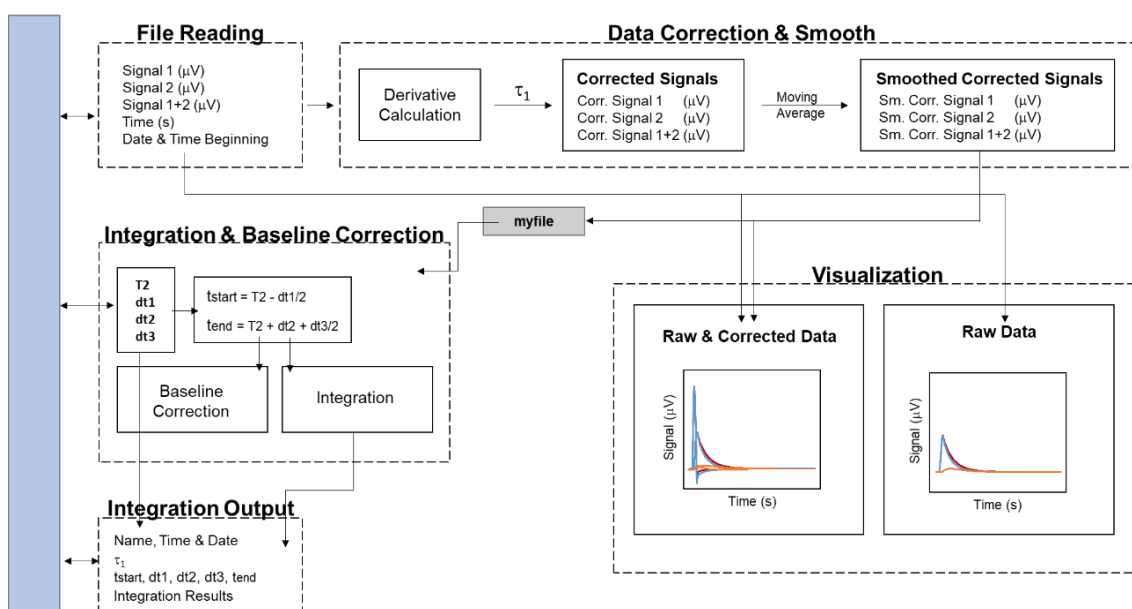


Figure B.3. Block diagram of the Data Treatment Software, developed in HPVEE, to integrate the peaks obtained in the experiments performed in μ FlowCal calorimeter.

File Reading

When initiated, the software reads and extracts the data of the “.txt” output file of the data acquisition software. The information on the time and date of the beginning of the experiment is stored and the “experimental time (s)”, the “signal 1 (μ V)”, the “signal 2 (μ V)” and the “signal 1+2 (μ V)” is transformed in 4 coordinates.

Data correction & Smooth

The software calculates the derivatives of the “signal 1” and “signal 2” using the correspondent coordinates and then calculates the “corrected signal 1” and the “corrected signal 2” using equation A.13. The time constant of the calorimeter used in the calculations can be modified by the user prior to data file upload. The “corrected signal 1” and the “corrected signal 2” is then summed originating “corrected signal 1+2”, which corresponds to a transformation of the raw data (calorimetric output data) into an approximation of the instantaneous thermal power generated by the process being investigated.

Due to the increase of the noise in the corrected signals caused by the multiplication of the derivative by the time constant, the corrected signals (“corrected signal 1”, “corrected signal 2” and “corrected signal 1+2”) were smoothed by application of a moving average of 10 experimental points.

The “corrected smoothed signal 1+2” and the correspondent experimental time is recorded in a temporary file (“myfile”).

Integration & Baseline Correction

The integration is made peak by peak, using the sum of the triangles method, within the limits of integration defined by the user. The user selects the point of the beginning of the integration (“T2”), the period that precedes the integration (“dt1”), the integration period (“dt2”), and the period after the integration (“dt3”).

The software will then use the triangles method to integrate the data existent in the temporary file (“myfile”) between the points correspondent to the interval between “T2-(dt1/2)” and “T2+dt2+(dt3/2)”, which are the integration limits.

The correction for the baseline is made from the defined limits of integration using three different methodologies:

B1 –Baseline defined as constant using the average of the signal that precede the integration interval (dt1);

B2 –Baseline defined as constant using the average of the signal that follow the integration interval (dt3);

B3 –Baseline is defined as the average of B1 and B2.

Visualization

In the front panel of the software (figure B.4), a graphical representation of the “signal 1”, “signal 2” and “signal 1+2” as a function of the “experimental time” is depicted, using the 4 coordinates extracted from the output file of the data acquisition software (raw data).

In one of these graphical representations is also shown the smoothed corrected data: “smoothed corrected signal 1”, “smoothed corrected signal 2” and “smoothed corrected signal 1+2” as a function of the “experimental time”. For detailed visualization, the zoom in and zoom out of the different regions of the graphical representations is available, as well as, the use of markers to identify specific experimental points.

The integration output, as well as the path and name of the file where the integration data is saved is also displayed in the front panel.

The interface of interaction with the user for integration of the peaks is also present at the front panel of the software.

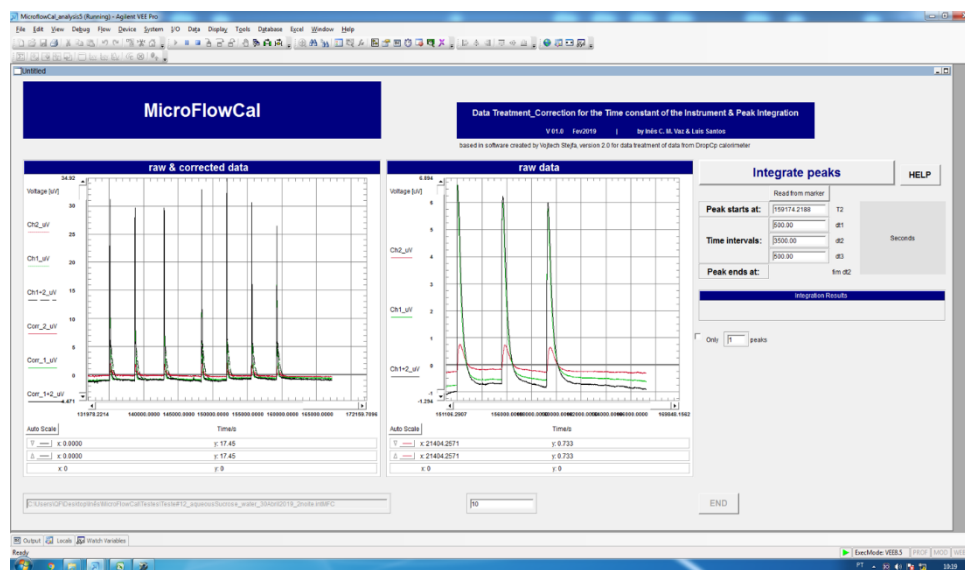


Figure B.4. Screenshot of the front panel of the Data Treatment Software, developed in HPVee, to integrate the peaks obtained in the calorimetric experiments performed in μ FlowCal.

Integration Output

An output file is created automatically when the program is initiated, with the same name of the raw data file and a different file name extension “.intMFC”. This output file is written in text mode file type.

In the output file is written, in a unique line, in the following order, the following information relative to the integration of each peak:

- the name of the input file,
- the time constant used to correct the data,
- the initial integration limit,
- dt1,
- dt2,
- dt3,
- the final limit of integration,
- the integration considering B1 baseline,
- the integration considering B2 baseline,
- the integration result considering B3 baseline.

B.3. Temperature Monitor Software of μ FlowCal Calorimeter

To monitor the thermostatzation of the calorimeter a software was created in HPVVEE. The software performs data acquisition from a data logger, allowing real time visualization of the temperature in the calorimeter, in the aluminium external box (calorimeter thermostat) and in the water / ethylene glycol thermostated bath. In figure B.5 is presented a block diagram, which summarizes the software operation, that consists in the following steps:

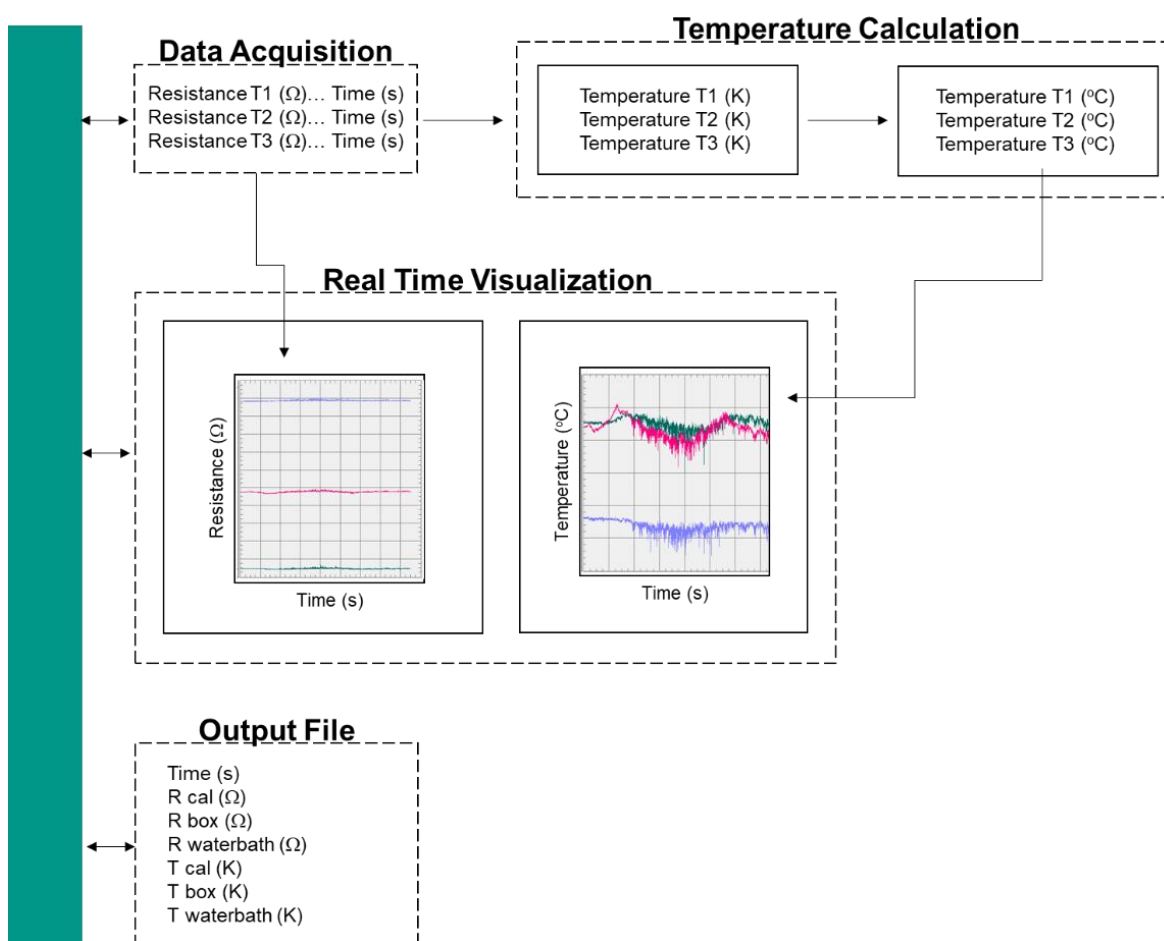


Figure B.5. Block diagram of the Temperature Monitor Software, developed in HPVVEE, to monitor the thermostatzation of the μ FlowCal.

Data Acquisition

The resistance of each thermistor is acquired from a data logger (Agilent, LXI Data acquisition 34972A) connected to the computer via TCP/IP.

When initiated, the software starts a timer and resets the data logger to factory preset state ("*RST"). Then, the software configures the device for 2-wire measurements of resistance in the "channel 218", "channel 219" and "channel 220" in the range of 10 k Ω with 0.01 Ω resolution ("CONF:RES 10000,0.01,(@218,219,220)") and 100 power line cycles, PLCs, ("SENS:RES:NPLC 100,(@218,219,220)").

After configuring the data logger, the software selects the "channel 218" ("ROUT:SCAN (@218)") and reads the existent value in the data logger memory ("READ?"). After, the software selects the "channel 219" ("ROUT:SCAN (@219)") and reads the existent value in the data logger memory ("READ?"), which is followed by the same procedure to read the resistance value in "channel 220". Reading the resistance signal in the three channels constitutes a cycle which is repeated at a period chosen by the user.

Every time this cycle is initiated, the software consults the timer initiated in the "start moment" and associates an experimental time in seconds to the resistance readings.

Temperature Calculation

The software converts the thermistor resistance measurements in temperature. The relation between the sensing temperature (K) and resistance (Ω) of the thermistor was determined by prior calibration of the thermistor used in the water / ethylene glycol thermostated bath, using precision thermometers in the range 293 to 313 K (20 to 40 $^{\circ}\text{C}$).

It was assumed that the resistance - temperature dependence was the same for all the three thermistors. After determining the sensing temperature (K), the software converts the temperature units from Kelvin (K) to Celsius ($^{\circ}\text{C}$). Despite the fact of the relation temperature - resistance being considered to be the same, an offset correction in order to anchoring the temperature readings at a fixed temperature.

Visualization

The front panel of the software (figure B.6) displays two graphical representations. The first graphical representation displays the resistance of the three thermistors as a function of the “experimental time”. The second graphical representation displays the sensing temperature in Celsius ($^{\circ}\text{C}$) of the three thermistors, in the thermostated bath, in the aluminium box and in the calorimeter, as a function of the “experimental time”. For detailed visualization, the zoom in and zoom out of the different regions of the graphical representations is possible, as well as, the use of markers to identify specific experimental points.

The last value acquired from the data logger, in the three channels is also displayed in the front panel of the software, as well as, the correspondent calculated temperature and the correspondent time of measurement.

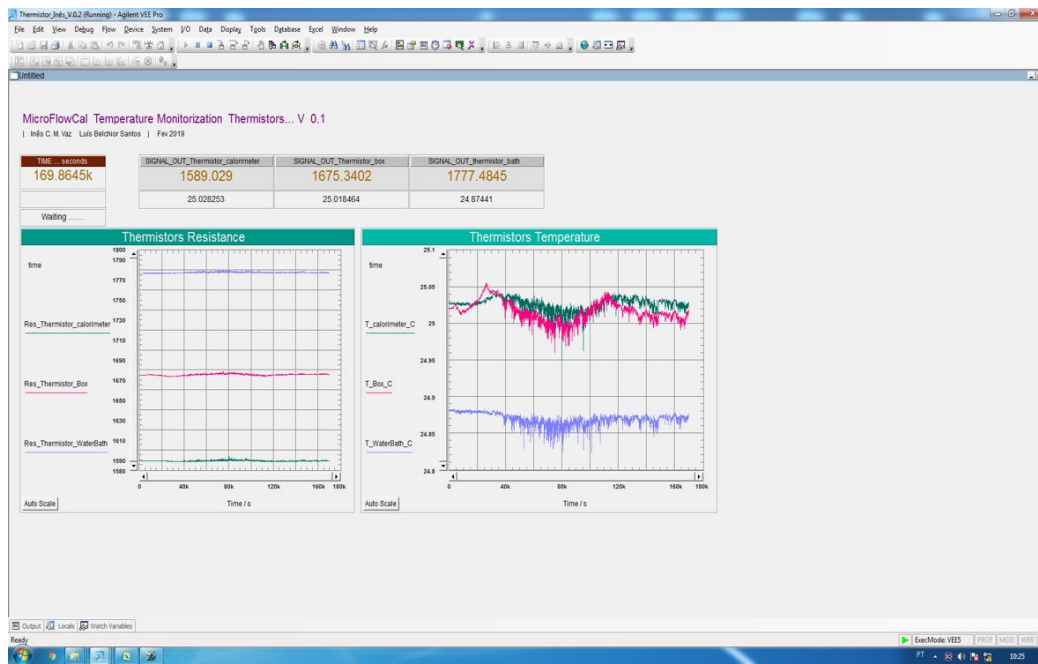


Figure B.6. Screenshot of the front panel of the Temperature Monitor Software, developed in HPVee, to monitor the thermostatzation of the $\mu\text{FlowCal}$.

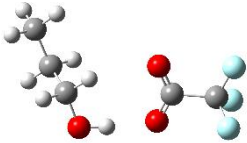
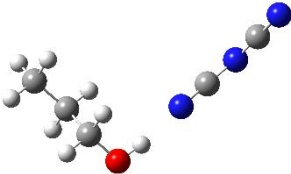
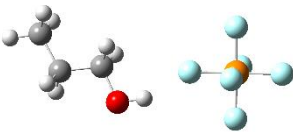
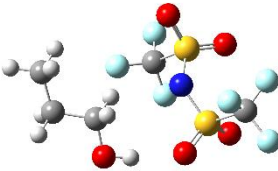
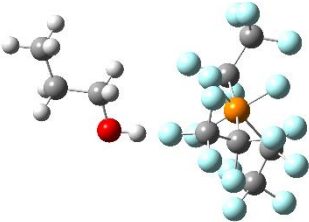
Output File

The software creates an output file when the program is initiated and writes in the first line of the file the actual date and time, followed by the description of what is going to be recorded in the file, in the respective order ("Time_s Rcal_ohm, Rbox_ohm, Rwaterbath_ohm, Tcal_C, Tbox_C, Twaterbath_C"). In the following lines the software records the experimental time together with the resistance of the three thermistors and the calculated sensing temperature. This output file is written in a text mode file, which allows the data to be read and analysed in commercial common programs like Origin or Excel.

Appendix C

C.1. Quantum Chemical Calculation of Propanol-Anion Interaction

Table C.1. Results of the quantum chemical calculations regarding the structure and orientation of the propanol-anion pair, as well as, the energy of interaction established in the gas phase

Anion	Structure / Orientation	$E_{\text{int}} / \text{kJ}\cdot\text{mol}^{-1}$
[TFA]		-62.90
[DCA]		-52.60
[PF ₆]		-30.24
[NTf ₂]		-28.03
[FAP]		-17.55

C.2. Quantum Chemical Calculation of Alcohol-[NTf₂] Interaction**Table C.2.** Results of the quantum chemical calculations regarding the structure and orientation of the BuOH-[NTf₂] pair (and BuOH derivatives), as well as, the energy of interaction established in the gas phase

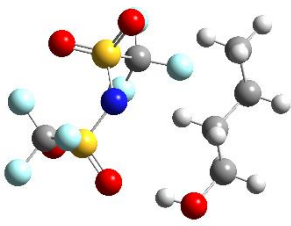
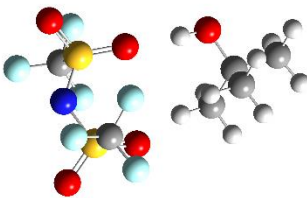
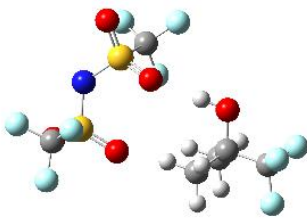
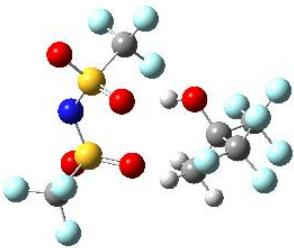
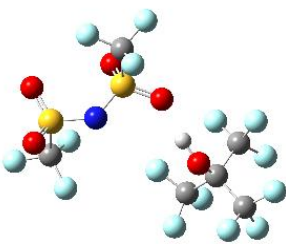

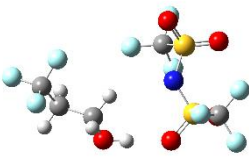
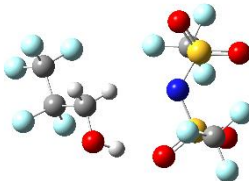
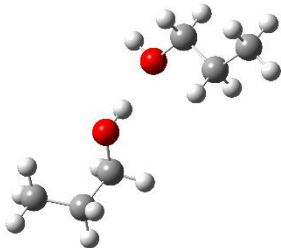
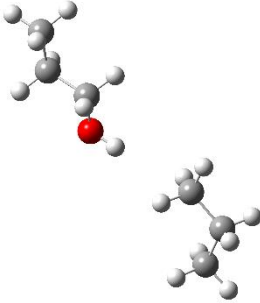
Alcohol	Structure / Orientation	$E_{\text{int}} / \text{kJ}\cdot\text{mol}^{-1}$
BuOH		-28.00
<i>t</i> -BuOH		-23.14
TF <i>t</i> -BuOH		-46.61
HF <i>t</i> -BuOH		-56.16
PF <i>t</i> -BuOH		-54.92

Table C.3. Results of the quantum chemical calculations regarding the structure and orientation of the PrOH-[NTf₂] pair (and PrOH derivatives), as well as, the energy of interaction established in the gas phase

Alcohol	Structure / Orientation	$E_{\text{int}} / \text{kJ}\cdot\text{mol}^{-1}$
PrOH		-28.03
TFPrOH		-42.46
PFPrOH		-60.81

C.3. Quantum Chemical Calculation of Alcohol-Alcohol and Alcohol-Alkane Interaction

Table C.4. Results of the quantum chemical calculations regarding the structure and orientation of the propanol-propanol and propanol – propane, as well as, the energy of interaction established in the gas phase

Molecule	Structure / Orientation	$E_{\text{int}} / \text{kJ}\cdot\text{mol}^{-1}$
propanol		-18.46
propane		-0.68

Appendix D

D.1. Redlich-Kister Fittings of the Mixture BuOH and [C₆C₁im][NTf₂]

Excess molar enthalpy of mixing of the binary mixture BuOH + [C₆C₁im][NTf₂] was obtained in μ FlowCal, at 298.15 K, in the molar fraction interval $0.16 < x_{\text{BuOH}} < 0.95$. In figure D.1, all the experimental data obtained is graphically represented, as well as, the correspondent average, at each concentration measured, with the correspondent confidence intervals at a confidence level of 95 % ($\pm 2\sigma$).

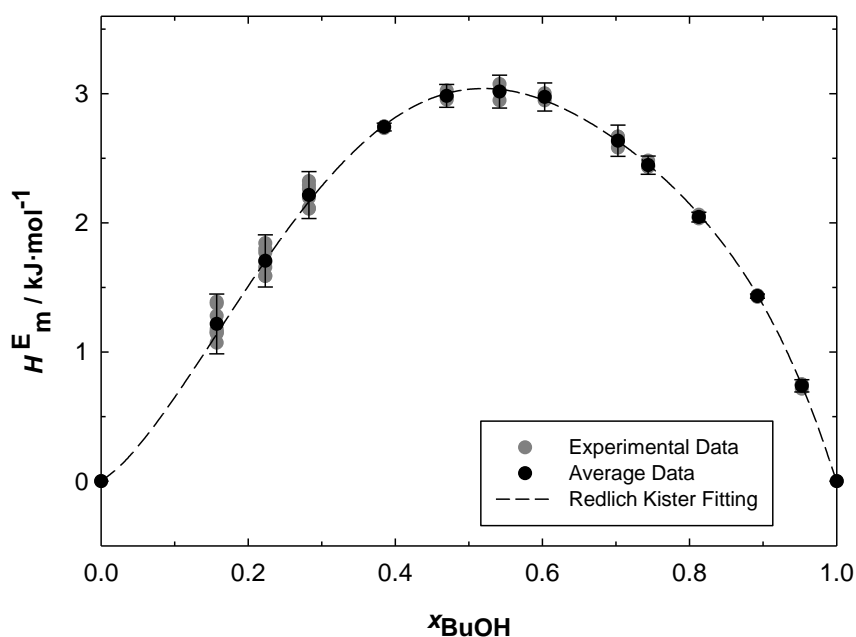


Figure D.1. Graphical representation of the excess molar enthalpy of mixing of the binary mixture BuOH + [C₆C₁im][NTf₂], determined experimentally in this work using μ FlowCal, at the reference temperature ($T = 298.15$ K), as a function of the molar fraction of 1-butanol in [C₆C₁im][NTf₂].

The data obtained was fitted using the Redlich-Kister equation. Given the dispersion of the calorimetric results verified at some concentrations, all experimental data was used in the fitting, and not only the average data. Data concerning the fitting is now presented.

Fitting with two parameters:**Table D.1.** Summary of the parameters used in the fitting of the experimental data with the Redlich-Kister equation using two parameters

	A_0	A_1
$A_k/\text{kJ}\cdot\text{mol}^{-1}$	11.890	3.585
$\sigma/\text{kJ}\cdot\text{mol}^{-1}$	0.096	0.175
R^2	0.890	

Table D.2. Comparison of the excess molar enthalpy obtained with the fitting of the experimental data with the Redlich-Kister equation using two parameters

x_{BuOH}	$H_{\text{m, exp}}^E / \text{kJ} \cdot \text{mol}^{-1}$	$H_{\text{m, fit}}^E / \text{kJ} \cdot \text{mol}^{-1}$	Rel Dev / %
0.1572	1.22	1.25	2.57
0.2233	1.71	1.72	0.72
0.2826	2.22	2.09	-5.47
0.3848	2.74	2.62	-4.47
0.4698	2.98	2.91	-2.53
0.5416	3.02	3.03	0.32
0.6031	2.97	3.02	1.61
0.7027	2.64	2.79	5.76
0.7436	2.45	2.60	6.24
0.8125	2.04	2.15	5.27
0.8921	1.43	1.42	-1.29
0.9526	0.74	0.68	-7.55
Average of Absolute Values			3.65

Fitting with three parameters:

Table D.3. Summary of the parameters used in the fitting of the experimental data with the Redlich-Kister equation using three parameters

	A_0	A_1	A_2
$A_k/\text{kJ}\cdot\text{mol}^{-1}$	11.677	3.493	0.709
$\sigma/\text{kJ}\cdot\text{mol}^{-1}$	0.160	0.181	0.429
R^2	0.895		

Table D.4. Comparison of the excess molar enthalpy obtained with the fitting of the experimental data with the Redlich-Kister equation using three parameters

x_{BuOH}	$H_{\text{m, exp}}^E / \text{kJ} \cdot \text{mol}^{-1}$	$H_{\text{m, fit}}^E / \text{kJ} \cdot \text{mol}^{-1}$	Rel Dev / %
0.1572	1.22	1.27	4.57
0.2233	1.71	1.73	1.28
0.2826	2.22	2.09	-5.82
0.3848	2.74	2.58	-5.80
0.4698	2.98	2.86	-4.23
0.5416	3.02	2.97	-1.45
0.6031	2.97	2.97	0.00
0.7027	2.64	2.76	4.71
0.7436	2.45	2.58	5.55
0.8125	2.04	2.15	5.33
0.8921	1.43	1.43	-0.27
0.9526	0.74	0.70	-5.80
Average of Absolute Values			3.73

Fitting with four parameters:**Table D.5.** Summary of the parameters used in the fitting of the experimental data with the Redlich-Kister equation using four parameters

	A_0	A_1	A_2	A_3
$A_k/\text{kJ}\cdot\text{mol}^{-1}$	11.965	1.103	-0.909	5.443
$\sigma/\text{kJ}\cdot\text{mol}^{-1}$	0.111	0.316	0.346	0.666
R^2	0.955			

Table D.6. Comparison of the excess molar enthalpy obtained with the fitting of the experimental data with the Redlich-Kister equation using four parameters

x_{BuOH}	$H_{\text{m, exp}}^{\text{E}} / \text{kJ} \cdot \text{mol}^{-1}$	$H_{\text{m, fit}}^{\text{E}} / \text{kJ} \cdot \text{mol}^{-1}$	Rel Dev / %
0.1572	1.22	1.20	-1.84
0.2233	1.71	1.76	3.23
0.2826	2.22	2.20	-0.57
0.3848	2.74	2.75	0.12
0.4698	2.98	2.96	-0.69
0.5416	3.02	2.99	-0.79
0.6031	2.97	2.92	-1.83
0.7027	2.64	2.64	0.07
0.7436	2.45	2.46	0.63
0.8125	2.04	2.08	1.53
0.8921	1.43	1.43	0.02
0.9526	0.74	0.73	-0.70
Average of Absolute Values			1.00

Fitting with five parameters:

Table D.7. Summary of the parameters used in the fitting of the experimental data with the Redlich-Kister equation using five parameters

	A_0	A_1	A_2	A_3	A_4
$A_k/\text{kJ}\cdot\text{mol}^{-1}$	12.112	1.448	-2.671	4.291	2.970
$\sigma/\text{kJ}\cdot\text{mol}^{-1}$	0.133	0.356	0.980	0.885	1.552
R^2	0.958				

Table D.8. Comparison of the excess molar enthalpy obtained with the fitting of the experimental data with the Redlich-Kister equation using five parameters

x_{BuOH}	$H_{\text{m, exp}}^{\text{E}}/\text{kJ}\cdot\text{mol}^{-1}$	$H_{\text{m, fit}}^{\text{E}}/\text{kJ}\cdot\text{mol}^{-1}$	Rel Dev / %
0.1572	1.22	1.21	-0.64
0.2233	1.71	1.74	2.12
0.2826	2.22	2.18	-1.81
0.3848	2.74	2.74	0.09
0.4698	2.98	2.99	0.32
0.5416	3.02	3.03	0.55
0.6031	2.97	2.95	-0.71
0.7027	2.64	2.64	0.08
0.7436	2.45	2.45	0.09
0.8125	2.04	2.05	0.38
0.8921	1.43	1.42	-0.65
0.9526	0.74	0.74	0.24
Average of Absolute Values			0.64

Fitting with six parameters:**Table D.9.** Summary of the parameters used in the fitting of the experimental data with the Redlich-Kister equation using six parameters

	A_0	A_1	A_2	A_3	A_4	A_5
$A_k/\text{kJ}\cdot\text{mol}^{-1}$	12.138	1.182	-3.116	5.947	3.952	-2.218
$\sigma/\text{kJ}\cdot\text{mol}^{-1}$	0.142	0.605	1.281	3.167	2.386	4.069
R^2	0.959					

Table D.10. Comparison of the excess molar enthalpy obtained with the fitting of the experimental data with the Redlich-Kister equation using six parameters

x_{BuOH}	$H_{\text{m, exp}}^{\text{E}}/\text{kJ}\cdot\text{mol}^{-1}$	$H_{\text{m, fit}}^{\text{E}}/\text{kJ}\cdot\text{mol}^{-1}$	Rel Dev / %
0.1572	1.22	1.21	-0.44
0.2233	1.71	1.74	1.75
0.2826	2.22	2.17	-1.89
0.3848	2.74	2.76	0.51
0.4698	2.98	3.00	0.65
0.5416	3.02	3.03	0.57
0.6031	2.97	2.95	-0.97
0.7027	2.64	2.63	-0.26
0.7436	2.45	2.45	-0.08
0.8125	2.04	2.06	0.60
0.8921	1.43	1.43	-0.26
0.9526	0.74	0.74	0.01
Average of Absolute Values			0.67

Fitting with seven parameters:**Table D.11.** Summary of the parameters used in the fitting of the experimental data with the Redlich-Kister equation using seven parameters

	A_0	A_1	A_2	A_3	A_4	A_5	A_6
$A_k/\text{kJ}\cdot\text{mol}^{-1}$	12.112	0.873	-2.188	8.309	-0.564	-5.933	5.651
$\sigma/\text{kJ}\cdot\text{mol}^{-1}$	0.152	0.846	2.181	5.494	8.884	8.144	10.701
R^2	0.959						

Table D.12. Comparison of the excess molar enthalpy obtained with the fitting of the experimental data with the Redlich-Kister equation using seven parameters

x_{BuOH}	$H_{\text{m, exp}}^{\text{E}} / \text{kJ} \cdot \text{mol}^{-1}$	$H_{\text{m, fit}}^{\text{E}} / \text{kJ} \cdot \text{mol}^{-1}$	Rel Dev / %
0.1572	1.22	1.21	-0.30
0.2233	1.71	1.73	1.34
0.2826	2.22	2.18	-1.67
0.3848	2.74	2.77	0.98
0.4698	2.98	3.00	0.61
0.5416	3.02	3.02	0.20
0.6031	2.97	2.94	-1.29
0.7027	2.64	2.63	-0.10
0.7436	2.45	2.45	0.19
0.8125	2.04	2.06	0.70
0.8921	1.43	1.42	-0.63
0.9526	0.74	0.74	0.16
Average of Absolute Values			0.68

Evaluation of the Best Fitting:

To evaluate the quality of the fitting and chose the appropriate number of parameters, the excess molar enthalpy of mixing obtained experimentally was graphically represented, in figure D.2, together with its fitting with Redlich-Kister equations with 2 to 7 parameters (“ A_k ”). From the analysis of this figure, is visible that the utilization of 2 and 3 parameters in the fitting is not enough to capture the correct curvature of the experimental values. In average, these fittings deviate from the experimental values 3.65 % (2 Parameters) and 3.73 % (3 Parameters).

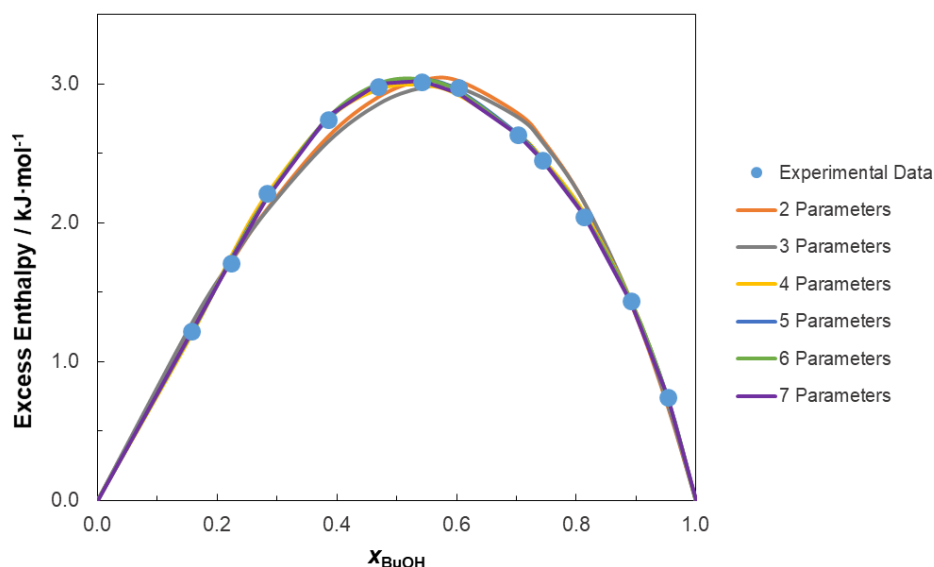


Figure D.2. Graphical representation of the excess molar enthalpy of mixing of the binary mixture BuOH + [C₆C₁im][NTf₂], determined experimentally in this work using μ FlowCal, at the reference temperature ($T = 298.15$ K), as a function of the molar fraction of 1-butanol in [C₆C₁im][NTf₂] and the fitting of the experimental data using the Redlich-Kister equation with 2 to 7 parameters.

In figure D.3 the relative deviation of the fitting towards the experimental data is presented. From the analysis of this representation, it stands out that the use of 2 and 3 parameters in the fitting is not enough to describe the experimental data, in agreement to what was already seen before. The utilization of 4 parameters seems to be enough to capture the main data behaviour. Nevertheless, the increase of the number parameters to 5 decreases the relative deviation towards the data and thus, fits better the experimental results. This was already evident in the reduction of the average deviation

from 1.00 % to 0.64 %, as summarized in tables D.6 and D.8. The further increase in the number of parameters does not seem to improve the fitting. Based only on these results, the number of parameters chosen would be 5.

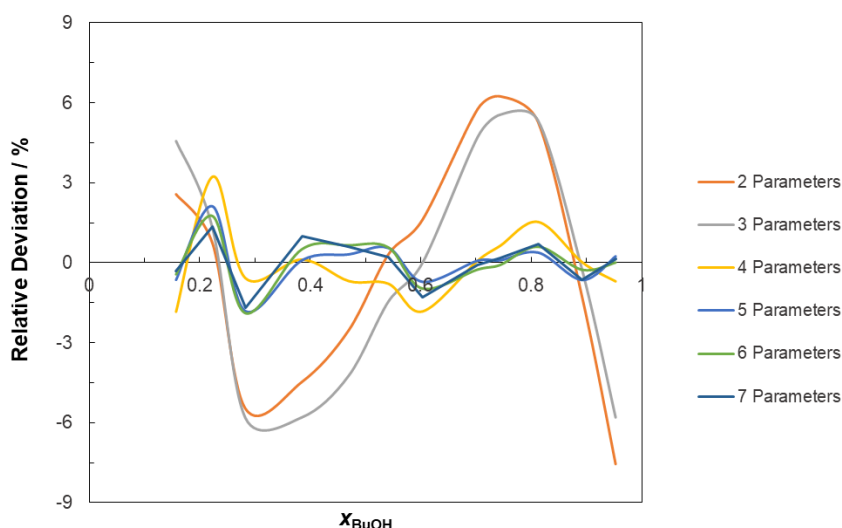


Figure D.3. Graphical representation of the relative deviation of the excess molar enthalpy of mixing, calculated using the Redlich-Kister equation with 2 to 7 parameters, to the experimental data obtained in μ FlowCal calorimeter.

To the selection of the appropriate number of parameters is important to choose a number of parameters that reproduces as close as possible the experimental data without introducing artefacts that do not correspond to the composition dependence of the enthalpy of mixing. In figure D.2, no artefact seems to be present independently of the number of parameters used in the fitting. To a better analysis, the partial molar excess enthalpy of both components of the mixture was generated using the derivative of the Redlich-Kister equation, as described in the Introduction.

In figure D.4 is represented the partial molar excess enthalpy of mixing of $[\text{C}_6\text{C}_{1\text{im}}][\text{NTf}_2]$ generated from the Redlich-Kister equation using 2 to 7 parameters as a function of the molar fraction of BuOH. The curve obtained from the generation of the property using 2 and 3 parameters is different from the others as the degree used in the equation was not enough to fully describe the concentration dependence of the property. Nevertheless, the utilization of 4 or more parameters does not seem to produce significant alterations in the partial molar excess enthalpy of mixing of $[\text{C}_6\text{C}_{1\text{im}}][\text{NTf}_2]$. No evidence of the presence of artefacts was found.

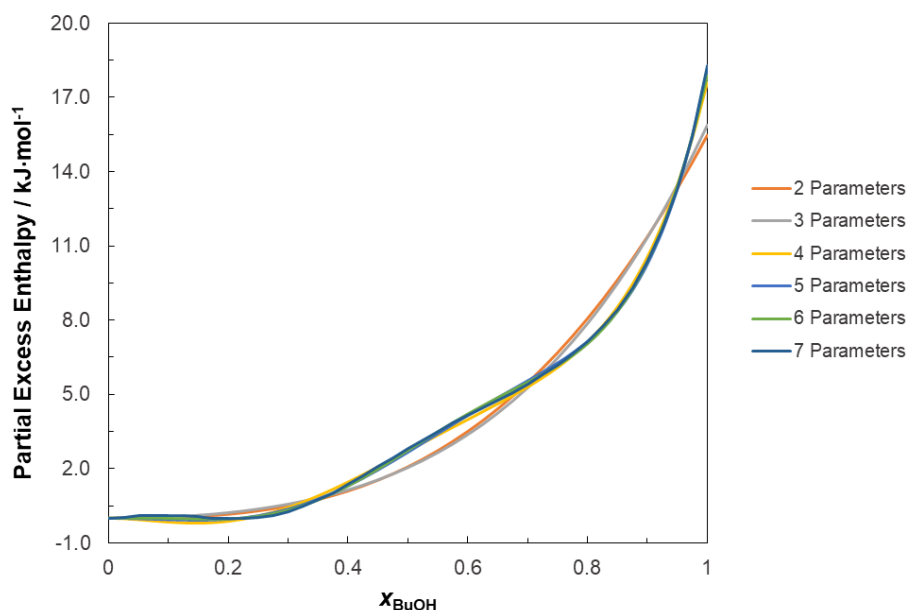


Figure D.4. Graphical representation of the partial molar excess enthalpy of mixing of $[\text{C}_6\text{C}_{1\text{im}}][\text{NTf}_2]$ calculated using the Redlich-Kister equation with 2 to 7 parameters.

In figure D.5 is represented the partial molar excess enthalpy of mixing of BuOH generated from the Redlich-Kister equation using 2 to 7 parameters as a function of its molar fraction. As before, the curves estimated from the derivative of the Redlich-Kister equation using 2 and 3 parameters were different from the ones with higher number of parameters, due to the lack of liberty degrees to describe correctly the concentration dependence. The curves generated from the derivative of the Redlich-Kister equation using 4 to 7 parameters display a similar concentration dependence to molar fractions superior to $x_{\text{BuOH}} > 0.22$. At low concentration of alcohol, each curve presents a different behaviour. The higher dispersion of the calorimetric results in this area, together with the relative high “distance” to the infinite dilution (lowest concentrations tested were $x_{\text{BuOH}} = 0.16$; $x_{\text{BuOH}} = 0.22$) may explain the difficulty of the equations to capture the real concentration dependence on this area.

To facilitate the task of the analysis of this area, the partial molar excess enthalpy of mixing of BuOH reported by Costa Gomes et al.^[3] and Heintz et al.^[4] were also represented in figure D.5, as well as, the enthalpy of solution at infinite dilution determined by ITC.

The curves generated with two and three parameters are in accordance with these data. The use of four parameters is hardly correct, as the partial enthalpy is decreasing with the decrease in alcohol content. Moreover, the excess enthalpy calculated using

four parameters presents a deviation of - 1.84 % and + 3.23% towards the average of the calorimetric results at the concentrations $x_{\text{BuOH}} = 0.16$; $x_{\text{BuOH}} = 0.22$.

The utilization of five parameters decrease these deviations to - 0.64 % and + 2.12 %. Nevertheless, the behaviour of the partial molar excess enthalpy is still the opposite of what is reported in the literature. It was considered that the utilization of six parameters was more adequate. The deviations of the calculated excess enthalpy are - 0.44 % and + 1.75 %. Furthermore, the curve of the partial molar excess enthalpy seems rather well behaved (without great changes in the concavity of the curves which could be associated to artefacts of the fitting) and seems to increase close to the infinite dilution, as described in the literature. Since, for higher concentrations, no significant difference was found towards the curves obtained with four or five parameters and that it seems the option to describe the low concentration in BuOH area, the number of parameters chosen was 6. Nonetheless, a higher uncertainty on the low concentration of alcohol area, should be considered. This higher uncertainty was indicated by the orange shaded area represented in D.5.

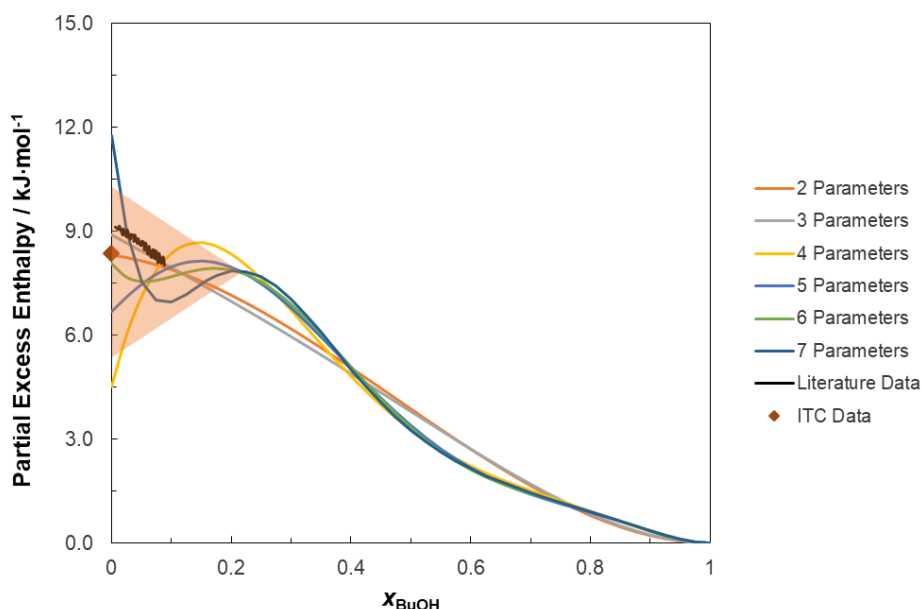


Figure D.5. Graphical representation of the partial molar excess enthalpy of mixing of BuOH calculated using the Redlich-Kister equation with 2 to 7 parameters. The partial molar excess enthalpy of mixing of BuOH reported by Costa Gomes et al.[3] and Heintz et al.[4] was also represented, as well as, the standard molar enthalpy of solution, at infinite dilution of BuOH, determined by ITC.

Appendix E

E.1. Cost Evaluation of μ FlowCal Calorimeter Prototype

Table E.1. Summary of the cost of the instrumentation

Material	Brand	Cost / euros
Nanovoltmeter (5 ½ Digit, Fluke 45)	Fluke	500
Data logger (Agilent, LXI Data acquisition 34972A)	Agilent	2 000
Nanovoltmeter (7 ½ Digit, Agilent/Keysight 34420A)	Agilent	4 500
Offline UPS		1 000
Timer Omron (H5CX-A-N) & Box	Omron	200
PC + monitor to data acquisition & system control		800
SUM Instrumentation		9 000

Table E.2. Summary of the cost of the materials used in the injection system

Material	Comment	Brand - Supplier	Cost / euros
4 x Syringe 5mL	Injection System	SETonic - Cetoni	310
4 x Syringe 2.5mL	Injection System	SETonic - Cetoni	310
Interconnect Cable	Injection System	Cetoni - Cetoni	200
2 x Syringe pump (CETONI, model low pressure pump neMESYS 290N)	Injection System	Cetoni - Cetoni	6 400
Nemesys Power & Communication Module	Injection System	Cetoni - Cetoni	2 000
10 Flasks 10 mL w/ GL25 screw cap		Schott - Schmidt-Stosberg	90
10 Flasks 25 mL w/ GL25 screw cap		Schott - Schmidt-Stosberg	70
4 x screw cap GL25 with three ports		Schott - Schmidt-Stosberg	190
10 x SEAL PTFE protected GL25		Schott - Schmidt-Stosberg	10
10 screw caps GL25		Schott - Schmidt-Stosberg	20
SUM Injection			9 600

Table E.3. Summary of the cost of the materials and parts used in the construction

Material	Brand - Supplier	Cost / euros
Clean-cut polymeric tubing cutter	VICI- Paralab	40
Tubing PTFE, L = 10 m, OD = 1/16", ID = 0.030"/0.75mm	VICI- Paralab	100
8 metallic unions 1/4"-28 to 10-32, for 1/16" OD tubing, 0.75mm bore	VICI- Paralab	680
2 x pkg 12, nuts w/ferrule CTFE 1/4"-28 for OD = 1/16" tubing	VICI- Paralab	100
8 Peltier Sensors (Laird, model HT4-6-F2-2143)	Laird - Digikey	500
4 x stainless steel tubing, L = 20 cm, OD = 1/16, ID = 0.030"/0.75mm	Sigma Aldrich	500
3 x Cheminert plug 1/4-28, pkg of 5, CTFE	VICI- Paralab	210
2 x Tampa Cheminert 1/4-28, CTFE	VICI- Paralab	260
5 x T Connection Cheminert 1/4-28, 0.75mm bore, CTFE	VICI- Paralab	330
pkg 12, nuts CTFE 1/4"-28 for OD = 1/16" tubing	VICI- Paralab	80
pkg 10, Cheminert ferrule collapsible, for tubing 1/16" OD	VICI- Paralab	60
Cheminert union 1/4-28, for tubing OD = 1/16", ID = 0.75 mm	VICI- Paralab	40
Tubing PTFE, OD = 1/16 ", ID = 0.030 " / 0.75 mm, L = 10 m	VICI- Paralab	130
5 x Cheminert union 1/4-28, 0.75mm bore, CTFE	VICI- Paralab	200
Aluminium Blocks (Material + Machining)	Lanema	1 200
PE tubing, OD = 4 cm	Termodinâmico	50
Diverse (connections for gas and liquid flow systems)	Termodinâmico	500
Workshop materials (copper, tubing...)		200
SUM Construction Materials		5 180

Table E.4. Summary of the cost of the parts and instrumentation used in the temperature control

Material	Brand - Supplier	Cost / euros
Flow Pump EHEIM universal 2400	EHEIM-hidraulicart	270
Cold source, Thermostatization Bath (Julabo F25)	Julabo	3 000
3 Thermistors (2 k Ω @20 °C, reference GL23, RS-stock No 151-029, glass bead type)	RS	100
Thermostatization Bath	Prototype	2 000
PID temperature controller (Fuji, model PXR4)	Fuji	100
Cartridge Resistance of 50 W		50
Air-to-Air Thermoelectric Assembly (Laird, Part Number AA-034-12-22-00-00)	Laird - Digikey	400
SUM Temperature Control		5 920

Table E.5. Summary of the cost of workforce involved in the design, construction and test

Working Force	Months	Cost / euros
Inês C. M. Vaz	24	24 000
Luís M. N. B. F. Santos	6	24 000
Workshop	1	2 000
SUM Workforce		50 000

Table E.6. Summary of the cost of the development of the μ FlowCal calorimeter prototype

Different Elements	Cost / euros
Instrumentation	9 000
Injection	9 600
Construction Materials	5 180
Temperature Control	5 920
Workforce	50 000
SUM	79 700

References:

- [1] F. P. Incropera and D. P. DeWitt, Introduction to Heat Transfer, 3rd, John Wiley & Sons, **1996**. ISBN:0-471-30458-1.
- [2] Randzio and Suurkuusk, - Interpretation of calorimetric thermograms and their dynamic corrections, Biological Microcalorimetry, Academic Press, London, **1980**, p. 311-341.
- [3] Y. Deng, P. Husson, J. Jacquemin, T. G. A. Youngs, V. L. Kett, C. Hardacre and M. F. Costa Gomes, Volumetric Properties and Enthalpies of Solution of Alcohols $C_kH_{2k+1}OH$ ($k=1, 2, 6$) in 1-Methyl-3-alkylimidazolium Bis(trifluoromethylsulfonyl)imide $\{[C_1C_nIm][NTf_2] \ n=2, 4, 6, 8, 10\}$ Ionic Liquids, *The Journal of Chemical Thermodynamics*, 43 (**2011**) p. 1708-1718. DOI:10.1016/j.jct.2011.05.033.
- [4] A. Heintz, S. P. Verevkin, J. K. Lehmann, T. V. Vasiltsova and D. Ondo, Activity Coefficients at Infinite Dilution and Enthalpies of Solution of Methanol, 1-Butanol, and 1-Hexanol in 1-Hexyl-3-methyl-imidazolium Bis(trifluoromethylsulfonyl)imide, *The Journal of Chemical Thermodynamics*, 39 (**2007**) p. 268-274. DOI:10.1016/j.jct.2006.07.006.